The Solidification of Niobium Silicides for Next Generation Gas Turbine Engines

CONOR MCCAUGHEY

Panos Tsakiropoulos & Russell Goodall

2016

Department of Materials Science and Engineering
University of Sheffield

ABSTRACT

The thesis is an experimental study of two near eutectic alloys Nb-8.3Ti-21.1Si-5.4Mo-4W-0.7Hf at. % (CM1) and Nb-20.5Si-5.8W-4Hf at. % (CM2) in the cast and heat treated (1500 ^{O}C/100 hrs) conditions. The alloys were in the form of 10 g button ingots, 6 mm and 8 mm suction cast bars and OFZ bars grown at 12, 60 and 150 mm/h using feed materials from 600 g (CM1) g and 500 g (CM2) ingots. In addition to stable OFZ growth, the non-stable growth of the alloy CM2 at the beginning and end of the OFZ process was also studied. The thesis starts with a brief review of relevant literature on Nb silicide based alloys and solidification followed by the experimental techniques used in this research.

The main aim of this study was to determine how the solidified microstructure varies due to changes in the solidification conditions (cooling rate, growth rate etc.) and concentrations of elements. Overall there was an aim to gain a better understanding of how an "ideal" microstructure (columnar eutectic aligned to the direction of force) could be gained in a multi-element niobium silicide based alloy using OFZ furnaces by varying the processing parameters. This "ideal" microstructure has a similar form to columnar NBSA (pre-single crystal blades) to reduce the effect of creep but with alternating phasing of Nb_{ss} and Nb_5Si_3 to create an improvement in the overall mechanical properties of the component. This aim was not realised and the conditions necessary to form an idealised structure could not be found

The range of solidification conditions employed in this research allowed us to capture the formation of Nb_3Si and its eutectoid decomposition in both alloys and the β-$Nb_5Si_3 \rightarrow \alpha$-$Nb_5Si_3$ transformation. In all forms of the two cast alloys the Nb_{ss}, Nb_5Si_3 and their eutectic with/out Nb_{ss} haloes were observed. The cast microstructures were dependent on cooling rate and/or solute additions. Anomalous eutectics were observed near the water cooled copper crucible walls and were attributed to de-coupled growth of the eutectic phases. The heat treated microstructures of both alloys in all studied forms had coarsened and only the Nb_{ss} and α-Nb_5Si_3 were present.

Formation of Nb_3Si and its eutectoid decomposition were observed in suction cast and OFZ grown bars of both alloys. The former respectively in the 8 mm and 6 and 8 mm suction cast bars of the alloys

CM1 and CM2. In the CM1 600 g ingot and OFZ bars and in all forms of the cast alloy CM2 the β-$Nb_5Si_3 \rightarrow$ α-Nb_5Si_3 transformation had occurred during solid state cooling.

The OFZ microstructures of both alloys depended on twelve inter-related parameters (phenomena) processes, according to OFZ literature. In the OFZ CM1 there were differences in chemical composition between the edge and centre of the bar, the edge was richer in Si and poorer in Ti. There were also differences in chemical composition of the lamellar microstructures between edge and centre, in the edge they were poorer in Si and Ti. In the stable OFZ CM2, the average chemical composition was significantly different than that of the parent (feed) ingot, owing to strong Si segregation during OFZ. In the non-stable OFZ CM2 the Nb_{ss} and Nb_5Si_3 and their eutectic were formed and the Nb_3Si and its eutectoid decomposition were observed in areas of low Si content.

The refractory metals partitioned to the solid solution in both alloys in all their cast and heat treated forms and Nb_{ss} free of Si was formed after heat treatment in both alloys. Relationships between solutes in the Nb_{ss} were found for both alloys showing that Ti and Mo and W *did not like each other* in the Nb_{ss}. Bulky and high aspect ratio precipitates formed with some orientation relationship were observed in the heat treated Nb_{ss} in CM2 500 g ingot and in the cast and heat treated stable OFZ grown alloy CM2 at all three growth rates.

In the alloy CM1 subgrains were observed in the α-Nb_5Si_3. Their formation was attributed to the effect of Ti on the anisotropy of CTE of the 5-3 silicide. Light and dark contrast areas were formed in α-Nb_5Si_3 grains in all three growth rates in CM1 OFZ. In the former areas fine spherical or needle like precipitates of light contrast (like the Nb_{ss}) were observed in the same α-Nb_5Si_3 grain. No subgrains were observed in the α-Nb_5Si_3 in all forms of the cast and heat treated alloy CM2.

Precipitates in the α-Nb_5Si_3 exhibiting contrast similar to that of the Nb_{ss} were observed when the α-Nb_5Si_3 was present in the microstructures of all forms of the alloy CM1 and were attributed to the β-$Nb_5Si_3 \rightarrow Nb_{ss} + \alpha$-$Nb_5Si_3$ transformation. Precipitates exhibiting contrast similar to that of the Nb_{ss} were rarely observed in the α-Nb_5Si_3 and only in some of the heat treated microstructures of the alloy CM2, namely the 6 mm suction cast bar and the 500 g ingot.

The data for eutectic spacing in CM1 OFZ did not follow the Jackson-Hunt relationship $\lambda^2.V_{S/L}$ = constant but instead obeyed the relationship $\lambda^3.V_{S/L}$ = constant. In the suction cast bars similar trends in the variation of λ and V_f were observed in sections along the edge and centre of the bars. The trends were dependent on alloy and condition. Differences in trends were particularly noticeable when Nb_3Si and the fine Nb_{ss} and α-Nb_5Si_3 products of its eutectoid transformation were present in the microstructure.

Sections from this thesis were presented at “Beyond Nickel Based Superalloys” International Conference, Bayreuth, 2013 and the TMS international conference, San Diego, 2014.

ACKNOWLEDGMENTS

The author of this thesis would first and foremost like to acknowledge the Engineering and Physical Sciences Research Council (EPSRC) and Rolls Royce plc. for their financial assistance via the Advanced Metallic Systems Centre for Doctoral Training (CDT), without which this work would not have been possible. The author would also like to acknowledge Rolls Royce plc. in facilitating the use of SEMs at Intertek as well as the help offered by Dr Neil Dsouza and Dr Neil Jones throughout this research project. The help of Ms Amanda Lowe with the operation and booking of the SEM at Intertek also be acknowledged for her help in the operation and booking of the SEM used at Intertek is also gratefully acknowledged.

I would also like to gratefully acknowledge Professor S. Miura (Hokkaido University) and Dr H. Stone (University of Cambridge) for their permission to use the optical float zone solidification facilities at Hokkaido and Cambridge for this investigation. Finally, I would also like to acknowledge the help of all of the support staff and technicians within materials science and engineering department as well as those in the Sorby Centre at Sheffield University.

I would also like to acknowledge the help and direction of Professor Panos Tsakiropoulos throughout the research which has culminated in this thesis. The work involved was made substantially easier by his keen mind and friendly smile. The help that Panos offered during this time was reinforced by my peers in the ultra-high temperature alloys research group. In particular I am grateful to them and would like to acknowledge discussions on numerous ideas and theories and informal chats, most of which helped me with the structure of my work. Finally, I would like to acknowledge Dr Claire Hinchliffe, the Advanced Metallic Systems CDT Project Manager, for her help and guidance in advancing my career throughout my research.

On a more personal note I would like to acknowledge the help of people who have surrounded me all the way through this research and helped me remain sane during this time. My loving fiancé,

Laura, who I met at the very beginning of my research, supported me and helped me through some rough times, mainly during writing, and it is inconceivable to me that this thesis would have been finished without her. I am so grateful to my family who supported me throughout my work, even though for the majority of the time they had no idea what I was working on or talking about. Finally my friends that gave me a rest bite from my work and helped me laugh during times of stress, they deserve a special mention; Brett, Stu, Lesley, Ollie, Lizzi, Carl and Shaun, thank you.

TABLE OF CONTENTS

INTRODUCTION

Nickel based superalloys (NBSA) have been the industry standard for use in the high temperature and pressure areas of gas turbine engines for aerospace and energy production since the end of WWII (Bowman 2000). In recent years research on NBSA has been accompanied with research on refractory metal-silicon based systems for high temperature applications in turbine engines. This move has been fuelled by the necessity to create more efficient engines in the aerospace sector. In the early 1990's systems containing a refractory element and silicon became the front runners to replace NBSA. Initially Cr, Mo, W and Nb were all considered for experimentation. However, due to the superior properties of niobium based silicides, they soon became the front runner for high temperature alloy research.

A significant reason for switching to Nb silicide based alloys over NBSA is the reduction in density that can be achieved. Typical 3rd generation NBSA have densities of 8.8 to 9.1 g/cm^3 (Bewlay, Jackson, et al. 1999) while a typical Nb silicide based alloy has a density range of 6.6 to 7.2 g/cm^3 (Bewlay et al. 2003). This equates to not only a significant reduction in the weight of the turbine section but will also have a knock on effect on the weight of supporting structures of the engine, e.g. the central shaft; reduced centripetal forces as the weight of the blades is reduced. This therefore will increase the power to weight ratio of the engine increasing the efficiency. The second factor in increasing the efficiency of turbine engines is the increase in the liquidus temperature of Nb silicide based alloys over NBSA. Typically, NBSA have a liquidus temperature of ≈ 1350 ^{O}C which translates to being able to withstand a metal surface temperature of 1150^{O}C. This is believed to be the maximum temperature that components based on NBSA can withstand and therefore the ceiling for inlet temperatures for jet engines unless there is a significant advance in thermal barrier coatings. Niobium-silicon alloys, based around the eutectic point, have a liquidus temperature of ≈ 1920 ^{O}C (Okamoto 2005) and even with alloying additions to increase strength, ductility, oxidation resistance etc. a melting temperature

in excess of 1650 ^{O}C is retained. This increase in the liquidus temperature of these alloys has a substantial effect on the efficiency of the engine. Niobium based silicides within a turbine section could allow for increased entry temperature of the turbine section of 200 ^{O}C to around 1900^{O}C. This could allow for increases in the efficiency in two ways; the temperature of the inlet could remain constant compared with NBSA turbines but with reduced internal cooling in the blades. This allows less compressed air to bypass the combustion stage increasing the efficiency of the turbine section to convert energy. Or the engine could be run at a higher combustion temperature allowing the fuel to burn more efficiently.

This thesis will focus on near eutectic Nb-Si based alloys. Intermetallics are strictly ordered structures that form between two (or more) metallic elements. They normally have larger, more complex structures than usual metallic systems based on FCC, BCC or HCP structures. The compositional range is usually very close to the stoichiometric value. These compounds also tend to have large Burgers vectors which inhibit the movement of dislocations creating a very brittle structure. However, their poor ductility can be improved by alloying (Fleischer 1989). The strong intermetallic bonds present also create a system that can retain structural integrity to extremely high temperatures. The Nb-Si based intermetallics also have good high temperature oxidation and creep resistance. Around the eutectic point in the Nb-Si binary there are up to 4 different intermetallic compounds (Nb_3Si, α-, β- and/or γ-Nb_5Si_3) which each have beneficial and detrimental properties to the overall system. These will be discussed in due course. The other important phase in the system is the Nb solid solution (Nb_{ss}). This retains many of the properties associated with the pure metal. It has a BCC structure, is ductile (especially when compared with the intermetallic phase) and has good low temperature strength but has poor high temperature strength and oxidation resistance. Therefore, both phases (i.e. the solid solution and intermetallic) have distinctly different properties but together they offer all of the properties necessary for a high temperature structural alloy. Solidification of these phases then becomes paramount to the exploitation of all of the properties that the phases possess.

This thesis will focus on two alloys of near eutectic composition. Eutectic solidification is the cooperative solidification of two phases from a single melt. This means that the solidified alloy will form an “in-situ composite” of the two phases benefiting from the advantageous properties of each of the phases, i.e. the intermetallic will support the structure at high temperature while at low temperatures the system will be able to resist crack growth due to the ductile Nb_{ss} phase. Although the solidification of some eutectics has been previously well examined these studies are usually focused on metal-metal (two non-faceted phases) eutectics whereas the solidification of faceted/non-faceted eutectics is less understood. This becomes even more complex when specifically looking at the Nb-Si system. Near the eutectic point, for which the composition of Si is under dispute, there are also eutectoid and peritectic reactions. This is made more complex by changes in the intermetallic phase present in the system. As stated previously, there are 4 intermetallics present within close proximity to the eutectic point and each one can solidify forming half of the eutectic. Which phase solidifies depends on the cooling rate and the alloying elements present in the system. Although solidification in the Nb-Si system has been studied previously, these studies have mainly been restricted to looking at binary or ternary systems. This, although helpful for a starting point, does not advance the research as a whole towards the industrial manufacture of turbine blades from Nb silicide based alloys. For these alloys to be commercially viable other elements must be used to improve the properties and more advanced solidification methods used.

To examine fully the complexities of multi-element Nb-Si eutectic solidification a number of different methods were used in this thesis to discover how the eutectics vary in a solidification technique as well as how the cooling rate affects the morphology. Initially, a base structure was assessed by using simple arc-melted buttons solidified in a water cooled cooper hearth. This allowed observations to be made on the bulk structure that solidifies, determining how the structure was affected by alloying elements compared with previous work. It also allowed some analysis on the variations in structure due to the cooling rate. Both alloys were then solidified using suction casting in water cooled copper cylindrical moulds so that the effects of cooling rate could be examined in more

detail due to the extreme variations that occurred depending on distance from the cooling surface. Finally, the alloys were solidified using an optical floating zone (OFZ) furnace creating a “directionally” solidified structure. This is a necessary step towards the industrialisation of these alloys as it is common practice within the industry for high temperature alloys. Previous research has also shown that, similar to NBSA, directional solidification of these alloys increased their mechanical properties compared with conventionally solidified alloys. This research however had been focused on binary and ternary compositions and the effects on more complex systems are still unknown.

In addition to the solidification conditions causing significant changes in the chemistry and morphology of the system they can also cause significant changes in the properties of the alloy. To increase the oxidation resistance Al, Cr, Ti and Hf are added. However, these elements can also have a detrimental effect on the properties. Ti and Al will decrease the melting temperature which, if added in too high a concentration can produce an alloy not fit for purpose. Cr and Al additions of above 8 at.% (Subramanian et al. 1996; Subramanian et al. 1997) or 6 at.% (Bewlay et al. 2002) respectively can have a detrimental effect on the toughness of the alloy. Finally, the synergy of Ti and Hf can also cause unwanted destabilising of the tetragonal Nb_5Si_3 creating an undesirable hexagonal γ-Nb_5Si_3 phase. This is just one example of how solutes added for one purpose can cause significant detrimental properties to the overall system if all of the factors are not understood. There are however cases where elements added for one reason can have other positive effects. Molybdenum and W are added to niobium silicides to increase the fracture toughness of the Nb_{ss} phases. A side effect of adding them is the solidification of Nb_5Si_3 directly from the melt at equilibrium rather than the Nb_3Si phase which is not stable at high temperature and will slowly transform to Nb_{ss} and Nb_5Si_3 via a eutectoid reaction.

The structure of the thesis is as follows. Chapter 1 reviews relevant literature on solidification, phase equilibria, mechanical properties and processing of Nb silicide based alloys. The experimental techniques used in the research are described in chapter 2. The results of this research are presented

in chapter 3 and discussed in chapter 4. Conclusions and suggestions for future research are given in chapter 5. The XRD data is given in Appendix B.

1. LITERATURE REVIEW

1.1 SOLIDIFICATION, EUTECTICS, EUTECTOIDS AND PERITECTICS

The Nb silicide based alloys studied in this thesis were prepared using solidification processing methods (see next chapter) namely clean melting, clean melting + suction casting and clean melting + optical floating (OFZ) zone "*directional*" solidification. Thus, it is appropriate a brief overview of some aspects of solidification theory to be given in this chapter.

The eutectic reactions L → Nb_{ss} + Nb_3Si and L → Nb_{ss} + β-Nb_5Si_3, the eutectoid reaction Nb_3Si → Nb_{ss} + α-Nb_5Si_3 and the peritectic reaction L + β-Nb_5Si_3 → Nb_3Si play a key role in the development of the microstructures of Nb silicide based alloys. Therefore, eutectic, peritectic and eutectoid transformations will be briefly reviewed in this chapter before an overview of phase equilibria relevant to the alloys of this research is presented.

1.1.1 Introduction

Solidification is a nucleation and growth phase transformation (phase change) of the melt (liquid - mother phase) to solid (product phase) in which diffusion, undercooling (drives transformation) and interfacial free energy (opposes transformation) are important. For a given material (pure element, alloy) thermal and solute diffusion and interfacial energy (are the physical processes that) control the solidification microstructure. Solute diffusion is slower (more than 100 times) than thermal diffusion. The relative differences in thermal diffusivity between liquid and solid are small compared with solute diffusivities.

Thermodynamics and kinetics "define" cast microstructures. For a given alloy, the latter are characterised by the phases (solid solution(s), intermetallic(s)) and growth morphologies (dendrites, cells, eutectics etc.) which are influenced by temperature gradient, solid-liquid interface velocity and alloy composition. Solidification theory considers growth morphology changes as stability problems

and uses the highest interface temperature criterion for predicting stability. This criterion is as follows: the phase/growth morphology that grows at the highest interface temperature is the most stable one.

Nucleation is crucial at large melt undercoolings. In solidification processing the nucleation of solidification is said to be heterogeneous because the melt can contain and/or be in contact with a variety of catalytic nucleation sites and nucleation occurs at lower undercooling. The nucleation undercooling in heterogeneous nucleation depends on the most potent of the catalysts. For homogeneous nucleation (which is possible in small free volumes of melt (e.g. droplets)) maximum nucleation undercoolings of up to $0.4T_m$ are possible (T_m is melting temperature). The primary phase establishes the solidification path and the latter is influenced (can change) by subsequent growth and possible solid state decomposition.

Gradients in temperature and/or composition that develop during solidification mean that the system is not at equilibrium (i.e., not at its lowest Gibbs free energy). However, the S/L interface might still be at equilibrium. In the latter case the phase diagram is used to determine temperature and composition at the interface. Departures from equilibrium mean the temperature and composition at the interface cannot be those given by the equilibrium phase diagram. These departures arise from the attachment kinetics of atoms at the interface, the curvature of the interface (surface energy effects) and solute trapping, the latter under rapid solidification with growth rates above the absolute stability velocity (see below). Under non-equilibrium solidification (e.g., rapid solidification) diffusion becomes localised and metastable phase formation is possible and even desirable. Departure from local equilibrium at the interface at high growth rates requires one to use the kinetic liquidus slope m_k and the kinetic solute partition coefficient k_k instead of the equilibrium values m_L and k_o.

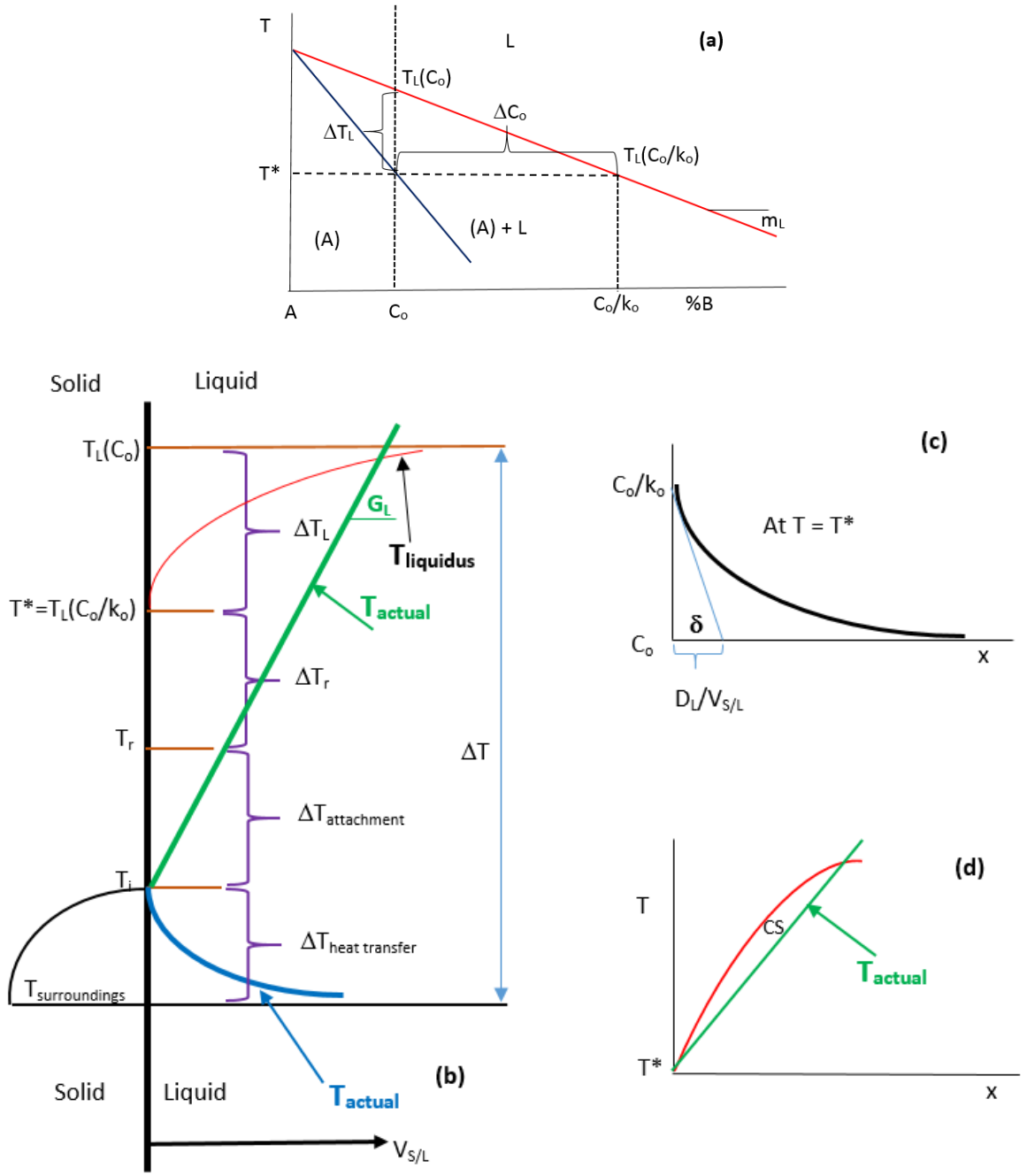

Figure 1: Schematic diagrams (a) of phase diagram of AB binary system showing alloy of composition C_o, (b) melt undercoolings at S/L interface, showing T_{actual} for unconstrained (blue) and constrained (green) growth, (c) solute rich boundary layer at S/L interface at T = T, see text and (d) constitutionally undercooled region (CS) ahead of the S/L interface for constrained solidification with $\Delta T_r = 0$ and $\Delta T_{attachment} = 0$.*

In solidification the growth of the solid can be unconstrained (solid hotter than melt, blue line in Figure 1b) or constrained (solid cooler than melt, green line in Figure 1b, constrained solidification conditions are met in directional solidification, DS). The undercooling ΔT at the S/L interface is made up of different terms, $\Delta T = \Delta T_L + \Delta T_r + \Delta T_{attachment} + \Delta T_{heat\ transfer}$, see Figure 1b (drawn following Tarshis

& Tiller (1966)). Some of the ΔT terms can have very low values depending on solidification conditions and can be ignored. For example, in pure metals solidifying at 1 m/s the $\Delta T_{attachment}$ (kinetic undercooling) is about 2 to 3 ^{O}C and may be neglected compared with the other contributions to undercooling. In near eutectic Al-Si alloys the estimated $\Delta T_{attachment}$ for Si crystals "*is dwarfed*" by the ΔT_L and ΔT_r (Steen & Hellawell 1975).

The Gibbs free energy change ΔG driving solidification depends on undercooling and is often approximated to $\Delta G \approx \Delta S\ \Delta T$. The Gibbs free energy change can be written as $\Delta G = \Delta G_L + \Delta G_r + \Delta G_{attachment} + \Delta G_{heat\ transfer}$ or $\Delta G = \Delta S \{\Delta T_L + \Delta T_r + \Delta T_{attachment} + \Delta T_{heat\ transfer}\}$ (Kotler & Tiller 1966) where each term can be considered to represent the part of the free energy that drives a particular process at the S/L interface. Thus, ΔG_L (or ΔT_L) drives the transport of matter, ΔG_r (or ΔT_r) corrects the equilibrium melting temperature for curvature (curvature undercooling $\Delta T_r = \Gamma_{S/L}\kappa$ where $\Gamma_{S/L} = \gamma_{S/L} / \Delta S_f$ (Gibbs-Thomson coefficient) and $\kappa = 1/r_1 + 1/r_2$ (i.e., κ is the curvature of the S/L interface where r_1 and r_2 are the principal radii of curvature), and $\gamma_{S/L}$ is the interfacial free energy of the S/L interface, for metals $\Gamma_{S/L} = 10^{-7}$ Km), $\Delta G_{attachment}$ (or $\Delta T_{attachment}$) drives attachment processes at the S/L interface (depends on the assumed mechanism of growth) and $\Delta G_{heat\ transfer}$ (or $\Delta T_{heat\ transfer}$) drives heat transfer processes at the interface (temperature field in the melt must be described).

In unconstrained solidification the solid phase grows in the undercooled liquid (negative temperature gradient at the S/L interface (Figure 1b blue line)) as equiaxed dendrites, the heat flow and dendrite growth directions are parallel, neighbouring dendrites influence the solute and thermal fields, and C_o and ΔT control the $V_{S/L}$, dendrite tip radius and secondary arm spacing. In constrained solidification the temperature gradient at the interface is positive (Figure 1b green line), the heat flow and dendrite growth directions are antiparallel and C_o, $V_{S/L}$ (imposed growth rate in DS) and G_L control the dendrite tip radius and the primary and secondary arm spacing.

The S/L interface is a sink of solute and a source of heat. Work must be done to "create" this interface, thus it has a free energy. In other words S/L interfaces have interfacial free energy $\gamma_{S/L}$ which

can vary with the orientation of the interface, i.e., the $\gamma_{S/L}$ can be anisotropic. The parameter used to describe this is the surface stiffness $\gamma_{S/L} + (d^2\gamma_{S/L}/d\theta^2)$ where θ is the angle between the normal to the interface and the direction of maximum interfacial free energy. In 2-D the interfacial free energy $\gamma_{S/L}$ can be written as $\gamma_{S/L} = \gamma^o_{S/L} [1 + \varepsilon_4 \cos(4\theta)]$ for fourfold cubic symmetry where $\gamma^o_{S/L}$ is the isotropic interfacial free energy and ε_4 is a measure of the strength of the anisotropy. Thus, cubic symmetry for the surface stiffness is $\gamma_{S/L} + (d^2\gamma_{S/L}/d\theta^2) = \gamma^o_{S/L} [1 - 15\ \varepsilon_4 \cos(4\theta)]$. This equation shows that the surface stiffness is positive for $\varepsilon_4 < 1/15$, but for strong anisotropy, i.e., for $\varepsilon_4 > 1/15$, the surface stiffness can be negative for some values of θ. This is not allowed by thermodynamics, meaning that these surface orientations (defined by θ) cannot appear on the crystal. Thus, the facet orientations of a facetted interface can change with its surface stiffness.

The anisotropy of $\gamma_{S/L}$ is important in (constrained and unconstrained) solidification. In a study of Al-Zn alloys using DS, the deviation (i.e., misorientation) of primary dendrite arms (the growth of dendrites and their features is discussed below) from <100> was measured (Gonzales & Rappaz 2006). It was observed that the growth direction shifted from <100> to <110> as the solute content (Zn) in the alloy increased. This was attributed to the effect of Zn (hcp) on the weak ($\varepsilon_4 = 0.01$) $\gamma_{S/L}$ anisotropy of Al (fcc).

The S/L interface advances with velocity (growth rate) $V_{S/L}$ (units m/s, the symbol R is often used instead of $V_{S/L}$), see Figure 1b. Growth can be visualised to occur as atoms arrive at and depart from the interface. Thus, the growth rate depends on the difference between the rates of arrival and departure of atoms at the interface. The structure of the S/L interface is therefore very important.

Different models have been proposed for the structure of a surface. The predictions of growth rate made using the different models do not agree. Furthermore, one model seems to "work" in one case but not in another case. Linear dependence of $V_{S/L}$ on ΔT was predicted by (Wilson 1900) and (Frenkel 1932) who considered the surface to be rough (on a rough surface atoms can be added at any side). For growth requiring nucleation of new layer on a (smooth) surface the model of Becker (1949)

predicted that the growth rate is proportional to exp(-A/ΔT). For growth "assisted" by screw dislocations, models predicted the growth rate to be proportional to ΔT^2 (Burton et al. 1951; Hillig & Turnbull 1956). Cahn (1960) and Temkin (1964) predicted a transition in growth rate from a low ΔT regime to a high ΔT regime with change in surface structure.

Jackson (1958) calculated the free energy change when a layer is added to a surface of ***pure metal A*** in equilibrium with its melt. He showed that the structure of the surface of pure A (i.e., whether the surface is "atomically" rough (diffuse) or smooth (facetted)) depends on the roughness parameter $\alpha = [\Delta S_f/R]\zeta$ where ΔS_f is the molar entropy of fusion of the pure A, R is the gas constant and ζ is the fraction of total binding energy binding an atom to the growth front (ζ varies with orientation). Surfaces with $\alpha > 2$ were "classified" as smooth and those with $\alpha < 2$ as rough. For a given growth rate, the undercooling for materials with large entropy of fusion will be larger than for materials with small entropy of fusion. Materials with large entropy of fusion will have growth rate anisotropy greater than materials with small entropy of fusion materials.

Kerr & Winegard (1967) and Taylor et al. (1968) considered ***alloy melts*** and calculated the free energy change when a layer is added to a surface of a solid solution in equilibrium with its binary melt. Their treatment showed that the surface structure (i.e., whether the surface is "atomically" smooth or rough) depends on the roughness parameter $[\Delta S/R](n/n_A)$ where ΔS is the entropy of solution, n is the total possible number of nearest neighbours per atom in the plane to which the atoms are added and n_A is the number of nearest neighbours of element A in its pure state (for example, for Bi and Ag grown along [110] and [111], respectively, the values of n/n_A are 0.66 and 0.5 (Hellawell & Herbert 1962; Wagner & Brown 1962). In other words, the entropy of fusion term in the roughness parameter α of Jackson (1958) was replaced by the entropy of solution.

Kerr & Winegard (1967) and Taylor et al. (1968) also called their roughness parameter α. The entropy of solution was calculated from the heat of solution. Given the dependence of the heat of solution on alloy composition, Taylor et al. (1968) showed that the parameter α (= $[\Delta S/R](n/n_A)$, i.e.,

the modified roughness parameter (α) of the Ag solid solution in Bi-Ag alloys changed with alloy composition, in other words that the Ag rich phase would be expected to change from facetted (smooth) at the eutectic composition to rough. This transition occurred for $\alpha \approx 2$ for the Ag rich solid solution. Alloy composition had no effect on the Bi rich solid solution, which had $\alpha < 2$ and was rough. Taylor et al. (1968) reported the same also to be the case for Al in Al-Sn alloys (i.e., a change from rough to smooth interface of Al with increase in Sn concentration in the alloy).

The morphological stability of an S/L interface, ahead of which a solute rich boundary layer is formed (see Figure 1c where δ is the thickness of the boundary layer, $\delta = D_L/V_{S/L}$, δ is the solute diffusion length (δ_D) for the solute diffusion process in solidification (Trivedi & Kurz 1994)), depends on the parameter $G_L/ V_{S/L} = \Delta T_L/D_L$ where G_L is temperature gradient (not the free energy of the liquid see Figure 1b) and D_L is the diffusivity of solute in the liquid. For $G_L/ V_{S/L} > \Delta T_L/D_L$ the S/L interface is said to be morphologically stable (remains planar or retains its planarity) and for $G_L/ V_{S/L} < \Delta T_L/D_L$ the S/L interface is said to be morphologically unstable (loses its planarity) owing to the existence of constitutionally undercooled (often referred to as constitutionally supercooled – CS) liquid ahead of the interface, see CS region in Figure 1d. The inequality $G_L/ V_{S/L} < \Delta T_L/D_L$ can be written as $G_L D_L/V_{S/L} < -m_L C_o(1-k)/k$ and the right hand side of the latter is often referred to as the constitutional undercooling parameter, m_L is the slope of the liquidus, which is negative for partition coefficient $k < 1$. In the latter case (i.e., $V_{S/L} > G_L D_L/\Delta T_L$), perturbations on the interface can grow to become cells at low $V_{S/L}$ and dendrites at high $V_{S/L}$. The cells have small length and large tip radius. At higher $V_{S/L}$ cellular dendrites are formed that are much longer than the spacing between the cells and have sharper tips. At even higher growth rates fine cells form again and for growth rates exceeding the absolute stability velocity the S/L interface becomes planar again.

Microsegregation of solute(s) can occur with the formation of cells, in other words there will be chemical inhomogeneity at the scale of the microstructure that evolves from a morphologically unstable S/L interface. The tip of the cell is at a higher temperature than the root (base) of the cell.

For k < 1, which is the case for the alloy of composition C_o shown in Figure 1a, the concentration at the tip of the cell will be lower than at its root. The microsegregation profile is given by the Scheil equation $C_S = k\ C_o\ (1 - f_S)^{k-1}$ where C_S is the composition of the solid phase (A) and f_S is the volume fraction of solid.

Dendrites develop when the $V_{S/L}$ exceeds that for cellular-dendritic structure. These dendrites grow along preferred crystallographic orientations, aligned (almost perfectly) with the temperature gradient and growth direction, and develop side branches (arms). The dendrites are characterised by dendrite primary and secondary (and possibly tertiary) arms. The primary arms are often referred to as dendrite trunks. The final spacing between arms in the base of a dendrite is larger than near the tip owing to coarsening. The final arm spacing controls the microsegregation profile. The length of dendrites is $\wr = (T_L - T_{root})/G_L$ where T_{root} is the temperature of the dendrite root (for eutectic systems with negligible solid diffusion $T_{root} = T_{eutectic}$).

The thermal diffusion length of the thermal diffusion process in the solidification of a pure metal or an alloy is $\delta_T = \alpha_{TD}/V_{S/L}$ where α_{TD} is thermal diffusivity. In DS the thermal diffusion length is $\wr_T = \Delta T_o/G_L$, where $\Delta T_o = \left| m_L \right| \Delta C_o$ (in Figure 1a, ΔT_L is the same as ΔT_o). The capillarity length in alloy solidification is $\delta_c = \Gamma/\Delta T_o$ (Trivedi & Kurz 1994). For an alloy with ΔT_o = 10 K and for DS with $G_L = 10^3$ K/m, $V_{S/L} = 10^{-6}$ m/s typical values of the three characteristic lengths δ_D, δ_T and δ_C are 3 mm, 10 mm and 28 nm respectively. When the temperature gradient and growth rate increase respectively to 10^5 K/m and 1 m/s the characteristic lengths δ_D, δ_T and δ_C are 3 nm, 0.1 mm and 28 nm, respectively (Trivedi & Kurz 1994).

Constitutional undercooled melt can occur ahead of cells and dendrites but the region of constitutionally undercooled melt is ***less*** than that formed in front of a planar S/L interface because cells and dendrites reject solute laterally as well as forward during their growth. Thus, the solute rich layer in front of dendrites is not of the order of $D_L/V_{S/L}$ (Figure 1c) but of the order of the radius of the tip of the dendrite (i.e., few microns). However, extensive undercooling exists at the tip of the

dendrites because their tips are at a temperature well below the equilibrium temperature of the alloy. The undercooling at the dendrite tip depends on temperature gradient, growth rate and alloy composition according to the equation $\Delta T = G_L D_L/V_{S/L} + [-8m_L(1-k)C_o V_{S/L}\Gamma_{S/L}/D_L]^{1/2}$ (Hunt 1977). The first term on the right hand side cannot be ignored when G_L is high and $V_{S/L}$ low. The undercooling at the dendrite tip will increase with increasing solute content, C_o. The previous equation can also be used to calculate the melt undercooling at the columnar front (Flood 1985).

If we were to ignore interface attachment kinetics, the growth of dendrites along preferred crystallographic orientations is attributed to the system attempting to minimise the area of surfaces with the highest $\gamma_{S/L}$. As the anisotropy of $\gamma_{S/L}$ increases (all other parameters do not change) the dendrite tip will become sharper and the dendrites will become facetted when the anisotropy of $\gamma_{S/L}$ is high. In metals the anisotropy of $\gamma_{S/L}$ controls the growth direction at low undercoolings. Experiments have shown that materials with high anisotropy of $\gamma_{S/L}$ tend to have large entropies of fusion. This has led to the "*rule of thumb*" that facetted crystals form in materials with $\Delta S_f/R > 2$ (some values of $\Delta S_f/R$ for facetted Bi – 2.5, H_2O – 2.65, Si – 3.6, and for non-facetted Sn – 1.7, Al – 1.3, SCN (succinonitrile) – 1.3). The two phases of interest to the research described in this thesis, namely the Nb and Nb_5Si_3 have $\Delta S_f/R$ values respectively 1.14 and 1.7 – 2.8 (Utton & Tsakiropoulos 2015; Li, Miura, et al. 2011).

Experimental work has shown that the dendrite spacing decreases with increasing temperature gradient G_L and growth rate $V_{S/L}$ and decreasing alloy composition C_o. The spacing L between dendrite trunks (often referred to as λ_1) is more sensitive to changes in temperature gradient than to changes in composition and growth rate according to a "*crude order of magnitude*" analysis by Hunt (1977) that linked L with growth rate and temperature gradient via the equation $V_{S/L}\, G_L^2\, L^4 = -64\, \Gamma\, D_L\, (-m_L)\, (1-k)\, C_o$, in other words L varies as $G_L^{-1/2}$ and as $V^{-1/4}$. This dependence of L on V and G_L has been confirmed also in "*more elegant*" treatments of dendrite growth.

A common configuration in solidification processing is the pouring of a liquid into a cold mould where solidification starts from a chill surface. The stability of this configuration depends on G_L and

$V_{S/L}$, see discussion above about constitutional undercooling and Figure 1d. In a "typical" casting equiaxed and columnar grain structures are found, the former type is observed near the walls of the mould (equiaxed chill zone) and may also be present in the centre of the mould where the melt is undercooled. During equiaxed growth dendritic grains grow radially. Directional solidification conditions give the columnar zone which forms from the chill zone. We discussed above that dendrites grow along preferred crystallographic orientations. Each dendrite will "produce" a grain and when several grains of different orientation grow in a columnar form, the "competition" between the grains eliminates the least favourably oriented ones.

A columnar to equiaxed transition (CET) might be present in a casting. It is believed that this transition occurs because of three mechanisms (Flood 1985), namely dendrite detachment (caused by convection in the melt and the low yield strength near the melting temperature), "big bang" mechanism (pre-dendritic nuclei formed during pouring by the chilling action of the mould are carried into the bulk of the casting by fluid flow and survive) and nucleation driven in constitutionally undercooled melt. Gandin (2000) has proposed an alternative mechanism for CET that leads to a breakdown of the columnar front and is based on a constraint to unconstraint growth transition.

1.1.2 Eutectics

Eutectics result from the solidification of at least two distinct phases from a single melt, where the melt and the two solid phases exist in a dynamic equilibrium. Due to the in-situ solidification of two dissimilar phases, eutectic structures have been used to create composite like structures from a single melt. Similarly to composite materials, this allows favourable properties from each constituent to be utilised. Looking at an example of an equilibrium phase diagram, Figure 2, eutectic solidification occurs at the invariant point (Z). This is the point at which two downward sloping liquidus lines (α and β liquidus) meet forming a two phase region (α + β) underneath Z and a single liquid phase above Z. The invariant point is also the lowest melting point of the microstructure of the two constituents, which is beneficial for melting and casting.

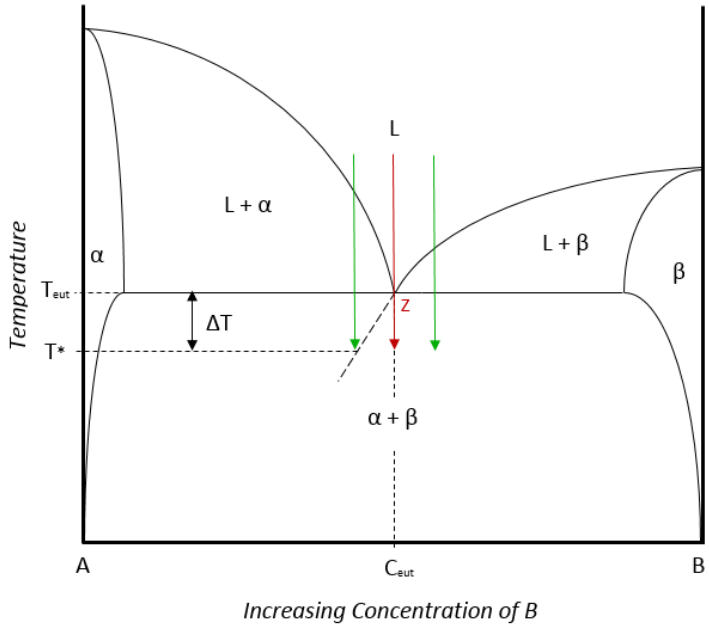

Figure 2: Schematic phase diagram showing a eutectic. Z highlights the invariant eutectic point at which L will solidify to an α+β eutectic.

Within well-known binary systems, e.g. Al-Cu and Sn-Pb, creating the correct conditions for a eutectic to form can almost be a formality. However, in higher order (ternary, quaternary etc.), more unknown systems, or systems where there is a very steep eutectic trough this can become more difficult. In the cases highlighted by the green arrows in Figure 2, dendrites form initially. These alloys can take two forms; hypereutectic, the concentration of B is higher than C_{eut}, and hypoeutectic, the concentration of B is lower than C_{eut}. In a hypoeutectic case cooling the melt will initially form α dendrites as the liquidus is crossed. This enriches the melt with B atoms. Once the temperature of the melt is reduced under the eutectic temperature (T_{eut}) to a critical temperature (T*) the eutectic will begin to grow in the inter-dendritic regions. The difference between these two temperatures T_{eut} and T*, is known as the undercooling, or supercooling, of the melt (ΔT) and is the driving force for solidification, as shown in Figure 2.

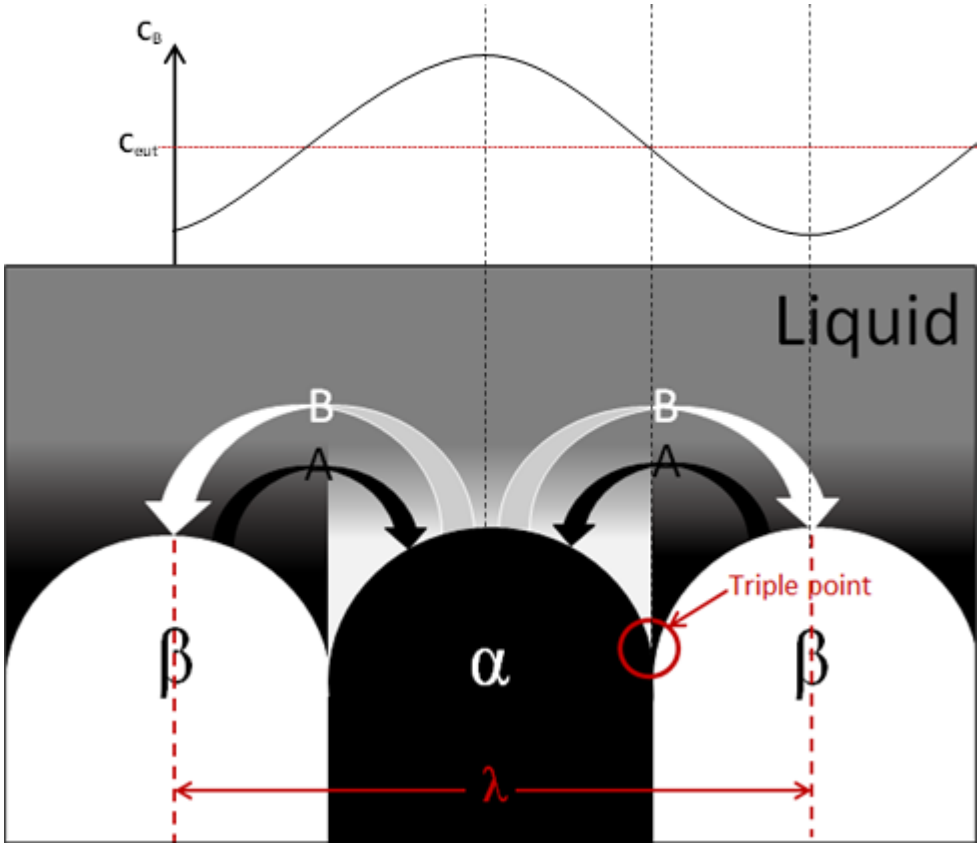

Figure 3: Schematic diagram showing coupled growth of the α/β eutectic. The movement of the phase constituents, the triple point, eutectic spacing (λ) of the lamellae and the concentration variation of B in the liquid along the S/L interface are shown.

Eutectics grow by way of coupled growth (Figure 3) which occurs in the couple growth zone located below the invariant point on the phase diagram (§ 1.1.2.1).The coupled zone represents the range of growth conditions within which morphologically stable two (or more) phase growth will be obtained. As the α phase grows it rejects excess B atoms into the melt creating a saturation of B atoms in the melt in front of the S/L interface at the α phase. As this is occurring the β phase, growing parallel to the α phase, rejects A atoms into the melt. The concentration difference in the melt in front of the isothermal S/L interface drives, parallel to the interface, diffusion of rejected atoms toward their respective phases (A → α and B → β). This creates a co-operative, mutually dependent growth around a stable triple point with interlamellar interfaces perpendicular to the S/L interface. To maintain a locally stable triple point the resolved interfacial forces at the S/L boundary must equal the interphase energies. The concentration of an element (e.g. B) in the melt ahead of the S/L interface will therefore

oscillate around C_{eut} throughout the length of the interface. The amplitude of these oscillations decreases with increasing distance from the S/L interface. The rejection of solute into the melt causes constitutional supercooling in the liquid at the S/L interface compared with the bulk melt temperature. This undercooling keeps the liquid at the S/L boundary undercooled below the T* temperature and drives the eutectic growth.

Cooperative growth of eutectics gives rise to a repetitive lamellar microstructure the scale of which can be measured. The conventional measurement taken is the lamellar spacing (λ), which is defined as the distance from the centre of one phase to the centre of the nearest similar phase (shown in Figure 3). The Jackson-Hunt theory quantifies the relationship between the cooling rate of materials grown by steady state methods (e.g. directional solidification (DS)) and regular lamellar spacing. This theory states that

$$\lambda^2 \mathrm{V}_{\mathrm{S/L}} = C \tag{1.1}$$

Where $V_{S/L}$ is the growth rate (m/s) and C is a constant. Therefore, plotting a graph of λ vs. $(V_{S/L})^{1/2}$ will give a straight line through the origin.

It is customary to say that the well organised eutectic structure arises from the cooperative (coupled) growth of the two eutectic phases, owing to the need of rejected solute from one phase for the growth of the other phase. However, the same microstructure would be produced if the eutectic formation was considered to occur as each phase of the eutectic prefers to grow along the interface between the other phase and the liquid. This then would be a battle between the two eutectic phases, as each one of them would try to isolate the other from contact with the melt.

In non-steady state growth conditions the relationship between spacing and cooling rate can be more ambiguous as the cooling rate of eutectic colonies can be hard to determine and the average of the entire ingot can be insufficient. The work of Li & Kuribayashi (2003) detailed the variances that

occur within measuring of freely solidifying eutectic of the same composition between different researchers.

In theory, metallic eutectics solidified in the coupled growth region will grow relatively long scale lamellar phases as long as the variables remain within reasonable limits. As the lamellae are solidified by coupled growth they have a tendency to form lower energy crystallographic orientations and therefore will have lower interphase energies than dissimilar phases solidified conventionally (Kurz & Fisher 1968). However, variations primarily in the composition of the melt at the S/L interface as well as temperature variations can cause instabilities in the microstructures forming shorter lamellae. Figure 4 shows the two main forms of instability that can form.

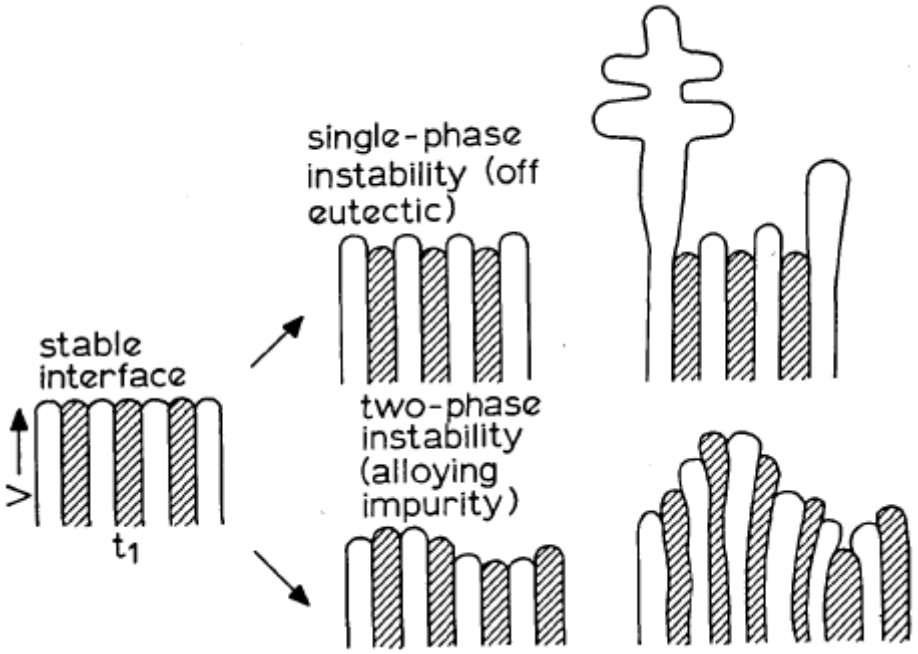

Figure 4: Schematic diagram showing schematic of single-phase and two-phase instabilities in eutectics (Kurz & Fisher 1979). *Copyright for the reproduction of this image granted by Taylor and Francis group (http://www.tandfonline.com)*

Single-phase instabilities, Figure 4, are caused by one of the phases growing out of the stable interface due to an off eutectic composition or accelerated growth of one phase due to undercooling. This creates a dendritic microstructure and an inter-dendritic eutectic. The two phase instability shown in Figure 4, is due to the rejection of one or more elements by both phases into the melt. This

causes instabilities in the solid/liquid interface causing eutectic cells, rods or eutectic dendrites to form instead of lamellae. Variations in morphology can also be caused from deviations in cooling rate as well as composition. For example, a fully eutectic microstructure that forms under slow cooling rate is replaced by an off eutectic one, consisting of primary phase + eutectic, at high cooling rate. In the latter case to obtain a fully eutectic microstructure a concentration higher than the eutectic concentration is required.

Continuous parallel lamellae are commonly thought to be the "perfect" structure for eutectics but other beneficial morphologies can result from a eutectic melt. Depending on the volume fraction of the phases and whether phases are faceted or not discontinuous morphologies can form within the coupled zone without instabilities forming (§ 1.1.2.1). In general, when the vol.% of one of the phases in the eutectic is lower than 28 % the eutectic will tend to be fibrous and when it is 28 % < vol.% <72 %, it will tend to be lamellar.

The morphology of eutectics depends on C_L and $V_{S/L}$. Many eutectic morphologies have been reported over the years. The roughness parameter α proposed by Jackson (§ 1.1.1) was used to classify eutectic structures (often referred to as the Hunt and Jackson classification of eutectics (Hunt & Jackson 1966)). When both phases have $\alpha < 2$ lamellar or regular-rod eutectics structures are formed and these were classified as non-facetted/non-facetted (NF/NF) eutectics. When one phase has $\alpha > 2$ and the other $\alpha < 2$ the eutectic was classified facetted/non-facetted (F/NF) eutectics. When both phases have $\alpha > 2$ irregular eutectics are formed and these were classified as facetted/facetted eutectics (F/F). The Hunt and Jackson classification applies to simple binary eutectics when the α values of the eutectics phases are calculated at $T_{eutectic}$ and $C_{eutectic}$.

The work of Kerr & Winegard (1967) and Taylor et al. (1968) showed that in alloys the surface roughness parameter depends on solute content and changes as $C_o \neq C_{eutectic}$ (§ 1.1.1). Fidler et al. (1972), based on the results of 14 binary eutectics with an intermetallic phase, proposed that the change from NF/NF to F/NF eutectics occurs when the entropy of solution exceeds 23 J/molK

($\Delta S_{solution}/R$ = 2.77). Croker, McParlan, et al. (1975) used the entropy of solution criterion and the volume fraction V_f of the facetted phase to classify F/NF eutectics as broken lamellar, irregular, complex regular and quasi-regular with increasing V_f. Members of the same research group showed that the structure of binary eutectics depends on $\Delta S_{solution}$, G_L, $V_{S/L}$, C_o and V_f (of the facetted phase) and also on thermal anisotropy, the value of $\gamma_{S/L}$ and the anisotropy of the interphase boundary free energy (Croker, Baragar, et al. 1975).

There are many ways eutectics can be grouped but they are usually bound into three main groups; non-faceted/non-faceted (regular), faceted/non-faceted (irregular) and faceted/faceted eutectics.

Faceted/faceted eutectics grow along very well defined directions. The triple point between the liquid and two solids (Figure 3) are **not** stable so the growth cannot be described as co-operative and leads to discontinuous phases within a matrix. Faceted/faceted eutectics are uncommon in metallic systems.

Non-faceted/non-faceted eutectics are considered the standard of eutectic solidification. This type of eutectic exhibits regular lamellar growth of both phases creating a “perfect” solidified eutectic microstructure due to coupled, mutually dependent growth. Examples of these are normally basic metal-metal systems such as Pb-Sn and Ag-Cu. These eutectics form in a symmetrical couple zone below the eutectic point.

1.1.2.1 Faceted/Non-faceted Eutectics

Faceted/non-faceted (F/NF) eutectics are of particular interest in this thesis due to the faceted nature of the silicides (§ 1.1.1) that solidify with metallic niobium solid solution (Nb_{ss}). F/NF eutectics are considered more complex than eutectics containing only non-faceted phases. Non-faceted systems have simple morphologies after solidification (§ 1.1.2), while F/NF eutectics have many including, lamellar, quasi-regular, Chinese script, anomalous, etc. These can all form in the same system by altering the solidification variables slightly. Regular, lamellar coupled growth, seen in the

NF/NF, systems occurs in a coupled zone under the invariant point. However, in F/NF systems the coupled zone is not symmetrical and tends to skew off to the faceted side of the phase diagram.

As will be discussed in the next chapter, the alloys studied in this thesis were near-eutectic Nb silicide based alloys. Alloys of this type are interesting because solidification processing could allow one to control the V_f of the primary phase (Nb_{ss} or Nb_5Si_3), which is important for achieving a balance of properties. Considering the values of the entropy of fusion of the two phases (§ 1.1.1) the silicide would be expected to be facetted and a eutectic between these two phases to be F/NF.

In eutectic alloys the range of compositions and solidification conditions that give a fully eutectic structure is described by the coupled zone. Facetted/non-facetted eutectics tend to have large interphase spacings and undercoolings that are influenced by the temperature gradient G_L..

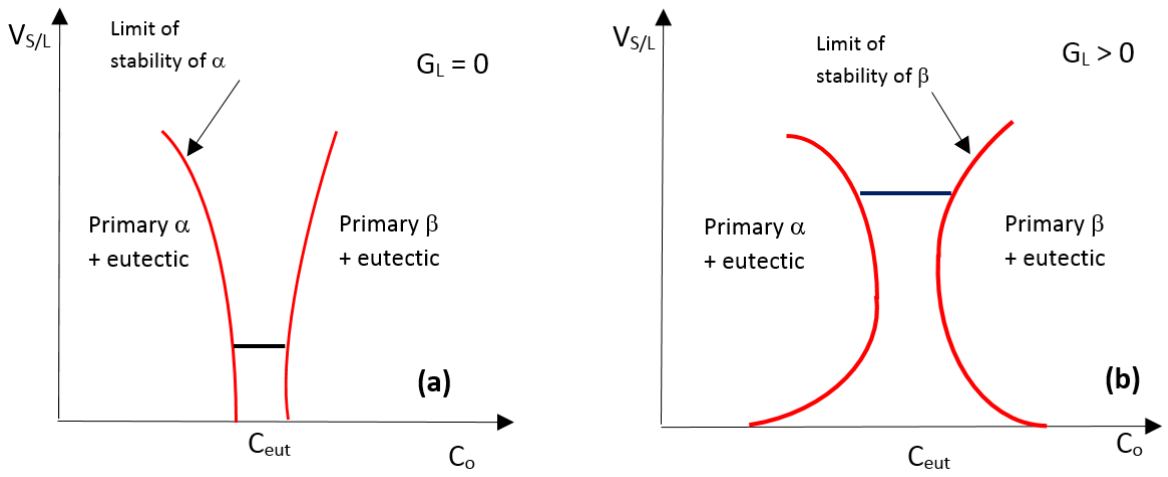

Figure 5: Schematic diagrams of coupled zones for NF/NF eutectics between α and β phases (a) for isothermal growth and (b) for growth in a temperature gradient. The horizontal lines indicate the growth rate below which oriented structures form in DS.

Typical coupled zones for NF/NF eutectics grown under isothermal conditions ($G_L = 0$) and temperature gradient ($G_L > 0$) are shown in Figure 5 (drawn after Fisher & Kurz (1977)). The zones include the eutectic composition C_{eut}. Figure 5 shows that the width of the coupled zones changes with growth rate, in (a) the zone widens only at high growth rates while in (b) the zone widens at high and low growth rates.

A skewed coupled zone formed under steady state conditions with $G_L > 0$ is shown in Figure 6b (where in the phase diagram of the A-B system shown on the left hand side the phase β is the facetted one) and for comparison purposes a symmetric coupled zone formed under steady state conditions with $G_L > 0$ is shown in Figure 6a. In both parts of the schematic the growth rate vs temperature relationships for plane front eutectic and primary dendrites are shown on the right hand side diagrams.

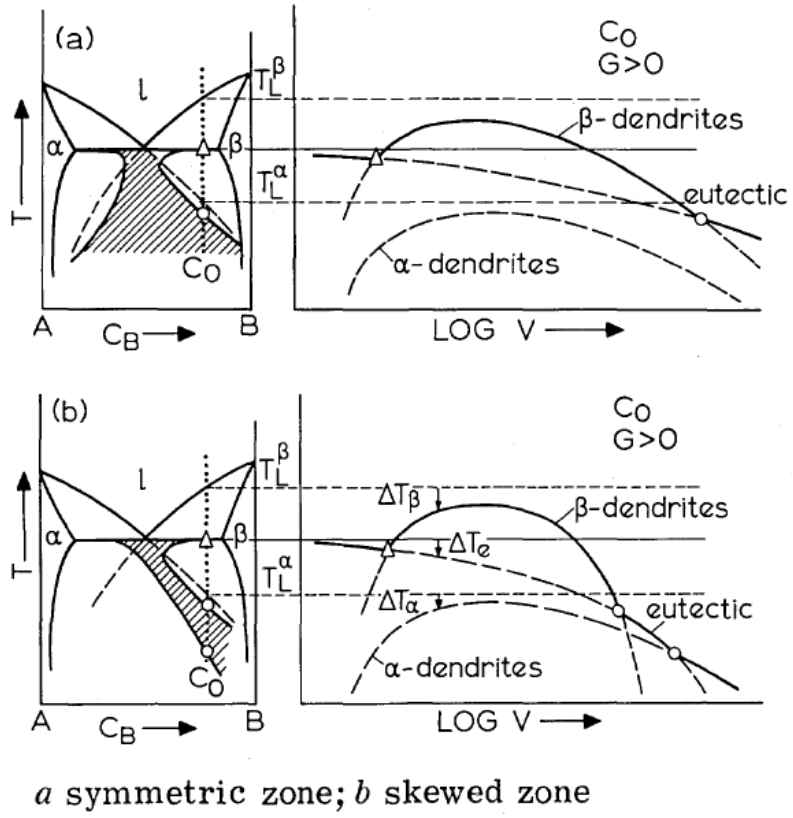

a symmetric zone; *b* skewed zone

Figure 6: Schematic diagrams showing the construction of coupled zones drawn as temperature versus composition and temperature versus growth rate, (a), (b) show different behaviour for eutectic and dendrites. In the phase diagrams the alloy composition is shown as C_o and metastable extensions of α and β liquidus as dashed lines. The facetted phase is β in (b) (Kurz & Fisher 1979). *Copyright for the reproduction of this image granted by Taylor and Francis group (http://www.tandfonline.com)*

The growth temperature (meaning the interface temperature) of ***NF/NF eutectic*** is given as $T_G = T_{eut} - B_{eu}\sqrt{V_{S/L}}$ where B_{eu} is a function of physical constants of the alloy, and the dendrite tip temperature for growth with $G_L > 0$ is given as $T_{den} = T_L - B_{den}\sqrt{V_{S/L}} - G_L D_L/V_{S/L}$ where B_{den} is a function of physical constants of the alloy and T_L is the stable or metastable liquidus of the alloy (Tsakiropoulos

2009). The curves defined by the latter equation exhibit a maximum and thus the curve for the eutectic (i.e., derived from the expression for T_G) is cut twice.

The coupled zone shown on the left hand side phase diagrams is derived by applying the competitive growth criterion according to which the morphology having the highest interface temperature for a given growth rate or the highest growth rate for a given undercooling will be observed. The superposition of interface temperature versus growth rate curves for the competing morphologies on the right hand side diagrams indicates the boundaries of the coupled zone at a given temperature.

From Figure 6b we deduce that to get the skewed zone the rate of change of ΔT_β must be greater than that for ΔT_{eut} (shown as ΔT_e). For the non-facetted dendrite the rate of change of ΔT_α must be smaller than ΔT_{eut}.

Experimental work has shown that facetted materials can have different morphologies at the same $V_{S/L}$. This is not the case for non-facetted materials. The former fact implies that facetted dendrites will grow with different tip temperatures at the same $V_{S/L}$ (meaning the local growth rates can be different between neighbouring facetted dendrites). Thus, it is unlikely that steady state growth conditions can be "easily" achieved (if at all) in the case of facetted phases and F/NF eutectics. Thus, for F/NF eutectics the growth rate applies to the S/L interface in an "average" sense (Fisher & Kurz 1977).

The equations for T_G and T_{den} given above, which were (are) used to calculate the skewed coupled zone, mean that the behaviour of eutectic and dendrites is described by mathematical curves even though the solidifying alloy should not be expected to respond in such a (continuous) way to growth conditions. Most likely the skewed shape of the coupled zone in F/NF eutectics arises because the anisotropic growth of the facetted phase (see § 1.1.1 for surface stiffness) causes non-optimum growth of eutectic and dendrites (Fisher & Kurz 1977).

The dependence of eutectic spacing on growth rate is shown schematically in Figure 7. In this figure macroscopic S/L interface morphologies are shown below the V vs λ diagram. For λ < LCL fluctuations in eutectic spacing squeeze off one phase and the space increases. For λ > UCL one phase falls back and the other phase becomes unstable (forms branches). Large λ is attributed to non-optimum growth.

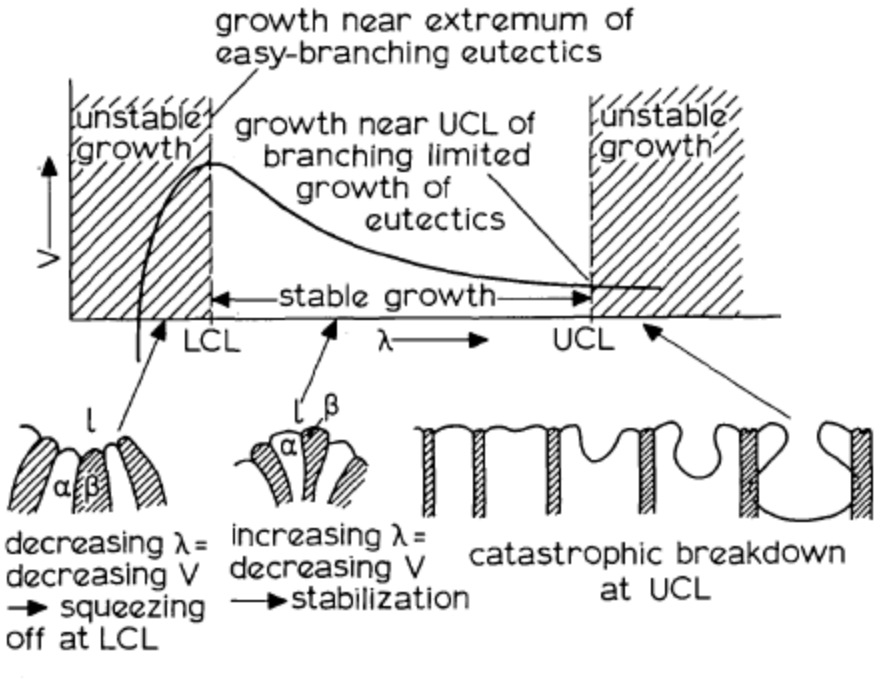

Figure 7: Schematic diagram of $V_{S/L}$ (shown as V) vs spacing λ showing range of possible eutectic spacings. LCL is the "lower catastrophic limit" and UCL is the "upper catastrophic limit" (see text) (Kurz & Fisher 1979). *Copyright for the reproduction of this image granted by Taylor and Francis group (http://www.tandfonline.com)*

An NF/NF eutectic grows with λ that gives the maximum $V_{S/L}$ (see LCL in Figure 7). The "stiffness" of facetted phases (i.e., their anisotropic growth) leads to branching limited growth, in other words F/NF eutectics change morphology as λ → UCL. Thus, the spacing of F/NF eutectics will be between LCL and UCL and will vary from place to place (meaning the S/L interface will be macroscopically irregular). Experiments have shown that depressions are not formed in the non-facetted phase with increase in G_L and that branching occurs at smaller λ (UCL shifts to the left in Figure 7), in other words finer eutectic spacings (smaller λ) at high G_L.

From the study of the bismuth-tin and bismuth-thallium systems (entropies of fusion ΔS_f^{Bi} = 20 J/mol.K, ΔS_f^{Sn} = 13.9 J/mol.K, ΔS_f^{Ti} = 7.2J/mol.K) Baragar et al. (1977) showed that solidification of faceted phases required much higher driving force (undercooling) and that a boundary layer rich in the faceted component must exist for coupled growth to occur. When the boundary layer was too rich, cellular eutectic formed with a central spine and radiating lamellae. At high cooling rates however the complex microstructure disappeared and full lamellar morphology dominated. It was proposed that if the non-faceted phase grows out dendritically then the undercooling will be increased allowing the growth rate to be equal.

Work on the growth of the Al_3O_3/$GdAlO_3$ eutectic (Andreeta et al. 2002) showed that in F/NF eutectics the V_f of a phase is related to the type of eutectic formed. A reduction of the volume fraction of the $GdAlO_3$ phase by 4% caused a change in structure from “Chinese script” morphology to a complex regular morphology. It was also shown that taking an average across the different microstructures the spacing obeyed the Jackson-Hunt relationship (Eqn. 1.1). However the spacing of individual morphologies varied drastically at the same growth rate. Irregular structures such as Chinese script eutectics (i.e. eutectic with faceted and non-faceted phases where one phase has relatively high entropy of melting) grow due to the high kinetic undercooling associated with the phase of high entropy of melting.

Extensive work was carried out on collating numerous publications on faceted/non-faceted eutectics Croker, Baragar, et al. (1975). This work found a link between the V_f and the growth rate. This was taken further and it was found that this could be used to predict the type of F/NF microstructure that will evolve. The diagram produced from this work is shown in Figure 8. It was also stated, though not shown, that these results were sensitive to the entropy of solution (see § 1.1.1) and a three dimensional plot can be constructed to more accurately account for variation in structures. The later work on the Bi-Th system Baragar et al. (1977) seemed to confirm this. They

found that increasing the V_f of the faceted phase creates a lamellar structure for the same growth rate.

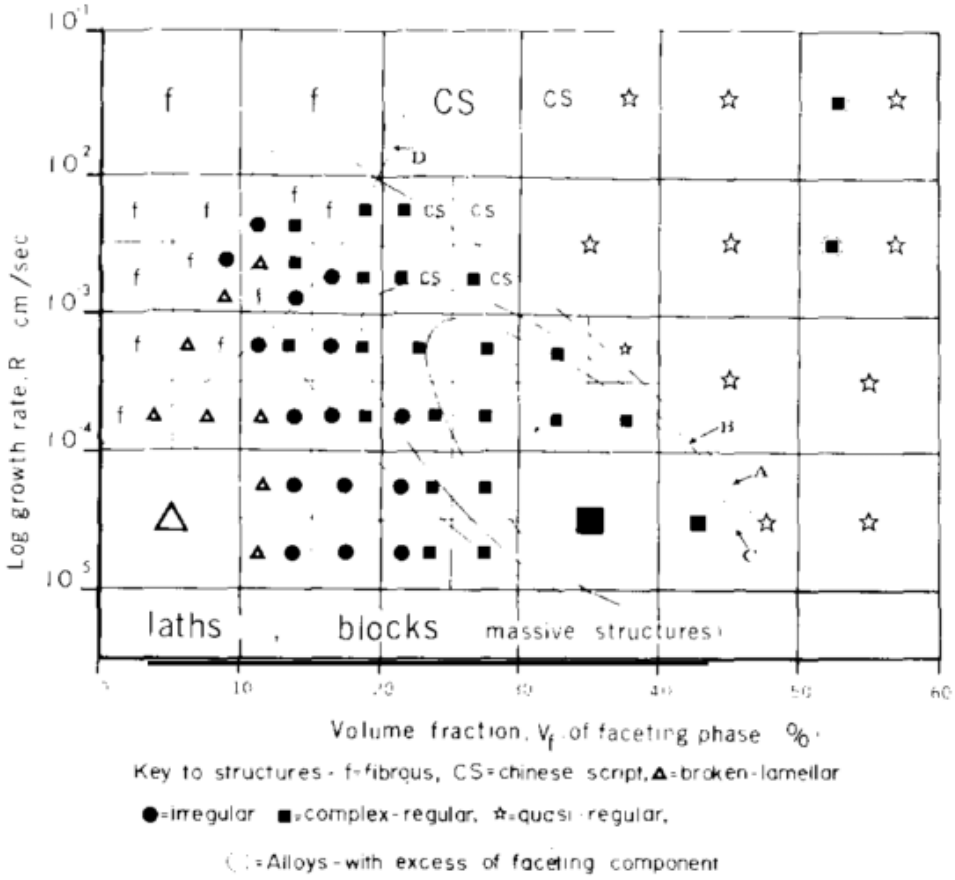

Figure 8: Variation in microstructure of a F/NF eutectic with varying V_f of the faceted phase and growth rate, compiled from published data. Republished with permission of Elsevier, from Croker, Baragar, et al. (1975); permission conveyed through Copyright Clearance Center, Inc.

A change of microstructure from regular lamellar formations to anomalous has also been studied. Work on the Ni-Si, Co-Sb and Ni-Al-Ti alloys (Goetzinger et al. 1998) showed evidence that anomalous eutectics can form in three ways;

- A supersaturated dendrite grows which, through solid state transformation, separates into two distinct phases.
- Both phases grow simultaneously in an uncoupled manner.
- Phases grow co-operatively from independently nucleating sites.

1.1.3 Eutectoids

Eutectoid reactions are, in effect, the "equivalent" of eutectic reactions, in solid state. A eutectoid reaction occurs when one phase becomes thermodynamically unstable at a certain temperature and composition (and pressure). To return to a stable state the phase needs to transform into two distinctly different phases. Diffusion in the solid state plays a key role in their transformation. The formation of pearlite from austenite via the eutectoid reaction γ-Fe = α-Fe + Fe_3C is one of the most studied eutectoid transformations

In the schematic phase diagram shown in Figure 9 cooling though the invariant point Z will cause the eutectoid transformation $\Upsilon_{solid} \rightarrow \alpha_{solid} + \beta_{solid}$ to occur.

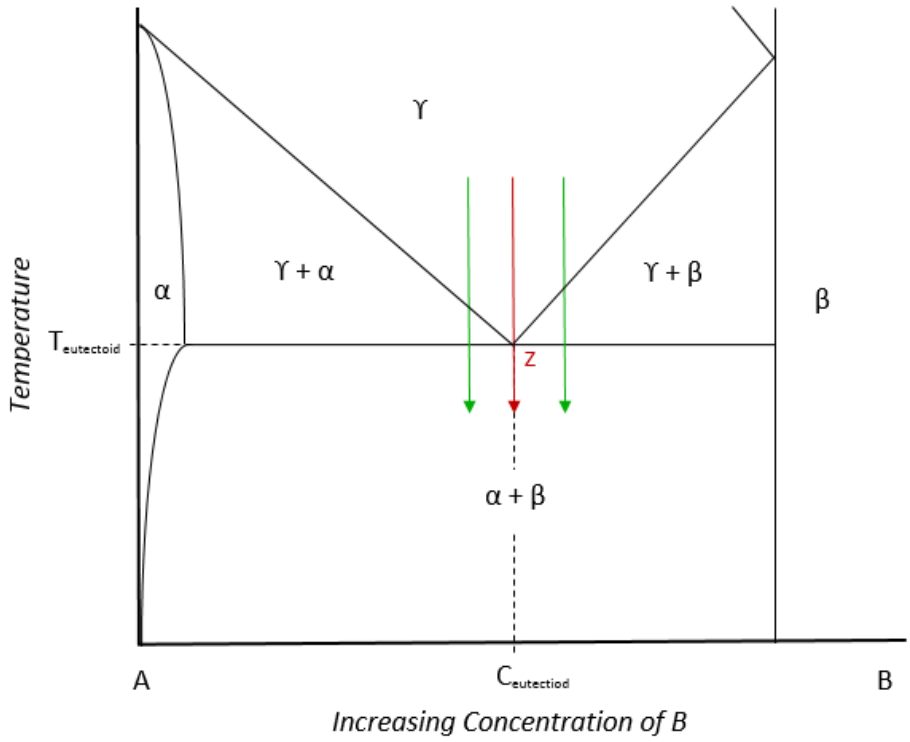

Figure 9: Schematic binary phase diagram showing the invariant eutectoid point Z at which Υ will transform to α+β.

During equilibrium solidification of an alloy of composition $C_{eutectoid}$ the solid solution γ phase could form. Upon solid state cooling to the temperature $T_{eutectoid}$ all three phases would be in equilibrium at $T_{eutectoid}$. At some temperature $T_G < T_{eutectoid}$ the eutectoid transforms to the two new phases α and β will start to form. T_G is the growth temperature of the eutectoid. The two phases will

grow by way of coupled growth similar and that of eutectics until the ϒ phase is completely transformed or the temperature drops below a point for which the diffusion driven growth is possible.

As with eutectics, eutectoids can form at either side of $C_{eutectoid}$. Green lines in Figure 9 show an example of this. As the α/ϒ or β/ϒ solidus is crossed that phase will nucleate and grow on the grain boundary of ϒ, as the ϒ rejects the B (or A) atoms. This continues until the ϒ phase reaches the eutectoid composition at which point the eutectoid forms. An orientation relationship between ϒ and α or β in a eutectoid structure has been postulated but never confirmed experimentally.

1.1.4 Peritectics

Figure 10 shows schematic diagrams of peritectics in binary systems. Consider the alloy of composition C_o. Equilibrium solidification starts with primary α, and below the peritectic temperature T_{per} phase β forms. The peritectic reaction is L + $\alpha \rightarrow \beta$ and requires L, α and β to be in contact with each other so that the L and α can react to form the β (β should grow where both the parent phases are present). The β forms along the α/L interface and thus it isolates the α from contact with the liquid.

Whether or not the reaction takes place depends on C_o and $\dot{T}$ (cooling rate) because these parameters affect the vol% and spatial distribution of primary α and the kinetics of the reaction. In a peritectic transformation however the L and α phases are not necessarily in contact and the β may be produced by long range diffusion (Kerr et al. 1974) which means that the former (i.e., the reaction) is a specific case of the latter (the transformation), in other words the *connectivity* of L, α and β determines whether the peritectic reaction can take place. The reaction is aided when primary α forms as small particles in the melt.

In binary alloys like the one of composition C_o shown in Figure 10, the α or β could form from the melt (meaning either the α or the β can be primary phases) depending on solidification conditions. If β were to be the primary, it would be metastable β. At low $V_{S/L}$ according to the stability criterion

(see § 1.1.1) the primary phase will be the α because it has a higher $T_{liquidus}$ (see Figure 10, $T_{Liquidus\alpha} > T_{Liquidus\beta}$).

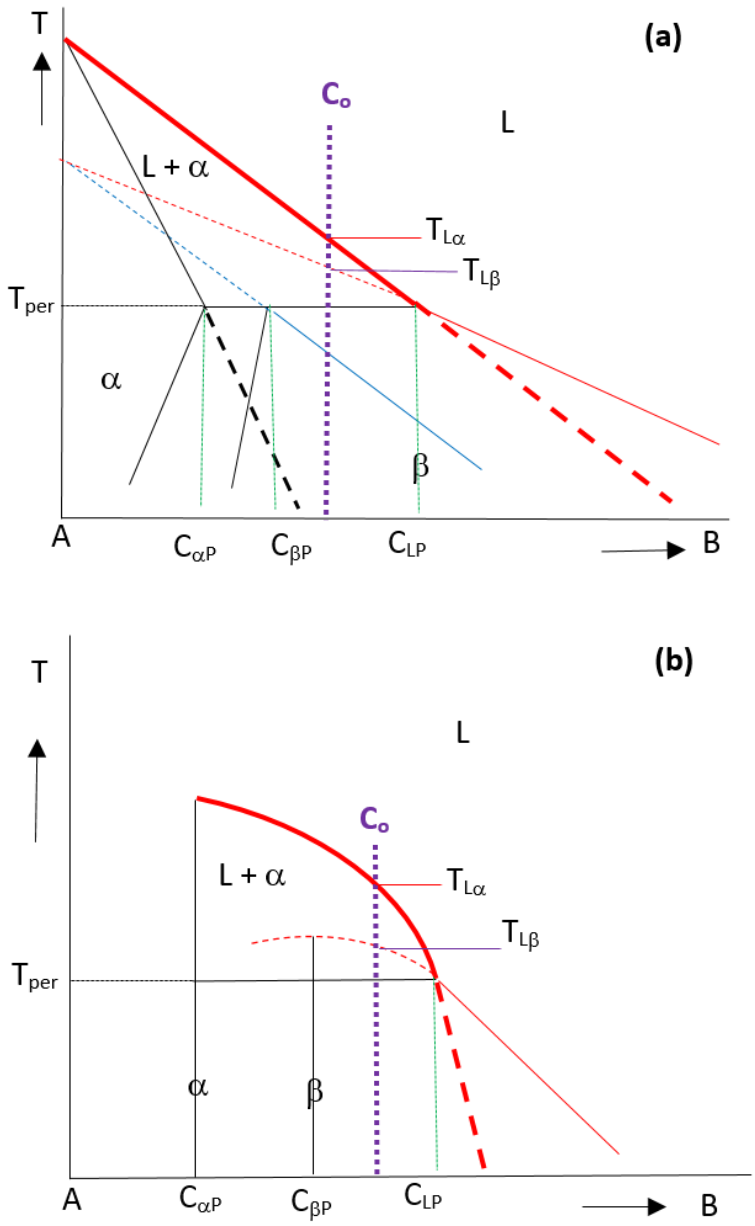

Figure 10: Schematic A rich corners of binary phase diagrams of AB systems showing two types of peritectics (a) most common (e.g., like the peritectic in the Fe-C diagram) and (b) in intermetallic forming systems. Thick and thin red continuous and dashed lines indicate the equilibrium and metastable liquidus respectively of α and β. The compositions of the phases at the peritectic temperature T_{per} are C_{iP} where i = α, β, L.

1.2 PHASE EQUILIBRIA

1.2.1 The Nb-Si Binary System

The Nb-Si binary phase diagram has been an area of research for a number of decades. This study will focus mainly on the metal-rich side of the system (i.e. Si concentration < 40%) as this allows the in-situ solidification of Nb_{ss} and, at least one, intermetallic phase. Looking at the phase diagram in Figure 11 (Schlesinger et al. 1993; Okamoto 2005) there are 4 invariant reactions of interest to this research;

i. $L \rightarrow Nb_{ss} + Nb_3Si$ – eutectic reaction at 18.7 at.%Si and 1920 ^{O}C
ii. $L + \beta\text{-}Nb_5Si_3 \rightarrow Nb_3Si$ – peritectic reaction at 25 at.%Si and 1980 ^{O}C
iii. $Nb_3Si \rightarrow \alpha\text{-}Nb_5Si_3 + Nb_{ss}$ – eutectoid reaction at 25 at.%Si and 1770 ^{O}C
iv. $\beta\text{-}Nb_5Si_3 \rightarrow \alpha\text{-}Nb_5Si_3 + NbSi_2$ – at 39.5 at.%Si and 1650 ^{O}C

The $\alpha\text{-}Nb_5Si_3$ and $\beta\text{-}Nb_5Si_3$ were defined as $rt\text{-}Nb_5Si_3$ and $ht\text{-}Nb_5Si_3$ respectively in the phase diagram shown in Figure 11. There is disagreement over the exact composition and temperature of the eutectic. Reported compositions tend to vary from 15.3 at.% (David et al. 2006) to 17.5 at.%Si (Amancherla et al. 2007) to 18.7 at.%Si (Schlesinger et al. 1993) and the temperature varies from 1880 ^{O}C (Bewlay et al. 2004) to 1920 ^{O}C (Okamoto 2005). This system allows one to use solidification of the alloys with composition near the eutectic and thus knowledge of the actual parameters needed to gain a purely eutectic alloy would be valuable. Furthermore due to the close proximity of the above invariant reactions there can be large variations in the final microstructure with relatively small changes in composition and/or temperature.

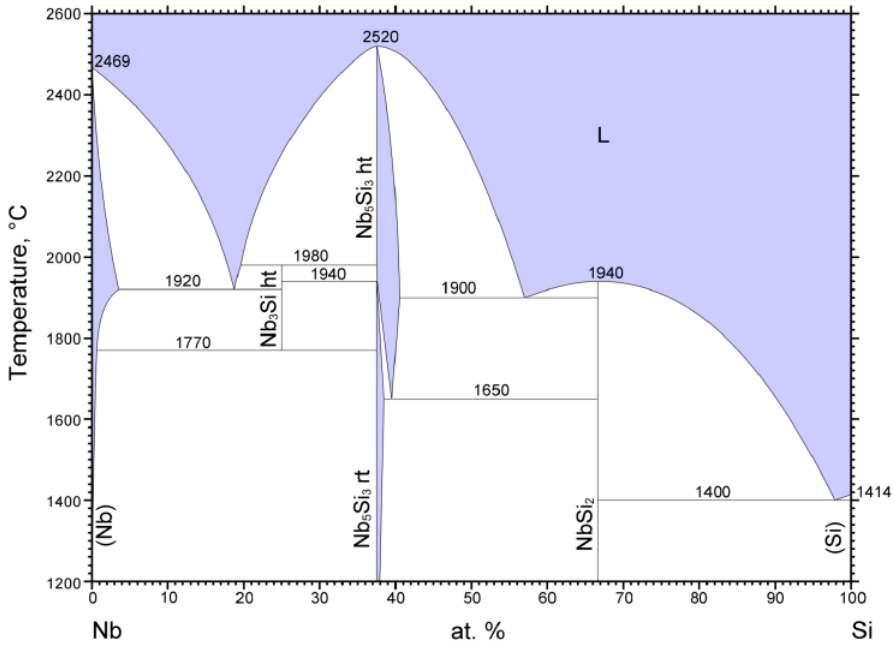

Figure 11: The binary Nb-Si system (Schlesinger et al. 1993; Okamoto 2005)

The crystallographic properties of the phases that are important to this research are shown in Table 1 (Schlesinger et al. 1993; Bewlay et al. 2004), which also includes the metastable phase γ-Nb_5Si_3.

Table 1: The phases present in the Nb-rich side of the Nb-Si binary system and their crystallographic properties (Schlesinger et al. 1993; Bewlay et al. 2004). **metastable phase*

Phase	*Composition (at.%Si)*	*Pearson symbol*	*Structure*	*Prototype*	*Lattice parameter(s) (Å)*
Nb_{ss}	0 – 3.5	*cI*2	BCC	W	a=3.306
Nb_3Si	25	*tP*32	Tetragonal	Ti_3P	a=10.224 c=5.1891
α-Nb_5Si_3	36.7 – 39.8	*tI*32	Tetragonal	Cr_5B_3	a=6.570 c=11.884
β-Nb_5Si_3	37.5 – 40.5	*tI*32	Tetragonal	W_5Si_3	a=10.026 c=5.0717
γ-Nb_5Si_3*	37.5	*hP*16	Hexagonal	Mn_5Si_3	a=7.536 c=5.249

It can been seen in Table 1 and Figure 11 that all of the phases have, either fixed (line compounds) or very limited solubility of Si over the entire temperature range. This led researchers in the field to create in-situ composites from this system that are thermodynamically stable (Mendiratta & Dimiduk 1991). The properties of both phases make the in-situ composite ideal for high temperature

structural applications. There were a number of metastable phases also present in the Nb-Si system that are largely stabilised by interstitials, most notably carbon (Shah et al. 1992). The γ-Nb_5Si_3 is of particular interest in this study and therefore will be discussed further in relation to Ti and Hf additions.

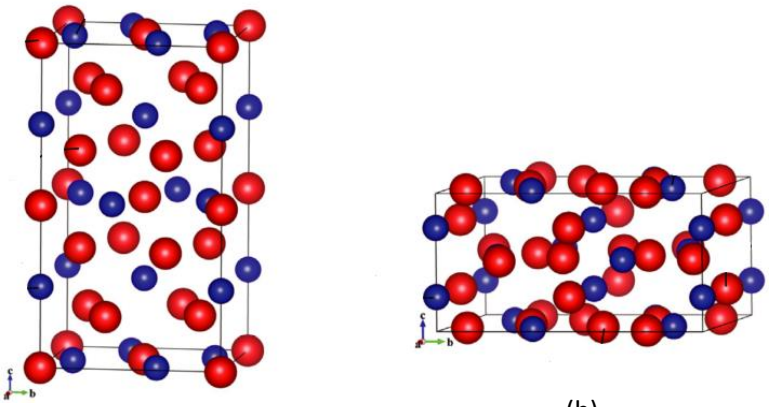

Figure 12: The crystal structures of (a) α-Nb_5Si_3 and (b) β-Nb_5Si_3 where the red and blue spheres denote Nb and Si atoms, respectively. Republished with permission of Elsevier, from (Xu et al. 2014)*; permission conveyed through Copyright Clearance Center, Inc.*

Diagrams of the crystal structures of α- and β-Nb_5Si_3 are shown in Figure 12 a and b respectively. Work by Xu et al. (2014) attempted to determine the temperature dependent mechanical properties of these phases from first principles. They showed that both phases have crystal anisotropy which becomes stronger with increasing temperature for α-Nb_5Si_3. Their results showed that, for the range of operational temperatures the α-Nb_5Si_3 had higher Bulk modulus and better compressive strength capabilities. Ductility was estimated from the ratio between bulk and shear modulus (B/G); 1.75 is considered the boundary between brittle (< 1.75) and ductile (>1.75). The α-Nb_5Si_3 showed increased ductility between 227 ^{O}C (B/G = 1.56) and 2227 ^{O}C (B/G = 1.75). Whereas β-Nb_5Si_3 showed very little increase in ductility over the entire range of temperatures, B/G increasing from 1.54 to 1.59 over the same temperature range.

1.2.2 The Nb-Ti-Si Ternary System

Titanium is one of the most studied alloying additions to Nb-Si based alloys due to its numerous benefits on mechanical and oxidation properties (§ 1.5.1). Thus, the Nb-Ti-Si ternary system is one of

the most researched in this field. Despite this there still is not full description of the system over the full range of temperatures and disagreement regarding the liquidus projection.

1.2.2.1 The Nb-Ti and Ti-Si Binary Systems

The Nb-Ti binary phase diagram is simple. A solid solution extends across all compositions with a liquidus and solidus stretching from 2469 ^{O}C at 100 at.%Nb to 1670 ^{O}C at 100 at.%Ti with a small L + Nb_{ss} region (Okamoto 2002). At very high concentrations of Ti and relatively low temperatures, > 95 at.%Ti and < 882 ^{O}C, a hexagonal Ti_{ss} formed.

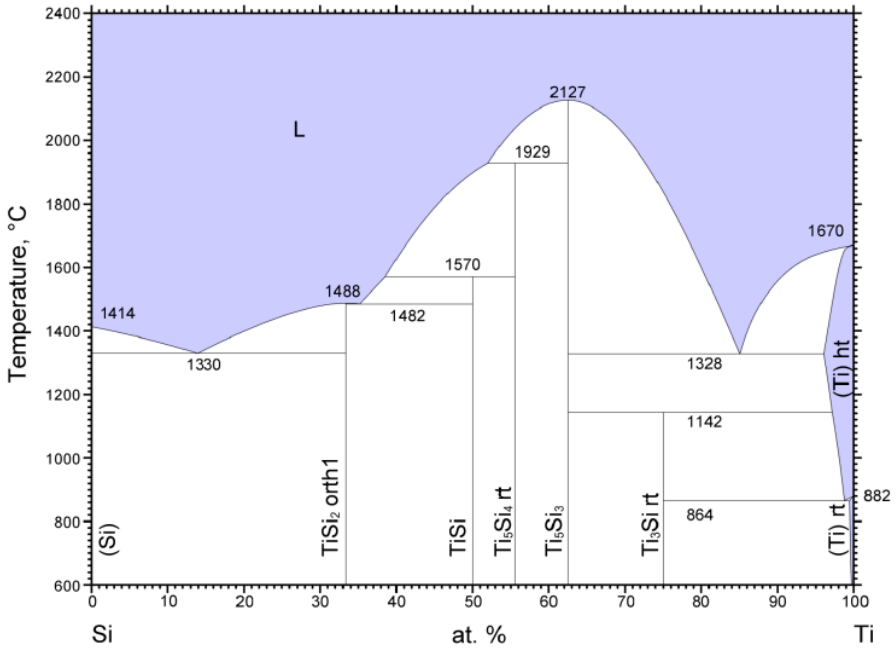

Figure 13: The phase equilibria of the Si-Ti binary system (Yang et al. 2007)

The binary phase diagram of the Ti-Si system is slightly more complex. Looking at the Ti-rich region (> 60%Ti) in Figure 13 there are four main phases and three invariant reactions of interest to this research. These reactions are:

i. $L \rightarrow Ti_5Si_3 + Ti_{ss}$ (ht) – eutectic reaction at 13.5 at.%Si and 1328 ^{O}C

ii. $Ti_5Si_3 + Ti_{ss}$ (ht) $\rightarrow Ti_3Si$ – peritectoid reaction at 25 at.%Si and 1142 ^{O}C

iii. Ti_{ss} (ht) $\rightarrow Ti_3Si + Ti_{ss}$ (rt) – eutectoid reaction at 1 at.%Si and 864 ^{O}C

The crystallographic properties of the four phases of interest to this research are shown in Table 2.

Table 2: The phases present in the Ti-Si binary system and their crystallographic properties (Meng et al. 2010; Antonova et al. 2003)

Phase	*Composition (at.%Si)*	*Pearson symbol*	*Structure*	*Prototype*	*Lattice parameter(s) (Å)*
Ti_{ss} (rt)	0 – 1.0	*hP2*	Hexagonal	Mg	a=2.9486 c=0.467
Ti_{ss} (ht)	0 – 4.5	*cI2*	BCC	W	a=3.33
Ti_3Si	25	*tP32*	Hexagonal	Ti_3P	a=10.206 c=5.069
Ti_5Si_3	37.5	*hP16*	Hexagonal	Mn_5Si_3	a=7.461 c=5.1508

Looking at the phases and invariant reactions in the Nb-Si and Si-Ti systems there seems to be some parallels. Both systems formed 5-3 and 3-1 type silicides with limited Si solubility and the Nb-Si (reaction i. § 1.2.1) and Ti-Si (reaction i. § 1.2.2.2) eutectic reactions formed a solid solution and an intermetallic. However, the Ti_5Si_3 and Nb_5Si_3 intermetallics although compositionally similar are not isomorphous, having hexagonal and tetragonal structures, respectively. Even though Nb_3Si and Ti_3Si are isomorphous they do not form in the same manner. The Nb_3Si forms via a peritectic or eutectic reaction and the Ti_3Si via a peritectoid reaction. The latter is also stable to room temperature. Finally the eutectics produce distinctly different intermetallic phases. The Nb-Si eutectic produces the Nb_3Si silicide while the Si-Ti forms the Ti_5Si_3 phase.

1.2.2.2 The Nb-Ti-Si Ternary Phase Equilibrium

Some of the earliest research on the Nb-Ti-Si system (Bewlay et al. 1997) was experimental work on ternary alloys with Si concentrations ≤ 35 at.%. Using binary phase diagrams two options were derived about the nature of the two invariant reactions in the liquidus surface. One predicted the invariant reactions;

i. $L + Nb(Ti)_5Si_3 \rightarrow (Nb,Ti)_3Si + Ti(Nb)_5Si_3$

ii. $L + (Nb,Ti)_3Si \rightarrow (Nb,Ti,Si)_{ss} + Ti(Nb)_5Si_3$

Whereas the other option predicted the invariant reactions;

iii. $L + Nb(Ti)_5Si_3 \rightarrow (Nb,Ti)_3Si + (Nb,Ti,Si)_{ss}$

iv. $L + Nb(Ti)_5Si_3 \rightarrow (Nb,Ti,Si)_{ss} + Ti(Nb)_5Si_3$

Where $Nb(Ti)_5Si_3$ denotes that Nb is substituted for Ti within the Nb_5Si_3 phase and vice versa, and $(Nb,Ti,Si)_{ss}$ denotes that all the elements are in a BCC solid solution.

Based on the results of the experimental work the first set of reactions was adopted with estimated temperature for the invariant reactions between 1600-1650 ^{O}C and 1350 ^{O}C, respectively. The experiments resulted in a phase equilibria with four phases and five monovariant reactions (monovariant reactions are represented as lines on phase equilibria as they change with a variable alteration). These reactions are;

v. $L + Nb(Ti)_5Si_3 \rightarrow Ti(Nb)_5Si_3$ – peritectic (not exhibited in either binary)

vi. $L + Nb(Ti)_5Si_3 \rightarrow (Nb,Ti)_3Si$ – peritectic (similar to reaction ii. § 1.2.1 with Ti substituting for Nb)

vii. $L \rightarrow (Nb,TI)_3 + (Nb,Ti,Si)$ – eutectic (similar to reaction i. § 1.2.1 with Ti substituting for Nb)

viii. $L + Ti(Nb)_5Si_3 \rightarrow (Nb,Ti)_3Si$ – peritectic (not exhibited in either binary)

ix. $L \rightarrow (Nb,Ti,Si) + Ti(Nb)_5Si_3$ – eutectic (similar to reaction i. § 1.2.2.1 with Nb substituting for Ti)

Subsequently, the liquidus projection shown in Figure 14 was compiled.

The above were confirmed by thermodynamic modelling (Liang & Chang 1999) and further experimental work by Jing et al. (2008). However there is one main discrepancy between the modelled and experimentally determined phase diagrams. The calculated temperature of the invariant reaction i. above was 1850 ^{O}C, 200 ^{O}C higher than that found experimentally. There was also a slight shift of the invariant reaction ii. towards the Nb-rich side of the diagram.

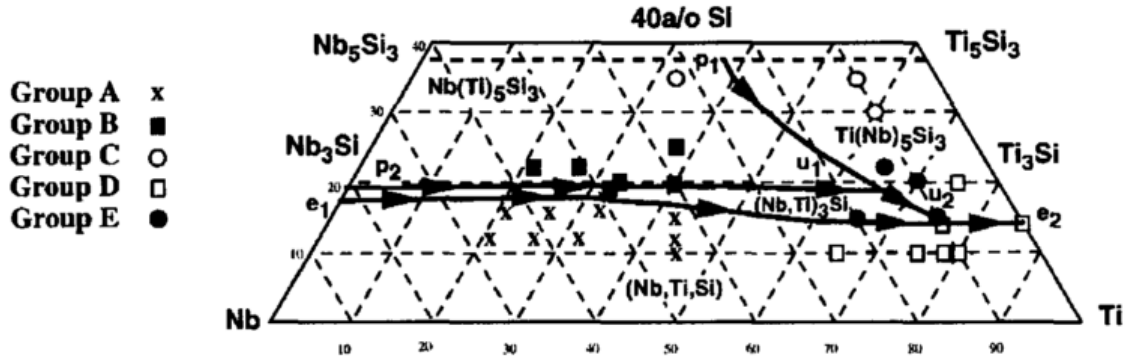

Figure 14: The prepared partial liquidus projection of the Nb-Ti-Si ternary phase diagram (Bewlay et al. 1997) *including experimental results, grouped depending on their composition. For meaning of group A – E, see paper.*

Further research has also been done on Nb-Ti-Si isothermal sections. Thermodynamic modelling was used to create isothermal sections at 1200 ^{O}C (Figure 15c), 1500 ^{O}C (Figure 15d) and 1800 ^{O}C (Liang & Chang 1999). Experimental work using diffusion multiples (Zhao et al. 2004) and directionally solidified samples (Bewlay, Jackson, et al. 1998) was used to map isothermal sections at 1000 ^{O}C, 1150 ^{O}C (Figure 15b) and 1200 ^{O}C and 1150 ^{O}C (Figure 15a), 1340 and 1500 ^{O}C (Figure 15e) respectively.

Examining the isothermal sections produced by Zhao et al. (2004) shows that as temperature increases from 1000 ^{O}C to 1200 ^{O}C the solubity of Ti in the tetragonal $Nb(Ti)_5Si_3$ increases from ≈ 20 at.% to ≈ 30 at.%. The hexagonal $Ti(Nb)_5Si_3$ on the other hand has increased solubilty of Nb from ≈ 18 to ≈ 25 at.% up to 1150 ^{O}C, which then reduces slightly at 1200 ^{O}C. This is in conflict with the 1150 ^{O}C isothermal section produced by Bewlay et al. (1998a) that showed a maximum solubility of ≈ 10 at.% Nb in $Ti(Nb)_5Si_3$ and 15 at.% Ti in $Nb(Ti)_5Si_3$. Bewlay et al. (1998a) also showed a $(Nb,Ti)_3Si$ primary phase region extending to 100 at.%Ti but Zhao et al. (2004) had a maximum Ti concentration of 85 at.%. This can be explained as the peritectiod reaction that forms Ti_3Si occurs at 1142 ^{O}C, which is very close to Bewlay et al. (1998a)'s isothermal section. As the temperature increases slightly to 1200 ^{O}C, the reaction producing Ti_3Si in the binary Ti-Si cannot occur (Figure 13), but small additions of Nb will allow the reaction to proceed. When comparing the two 1200 ^{O}C isothermal sections, there are some discrepancies between the solubilities of Ti and Nb in the 5-3 silicide phases. The modelling results, Figure 15c, show $Ti(Nb)_5Si_3$ has a maximum solubility of ≈ 10 at.%Nb whereas in the experimental

results, Figure 15b, the solubility increases to ≈ 20 at.%Nb. In the $Nb(Ti)_5Si_3$ phase the solubility of Ti was found to be ≈ 30 at.%Ti but modelling showed this to be limited to ≈ 15 at.%. This indicates that the results of Zhao et al. (2004) (modelling) do not conform with those of Bewlay et al. (1998a) (experimental) and Liang & Chang (1999). When examining the two 1500 ^{O}C isothermal sections some disparities also come to light. Bewlay et al. (1998a) show a maximum solubility of Nb in $Ti(Nb)_5Si_3$ about ≈ 15 at.% higher than calculated. Also the maximum solubility of Nb in $(Nb,Ti)_3Si$ is higher in Liang & Chang (1999) (≈70 at.%) compared to Bewlay et al. (1998a) (≈47 at.%)

1.2.3 The Nb-Si-Hf Ternary System

1.2.3.1 The Nb-Hf and Hf-Si Binary Systems

The Nb-Hf binary has many similarities to the Nb-Ti system. At temperatures and concentrations in excess of 1743 ^{O}C and 6 at.%Nb, Hf and Nb form a continuous BCC solid solution across the entire diagram (Guillermet 1996). There is a small phase field of hexagonal Hf at high concentrations of Hf and temperatures lower than 1743 ^{O}C.

Similar to the previous Ti-Si system, at the metal rich end (< 40 at.%Si), there are many phases and invariant reactions present. Looking at the phase diagram in Figure 16 (Zhao et al. 2000), 5 equilibrium phases and 4 invariant reactions are present. These reactions are:

i. $L \rightarrow \beta\text{-}Hf_{ss}(ht) + Hf_2Si$ – eutectic reaction at 11.1 at.%Si and 1828 ^{O}C
ii. $L + Hf_5Si_3 \rightarrow Hf_2Si$ – peritectic reaction at 33.3 at.%Si and 2086 ^{O}C
iii. $L + Hf_3Si_2 \rightarrow Hf_5Si_3$ – peritectic reaction at 37.5 at.%Si and 2357 ^{O}C
iv. $Hf_5Si_3 \rightarrow Hf_2Si + Hf_3Si_2$ – eutectoid reaction at 37.5 at.%Si and 1924 ^{O}C

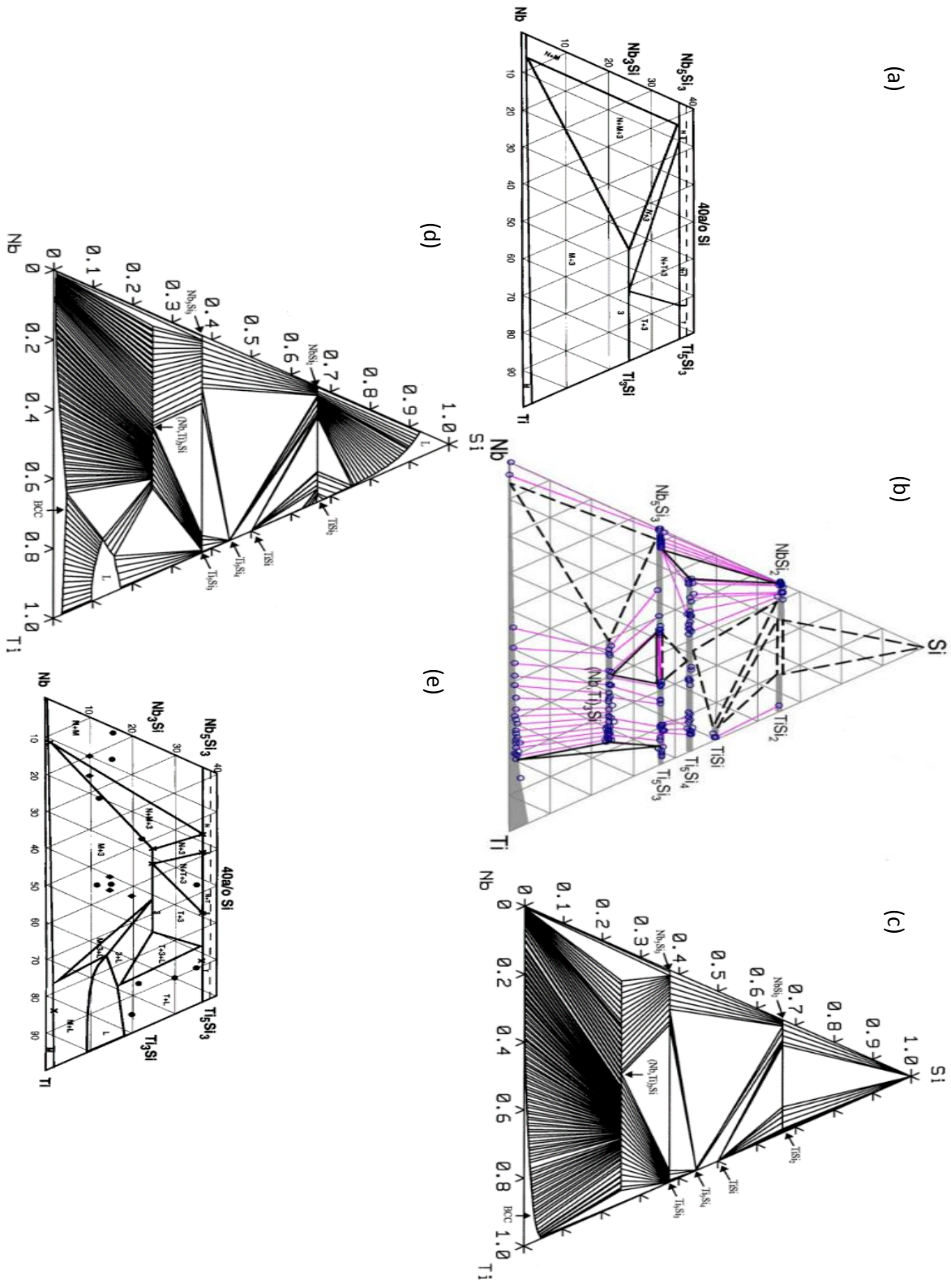

Figure 15: Showing the Nb-Ti-Si isothermal phase diagram at (a) 1150 ^{O}C (Bewlay, Jackson, et al. 1998), *(b) 1200 ^{O}C* (Zhao et al. 2004)*, (c) 1200 ^{O}C* (Liang & Chang 1999)*, (d) 1500 ^{O}C* (Liang & Chang 1999)) *and (e) 1500 ^{O}C* (Bewlay, Jackson, et al. 1998)*. Images (b), (c) and (d) republished with permission of Elsevier; permission conveyed through Copyright Clearance Center, Inc.*

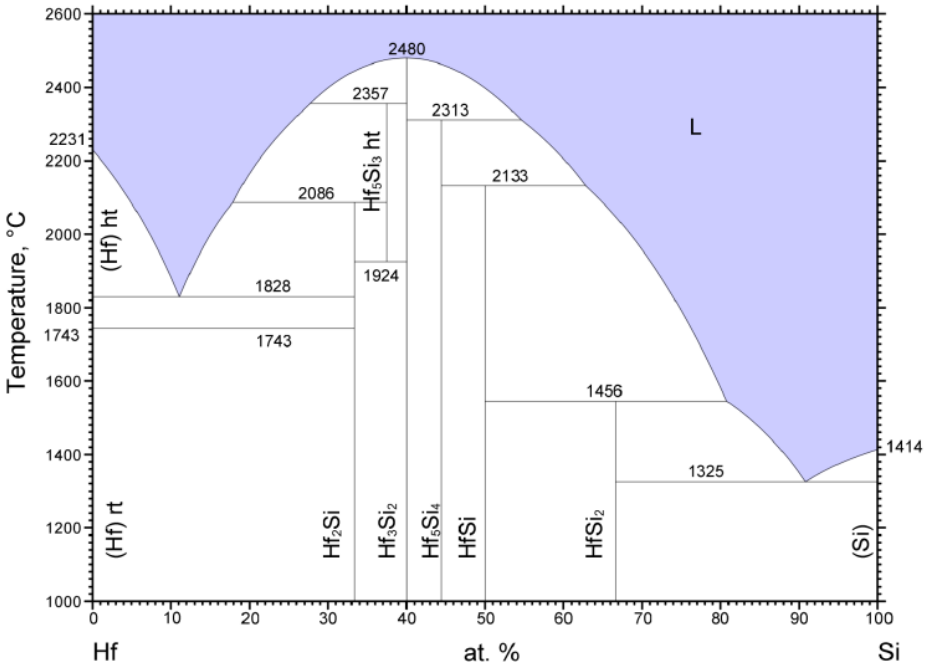

Figure 16: The phase equilibria of the Hf-Si system (Zhao et al. 2000).

The primary equilibrium phases and their crystallographic data are presented in Table 3

Table 3: The phases present in the Hf-Si system and their crystallographic properties (Zhao et al. 2000)

Phase	*Composition (at.%Si)*	*Pearson symbol*	*Structure*	*Prototype*	*Lattice parameter(s) (Å)*
β-Hf_{ss} (ht)	0	*cI2*	BCC	W	a=3.625
α-Hf_{ss} (rt)	0	*hP2*	Hexagonal	Mg	a=3.1965 c=5.058
Hf_2Si	33.3	*tI12*	Tetragonal	$CuAl_2$	a=6.553 c=5.186
Hf_5Si_3	37.5	*hP16*	Hexagonal	Mn_5Si_3	a=7.844 c=5.492
Hf_3Si_2	40	*tP10*	Tetragonal	U_3Si_2	a=6.988 c=3.675

The Hf-Si phase equilibria has also been studied using thermodynamic modelling (Yang et al. 2003). The data from this work correlated well with that presented here with any difference in temperature being less than 6 ^{O}C and no difference in composition. However, a 5th invariant reaction was proposed between the two Hf_{ss} phases;

v. β-Hf_{ss} + Hf_2Si → α-Hf_{ss} – peritectoid reaction at ≈ 0 at.%Si and 1743 ^{O}C

Early work on the Hf-Si system reasoned that the Hf_5Si_3 phase was a metastable one that only existed in the presence of N, C or O interstitials. The work of Bewlay et al. (1999) however showed that this phase exists with interstitial levels lower that 100 ppm. This work also showed good correlation in the positions of the invariant reactions within the phase diagram.

1.2.3.2 The Nb-Si-Hf Ternary Phase Equilibria

In Nb-Si-Hf there are less similarities between the phases than those presented in the Nb-Ti-Si system (see also Table 1 and Table 3). Yang et al. (2003), used CALPHAD, to model the Nb-Si-Hf liquidus projection. They showed six primary phase regions in the Nb-Hf-rich end of the phase equilibria (Si < 40 at.%Si), as shown in Figure 17. The results of the model were also backed up by some experimental results.

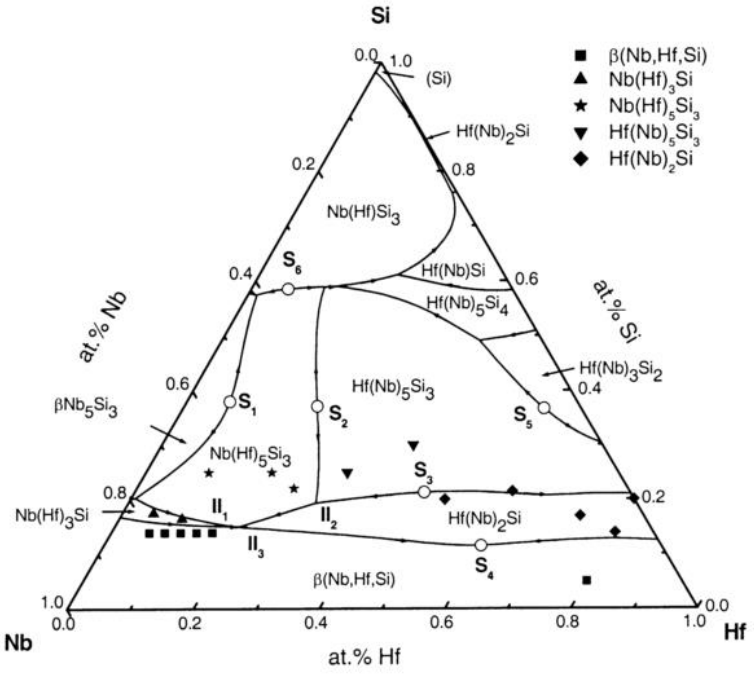

Figure 17: The calculated Nb-Si-Hf liquidus projection, including experimental results. Republished with permission of Elsevier, from (Yang et al. 2003)*; permission conveyed through Copyright Clearance Center, Inc.*

From Figure 17 it can be seen that there are three invariant reactions, labelled II_1, II_2 and II_3. Respectively, these are:

i. $L + Nb(Hf)_3Si \rightarrow Nb(Hf)_5Si_3 + \beta\text{-}(Nb,Si,Hf)_{ss}$ – liquid composition Nb-21Hf-16Si at 1850 ^{O}C

ii. $L + Hf(Nb)_5Si_3 \rightarrow Hf(Nb)_2Si + Nb(Hf)_5Si_3$ – liquid composition Nb-27Hf-22Si at 2040 ^{O}C

iii. $L + Nb(Hf)_5Si_3 \rightarrow Hf(Nb)_2Si + \beta\text{-}(Nb,Si,Hf)_{ss}$ – liquid composition Nb-26Hf-14Si at 1840 ^{O}C

These invariant reactions are connected in turn by 7 monovariant reactions.

iv. $L + \alpha\text{-}Nb(Hf)_5Si_3 \rightarrow Nb(Hf)_3Si$ – peritectic (similar to reaction ii. § 1.2.1 with Hf substituting for Nb)

x. $L \rightarrow Nb(Hf)_3Si + \beta\text{-}(Nb,Si,Hf)$ – eutectic (similar to reaction i. § 1.2.1 with Hf substituting for Nb)

v. $L \rightarrow Nb(Hf)_5Si_3 + \beta\text{-}(Nb,Si,Hf)$ – eutectic (not exhibited in either binary)

vi. $L + \alpha\text{-}Nb(Hf)_5Si_3 \rightarrow Hf(Nb)_2Si$ – peritectic (similar to reaction ii. § 1.2.3.1 with Nb substituting for Hf)

vii. $L \rightarrow Hf(Nb)_2Si + \beta\text{-}(Nb,Si,Hf)$ – eutectic (similar to reaction i. § 1.2.3.1 with Nb substituting for Hf)

viii. $L + \alpha\text{-}Nb(Hf)_5Si_2 \rightarrow Hf(Nb)_5Si_2$ – peritectic (not exhibited in either binary)

ix. $L + Hf(Nb)_5Si_3 \rightarrow Hf(Nb)_2Si$ – peritectic (similar to reaction ii. § 1.2.3.1 with Nb substituting for Hf)

Yang et al. (2003) also produced an isothermal section for the ternary equilibrium at 1500 ^{O}C (Figure 18a). The calculated phase diagram was in good agreement with the experimentally produced section (Figure 18b, (Zhao et al. 2001)).

Comparing these isothermal sections with the liquidus projections we see that the $Nb(Hf)_3Si$ phases does not exist at this temperature. Looking back at the Nb-Si binary phase diagram (Figure 11) we see that the Nb_3Si phase does not exist below 1770 ^{O}C and so would not be expected in the 1500 ^{O}C isothermal section. Comparing the Hf-Si binary (Figure 16) with the isothermal section in Figure 18b it can be reasoned that small amounts of Nb allow for increased levels of Si within the two forms of the (Nb,Si,Hf) solid solution. The phase extends up to ≈ 5 at.%Si in the ternary isotherm whereas in the binary no Si was dissolved within the Hf_{ss} in either crystallographic form

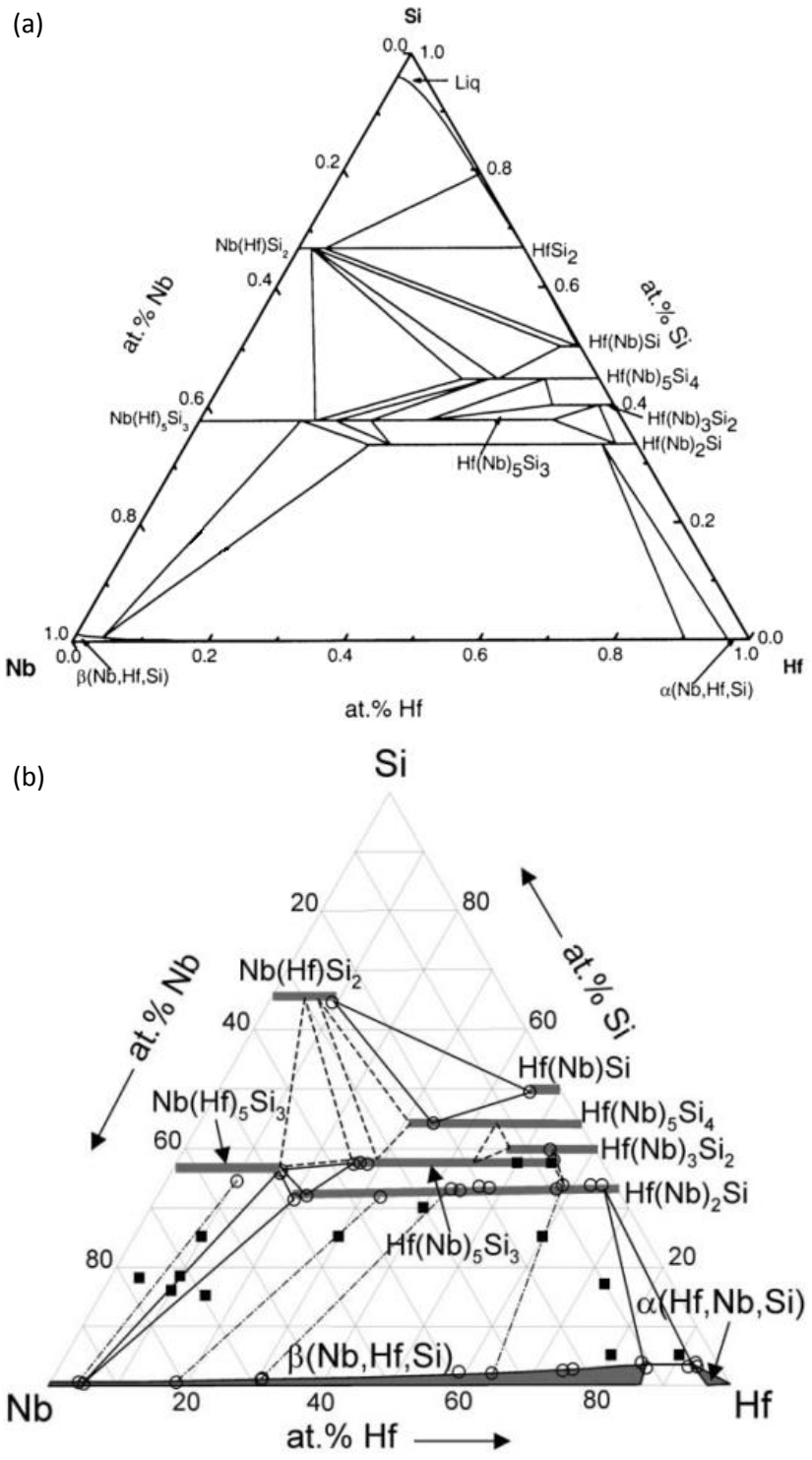

Figure 18: The 1500 ^{O}C isothermal sections from (a) thermodynamic modelling (Yang et al. 2003) *and (b) experimental data* (Zhao et al. 2001).

1.2.4 The Quaternary Nb-Si-Ti-Hf Phase Equilibrium

A partial (< 40 at.%Si) liquidus projection of the Nb-Si-Ti-Hf, created using CALPHAD and by extrapolating the four ternary diagrams (Yang et al. 2007), is shown in Figure 19.

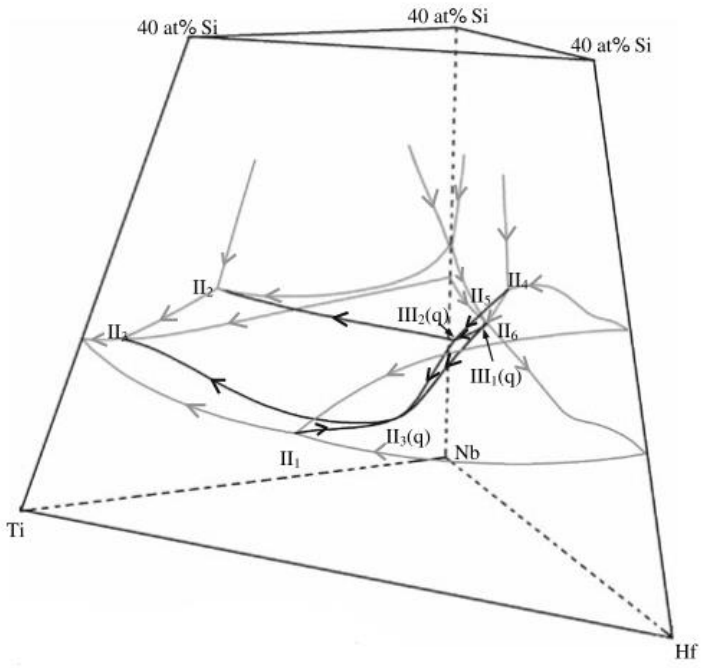

Figure 19: The partial (< 40 at.%Si) liquidus projection of the Nb-Si-Ti-Hf system (Yang et al. 2007)*, including transition reactions with four phases ($II_{1,2,4,5,6}$) and five phases (III_{1-2} and II_3) in equilibrium.*

Grey lines in the diagram represent monovariant reaction in the ternary and black lines represent the monovariant reactions (in the ternary) that have been extrapolated from the invariant reactions ($II_{1,2,4,5,6}$) in the ternary systems. The two invariant and one monovariant reactions with 5 phases in equilibrium are labelled III_1, III_2 and II_3, respectively, in Figure 19. Respectively, they are;

i. $L + (Nb,Si,Ti,Hf)_{ss} + \alpha\text{-}Nb(Ti,Hf)_5Si_3 \rightarrow Hf(Ti,Nb)_2Si + (Nb,Ti)_3Si$ – at 1814 ^{O}C

ii. $L + Hf(Ti,Nb)_2Si + \alpha\text{-}Nb(Ti,Hf)_5Si_3 \rightarrow (Hf,Ti)_5Si_3 + (Nb,Ti)_3Si$ – at 1739 ^{O}C

iii. $L + Hf(Ti,Nb)_2Si \rightarrow (Nb,Ti,Hf,Si)_{ss} + (Hf,Ti)_5Si_3 + (Nb,Ti)_3Si$ – at 1400 ^{O}C

From the sequence of invariant reactions it is predicted that the overall “temperature slope” of the liquidus is at a maximum in the Nb-Hf-Si-rich region and decreases to the Nb-Ti-Si region. Twelve alloys were directionally solidified to determine the validity of the above phase diagram. The as-cast

microstructures seemed to prove that the projection shown in Figure 19 accurately represents the liquidus projection for this section of the quaternary diagram. The authors stated that further work must be done to confirm the positions of the reaction i., ii. and iii..

1.2.5 The Nb-Si-Mo Ternary System

1.2.5.1 The Nb-Mo and Si-Mo Binary Systems

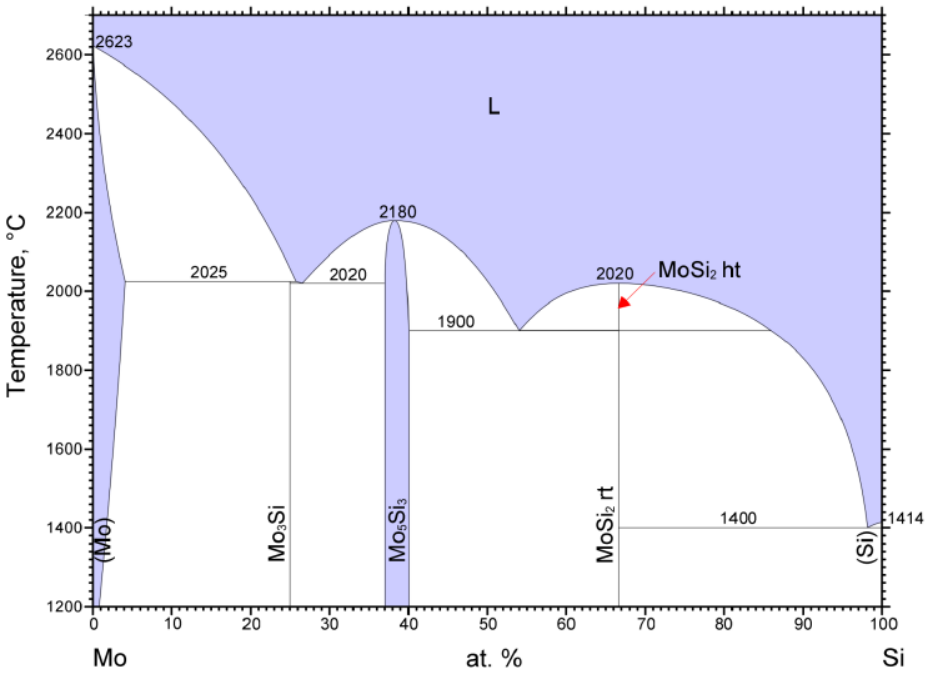

Figure 20: The phase equilibria of the Mo-Si system (Gokhale & Abbaschian 1990).

The Nb-Mo binary system (Wang & Sundman 2000) is simple. There is a small two phase region of L + $(Nb,Mo)_{ss}$ between the temperatures of 2623 ^{O}C at 0 at.%Nb and 2469 ^{O}C at 100 at.%Nb. Below the solidus is a $(Nb,Mo)_{ss}$ BCC single phase region at all compositions and temperatures.

The Mo-Si binary system, Figure 20, has 3 phases and 2 invariant reactions in the region of interest (< 40 at.%Si). Theses invariant reactions are:

i. L + Mo_{ss} → Mo_3Si – peritectic reaction at 25 at.%Si and 2025 ^{O}C

ii. L → Mo_3Si + Mo_5Si_3 – eutectic reaction at 26.4 at.%Si and 2020 ^{O}C

The phases present and their crystallographic data is shown in Table 4.

Table 4: The phases present in the Mo-Si system and their crystallographic properties (Gokhale & Abbaschian 1990).

Phase	*Composition (at.%Si)*	*Pearson symbol*	*Structure*	*Prototype*	*Lattice parameters (Å)*
Mo_{ss}	0 – 4	*cI*2	BCC	W	a=3.147
Mo_3Si	25	*cP8*	Cubic	Cr_3Si	a=4.897
Mo_5Si_3	37 - 40	*tI*12	Tetragonal	W_5Si_3	a=9.65 c=4.911

There are many similarities between the Mo-Si and Nb-Si binary phase diagrams. Both have exhibited a BCC solid solution with limited, temperature dependent, solubility of Si. The Mo_5Si_3 is isomorphous with the β-Nb_5Si_3. The Mo_3Si is formed by a peritectic reaction with liquid and Mo_{ss} but the Nb_3Si is formed by a eutectic, these silicide phases are non-isomorphous.

1.2.5.2 The Nb-Mo-Si Ternary Phase Equilibrium

There is limited literature on the Nb-Mo-Si ternary system. However experimental work of Ma et al. (2000) has helped to gain a better understanding of this system. The liquidus projection proposed by Ma et at. (2000) is shown in Figure 21.

As would be expected the isomorphous phases (i.e. the 5-3 silicides and the solid solution) β-$(Nb,Mo)_5Si_3$ and $(Nb,Mo,Si)_{ss}$, extend from the Nb-Si-rich side to the Mo-Si-rich end of the diagram. There are only two other phases within this area of the diagram, $Nb(Mo)_3Si$ and $Mo(Nb)_3Si$. Within the system there are two invariant reactions, U_1 and U_2 shown in Figure 21. These are respectively:

i. $L + Mo(Nb)_3Si \rightarrow \beta\text{-}(Nb,Mo)_5Si_3 + (Nb,Mo,Si)_{ss}$

ii. $L + \beta\text{-}(Nb,Mo)_5Si_3 \rightarrow Nb(Mo)_3Si + (Nb,Mo,Si)_s$

There are also 5 monovariant reactions:

iii. $L \rightarrow (Nb,Mo,Si)_{ss} + Nb(Mo)_3Si$ – eutectic (similar to reaction i. in § 1.2.1 with Mo substituting for Nb)

iv. $L + \beta\text{-}(Nb,Mo)_5Si_3 \rightarrow Nb(Mo)_3Si$ – peritectic (similar to reaction iii. In § 1.2.1 with Mo substituting for Nb)

v. $L \rightarrow \beta\text{-}(Nb,Mo)_5Si_3 + (Nb,Mo,Si)_{ss}$ – Not exhibited in either binary

vi. $L + (Nb,Mo,Si)_{ss} \rightarrow Mo(Nb)_3Si$ – peritectic (similar to reaction i. in § 1.2.5.1 with Nb substituting for Mo)

vii. $L \rightarrow Mo(Nb)_3Si + \beta\text{-}(Nb,Mo)_5Si_3$ – eutectic (similar to reaction ii. In § 1.2.5.1 with Nb substituting for Mo)

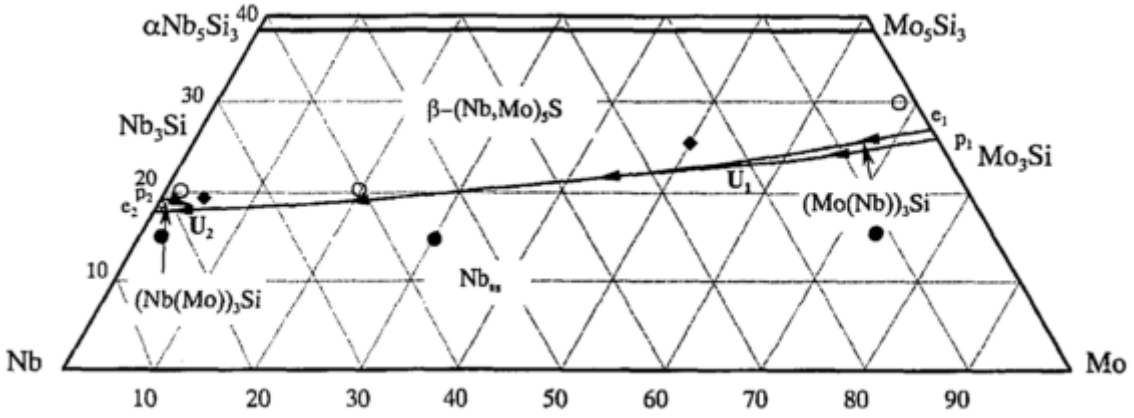

Figure 21: The partial liquidus projection of the Nb-Mo-Si system including experimental results. Nbss in this diagram is defined as (Nb,Mo,Si)ss in the rest of this report. The liquidus diagram shows the phase β-(Nb,Mo)5S, this is a mistake and is named within the text as β-(Nb,Mo)5Si3. Republished with permission of Japanese Institute of Metals and Materials, from (Ma et al. 2000).

There is small solubility of Mo in $Nb(Mo)_3Si$, and alloys with more than 3 at.%Mo did not show $Nb(Mo)_3Si$ in the cast microstructure. This is in contradiction to the effect of Ti and Hf additions where $Nb(X)_3Si$ is stabilised in the liquidus over the solubility ranges of 0-75 at.%Ti and 0-18 at.%Hf. The experimental work showed EDS data for concentrations of up to 5.2 at.%Si in the $(Nb,Mo,Si)_{ss}$ phase, this has not been included in Figure 21. Ma et al. (2000) attributed this solubility to be a result of solidification not allowing enough time for the diffusion of Si and therefore is not the equilibrium solubility. Both the binary Nb-Si and Mo-Si however do have small amounts of Si in their respective solid solutions. Therefore it can be assumed that there is some level of silicon in the equilibrium $(Nb,Mo,Si)_{ss}$.

An isothermal section at 1700 ^{O}C was proposed Ma et al. (2000), Figure 22.

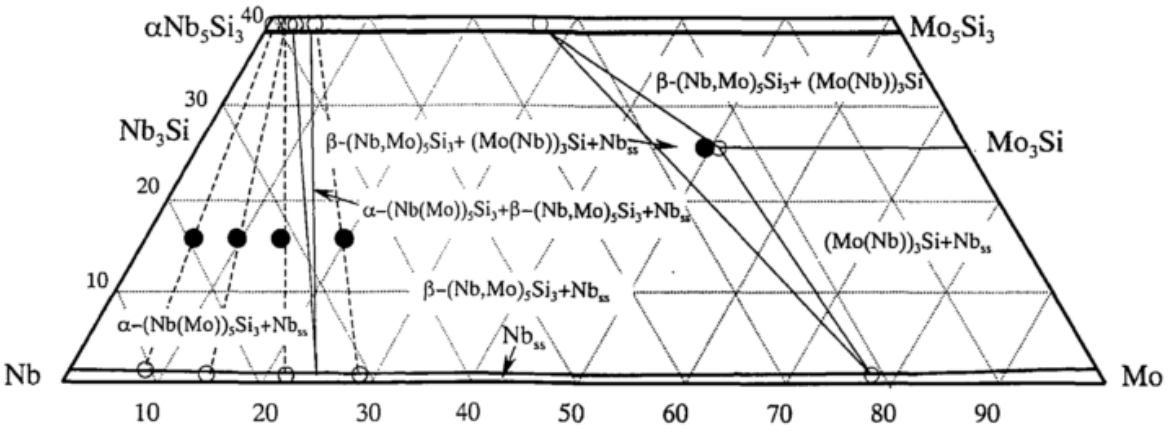

Figure 22: The partial isothermal section of the Nb-Mo-Si system at 1700 ^{O}C including experimental results. Nb_{ss} in this diagram is defined as $(Nb,Mo,Si)_{ss}$ in the rest of this report. Republished with permission of Japanese Institute of Metals and Materials, from (Ma et al. 2000).

At this temperature there is no Nb_3Si present, which is expected from the binary Nb-Si. On the other hand, there is the α-$Nb(Mo)_5Si_3$ phase present. The phase is present in alloys with composition of up to 25 at.%Mo if the silicon concentration is sufficiently low. The size of the α-$Nb(Mo)_5Si_3$ single phase region is thought to be small with a maximum solubility of only 1.5 at.%Mo at this temperature. The isothermal section also shows $(Nb,Mo,Si)_{ss}$ having a solubility of ≈ 2 at.%Si.

1.2.6 The Nb-Si-W Ternary Diagram

1.2.6.1 The Nb-W and Nb-Si Binary Systems

The Nb-W system is very similar to the Nb-Mo system. There is a two phase region between the liquidus and the solidus lines that extends from 2469 ^{O}C at 0 at.%W and 3422 ^{O}C at 100 at.%W. At temperatures below the solidus at all compositions there exists a single phase region of BCC $(Nb,W)_{ss}$.

Within the area of interest (< 40 at.%Si) the Si-W system shown in Figure 23 has only two phases and one invariant reaction. The invariant reaction is:

i. $L \rightarrow W_{ss} + W_5Si_3$ – eutectic reaction at 31.5 at.%Si and 2180 ^{O}C

The crystallographic data of the two phases are shown in Table 5.

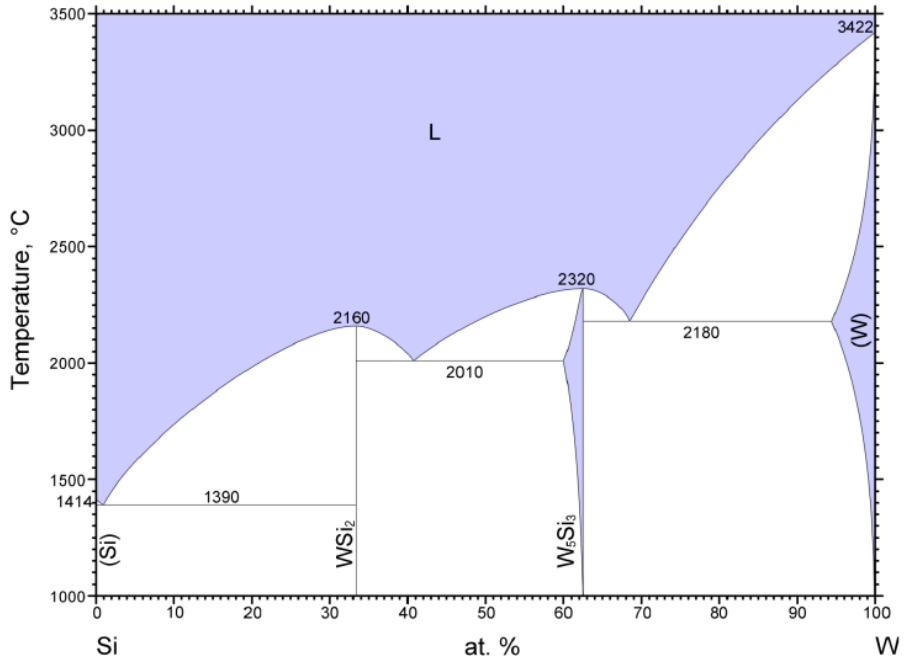

Figure 23: The phase equilibria of the Si-W system (Naidu 1990).

Comparing the phases in the Nb-Si and the W-Si binary shows that the solid solution phases are isomorphous and have limited, temperature depended, solubility of silicon. The W_5Si_3 and β-Nb_5Si_3 phases are isomorphous.

Table 5: The phases present in the W-Si system and their crystallographic properties (Naidu 1990).

Phase	*Composition (at.%Si)*	*Pearson symbol*	*Structure*	*Prototype*	*Lattice parameter(s) (Å)*
W_{ss}	0 – 5.5	*cI*2	BCC	W	a=3.1649
W_5Si_3	37.5 - 40	*tI*32	Tetragonal	W_5Si_3	a=9.645 c=4.97

1.2.6.2 The Nb-Si-W Ternary Phase Equilibria

There is limited data on this system. The experimental work of Ma et al. (2002) proposed a partial liquidus projection and an isothermal section at 1700 ^{O}C for the Nb-W-rich section. The liquidus projection is shown in Figure 24.

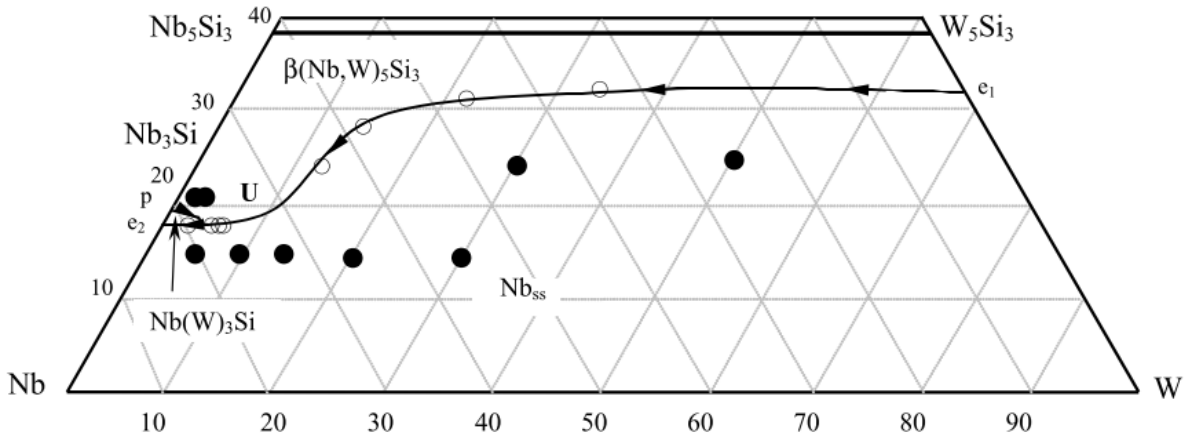

Figure 24: The partial liquidus projection of the Nb-W-Si system including experimental results. Nb_{ss} in this diagram is defined as $(Nb,W,Si)_{ss}$ in the rest of this report. Republished with permission of Japanese Institute of Metals and Materials, from (Ma et al. 2002).

As would be expected, there are two large regions across the entire partial liquidus projection where the $(Nb,W,Si)_{ss}$ and β-$(Nb,W)_5Si_3$ are the primary phases. There is only one other phase present, namely the $Nb(W)_3Si$, which has a small primary phase field at the Nb-Si–rich side with only a small solubility of W. There is only one invariant transition reaction in this partial liquidus projection:

i. $L + \beta\text{-}(Nb,W)_5Si_3 \rightarrow Nb(W)_3Si + (Nb,W,Si)_{ss}$

There are 3 monovariant reactions in this section:

ii. $L + \beta\text{-}Nb(W)_5Si_3 \rightarrow Nb(W)_3Si$ – peritectic reaction similar to reaction ii. In § 1.2.1 with W substituting for Nb.

iii. $L \rightarrow Nb(W)_3Si + (Nb,W,Si)_{ss}$ – eutectic reaction similar to reaction i. in § 1.2.1 with W substituting for Nb.

iv. $L \rightarrow (Nb,W,Si)_{ss} + \beta\text{-}Nb(W)_5Si_3$ – eutectic reaction similar to reaction i. § 1.2.6.1 with Nb substituting for W.

Tungsten additions to the Nb-Si system have more similarities to the addition of molybdenum than titanium and hafnium. There was only a small region of W where the $Nb(W)_3Si$ exists and alloys with concentrations above 3 at.%W do not show $Nb(W)_3Si$. There was a large eutectic valley between the $(Nb,W,Si)_{ss}$ and β-$Nb(W)_5Si_3$. However, whereas the 5-3 and solid solution eutectic valley in the Nb-

Mo-Si system was unique to the ternary, the same eutectic is present in the Si-W system (Figure 23). The eutectic valley showed a sharp change towards the Si region, at W concentrations of 10 -15 at.%. It was suggested (Ma et al. 2004) that this will have a big effect on the solidification of Nb-Si-W alloys.

A partial isothermal section of the Nb-Si-W equilibria at 1700 ^{O}C is shown in Figure 25. Again, similar to the Nb-Si-Mo isotherm, α-Nb(W)$_5$Si$_3$ has a low solubility of W. Maximum concentrations of W in this phase were found to be in the region of 2 at.%W. The two phase region including α-Nb(W)$_5$Si$_3$, is much larger in this system extending out to include alloy compositions over 50 at.%W when silicon concentrations are sufficiently low.

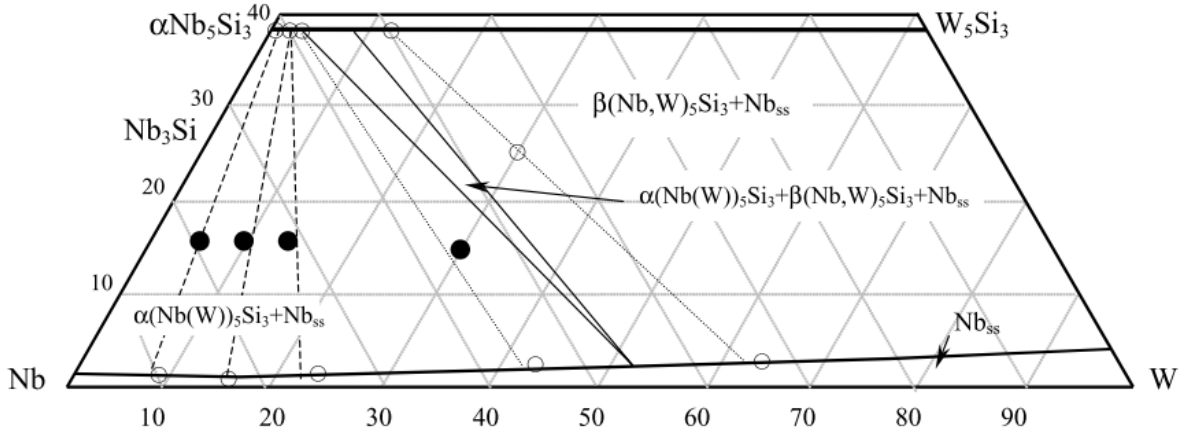

Figure 25: The partial isothermal section of the Nb-W-Si system at 1700 ^{O}C including experimental results. Nb$_{ss}$ in this diagram is defined as (Nb,W,Si)$_{ss}$ in the rest of this report. Republished with permission of Japanese Institute of Metals and Materials, from (Ma et al. 2002).

1.3 SOLIDIFICATION OF NB-SI BINARY ALLOY

1.3.1 Nb-Si Binaries near Alloys the Eutectic Composition

Abbaschian & Lipschutz (1997) studied Nb-Si binaries near the Nb-Si eutectic. They were able to undercool and quickly quench the alloys, which enabled them to study the coupled zone. Nb-15Si alloy was undercooled 80 K below the T_{eut} and quenched. The study of the microstructure that was supported by EDS data showed that a fine anomalous eutectic had formed at the quenched surface. An example (Abbaschian & Lipschutz) of an anomolous Nb-Si eutectic is shown in Appendix A, Figure 1. It's composition was 15 at.%Si, i.e., 3.7% lower than the "accepted" eutectic composition, see § 1.2.1. The microstructure indicated that the eutectic had grown within the coupled zone. Moving away from the quenched surface the morphology altered to one consisting of primary Nb_{ss} dendrites with an interdendritic eutectic which was the expected microstructure at this composition. The hypereutectic alloy Nb-20Si was undercooled 390 K below T_{eut} and quenched. Eutectic cells of fine Nb_{ss}/Nb_3Si lamellae were observed in the sample with no difference at the quenched surface. This was in contrast to the equilibrium solidification of a hypereutectic Nb-Si alloy, which depending on the initial composition, can have primary dendrites of Nb_3Si or β-Nb_5Si with a peritectic Nb_3Si (Bewlay et al. 1995). The composition of the eutectic was deemed to be the same as the initial alloy composition.

Using the experimental data and solidification theory Abbaschian & Lipschutz (1997) derived the coupled zone shown in Figure 26a. The diagram shows how undercooling affects coupled growth at ≈ 16 at.%Si (red line). Samples with very high and low undercoolings showed uncoupled growth while those with mid range undercoolings showed coupled growth.

The metastable $Nb_{ss}/β\text{-}Nb_5Si_3$ eutectic was initially found in work done on rapidly solidified Nb-Si alloys using melt-spinning (Bendersky et al. 1987). Where undercooling of $0.19T_{eut}$ was achieved in the melt which did not nucleate homogeneously. Bendersky et al. (1987) proposed that the metastable eutectic point is 19 at.%Si. Abbaschian & Lipschutz (1997) formed a metastable $Nb_{ss}/β\text{-}Nb_5Si_3$ eutectic in an undercooled alloy of hypoeutectic composition. This metastable eutectic was

attributed to Nb_{ss}/Nb_3Si eutectic growth being kinetically limited by the recalesence of the primary Nb_{ss}. The liquid therefore continued to become richer in Si concentration with the growth of the Nb_{ss}. This led to the liquid entering the metastable Nb_{ss}/Nb_5Si_3 coupled zone Figure 26b. Studies of undercooled Nb-Si alloys (Wang et al. 2006; Kashyap et al. 2013a) showed that this metastable eutectic would form at undercooling predicted to be as high as 480 K.

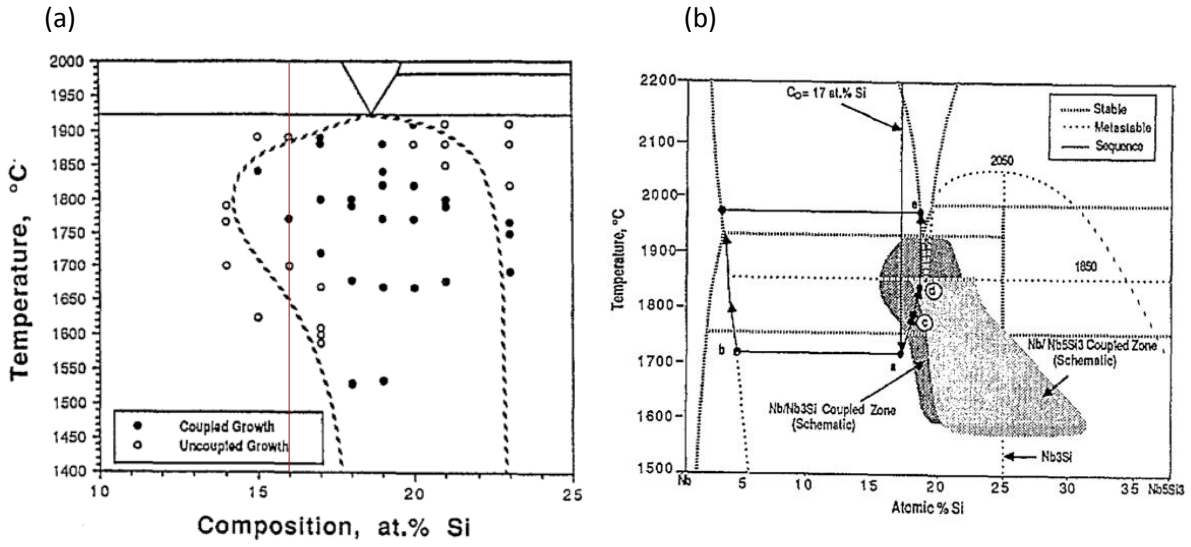

Figure 26: Phase diagrams showing (a) the theoretically stable Nb_{ss}/Nb_5Si_3 coupled zone represented by the dashed line and how the experimental data (points) aligns with it, (b) both the metastable Nb_{ss}/Nb_5Si_3 (light contrast) and stable Nb_{ss}/Nb_3Si (dark contrast) coupled zones. Republished with permission of Elsevier, from (Abbaschian & Lipschutz 1997)*; permission conveyed through Copyright Clearance Center, Inc.*

The growth of eutectic from primary phases was examined by Kashyap et al. (2013a). In a hypereutectic alloy where the Nb_3Si was the primary phase the eutectic tended to grow directly from the Nb_3Si dendrites. However, in hypoeutectic alloys the primary phase (Nb_{ss}) was surrounded by a thin shell of Nb_3Si before the eutectic would nucleate and grow. This work also showed a variation in eutectic lamellar spacing with variation in Si content. In hypoeutectic alloys the spacing remained relatively constant at ≈ 600 nm in the as-cast condition. Increasing the silicon content past the eutectic point reduced the spacing dramatically to ≈ 225 nm at 25 at.%Si. No explanation was presented for the variation in spacing in this work, but the formation of the β-Nb_5Si_3 phase, which was not present in the hypoeutectic alloys, could be a possible reason.

1.3.2 Nb-Si Binaries near the Eutectoid Composition

Not only eutectics, but eutectoids can also be used to produce fine lamellar structures in the Nb-Si binary alloy system. As seen in reaction iii. § 1.2.1 the Nb_3Si silicide, through a solid state eutectoid reaction, forms Nb_{ss} + α-Nb_5Si_3 at 25 at.%Si and 1770 ^{O}C.

Early studies to determine the temperature at which this reaction takes place were uncertain (Schlesinger et al. 1993). Estimates of the reaction temperature vary from 1660 ^{O}C (Mendiratta & Dimiduk, 1991) to 1770 ^{O}C (Okamoto 2005). This is due to extremely slow kinetics of the system taking roughly 100 hrs at 1500 ^{O}C to generate the typical Nb_{ss} + α-Nb_5Si_3 lamellar structure (Bewlay et al. 1995).

Miura et al. (2007) studied the eutectoid reaction in the Nb-Si binary system to determine whether an optimum microstructure could be gained through eutectic and eutectoid reactions. The target microstructure was a Nb_{ss} matrix with evenly dispersed Nb_5Si_3, similar to that of nickel based superalloys. They aimed for the solidification sequence;

$$L \rightarrow (Nb_{ss} + Nb_3Si)_{eut} \rightarrow Nb_{ss} + (Nb_{ss} + \alpha\text{-}Nb_5Si_3)_{eutectoid}$$

The eutectoid transformation would mean the decomposition of Nb_3Si creating the optimised microstructure. Hyper- and hypo-eutectic alloys (25 and 16 at.%Si, respectively) were doped with Mg to decrease the time at the nose temperature of the reaction from 100 to 20 hrs at 1500 ^{O}C. The final microstructure, although not optimised as the authors would have liked, showed some interesting features. In the hypoeutectic alloy the rods of the Nb_{ss} formed during the eutectic reaction were found to have the same orientation relationship as the Nb_{ss} formed in the eutectoid reaction. This gave the appearance of a “single grain” matrix structure. This work was then extended (Miura et al. 2009) and small amounts of Zr (1.5 at.%) were added to binary alloys as it was found that this also quickened the eutectoid reaction. The effect of Mg and Zr additions as well as Ti can be seen in the Time-Temperature transformation diagram in Figure 27.

This work showed that Mg addition not only decreased the time of the reaction but also increased the spheroidization of the Nb_5Si_3. Due to this beneficial effect on the eutectoid reaction Tiwary et al. (2013) looked at the effect of Mg on material properties. It was shown that Mg also promoted an orthorhombic δ-$Nb_{11}Si_4$ phase to precipitate within the Nb_{ss} with a coherent interface. The Mg containing alloy showed improved oxidation resistance with the weight gain being reduced by ≈ 10 % after an hour at 1000 ^{O}C. There were also large increases in strength and ductility compared with binary alloys at room temperature and 700 ^{O}C.

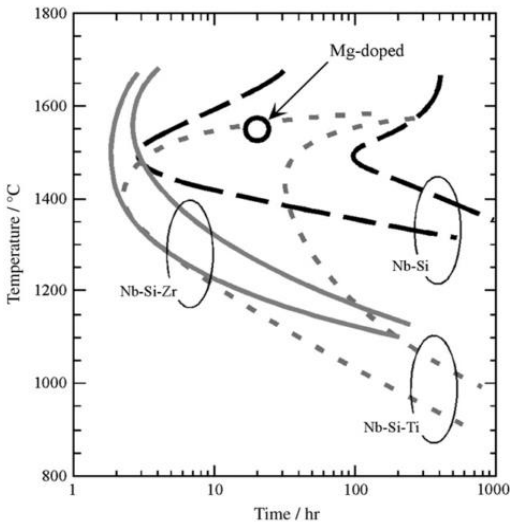

Figure 27: The TTT diagram for the eutectoid transformation of Nb_3Si in Nb-si binary alloy and in Nb-rich ternaries with Ti, Mg and Zr additions. Republished with permission of Elsevier, from (Miura et al. 2007); permission conveyed through Copyright Clearance Center, Inc.

1.3.3 Nb-Si Binaries near the Peritectic Composition

As can be seen from reaction ii. § 1.2.1 and Figure 11 the peritectic reaction in Nb-Si binary alloys produces the β-Nb_5Si_3 and Nb_3Si silicides with the former being the core surrounded by a shell of the latter. This reaction is the least examined. The double silicide based microstructure does not have the Nb_{ss} phase to increase ductility and toughness.

Kashyap et al. (2013a) studied binary alloys with composition near the peritectic reaction (Nb-18.9Si). They produced the expected peritectic morphology and after heat treatment the Nb_3Si transformed eutectoidally producing a microstructure consisting of β-Nb_5Si_3 surrounded by lamellar

Nb_{ss} + α-Nb_5Si_3. In this peritectic/eutectoid formation the Nb_5Si_3 had a higher toughness (K_q = 6.4 $MPa.m^{1/2}$) compared with its intrinsic value (K_q = 3.4 $MPa.m^{1/2}$), (Sekido et al. 2004). The lamellar peritectic/eutectoid morphology was given as the primary reason for the increase in the toughness.

1.4 Fracture and Strength of Nb-Si Alloys

The fracture of Nb silicide based alloys usually occurs in three main steps (Chan 2002).

1. Cracking of the silicide phase: This usually initially takes the form of microcracks (Chan & Davidson 2003) beginning at grain boundaries or triple points (Sha, Hirai, Ueno, et al. 2003b). This is due to the significantly lower toughness of the silicide phase compared with the solid solution phase.
2. These microcracks widen and form the main crack. The latter will eventually come in contact with the more ductile Nb_{ss} phase, blunting the tip. The adjacent silicide grains however will begin to form microcracks parallel to the crack direction, leaving the Nb_{ss} bridging the main crack and the toughening of the entire system occurs by lowering the crack tip intensity factor.
3. Increasing the stress on the system causes plastic deformation of the toughening Nb_{ss} and eventually failure of the bridge and the test piece.

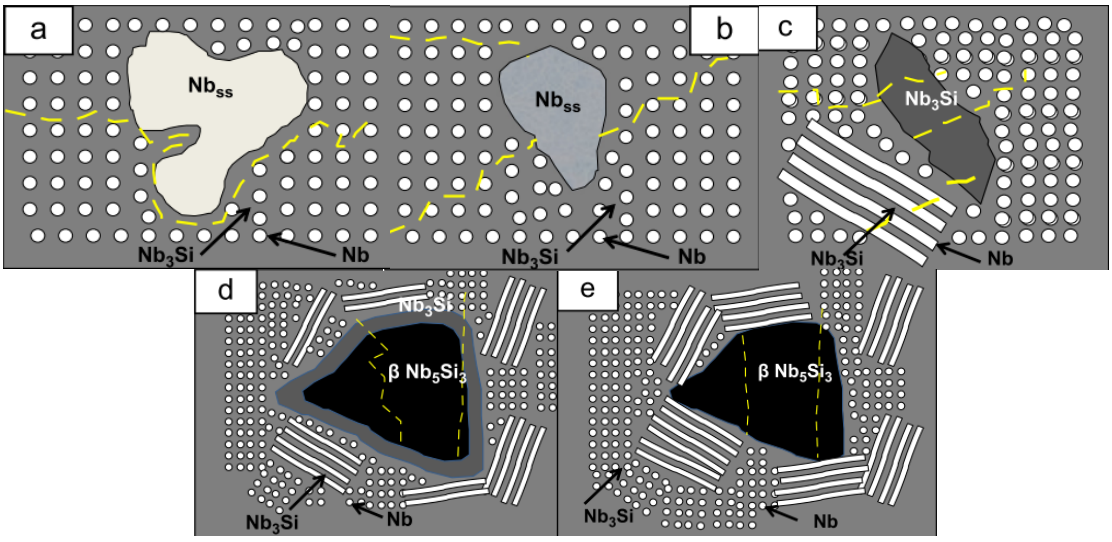

Figure 28: Schematic diagram showing how a crack is perceived to grow through different phases and microstructures. Republished with permission of Elsevier, from (Kashyap et al. 2013a)*; permission conveyed through Copyright Clearance Center, Inc.*

Although crack bridging is thought to be one mechanism improving crack resistance, there is evidence of other mechanisms that increase the fracture toughness. It was noted that in hypoeutectic alloys crack deflection occurred around the large primary Nb_{ss} grains (Kim et al. 2001; Kashyap et al.

2013a). These reports also noted toughening phase bridges forming and toughening phase pull out, especially in lamellar eutectics. In eutectic areas consisting of Nb_{ss} rods embedded in the silicide (the predominant morphology of Nb_{ss}/Nb_3Si eutectics) the cracks proceeded through the matrix avoiding the eutectic Nb_{ss}, see Figure 28.

Fracture toughness of Nb silicide based alloys decreases with increasing levels of silicon (Li & Peng 2007). In this work it was noted that as the silicon in the alloys increased from 11 to 18 at.% the fracture toughness decreased from 13 to 8.5 $MPa.m^{1/2}$. The main reason for this was the increased volume fraction (V_f) of the brittle silicide. The fracture surfaces of the alloys with higher silicon concentrations (18 at.%Si) showed entirely brittle fracture, whereas the alloys with lower silicon levels (11 and 16 at.%Si) showed signs of plastic deformation of the Nb_{ss} before catastrophic failure. Debonding at the interfaces was also evident at the fracture surface of all the alloys. The effect of increased V_f of silicide on fracture toughness was noted in other work on binary systems (Chan & Davidson 2003), see Figure 29.

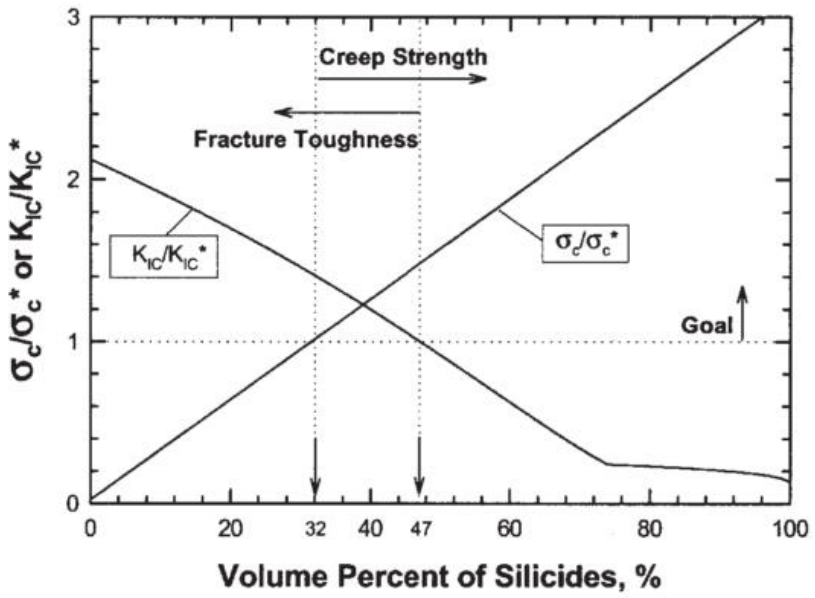

Figure 29: Variation of fracture toughness and strength of Nb silicide based alloys with volume fraction of the silicide phase. Fracture toughness and strength are shown as a ratio to the ideal goal. Republished with permission of Elsevier, from (Chan & Davidson 2003)*; permission conveyed through Copyright Clearance Center, Inc.*

There are two main strengthening mechanisms acting in Nb-Si alloys; hard phase strengthening and solid solution strengthening, both of which depend on the concentration of Si. Increases in the Si content of the alloys up to ≈ 2 at.% increases the strength of the material by solid solution strengthening. However, due to the low solubility of Si in the Nb_{ss} (see Figure 11) further increases in Si increase the silicide V_f and therefore the hard phase strengthening mechanism become important (Kim et al. 2001). Li & Peng (2007) showed that the hardness increased from 2.61 to 3.75 GPa as the Si increased from 11 to 18 at.%Si.

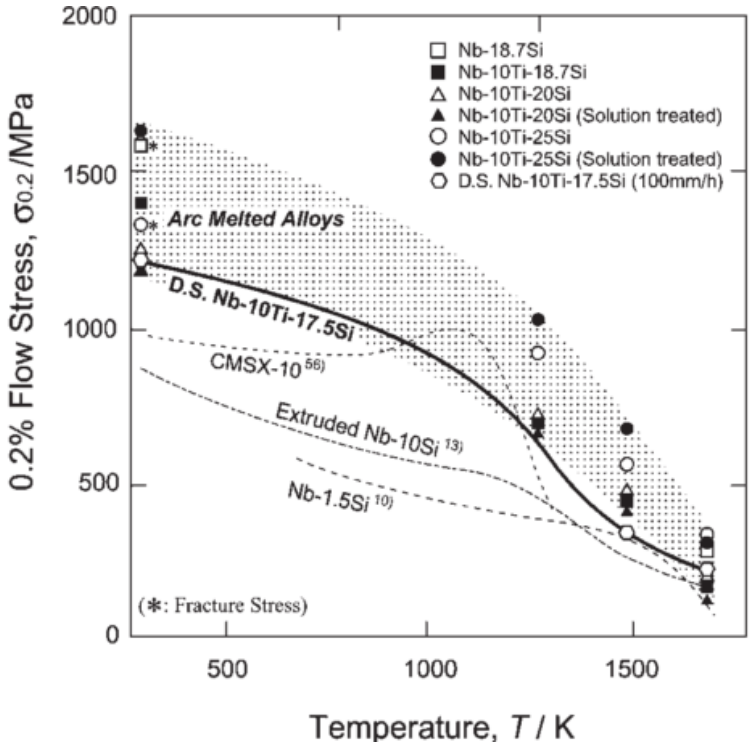

Figure 30: Variation of strength with Si concentration and temperature. Republished with permission of Japanese Institute of Metals and Materials, from (Sekido et al. 2004).

At high temperatures the strength increases by increasing additions of Si (0-10 at.%Si) due to the silicide acting as a hard phase strengthener (Sha, Hirai, Ueno, et al. 2003b). This was also noted in ternary Nb-Si alloys containing Ti. An addition of 1 at.%Si to pure Nb increased the hardness from ≈ 100 Hv to ≈ 300 Hv (Sekido et al. 2004). Increased additions to 4 at.%Si however had very little effect on the hardness. This showed that the solid solution strengthening effect of Si at low volume fractions of silicide is much more potent than hard phase strengthening. However, the latter was much more

effective at higher temperatures and higher Si concentrations. Figure 30 illustrates the variation in strength over a range of temperatures and Si concentrations. It shows that the binary Nb-18.7Si alloy out performs the Nb-1.5Si alloy over the entire range of temperatures (Sekido et al. 2004). Increased strength with increased V_f of silicide was also shown by Li & Peng (2007) who studied the compressive strength of alloys with varying Si concentrations. At 11 and 18 at.%Si the compressive strength at a strain rate of 2.8×10^{-5} s^{-1} was 770 and 994 MPa, respectively. Improvement in fracture behaviour and strength were sought via alloying. We have already seen the affect of Ti additions on strength in Figure 30. In the next section the effect of key alloying additions on microstructure and properties are briefly reviewed.

1.5 Effect of Alloying Additions

1.5.1 Titanium

1.5.1.1 Microstructural Effects

The addition of titanium benefits mechanical properties and oxidation. Most literature has focused on slightly hyper- and hypo-eutectic compositions as these are perceived to have the most beneficial microstructure for the ternary system to be used for further alloy development. As can be seen in Figure 14 the $(Nb,Ti)_3Si/(Nb,Ti,Si)_{ss}$ eutectic has a constant Si concentration for Ti concentration in the range 0 to 40 at.%.

"Directional" solidification using OFZ processing of Nb-17.5Si-xTi alloys (x=0,2,5,10) examined the effect that Ti had on eutectic solidification (Sekido et al. 2007). The 17.5 at.%Si concentration was used as it was determined by the authors in a previous study (Sekido et al. 2004) to be the eutectic point for the levels of Ti tested. The eutectic morphology was Nb_{ss} plates/rods in a Nb_3Si matrix, similar to that of Nb-Si binary alloys. At the slowest growth rate (10 mm/hr) the microstructure of the binary alloy was extremely regular and had intercellular products; indicating eutectic growth with a planer front. In the Ti containing alloys the regular structure did not form at 10 mm/hr, instead the structure consisted of fine two phase cellular regions with a coarser two phase region surrounding the finer region. An explanation for this put forward by the author is two-phase instabilities forming in the S/L front caused by the build-up of a third element ahead of the front. Sekido et al. (2004) also explained the non-planar fronts with increasing growth rate. At higher growth rates solidification of the monovariant reactions forms a mushy zone as the liquid and solid were in equilibrium, which reduced the chances of forming a planar S/L front. The Nb-2Ti-17.5Si alloy (Sekido et al. 2007) was quenched during solidification. The result was an undulating S/L front not a planar one, proving that the growth front of the ternary eutectics was not stable. With increasing Ti additions the microstructure became coarser and the larger $(Nb,Ti)_3Si$ grains showed some evidence of microsegregation at Ti = 10 at.%.

The segregation was not discussed in the paper but segregation of Ti to the edges of silicide phases and interphase regions has been noted in other works (Bewlay et al. 1997; Sekido et al. 2004; Li & Tsakiropoulos 2013).

The $(Nb,Ti,SI)_{ss}/Nb(Ti)_3Si$ eutectic is the "most normal" microstructure formed when solidifying around the eutectic ridge, but is not always formed. Alloys with compositions Nb-Si(11,16,18)-6Ti were manufactured by initially cold pressing the elemental powders to a compact and then formed via hot pressed reactive sintering at 1500 ^{O}C for 1 hr. This produced a microstructure in which only the Nb_5Si_3 silicide was present with Nb_{ss} (Li & Peng 2007). Given that Ti stabilises the Nb_3Si to lower temperatures (Bewlay et al. 2004) this would suggest that the eutectoid decomposition time was reduced from 100 hrs in the binary to less than 1 hr with concentrations of 6 at.%Ti at 1500 ^{O}C in the ternary. Enhanced eutectoid decomposition was also noted by Geng & Tsakiropoulos (2007). Sekido et al. (2004) showed that Ti addition of 20 at.% can stabilise the $Nb(Ti)_3Si$ below 1400 ^{O}C.

For high temperature structural applications the structural integrity of an alloy is paramount. One main disadvantage of alloying with Ti is the reduction in liquidus temperature. Taking the eutectic as a point of reference, the temperature drops from 1920 ^{O}C to 1330 ^{O}C at 0 and 100 at.%Ti respectively (Figure 11 and Figure 13). At 42.5 at.%Ti the eutectic was measured at 1700 ^{O}C (Bewlay et al. 1997). Thus, to keep the liquidus temperature above the goal value for Nb silicide based alloys the Ti additions have to be limited to 25 at.%.

Titanium does not have a strong tendency to segregate only to a certain phase (Li & Tsakiropoulos 2013). It segregates in both the Nb_{ss} and the silicides with slightly more affinity for the Nb_{ss} with Ti concentrations of 29.3, 22.0 and 25.5 at.%Ti for the Nb_{ss}, β-Nb_5Si_3 and Ti-rich β-Nb_5Si_3, respectively. Another report from the same research group found more than one Ti-rich solid solution phase (Geng et al. 2007). Alloys with Sn, Si, Ti and Cr additions had two distinct solid solution types; one that was Ti-Cr-rich (36.4 at.%Ti) and another Sn-Si-rich (25.5 at.%Ti). Li & Peng (2007) noted that additions of Ti can coarsen the ductile solid solution phase.

1.5.1.2 Mechanical Properties and Oxidation

Due to the toughening effect the Nb_{ss} has in the Nb silicide based alloys it is necessary to keep the brittle to ductile transition temperature (BDTT) of this phase low. The only known alloying elements to do this are Ti and Hf (Chan 2002). The BDTT of the Nb_{ss} phase remained unchanged for alloying additions of up to 13 at.%Ti. The effect that alloying elements have on the BDTT is important when considering the alloy in service. Increases in the BDTT will have little effect at the engines operating temperature, but if the metal becomes brittle at temperatures in the atmospheric range (-30 ^{O}C to 40 ^{O}C) then any damage caused to the cold blades, e.g. a stray stone while the engines are initiating, could cause damage that could lead to catastrophic failure. Chan (2002) showed that elements such as Al and Cr in high enough concentrations (5 and 3 at.% respectively) can move the BDTT close to this critical range.

The increased fracture toughness is one of the main advantages of alloying with Ti. Work looking at binary Nb-Si and ternary alloys with Ti (Sekido et al. 2004) showed that a 10 at.% addition of Ti to the eutectic Nb-18.7Si composition raised the fracture toughness from 3.4 MPa.m$^{1/2}$ to 11.8 MPa.m$^{1/2}$. These results were supported in later work (Sekido, Kimura, et al. 2006) where the toughness was increased by 6.9 MPa.m$^{1/2}$ with 10 at.%Ti addition. Sekido et al. (2004) also reported the variation of hardness with Ti additions from 0 – 10 at.% with changing Si concentrations in the alloy. Within the Nb-Ti binary system increased Ti concentration had little effect. However, an addition of 1 at.%Si caused a decrease in the hardness with Ti additions from 0 to 5 at.%Ti. This increased again but did not exceed that of the binary Nb-1Si for Ti < 10 at.%. The pattern was repeated at 4 at.%Si. At 20-25 at.%Si the hardness decreased dramatically with Ti additions from Ti 0 to 5 at. %, e.g. in the Nb-20Si-xTi alloy the hardness at x=0 was ≈ 825 Hv and reduced to ≈ 500 Hv at x=5. The hardness then remained constant up to additions of 10 at.%Ti. Softening of the alloy was thought to be caused primarily by the softening of the $(Nb,Ti,Si)_{ss}$ phase. This was mirrored in the toughening of this phases. This softening also reduced the high temperature strength of Nb-Si alloyed with Ti (Sekido et al. 2004; Sekido, Kimura, et al. 2006), as shown in Figure 31.

Alloying with, relatively, small concentrations of titanium (Nb-6Ti-18Si) resulted in a slight increase in compressive yield strength over a range of strain rates as well as increased flexural strength and fracture toughness. There was however a decrease in percentage strain to failure with Ti additions, except for tests done at the highest strain rate where the ternary alloy showed a higher strain to failure. The hardness of the alloy also decreased with the Ti addition (Li & Peng 2007).

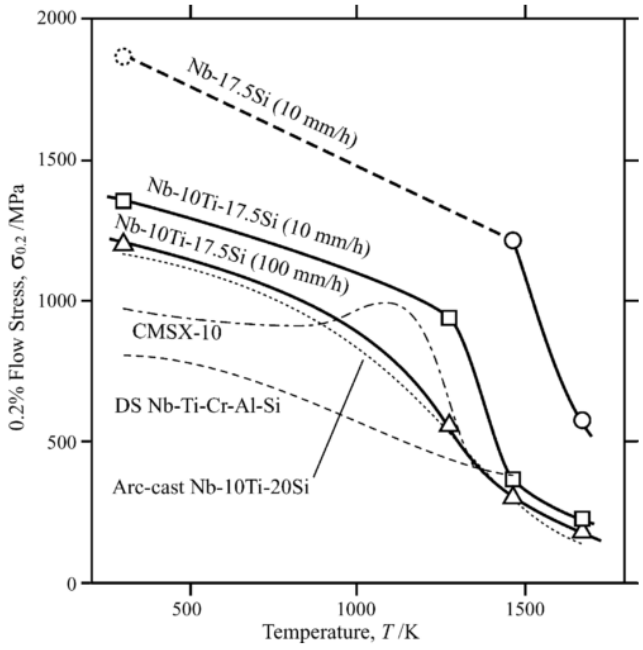

Figure 31: Plot of flow stress vs. temperature showing the effect of temperature on the strength of binary and ternary Nb-Si-(Ti) alloys. Republished with permission of Elsevier, from (Sekido, Kimura, et al. 2006)*; permission conveyed through Copyright Clearance Center, Inc.*

It has been widely accepted that Ti can increase the fracture toughness of Nb silicide based alloys. The main resistance to fracture in these alloys arises from the resistance to crack propagation from the ductile solid solution phase. The increased V_f of the solid solution phase with increasing Ti addition is the reason for toughening (Li & Peng 2007; Sekido et al. 2004; Sekido, Kimura, et al. 2006). Sekido et al. (2006) showed that the addition of 10 at.%Ti increased the $(Nb,Ti,Si)_{ss}$ size and also increased the amount of bridging compared with the binary. Other factors have been also considered. Alloying additions, such as Ti, which have 4d+s electrons compared with 5d electrons of Nb, reduce the anisotropic shear modulus of the solid solution (Chan 2005). This in turn decreases the Peierls-

Nabarro (P-N) barrier energy, thus increasing the ductility and therefore the fracture toughness of the alloy.

The fracture toughness of the Nb_5Si_3 silicide phase has also been studied (Chan 2005; Chan & Davidson 2003). The data is shown in Figure 32.

Figure 32 shows that increasing the Ti solubility in the Nb_5Si_3 silicide increased the fracture toughness until the Ti concentration was high enough to transform the tetragonal $Nb(Ti)_5Si_3$ to hexagonal $Ti(Nb)_5Si_3$. The increased fracture toughness of $Nb(Ti)_5Si_3$ with increasing Ti content is thought to be due to either;

1. Reduction of the Peierls-Nabarro energy similar to the solid solution
2. Reduction of the stacking fault energy
3. Stress induced transformation of the silicide phase, adding a deformation mechanism and blunting the crack tip.

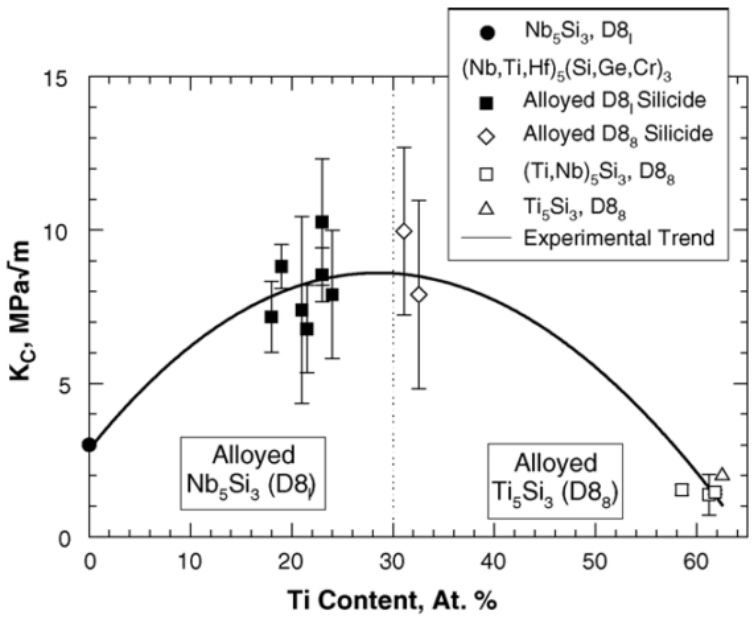

Figure 32: Effect of Ti on the fracture toughness of the $(Nb,Ti)_5Si_3$ silicide. Republished with permission of Elsevier, from (Chan 2005)*; permission conveyed through Copyright Clearance Center, Inc.*

Study of the oxidation resistance of multi-phase Nb silicide based alloys with and without an addition of 24 at.%Ti showed that at 800 ^{O}C the weight gain was reduced by 22.5 mg/cm^2 to ≈ 7.5

mg/cm^2 in the presence of Ti (Geng & Tsakiropoulos 2007; Geng et al. 2006a). The non-titanium containing alloy suffered from pest oxidation after 48 hrs at temperature. Even though some pesting was seen in the Ti containing alloy it was still solid (did not disintegrate) after 100 hrs. It has been suggested that Ti additions help increase the oxidation resistance of the alloy by reducing the surface area of the solid solution phase relative to its volume.

1.5.2 Hafnium

1.5.2.1 Microstructure Effects

In Nb silicide based alloys containing 5 at.%Hf, Hf-rich areas were present in the Nb_5Si_3 (Geng et al. 2007; Grammenos & Tsakiropoulos 2011). The Hf-rich areas of the silicide were formed in interfacial regions next to Nb_{ss} and remained after heat treatment (1500 ^{O}C/100 hrs). In the Hf-rich areas there was no solubility for refractory metals W and Mo. The presence of metastable γ-Nb_5Si_3 was also noted in these Hf containing alloys pre- and post-heat treatment. It was concluded that this phase could be stable in the presence of Hf as well as interstitials.

Geng et al. (2007) did not detect Nb_3Si phase in Nb-24Ti-18Si-5Al-5Cr-2Mo-5Hf by XRD. However, the same study observed Nb_3Si, by XRD, in identical alloys without 5 at.%Hf addition. The liquidus projection in Figure 17 shows that the $Nb(Hf)_3Si$ can form at this concentration of Hf. This was confirmed in Nb-16Si alloyed with 0-7 at.%Hf (Tian et al. 2008) and Nb-10Hf-(16,18.7)Si (Zhao et al. 2001) where the as-cast microstructure consisted of $(Nb,Hf,Si)_{ss}$ and $Nb(Hf)_3Si$. This could suggest that destabilisation of this phase occurred due to the effect that Hf and one (or more) of the other alloying element(s) (Cr, Al, Mo) had. This however is not supported by the result of alloys containing Hf, Mo and W (Grammenos & Tsakiropoulos 2011). In the alloys with Hf, Mo and W and Hf and W, Nb_3Si was detected by XRD whereas in alloys with just refractory metal additions and no Hf the Nb_3Si was not found. Therefore it might not be only the action of alloying elements that can prevent/promote the formation of Nb_3Si but also the solidification conditions applied or even the synergy of both

In the alloy containing 5 at.%Hf J Geng et al. (2007) reported an increase in the V_f of the Nb_{ss}, from ≈ 0.09 to 0.17 pre-and post-heat treatment respectively. Hafnium, although present in the Nb_{ss}, had more affinity for the silicides (in the as-cast alloy there was ≈ 100% more Hf in the Nb_5Si_3 than the Nb_{ss} and ≈ 300% more in the Hf-rich Nb_5Si_3 and increased further in the heat treated alloy (Guo & Guo 2011a)). Therefore Hf having an affinity for Nb_{ss} is not a reasonable argument for those increases in V_f. However, since the concentrations of other alloying elements (Ti, Si, Cr and Al) in the Nb_5Si_3 do not change significantly from Hf-poor to Hf-rich areas it is reasonable to conclude that the Hf mainly substitutes for Nb in this phase. Therefore, the increased rejection of Nb from the solidification of the silicides increased the V_f of the Nb_{ss}. The conclusion that Hf preferentially substitutes for Nb and not for other alloying additions in 5-3 silicides was looked at from first principles (Chen et al. 2007). It was shown that elements with larger atomic radii (e.g. Hf, Zr) tend to occupy close packed planes in β- and γ-Nb_5Si_3 and less close packed planes in α-Nb_5Si_3. Alloying elements with smaller radii (e.g. Ti, V, Mo, Cr, W) tend to favour the opposite position. Therefore there is no competition for positions between these two sets of alloying additions and Hf, when no other larger radii element is present, only replaces Nb.

A thermodynamic explanation has also been offered for the increased V_f of Nb_{ss} (Tian et al. 2008). It was shown that as Hf concentrations surpassed 4 at.% the mixing entropy exceeded that of the silicide phase. In turn this decreased the Gibb's free energy of the system making it less favourable to form ordered phases such as silicides. The increase of the V_f of Nb_{ss} had a detrimental effect on the eutectic structure (Tian et al. 2008). As the Hf concentration in the alloy Nb-16Si was increased from 0 to 7 at.% the fraction of interdendritic eutectic decreased, with little evidence of eutectic cells left at 7 at.%Hf.

1.5.2.2 Mechanical Properties and Oxidation

To determine the effect that Hf has on fracture toughness a three point bend test was done on Nb-16Si-xHf alloys where x=0,1,3,7 at.%Hf (Tian et al. 2008). There was an increase in the fracture

toughness of the alloy with addition of 1 at.%Hf, from 5.5 to 7.25 MPa.$m^{1/2}$, and then a gradual increase from this value to 8.5 MPa.$m^{1/2}$ at 7 at.%Hf. Fractographs showed clearly deflection and bridging of the crack when it came in contact with primary Nb_{ss}. It was suggested however that the eutectic Nb_{ss} was below a critical size for these mechanisms to operate and thus cracks propagated straight through. In binary Nb-Si alloys fracture of both primary Nb_{ss} and Nb_3Si was due to cleavage with large cleavage facets and river patterns seen on the fracture surface. Eutectic Nb_{ss} however was pulled out of the matrix. The additions of Hf changed this. There was evidence of plastic deformation with no large facets for the primary $(Nb,Hf)_{ss}$. The eutectic showed signs of $(Nb,Hf)_{ss}$ remaining adhered to the matrix and definite signs of plastic deformation. Two main reasons were given for the increased fracture toughness due to increased Hf content;

1. Increased width of primary Nb_{ss} which, due to its size, was more beneficial for crack bridging.
2. Similar to Ti additions Hf also lowers the Peierls-Nabarro energy increasing ductility and therefore toughness by allowing easier movement of dislocations.

To examine the effect of Hf on mechanical properties of Nb_{ss} further the solid solution alloy Nb-15W-0.5Si-2B-(0,5,10,15)Hf was studied (Zheng et al. 2008). The results indicated that the strength of the solid solution alloy increased with increased Hf additions. The 0.2% yield stress increased from 775-870 MPa at room temperature, from 295-448 MPa at 1200 ^{O}C and from 180-365 MPa at 1400 ^{O}C as the concentration of Hf increased from 0-15 at.%. The 9 % difference in atomic size between Nb and Hf atoms was proposed to be the reason for increased strength with Hf additions. Therefore additions of Hf to Nb_{ss} not only cause increase of ductility/toughness but also increased strength which is contrary to the general relationship between ductility and strength.

The effect of Hf on the oxidation resistance of Nb silicide based alloys has also been studied. A 5 at.%Hf addition to Nb-24Ti-18Si-5Al-5Cr-2Mo changed the oxidation behaviour in static air at 1200 ^{O}C depending on the alloy condition (Geng & Tsakiropoulos 2007; Geng et al. 2006a). As-cast and heat treated (1500 ^{O}C/100 hrs) samples showed very similar rates of weight gain up to ≈ 56 hrs and ≈ 24

hrs respectively, with the heat treatmented sample showing a steeper weight gain. This increase in weight gain was expected because of the increased V_f of the Nb_{ss} after heat treatment. However, after the aforementioned times the rate of weight gain in the as-cast sample began to decrease while the rate of weight gain in the heat treated sample increased. This result was mirrored in static air oxidation tests run at 800 ^{O}C.

1.5.3 Hafnium and Titanium

As discussed in the previous sections, Hf- and Ti-rich areas in Nb_5Si_3 have been identified in Ti and Hf containing Nb silicide based alloys. These regions are formed by the partitioning of solute into the melt (Tian et al. 2009; Cheng & He 2011). XRD studies of Ti and Hf containing alloys showed that metastable γ-Nb_5Si_3 was present in the microstructure with no indication of hexagonal (Ti or Hf)$_5Si_3$ phase formation. Based on the quantitative EPMA data for silicides and the "Bewlay rule" (see below) it has been suggested (Geng et al. 2007; Geng & Tsakiropoulos 2007) that some Hf-rich Nb_5Si_3 corresponds to γ-Nb_5Si_3.

The role of Hf additions on the solidification of Ti containing Nb silicide based alloys has also been studied (Bewlay et al. 2004), focusing on the eutectoid decomposition of Nb_3Si in the Nb-12.5Hf-33Ti-16Si alloy. Hafnium had partitioned (segregated) in the Nb_{ss} and (hexagonal) γ-Nb_5Si_3 phases (mainly to the silicide phase) after eutectoid decomposition. Bewlay et al. (2004) suggested that hexagonal silicides are stabilised when the alloy and silicide have Nb:(Ti+Hf) < 1 ("Bewlay Rule").

1.5.4 Refractory Metal Alloying Additions

Refractory metals have been added to Nb silicide based alloys to increase the strength of Nb_{ss} and gain a more beneficial morphology by promoting the solidification of the more favourable Nb_5Si_3 rather than the Nb_3Si silicide. The refractory metal additions form a continuous solid solution with niobium, see § 1.2.5.1 and 1.2.6.1. The effects of W and Mo additions have been studied in some detail.

1.5.4.1 Microstructural Effects

Early work in this area focused on basic microstructural changes that occur with Mo and W additions around the eutectic point (Ma et al. 2004). This work looked at how the microstructure of Nb-16Si evolved with Mo and W concentrations increasing from 5 to 20 at.% and 5 to 30 at.%, respectively. It was observed that increasing additions of W caused coarsening of the eutectic microstructure. However, no similar effect was observed with increasing levels of Mo. Coarsening of primary $(Nb,Mo,W,Si)_{ss}$ with increasing Mo and W additions has also been noted in other work on near-eutectic ternary alloys (Chattopadhyay et al. 2006; Chattopadhyay et al. 2007; Sha, Hirai, Ueno, et al. 2003a). This was quantified by Chattopadhyay et al. (2007) for additions of Mo. As Mo concentrations in the alloy increased from 4 to 15 at.% there was a 22 % increase in the V_f of primary $(Nb,Mo,Si)_{ss}$ in hypoeutectic alloys. In hypereutectic alloys there was an increase in the V_f of the eutectic and a similar decrease in the V_f of the primary $Nb(Mo)_5Si_3$ but these changes were not quantified. It was speculated that this stabilisation of $(Nb,Mo,Si)_{ss}$ was due to the nucleation and growth kinetics of $(Nb,Mo,Si)_{ss}$ being altered by increased Mo additions. In this study changes in the morphology of the eutectics with changing Mo content were noted. As the Mo concentration in the alloy increased the V_f of non-lamellar eutectic increased and the V_f of lamellar eutectic decreased. However other work in this area, (Kim et al. 2002b), demonstrated that increasing Mo addition reduced eutectic spacing.

After heat treatment at 1700 ^{O}C for 48 hrs (Ma et al. 2004) complete transformation of β-Nb_5Si_3 to α-Nb_5Si_3 was observed over all concentrations of Mo or W in both ternary alloys that were made using conventional arc melting, see Figure 22 and Figure 25. Full transformation of β-Nb_5Si_3 to α-Nb_5Si_3 at low Mo concentrations has also been reported by Li et al. (2006), who studied alloys Nb-xSi-yMo (where x = 57, 39.5, 37.5 at.% and y = 0 - 3 at.%) that were made using conventional arc-melting. At slightly higher concentrations of Mo the α-Nb_5Si_3 silicide was the only silicide in the as-cast condition of Nb-xSi-yMo (where x = 19.1, 17.9, 12.8 or 12.3 at.% and y = 5.2, 26.3, 4.1 or 14.8 at.%) made via conventional arc melting (Chattopadhyay et al. 2006). The results obtained by Chattopadhyay et al.

(2006) could also be attributed to a slower cooling rate of the ingot allowing for solid state trasformation of β-Nb_5Si_3 to α-Nb_5Si_3 to occur. This seems to be supported by other work by this group (Chattopadhyay et al. 2007) where in the cast binary Nb-10Si alloy which was solidified via arc melting only the low temperature α-Nb_5Si_3 was identified. The β-Nb_5Si_3 to α-Nb_5Si_3 transformation was studied to determine the effect that Mo has on the stability of β-Nb_5Si_3 at high Si (> 36 at.%Si) alloy concentrations (Sekido et al. 2013; Li et al. 2006). It was found that at 0 at.%Mo the β-Nb_5Si_3 fully transformed to α-Nb_5Si_3 after 20 hrs at 1200 ^{O}C for silicon concentration in the alloy of 57 at.% (Li et al. 2006). The α-Nb_5Si_3 is stable at 1200 ^{O}C according to the Nb-Si binary phase diagram, see Figure 11. With additions of 2 at.%Mo and for similar Si concentration the results showed no transformation. Addition of 6 at.%Mo was shown to stabilise the β-Nb_5Si_3 (Sekido et al. 2013) after heat treatment temperatures at 1600 ^{O}C in the alloy Nb-37.5Si-6Mo. Full transformation of β-Nb_5Si_3 did not occur unless the concentration of Mo in the alloy was less than 4 at.% The increased β-Nb_5Si_3 stability with Mo additions was also confirmed by the work of Sekido et al. (2013). Kim et al. (2002b) studied the different allotropes of $(Nb,Mo)_5Si_3$ and showed that the α-Nb_5Si_3 has a higher yield strength and the β-Nb_5Si_3 exhibited more plastic deformation at room temperature prior to failure.

Tungsten has a similar effect to Mo on the phase transformation of Nb_5Si_3, at alloy Si concentrations of interest in this research. Tungsten in the presence of Hf stabilised the α-Nb_5Si_3 to higher temperatures (Grammenos & Tsakiropoulos 2011).

With the transformation of β-Nb_5Si_3 to α-Nb_5Si_3 in the heat treated (1500 ^{O}C) alloy Nb-36Si-4Mo precipitates of Nb_{ss} formed in the α-Nb_5Si_3 (Sekido et al. 2013). These precipitates had two orientation relationships ($(01\bar{1})_{\mathrm{Nb}}//(12\bar{3})_{\alpha}, [133]_{\mathrm{Nb}}//[111]_{\alpha}$ and $(\bar{1}12)_{\mathrm{Nb}}//(1\bar{1}0)_{\alpha}, [110]_{\mathrm{Nb}}//[110]_{\alpha}$) with the surrounding silicide, the same OR that Nb_{ss} and α-Nb_5Si_3 share after eutectoid decomposition of Nb_3Si. The cause of the precipitation was determined to be the temperature dependent solubility of Nb and Mo in β-Nb_5Si_3. As the transformation of β-to α-Nb_5Si_3 occurs the excess Nb and Mo are rejected from the silicide and form $(Nb,Mo)_{ss}$ precipitates.

The microstructure of the eutectic formed in the alloys studied by Ma et al. (2004) changed after heat treatment. The silicide matrix in the eutectic changed to a $(Nb,Mo,Si)_{ss}$ matrix in the Mo containing alloys. This however was not the case in the W containing alloys (Kim et al. 2002a).

EDS analysis indicated low solubility of the refractory metals in the silicide. The maximum concentration of Mo and W were 1.5 and 1.3 at.%, respectively in the α-Nb_5Si_3 at 1700 ^{O}C (Ma et al. 2004). In the as-cast alloy Nb-12.3Si-14.8Mo studied by Chattopadhyay et al. (2006) there was saturation of Mo in α-Nb_5Si_3 at 4.5 at.%Mo. The affinity of BCC Mo and W for the solid solution phase can be explained since Mo and W form BCC solid solutions with Nb.

Chattopadhyay et al. (2006) attributed the lack of Nb_3Si peaks in their XRD data either to increased Mo levels altering the thermodynamics of the eutectoid or inhibiting the formation of Nb_3Si altogether. In other work looking at the effects of W and Mo additions on phase stability, (Grammenos & Tsakiropoulos 2011; Geng et al. 2006b), the Nb_3Si was identified. A V_f of 2 % was noted for the Nb_3Si in a quaternary alloy containing 5Mo-3W (Grammenos & Tsakiropoulos 2011). This indicates that rather than inhibiting Nb_3Si formation refractory metal additions may have just decreased the time of the eutectoid reaction dramatically.

Chattopadhyay et al. (2006) also noted two types of eutectic a coarse and a fine eutectic with the same two phase α-Nb_5Si_3 and Nb_{ss} in the alloy Nb-xSi-yMo (where x = 19.1, 17.9, 12.8 or 12.3 at.% and y = 5.2, 26.3, 4.1 or 14.8 at.%) made via conventional arc melting. This was thought to be due to the large range of temperatures over which the eutectic exists, with the fine forming after the coarse one at a relativly lower temperature. Looking at the microstructural images, however, the fine eutectic seems to form close to primary silicide dendrites indicating that it formed first. The coarser structure could therefore be due to the formation of fine eutectic increasing the temperature of the remaining melt during recalesence. This decreased the driving force of eutectic growth creating a coarser structure.

Grammenos & Tsakiropoulos (2011) also showed that Mo, W and Hf have an effect on the macrosegregation of Si in Nb silicide based alloys. In a quaternary alloy with 5Mo and 3W additions the difference between maximum and minimum Si concentations over the entire ingot was 4.4 at.%. However, when 5 at.% Hf was added to the alloy the Si variation across the ingot decreased to 1.9 at.%. Alloys with 5W and 5Hf and no Mo also showed less Si macrosegregation with the difference between maximum and minimum concentration being only 2.5 at.%. Kim et al. (2002b) reported no Si macrosegregation in ternary alloys with a range of Mo additions. Therefore it was deduced Mo and W in synergy increase the macrosegregation of Si and this effect is reduced by Hf additions.

1.5.4.2 Mechanical Properties and Oxidation

Chattopadhyay et al. (2006) studied the microhardness of $(Nb,Mo)_{ss}$, α-$Nb(Mo)_5Si_3$ and the $(Nb,Mo)_{ss}/\alpha$-$Nb(Mo)_5Si_3$ eutectic. They reported a slight increase in hardness with increasing Mo concentration in all phases. For the α-$Nb(Mo)_5Si_3$ silicide and solid solution the hardness increased roughly linearly with Mo at.% with the silicide hardness increasing with a steeper gradient. The eutectics hardness on the other hand increased up to an alloy concentration of ≈ 25 at.%Mo and then levelled off. Looking at the hardness of the alloys there were significant increases in hardness with increased Mo content when compared with alloys with similar Si levels and no Mo. Increasing the Mo concentration from 5.2 to 26.3 at.% and from 4.1 to 14.8 at.% increased the hardness by 0.8 and by 0.9 GPa in hyper-and hypo-eutectic alloys, respectively. Alloying with W also increased the hardness of the constituent phases (Xiong et al. 2014) indeed the addition of 10 at.%W to the binary alloy Nb-20Si increased the hardness of the $(Nb,W,Si)_{ss}$ from 521 Hv to 726 Hv and of $Nb(W)_5Si_3$ from 1437 HV to 1783 HV.

As would be expected from the hardness data, for similar levels of Si content in the alloys increasing the Mo content in the alloy decreased the room temperature fracture toughness (Kim et al. 2001; Chattopadhyay et al. 2006), in line with the general trend exhibited by hardness and fracture toughness of the alloys. The fracture toughness of the hypereutectic and hypoeutectic alloys was

reduced by 3.3 MPa.$m^{1/2}$ from 8.8 MPa.$m^{1/2}$ and 1 MPa.$m^{1/2}$ from 6.6 MPa.$m^{1/2}$, respectively (Chattopadhyay et al. 2006). Decreased ductility with increased refractory metal additions was also reported in tungsten containing alloys (Sha et al. 2000). The ductility decreased from 2.3 to 1.2% as the W content increased from 0 to 15 at.%, respectively.

Increased hardness and decreased fracture toughness/ductility have been attributed to solid solution strengthening caused by the refractory metal additions. Molybdenum and W atoms both have relatively large misfit parameters with the larger Nb atom, 5% and 4%, respectively (Chattopadhyay et al. 2006; Sha et al. 2000). The resulting increase in strain energy makes the movement of the dislocations more difficult, thus higher stresses are required to move the dislocations increasing yield strength/hardness and decreasing ductility/toughness.

Kim et al. (2002b) studied the high temperature (1773 K) compressive yield strength of Nb silicide based alloys with Mo additions. The general trend in both hypo-(16 at.%Si) and hyper-(22 at.%Si) eutectic alloys was increased strength with Mo concentration. This was attributed to solid solution hardening of Nb_{ss} by Mo. However, there were some irregularities in the above trend. There was a drop in the yield strength between 0 and 5 at.%Mo and between 15 and 20 at.%Mo for the hyper-and hypo-eutectic alloys, respectively. In the hypereutectic alloys the drop from ≈ 325 MPa to a minimum at ≈ 275 MPa seemed to be a microstructural effect as the microstructure changed from $(Nb,Mo,Si)_{ss}$ particles distributed in a silicide matrix to a “maze” or “Chinese script” morphology, with the V_f of the phases remaining constant. An example of the “Chinese script” morphology is shown in Appendix A Figure 2. However, in the hypoeutectic alloys the drop in yield strength from a maximum of ≈ 325 MPa to ≈ 300 MPa coincided with the transition from β- to α-Nb_5Si_3. These results compare well with other results for alloys of similar composition and processing history (Ma et al. 2004). At 16 at.%Si the yield strength of W containing ternary alloys increased from ≈ 150 MPa to ≈ 550 MPa with an increase of W from 0 to 15 at.%, in other words the addition of W did not cause a decrease in the yield strength. The monotonous increase in yield strength with W additions was also seen at 1670 K

(Sha et al. 2000). This was further reinforced by work done on the yield strength of quaternary alloys Nb-16Si-5Mo-xW, where x=0,5,10,15 at.%W (Kim et al. 2002a), see Figure 33 which also shows how the fracture toughness decreased with increased W content. Increasing strength with W additions have again been attributed to solid solution strengthening of the Nb_{ss}.

Ma et al. (2004) also compared the true stress and strain at room temperature of ternary (Mo and W additions) alloys with varying refractory metal additions. The alloy with 5 at.%Mo had the most plastic deformation to failure however it's yield strength was 600 MPa lower than the 15 at%Mo alloy (≈ 2300 MPa). Tungsten additions in the ternary alloys showed a very similar trend, with the alloy with 5 at.%W showing most deformation to failure but also having a lower yield strength (≈ 1750 MPa) compared with the alloy with 20 at.%W (≈ 2300 MPa). Weaker solid solution strengthening with lower refractory metal additions was thought to be the cause of the increased plastic deformation. At 1773 K (1500 ^{O}C) the stress stain curves for both alloying additions showed high strength even at strains approaching 20% (≈ $0.7\sigma_{yield}$ for Mo and ≈ 0.8 σ_{yield} for W).

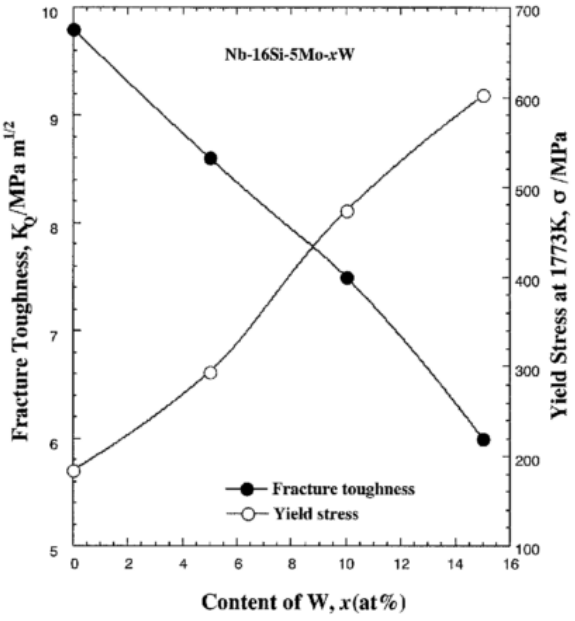

Figure 33: Variation of yield strength and fracture toughness with increasing W concentration in the alloy Nb-16Si-5Mo-xW alloys. Republished with permission of Japanese Institute of Metals and Materials, from Kim et al. (2002a).

In W containing hypoeutectic ternary alloys (Sha, Hirai, Ueno, et al. 2003b) the main fracture mechanism was cleavage for all alloys. The highest fracture toughness was for the binary Nb-10W solid solution alloy. This alloy did not show signs of transgranular cleavage that was shown in the ternary alloys but exhibited intergranular cracking. The lowest fracture toughness was exhibited by the Nb-10Si-10W alloy, whose fracture surface was planar and both phases fractured in a brittle manner. The decreased ductility of the Nb_{ss} phase was attributed to the addition of silicon increasing solid solution strengthening.

The effect of refractory metal additions on the oxidation behaviour of Nb silicide based alloys has also been studied. One study focused on the oxidation behaviour of ternary alloys based on the binary Nb-20Si with 10 at.% of W or Mo (Xiong et al. 2009). This work showed that in Nb-20Si the oxidation resistance was increased by alloying with 10 at.%W. It was shown that W additions caused the formation of a dense WO_3 scale and was claimed that this had enhanced the scale adhesion (reducing the cracking of the Nb_2O_5 scale) and therefore reduced oxygen penetration. When compared with the best performing binary alloy (Nb-20Si) the W additions showed a ≈ 50% reduction in weight gain over 100 hrs at 1000 ^{O}C and ≈ 75% reduction at 1200 ^{O}C. However, the addition of 10 at.%Mo reduced oxidation resistance. This was attributed to the creation of a porous MoO_3 scale. The weight gain increased from ≈ 30 mg/cm^2 in the ternary alloy to ≈ 50 mg/cm^2 in the Nb-20Si-10Mo-10W quaternary alloy at 1000 ^{O}C. This was further exaggerated at 1200 ^{O}C, with the weight gain increasing from 35 mg/cm^2 to 95 mg/cm^2. The effect of Mo additions without the presence of W has also been studied (Geng & Tsakiropoulos 2007). This work showed that in higher order alloys with 4.5 at.%Mo at 800 ^{O}C the weight increased by ≈ 15 mg/cm^2 more than in alloys with only 1.8 at.%Mo, confirming the work in the previous study.

1.6 Processing Nb Silicide Based Alloys

The processing route of Nb silicide based alloys have been shown to have, as would be expected, significant influence on their microstructure and properties. Due to the nature of these alloys a range of different methods have been used for their preparation. Solidification methods include; Directional Solidication and conventional clean melting and casting. Powder metallurgy routes have also been used. In most cases heat treatment of the alloys is required.

1.6.1 Clean Melting

The most used conventional solidifcation technique to prepare these alloys is non-consumable W arc melting in an inert gas (Ar typically) atmosphere. The melting/casting chamber (furnace) is vacuated using a rotary and diffusion or turbo pump systyem and back-filled with inert gas prior to melting. The alloy charge is melted in a water-cooled copper crucible. This technique will be the reference against which the other techniques will be compared with. Within this technique there are examples of altering solidification conditions to observe microstructural changes and evaluate their effect on properties. Non-consumable W arc melting with suction casting uses a pressure difference in the vacuum chamber to force the melt into a mould inducing faster cooling rates during solidifcation (Kashyap et al. 2013a; Kashyap et al. 2013b). This method does not allow one to explore systematic variations in microstructure in any great detail. It has been used to study differences between suction cast and as-cast alloy microstructure and has concentrated mainly on measurement of average eutectic spacing in the bulk microstructure of suction cast ingots, not including any scope for variation of the latter with length or diameter of the suction cast rod. Other casting methods, including vacuum induction melting (VIM) and induction skull melting (ISM) have been studied using multi-element Nb-Si alloys (Li et al. 2010). However, microstructural and mechanical property comparisons are hard to make owing to difference post-pocessing. Isothermal forging of arc melted alloys (Kim et al. 2002b) has also been studied. This process produced a more equiaxed coarser structure with lower yield strength compared with the cast alloy.

1.6.2 Powder Metallurgy

The powder metallurgy processing of Nb silicide based alloys was concentrated on hot isostatic pressing (HIP) or spark plasma sintering (SPS) of elemental or pre-alloyed powders manufactured via ball milling. New powder processing techniques such as additive layer manufacturing (ALM) and direct laser fabrication (DLF) have not been possible owing to the unavailability of powders.

In the few occasions where DLF was used some serious problems with the microstructure of the alloy were reported. These included locally high concentrations of Si due to an initially inhomogeneous mixture leading to the formation of $NbSi_2$ in compositions with less than 35 at.%Si (Brice 2000) and variations in the scale of the solidified microstructure from largely dendritic structure at the base to a finer equiaxed structure at the top (Dicks et al. 2009). The research using DLF did however show that some directionality could be achieved using this method.

1.6.3 Directional Solidification

As with Ni based superalloys directional solidification (DS) has been implemented in the solidification processing of Nb silicide based alloys to improve mechanical properties via microstructural alignment. Having a microstructure aligned parallel to the direction of tensile force can increase the mechanical properties in that direction. Hard, strong silicides can form as aligned fibres in in-situ composites. Periodic arrangement of the toughening solid solution phase increases resistance to crack propagation via crack bridging and blunting (see § 1.4). Crack deflection will also increase toughness due to high aspect ratio phases the crack has to circumvent. Creep due to grain boundary sliding is also reduced by increasing the directionality of phases.

Different methods of directional solidification have been applied in the solidification processing of Nb silicide based alloys; optical float zone (see below), electron-beam float zone (Guo, Gao & Guan 2007), liquid-metal cooled furnace (Sainan et al. 2013; Fei et al. 2013), Bridgman (Wang et al. 2013; Su et al. 2013; Ma et al. 2012), Czochralski (Bewlay, Sutliff, et al. 1999; Bewlay, Jackson, et al. 1999; Bewlay et al. 1995; Bewlay et al. 1996), and self-made facilities (Guo & Guo 2011b).

Initial research into directional solidification (DS) of Nb-Si based alloys used the Czochralski method. This uses induction levitation to partially raise melts over a skull of the material on a water cooled copper crucible. A seed rod is then lowered into the melt and retracted at a constant rate to remove a directionally solidified material. These early results showed the major benefits of DS. Near eutectic alloys solidified with Nb_{ss} rods parallel to the growth direction within a Nb_3Si matrix (Bewlay et al. 1995). Off eutectic alloys also showed alignment of dendrites in both hyper- or hypo- eutectic alloys. Due to the alignment of the toughening phase, the fracture toughness was increased by 50% when binary arc-melted samples were compared with DS samples of similar Si concentrations (Bewlay et al. 1995). Research then moved onto multi-element Nb silicide based alloys (Bewlay et al. 1996), and concentrated on MASC ("Metal and Silicide Composite Alloy" of composition Nb-25Ti-8Hf-2Cr-2Al-16Si) and MASC type alloys patented by General Electric. In their alloys the Nb_{ss} and silicide dendrites were aligned with the growth direction as in the binary alloys. A similar increase in fracture toughness was reported for the MASC alloy compared with the binary. The K_{IC} values reported for arc-melted MASC and DS alloys were in the region 7.5-9.2 MPa.$m^{1/2}$ and 19-22 MPa.$m^{1/2}$, respectively (Li et al. 2010).

In more recent research the Bridgman method and liquid-metal cooled furnace techniques were used. The Bridgman method is similar to the Czochralski method. However, where the Czochralski method uses a seed material to pull the melt out of the crucible, in the Bridgman method the seed is stationary and the crucible moves away (either vertically or horizontally), effectively forcing the melt out of the crucible and away from the hot zone. Research on the Bridgman method (Wang et al. 2013; Su et al. 2013) showed very similar microstructures as the Czochralski method. In interdendritic regions however, described by the author as a "petaloid" eutectic structure, was shown when examined transverse to the growth direction. An example of the petaloid eutectic morphology described by Wang et al. 2013 is shown in Appendix A, Figure 3. Consisting of finer Nb/Nb_5Si_3 eutectics radiating from the centre of the cells surrounded by coarser, anomalous morphologies at the edges. Su et al. (2013) reported variation of fracture toughness and microstructure with changing growth

rates. At growth rates lesser than 18 mm/hr there was no significant fraction of Nb_3Si formed. This was thought to be due to the cooling rate being low enough to complete the eutectoid transition. As the growth rate increased there was a distinct reduction in the formation of Nb_{ss}/Nb_5Si_3 eutectic at 70 and 100 mm/hr. The room temperature fracture toughness of specimens was highest at low growth rates with K_Q values of 8.8, 9.7 and 9.6 $MPa.m^{1/2}$ for 6, 18 and 30 mm/hr, respectively. Between 30 and 50 mm/hr there was a sudden drop in fracture toughness to 7.5 $MPa.m^{1/2}$ which then plateaued for the remaining growth rates. Su et al. (2013) did not give an explanation for this phenomenon. Wang et al. (2013) also showed some changes in morpholgy with increasing solidification rates. Eutectics had three distinct formations with increasing growth rate. Generally speaking these were irregular lamellar, complex regular and quasi-regular. Examples of the irregular laminar, complex regular and quasi-regular eutectics are shown in Appendix A Figures 4, 5 and 6 repectively. At the highest growth rate (50 mm/hr) the formation of the γ-Nb_5Si_3 phase was eliminated. This was thought to be due to entrapment of Ti and Hf in the initial stages of solidification. This is contrary to the normal solidifcation sequence where a Ti rich melt would be the last to solidify increasing the chances of the γ-Nb_5Si_3 forming.

Yuan et al. (2012) studied DS micorstructure produced with liquid-metal-cooled furnace to examine microstructure development under different conditions. Due to the technique used there was an initial unmelted zone and an initial transition region before a “quasi-steady-state” growth region developed. After this area of interest there was also a mushy zone, which was examined after quenching the specimen before the end of the solidification, and quenched region. Similar to the Bridgman method this work defined three different eutectic structures within the DS area of the ingot; Petaloid Nb_{ss}/ Nb_5Si_3 eutectic, fine scale lamellar eutectics Nb_{ss}/Nb_5Si_3 and fibrous Nb_{ss}/Nb_5Si_3 with increasing scale as the DS continued. The silicide was not defined as either α, β or γ. The first and third eutectic had similar concentrations of alloying elements apart from Si which was 6.4 at.% higher in the petaloid eutectic. This was accompanied with an increase of the V_f of the silicide in these areas. Further study showed that in some of the eutectics the Nb_5Si_3 phase was defined as non-faceted phase

compared with other eutectics where the Nb_5Si_3 was claimed to be faceted. The authors believed the transition from faceted to non-faceted was due to faster solidification of the former eutectics compared with the latter (this was also examined in the work of Fu et al. (2008)). This is offered as the main reason for the change in the eutectic structure along with the changes in eutectic composition. The liquid-metal-cooled technique used by Yuan et al. (2012) uses an yttria mould during solidification. Using a ceramic mould allows for better control of temperature and cooling rate. However, it has been shown that these moulds react with alloying additions in Nb silicide based alloys creating an yttrium and hafnium rich layer between the mould and the DS ingot (Ma et al. 2012).

DS alloys procured using the Bridgman method and liquid-metal-cooled furnace technique have shown similarities in their microstructures with increasing growth rate (Fei et al. 2013). As the growth rate increased there was a distinct rise in the concentrations of Cr and Ti in the Nb_{ss} phase. This was attributed to increased rate of solidification of the Nb_{ss} hindering the diffusion of Cr and Ti out of the solid solution. A relationship between Cr and Ti concentrations in Nb_{ss} has been identified by Zelenitsas & Tsakiropoulos (2006) and H. Guo & Guo (2011). This indicates that the concentration of Cr in the Nb_{ss} increases as the Ti/Nb ratio increases.

Work on alloys processed using electron beam floating zone (similar to the optical float zone technique, see § 1.6.3.1, but melted using electrons rather than focused light) showed how tensile strength, fracture toughness and elongation were affected by DS growth rate (Guo, Gao & Guan 2007). This work showed that high temperature (1250 ^{O}C) and room temperature tensile strength were higher in DS samples compared with arc melted samples. As withdrawal rates increased (2.4, 4.6 and 7.2 mm/min) the tensile strength decreased but even at its lowest it was nearly twice that of the arc melted samples. Fracture toughness increased from 12.1 MPa.m$^{1/2}$ in the arc melted sample to 19.4, 16.9 and 19.7 MPa.m$^{1/2}$ for 2.4, 4.6 and 7.2 mm/min, respectively. Increases compared with the arc melted condition were attributed to aligned phases. There was however a decrease in elongation at 1250 ^{O}C compared with the arc-melted one in the DS alloys that was attributed to the aligned

microstructure. The elongation of the arc-melted sample was 142.3 % and for the DS sample was 53.1, 19.2 and 19.8 % with decreasing growth rate. This was taken to be an indication that DS prepared samples will have increased creep resistance.

1.6.3.1 Optical Float Zone Processing

A widely researched method for producing directionally solidified metal/intermetallic systems such as Nb silicide based alloys is the optical floating zone (OFZ) method. The OFZ furnace consists of a number of halogen lamps (normally 2 or 4) surrounding a central vertical tube inclosing the specimen in an inert atmosphere. The halogen lamps are surrounded on one side by concave mirrors that focus the light emitted onto a small section of the specimen. This results in heating the sample to temperatures in excess of 2000 ^{O}C. This temperature however is dependent on certain properties of the material in question, such as surface reflectivity. The material to be directionally solidified (feed rod) is hung from an upper piston via a metallic wire (usually molybdenum or tungsten). A smaller seed rod is attached to the bottom piston; to which the melted sample will be adhered to once solidification has begun. Once the feed rod is adhered both pistons begin to move down, either at the same or different rates, moving the upper sample through the stationary hot zone. This creates the directional solidification of the sample with the growth of the microstructure in the opposite direction to the motion of the specimen. As well as vertical movement the upper and lower pistons are able to rotate independently of each other. This allows the feed and seed rods to be rotated in opposite directions. This reduces any axial misalignment between the two rods, creates more uniform heating and increases the homogeneity of the system. This coupled with a constant temperature gradient within the furnace due to the lack of crucible allows for good microstructural control. Rotational speed are denoted as X-Y rpm where X = feed rod rotation and Y = seed rod rotation. Relative rotation of the system is defined as the sum of the two rotational speeds.

As with other DS systems there was reduction of lamellar spacing with increased growth rate in OFZ (Tian et al. 2009; Sekido et al. 2007). The size of the eutectic cells also show a relationship with

growth rate defined as the diagonal distance across the "hexagonal" eutectic, increasing with increasing growth rate (Sekido et al. 2007).

In Nb-Si alloys with titanium additions it has been shown (Tian et al. 2009) that increased growth rate reduced Ti segregation.

The microstructure that developed during the OFZ process is similar to that in other DS processes, namely elongated Nb_{ss} and silicide phases along the growth direction (Huang et al. 2011; Sekido et al. 2004). Increasing the growth rate led to a reduction of the radial width of the phases. Slower growth rates benefit the coupled growth of laminar eutectics. However, when growth is too slow, say 3 mm/hr, it can cause radial growth of silicides creating extremely large unwanted silicide phases (Huang et al. 2011). It was also shown (Sekido et al. 2004) that increasing the growth rate changes the S/L interface from planar to a unstable, undulating front.

Looking at the effect that rotation has Li, Miura, et al. (2011) noted that at 5-5 rpm the radial morphology changed from the centre to the edge in the alloys Nb-17Si-10Mo-3Al and Nb-18Si-10Mo. The morphology in the centre consisted of spherical Nb_{ss} grains and a lamellar eutectic and the microstructure at the edge was equiaxed with no obvious directionality. Maintaining relative rotation but altering actual rotation to 10-0 rpm showed less equiaxed grains and more regular eutectic. It was concluded that irregularities at the edge were due to the rotation of the seed rod causing liquid flow near the S/L boundary, especially at the edge. This was supported by the result at 40-0 rpm where the edge only had regular eutectics.

At a rotation of 10-0 rpm and growth rates of 3, 5, and 10 mm/hr lamellar spacing (λ) obeyed the Jackson-Hunt theory $\lambda^2 R = C$ as shown in Figure 34 (Li, Miura, et al. 2011) where C = a constant, calculated to be 170 μm^2.mm/hr.

Orientation relationships, determined using EBSD, between the Nb_{ss} and α-Nb_5Si_3 were shown to be $<210>_{Nbss}//<101>_{Nb5Si3}$ and $\{001\}_{Nbss}//\{001\}_{Nb5Si3}$, $<111>_{Nbss}//<001>_{Nb5Si3}$ and $\{011\}_{Nbss}//\{110\}_{Nb5Si3}$,

Whereas in eutectics containing the β- form of Nb_5Si_3 the ORs was $\{112\}_{Nbss}//\{100\}_{Nb5Si3}$ and $<113>_{Nbss}//[001]_{Nb5Si3}$ at a growth rate of 5mm/hr (Li, Miura, et al. 2011). However, in the hypoeutectic alloy Nb-16Si (doped with Mg) no ORs were formed between the primary Nb_{ss} and the eutectic, thought to be due to the silicide shell that had formed around the Nb_{ss} before eutectic solidification (Miura, Ohkubo, et al. 2007). ORs were also noted in Nb_{ss}/Nb_3Si eutectics in Nb-25Si alloys (Sekido et al. 2007). These were determined to be $\{110\}_{Nbss}//\{110\}_{Nb3Si}$ and $\{112\}_{Nbss}//\{001\}_{Nb3Si}$.

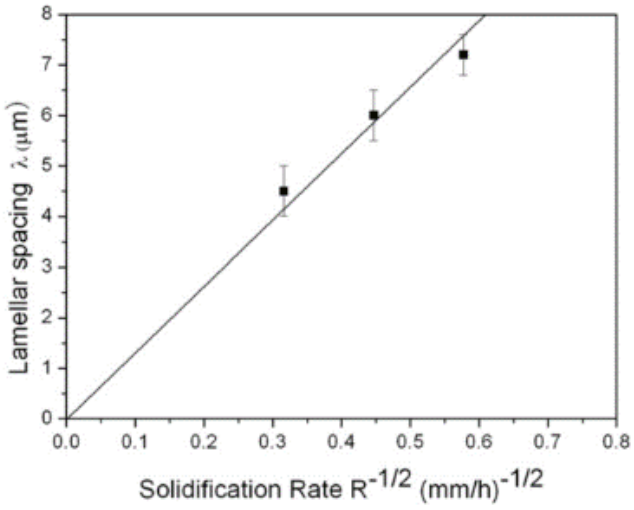

Figure 34: The Jackson-Hunt relationship between the lamellar spacing and the solidification rate for the OFZ alloy Nb-17Si-10Mo-3Al at rotational speed 10-0 rpm. Republished with permission of Elsevier, from (Li, Miura, et al. 2011)*; permission conveyed through Copyright Clearance Center, Inc.*

Comparison of the yield strength and fracture toughness between conventionally arc melted and DS OFZ alloys, Nb-22Ti-16Si-7Cr-3Al-3Ta-2Hf-0.1Ho, showed that the former had yield strength of 1779 MPa and toughness of 11.2 $MPa.m^{1/2}$, while the latter grown at 6, 9 and 12 mm/hr has yield strengths of 1884, 1950, 1981 MPa and fracture toughness's of 13.4, 13.1, 12.9 $MPa.m^{1/2}$, respectively (Tian et al. (2009)). Higher strength and work hardening rate in the DS samples compared with the as-cast ones were thought to be due to coarser microstructure in the DS alloy (Sha, Hirai, Tabaru, et al. 2003).

High temperature (1250 ^{O}C) compressive yield strength of OFZ DS alloy Nb-21Ti-16Si-7Cr-3Al-2Hf at different growth rates showed that as the growth rate increased from 3 to 12 mm/hr the yield

strength decreases from 445 to 285 MPa with a sudden drop of 153 MPa between 5 and 8 mm/hr. The arc-melted master alloy from which the DS samples were prepared however had a strength of 326 MPa. Continuous, high aspect ratio phases grown at the low growth rates gave high compressive strengths. The higher the growth rate however the more interfaces were introduced to the system, this had a negative effect on strength (Huang et al. 2011).

Room temperature fracture toughness of the alloy Nb-21Ti-16Si-7Cr-3Al-2Hf grown at 5 mm/hr was highest at K_Q = 22.4MPa.$m^{1/2}$ followed by 3 mm/hr, the master alloy, 8 and 12 mm/hr at 17.99, 14.12, 13.6 and 11.0 MPa.$m^{1/2}$, respectively. The highest fracture toughness in the 5 mm/hr alloy was attributed to this alloy having a higher number of smaller silicide phases compared with the 3 mm/hr sample, increasing the interfaces for crack deflection and microcracking ahead of the main crack (Huang et al. 2011). Other work on the alloy Nb-17Si-10Mo-0.1Ga also showed this pattern of increasing fracture toughness with decreasing phase radii (Li, Ma, et al. 2011). This showed that grains with smaller diameter (≈ 1 mm) had a higher fracture toughness (11.5 MPa.$m^{1/2}$) than those with higher diameters (≈ 6 mm diameter grain had a fracture toughness of 9.3 MPa.$m^{1/2}$).

In crystal growth methods such as Bridgman, Czochralski and floating zone, all of which have been used for directional solidification processing of Nb silicide based alloys, the surface tension will vary because of gradients in temperature and solute concentration and the liquid will be in motion owing to surface tension gradients, gravity driven (natural) convection and stirring arising from rotation of the solid (and crucible), see below.

The floating zone process is containerless, (the melt is not in contact with a crucible), and surface tension forces (in opposition to gravity) “hold” the melt. The upper limit of the length of the melt zone (meaning the length beyond which the zone becomes unstable and collapses) is proportional to $(\gamma_{LV}/\rho g)^{1/2}$ where γ_{LV} is the surface tension of the melt, ρ is melt density and g is the gravitational acceleration (Lan & Kou 1992). For elemental Si, Nb, Mo the ratio $(\gamma_{LV}/\rho g)^{1/2}$ is large (respectively 0.17, 0.16 and 0.15) which means that necking (Figure 36) in the melt zone is not severe.

For Nb silicide based alloys with densities in the range $6.5 < \rho < 7.5$ g/cm^3 this ratio is in the range 0.167 to 0.18 (not accounting for changes in γ_{LV}).

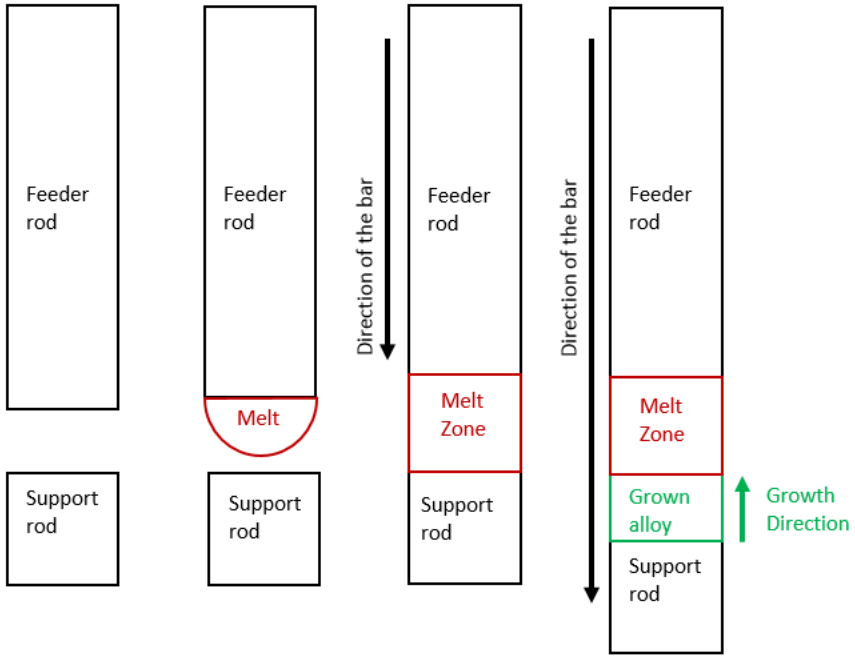

Figure 35: Schematic diagram showing the OFZ arrangement at three different times, t= 0 before start of OFZ, t = t_1 start of OFZ (with enlarged melt zone for visual purposes) and t = $t_2 > t_1$ showing part of grown alloy and melt zone.

Under normal gravity a short melt zone is desirable owing to its greater stability compared with long zones. Usually the ratio of the length to the diameter of the melt zone is 1 (see Figure 36i and ii). The floating zone moves through the solid by moving the solid rods (feeder and grown solid (crystal)) that border the zone or by moving the heater. The former is the case in this research.

In gravity conditions convection in the liquid can arise from surface tension gradients thermocapillary convection (owing to temperature and concentration gradients, see below) and from buoyancy (natural convection). Convection in the liquid zone can have an effect on liquid zone length, the shape of the S/L interface and on zone stability.

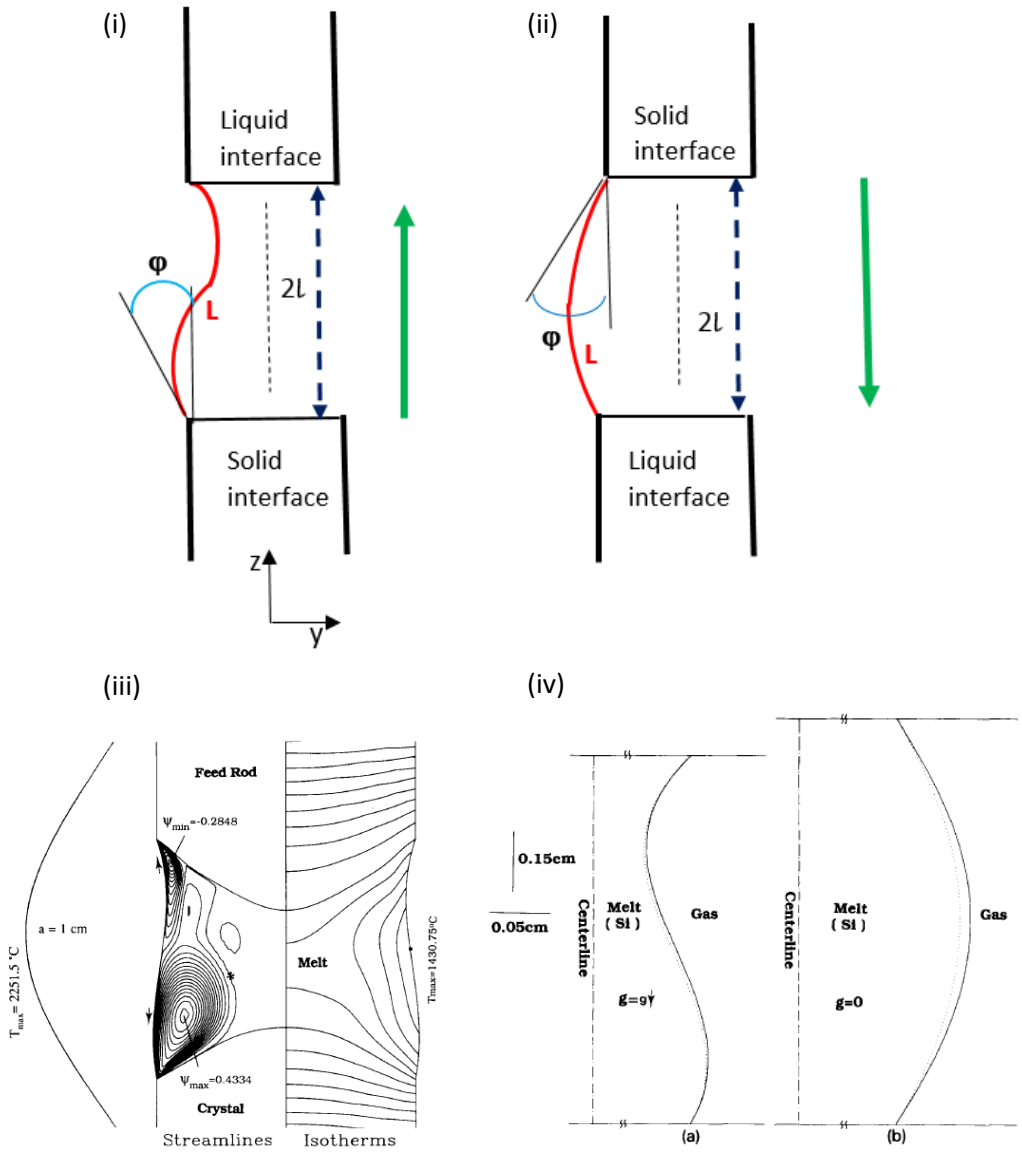

Figure 36: (i) and (ii) schematic diagrams showing floating zones and angle φ for a cylindrical solid. The arrows indicate the directions of growth (i.e., the direction of movement of the S/L interface). Only one side of the floating zone is shown. Growth axes indicated by dashed lines. The length of the floating zone is 2ℓ. (iii) Calculated (Lan & Kou 1991b) *flow and temperature in float zone for natural and thermocapillary convections for Si rod of 10 mm diameter OFZ processed under normal gravity with growth rate 150 mm/h and $\Delta T = T_{max} - T_m$ (T_{max} is the maximum temperature in the float zone) and (iv) effect of convection on the shape of L-V surface where (a) corresponds to the flow shown (iii) (radial scale is enlarged in (iv)).*

Floating zone processing can involve counter-rotation of feeder and grown solid, single rotation of feeder or grown solid or no rotation at all. Forced convection can be introduced by such rotations. Often slow rotation rates are used to achieve uniform (axisymmetric) heating.

In the floating zone melting process there is a liquid-vapour (L-V) interface (often referred to as the liquid surface) with an imposed temperature gradient. The surface tension is a function of

temperature. Thus, the temperature gradient will produce motion in the liquid (convection). The shape of the solid (S) depends on the L-V interface at the S-L-V junction. Figure 36i and ii shows the angle φ formed between the tangent to the L-V interface and the growth axis (i.e., the angle of the meniscus formed at the S-L-V junction). Every material will have a characteristic value of this angle, which we shall call φ^* (for Si $\varphi^* = 11^o$, for Ge $\varphi^* = 10^o$), and the latter will; (a) depend on the crystal orientation (the relative orientations of the three interfaces at the S-L-V junction will depend on the γ_{SV}, γ_{SL} and γ_{LV} surface tensions, the former two will also depend on surface orientation) and (b) be affected by the type of solutes and their concentrations in the liquid and by the gaseous environment in the OFZ process (Surek 1976).

Steady state growth occurs with $\varphi = \varphi^*$. If for some reason (see discussion above and below) there was a change in shape of the meniscus (i.e., growth with $\varphi \neq \varphi^*$), then the solid will not grow with a constant cross section, i.e., its dimensions will change. If the latter were to occur so that $\varphi \rightarrow \varphi^*$ a new steady state condition will be reached and stable solid shape can be achieved. However, if φ deviates significantly from φ^* then the shape of the solid will become unstable. Thus, there can be oscillations about the steady state when the system is perturbed ($\varphi \neq \varphi^*$). When the radii of the upper and lower solid (Figure 35, Figure 36i, ii and Figure 37c, d) are different, at steady state the decay time of a perturbation increases but the period of oscillation does not change. Temperature gradients will also be affected by changes in the shape of the solid and of the meniscus and in turn will influence these changes (Surek & Coriell 1977).

Oscillatory thermocapillary convection in crucible-less zone melting of Mo and Nb has been confirmed in the experimental work of Jurisch (1990). In W doped Mo as the power increased there was a significant change in the distribution of W from radial inhomogeneities to periodic and irregular non-rotating W striations. The latter were formed in Mo single crystals grown without rotation from the transition from steady thermocapillary flow to a single mode oscillatory state at a critical Marangoni number (see below) (Jurisch & Loser 1990).

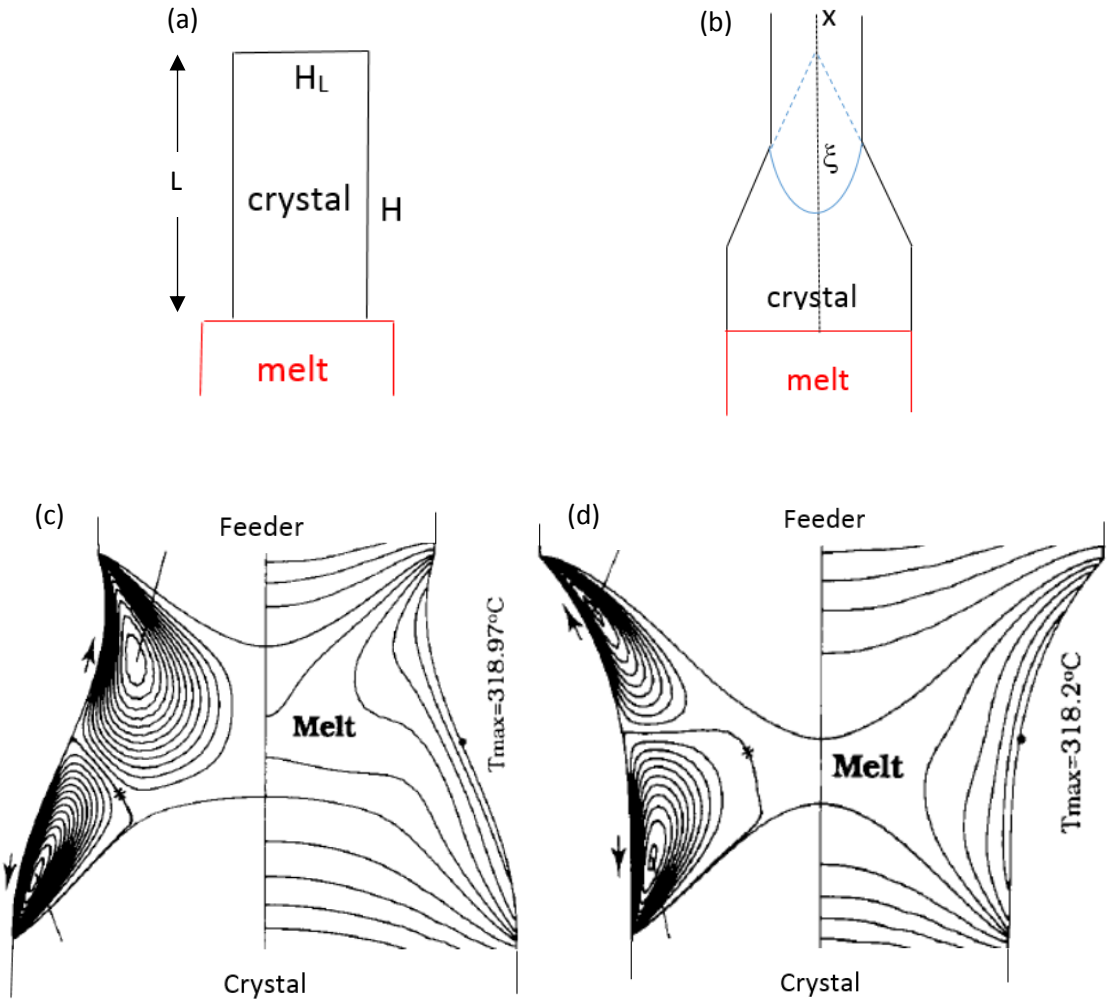

Figure 37: Schematic diagrams showing the geometries considered drawn from (a) Kuo & Wilcox (1972) *and (b)* (Louchev et al. 2004). *H is the Biot number (= hR/k for cylindrical surface, where h is the heat transfer coefficient, R is the radius of the crystal and k is the thermal conductivity). In (b) ξ is the angle at which crystal shoulder is formed if there were to be change in cross section area with distance from the growth interface. (c) and (d) calculated flowlines (left) and isothermal lines (right) under normal gravity for NaNO3 for feeder and crystal of different diameters of 4 mm and 6 mm* (Lan & Kou 1991b)

The 1D heat transfer problem for the interface temperature gradient *in the solid* was solved by Kuo & Wilcox (1972) for the geometry shown in Figure 37a, for materials with Biot number (see above figure) H < 0.2. For the conditions $H_L/H = \infty$, i.e., for perfectly cooled end of the crystal and taking the interface temperature equal to the melting point, the data in Table 1 of their paper gives, for a cylindrical crystal of radius 10 mm respectively for W (H = 0.071) and Nb (H = 0.063), the temperature gradient at the interface equal to 1365 K/cm and 973 K/cm, respectively (emissivity ε_{Nb} = 0.29 (Sakata et al. 2015)). The radiation heat losses to the surroundings increase with increasing diameter of the

processed rod (the radiation Biot number H increases). As H increases the curvature of the S/L interface increases (Chen & Chu 1995).

(Louchev et al. 2004) also used an 1D heat transfer problem to study the thermal stresses in the initial stages of crystal growth from the melt for the geometry shown in Figure 37b and considered the effect of change in cross sectional area with distance from the growth interface using the angle ξ. They proposed that the thermal stress is $\sigma_{thermal} \approx \alpha EW^2 d^2T/dx^2$ where α is the linear CTE, E is the Young's modulus of elasticity, W=0.2R (R is the diameter of the crystal) and dT/dx is the temperature gradient in the crystal. Tensile stress ($\sigma_{thermal} > 0$) arises from the heat dissipation from the lateral surface and compressive stress ($\sigma_{thermal} < 0$) from the radiation heat flux incoming to the crystal surface and from the geometry of the growing crystal (the effect of the latter was described using the angle ξ, see Figure 37b). For small ξ (< 30°) the thermal stress is tensile ($\sigma_{thermal} > 0$). The temperature gradient in the solid $(dT/dx)_S$ decreases with increasing ξ with the highest temperature gradient occurring for $\xi = 0$.

In floating zone melting with radiation heating (radiation heating is modelled using parabolic temperature profiles with a maximum at the centre) there are four sources of convection in the liquid, namely (i) surface tension driven flow, (ii) buoyancy driven natural convection, (iii) convection arising from rotation of the feeder and (grown) solid and (iv) flow generated by melting at the liquid interface and solidification at the solid interface (see Figure 36i and ii). The (i) arises from changing surface tension along the liquid surface owing to changes in temperature along the surface. The magnitude of this convection depends on the processing conditions and material. The flow will change from laminar to oscillatory to turbulent as the driving force increases.

The surface tension of hot liquid is lower compared with that of colder liquid. Thus, the system will attempt to lower its free energy via movement of the liquid from areas of low surface tension to areas of high surface tension. The resulting convection is referred to as surface driven flow, thermocapillary flow or Marangoni flow or Marangoni convection in temperature gradient (MCT). This

is described by the thermal Marangoni number Ma(T) = PrM, where Pr is the Prandtl number and M is the surface tension parameter (see below). Gradients in composition will also produce such a flow (gradients in surface energy at the S/L interface will not produce liquid motion owing to the no-slip condition) that is referred to as Marangoni convection in concentration gradient (MCC). The buoyancy driven convection arises from interaction of density variations in the liquid (due to temperature variations) with gravity or acceleration fields. The (iv) in the previous paragraph is attributed to the movement of the zone (through the solid).

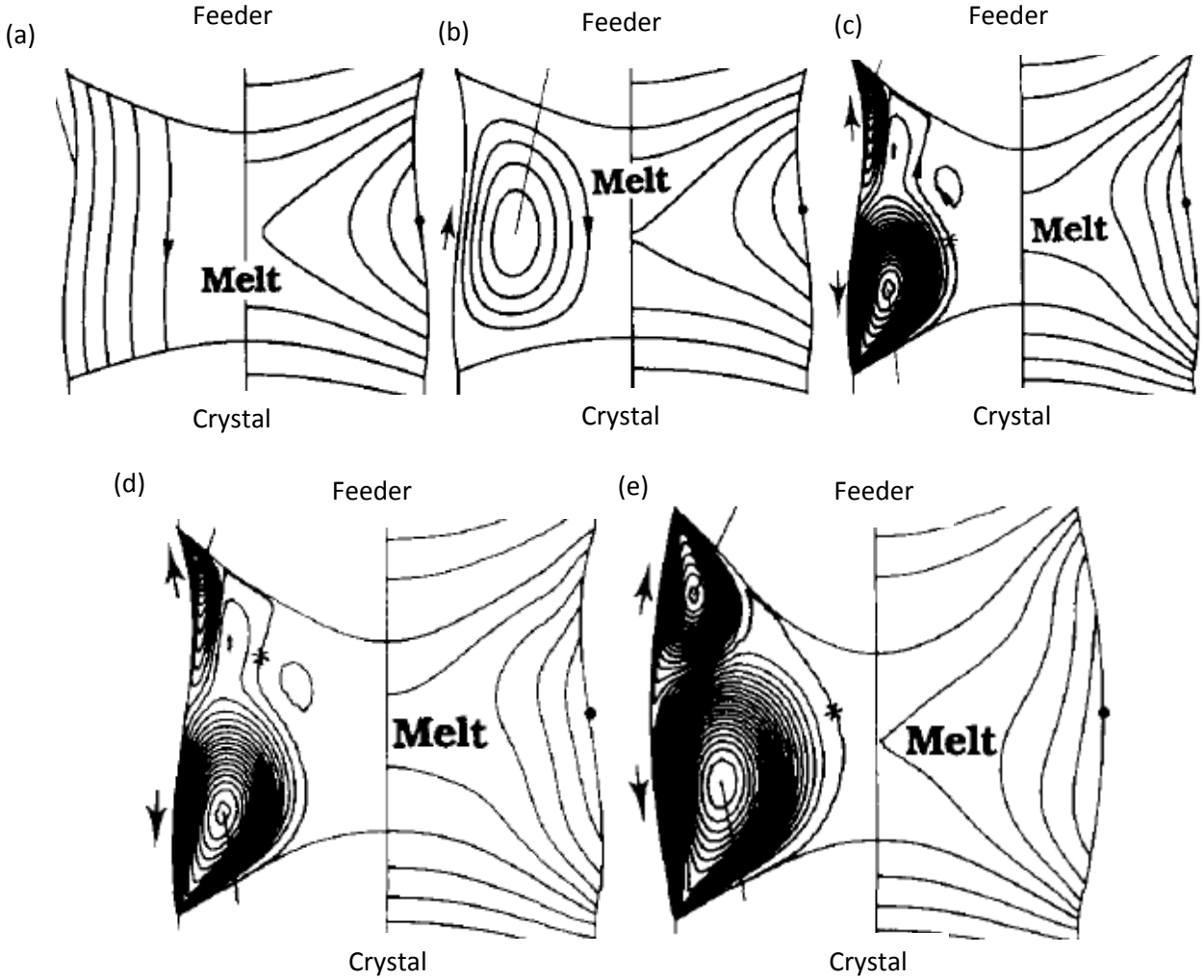

Figure 38: (a) to (e) calculated flowlines (left) and isotherms (right) for OFZ 10 mm Si rod grown at 150 mm/h with $\Delta T = T_{max} - T_m$ (T_{max} is the maximum temperature in the float zone) for (a) conduction, (b) natural convection and (c) thermocapillary and natural convection, (d) normal gravity and (e) zero gravity (Lan & Kou 1991b).

The Prandtl number Pr is important for the shape of the melt zone. Liquid metals have small Pr. When the power input increases the shape of the S/L interface changes from convex towards the

liquid to flat to concave (Chen et al. 1994). Thermocapillary flow instability in the liquid may appear before instability from the L-V interface sets in. Large surface deformation of the latter can modify the flow and temperature fields, see Figure 36iii and iv and Figure 38 (Lan & Kou 1991b).

The Marangoni flow has an effect on transport phenomena (i.e., mass and heat transfer) during OFZ. The shape of the S/L interface and the distribution of solute (i.e., the development or not of chemical inhomogeneities) depend on the mass and heat transfer. The homogeneity of the solid is influenced by mass transfer (and heat transfer, due to its effect on the shape of the S/L interface) and the shape of the solid and the stability of the floating zone are influenced by heat transfer. For Pr << 1 laminar flow has a small influence on the heat transfer.

Dimensionless numbers that are important for understanding floating zone processing include the surface tension parameter M, and the Prandtl Pr and Schmidt Sc numbers. The surface tension parameter that is given by the equation $M = \rho(T_o - T_m)(-\partial\gamma_{LV}/\partial T)\alpha/\mu^2$ is used to characterise thermocapillary flow in OFZ. In this equation ρ is the density of the liquid, α is the radius of the zone, μ is the liquid viscosity, T_o is the temperature of the liquid surface at the centre of the zone (K) and T_m is the interface temperature taken to be the melting point (K). For elemental Nb the term $-\rho(\partial\gamma_{LV}/\partial T)/\mu^2$ is equal to 1380 (the data for Nb is γ_{LV} = 2050 dyne/cm, $-\partial\gamma_{LV}/\partial T$ = 0.43 dyne/cm K, ρ = 8 g/cm^3, μ = 5 cP (1 centipoise (cP) = 1 mPas = 0.001Nsm^{-2} = 0.001 kgm^{-1}s^{-1}) and is from Chang & Wilcox (1975)). Compared with M = 14000 for Si (the most studied element in models of floating zone melting) (Chang & Wilcox 1975). Thus, for elemental Nb and α = 5 mm (the diameter of the solid rods used for OFZ in this thesis was 10 mm) the value of M is 690, 345 and 34.5 for $T_o - T_m$ equal to 1, 0.5 and 0.05 K, respectively. According to Chang & Wilcox (1975) buoyancy driven convection in enclosed spaces is oscillatory for $T_o - T_m$ above 0.1 K and turbulent above 2 K.

The Prandtl (Pr) number ($= C_p \mu/k$) is the ratio of momentum diffusivity (μ/ρ = kinematic viscosity) to thermal diffusivity ($k/\rho C_P$) where C_P is the specific heat at constant pressure and k is the thermal conductivity. The Schmidt (Sc) number is the ratio of momentum diffusivity to molecular

diffusion coefficient and is given as Sc = $\mu/\rho D$, where D is the diffusion coefficient. For elemental Nb the values are Pr = 0.026 (compared with Pr = 0.023 for Si and Pr=0.025 for Mo) and Sc = 145 (compared with Sc = 5 for Si) (the data for elemental Nb is D = 4.3 10^{-4} cm^2/s, k = 0.19 cal/cm K s, and is from Chang & Wilcox (1975)).

Transport by convection becomes more significant compared with transport by conduction or diffusion as Pr or Sc increases. Liquid metals are low Pr number materials. Small values of the Prandtl number, Pr << 1, means the thermal diffusivity dominates and large Prandtl number, Pr >> 1, means the momentum diffusivity dominates. The Pr values for elemental Si and Nb indicate that the heat conduction is more significant compared with convection and that thermal diffusivity is dominant. Thus, if these elements were to be grown using floating zone melting, it is most likely that they will exhibit thermocapillary flow. The latter can introduce considerable inhomogeneities even at gentle flow.

Calculated flowlines and isothermal lines for elemental Si by Lan & Kou (1993) are shown in Figure 38 for the conditions (a) of zero volume expansion coefficient β and $|\partial\gamma/\partial T| = 0$ (conduction), (b) for $\beta \neq 0$ and $|\partial\gamma/\partial T| = 0$ (natural convection) and (c) for $\beta \neq 0$ and $|\partial\gamma/\partial T| \neq 0$ (thermocapillary and natural convection). In (b) the upward shift of the melt zone and the change of the shape of the S/L interface are not significant. In (c) the shape of the S/L interface is more convex compared with (a), the lower flow loop is larger and stronger than the one above it which has less space to develop and the highest temperature of the liquid is closer to the feeder side than the crystal side. The small flow loop in the upper half of the melt zone in (c) is attributed to natural convection. Figure 38e shows the bulging of the L-V interface under zero gravity.

Experiments (Schwabe et al. 1978) making use of the similarity law of hydrodynamics with $NaNO_3$ (material considered to be comparable with Si for float zone modelling, even though it has Pr > 1) have confirmed the calculated (e.g., see Chang & Wilcox (1975)) streamlines for Si for M = 35, Pr = 0.023, α = 5 mm and $T_o - T_m$ = 0.005 K. Schwabe et al. (1978) showed (see Figure 39); (a) the

streamlines are concentrated at the surface, with their centre of the vortex being near the surface, (b) the direction of the streamlines was from hot to cold in both halves of the zone, (c) the flow of hot liquid was along the surface directed to the interface in both half zones and (d) flow and mixing in the floating zone were significant.

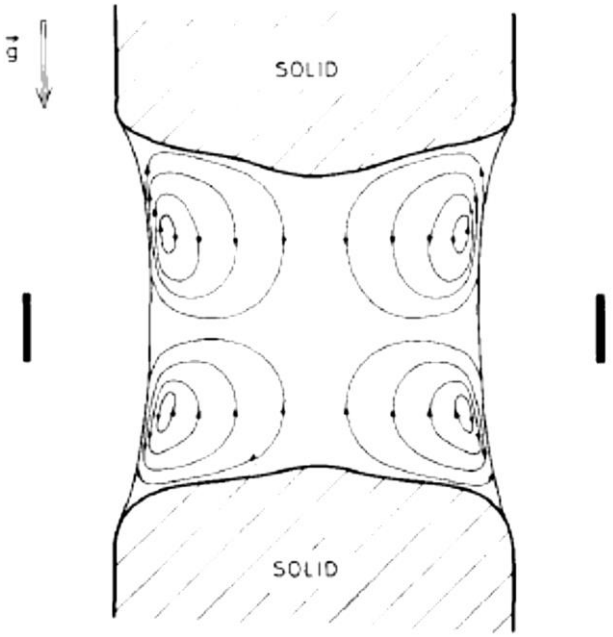

Figure 39: Schematic of MCT in a $NaNO_3$ floating zone (Schwabe et al. 1978). *The vertical black lines indicate radiation heating (parabolic temperature profile).*

The experiments of Schwabe et al. (1978) also showed; (i) for short floating zones the heat transfer was mainly by diffusion and the contribution of MCT to the latter became significant when the zone length exceeded 1 mm, and (ii) the Marangoni vortices moved from near the surface (where they were confined for short zones (compared with their width (radius)) towards the zone interior as the zone length was increased. The calculations showed formation of secondary cells as the M increased. The experiments of Schwabe et al. (1978) and others have also indicated that flow instability occurs when the Marangoni number exceeds some critical value, or critical Marangoni number, which depends strongly on the aspect ratio of the zone and the properties of the liquid.

Schwabe et al. (1978) also studied $NaNO_3$ doped with CH_3CH_2COOK to find out the effect of the solute (CH_3CH_2COOK). They reported; (a) the flow velocity induced by MCC was significantly lower than that of MCT and (b) the flow of the hot liquid was to the zone interior.

Chang and Wilcox studied the effect of increasing M on flow induced by MCT for floating zone melting of Si using parabolic temperature profiles (Chang & Wilcox 1976). Donut shaped vortex cells were formed in all cases, see streamlines in Figure 40. For M equal to 35 and 350 only two cells were formed and their centres moved closer towards the S/L interfaces as M increased. When M increased to 3500 secondary vortex cells were formed behind the primary cells. As the value of M increased further to 7000 third and fourth vortices were produced, see Figure 40. Chang & Wilcox (1976) concluded that *"…with laminar flow, the convection had only a small influence on heat transfer at small Pr (<< 1) and that the laminar flow cells would lead to significant inhomogeneities in the melt during zone melting, which in turn would cause inhomogeneities in the solidified material".*

Convection and temperature fields arising from rotation of the feeder and grown solid in floating zone melting using cylindrical rods have also been studied (e.g., see Kobayashi & Wilcox (1982)). The convection was described using the dimensionless numbers $S = \omega_f/\omega_S$ and $A = l/\alpha$, where ω_f and ω_S are the rotation speeds of the feeder and solidified specimen, respectively, and l and α are the half zone length (see Figure 36i) and the rod radius, respectively, and the Reynolds number due to rotation $Re_S = \alpha^2\omega_S/\nu$, where ν is kinematic viscosity. Figure 41 shows the calculated patterns for the case where there is no free convection (i.e., Gr = 0, the Grashof number Gr is the ratio of the buoyancy (upward) force on the fluid to viscous force acting on a fluid) and no Marangoni convection (i.e., Ma(T) = 0).

According to Kobayashi & Wilcox (1982) *"…for S = 1 the fluid rotates as if it were a solid body, for $1 > S \geq -0.25$ a single cell forms in the zone and the fluid at the axis flows from the slower rotating rod to the faster rod and returns along the zone surface in the opposite direction, for S = - 0.5 another cell rotating in the opposite sense appears near the edge of the slower rotating rod, as S becomes more*

negative this cell becomes more larger and completely covers the interface, the fluid near the axis flows towards each interface and two circulating cells are divided by a stagnant surface, and when S = -1 the flow in the zone is divided into two equal cells by the mid-plane of the zone.".

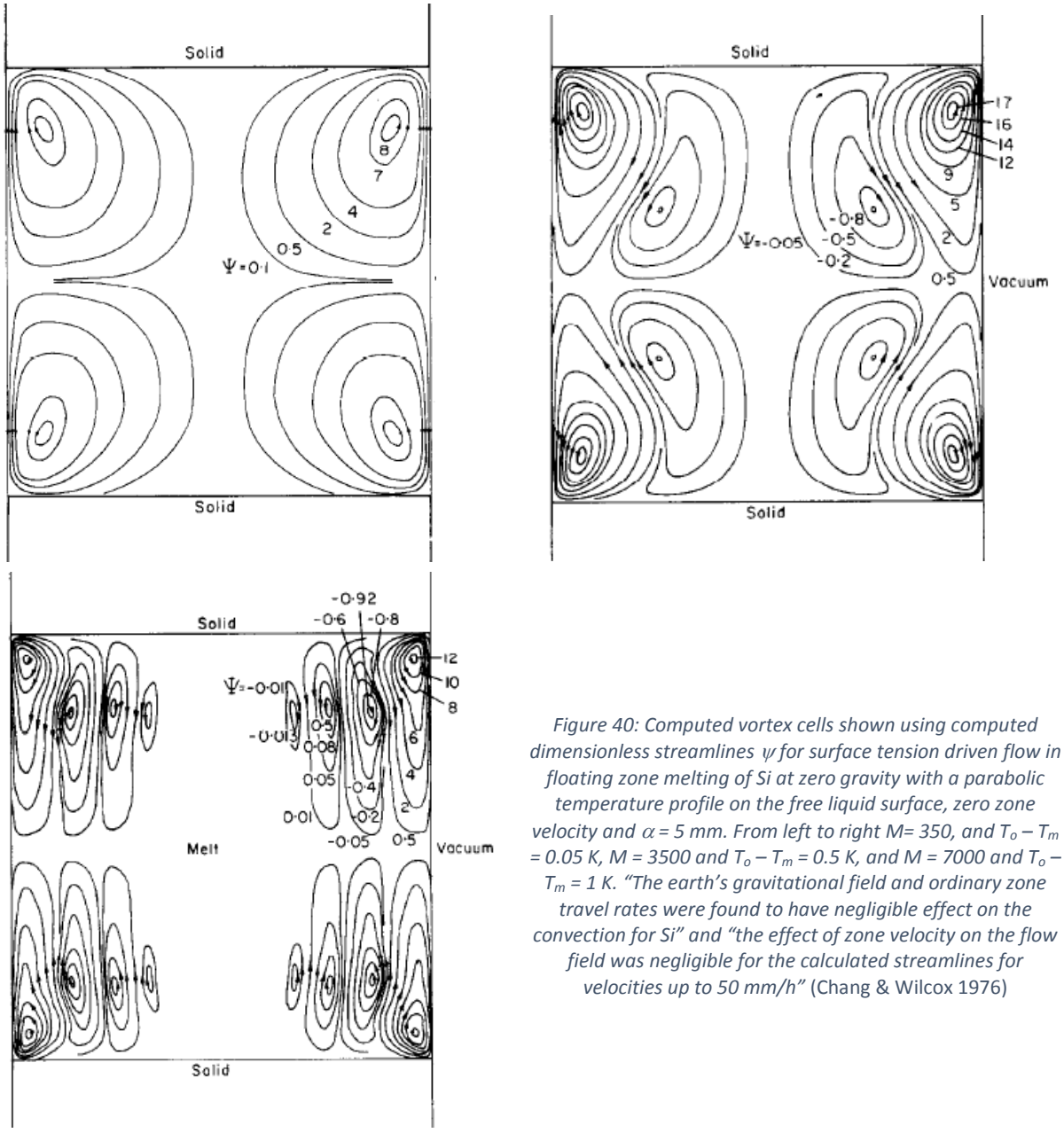

Figure 40: Computed vortex cells shown using computed dimensionless streamlines ψ for surface tension driven flow in floating zone melting of Si at zero gravity with a parabolic temperature profile on the free liquid surface, zero zone velocity and α = 5 mm. From left to right M= 350, and $T_o - T_m$ = 0.05 K, M = 3500 and $T_o - T_m$ = 0.5 K, and M = 7000 and $T_o - T_m$ = 1 K. "The earth's gravitational field and ordinary zone travel rates were found to have negligible effect on the convection for Si" and "the effect of zone velocity on the flow field was negligible for the calculated streamlines for velocities up to 50 mm/h" (Chang & Wilcox 1976)

The dependence of the temperature field on convection in the floating zone depends on Pr, the Biot number H and dimensionless power density Q. The Biot number (an index of the ratio of the heat transfer resistances inside of and at the surface of a body, small H (< 1) means uniform temperature

inside the body) is $H = \varepsilon\sigma T_m^3\alpha/k$, where ε is the emissivity, α is the radius of the crystal (rod) and σ is the Stefan-Boltzmann constant ($5.67\ 10^{-8}$ W/m^{2}K^4), and $Q = q\alpha/kT_m$ where q is input power density.

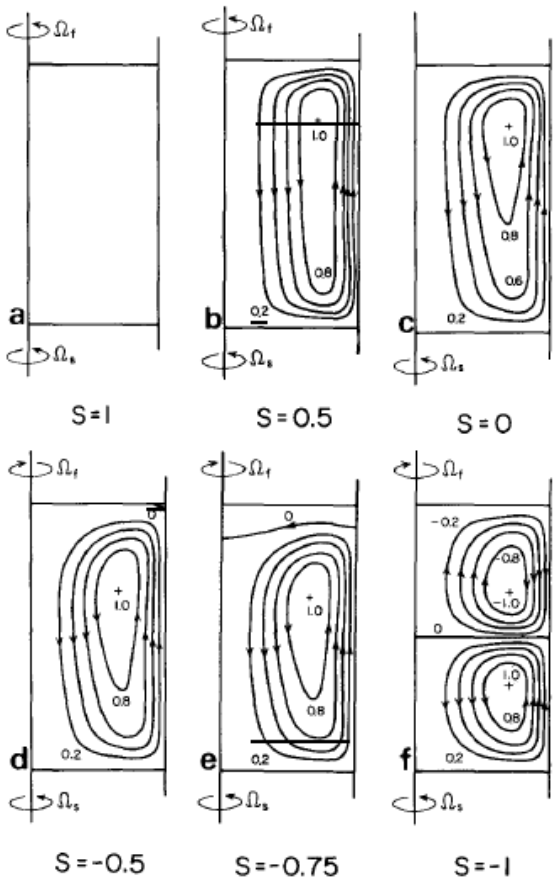

Figure 41: Calculated flow patterns shown as equi-contours of a stream function for Re_S = 100 and A = 1 and indicated values of S (Kobayashi & Wilcox 1982)*. No free convection and no Marangoni convection.*

Calculated temperature fields for Re_S = 100, A = 1 and H = 0.01 are shown in Figure 42 for two Pr and three S numbers, namely 0.10 and 1 for Pr and 1, 0 and -1 for S assuming no free convection (Gr = 0) and no Marangoni convection (Ma(T) = 0). Remembering that liquid metals have low Prandtl values, for such small Pr numbers when $PrRe_S$ = 1 the temperature field is determined by conduction.

When $PrRe_S$ = 100 the temperature profile depends strongly on fluid flow. For S = 1 the temperature field is the same as that for conduction (no circulating flow in the zone). For S = 0, there is no symmetry of the temperature profile along the surface about the mid-plane, the isotherms near the axis are pushed to the faster rotating rod and away from the slower and the highest temperature

is closer to the slower rotating rod. "*For S = - 1, the isotherms near the axis are pushed to each rod and those near the periphery move away from each rod along the flow direction.*"

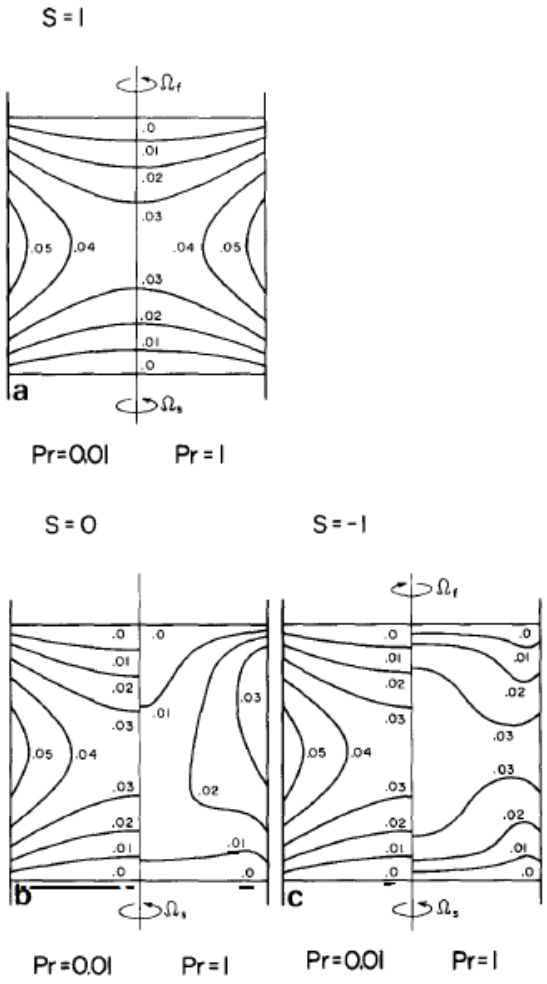

Figure 42: Calculated temperature fields (temperature shown with isotherms) for Re_S = 100, A = 1, H = 0.01, $\theta_o = (T_o - T_m)/\Delta T$ = - 1 and dimensionless power density Q = 0.0575 for the indicated values of S and Pr number, where T_o is the temperature of the surroundings and ΔT a characteristic temperature difference, see (Kobayashi & Wilcox 1982).

Lan and Kou studied the effects of counter-rotation and single rotation on heat transfer, fluid flow and shape of the S/L interface *in normal gravity* OFZ processing of cylindrical rods of $NaNO_3$ (Lan & Kou 1991a). The $NaNO_3$ has properties close to those of elemental Si and thus it is often used in studies of floating zone behaviour (see above the discussion of the work of Schwabe et al. (1978)), but its higher (compared with Si) Pr number means that the effects of rotation discussed below should be expected to be more significant than those for lower Pr number materials like Si, Mo and Nb. Lan and Kou considered upward and downward growth, counter-rotation speeds of 140, 200 and 400 rpm

(significantly higher than the rotation speeds used in this research and reported for one study in the literature, see below), single rotation speeds of 150 and 400 rpm and growth rates up to 20 mm/h.

First we shall consider the results of Lan & S. Kou (1991) for *upward* growth. For each of the three counter-rotation speeds four flow cells were formed in the melt zone, two near the L-V surface and two further in (to visualise this consult the image in the middle of Figure 40 and imagine the outer cells being squeezed and very narrow). The former were attributed to surface tension gradients (Marangoni convection or thermocapillary convection) and the latter to the centrifugal force arising from the counter-rotation, i.e., were attributed to forced convection. The latter increased with increasing counter-rotation speed and as a result the two inner cells expanded at the expense of the two outer cells. As the counter-rotation speed increased further the forced convection was further enhanced, “its” two cells expanded further, the two outer cells almost disappeared, the maximum velocity in the liquid was near the vertical centre line directed towards the horizontal centre line of the melt, the convective heat transfer to the centre of the S/L interface was significant and the shape of the latter became concave. As the growth rate increased from 3.6 to 20 mm/h for counter-rotation speed of 200 rpm, the position of the zone moved towards the grown solid and the liquid/feeder interface became more convex. For counter-rotation speed of 200 rpm and growth rate 10 mm/h, as the peak temperature in the Gaussian temperature distribution increased (i.e., the temperature distribution became sharper) the maximum surface temperature increased and the thermocapillary convection became stronger.

Next we consider the results of Lan & S. Kou (1991) for *downward* growth. For counter-rotation speed of 200 rpm and growth rate of 10 mm/h the free surface bulged (necked in upward growth). Owing to gravity, in upward growth the diameter of the upper half of the zone was smaller than that of the lower half. In downward growth the free surface had a significantly larger average diameter (and total area). The larger area received more heat from the heater, meaning the heat input was significantly greater in downward growth, and this resulted in larger volume of liquid and zone length.

In other words, the zone stability was sensitive to heat input in downward growth. Too high a heat input bulged the L-V surface which in turn caused more heat input. As the zone length increased, the free surface near the upper S-L-V junction started to neck leading to the condition $\varphi < \varphi^*$ and a reduction in the diameter of the solid. This in turn caused the liquid volume to increase and the free surface to bulge more and eventually the liquid broke out. As the counter-rotation speed increased to 400 rpm for the same growth rate the liquid zone became significantly shorter and its free surface bulged slightly. The latter helped to keep the heat input low and thus the zone was short, which ensured slight bulging. The resultant zone was thus very stable.

Let us now pay attention to the results of Lan & S. Kou (1991) for *single rotation*. When the speed was 400 rpm and the growth rate 10 mm/h only one cell formed and it was attributed to forced convection. Comparison of results for rotation speeds of 150 and 400 rpm and growth rate of 10 mm/h showed that as the speed increased the zone length decreased slightly but the separation between the S/L interfaces increased at the centreline. It must be realised that when it comes to single rotation there are four possibilities, namely upward growth with rotation of the feeder rod or the grown solid and downward growth with rotation of the feeder rod or the grown solid. The shape of the S/L interface depends on the rotation mode, it is convex when the feeder rod is rotated and flat when the grown solid is rotated. The free surface necks in upward growth and bulges in downward growth (the same behaviour was discussed above for counter-rotation of the feeder and grown solid rods). The position of the zone is also affected when single rotation is used, the zone shifts towards the feeder rod when the grown solid rod is rotated and vice versa.

In OFZ with mirror furnaces the radiation for the heating of the material is provided either from the (finite size) filament of a halogen (or xenon) lamp or from a (finite size) arc of arc lamp, both of which can be of a size comparable with the diameter of the material rod. In this type of OFZ it is difficult to measure and control the temperature distribution. The radiation is directly or indirectly reflected from the mirror to the material. The energy flux depends on the volume of the heating

source V_L, the lamp power W_L and the lamp emissivity ε_L. The power intensity $\kappa = \varepsilon_L W_L/(4\pi V_L)$ is a lamp property.

The size of most commercially available lamps is larger than the diameters of OFZ processed samples. Spherical lamps provide quite uniform heating but many OFZ systems do not use spherical lamps, instead long cylindrical lamps are preferred as these are expected to produce sharper axial energy distribution and thus higher $G_L > 0$ at the S/L interface (to prevent formation of constitutionally undercooled liquid, desirable for single crystal growers). Heat transport between the sample and the environment is by convection and radiation.

The energy distribution (direct and indirect radiation) from the lamps in OFZ processing using mirror furnaces with upward growth in normal gravity *without rotation* has been modelled by Lan & Tsai (1997) with vacuum as the growth atmosphere (heat transfer coefficient h = 0) and room temperature as the ambient temperature. Their results can be summarised as follows: (1) When spherical lamps are used the energy distribution is affected by the lamp size, for small lamps it is sharper but less uniform in the middle of the zone and becomes more uniform when the lamp radius is larger than the sample radius. (2) When elongated lamps are used the heating is less uniform, the axial flux distribution becomes sharper but the intensity is reduced. (3) Modulation of the energy distribution is possible by defocusing the lamps. For spherical lamps slight defocusing does not improve heating. However, slight defocusing in the axial direction produces an asymmetric heating profile that is beneficial (more heat on the feeder side to melt the material and less heat on the grown solid side to aid solidification). (4) For spherical lamps the maximum temperature is slightly higher in the zone that is near the lamps and the zone in this case becomes longer. Lamps of the same power as spherical lamps but elongated along the y axis (or squeezed along the z axis, see Figure 36) give significantly shorter zone and when the lamps are squeezed more along the z axis some of the core of the zone is not melted. (5) Significantly non-uniform heating results when non-spherical lamps are placed vertically so that their fatter side is parallel to the z axis, the uniformity of heating is much

improved when the fatter side is parallel to the y axis, in this case the zone shape is more axisymmetric. (6) When non-spherical lamps placed parallel to the y axis are moved toward the sample (defocussed) the liquid zone becomes shorter and less uniform, the S/L interface more convex in the y-z plane and the zone significantly shorter in the x-z plane. (7) The opposite effects occur when non-spherical lamps placed parallel to the y axis are moved away from the sample (defocussed). The (6) and (7) suggest that use of non-spherical lamps at their foci may not always be the best choice.

We discussed in § 1.1.1 that the formation of constitutionally undercooled liquid ahead of an S/L interface depends on concentration and temperature gradients. The S/L interface becomes morphologically unstable (i.e., it "breaks down" to cells and dendrites) as the former increases and the latter decreases. In floating zone processing the formation of constitutionally undercooled liquid and therefore the "breakdown" of the interface is most likely at the centre rather than at the periphery of the solidifying solid. At low M values if the growth rate is not low there will be radial variations in solute concentration. At intermediate M values oscillations and formation of striations parallel to the S/L interface are likely.

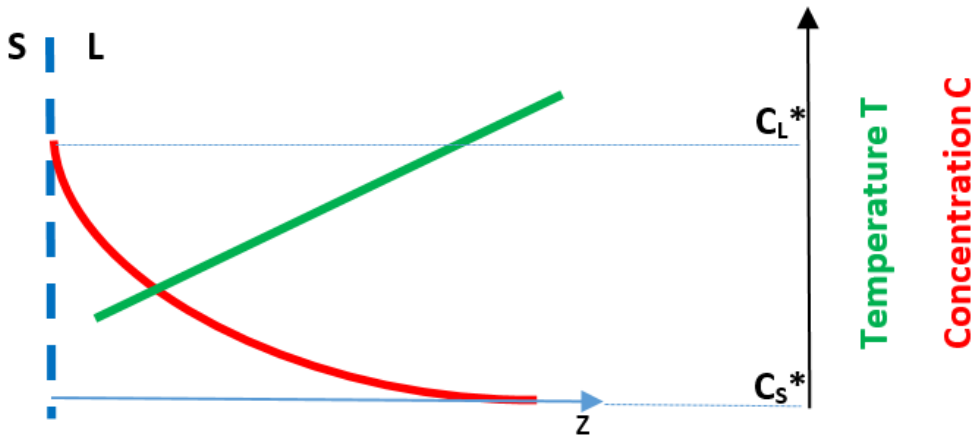

Figure 43: Schematic diagram showing concentration and temperature gradients ahead of an S/L interface.

Consider an alloy of composition C_o with solute having partition coefficient $k < 1$ and reducing the surface tension of the melt. Figure 1a shows the relevant part of the phase diagram and Figure 1c shows the solute boundary layer of thickness δ formed ahead of the S/L interface. A positive

temperature gradient in the melt is shown in Figure 1d. The information of these three figures is "captured" in the Figure 43 which shows the position of the S/L interface at T = T* with the vertical dashed line (with the compositions of the solid and liquid at this temperature as C_S* and C_L*, respectively, which can be read on the axis on the right hand side), the solute rich boundary layer ahead of the interface (red curve) and the temperature gradient in liquid (green line). Assume that the alloy is processed using OFZ and allow for oscillations of temperature in the liquid.

The opposite forces, f_i, acting on the S/L interface due to the temperature and concentration gradients will be $f_z(T) = (\partial\gamma/\partial T)(\partial T/\partial z)$ and $f_z(C) = (\partial\gamma/\partial C)(\partial C/\partial z)$ where γ is surface tension (Schwabe et al. 1978). Assume that $f_z(T) > f_z(C)$. The resultant force means that phenomena will be driven by Marangoni convection in temperature gradient. This MCT will carry hot liquid to the interface and will support the heat transfer to the interface from the liquid ahead of the S/L interface. If there were to be an increase in $V_{S/L}$ this will change the solute profile in the boundary layer and the $f_z(C)$ will increase, which means that the resulting force on the interface will be reduced, i.e., the MCT will be reduced and this will result in an increase in $V_{S/L}$. If instead there were to be a decrease in $V_{S/L}$ this will change the solute profile in the boundary layer and the $f_z(C)$ will decrease, which means that the resulting force on the interface will be increased, i.e., the MCT will be increased meaning the MCT carries more hot liquid to the interface making it more morphologically stable. This simple argument shows how growth instabilities can arise because of MCT and MCC.

In floating zone melting the temperature gradient in the liquid $(dT/dx)_L$ is linked with that in the solid $(dT/dx)_S$ via the equation $k_S(dT/dx)_S = k_L(dT/dx)_L - V_{S/L}\Delta H\rho_S$ where k_i (i=S, L) is thermal conductivity and ρ_S is the density of the solid. For constant growth rate a decrease in $(dT/dx)_S$ is linked with a decrease in $(dT/dx)_L$ and thus would affect the conditions for forming constitutionally undercooled liquid ahead of the S/L interface and therefore the morphological stability of the latter. As $(dT/dx)_S$ decreases with increasing ξ (see Figure 37b) a change in cross section of the crystal (change in ξ), which brings in compressive thermal stress in the crystal (see above), will also reduce $(dT/dx)_L$ (G_L in

Figure 1b) and thus encourage the onset of constitutional undercooling (Louchev et al. 2004). Notice also change in flowlines and isothermal lines with change in cross section in Figure 37c and d.

Let us now consider the morphological stability of the S/L interface in more detail. This is important for the research presented in this thesis because the way the S/L interface "breaks down" (i.e., becomes destabilised) will have an effect on the scale of the microstructure (eutectic spacing). A detailed theoretical study of the morphological stability of the S/L interface was made by Mullins & Sekerka (1963) and numerous researchers after them who only changed slightly the conclusions of the original theory (e.g. see Coriell & Sekerka (1976)). This research predicted correctly the threshold growth rate for marginal stability. However, experimental work did not agree with the wavelength of the first stable perturbation predicted by the theories (in other words the observed primary arm spacings (linked with the critical wavelength) were much smaller than the predicted wavelength at the onset of instability). Mullins & Sekerka (1963) and those after them considered the melt to be quiescent and diffusion to be the only mechanism of mass transport in the melt. The convective motion in the liquid distributes solute laterally and thus should be expected to morphologically stabilise the S/L interface (and thus to have an effect on the wavelength at which the interface breaks down, i.e., instability occurs). What is the effect for solutes with $k < 1$ and $k > 1$?

Experimental study using succinonitrile-alcohol (solidification analogue material) showed that convection caused by radial temperature gradients induced macroscopic distortion of the S/L interface which developed deep (≤ 3 mm) depressions at $V_{S/L} > V_{(S/L)}^{critical}$ (where $V_{(S/L)}^{critical}$ is the critical growth rate at which the interface becomes unstable). The "breakdown" of the interface started at these depressions (Schaefer & Coriell 1984). Experimental study of DS Pb-Sn eutectic (Bridgman with $(dT/dx)_L$ = 20 K/cm) showed that as convection increased (rotation speed changed from 250 rpm to 500 rpm, growth rates in the range 8 mm/h to 22.5 mm/h) there was segregation at the S/L interface (there was negligible segregation at 250 rpm) and the eutectic spacing changed (Quenisset et al. 1983), see below.

The effect of convection has been studied theoretically by considering (i) the effect of the latter on the boundary layer at the S/L interface and (ii) that at distances from the unperturbed S/L interface greater than δ_m (see below) the concentration is uniform and equal to the concentration of the bulk liquid. The mass flow boundary layer (thickness δ_m) resulting from thermosolutal convection is smaller than the thermal flow boundary layer (thickness δ_t) owing to the much higher thermal diffusivity compared with the mass diffusion of solute in liquids (Hurle 1969). Smaller δ_m corresponds to larger convection ($\delta_m = \infty$ corresponds to diffusive mass transport, the case considered by Mullins & Sekerka (1963). Thus, because $\delta_m << \delta_t$ mixing affects the mass flow more strongly compared with the thermal flow.

Hurle (1969) studied theoretically the influence of convection on morphological stability for a stagnant boundary layer in DS solidification with constant $V_{S/L}$, temperature gradient G_L and concentration gradient dC/dx at the interface and concluded that convection made the S/L interface less morphologically stable for solute with k > 1 but could either increase or decrease morphological stability for k < 1. Hurle (1969) did not allow for coupling of the fluid flow field and morphological perturbations of the S/L interface. When Favier & Rouzaud (1983) considered a deformable boundary layer (meaning the boundary surface in the liquid is deformed in the same way as the perturbed S/L interface), i.e., allowed for the fluid flow field to be changed in front of the perturbation, they concluded that convection always stabilises morphologically the S/L interface for solute with k < 1, that for k > 1 convection destabilises the S/L interface and that capillary stabilises the interface quickly when convection is strong (or $\delta_m(D_L/V_{S/L})^{-1}$ is small). Experimental work (Tewari & Chopra 1992) using succinonitrile-acetone (transparent organic analogue for solidification) and Pb-10Sn (wt%) alloys supported the conclusions of Favier & Rouzaud (1983). Tewari & Chopra (1992) reported that two dimensional waves formed first on the S/L interface and then “broke down” resulting in the formation of 3D cells.

The above discussion would suggest that if fluid flow were to exist in the melt it should be expected to alter the thermal and solutal gradient ahead of the S/L interface and therefore to affect (i) the critical $V_{S/L}$ at which the interface becomes morphologically unstable and (ii) the scale of the microstructure (effect on the magnitude of the primary arm spacing). What would be the effect of convection on eutectic growth?

We are interested in the effect of convection on eutectic growth because it is possible to "grow" near eutectic Nb silicide based alloys as in situ eutectics using DS (in fact this new family of ultra-high temperature alloys is often referred to as Nb in situ composites because the "reinforcing" phase is formed ("grown") in situ during processing). Would convection have any effect on the aligned growth of the eutectic?

Moderate convection will result in laminar flow. In eutectic solidification flow parallel to the interface leads to mass transfer in orthogonal direction to the lamellae, which is superposed on the diffusional mass transfer between the liquid in front of each phase.

Quenisset & Naslain (1981) theoretically studied liquid flow within the liquid boundary layer parallel to the S/L interface in DS solidification of eutectic alloys and showed that it had strong effects on the size of eutectic phases and on lamellar $\leftrightarrow$ fibre eutectic microstructure transitions. They considered a binary A-50B alloy (i.e., C_{Eu} = 50%) with no terminal solid solutions (i.e., no solid solubility of A in B and of B in A), and equal volume fractions of the phases α and β that were assumed to form a lamellar eutectic. They considered that eutectic growth occurs at the extremum (i.e., at the spacing giving the minimum interfacial undercooling) and modified the Jackson-Hunt well known relationship $\lambda^2 V_{S/L}$ = constant to $\lambda^2 V_{S/L} = E(1 - [FG_u\lambda^2/D])^{-1}$ where E and F are constants the values of which depend on the alloy ($E = 2\Gamma_{S/L}D/mC_{Eu}$ and $F = 3\zeta/16$) , D is the interdiffusion coefficient of the elements A and B in the liquid, $\Gamma_{S/L}$ is the Gibbs-Thomson coefficient, m is the liquidus slope, ζ is a dimensionless constant and G_u is a (constant) gradient of velocity (u) of the transverse flow perpendicular to the lamellae. Quenisset & Naslain (1981) showed that; (a) for large D of each element, small λ and small

flow velocity, "u", the effect of forced convection is negligible, (b) λ increases as forced convection increases, (c) the lamellar $\rightarrow$ fibre eutectic microstructure transition becomes easier when convection is present and (d) points (a) to (c) become important at low growth rates (or large eutectic spacing λ). They compared the above prediction with the experimental data for eutectic spacing and growth rate for Ti-Ti_5Si_3 eutectic alloy that was solidified directionally using floating zone and showed good agreement, namely the increase of λ, particularly at low growth rates, with increased convection. In a subsequent paper based on an experimental study Quenisset et al. (1983) reported (i) there was agreement with experimental results for λ versus growth rate for the Pb-Sn eutectic, (ii) that the effect of convection on the eutectic solidification of the Cd-Zn eutectic was not as strong as for Ti-Ti_5Si_3 and Pb-Sn and (iii) increases in rotation speed that led to turbulent flow resulted in the development of transverse macrosegregation. They also concluded that convection increased the tendency to initiate a morphological transition and to degenerate eutectic microstructures.

Wilcox and co-workers also studied theoretically the effect of convection on the solute concentration in front of a lamellar eutectic but unlike Quenisset & Naslain (1981) they considered eutectics with volume fractions of 50 and 33% (Baskaran & Wilcox 1984) and 10 and 30% (Chandrasekhar et al. 1986). Wilcox and co-workers reported (1) that for eutectic volume fraction > 10% the eutectic spacing λ/λ_o (where λ_o is the spacing in the absence of convection) increases with Ω^2 (Ω is the convection intensity given by $\Omega = G_u\lambda^2/D$), particularly at low $V_{S/L}$ (see also (b) in previous paragraph) and increases with $\Omega^{1.32}$ for volume fraction of 10%, (2) that convection has less influence at high $V_{S/L}$, (3) that the change in λ depends on the orientation of the lamellae relative to the flow (maximum effect when the flow is perpendicular to the lamellae) and (4) the maximum change in λ occurs for equal volume fractions of the phases α and β in the eutectic.

Wilcox and co-workers also reported that in the presence of convection (i) the iso-concentration lines were found to shift in the direction of the flow (Ω = 500), (ii) the point on the interface where the eutectic composition was reached shifted downstream (i.e., in the direction of flow) and (iii) the

lamellae could grow at an angle to the interface (in the absence of strong crystallographic effects). The undercooling at the S/L interface $\Delta T = \Delta T_L + \Delta T_r$ (see § 1.1.1) had a contribution from convection in the first term (the second term equal to $\Gamma_{S/L}/\lambda$, i.e., unchanged). The ΔT was predicted to decrease linearly with intensity of convection, especially at low $V_{S/L}$.

Radial segregation of solutes with k<1 and k>1 has been modelled for floating zone crystal growth *in zero gravity* by Lan & Kou (1993) for $NaNO_3$ with KNO_3 solute (k=0.2) and Sc = 793. Note that in the Figure 44 and Figure 45, owing to the large Schmidt number (for Nb the Sc = 145), the axial concentrations gradients near the feeder and crystal fronts are very steep. Both fronts are non-isothermal owing to variation in solute concentration. Even though their results are for zero-gravity, they are interesting and thus will be considered in some detail here.

Lan & Kou (1993) separated the effect of growth front from that of thermocapillary convection by setting $d\gamma/dT = 0$ first. In this case the shape of the growth front was changed by altering the peak temperature T_{peak} giving convex interface for low T_{peak} and concave for higher T_{peak}. For solute with k<1, for a strongly convex interface the solute diffused (radial segregation) to the liquid surface and for concave interface the solute segregated towards the centre of the crystal. The effect of increasing $d\gamma/dT$ on segregation for solute with k<1 is shown in Figure 44. As $d\gamma/dT$ increases two flow loops form in the liquid (Figure 44b) with the lower causing the solute to move inward towards the centre (Figure 44e) and segregation in the centre (Figure 44g). When the $d\gamma/dT$ is the highest (considered by Lan & Kou (1993)) the flow loops mix the solute (Figure 44f) and the radial segregation in the centre decreases (Figure 44g). Since in the case k<1 the higher the solute concentration the lower the liquidus of the melt, the segregation in the centre means lower growth front temperature there (indicated by square in Figure 44f). The solute concentration changes longitudinally (i.e., varies along the axis) but not near the liquid surface (Figure 44h).

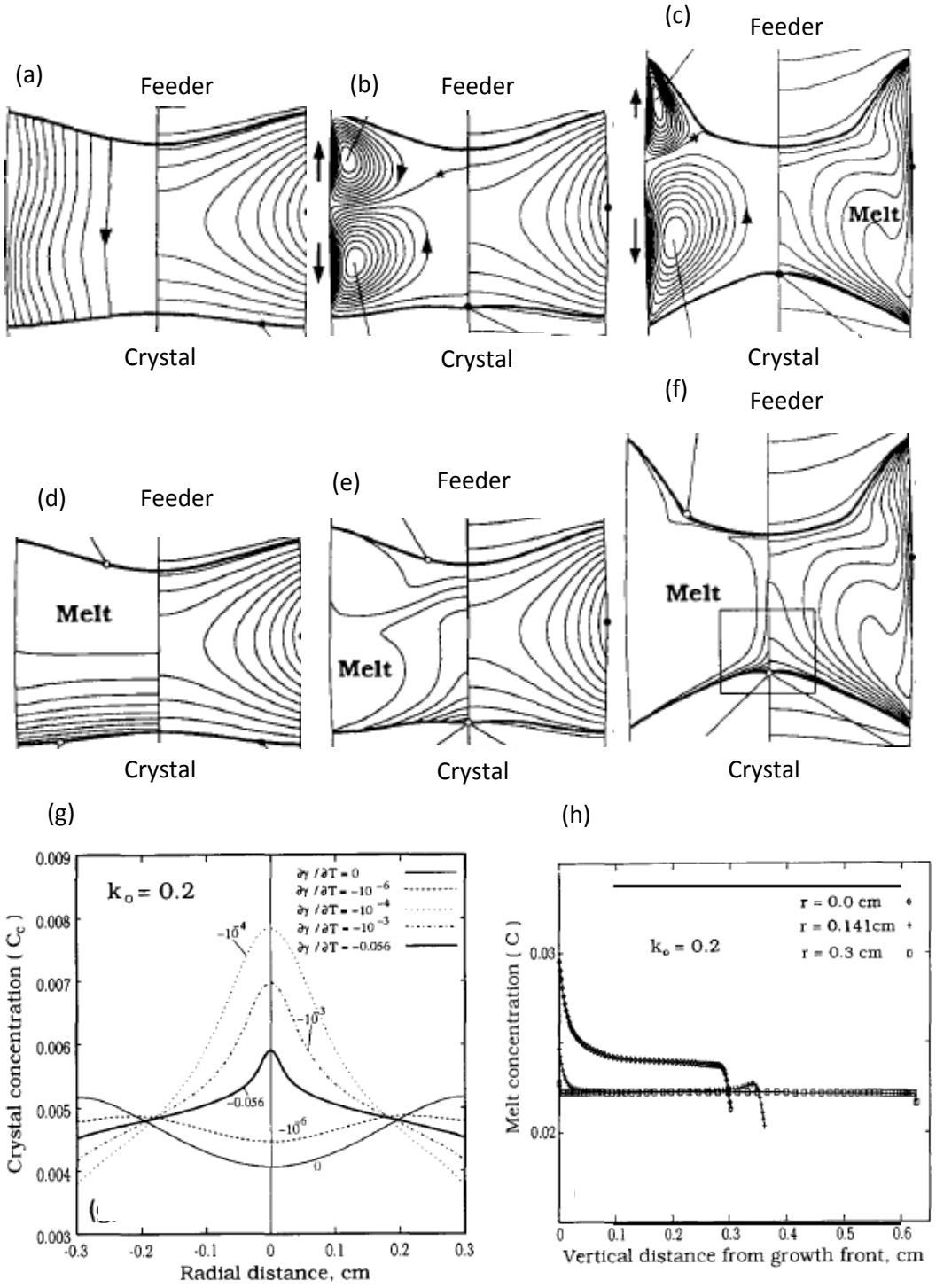

Figure 44: Effect of increasing dγ/dT on streamlines and isotherms (a to c) and concentration and isotherms (d to f) for k<1 for zero-gravity floating zone crystal growth. In all parts the feeder rod is on the top and the grown crystal in the bottom. The isotherms are shown on the right hand side of each part. (g) and (h) respectively show the solute segregation with radial distance and vertical distance (at three darial positions) for different dγ/dT values in (g) and for dγ/dT = - 0.056 in (h) (Lan & Kou 1993).

The case for k>1 is shown in Figure 45a and b for the highest dγ/dT (considered by Lan and Kou [1993]). Comparison with Figure 44c and f shows that the melt zone is shorter and the concentration field is reversed, meaning the maximum solute concentration is at the feeder front and the minimum

at the crystal front. In this case (k>1) the convection arising from thermocapillary causes the solute to segregate toward the surface (Figure 45c). Figure 45d shows that as dγ/dT increases to the highest value (considered by Lan & Kou (1993)) the solute segregation increases and then decreases due to mixing. There is also longitudinal variation in solute concentration but not near the L-V interface.

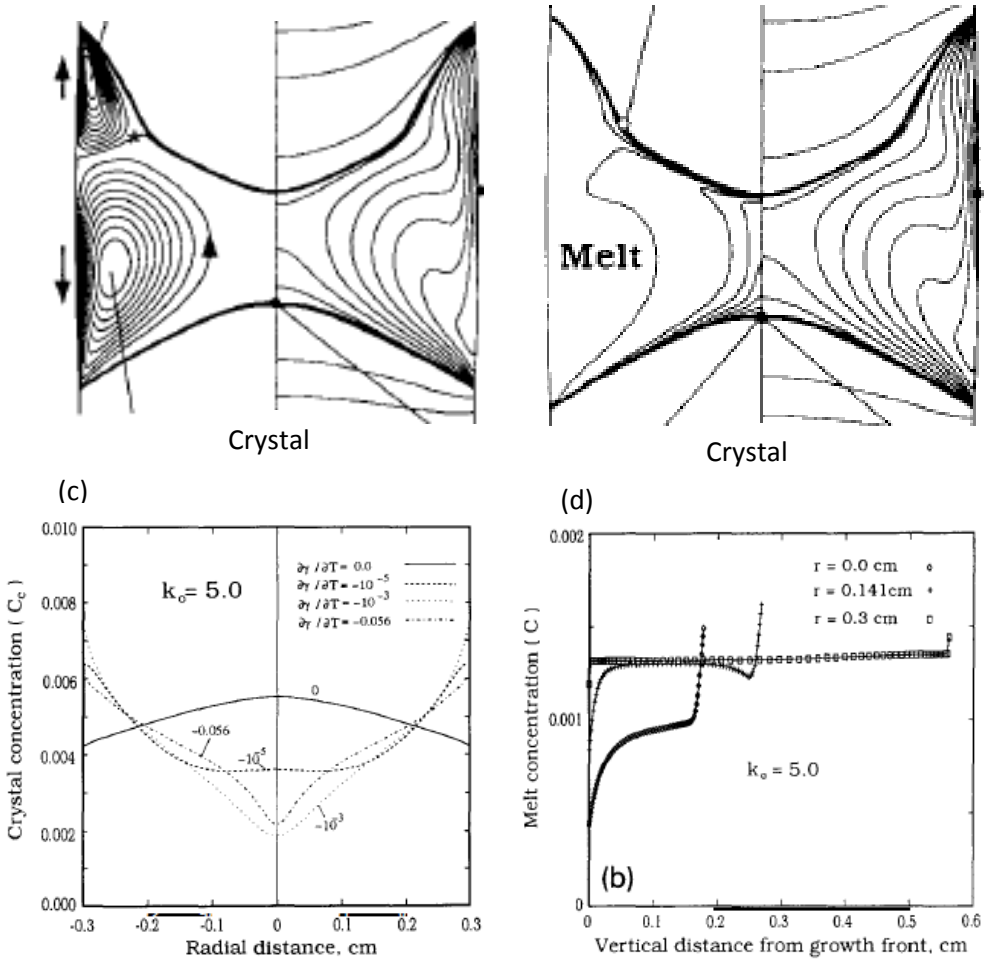

Figure 45: Streamlines and isotherms (a) and concentration and isotherms (b) for k>1 for zero-gravity floating zone crystal growth. In both parts the feeder rod is on the top and the grown crystal in the bottom. The isotherms are shown on the right hand side of each part. (c) and (d) respectively show the solute segregation with radial distance and vertical distance (at three darial positions) for different dγ/dT values in (c) and for dγ/dT = - 0.056 in (d) (Lan & Kou 1993).

2. EXPERIMENTAL

2.1 ALLOY SOLIDIFICATION AND SPECIMEN PREPARATION

Two "eutectic" alloys, namely CM1 and CM2 with compositions Nb-8.3Ti-21.1Si-5.4Mo-4W-0.7Hf and Nb-20.5Si-5.8W-4Hf (at. %) respectively, were selected for this study. These eutectic compositions were selected on the basis of previous research on non-eutectic alloys in the group with promising creep data, see Table 6.

*Table 6: Creep rates (s^{-1}) data of polycrystalline Alloys 1 and 2, on which the alloys CM1 and CM2 were respectively based, compared with the single crystal nickel based superalloy CMSX4. (*at 1050 ^{O}C)*

	Stress (MPa) at 1200 ^{O}C			
	150	**200**	**300**	**400**
Alloy 1		1.2×10^{-8}	6.8×10^{-8}	2.4×10^{-7}
Alloy 2		9.1×10^{-8}	4.5×10^{-7}	1.4×10^{-6}
CMSX4	6.3×10^{-8}	$*1.3 \times 10^{-7}$		

The two alloys were studied in 5 different conditions; 10g arc-melted buttons, 6 and 8 mm diameter suction cast ingots, 600 g plasma arc and 500 g arc-melted buttons (CM1 and CM2 respectively) and "directionally" solidified (inverted commas are used for directional, to signify that in this experiment the temperature gradient is not controlled as in traditional directional solidification) in an optical float zone furnace. This allowed study of the dependence of microstructure on different casting conditions. All castings were made using high purity elements.

Button ingots of the alloys CM1 and CM2 were solidified in an arc-melter in a water cooled copper crucible. The arc-melting atmosphere was prepared firstly by creating a vacuum better than 8 x 10^{-5} torr and back filling with Ar prior to melting. Ingots were melted at least 5 times; turning the sample between melts to improve homogeneity. The 6 and 8 mm diameter suction cast samples of the alloys CM1 and CM2 were prepared from 10 and 15 g buttons respectively. A pressure difference between the melting chamber and an external vacuum chamber was used. This "pulled" the melt

through into a water cooled copper crucible. Accurate control of bar lengths was not possible in this process which gave bars between 14 and 21 mm long. In both processes, i.e. arc melting and suction casting, melt super heat could not be controlled and the arc was moved manually by the operator.

The 600 g ingot of the alloy CM1 was prepared using plasma arc melting at the University of Birmingham casting and research facility (Birmingham 2016). The 500 g ingot of the alloy CM2 was processed in the University of Sheffield using a vacuum arc melter that was brought to a vacuum better than $8x10^{-5}$ torr and back filled with Ar and a large water cooled copper crucible. To improve homogeneity the alloy was melted 5 times. The ingots of CM1 and CM2 were sectioned using electrical discharge machining to get samples for microstructural examination, heat treatment and for "directional" solidification in the optical float zone furnace.

Optical floating zone melting and solidification is a "directional" solidification technique which uses focused light to melt the material. The latter moves through the stationary hot zone with the surface tension holding the melt zone between the solid sections to allow for containerless solidification. For more detail about the OFZ process see § 1.6.3.1

Two optical float zone furnaces were used in this study; a two-mirror furnace in Hokkaido University and a four-mirror furnace in the University of Cambridge. The alloy CM1 600 g ingot was electrically discharged machined (EDM) into bars of 10 mm diameter and 50 to 80 mm in length and solidified in the facility in Hokkaido University. The author was not present in their experiments. The alloy CM2 500 g ingot was EDM into bars of 8 mm in diameter and 60 to 90 mm in length and solidified in the facility in the University of Cambridge. This facility was used for the first time for the OFZ of Nb silicide based alloys using the alloy CM2.

All samples were subjected to a heat treatment of 1500 ^{O}C for 100 hrs under an inert, argon atmosphere to study the heat treatment microstructure and compare it with that of the cast alloys.

2.2 Microstructural and Phase Analysis

The button ingot and suction cast bars, in both the as-cast and heat treated conditions, were sectioned using an Isomet precision cutting machine. Sectioned samples were mounted in conductive Bakelite. Samples were ground using SiC abrasive papers and polished using polishing cloths and water based monocrystalline diamond suspension solution. Standard metallographic methods were used to prepare samples to a 1 µm finish and then finished on a cashmere cloth with colloidal silica.

Microstructure characterisation was done using InspectF, JEOL 6400, Camscan Mk2 and Phillips 500 and XL30 scanning electron microscopes (SEM). Quantitative chemical analysis was done using EDS in the JOEL 6400, Camscan Mk2 and Phillips 500 (Sheffield 2016) that were equipped with a high purity Co standard. Qualitative X-ray maps were produced on the Phillips XL 30 FEG SEM using a Bruker AXS XFLASH Detector 4010 and Bruker Espirit EDX analysis software. All imaging and EDS analysis was done with an accelerating voltage of 20kV.

X-ray diffraction (XRD) was done using powered samples and copper radiation, filtered to a monochromatic state via a nickel filter, on a STOE machine; 2θ range of 20-120 ^{O} and step size of 0.05^{O}. Phases determined using WINDEX POW and CDD PDF-4+ 2012 software packages. Powder XRD can be affected by the introduction of plastic strain in the samples. There is sufficient evidence, (Li et al. 2006), that powders of Nb silicide based alloys are not significantly deformed during their preparation.

2.3 Microstructural Measurements

To quantify changes in the microstructures between the different solidification techniques and pre- to post- heat treatment the spacing between lamellae in the eutectic and prior-eutectic were measured.

In a eutectic microstructure the eutectic spacing (λ) is defined as the distance between the centres of two adjacent similar phases, see Figure 3. To get an average eutectic spacing the spacing between the centres of two similar phases across a number of lamellae was measured and divided by

one minus the number of boundaries between dissimilar phases met (N). For increased accuracy the ImageJ image manipulation software was also used. This allowed scales to be incorporated into the lines drawn between two dissimilar phases and by creating a binary image (black and white based on the contrast difference of phases) the phase boundaries could be easily identified. In non-lamellar structures a fragmented line was used to allow the measurements between two adjacent phases to be incorporated into an average spacing across the entire eutectic structure.

The ImageJ was also used for measuring the volume fraction (V_f) of the phases. By creating a binary image the software identifies the number of pixels highlighted and calculates the area fraction of these highlighted areas. Since there were more than 2 phases present, mainly in the heat treated samples, images were manipulated slightly. First the software calculated the area fraction of darker contrast phases (silicides + nitrides + pores) compared with lighter contrast phases (niobium solid solution + hafnia). The contrast boundary for measuring was then altered to take into account only the brightest (hafnia) and then the darkest (nitrides and pores) phases. These were then taken away from the lighter contrast and darker contrast results respectively, to get area fractions for silicides, solid solution, hafnia and nitrides + pores.

3. RESULTS

3.1 ARC MELTED ALLOYS

3.1.1 Small (10 g) Button Ingot

The microstructure of the cast alloy CM1 10 g button is shown in Figure 46. The EDS analysis data of the CM1 alloy as-cast 10 g button is given in Table 7. Compared with the nominal composition (§ 2.1) the 10 g button of the alloy CM1 was richer in Si and leaner in Mo and W. Image A in Figure 46 shows that the microstructure consisted of dendrites, exhibiting a dark contrast, and interdendritic eutectic. The EDS analysis of the dendrites indicated that they were Nb_5Si_3 type silicide. This was confirmed by XRD, Appendix B Fig 1, which indicated that the Nb_5Si_3 dendrites were the high temperature allotrope β-Nb_5Si_3. The interdendritic region, Figure 46B, contained fine eutectic cells surrounded by a coarser eutectic. In both eutectics the phases exhibited dark and light contrast. The latter was from the Nb_{ss}, see Table 7 and Appendix B Fig 1. The darker contrast phase in the eutectic was the β-Nb_5Si_3. A third, bright white contrast phase was also present, Figure 46. Analysis of this phase showed it to be Hf rich, most likely hafnia formed from scavenging of oxygen during arc-melting, (Tian et al. 2008).

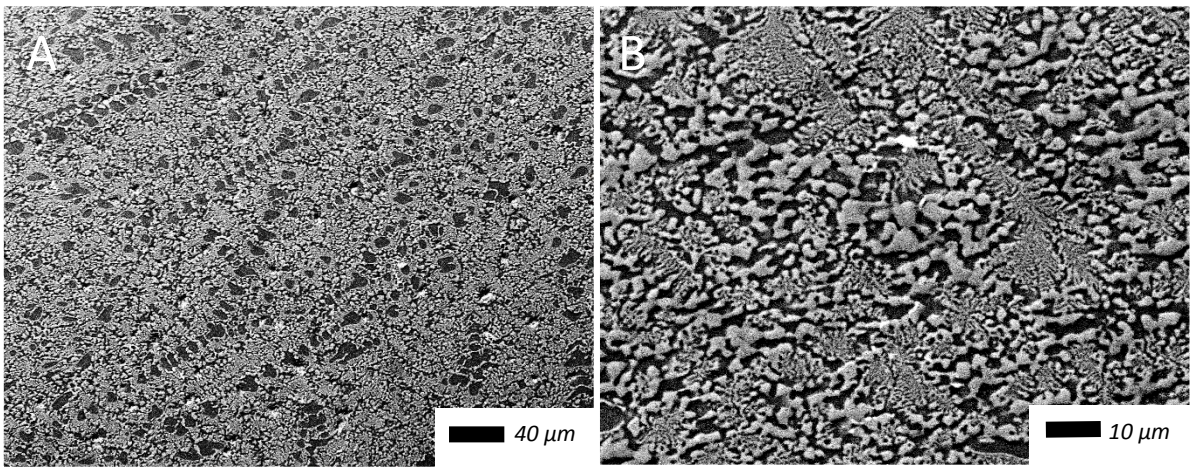

Figure 46: Backscattered electron images of the bulk microstructure of as-cast alloy CM1 10 g button at (A) low and (B) high magnification.

Table 7: Summary of EDS analysis data (at.%) of the as-cast alloy CM1 10 g button, including SD, minimum and maximum analysis values.

Element	*Large Area*	*Eutectic*	*Silicide*	*Solid Solution*
Nb	60.0 ± 0.30 59.7 - 60.5	60.7 ± 0.23 60.4 - 60.9	52.8 ± 0.57 51.7 - 53.3	74.7 ± 0.62 73.2 - 75.6
Ti	8.8 ± 0.09 8.6 - 8.9	9.5 ± 0.16 9.3 - 9.7	6.6 ± 0.84 6.0 - 8.2	8.0 ± 1.33 6.5 - 10.6
Si	22.6 ± 0.35 22.0 - 23.0	19.9 ± 0.79 19.0 - 20.7	37.4 ± 0.45 36.6 - 37.9	1.6 ± 0.55 0.7 - 2.2
Mo	4.7 ± 0.09 4.6 - 4.9	6.0 ± 0.60 5.2 - 6.7	2.5 ± 0.33 2.0 - 2.9	9.6 ± 0.46 8.7 - 10.5
Hf	0.8 ± 0.04 0.8 - 0.9	0.5 ± 0.16 0.3 - 0.7	0.2 0.1 - 0.7	0.4 ± 0.15 0.2 - 0.6
W	3.1 ± 0.05 3.0 - 3.1	3.4 ± 0.16 3.2 - 3.6	0.5 ± 0.27 0.1 - 0.8	6.4 ± 1.41 4.1 - 8.5

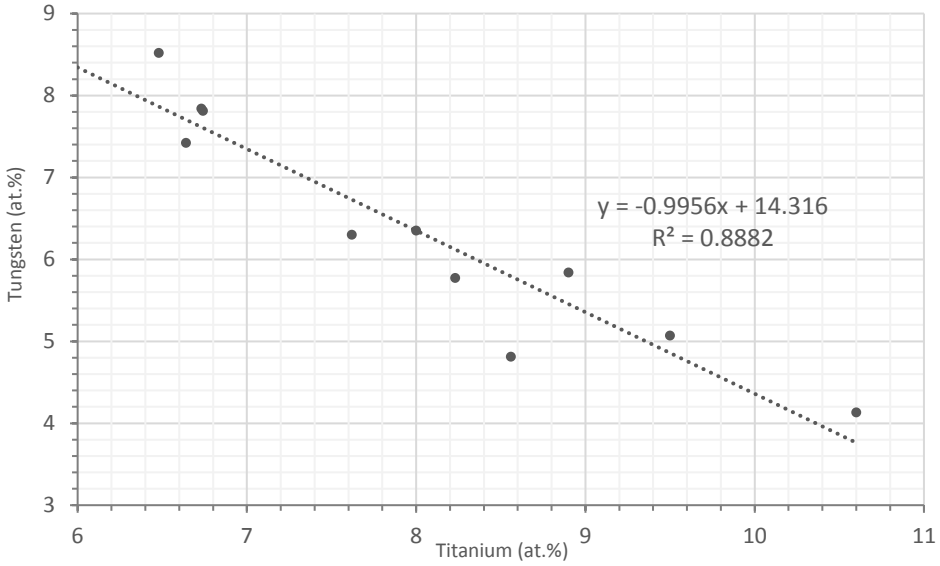

Figure 47: Relationship between W and Ti contents in the Nb_{ss} in as-cast CM1 10 g buttons.

The Si concentration of the eutectic was close to that reported for the Nb_{ss} + β-Nb_5Si_3 metastable eutectic in the Nb-Si binary, see § 1.3.1. In the silicide analysis there was a difference of about 2.2 at.%Ti between grains; with the lowest levels of Ti present in the grains with the highest Hf concentration. However, owing to the low concentration of Hf in the alloy it was not possible to establish whether a trend between the concentrations of the two elements existed. The Si

concentration in the silicide was in the range reported for the unalloyed Nb_5Si_3, see Figure 11 and Table 1. The solid solution data showed significant variation in Ti and W content. Highest levels of Ti and Hf were analysed in the same Nb_{ss} grains that had the lowest levels of W and Mo. In other words the Ti and Hf rich Nb_{ss} was poorer in Mo and W than the "normal" Nb_{ss}. Figure 47 shows the linear relationship between W and Ti in the Nb_{ss}. The figure shows that Ti and W in Nb_{ss} *"do not like each other"*.

The microstructure of the alloy CM2 10 g cast buttons is shown in Figure 48. The EDS data for the alloy and phases is given in Table 8. The average composition of the alloy was very close to the nominal one, § 2.1. However, there was weak macrosegregation of Si ($C_{max}^{Si} - C_{min}^{Si} = 1.9\ at.\%Si$). In contrast to the button of alloy CM1 dendrites of a lighter contrast phase were surrounded by eutectic. The EDS and XRD data, Table 8 and Appendix B Fig 2 respectively, confirmed this phase was the Nb_{ss}. The darker contrast phase in Figure 48B, was the α-Nb_5Si_3. Similarly to the alloy CM1, the interdendritic regions comprised of eutectic cells of fine microstructure surrounded by coarser eutectic. This eutectic, especially the cells with finer microstructure, showed more regular features than the largely irregular, Chinese script, morphology reported in the literature review (§ 1.1.2 and § 1.3.1). The fine eutectic cells consisted of Nb_{ss} rods in a Nb_5Si_3 matrix surrounding a central spine of Nb_5Si_3, "Fish-Spine" eutectics, see Figure 48C. A third, bright white contrast Hf-rich phase was present in the microstructure, as was the case in alloy CM1.

The Si concentration of the eutectic was within the range of Nb_{ss}+Nb_5Si_3 eutectic in alloys studied in the research group and close to that of the metastable Nb_{ss}+β-Nb_5Si_3 eutectic in the Nb-Si binary, see § 1.3.1. There was some variation of the silicon concentration in the silicide grains, Table 8, but within the expected range, see Figure 11 and Table 1. The Nb_{ss} was very rich in W with the concentration effectively the same as the total RM content of the Nb_{ss} in the alloy CM1 (Table 7).

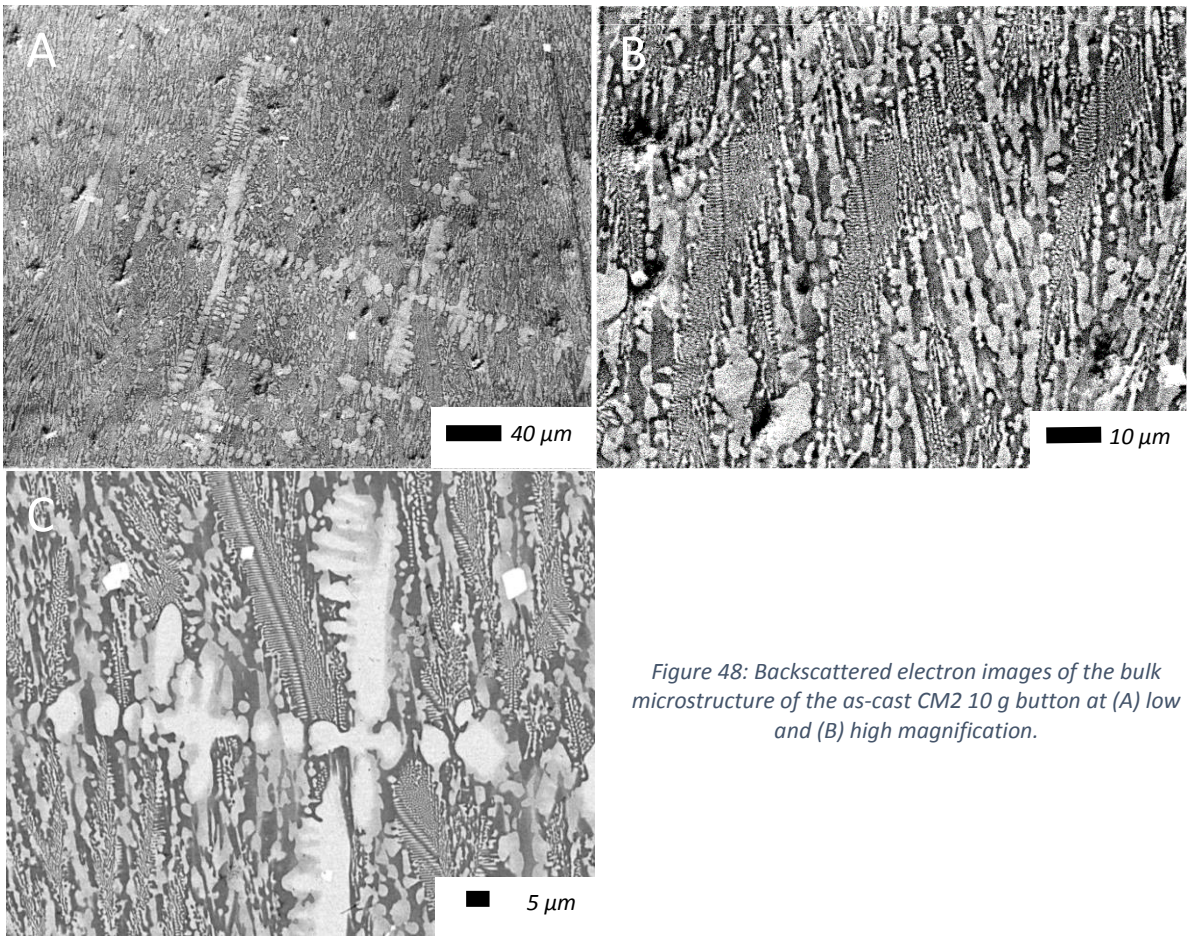

Figure 48: Backscattered electron images of the bulk microstructure of the as-cast CM2 10 g button at (A) low and (B) high magnification.

Table 8: Summary of EDS analysis data (at.%) of the as-cast CM2 10 g button, including SD, minimum and maximum analysis values.

Element	*Large Area*	*Eutectic*	*Silicide*	*Solid Solution*
Nb	69.6 ± 0.27 69.4 - 70.1	69.7 ± 0.36 68.7 - 69.6	55.7 ± 1.18 54.1 - 58.2	81.4 ± 0.32 80.8 - 81.8
Si	20.7 ± 0.7 19.4 – 21.3	21.3 ± 0.48 20.6 - 22.0	38.4 ± 1.10 36.2 - 39.4	0.3 0.0 - 0.8
W	5.2 ± 0.56 4.8 – 6.2	4.9 ± 0.36 4.5 - 5.4	0.1 0.0 - 0.9	16.8 ± 0.64 15.4 - 17.4
Hf	4.5 ± 0.15 4.3 - 4.7	4.5 ± 0.23 4.1 - 4.7	5.7 ± 0.34 5.2 - 6.5	1.5 ± 0.26 1.3 - 2.1

The microstructure of the alloy CM1 10 g button after heat treatment at 1500 ^{O}C for 100 hrs is shown in Figure 49 and the EDS and XRD data is given in Table 9 and Appendix B Fig 1, respectively. Comparing Figure 46 with Figure 49 we notice that a similar two phase structure was present after the heat treatment, that the microstructure had coarsened and there was no evidence of the fine cellular eutectic structure seen in the cast alloy. The microstructure seems to be a co-continuous mixture of

the two phases. The silicide was the α-Nb_5Si_3, i.e. the low temperature form of the 5-3 silicide, according to XRD, Appendix B Fig 1. The light contrast phase in Figure 49 was the Nb_{ss}.

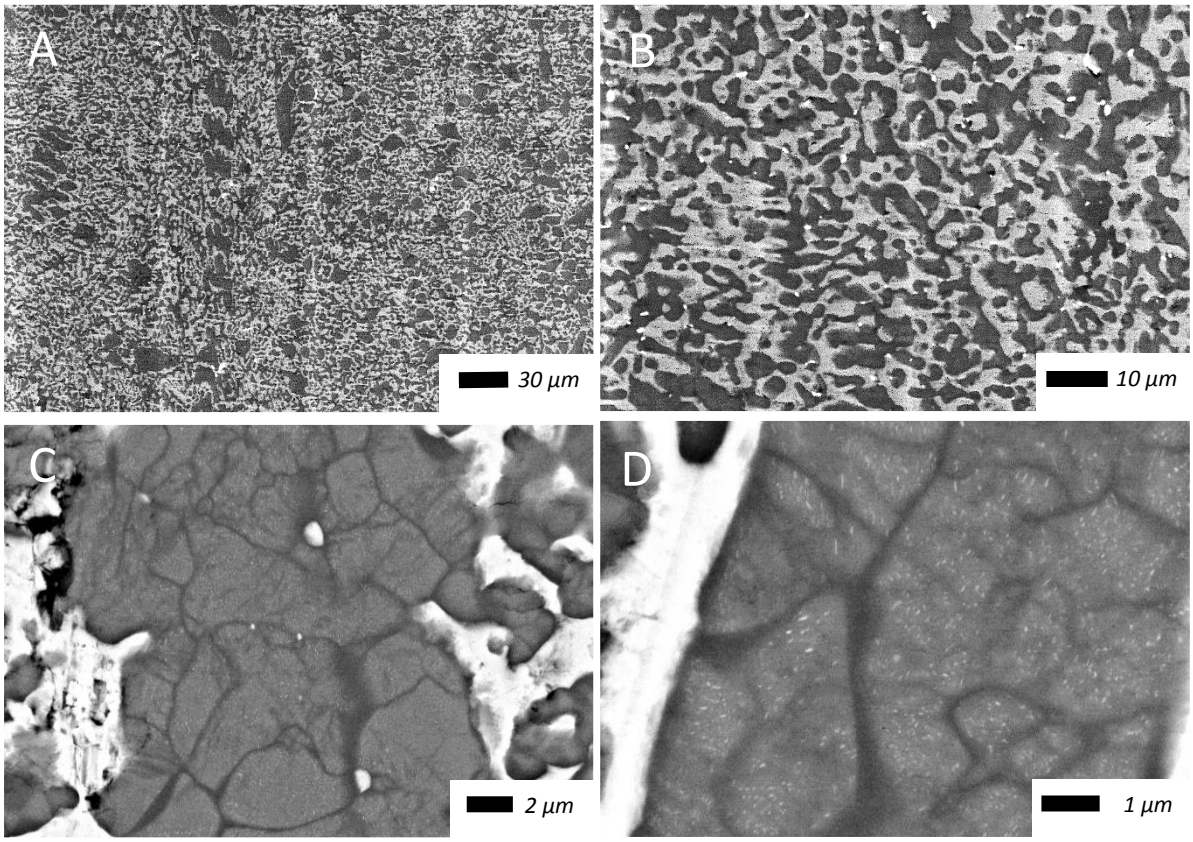

Figure 49 Backscattered electron image of the bulk microstructure of heat treated CM1 10 g button at (A) low and (B) high magnification as well as (C) subgrain structure and (D) precipitates within the α-Nb_5Si_3 phase.

The large area EDS analysis in Table 9 shows very little difference in the concentrations of elements compared with the cast button. The interdendritic prior-eutectic areas exhibited large variations in Si concentration from one area to the next. There was also a small reduction in Mo content in the prior eutectic after the heat treatment. The lowest values of Si concentration in the eutectic were associated with the highest values of tungsten concentration in these regions and vice versa. There was also variation in the concentration of Ti in the silicides. The highest Ti values were seen in the same grains with the highest Si and Hf values and the lowest Mo and W concentrations.

In the silicide there was a slight reduction in the total Mo + W content post-heat treatment. This was mirrored by increased W and Mo concentrations in the solid solution post-heat treatment. No Si or Hf were detected in the solid solution after heat treatment.

After the HT there was strong evidence of internal structures in the Nb_5Si_3 grains, see Figure 49C and D. Figure 49C shows "subgrains" of various sizes in the Nb_5Si_3 and Figure 49D shows precipitations of a second phase inside the "subgrains", with the precipitates exhibiting contrast similar to that of the Nb_{ss}. Some of the precipitates appear to be elongated and their orientation in different "subgrains" would suggest that they have formed with some orientation relationship.

Table 9: Summary of EDS analysis data (at.%) of heat treated alloy CM1 10 g button, including SD, minimum and maximum analysis values.

Element	*Large Area*	*Prior-eutectic*	*Silicide*	*Solid Solution*
Nb	60.6 ± 0.18 60.4 - 60.8	61.7 ± 0.80 60.4 – 63.7	54.3 ± 0.46 53.6 - 55.0	75.9 ± 0.54 75.2 - 77.2
Ti	8.4 ± 0.19 8.3 - 8.8	8.5 ± 0.39 7.6 - 9.2	7.5 ± 0.97 5.8 - 9.6	6.0 ± 0.65 5.2 - 7.2
Si	22.9 ± 0.47 22.2 - 23.5	21.1 ± 1.21 18.9 - 23.5	36.7 ± 0.32 36.1 - 37.3	0
Mo	4.8 ± 0.23 4.5 - 5.2	5.0 ± 0.31 4.6 - 5.6	1.4 ± 0.31 0.9 - 2.0	10.4 ± 0.30 9.9 - 11.0
Hf	0.5 ± 0.09 0.4 - 0.64	0.4 0.0 - 0.8	0.3 0.0 - 1.1	0
W	2.8 ± 0.15 2.5 - 3.0	3.2 ± 0.33 2.6 - 3.6	0.2 0.0 - 0.6	7.6 ± 0.35 7.2 - 8.4

The microstructure of the alloy CM2 10 g button after the heat treatment at 1500 ^{O}C for 100 hrs is shown in Figure 50. The EDS and XRD data is given in Table 10 and Appendix B Fig 2 respectively. There were strong similarities between the pre- and post- heat treatment microstructures, confirming the stability of the microstructure of CM2. The large solid solution dendrites were clearly seen, Figure 50A, and the interdendritic regions, Figure 50B, had become coarser and exhibited a co-continuous two phase structure. However, unlike the alloy CM1, there was still evidence of fine eutectic cells seen in the as-cast condition, but the majority of the lamellar morphology had disappeared. The XRD, Appendix B Fig 2, confirmed the presence of Nb_{ss} and α-Nb_5Si_3, similar to the as-cast condition. The

large area analysis of the heat treated specimen showed higher Si concentration compared with the cast alloy, with the minimum analysis value (21.4 at.%Si) higher than the maximum value (21.3 at.%Si) in the cast alloy. This could be attributed either to the macrosegregation of Si in the CM2-AC or, more likely, to error in the analysis of Si owing to the presence of Hf in the alloy at high concentration as well as to the HT and AC samples not from the same button.

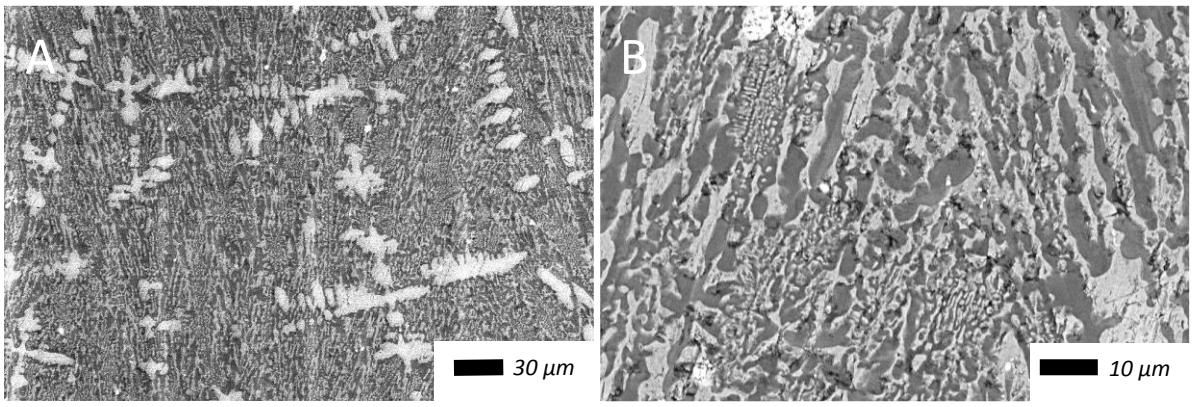

Figure 50: Backscattered electron image of the bulk microstructure of heat treated CM2 10 g button at (A) low and (B) high magnification.

In the heat treated button the Hf and especially the Si concentrations in the prior eutectic varied from one eutectic region to the next. The EDS analyses of the prior eutectic showed that the highest Si content was associated with the lowest W content. This was also the case in the analysis of the silicide phase. Variations in W content were also seen in the Nb_{ss} which was free of Si and poorer in W compared with the cast button.

Table 10: Summary of EDS analysis data (at.%) of the heat treated CM1 10 g button, including SD, minimum and maximum analysis values.

Element	*Large Area*	*Prior Eutectic*	*Silicide*	*Solid Solution*
Nb	68.5 ± 0.50 67.9 - 69.2	67.5 ± 0.95 65.5 - 69.0	55.8 ± 0.32 55.4 - 56.3	83.8 ± 0.96 82.6 - 85.6
Si	22.3 ± 0.62 21.4 - 23.1	23.7 ± 1.27 21.7 - 26.1	38.2 ± 0.57 36.9 - 38.7	0.0
W	4.1 ± 0.21 3.8 - 4.5	3.8 ± 0.5 3.0 - 4.2	0.0	14.8 ± 0.97 13.3 - 16.3
Hf	5.0 ± 0.13 4.8 - 5.2	5.0 ± 0.61 3.2 - 5.5	6.1 ± 0.70 5.5 - 7.6	1.1 ± 0.17 0.9 - 1.5

3.1.2 Intermediate (500 and 600 g) Ingots

The microstructure of the alloy CM1 600 g ingot is shown in Figure 51. Table 11 and Appendix B Fig 1 respectively show the EDS and XRD data. Compared with the 10 g button, this ingot was slightly leaner in W. Similar to the 10 g button the microstructure comprised of silicide dendrites (dark contrast) with an interdendritic eutectic of silicide and Nb_{ss} (light contrast). Nb_{ss} halos can be seen in Figure 51C. "Subgrain" formation and fine precipitates of a second phase with contrast similar to Nb_{ss} were formed in Nb_5Si_3 as was the case in the heat treated CM1 10 g button, see Figure 49 However, in this case, fine precipitates were also formed on the "subgrain" boundaries. The EDS analysis confirmed the presence of Nb_5Si_3 and the XRD determined it to be the low temperature α-Nb_5Si_3, unlike the cast 10 g button where the β-Nb_5Si_3 was formed. The eutectic morphology remained very similar to that of the 10 g button. The eutectic formed the fine eutectic cells observed in the 10 g ingot.

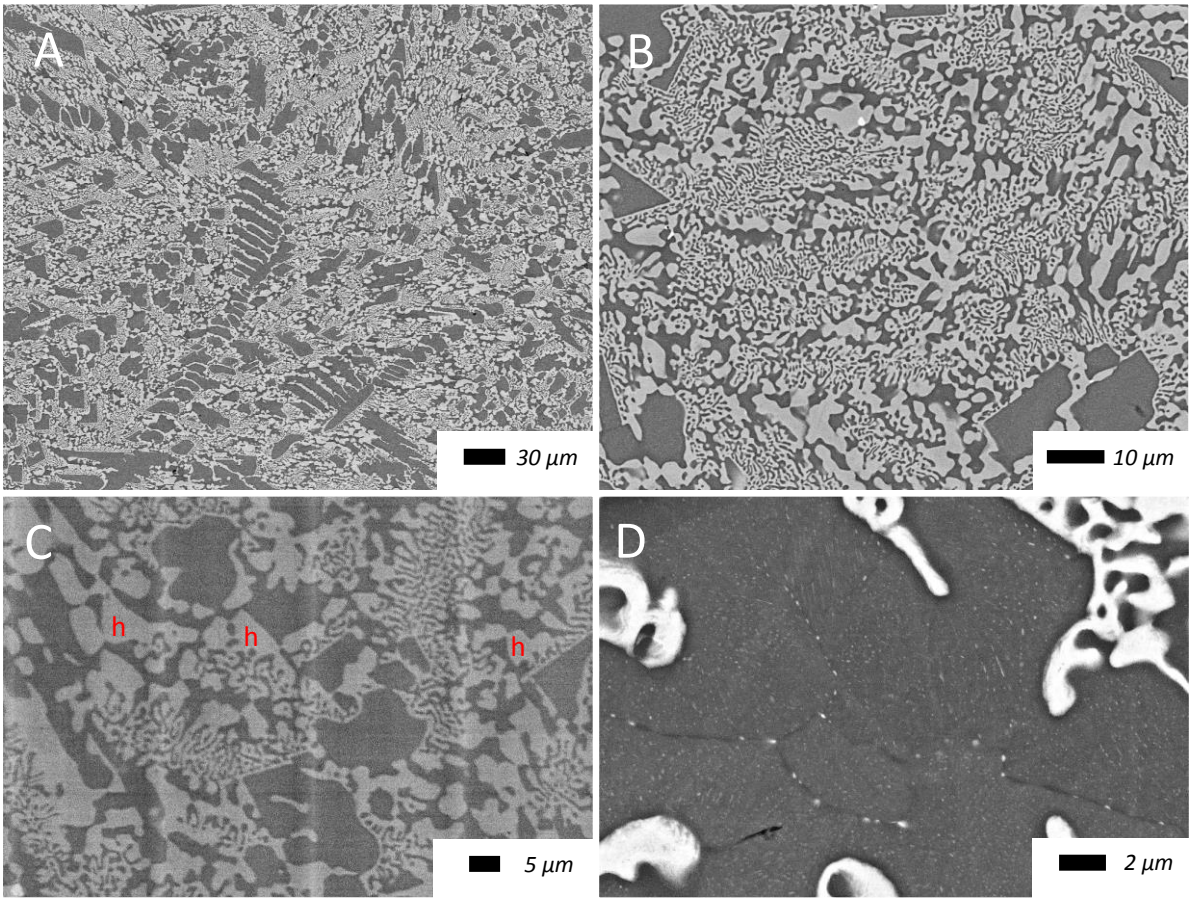

Figure 51: Backscattered electron images of the bulk microstructure of the as-cast alloy CM1 600 g ingot at (A) low and (B) high magnification as well as (C) subgrain structure and (D) precipitates within the α-Nb5Si3 phase. Nbss haloes are shown by h in (C).

Table 11: Summary of EDS analysis (at.%) of as-cast CM1 600 g ingot including SD, minimum and maximum analysis values.

Element	*Large Area*	*Eutectic*	*Silicide*	*Solid Solution*
Nb	60.8 ± 0.29	62.5 ± 0.77	54.3 ± 0.08	73.5 ± 0.68
	60.4 – 61.1	61.4 - 63.6	54.0 - 54.2	72.8 - 74.7
Ti	8.5 ± 0.22	8.8 ± 0.35	6.1 ± 0.19	9.4 ± 0.59
	8.0 - 8.7	8.2 - 9.2	5.8 - 6.4	8.6 - 10.1
Si	22.7 ± 0.61	19.4 ± 0.78	37.1 ± 0.39	1.7 ± 0.94
	22.0 - 23.8	18.3 - 20.4	37.1 - 38.2	0.8 - 3.2
Mo	5.2 ± 0.33	5.9 ± 0.19	2.0 ± 0.18	10.0 ± 0.39
	4.8 - 5.7	5.5 - 6.1	1.6 - 2.1	9.6 - 10.6
Hf	0.7 ± 0.07	0.8 ± 0.14	0.3 ± 0.06	0.7 ± 0.09
	0.6 - 0.8	0.6 - 1.0	0.2 - 0.4	0.6 - 0.9
W	2.1 ± 0.03	2.5 ± 0.31	0.1 ± 0.02	4.6 ± 1.08
	2.1 - 2.2	2.2 - 3.2	0.1 - 0.1	3.5 - 6.3

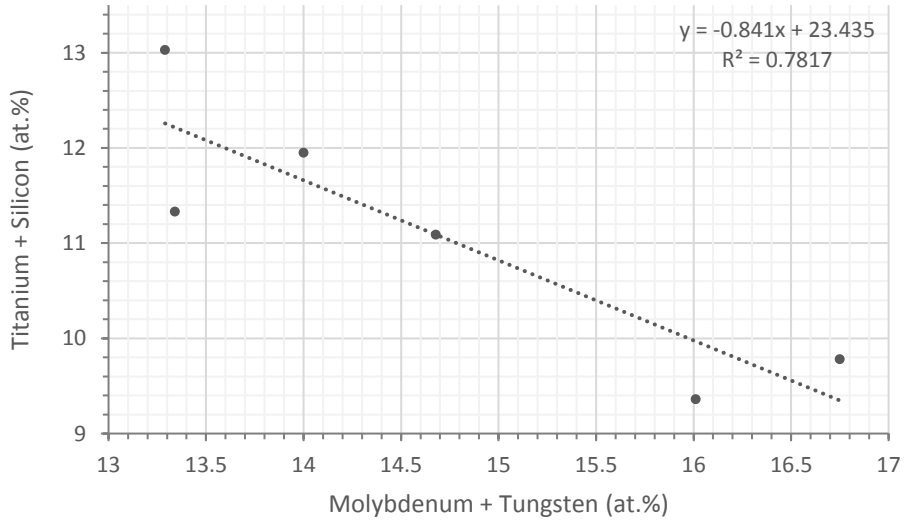

Figure 52: Relationship between Ti + Si and Mo + W contents in the Nb_{ss} in as-cast CM1 600 g ingot.

There was no macrosegregation of elements across the ingot. There was a variation in the Si content of the eutectic. Spot analyses showed variations in the concentrations of W and Si in the Nb_{ss} grains. Individual Nb_{ss} analyses alluded to a relationship between the grains with higher Mo and W levels and lower Si levels and vice versa. At Si levels over 1 at.% the concentrations of Mo and W were

lower than 9.8 and 4.2 at.%, respectively. At concentrations below 1 at.%Si the Mo and W concentrations were above 10.4 and 6.3 at.% respectively. The concentration of Ti showed a similar pattern to Si. The lowest values of Ti (< 9 at.%) correspond to the highest in Mo and W and the highest (> 9 at.%) corresponded to the lowest in Mo and W. This would therefore suggest the presence of Ti and Si rich Nb_{ss} and Mo and W rich Nb_{ss}. Figure 52 shows the relationship between the W and Mo in the Nb_{ss} with Si and Ti concentration

The microstructure of the cast alloy CM2 500 g ingot is shown in Figure 53. The EDS and XRD analysis is given in Table 12 and Appendix B Fig 2. The phases present in the microstructure were the Nb_{ss} and Nb_5Si_3 (Table 12) and the latter was the low temperature allotrope (α-Nb_5Si_3) Unlike the 10 g button, the CM2 500 g ingot had large areas of dramatically different microstructures, see Figure 53 (A to E). Throughout this thesis these microstructures will be known by the image they are shown in, i.e. image A shows morphology A etc. Morphologies A, B and E all had primary dendrites with an interdendritic eutectic. Structures A and E both comprised of a light contrast primary Nb_{ss}, confirmed by EDS and XRD, with a Nb_{ss}+Nb_5Si_3 interdendritic eutectic. The eutectic morphology however was distinctly different between these two regions. The eutectic in microstructure A was very similar to that seen in the CM2 10 g button (Figure 48). Small cells of fine, lamellar eutectic encompassed by an irregular, coarser eutectic. The microstructure in E had a much higher volume fraction of fine eutectic. These eutectics were more regular and the average eutectic spacing was half that of the eutectics in A, see § 3.4.1. Microstructure B on the other hand had faceted Nb_5Si_3 dendrites with an interdendritic structure of cells of fine regular eutectic and a surrounding coarser irregular eutectic. This eutectic morphology was similar to that seen in CM2 10 g button (Figure 48). However, the eutectic cells had a much more regular, lamellar morphology. The cells consisted of Nb_{ss} rods in a silicide matrix emanating from a central spine of Nb_5Si_3. The microstructures in C and D showed areas that were fully eutectic. The eutectic in C was comparable with that of the interdendritic region of B in that it had fine lamellar eutectic cells, around a central spine of silicide in a “fish bone” manner with coarser, irregular boarders. Morphology D was made up of very fine eutectic in cellular morphology with very little to

no surrounding coarser, irregular eutectic. Eutectic spacing in this region was around a quarter of that in interdendritic region of A.

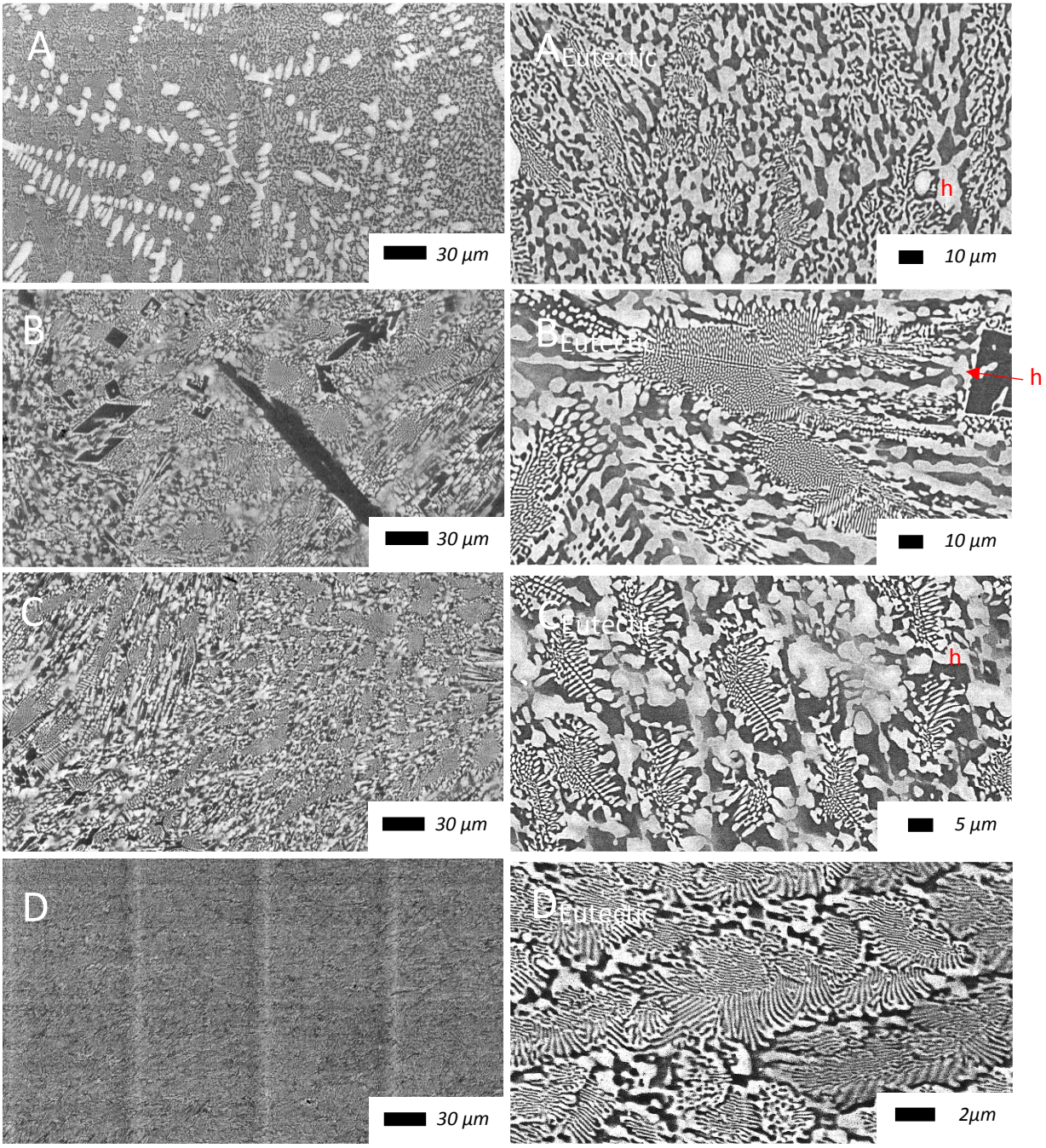

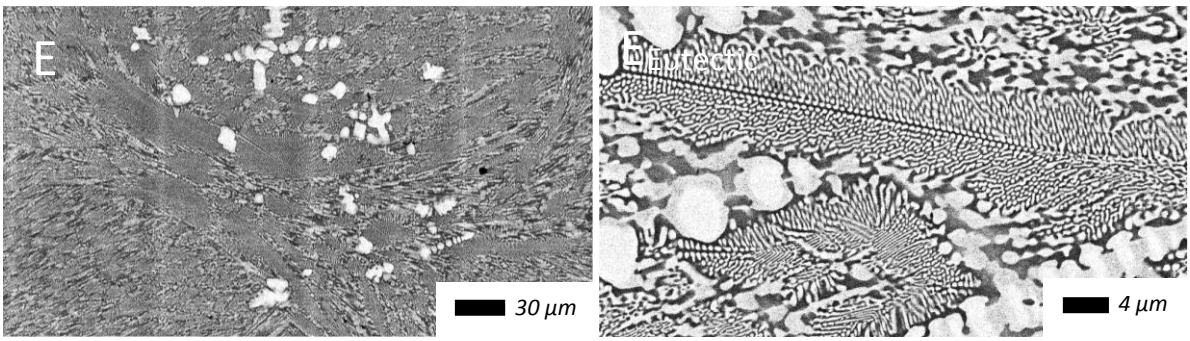

Figure 53: Backscattered electron images of bulk, in the left hand column, and eutectic, in the right hand column, microstructure of the as-cast CM2 500 g with 5 distinctly different morphologies (A – E). Nb_{ss} haloes are shown by h.

Table 12: Summary of EDS analysis (at.%) of the as-cast alloy CM2 500 g ingot, including SD, minimum and maximum analysis values.

Element	*Large Area*	*Eutectic*	*Silicide*	*Solid Solution*
Nb	71.3 ± 1.11	70.3 ± 1.12	54.9 ± 0.79	85.7 ± 1.29
	69.3 - 72.7	68.3 - 71.6	53.6 - 56.7	84.1 - 88.3
Si	19.8 ± 0.89	20.6 ± 0.99	39.5 ± 0.59	1.1 ± 0.30
	19.0 - 21.6	19.0 - 22.4	38.0 - 40.1	0.6 - 1.6
W	3.7 ± 0.14	4.2 ± 1.73	0.0	10.4 ± 1.97
	3.5 - 3.9	2.6 - 6.7		7.0 - 12.1
Hf	5.2 ± 0.25	4.9 ± 0.45	5.5 ± 0.42	2.8 ± 0.77
	4.8 - 5.4	4.2 - 5.7	5.2 - 6.7	2.0 - 4.4

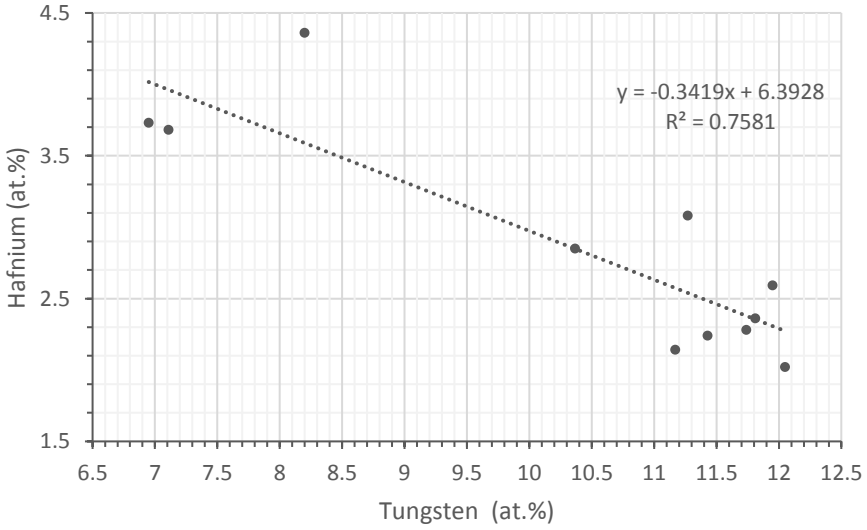

Figure 54: Relationship between the Hf and W contents in the Nb_{ss} in the as-cast alloy CM2 500 g ingot.

According to the EDS analysis, Table 12, there was weak macrosegregation of Si, $C_{max}^{Si} - C_{min}^{Si} = 2.6\ at.\%Si$. The highest Si content was recorded in the area C with the rest having 19.0 – 19.7 at.%Si. The Si content of the eutectic and the alloy and the microstructure in Figure 53 would suggest that this alloy solidified mostly as a eutectic. Highest levels of tungsten in the eutectic were in the area B, which was the only area with levels of tungsten in excess of 4 at.% and the majority of the eutectics in this area had concentrations between 6.2 and 6.8 at.%W. In the Nb_{ss} the W and Hf analyses also showed large disparities between grains. An overall trend could be deduced from the individual Nb_{ss} point analysis, as the W content increased the Hf content decreased, see Figure 54. However, as there were no concentrations of W between 8.2 and 11.2 at.% the phases could be classed as either Hf or W-rich. Compared with the alloy CM2 10 g button, the Nb_{ss} in the 500 g ingot was poorer in W but richer in Hf and Si.

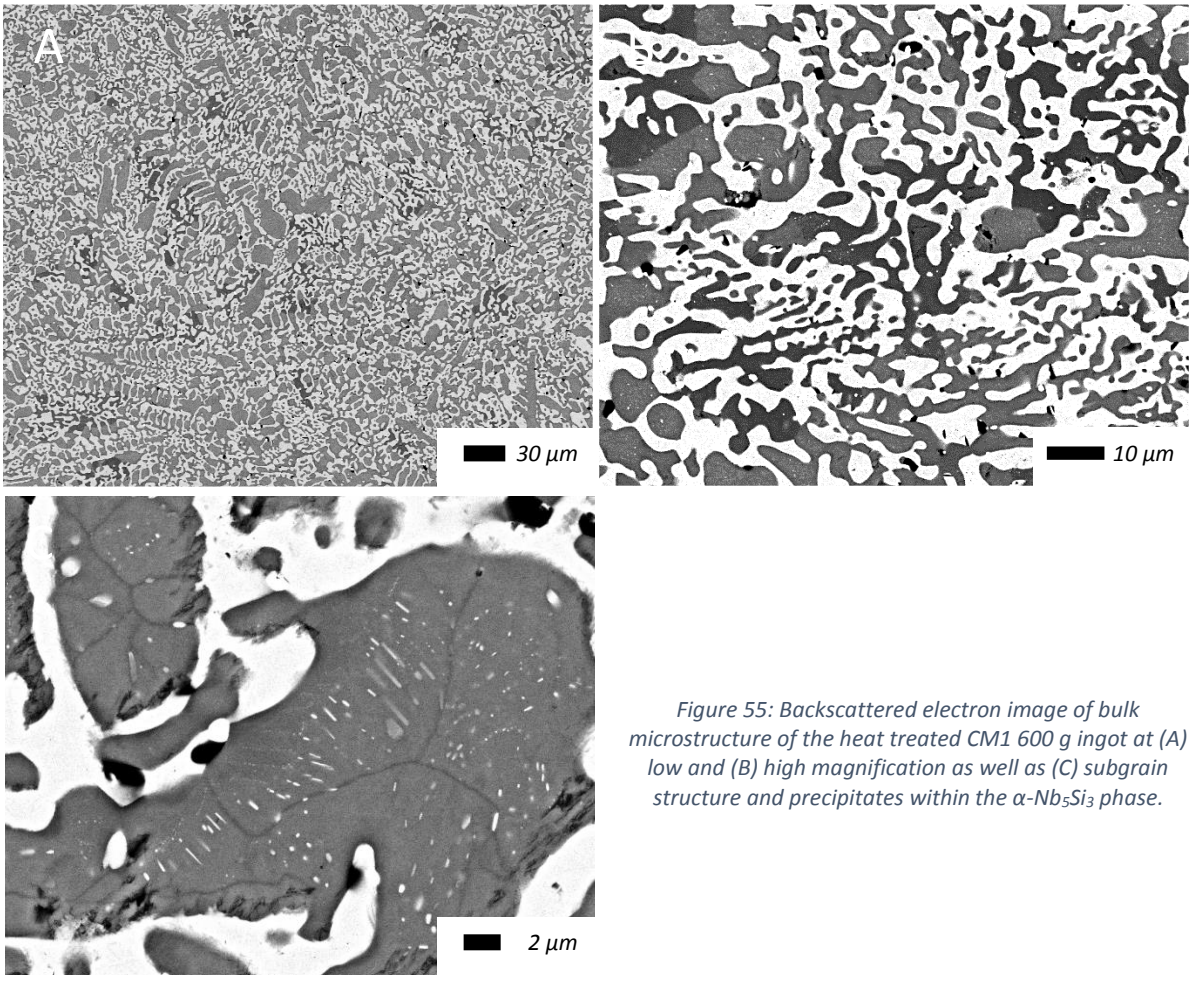

Figure 55: Backscattered electron image of bulk microstructure of the heat treated CM1 600 g ingot at (A) low and (B) high magnification as well as (C) subgrain structure and precipitates within the α-Nb_5Si_3 phase.

The microstructure of the heat treated alloy CM1 600 g ingot is shown in Figure 55. Data for the chemical analysis of the phases and their crystal structure in given in Table 13 and Appendix B Fig 1. The chemical composition of the heat treated specimen was essentially the same as that of the cast alloy. The α-Nb_5Si_3 silicide grains were surrounded by coarsened interdendritic prior-eutectic. Different areas of the silicides exhibited a contrast difference, see image B in Figure 55. EDS analysis of these dissimilar contrast phases revealed that the average concentration (and range) of Ti was 15.4 at.% (14.7 - 15.6 at.%) and 6.8 at.% (6.1 – 8.0 at.%) for the dark and light phases, respectively. This disparity was mainly at the expense of Nb, but there was also an average reduction of 1.0 at.%Mo from the dark to the light contrast. Owing to this partitioning of Ti in the α-Nb_5Si_3 the average Ti content of the latter was higher compared with the cast alloy. In Nb_{ss} the Ti concentration had decreased compared with the cast alloy, which would suggest that the Ti had partitioned to the α-Nb_5Si_3 from the Nb_{ss}.

Table 13: Summary of the EDS analysis (at.%) of heat treated CM1 600 g ingot including minimum and maximum analysis values.

Element	*Large Area*	*Prior-eutectic*	*Silicide*	*Solid Solution*
Nb	60.7 ± 0.35 60.2 - 61.0	61.3 ± 1.87 57.7 - 62.0	51.4 ± 3.47 46.2 - 54.4	75.6 ± 0.92 73.7 - 76.5
Ti	8.7 ± 0.21 8.5 - 9.2	9.4 ± 1.51 8.3 - 12.7	9.7 ± 4.20 6.1 - 15.6	7.3 ± 0.92 6.1 - 8.2
Si	22.7 ± 0.49 22.0 - 23.4	21.1 ± 1.79 17.7 – 23.3	36.9 ± 0.56 35.8 - 37.6	0.6 ± 0.64 0.0 - 2.0
Mo	5.1 ± 0.14 4.9 - 5.4	5.4 ± 0.59 4.4 - 5.6	1.5 ± 0.54 0.6 - 2.0	10.9 ± 0.46 10.2 - 11.4
Hf	0.6 ± 0.09 0.5 - 0.7	0.6 ± 0.26 0.4 - 1.2	0.4 ± 0.23 0.0 - 0.8	0.0 ± 0.02 0.0 - 0.1
W	2.2 ± 0.08 2.1 - 2.3	2.3 ± 0.73 0.9 - 3.3	0.1 ± 0.12 0.0 - 0.3	5.5 ± 0.41 4.7 - 6.0

Comparing the EDS analysis of the heat treated CM1 600 g ingot, Table 13, with the cast alloy, Table 9, shows no significant differences between the analyses of eutectic and prior-eutectic areas except for Si. Indeed, different prior-eutectic areas did show some difference in composition

particularly for Si, Ti and W. The variation in the Ti content could be attributed to the ratio of Ti-rich to Ti-poor silicides in that particular prior-eutectic. Similar to the as-cast alloy, there were some noteworthy variations in Si content of the prior-eutectic. Unlike the as-cast alloy there were also noteworthy variations in W content of the prior-eutectic. Plotting the individual data of Si against W in the prior-eutectic, Figure 56, showed a relationship between these two elements, the extremes of which could be defined as W-rich and Si poor and Si-rich and W-poor due to the difference in Si (5.6 at.%) and W (2.4 at.%) content. The only significant variations in the phase analysis were the Ti and Mo in the silicide phase and the Ti and Si variations in the Nb_{ss}. Unlike the heat treated samples of the CM1 10 g buttons Si was still detected in the solid solution. Figure 55C showed that the fine precipitates formed inside the α-Nb_5Si_3 had grown, with some becoming needle like long precipitates.

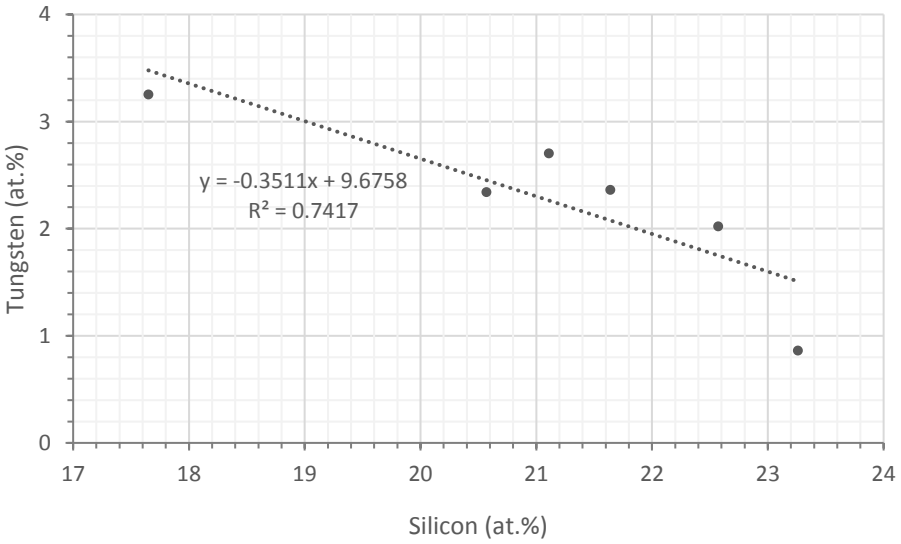

Figure 56: Relationship between W and Si contents in the prior-eutectics in the heat treated CM1 600 g ingot.

The microstructure of the heat treated alloy CM2 500 g ingot is shown in Figure 57. The EDS analysis and XRD data is shown in Table 14, and Appendix B Fig 2, respectively. The large area analysis confirmed very significant chemical inhomogeneity for Si and W that could be attributed to strong partitioning of these elements during the heat treatment. Furthermore, the average W and Hf concentrations were higher and lower, respectively, than those in the cast alloy, which could be attributed to there being W and Hf macrosegregation in the 500 g ingot of the alloy CM2.

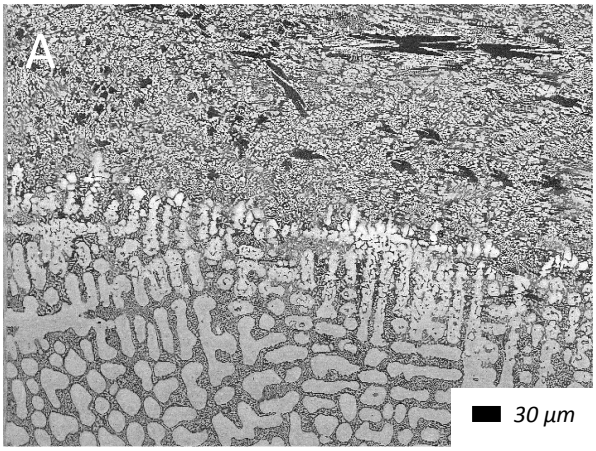
A
30 µm

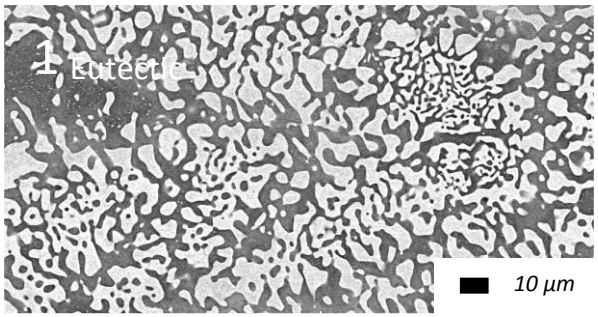
1 Eutectic
10 µm

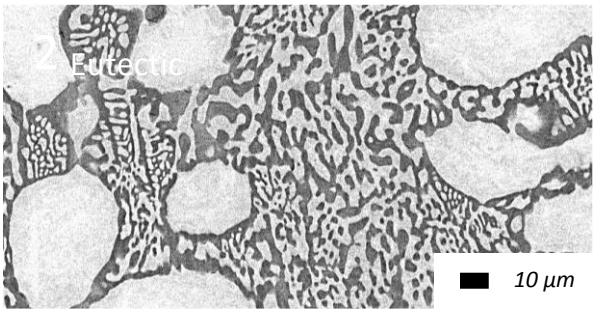
2 Eutectic
10 µm

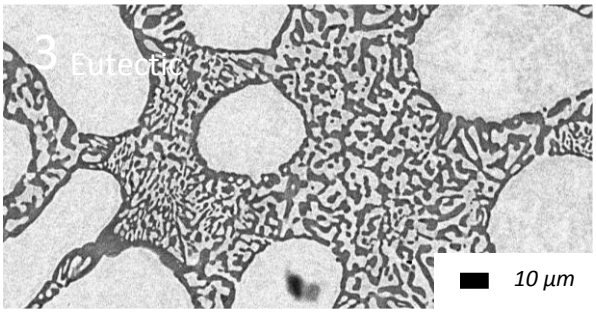
3 Eutectic
10 µm

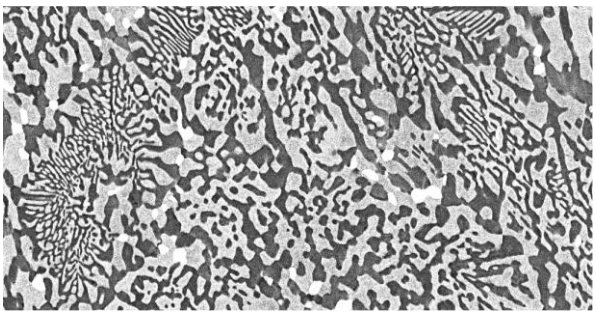

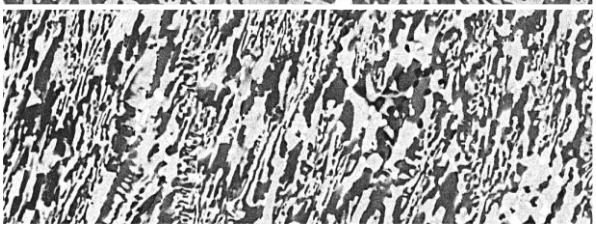

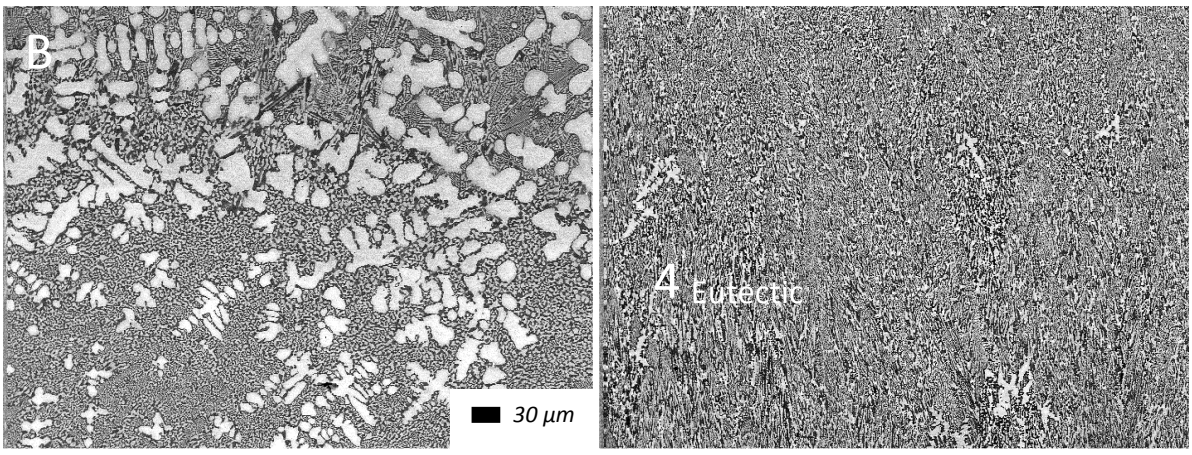

Figure 57: Backscattered electron images of the bulk, in the left hand column, and prior-eutectic areas, in t column, microstructure of the heat treated alloy CM2 500 g ingot, showing 5 distinctly different morphologies.

Image A in Figure 57 shows a boundary between two microstructures. The upper section of the image, we shall consider this microstructure 1, was more morphologically similar to the alloy CM1 600 g than any CM2 specimen, dendrites of α-Nb_5Si_3 surrounded by an interdendritic prior-eutectic of Nb_{ss}+α-Nb_5Si_3. There was also evidence of cells of prior fine eutectic regions and some variation in the silicide contrast, but not as pronounced as in the heat treated alloy CM1 600 g ingot. The bottom section of image A, we shall call this microstructure 2, had a high volume fraction of Nb_{ss} dendrites surrounded by a prior-eutectic of Nb_{ss} + α-Nb_5Si_3. Some lamellar morphologies were still present in the interdendritic Nb_{ss}+Nb_5Si_3 prior-eutectic. Microstructure 2 gradually evolved into microstructure 3, shown at the top of image B, Figure 57. Although similar in the interdendritic region, the volume fraction of the Nb_{ss} dendrites was reduced and some larger Nb_5Si_3 grains formed. At the bottom of image B, we shall call this microstructure 4, the volume fraction of the dendrites was reduced again and the larger second phase silicides did not form. The final microstructure in image C, we shall call this microstructure 5, was almost fully made up of prior eutectics with minimal formation of Nb_{ss} dendrites. This retained some areas of lamellar morphology surrounded by coarser prior-eutectics.

Table 14: Summary of EDS analysis (at.%) of heat treated CM2 500 g ingot, including SD, minimum and maximum analysis values.

Element	*Large Area*	*Prior-eutectic*	*Silicide*	*Solid Solution*
Nb	74.1 ± 4.59	71.5 ± 1.92	58.1 ± 0.37	89.6 ± 2.87

	68.5 - 81.2	67.8 - 74.7	57.7 - 58.5	85.7 - 92.8
Si	17.1 ± 3.27	20.6 ± 1.32	37.8 ± 0.41	0.3 ± 0.30
	12.9 - 21.9	17.7 - 22.6	37.3 - 38.3	0.0 - 0.84
W	5.7 ± 1.63	4.5 ± 2.4	1.2 ± 0.34	9.2 ± 3.26
	3.6 - 8.4	8.9 - 1.3	0.8 - 1.7	5.7 - 13.3
Hf	3.0 ± 0.40	3.3 ± 0.67	2.8 ± 0.24	0.9 ± 0.21
	2.4 - 3.4	2.5 - 5.3	2.5 - 2.9	0.5 - 1.2

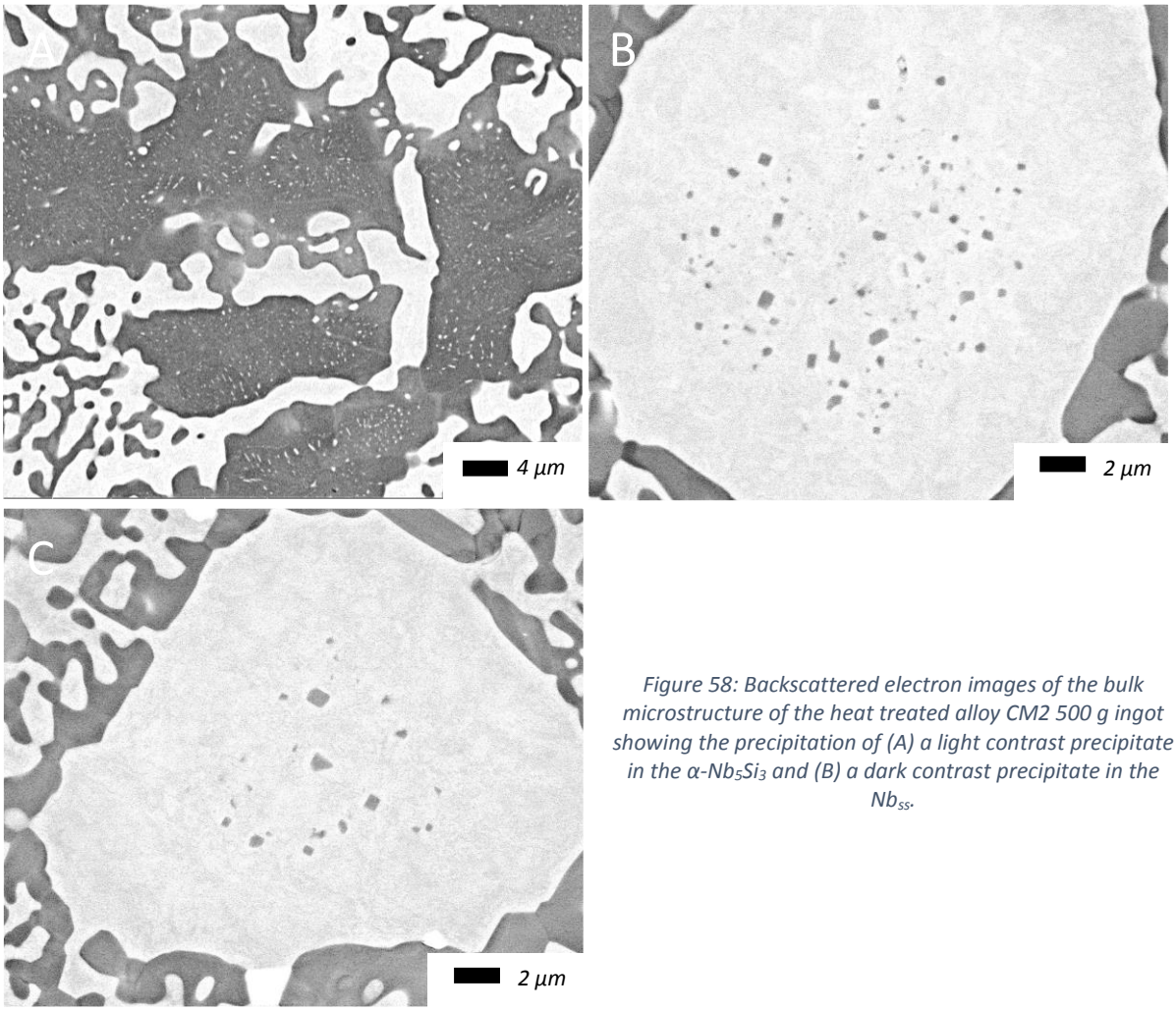

Figure 58: Backscattered electron images of the bulk microstructure of the heat treated alloy CM2 500 g ingot showing the precipitation of (A) a light contrast precipitate in the α-Nb_5Si_3 and (B) a dark contrast precipitate in the Nb_{ss}.

Compared with the cast alloy (Table 12) there were differences in the Si, W and Hf content of the HT specimen, Table 14, and larger standard deviation for Si and W in the prior eutectic. The concentration of silicon varied dramatically depending on the microstructure analysed. The highest Si concentrations were found in microstructure 1 and the lowest in microstructure 2. Concentrations of elements in the large area analysis of microstructure 5 were very similar to the overall average for the prior-eutectic. Variations in W within the prior-eutectic were at a maximum in microstructure 5 and a

minimum in 2. The prior-eutectic also showed variations in W content, the average for microstructure 1 and 5 was 6.5 and 5.9 at.%W, respectively and the prior-eutectic in microstructure 2 had an average of 1.5 at.%W. There was however an increase in the average Si content of the prior-eutectic from 19.6 to 20.4 to 21.8 at.% from microstructure 5 to 1 to 2, respectively. Within their respective phases, minimal variations in the spot analysis was noted, except for W concentrations in the solid solution. Tungsten levels in the Nb_{ss} in microstructure 1 were significantly higher than in microstructure 2, averaging 12.5 at.%W compared with 6.0 at.%W. Comparing the average compositions of the Nb_{ss} in the cast and the heat treated conditions, the Hf content was significantly reduced in the latter. The same was seen for Hf in the Nb_5Si_3, however the solubility of W had increased after HT. There was evidence of fine bright contrast precipitates forming inside α-Nb_5Si_3 grains but no evidence for "subgrain" formation, see Figure 58. There was also evidence of dark contrast precipitates in the bulk of large Nb_{ss} grains, see Figure 58. No precipitates were observed in the small Nb_{ss} grains.

3.1.3 Conclusions

Two near eutectic alloys with nominal compositions Nb-8.3Ti-21.1Si-5.4Mo-4W-0.7Hf (CM1) and Nb-20.5Si-5.8W-4Hf (CM2) were studied in the cast and heat treated (1500 ^{O}C/100 h) conditions in the form of 10 g button ingots (CM1, CM2) and 600 g (CM1) g and 500 g (CM2) ingots.

The Nb_{ss} and Nb_5Si_3 and eutectics of these two phases were formed in the cast alloys.

The refractory metals partitioned to the Nb_{ss} rather than the Nb_5Si_3 silicide.

The Nb_5Si_3 was the β-Nb_5Si_3 allotrope only in the CM1 10 g button. In the other cast alloys and in all the heat treated alloys the α-Nb_5Si_3 allotrope was formed.

In the heat treated 10 g buttons Nb_{ss} with no Si was formed.

Relationships between solutes in the Nb_{ss} and in prior-eutectic areas in the heat treated alloys have been found for both alloys.

In the alloy CM1 10g HT and 600 g AC and HT, precipitation of a second light contrast phase was observed in subgrains formed in the Nb_5Si_3.

In the alloy CM2 500 g HT precipitation of a second light contrast phase was observed in the Nb_5Si_3, but not subgrains and dark contrast precipitates of a second phase were formed in the bulk of large Nb_{ss} grains.

3.2 SUCTION CAST ALLOYS

Suction cast bars were studied to investigate the effect of cooling rate on the microstructure of the alloys CM1 and CM2.

The images in the following sections show the variation of the microstructure at the edge and the centre of the bars. The images are labelled A, B, C etc. to denote the location along the length of the bar. Each bar was split into 10 evenly spaced parts (A to J) with A at the end of the bar and closest to the bottom of the water cooled copper mould and J at the top of the bar in contact with the Ar atmosphere.

3.2.1 6 mm Diameter Bars

Images of the microstructure of the 6 mm diameter suction cast bar of the alloy CM1 at the edge and the centre are shown in Figure 59 and Figure 60, respectively.

Figure 59 shows the 4 different microstructures observed at different locations down the edge of the bar. In the area of the highest cooling rate, the microstructure was primarily as shown in Image A. It consisted of a fine mixture, sometimes lamellar, of dark and light contrast phases in cells surrounded by a light contrast phase. The next area along the edge of the bar, namely area B, consisted of very fine, regular, lamellar two phase eutectic cells surrounded by coarser two phase region. Although predominantly these structures were seen in their respective areas A and B, there was some cross over between them. Moving to area C, the microstructure changed again to a coarser mixture of light and dark contrast phases. There were elements of directionality in this morphology typically perpendicular to the cooling surface. The EDS analyses of individual phases was impossible due to their fine size. However XRD, Appendix B Fig 3, determined that there were only two phases present in this alloy, namely the Nb_{ss} and β-Nb_5Si_3. This, with our previous knowledge of this alloy and the spot analyses of the bulk phases, led to the conclusion that the dark and light contrast phases were the β-Nb_5Si_3 and Nb_{ss}, respectively. After initial variations in microstructure the morphology stabilised to a

structure of β-Nb_5Si_3 dendrites surrounded by an interdendritic eutectic similar to that seen in the 10 g buttons of the alloy CM1. This morphology continued uninterrupted from location D to J.

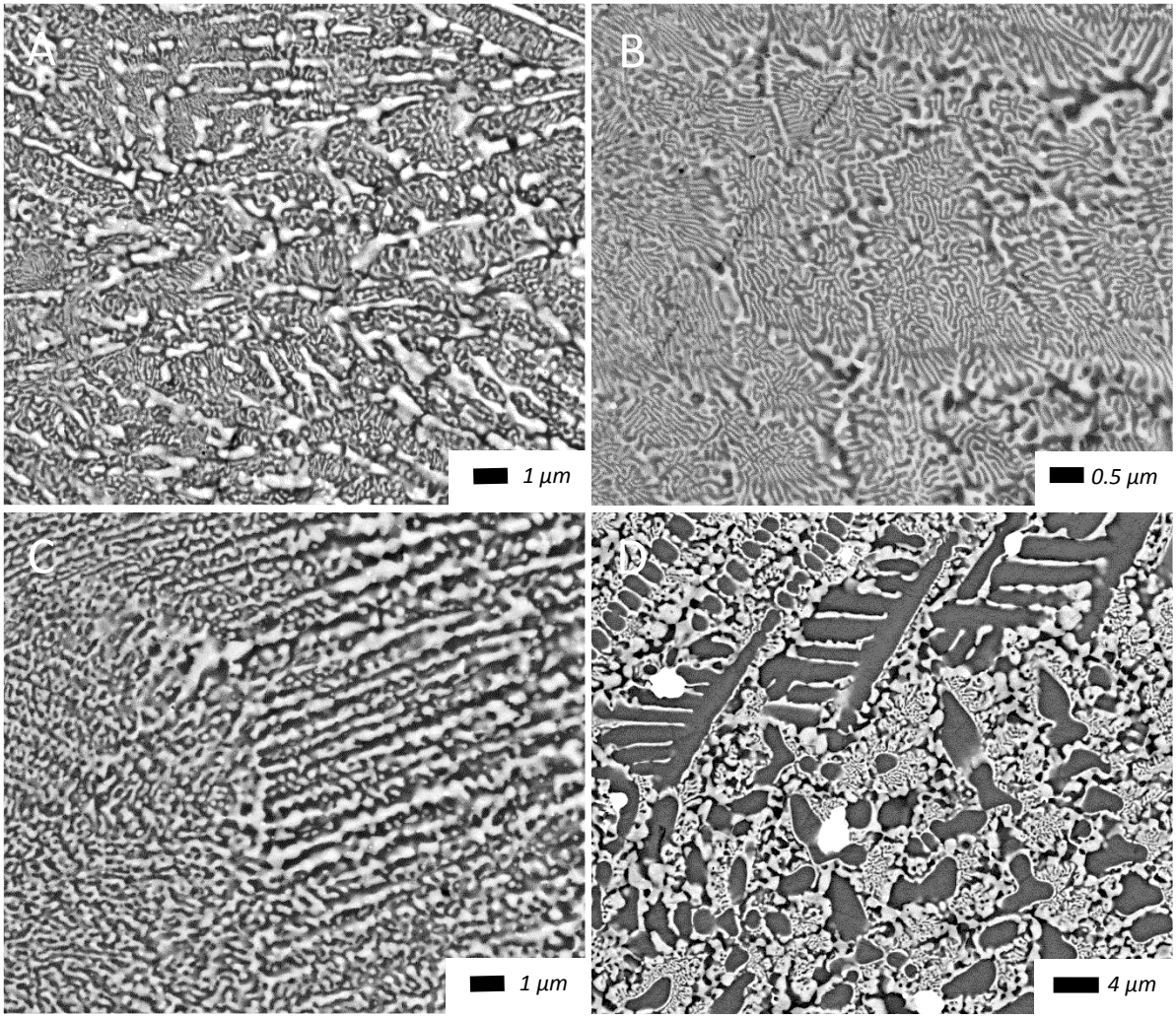

Figure 59: Backscattered electron images of the microstructure of the alloy CM1 6mm suction cast at the edge of the bar at areas A, B, C and D.

Changes in the morphology of the microstructure in the central region, Figure 60, were much less pronounced than at the edge of the bar. At the highest cooling rate, area A in Figure 60, the morphology was very similar to that of area C at the edge of the bar (Figure 59). This consisted of a fine, quasi-regular eutectic between Nb_{ss} and β-Nb_5Si_3. Right next to the cooling surface the eutectic was anomalous, as can be seen in the right hand side of the image A in Figure 60. Directionality became stronger slightly further from the cooling surface. The morphology steadily changed to include cells of finer, quasi-regular eutectic with larger areas of coarser eutectics. This gradually began to include

more of these cells and β-Nb_5Si_3 dendrites formed, creating the typical CM1 microstructure seen in the arc melted buttons and shown in image J, Figure 60. This microstructure dominated the centre of the bar from area B to J.

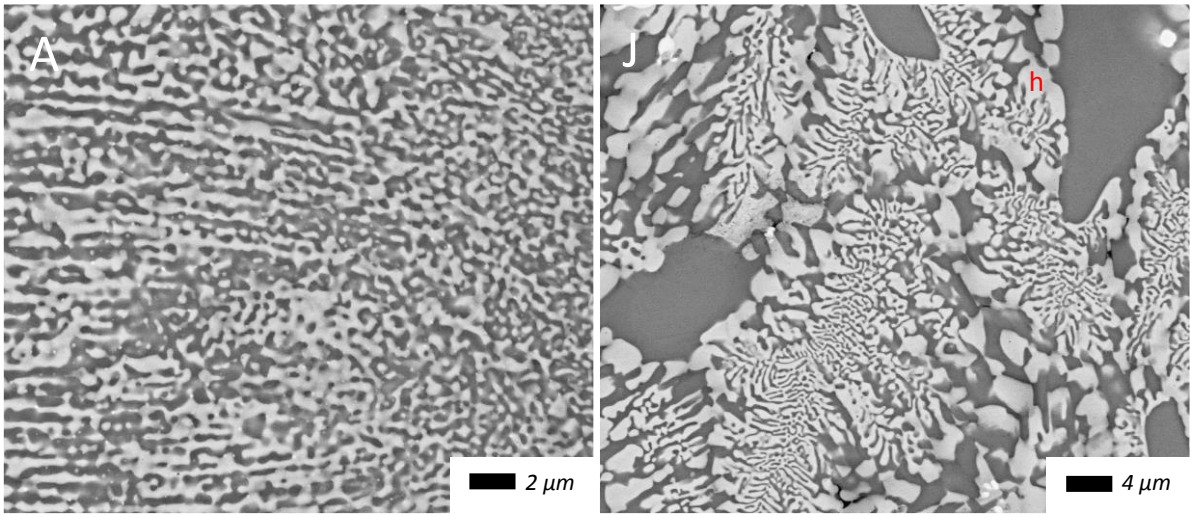

Figure 60: Backscattered electron images of the microstructure of the alloy CM1 6mm suction cast at the centre of the bar at areas A and J. Nb_{ss} halo is shown by h in J.

Table 15 shows the EDS data for the alloy CM1 6 mm suction cast bar. The data did not indicate any macrosegregation of elements over the length and diameter of the bar. The only phase that exhibited a significant variation in alloying elements between grains was the Nb_{ss} regarding the W concentration, seen previously in the CM1 10 g button and 600 g ingots. This would suggest that the changes in the morphology of the microstructure seen in Figure 59 and Figure 60 were caused by the changes in solidification conditions, not segregation of elements. The spot analyses showed very little discrepancy in the concentrations of the elements between similar phases.

To confirm whether changes in the morphology of the microstructure observed in the bar were driven by cooling rate changes or chemical effects the interface between microstructures seen in Figure 59C and D was studied by EDS. The analyses showed a maximum difference of 0.2 at.% between these two areas for all elements. Therefore, it was concluded that changes in microstructure of this nature were not driven by differences in elemental concentration.

Table 15: Summary of EDS analysis data (at.%) of the alloy CM1 6 mm suction cast, including SD, minimum and maximum values.

Element	*Large Area*	*Eutectic*	*Silicide*	*Solid Solution*
Nb	58.0 ± 0.57	55.8 ± 0.32	50.8 ± 0.19	72.3 ± 0.56
	57.5 - 59.8	55.2 - 56.1	50.4 - 51.0	71.7 - 73.0
Ti	9.7 ± 0.29	10.0 ± 0.18	7.0 ± 0.11	7.5 ± 0.33
	9.0 - 10.1	9.8 - 10.2	6.8 - 7.2	6.2 - 7.9
Si	23.4 ± 0.46	22.5 ± 0.33	37.4 ± 0.36	1.2 ± 0.52
	22.5 - 24.2	22.1 - 23.0	37.0 - 38.1	0.7 - 1.9
Mo	5.4 ± 0.31	8.0 ± 0.33	4.0 ± 0.27	11.1 ± 0.25
	4.7 - 5.7	7.6 - 8.4	3.5 - 4.5	10.9 - 11.4
Hf	0.6 ± 0.52	0.7	0.3	0.2
	0.2 - 0.7	0.5 - 1.1	0.1 - 0.5	0.2 - 0.3
W	2.9 ± 0.20	2.9 ± 0.07	0.6	7.7 ± 0.98
	2.6 - 3.2	2.8 - 3.0	0.3 – 0.9	6.8 - 9.0

Images of the microstructure formed in the cast 6 mm diameter suction cast bar of the alloy CM2 at the edge and the centre are shown in Figure 61 and Figure 62, respectively. The XRD and EDS data are shown in Appendix B Fig 4 and Table 16, respectively.

In the area of highest cooling rate, A, the microstructure at the edge of the alloy CM2 6 mm suction cast bar appeared to be very irregular and “disjointed”. There were some small cells consisting of Nb_{ss} rods embedded in a silicide matrix and some lamellar formations within this section. Along the length of the remaining bar the microstructure then alternated between the two microstructures seen in images D and I in Figure 61. Image D is representative of the microstructures seen in areas C, E, F and J as well as D. The main morphology was regular lamellae, forming in cells, surrounded by coarser semi-regular eutectics. There were however areas of anomalous eutectic seen in the top right hand side corner of image D. Image I represents the microstructure seen in areas B, G, H as well as I, a purely eutectic microstructure with a mixture of the silicide and solid solution phases. Within this image there was also a noticeable change in contrast of the silicide phase. At the right side of the image, closer to the cooling surface, the silicide had a darker contrast compared with the left image, further from the cooling surface. This was seen in all areas with similar microstructure. There was also a slight change

in morphology from the dark to the light silicide. In the dark contrast area it was very hard to define which, if any phase, was the matrix as both have a continuous nature. In the light contrast it was obvious that the silicide was the continuous phase with a discontinuous solid solution.

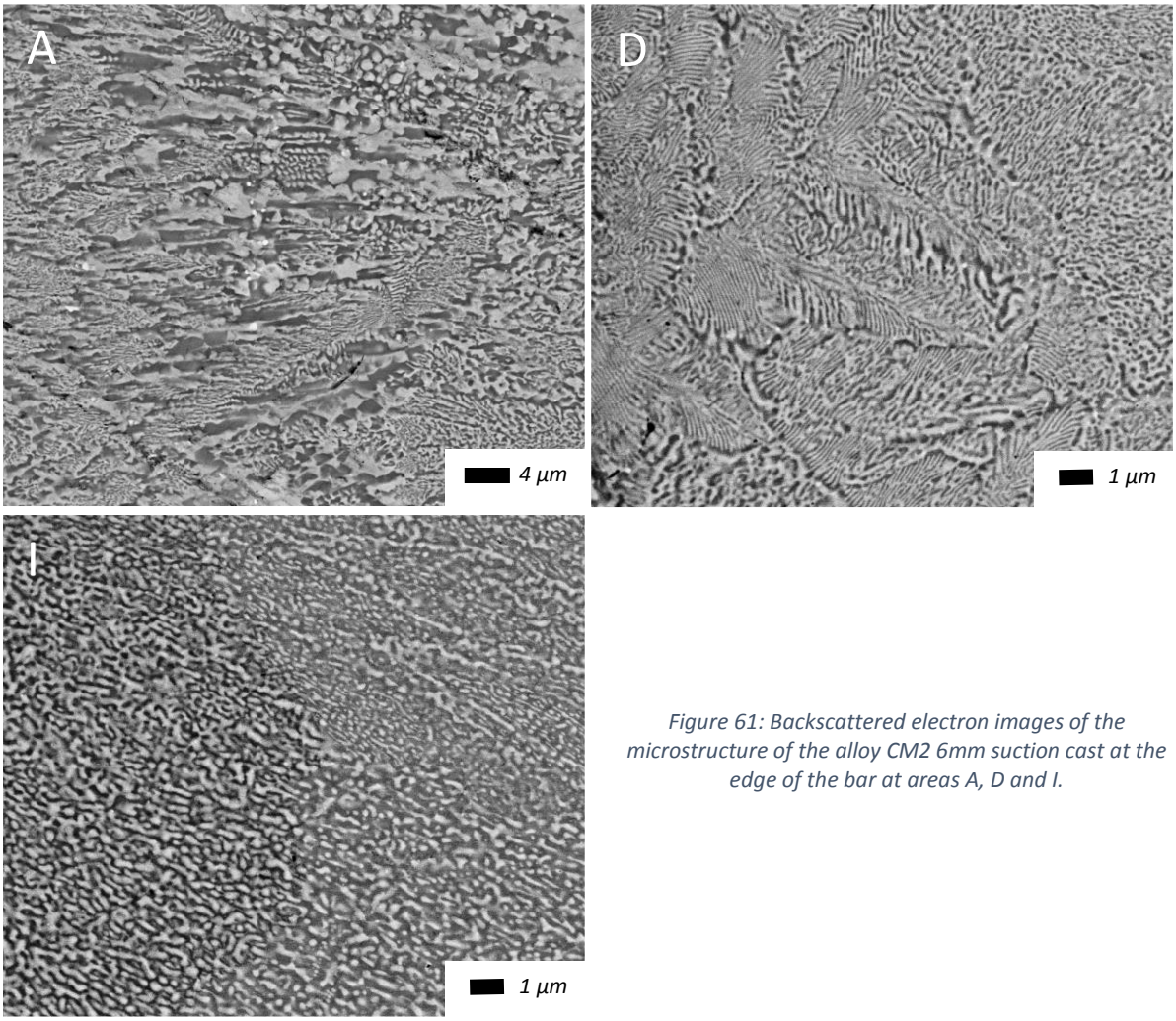

Figure 61: Backscattered electron images of the microstructure of the alloy CM2 6mm suction cast at the edge of the bar at areas A, D and I.

Unlike the central region in the alloy CM1 6 mm suction cast bar, the central images of the alloy CM2 6 mm bar, Figure 62, showed quite a lot of variation along the length of the bar. In the area A the microstructure was similar to that of image D in Figure 61 but the regions between the lamellar eutectic cells were much better defined. This continued until large regions of the microstructure seen in image C started to appear. The regions of Nb_{ss} dendrites surrounded by a second phase silicide and eutectics appeared periodically throughout the length of the bar. They were intercut with the image seen in D, similar to A but including Nb_{ss} dendrites. The periodic repetition of these microstructures

continued until area F/G where the microstructure shown in image I formed and continued to the end of the bar in area J.

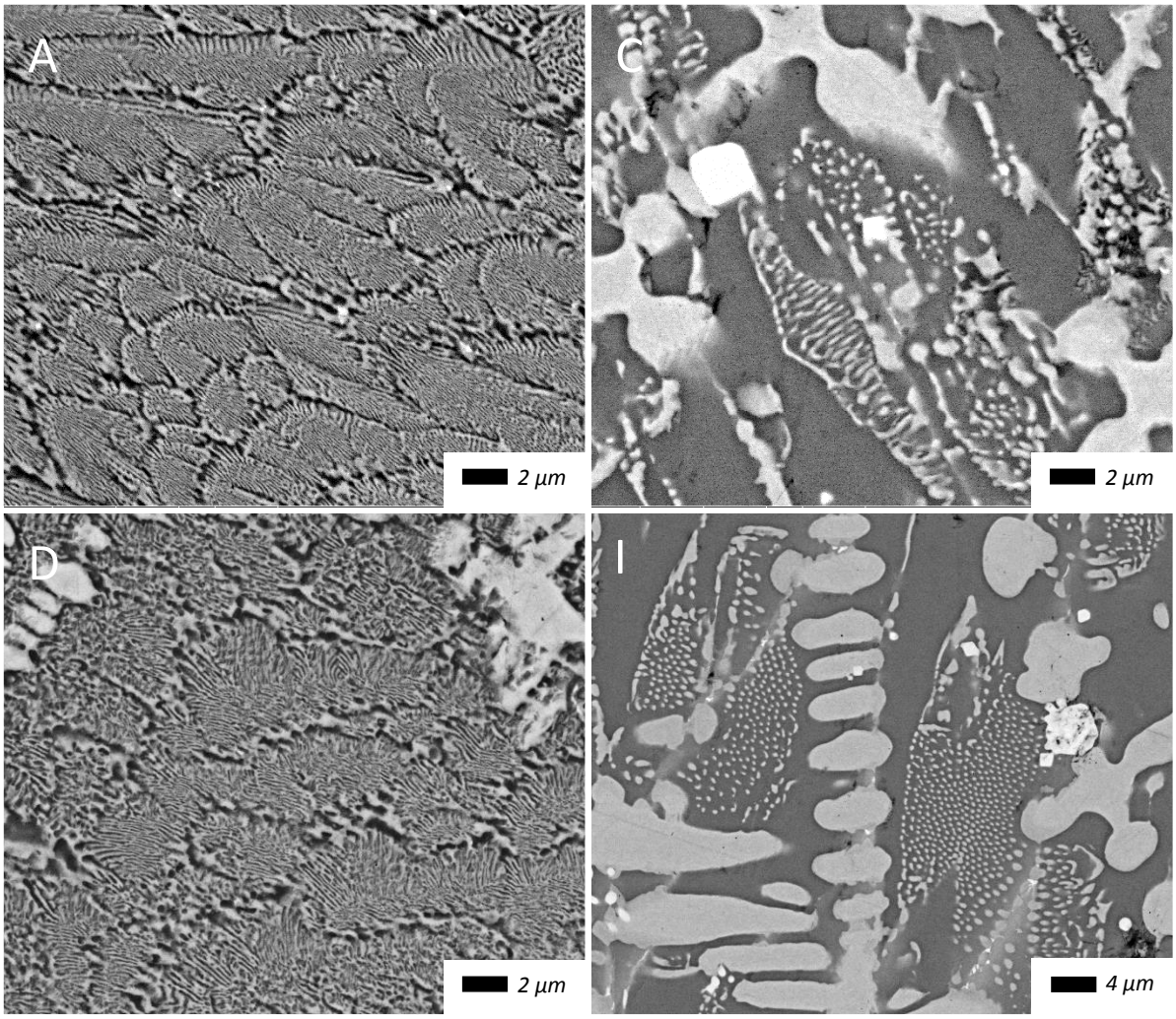

Figure 62: Backscattered electron images of the microstructure of the alloy CM2 6mm suction cast at the centre of the bar at areas A, C, D and I.

Table 16 shows the EDS analysis data of the 6 mm suction cast bar of the alloy CM2. The large area analysis data did suggest some segregation of Si throughout the bar. Looking at the individual analyses, the Si reached a maximum concentration in the centre of the bar in areas H to J. These areas, similar to Figure 62I, had a very high ratio of silicide to solid solution and thus the higher levels of Si were present. The rest of the EDS analysis showed no significant variations from area to area or phase to phase. The analysis indicated that the alloy was very close to the eutectic composition. The concentration of Si in the silicide was of interest. An average concentration of 25.4 at.%Si indicates

that the silicide was not a Nb_5Si_3-type silicide, which was present in the 10 g button and 500 g ingot. The XRD analysis, shown in Appendix B Fig 4, confirmed that the alloy had two types of silicide; Nb_3Si and α-Nb_5Si_3. The EDS data for the silicide in Table 16 was taken from the larger silicide grains seen at the centre, images C and I in Figure 62.

Table 16: Summary of EDS analysis data (at.%) of the alloy CM2 6 mm suction cast bar, including SD, minimum and maximum values.

Element	*Large Area*	*Eutectic*	*Silicide*	*Solid Solution*
Nb	70.5 ± 0.37	70.3 ± 0.35	68.6 ± 0.15	81.7 ± 0.43
	70.1 - 71.3	69.7 - 70.8	68.5 - 68.9	81.4 - 82.5
Si	19.9 ± 0.72	20.0 ± 0.33	25.4 ± 0.16	1.3 ± 0.30
	18.6 - 21.0	19.5 - 20.5	25.2 - 25.6	1.0 - 1.7
W	5.1 ± 0.46	5.2 ± 0.11	2.3 ± 0.19	15.4 ± 0.36
	4.5 - 6.0	5.0 - 5.3	2.0 - 2.6	15.2 - 16.0
Hf	4.5 ± 0.19	4.5 ± 0.18	3.8 ± 0.09	1.5 ± 0.12
	4.2 - 4.7	4.1 - 4.6	3.7 - 4.0	1.4 - 1.7

Further study of the central areas with larger Nb_3Si grains, Figure 62C, started to show areas of interest. Presented in Figure 63centre is a transition region around area C where the two microstructures meet. In this region, and others similar to it in the centre of the bar, the single Nb_3Si phase was transforming via the eutectoid reaction $Nb_3Si \rightarrow (Nb_{ss} + \alpha\text{-}Nb_5Si_3)_{eutectoid}$. It was clear from the magnified image on the right that a regular, quasi-lamellae, solid solution/silicide morphology evolved from a single Nb_3Si phase.

As well as regions in the centre, coarser silicide phases were also found close to the edge. In border regions between the irregular, anomalous eutectic at the edge and the quasi-regular cells, larger silicide phases were seen, Figure 63edge. Similar to the centre a two phase, Nb_{ss}/silicide, can be seen forming from a single larger silicide phase.

EDS analysis of these areas, both at the centre and the edge, showed no significant variations in the concentration of the alloying elements. The variation in silicon content was the largest seen, with an increase of 0.4 at.% from the fine structures to the coarser Nb_3Si and Nb_{ss} region.

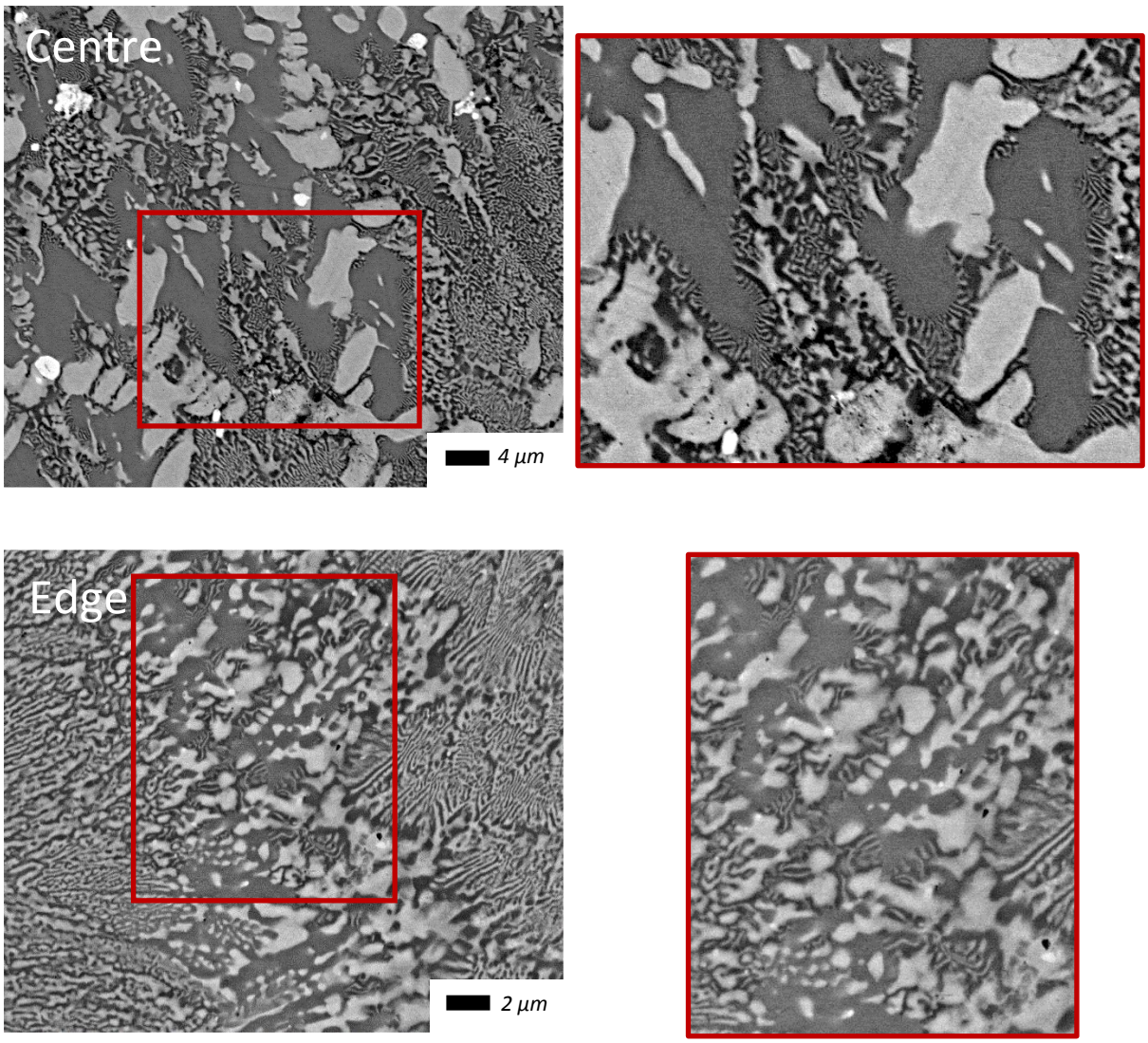

Figure 63: Backscattered electron images of the frozen eutectoid decomposition $Nb_3Si \rightarrow (Nb_{ss} + Nb_5Si_3)_{eutectoid}$ at the centre and the edge of the alloy CM2 6 mm suction cast bar.

Another area of interest in the as-cast CM2 6 mm bar was the contrast difference shown in the eutectic in Figure 61I. The change in contrast from the dark contrast, top of the image, to the light contrast, bottom of the image, also exhibited a slight change in morphology. The eutectics seen in the lighter region, morphologically had more in common with the eutectics seen between Nb_3Si and Nb_{ss}, Figure 62C and I, than the eutectic between Nb_5Si_3 and Nb_{ss}. This change in morphology can be better observed in Figure 64. EDS analysis of these regions did not show any variation in the concentrations of alloying elements higher than 0.1 at.%, seen for Hf, W and Si.

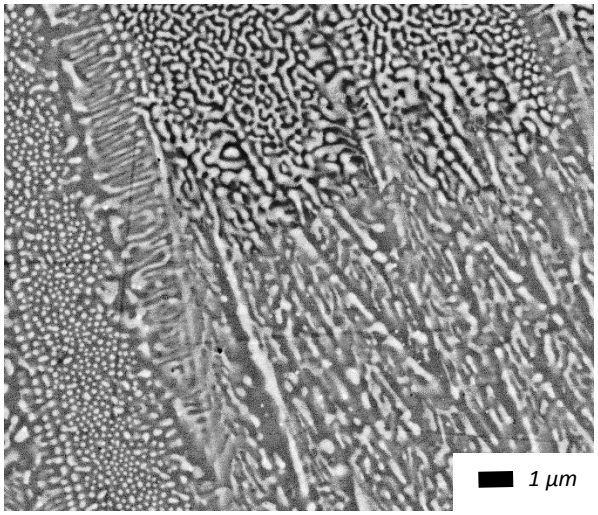

Figure 64: Backscattered electron image showing the difference in morphology between the darker silicide eutectic and the lighter silicide eutectic.

Figure 65 shows images of the edge and the centre of the alloy CM1 6mm suction cast bar sample after heat treatment at 1500 ^{O}C/100 hrs. On the basis of contrast in the SEM four phases were present in the microstructure. Only two of these were in significant enough volume fraction to register on XRD (Appendix B Fig 3); namely the α-Nb_5Si_3 and Nb_{ss}. Using EDS analysis (Table 17) these were identified as the dark grey and light grey contrast phases, respectively. The other two phases were identified in the images as a bright white phase, identified earlier in CM1 10 g as hafnia, and a dark black phase. The black phase was too small to be identified but it is accepted in the literature to be a titanium nitride (Zelenitsas & Tsakiropoulos 2005) formed from contamination by nitrogen during the heat treatment. Figure 65 is typical of all the microstructures present throughout the sample that consisted of co-continuous prior eutectic of Nb_{ss} and α-Nb_5Si_3, where both phases were continuous. The size and frequency of the silicide grains increased with increasing distance from the higher cooling areas. This was the only significant change in the structure throughout the bar.

EDS analysis of the bar showed, similar to the as-cast bar, small standard deviation for all the elements. In the large area analysis the difference between maximum and minimum Si concentration was 2.3 at.% but there was no apparent pattern between this difference and regions in the bar. The

difference between the maximum and minimum Ti concentrations increased in the silicide compared with the cast bar but not to the range seen in the 600 g ingot, Table 13.

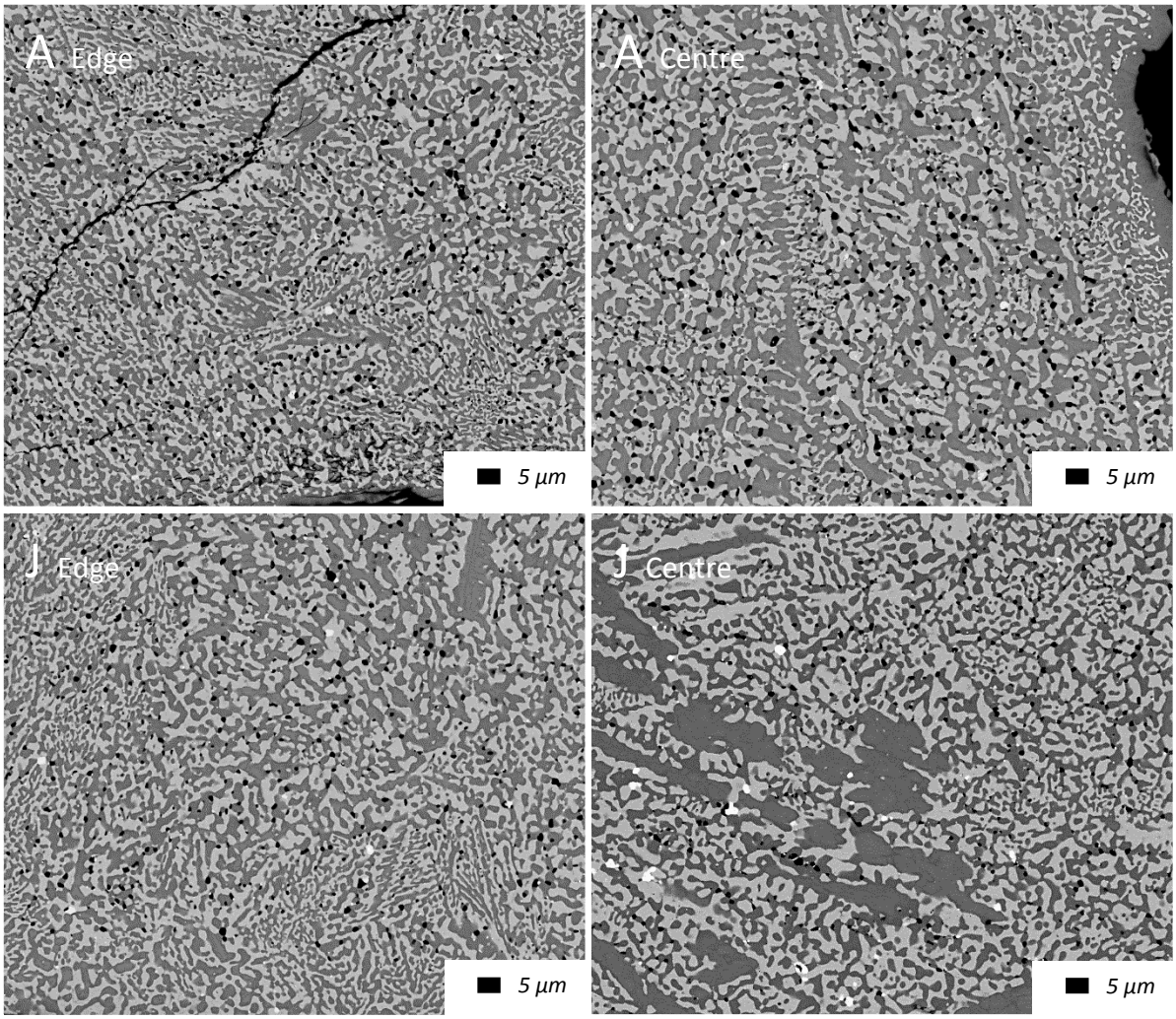

Figure 65: Backscattered electron images of the microstructure of the heat treated alloy CM1 6mm suction cast at the edge (left) and centre (right) of the bar at areas A and J.

Comparing the EDS analysis data for the as-cast and heat treated alloy CM1 6 mm bars, on average, the heat treated bar was leaner in Ti and Si. The reductions in Ti and Si concentration were also seen in the average eutectic composition with reductions of 1.1 and 2.5 at.%, respectively. The heat treated eutectic was also leaner in Mo and slightly leaner in W. Reductions in the Mo concentration in the eutectic were however maybe explained by the 2.6 at.% reduction seen in the silicide from the as-cast to heat treated alloy. Finally, the solid solution was also poorer in titanium and silicon. There was subgrain formation in Nb_5Si_3 with fine precipitates of a light contrast phase

(Figure 66), as seen in CM1 10 g HT, but the size of the precipitates was finer and comparable to those seen in CM1 600 g AC. Subgrains and fine precipitates were observed in area B to J.

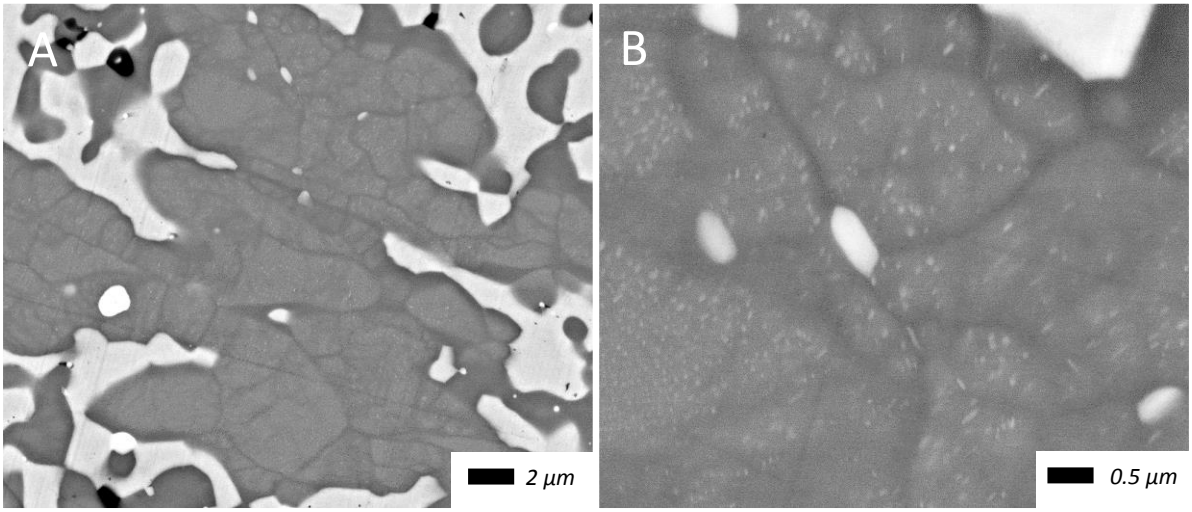

Figure 66: Backscattered electron images of the microstructure of the heat treated alloy CM1 6mm suction cast at the centre of the bar at areas J showing (A) the subgrain formation and (B) the precipitates in the β-Nb_5Si_3 grains.

Table 17: Summary of EDS analysis data (at.%) of heat treated CM1 6 mm suction cast bar, including SD, minimum and maximum values.

Element	*Large Area*	*Prior Eutectic*	*Silicide*	*Solid Solution*
Nb	60.6 ± 0.39	61.9 ± 0.65	53.9 ± 0.43	74.5 ± 0.3
	60.1 - 61.3	61.4 - 62.8	53.4 - 54.6	74.0 - 74.8
Ti	8.9 ± 0.29	8.9 ± 0.63	7.1 ± 0.76	5.7 ± 0.12
	8.3 - 9.4	8.3 - 9.8	6.1 - 8.3	5.6 - 5.9
Si	21.6 ± 0.56	19.9 ± 0.38	36.8 ± 0.31	0.1
	20.4 - 22.7	19.4 - 20.6	36.4 - 37.1	0.0 - 0.3
Mo	5.2 ± 0.41	5.5 ± 0.21	1.4 ± 0.07	11.5 ± 0.03
	4.6 - 6.0	5.1 - 5.8	1.0 - 2.1	11.3 - 11.9
Hf	0.5 ± 0.11	0.3 ± 0.12	0.3 ± 0.07	0.0
	0.3 - 0.7	0.2 - 0.5	0.2 - 0.4	0.0 - 0.1
W	3.2 ± 0.22	3.6 ± 0.09	0.4 ± 0.25	8.1 ± 0.13
	2.8 - 3.6	3.5 - 3.7	0.0 - 0.7	7.9 - 8.3

Figure 67 shows the microstructure of the heat treated alloy CM2 suction cast 6 mm diameter bar. The EDS and XRD data is given in Table 18 and Appendix B Fig 4, respectively. In image A, corresponding to the highest cooling rate, the microstructure consisted of discontinuous Nb_{ss} within an α-Nb_5Si_3 matrix. Only two phases were identified by XRD, Nb_{ss} and α-Nb_5Si_3, see Appendix B Fig 4.

This confirmed that the Nb_3Si present in the as-cast bar had fully transformed via the eutectoid reaction. The microstructure then subtly changed to the microstructure seen in image B of Figure 67. Both Nb_{ss} and Nb_5Si_3 were continuous phases and also retained some of the directionality formed during casting. This continued down the edge of the bar until reaching the area F. At this point the microstructure gradually changed from the structure seen in area B to a morphology similar to that in A and then to the structure in G. The microstructure shown in image G was similar to that seen in A but had more well defined Nb_{ss} dendrites and evidence of prior interdendritic eutectics. The interdendritic region had a continuous silicide matrix with embedded Nb_{ss}. This morphology did not change up to the area J where it then reverted back to area A type microstructure.

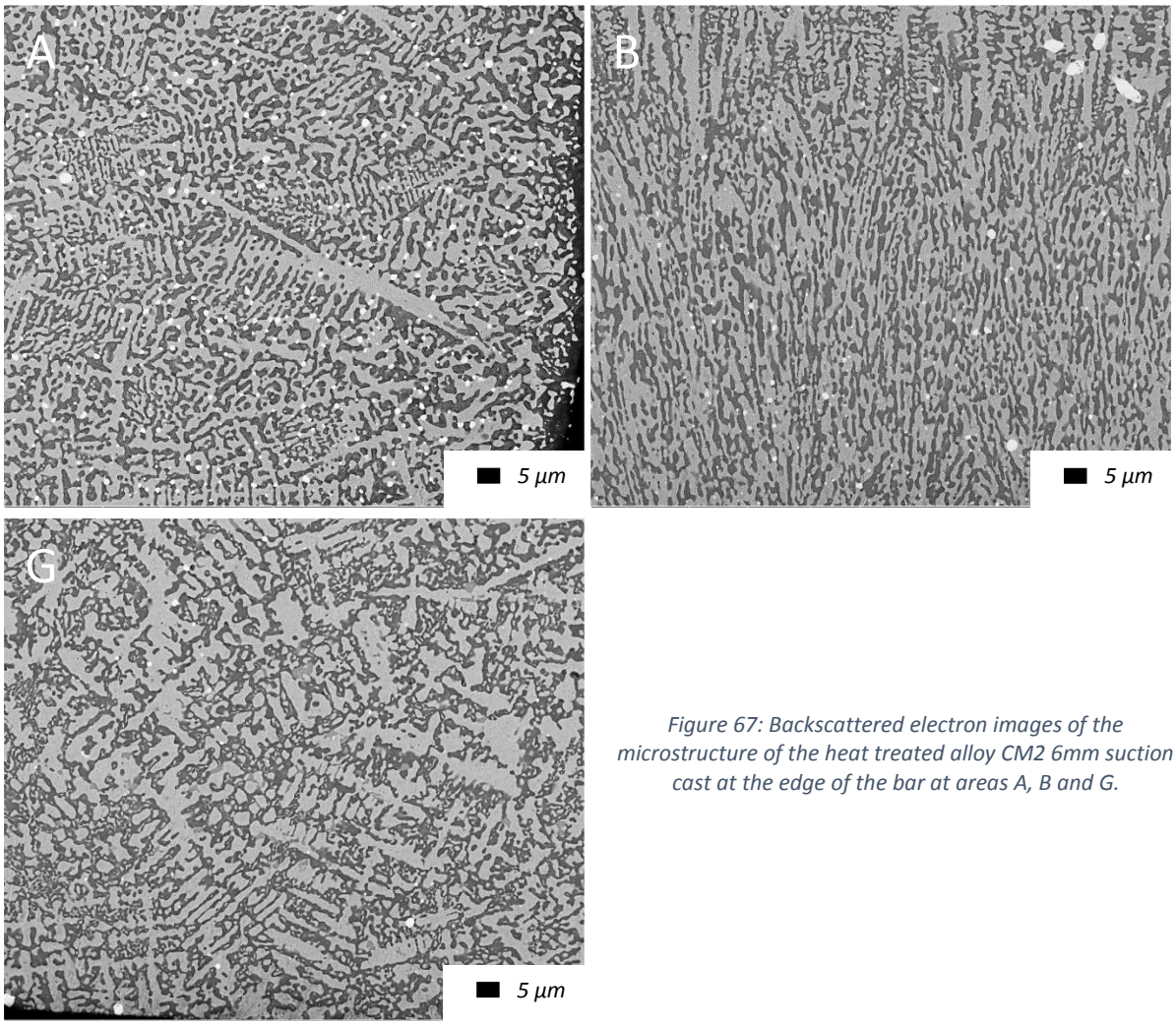

Figure 67: Backscattered electron images of the microstructure of the heat treated alloy CM2 6mm suction cast at the edge of the bar at areas A, B and G.

The images of the central area of the heat treated alloy CM2 6 mm suction cast bar are shown in Figure 68. There was a very similar progression of microstructure morphology as that seen at the edge. The microstructure started, at area A, with the same mix of Nb_{ss} in a α-Nb_5Si_3 matrix. This gradually transformed to the main microstructure seen in image E, consisting of well-defined Nb_{ss} dendrites surrounded by a prior-eutectic. The prior-eutectic had the same morphology as seen at the edge, discontinuous Nb_{ss} in a α-Nb_5Si_3 matrix.

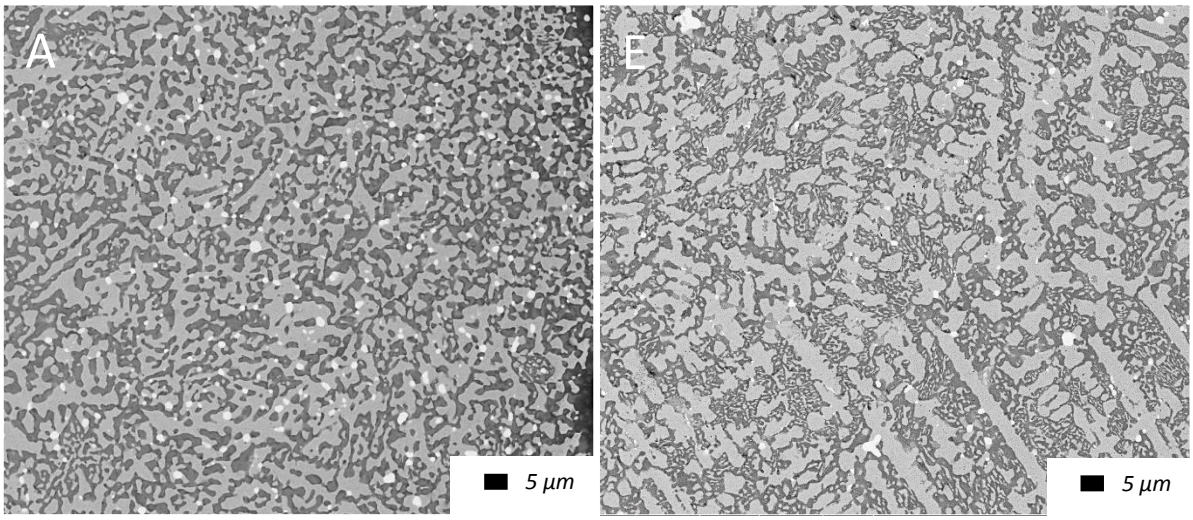

Figure 68: Backscattered electron images of the heat treated alloy CM2 6mm suction cast at the centre of the bar at areas A and E.

The EDS analysis data of the heat treated suction cast alloy CM2 6 mm bar is presented in Table 18. The large area analyses showed small standard deviations of the elements. Compared with the large area EDS analysis of the cast bar, the heat treated specimens were significantly poorer (3 at.%) in silicon, this is due to the heat treated and cast material not being from the same bar. This occurred due to a leak in the heat treatment chamber during the initial heat treatment rendering the sample (which was from the same bar as the cast sample) useless. The analysis of the prior eutectic showed that it was a lot richer in Si and with significant standard deviation (ranging from 20.7 to 24.3 at.%Si) and also richer and poorer in Hf and W, respectively. The increase in Si concentration in the prior eutectic areas is attributed to the presence of α-Nb_5Si_3 rather than Nb_3Si in these areas. No W and Si

were detected in the silicide and solid solution phase, respectively. However, there were significant increases in the concentration of Hf and W in the silicide and Nb_{ss}, respectively.

Table 18: Summary of EDS analysis (at.%) of the heat treated alloy CM2 6 mm suction cast bar, including SD, minimum and maximum values.

Element	*Large Area*	*Prior Eutectic*	*Silicide*	*Solid Solution*
Nb	73.1 ± 0.35 72.4 - 73.6	69.0 ± 1.23 67.2 - 70.7	55.4 ± 1.35 53.8 - 57.0	88.0 ± 0.7 87.1 - 88.9
Si	16.9 ± 0.44 15.7 - 17.5	22.4 ± 1.20 20.7 - 24.3	36.7 ± 0.42 36.3 - 37.3	0
W	5.2 ± 0.18 4.7 - 5.5	3.1 ± 0.22 3.0 - 3.4	0	10.8 ± 0.69 9.9 - 11.7
Hf	4.9 ± 0.27 4.5 - 5.3	5.4 ± 0.15 5.2 - 5.7	7.9 ± 0.94 6.7 - 8.9	1.2 ± 0.06 1.1 - 1.3

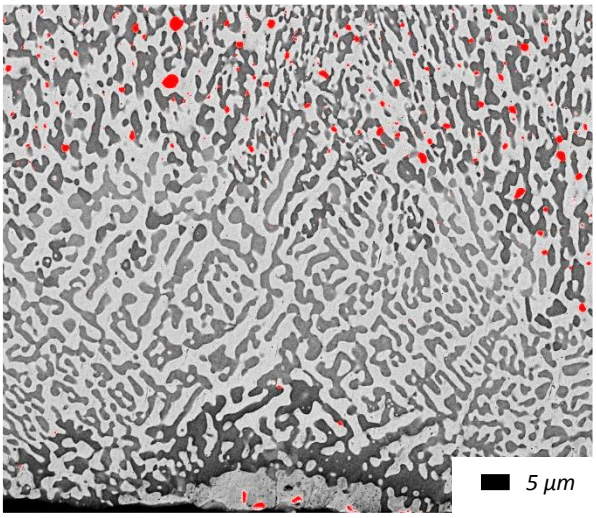

Figure 69: Backscattered electron image of the heat treated alloy CM2 6mm suction cast at the edge of the bar at area E showing the contrast difference in the silicides. The image shows how hafnia, highlighted red, varies in relation to the variation of the silicide contrast.

Close study of the microstructure detected a distinct contrast change in the silicide, see Figure 69 that was taken from the edge at area E. Areas of darker and lighter contrast silicide grains were seen throughout the bar. Starting at the bottom of the image in Figure 69 there was a large Nb_{ss} area at the edge of the bar surrounded by a dark contrast silicide matrix. This was in turn surrounded by Nb_{ss} and Nb_5Si_3, with a distinctly lighter contrast silicide, returning to the dark silicide after 15 -20 µm away from the edge. EDS analyses of the two silicides showed significant variations in the

concentration of Hf and some less significant variations in the silicon concentration. The darker contrast phase, on average, had 0.9 at.% less silicon and 3.4 at.% less hafnium than the lighter silicide. Minimal W content was detected in either phase with niobium balancing out. The volume fraction of hafnia was virtually zero within the areas of light contrast, Hf-rich, region compared with an overall volume fraction average of 1.6 %. This is highlighted in Figure 69 where the hafnia is in red.

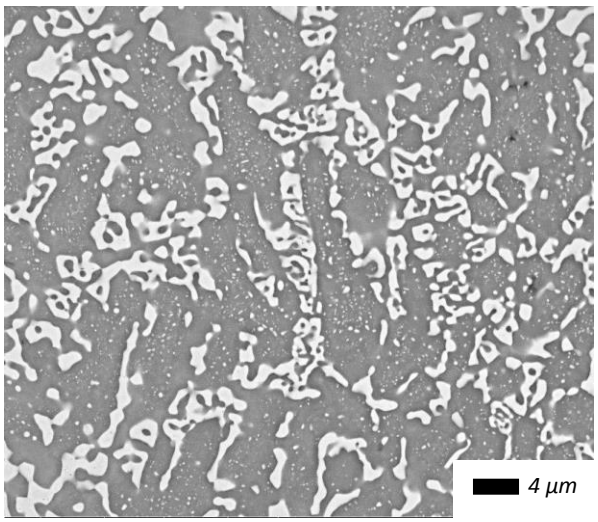

Figure 70: Backscattered electron image of the heat treated alloy CM2 6mm suction cast at the centre of the bar at area B showing light contrast precipitates forming in the Nb_5Si_3.

There was no evidence of subgrain formation in Nb_5Si_3 in all areas. Furthermore there was precipitations of a bright contrast phase in Nb_5Si_3 only in area B2, see Figure 70.

3.2.2 8 mm Diameter Bars

The microstructure at the edge of the alloy CM1 suction cast 8 mm diameter bar is shown in Figure 71. The edge of the bar contained a great variety of microstructural morphologies, as can be seen in Figure 71. In the area of highest cooling, image A, there was a distinct transition of morphologies from the corner of highest cooling inwards. The microstructure started at the edge as an anomalous eutectic between Nb_{ss} and β-Nb_5Si_3 (phases confirmed with XRD, Appendix B Fig 3, and EDS, Table 19) similar to that seen at the bottom of image D. This quickly progressed to the microstructure seen in image A, a very fine lamellar structure surrounded by Nb_{ss} and some silicide grains. This developed into what is seen at the extreme left of the image A, a cellular lamellar structure

surrounded by a second lamellar structure with a different contrast. In areas B through D the morphology did not change and consisted of an anomalous eutectic between Nb_{ss} and β-Nb_5Si_3. As can be seen in image D this anomalous eutectic had directionality (bottom left corner) and evolved to have larger Nb_{ss} surrounding finer mixtures of the two phases (top right corner). Between areas D and E a relatively sudden change from anomalous eutectic to the structure seen in image F occurred. This happened with Nb_{ss} halos formed around cellular eutectics. After the halos were formed a fine eutectic structure was surrounded by coarser eutectics, similar to that in the interdendritic area in image F. Areas E and F were very similar with the morphology of the microstructure seen in as-cast 10 g button and 600 g ingot of the alloy CM1. Nb_5Si_3 dendrites were surrounded by an interdendritic Nb_{ss}+Nb_5Si_3 eutectic with varying lamellar spacing. The microstructure in area G then regressed to the microstructure seen in image A, possibly due to a local high cooling rate. This was followed by the structure seen in image H, which is comparable with that seen in the transition between area D and E, a fine cellular eutectic surrounded by an area of coarser products made of the same phases, Nb_{ss} and β-Nb_5Si_3. This progressed to area I where the more conventional microstructure of the alloy CM1 was seen, and continued to the end of the bar. This structure however did have one main difference compared with the conventional morphology. The eutectics seemed to grow out from a silicide spine, similar to the interdendritic region in Figure 53B in the as-cast CM2 500 g ingot.

The microstructures in the central area of this bar, Figure 72, exhibited less variation in morphology throughout the length of the bar. At the central area of highest cooling rate, area A, the microstructure started off as an anomalous eutectic between Nb_{ss} and β-Nb_5Si_3. As can be seen in image A these eutectics had directionality, with the interfaces between the phases in general being perpendicular to the cooling surface. The transition to the conventional CM1 structure, Figure 72B, occurred in a similar fashion to the transition described between areas D and E for the edge microstructure. Dendritic β-Nb_5Si_3 with interdendritic Nb_{ss} and Nb_5Si_3 eutectic continued unabated for the rest of the central section of the bar.

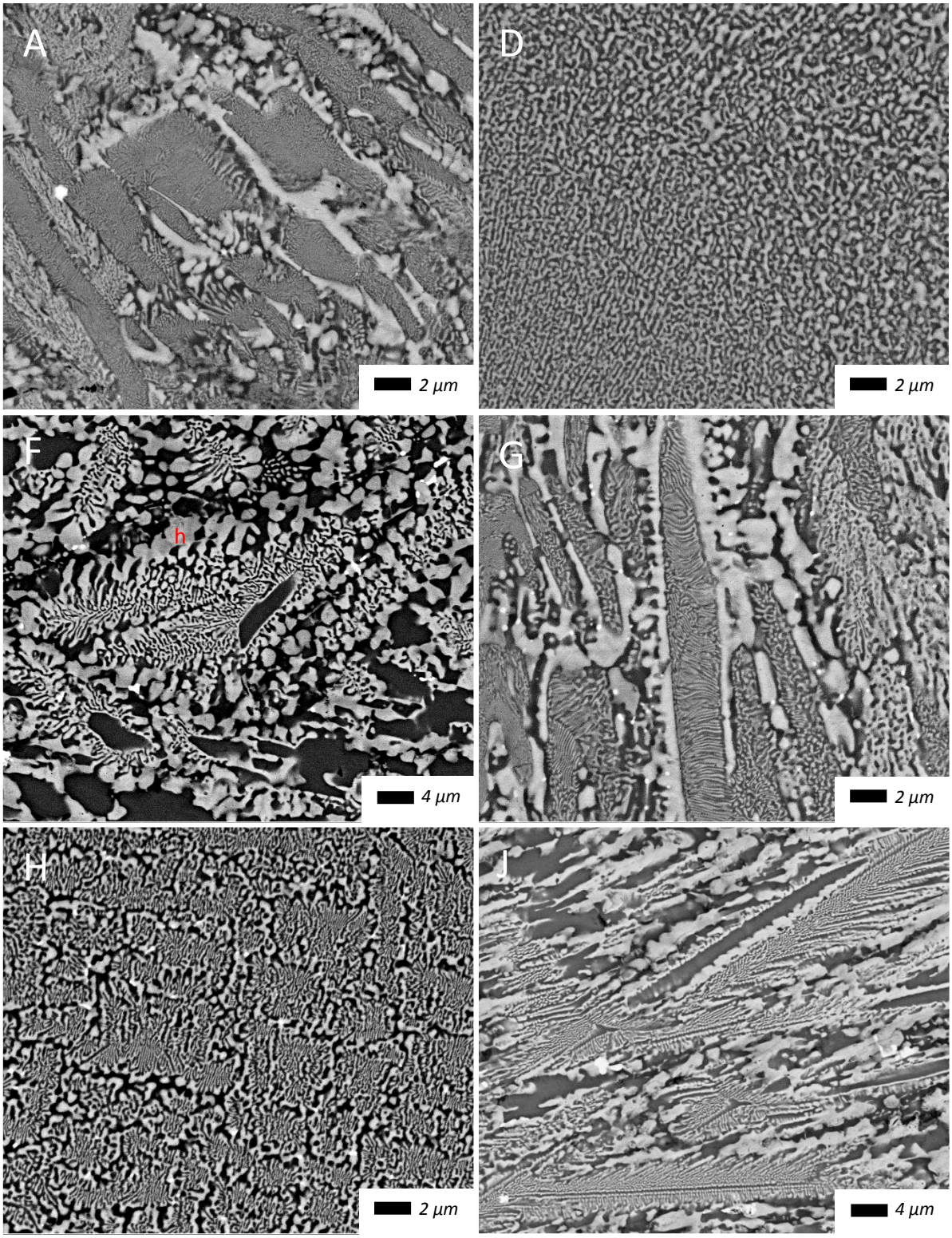

Figure 71: Backscattered electron images of the alloy CM1 8mm suction cast bar at the edge of the bar at areas A, D, F, G, H and J. Nb_{ss} halo is shown by h in image F.

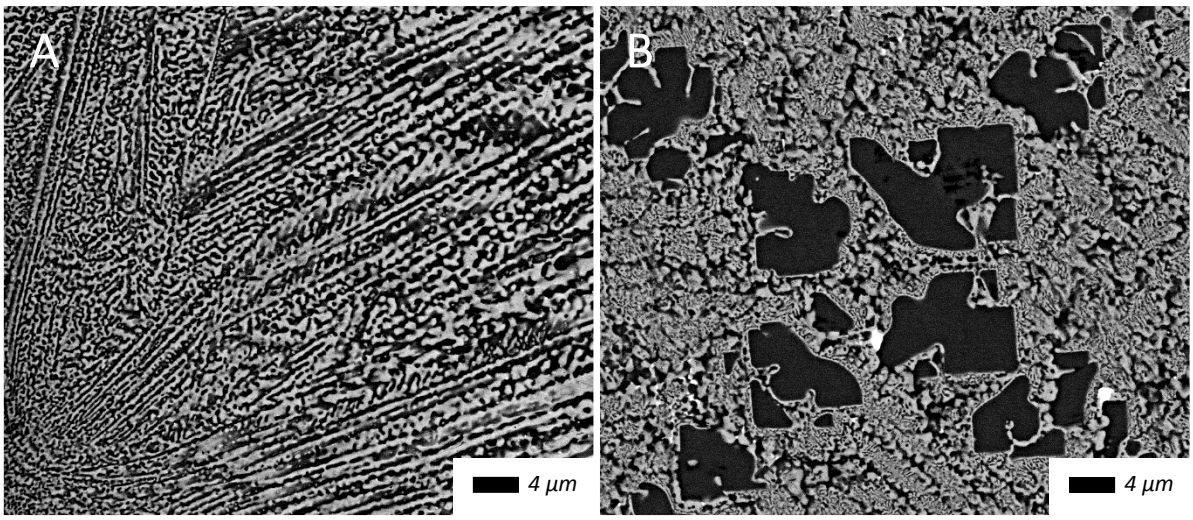

Figure 72: Backscattered electron images of the alloy CM1 8mm suction cast at the centre of the bar at areas A and B.

The EDS analysis, Table 19, showed that the alloy CM1 was near the eutectic composition of the metastable Nb_{ss}+β-Nb_5Si_3 in the binary. In the larger area and eutectic analysis data there was only one element that varied significantly, this was the Si in the eutectic. The areas of maximum and minimum silicon content were at the edge in areas C and G, respectively. This would suggest that the sudden change in microstructure seen at area G might be due to the reduction in silicon content rather than higher cooling rate locally.

Table 19: Summary of EDS analysis (at.%) of the alloy CM1 8 mm suction cast bar, including SD, minimum and maximum values.

Element	*Large Area*	*Eutectic*	*Silicide*	*Solid Solution*
Nb	57.5 ± 0.37	58.3 ± 0.48	51.9 ± 0.44	73.7 ± 0.65
	57.1 - 58.3	57.3 - 59.0	51.1 - 52.4	72.6 - 74.5
Ti	9.2 ± 0.14	9.4 ± 0.14	6.4 ± 0.08	6.9 ± 0.49
	9.0 - 9.4	9.1 - 9.7	6.2 - 6.5	6.1 - 7.7
Si	21.8 ± 0.47	20.4 ± 1.05	37.0 ± 0.37	1.6 ± 0.89
	21.1 - 22.4	18.6 - 21.8	36.2 - 37.5	0.6 - 3.2
Mo	7.6 ± 0.19	8.0 ± 0.41	3.7 ± 0.19	9.9 ± 0.41
	7.3 - 8.0	7.1 - 8.6	3.4 - 4.0	9.3 - 10.5
Hf	0.7	0.7	0.4	0.1
	0.6 - 0.8	0.6 - 0.8	0.3 - 0.5	0.0 - 0.3
W	3.2 ± 0.08	3.3 ± 0.23	0.7	7.8 ± 0.68
	3.1 - 3.3	3.0 - 3.8	0.5 - 0.8	6.9 - 8.7

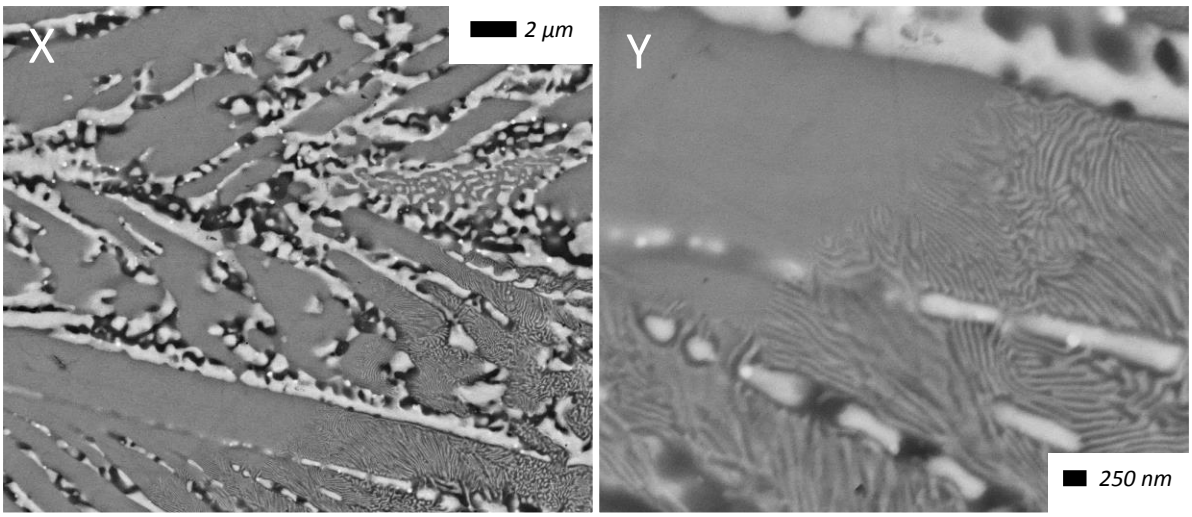

Figure 73: Backscattered electron images showing single phase Nb_3Si in as-cast alloy CM1 8mm suction cast bar decomposing eutectoidally to Nb_{ss} and α-Nb_5Si_3.

Figure 73 shows two images taken from a region of the alloy CM1 8 mm bar between areas A and B between the centre and the edge. Image X appeared to have the same morphology as that seen in images A and G in Figure 71. Very fine regular Nb_{ss} and Nb_5Si_3 lamellae surrounded by a Nb_{ss} shell and some silicide grains. However, the single phase in these images had 23.7 at.%Si and therefore was probably the Nb_3Si silicide. The XRD did not indicate that this phase was present, which is reasonable given the very precise location and its small volume fraction. Looking at the bottom right corner of image X a regular mixture of phases forming from the single phase can be seen. This is similar to the reaction seen in Figure 63, for the CM2 6 mm as-cast bar. Image Y therefore must be showing the eutectoid reaction $Nb_3Si \rightarrow (Nb_{ss} + \alpha\text{-}Nb_5Si_3)_{eutectoid}$ frozen before the phase could fully transform.

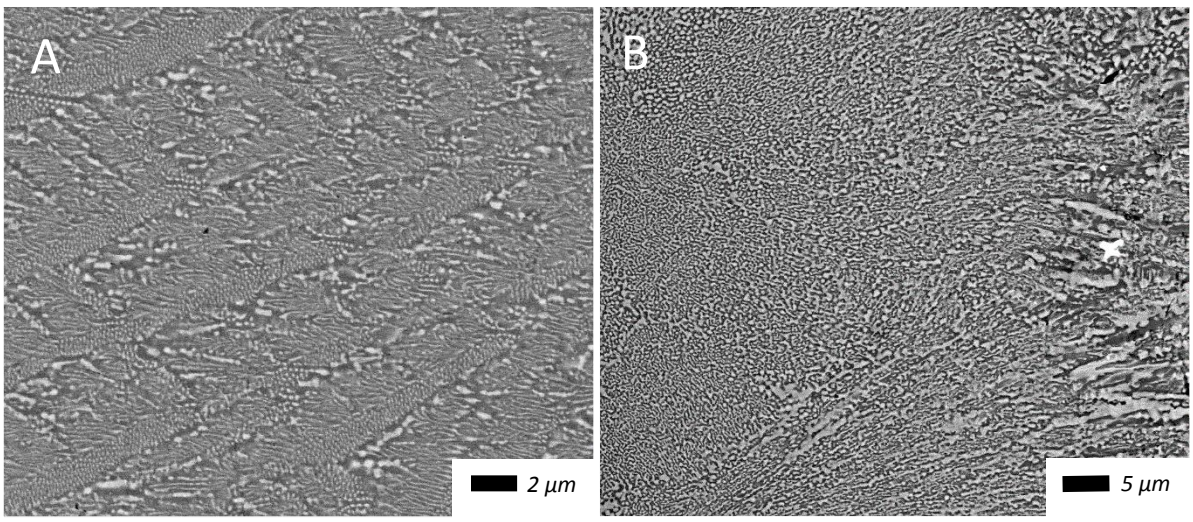

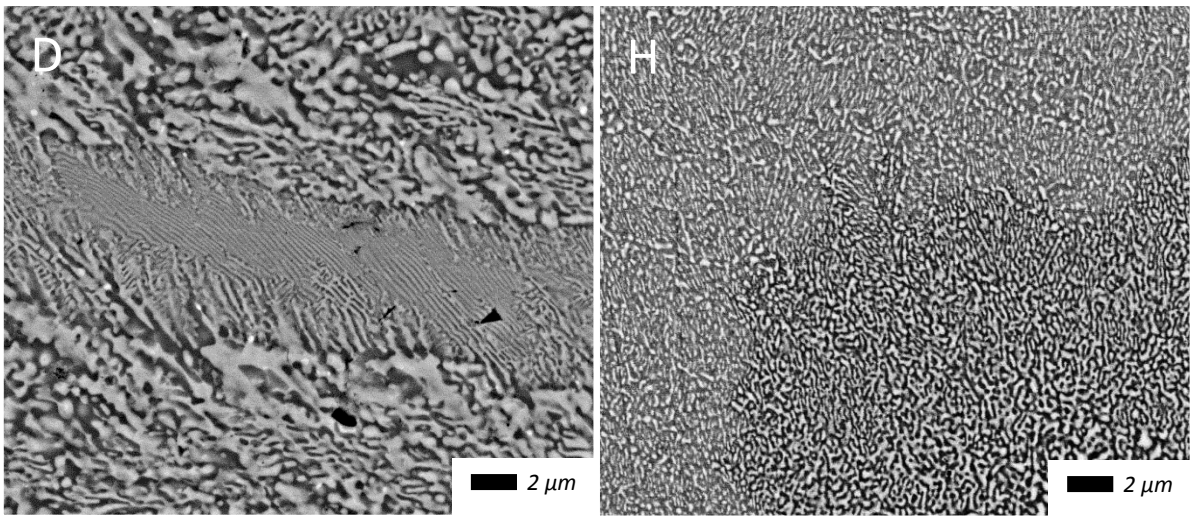

Figure 74: Backscattered electron images of the alloy CM2 8mm suction cast bar at the edge of the bar at areas A, B, D and H.

Figure 74 and Figure 75 show the microstructure of the alloy CM2 suction cast 8 mm diameter bar along the edge and in the centre, respectively. According to the XRD data, the Nb_{ss} and α-Nb_5Si_3 were present in the microstructure. The microstructure at the edge in the area with the highest cooling rate, image A, was eutectic and it consisted of a silicide matrix with a discontinuous Nb_{ss}. The eutectic had grown along well defined orientations in a "woven" pattern. Moving down the edge of the bar to area B, the morphology changed to an anomalous eutectic and in certain areas there was Nb_{ss} at the eutectic cell boundaries. Moving from left to right in image B (highest cooling rate to lowest) larger Nb_{ss} and silicide were formed which eventually evolved into a fine cellular eutectic surrounded by a coarser eutectic seen in the centre of the bar. The large Nb_{ss} formed in this transition zone then formed the Nb_{ss} dendrites seen throughout the microstructure. Moving further down the bar towards area C and D the anomalous eutectic gradually changed to form distinct eutectic cells surrounded by a coarser anomalous eutectic, Figure 74D. Proceeding along the edge, to area H, the volume fraction of eutectic cells increased in relation to the anomalous eutectic, eventually forming a microstructure similar to that in Figure 71H. The microstructure then regressed back to the fully anomalous eutectic, Figure 74H. This anomalous eutectic exhibited a similar contrast change from dark to light with increased cooling rate, as seen in the alloy CM2 6 mm as-cast bar. From the area H

the eutectic cell formation increased within the anomalous eutectic with increasing length down the bar. According to the XRD data the Nb_{ss} and α-Nb_5Si_3 were present in the microstructure.

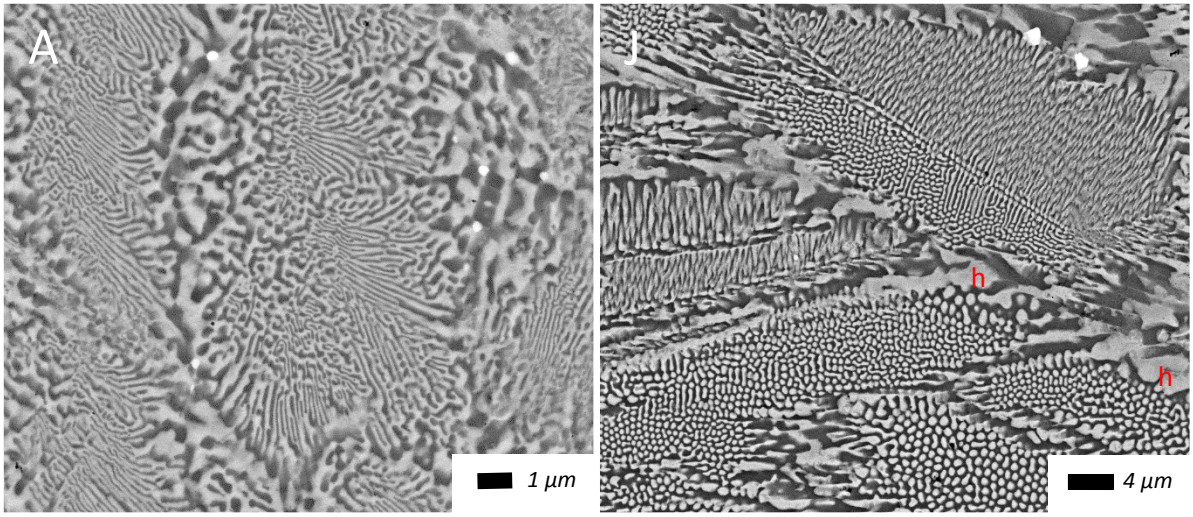

Figure 75: Backscattered electron images of the alloy CM2 8mm suction cast bar at the centre of the bar at areas A and I. Nb_{ss} halos are shown by h in image J.

The microstructure in the central region at area A, Figure 75, was fully eutectic with cells of quasi-regular eutectic surrounded by irregular (anomalous) eutectic boundaries. Progressing up the centre of the bar to areas B, C, and D the eutectic did not change dramatically other than coarsening slightly. However, at some point between areas B and C the Nb_{ss} dendrites formed and were present for the rest of the bar. The quasi-regular eutectic cells, present up to this point, gradually began to get replaced by regular cells of eutectic forming around a spine of silicide, Figure 75J. All three eutectics (regular, quasi-regular and irregular) co-existed until the later stages of the bar, approximately area I, where the quasi-regular eutectic was completely replaced by the regular one.

The EDS data for the alloy CM2 8 mm bar, Table 20, showed small standard deviations for the elements in the large area and eutectic analysis across the bar. The Si contents of the large area and eutectic would suggest that the bar was of near eutectic composition. In the central areas there were Nb_{ss} dendrites and the Si content of the eutectic was 22.0 at.%Si. Spot analysis of the phases showed that the silicide did not contain any W. The concentration of W varied significantly in the Nb_{ss}.

Table 20: Summary of EDS analysis data (at.%) of the alloy CM2 8 mm suction cast bar including SD, minimum and maximum values.

Element	*Large Area*	*Eutectic*	*Silicide*	*Solid Solution*
Nb	69.1 ± 0.42	69.2 ± 0.54	56.9 ± 0.42	81.7 ± 1.73
	68.4 – 69.7	68.6 - 69.9	56.0 - 57.7	79.5 - 84.2
Si	21.8 ± 0.48	21.7 ± 0.75	38.9 ± 0.50	2.2 ± 0.48
	21.0 - 22.4	20.4 - 22.1	38.3 – 39.7	1.6 - 3.0
W	4.8 ± 0.19	4.9 ± 0.26	0.0 ± 0.07	14.4 ± 2.39
	4.6 - 5.1	4.5 - 5.3	0.0 - 0.3	10.9 - 17.4
Hf	4.3 ± 0.10	4.3 ± 0.14	4.5 ± 0.34	1.6 ± 0.18
	4.2 - 4.5	4.1 - 4.6	4.2 - 5.6	1.4 - 1.9.

Along the edge of the alloy CM2 8 mm bar there was a significant number of microstructural changes, shown in Figure 76. Image W was taken from area B where three distinctive microstructures existed. Areas closest to the edge, top left corner of the image, were anomalous eutectics in nature. This microstructure transformed into a border area of coarser Nb_{ss} and silicide phases. This transformed into eutectic cells of the same two phases present in the coarse border region. After this there was a more subtle shift in the morphology as well as the contrast of the silicide, an example of which is shown in image Y. A less “ordered” transition of the same type is shown in image X where the coarse and eutectic cell regions were intertwined before a sudden change to the very fine cellular region on the right, similar to that seen at the right of images W and Y. Figure 76 image Z shows the transitional region between a dark contrast silicide and the light contrast silicide. The right hand, dark contrast, side of the image exhibited a continuous mix of both the solid solution and the silicide phase. The left-hand, lighter contrast, side of the image on the other hand has a distinct silicide matrix with discontinuous Nb_{ss}. EDS analysis of the transition shown in Figure 76W showed no major change in alloying elements between any of the three regions. There was a 0.4 at.% reduction of Si from the anomalous eutectic area at the edge to the coarser microstructure in the middle of image W.

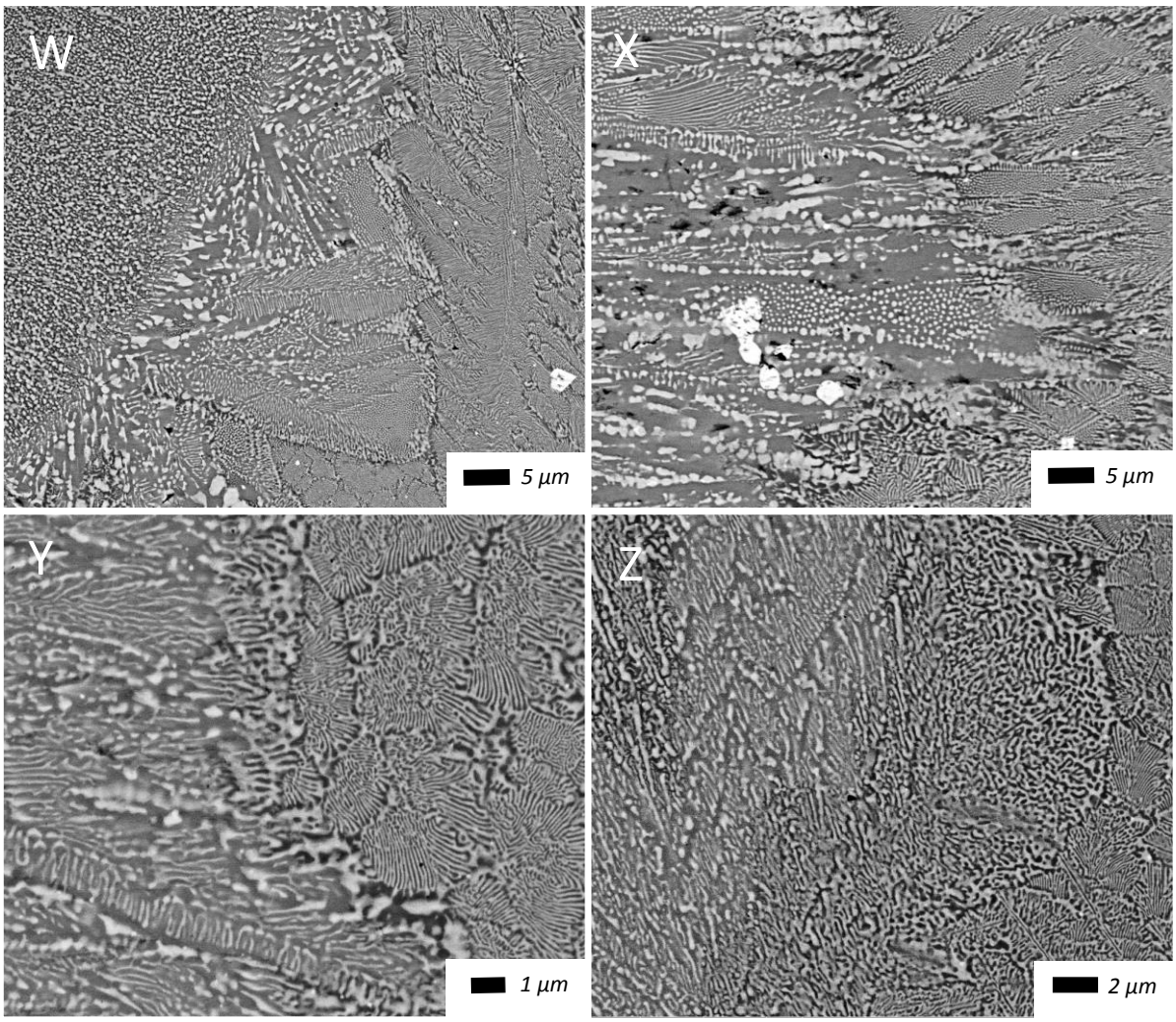

Figure 76: Backscattered electron images of microstructure transitions at the edge of the as-cast alloy CM2 8mm bar.

Through the centre of the alloy CM2 8 mm bar, in the eutectic regions, minor differences in contrast were seen in the eutectic phases. This manifested as regular eutectic cells containing brighter Nb_{ss} phases and darker Nb_5Si_3 phases than the surrounding irregular formations, Figure 77-BSE. The X-ray maps in this figure clearly show that there was a distinct deficit of W in the intercellular regions of these eutectics. Nb and Hf on the other hand had an affinity for the intercellular region, shown by the brighter contrast. Silicon remained highly concentrated in the silicide phase compared with the Nb_{ss}.

The top left side of image X in Figure 76, and the images in Figure 78 provide evidence (via the morphology of the lamellar microstructures) of a lamellar eutectiod microstructure like those resulting

from the transformation $Nb_3Si \rightarrow Nb_{ss} + \alpha\text{-}Nb_5Si_3$. Thus, it is likely that the microstructure transformations were also linked to the above transformation.

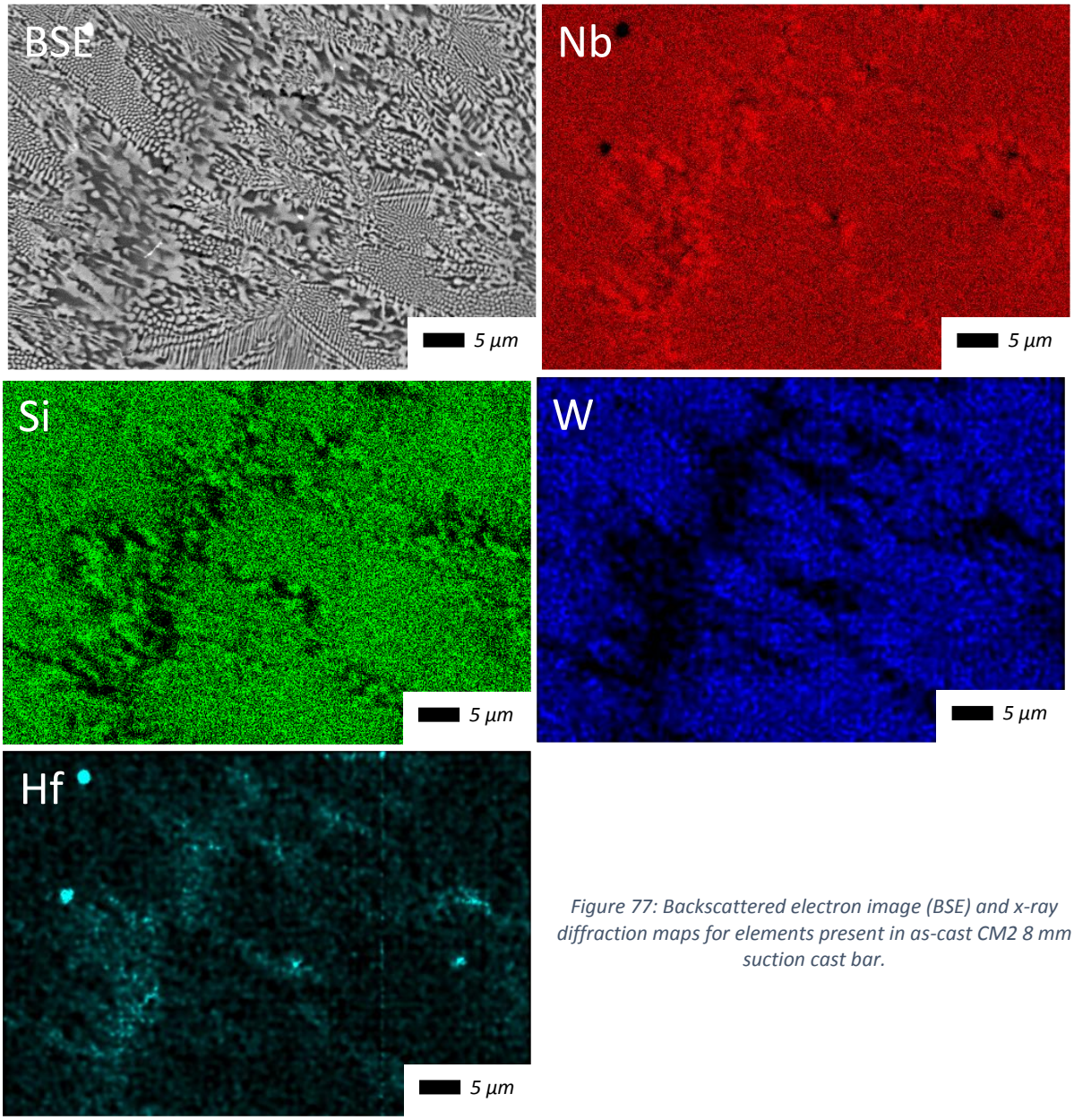

Figure 77: Backscattered electron image (BSE) and x-ray diffraction maps for elements present in as-cast CM2 8 mm suction cast bar.

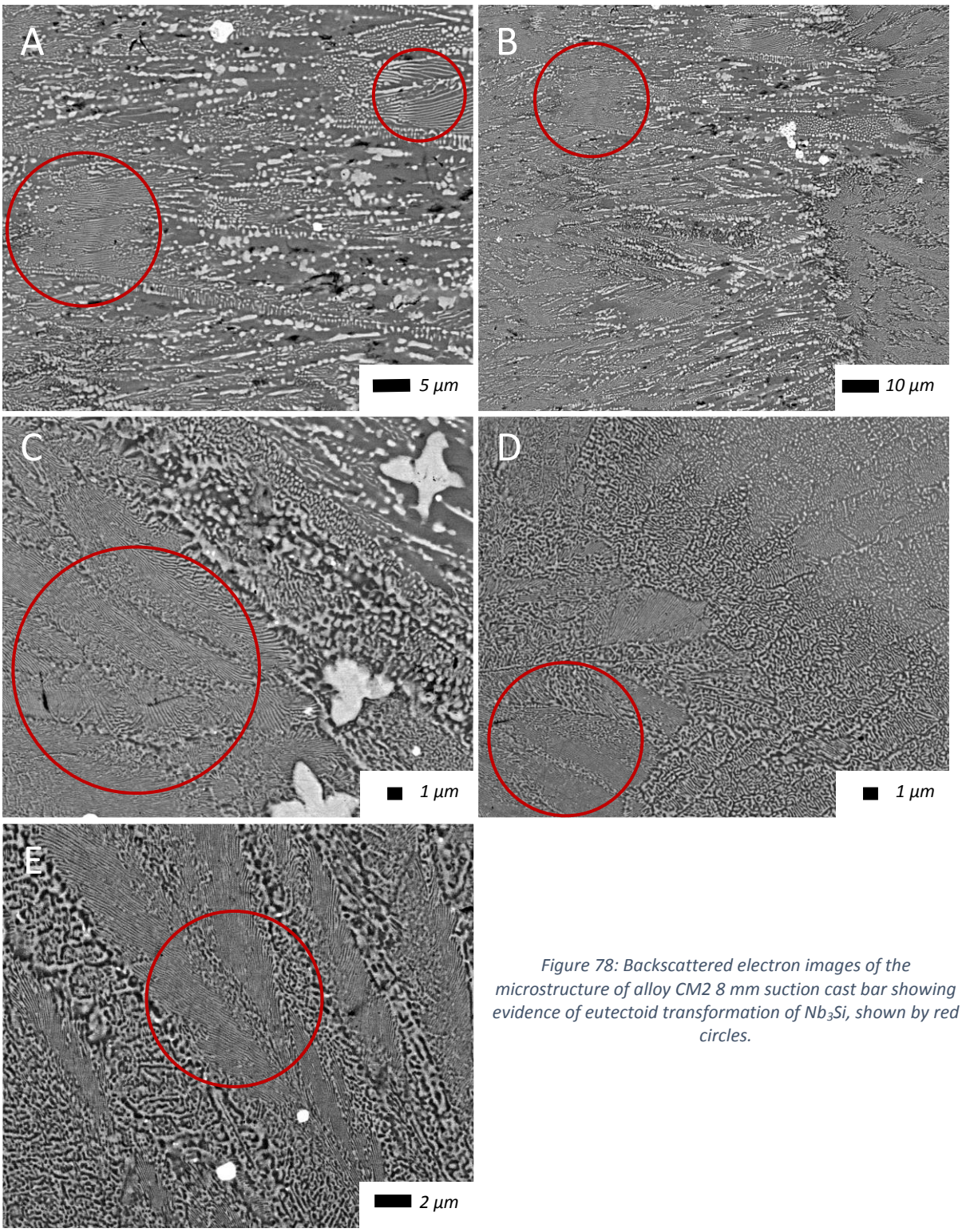

Figure 78: Backscattered electron images of the microstructure of alloy CM2 8 mm suction cast bar showing evidence of eutectoid transformation of Nb_3Si, shown by red circles.

Backscatter electron images of the microstructures in the centre and edge of the heat treated alloy CM1 8 mm bar are shown in Figure 79. In general, the microstructures had coarsened and were very similar to those seen in the 6 mm bar after heat treatment. The microstructure at the edge area A shown in image A had two phases, Nb_{ss} and α-Nb_5Si_3 as confirmed by EDS, Table 21, and XRD,

Appendix B Fig 3. The microstructure seen in image A Figure 79 continued for the entire length of the bar. In areas B to I some fine cells of the prior eutectics were also present, see Figure 79H. Areas A at the edge and the centre were very similar. This morphology did not change dramatically through the length of the bar. From area B to J however larger α-Nb_5Si_3 and Nb_{ss} grains were present after the heat treatment, as can be seen in Figure 79J.

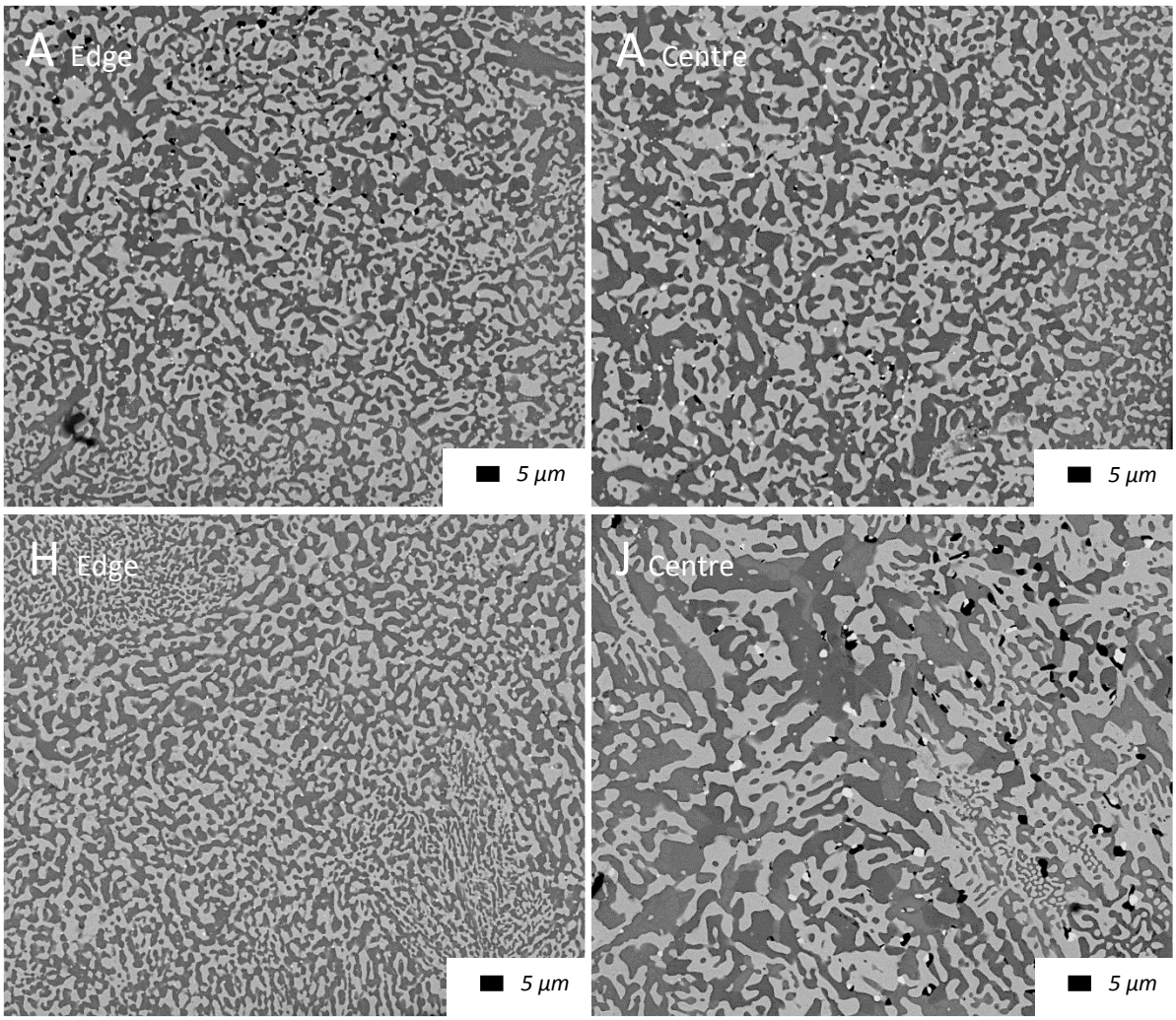

Figure 79: Backscattered electron images of the heat treated CM1 8mm suction cast bar at the edge (left) and centre (right) of the bar at areas A and J.

Table 21 shows the EDS analysis data of the heat treated alloy CM1 8 mm suction cast bar. For the large area and prior-eutectic area analyses the standard deviations were small. However, for the silicide and the Nb_{ss} the standard deviation for Ti was significant. Spot analysis of the phases indicated that they were either Ti rich or Ti poor. Considering the individual spot analyses of Ti in the solid

solution there were two distinct concentration ranges, 2.6 – 3.5 and 5.4 – 6.8 at.%Ti. This was also the case for the silicide where there was Ti-rich and Ti-poor silicide, with 6.9 – 8.7 and about 11.4 at.%Ti, respectively. The latter was similar to the concentration of Ti in the silicide in the heat treated CM1 600 g ingot. Variation in the concentration of W within the solid solution was also significant (difference of 2.5 at.% between maximum and minimum values) but unlike the other forms of the CM1 alloy studied in this thesis, this did not seem to relate to the concentration variation seen in Ti.

Comparing the EDS data for the heat treated and cast bars there was respectively increase and decrease in the average Ti concentration in the silicide and solid solution while in the same phases the opposite was the case for the concentrations of Mo.

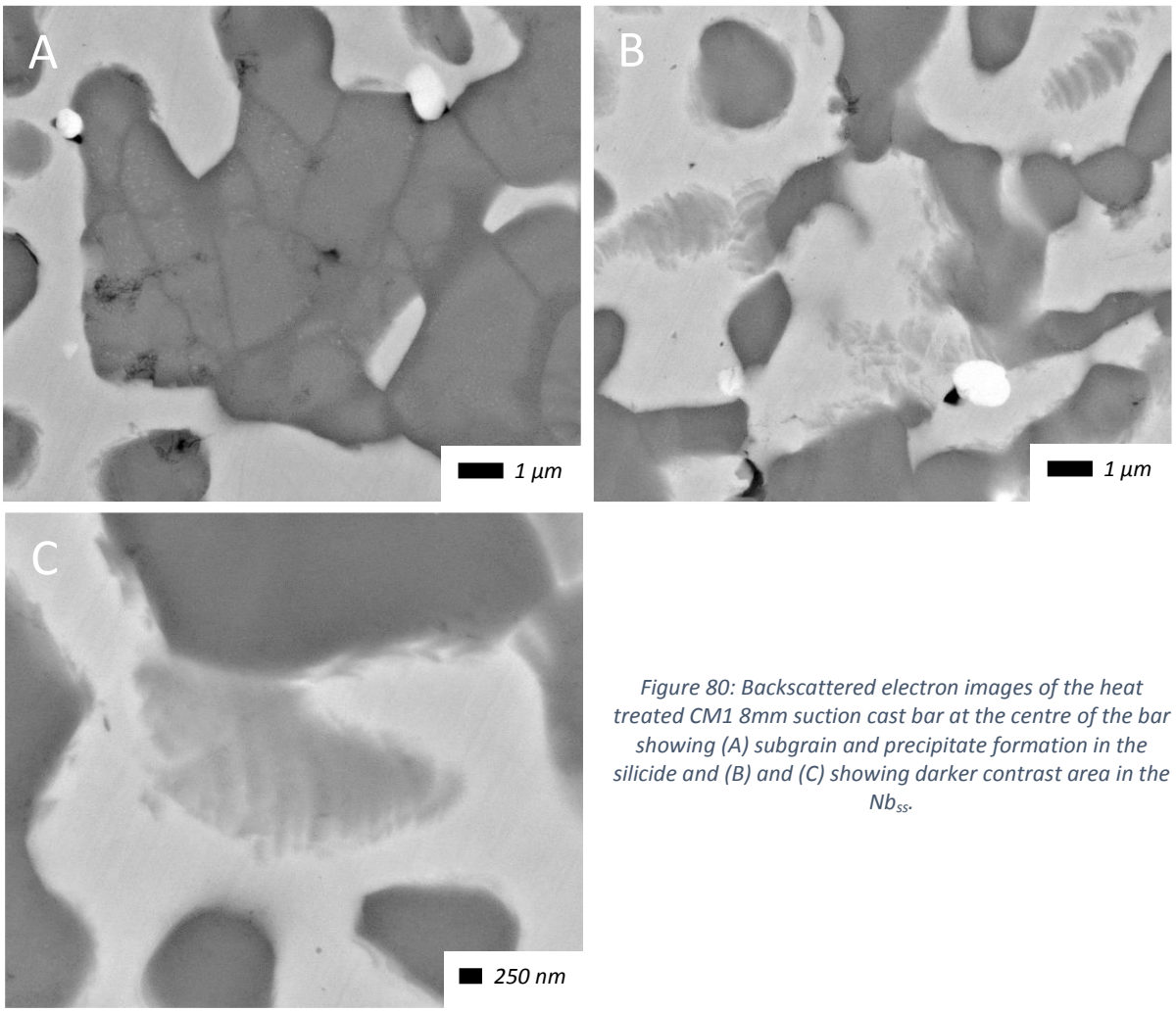

Figure 80: Backscattered electron images of the heat treated CM1 8mm suction cast bar at the centre of the bar showing (A) subgrain and precipitate formation in the silicide and (B) and (C) showing darker contrast area in the Nb_{ss}.

There was evidence of subgrain formation predominantly in the central (bulk) area of the bar at all locations with fine second phase precipitates seen in the central G to J areas, see Figure 80A. In some of the central (bulk) areas of the bar, namely B and D, darker contrast areas, not seen before, were noticed in the Nb_{ss}, see Figure 80B.

Table 21: Summary of EDS analysis (at.%) of the heat treated alloy CM1 8 mm suction cast bar, including SD, minimum and maximum analysis values..

Element	*Large Area*	*Prior-eutectic*	*Silicide*	*Solid Solution*
Nb	60.7 ± 0.31	61.2 ± 0.51	52.5 ± 1.20	75.6 ± 1.32
	60.2 - 61.1	60.4 - 62.2	51.1 - 54.1	74.0 - 77.9
Ti	8.5 ± 0.33	8.3 ± 0.66	9.4 ± 1.80	4.3 ± 1.50
	8.0 - 8.9	6.8 - 9.2	6.9 - 11.6	2.6 - 6.8
Si	21.8 ± 0.15	21.2 ± 0.58	36.2 ± 0.55	0
	21.4 - 21.9	20.2 - 22.3	35.0 - 36.9	
Mo	5.1 ± 0.10	5.1 ± 0.24	1.3 ± 0.54	11.3 ± 0.21
	5.0 - 5.3	4.7 - 5.7	0.6 - 2.2	10.9 - 11.6
Hf	0.7 ± 0.10	0.8 ± 0.13	0.4 ± 0.22	0.1 ± 0.09
	0.6 - 0.9	0.6 - 1.0	0.1 - 0.6	0.0 - 0.2
W	3.3 ± 0.08	3.4 ± 0.15	0.2 ± 0.22	8.6 ± 0.73
	3.2 - 3.4	3.2 - 3.7	0.0 - 0.6	7.8 - 10.3

Backscatter electron images of the microstructure in the centre and edge of the heat treated alloy CM2 8 mm bar are shown in Figure 81. Looking at the edge microstructure, throughout the length of the bar there were three distinctly different morphologies. Staring in area A, the majority of the microstructure was made up of a mixture of Nb_{ss} and α-Nb_5Si_3 phases, confirmed by XRD (Appendix B Fig 4) and EDS (Table 22), neither of which could be described as continuous or discontinuous. In this area and throughout the length of the bar hafnia was also observed in the microstructure. The most notable difference in the microstructure in area A compared with the rest of the alloy was the ≈ 10 µm thick zone of solid solution with hafnia particles surrounding the edge. This zone reduced in thickness gradually from this area and disappeared before area B at the edge or A in the centre, Figure 81. In area B the morphology was very similar to that of A, without the solid solution zone. This microstructure was also seen in areas E, G, H and I along the edge of the bar. The other areas were typified by the morphology seen in image C. This microstructure had distinct dendrites of Nb_{ss}

surrounded by a fine mixture of Nb_{ss} and α-Nb_5Si_3. The interdendritic region was distinct from the other morphology as it had a continuous, α-Nb_5Si_3, and discontinuous, Nb_{ss}.

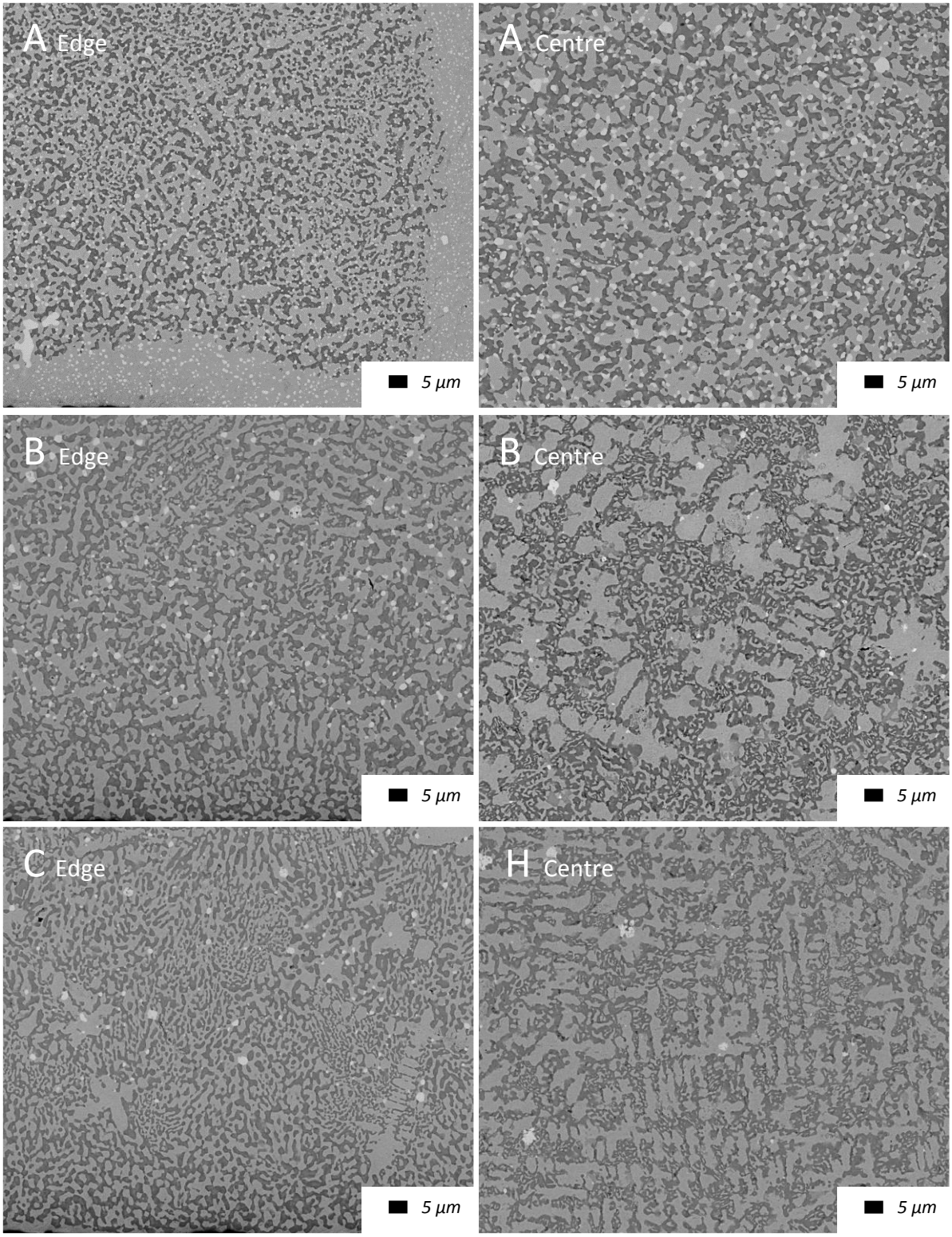

Figure 81: Backscattered electron images of the heat treated CM2 8mm suction cast bar at the edge (left) and centre (right) of the bar at areas A, B, C and H.

In the central region the microstructure in area A had many similarities to those seen in the edge areas B, E, G, H and I, two phase microstructure with no definitive dendrites or fine cellular regions. The centre of the bar from areas B to G was very similar to that seen in C, D, F, and J at the edge. Large Nb_{ss} dendrites surrounded by a two phase microstructure consisting of continuous α-Nb_5Si_3 with a smaller discontinuous Nb_{ss} phase were also present in the interdendritic region. A sudden transition occurred between the microstructure at G, image B, and the microstructure seen in image H, which persisted for the remainder of the bar. The new morphology in area G had distinctly smaller Nb_{ss} dendrites with higher volume fraction of Nb_{ss} than seen previously.

The EDS analysis data of the heat treated alloy CM2 8 mm suction cast bar is presented in Table 22. The analysis showed significant standard deviation for Si in the prior-eutectic. The variation of both Si and W in the prior eutectic stemmed from a variation from the centre and the edge. The average concentration of W at the edge and the centre was 4.1 and 3.0 at.%, respectively, with maximum values at the centre only equalling minimum values at the edge. This was mirrored in the Si content, average concentrations of silicon at the edge and centre were 19.2 and 23.0 at.%, respectively. There was also a less significant variation of Hf with an average increase of 0.9 at.%Hf when moving from the edge to the centre. The EDS data also showed that there was two types of silicide, Hf-rich and Hf-poor. The latter had an average concentration of 3.2 at.%Hf and the former 8.2 at.%Hf. Hf-rich phases exhibited lighter contrast and Hf-poor dark contrast, similar to that seen in the heat treated alloy CM2 6 mm bar. There was also a significant disparity in the Si content in the silicide, however this and the Hf concentration variations did not seem to be linked. Finally, there was a large variation in the W content of the solid solution whose average concentration in W had dropped compared with the concentration in the cast alloy. There was no evidence of a W-rich or W-poor Nb_{ss}, as there was an even distribution of tungsten throughout the Nb_{ss} grains.

Comparing the EDS analysis data for the as-cast with the heat treated condition, there was a distinct reduction in the Si content in the large area analysis with no noteworthy change in the eutectic

concentration. The silicide was richer in Hf by 2 at.%. Tungsten was reduced by 3.3 at.% in the solid solution.

Table 22: Summary of EDS analysis (at.%) of the heat treated alloy CM2 8 mm suction cast bar including SD, minimum and maximum analysis values..

Element	*Large Area*	*Prior-eutectic*	*Silicide*	*Solid Solution*
Nb	72.6 ± 0.31 72.2 - 73.2	69.8 ± 2.03 67.1 - 73.3	56.3 ± 3.32 52.2 - 61.4	87.9 ± 1.61 84.3 - 90.1
Si	17.6 ± 0.41 16.9 - 18.2	21.3 ± 2.22 17.4 - 24.6	37.2 ± 1.37 35.7 - 39.7	0
W	4.7 ± 0.19 4.4 - 5.0	3.5 ± 0.69 2.6 - 4.8	0	11.1 ± 1.39 9.3 - 14.1
Hf	5.1 ± 0.24 4.6 - 5.4	5.5 ± 0.60 4.6 - 6.0	6.5 ± 2.40 2.9 - 8.6	1.0 ± 0.64 0.0 - 1.6

3.2.3 Conclusions

Two near eutectic alloys with nominal compositions Nb-8.3Ti-21.1Si-5.4Mo-4W-0.7Hf (CM1) and Nb-20.5Si-5.8W-4Hf (CM2) were studied in the form of suction cast bars of 6 mm and 8 mm diameter in the cast and heat treated (1500 ^{O}C/100 hrs) conditions.

This study revealed dependence of microstructure type on cooling rate or specific solute concentration as well as the formation of Nb_3Si and its eutectoid decomposition even in cast bars, in other words the solidification conditions in bars allowed us to capture the formation of Nb_3Si and its eutectoid decomposition in both alloys.

The microstructures of the cast bars were similar to those of the 10 g buttons and larger ingots only in areas of lower cooling rate in the bars.

The Nb_{ss} and Nb_5Si_3 and eutectics and eutectoids of these two phases were formed in cast alloys.

In CM1 6 mm SC AC bar the phases were the Nb_{ss} and β-Nb_5Si_3, and Nb_{ss} + β-Nb_5Si_3 eutectics were formed.

In CM2 6 mm SC AC bar the phases were the Nb_{ss}, Nb_3Si and α-Nb_5Si_3 with evidence of the eutectoid $Nb_3Si \rightarrow Nb_{ss} + \alpha$-$Nb_5Si_3$

In CM1 8 mm SC AC bar the phases were the Nb_{ss} and β-Nb_5Si_3, with Nb_{ss} + β-Nb_5Si_3 eutectic, with evidence for some α-Nb_5Si_3 and the eutectoid $Nb_3Si \rightarrow Nb_{ss} + \alpha$-$Nb_5Si_3$

In CM2 8 mm SC AC the phases were the Nb_{ss} and α-Nb_5Si_3, with evidence of the eutectoid $Nb_3Si \rightarrow Nb_{ss} + \alpha$-$Nb_5Si_3$

In all the heat treated bars of 6 mm and 8 mm diameters the microstructure had coarsened and Nb_{ss} and α-Nb_5Si_3 were observed. The Nb_3Si was not observed in CM2 6 mm SC HT.

Subgrains were formed in CM1 6 mm SC HT and CM1 8 mm SC HT with evidence of fine precipitates of a second phase of light contrast in the 5-3 silicide.

Fine precipitates in α-Nb_5Si_3 without subgrain formation were observed in CM2 6 mm SC HT and CM2 8 mm SC HT.

In CM1 8 mm SC HT darker contrast fringe like areas in Nb_{ss}, not seen before in the group or reported in the literature, were observed.

3.3 Directional Solidification Using OFZ Processing

The two alloys in this study were directionally solidified to understand how solidification microstructures develops at different growth rates. The as-cast and heat treated conditions for both alloys were studied.

3.3.1 As-cast OFZ Alloys

Figure 82 shows the microstructure of the directionally solidified alloy CM1 at three different growth rates; 150, 60 and 12 mm/hr. Images in the left and right hand columns relate to the microstructure in the edge and bulk of the OFZ cast bars, respectively. Appendix B Fig 5 and Table 23 present the XRD and EDS analysis data, respectively.

The images in Figure 82 show a similar overall microstructure for all growth rates. Large primary silicide grains, identified as α-Nb_5Si_3 by XRD and EDS, were elongated in the direction of growth. The silicide grains were typically surrounded by solid solution. Between the silicide grains, a cellular Nb_{ss}/α-Nb_5Si_3 lamellar microstructure formed. Typically, these cells were elongated in the direction of growth and were surrounded by a coarser more randomly orientated microstructure. The cellular lamellar microstructural morphology did not change and consisted of a silicide matrix with discontinuous Nb_{ss} rods. These Nb_{ss} rods, on occasion, formed around a silicide spine but always grew perpendicular to the growth direction. Comparison of the bulk and edge microstructures for all growth rates showed a number of similarities, most obvious of which was the increased number of large silicide grains at the edge compared with the bulk. This coincided with the reduction in volume fraction of the lamellar microstructure.

The EDS analysis data, Table 23, supported the conclusion that there was more silicide present at the edge than the bulk. The large area analysis, especially for the 150 and 60 mm/hr growth rates, gave a higher concentration of silicon at the edge compared with the bulk. Differences in Si concentration in the analysis of the phases were minimal between the edge and the bulk with the

lamellar microstructure showing higher Si concentration in the bulk. Therefore, the increased concentration of Si in the edge gave the higher volume fraction of silicide in that area of the OFZ bar.

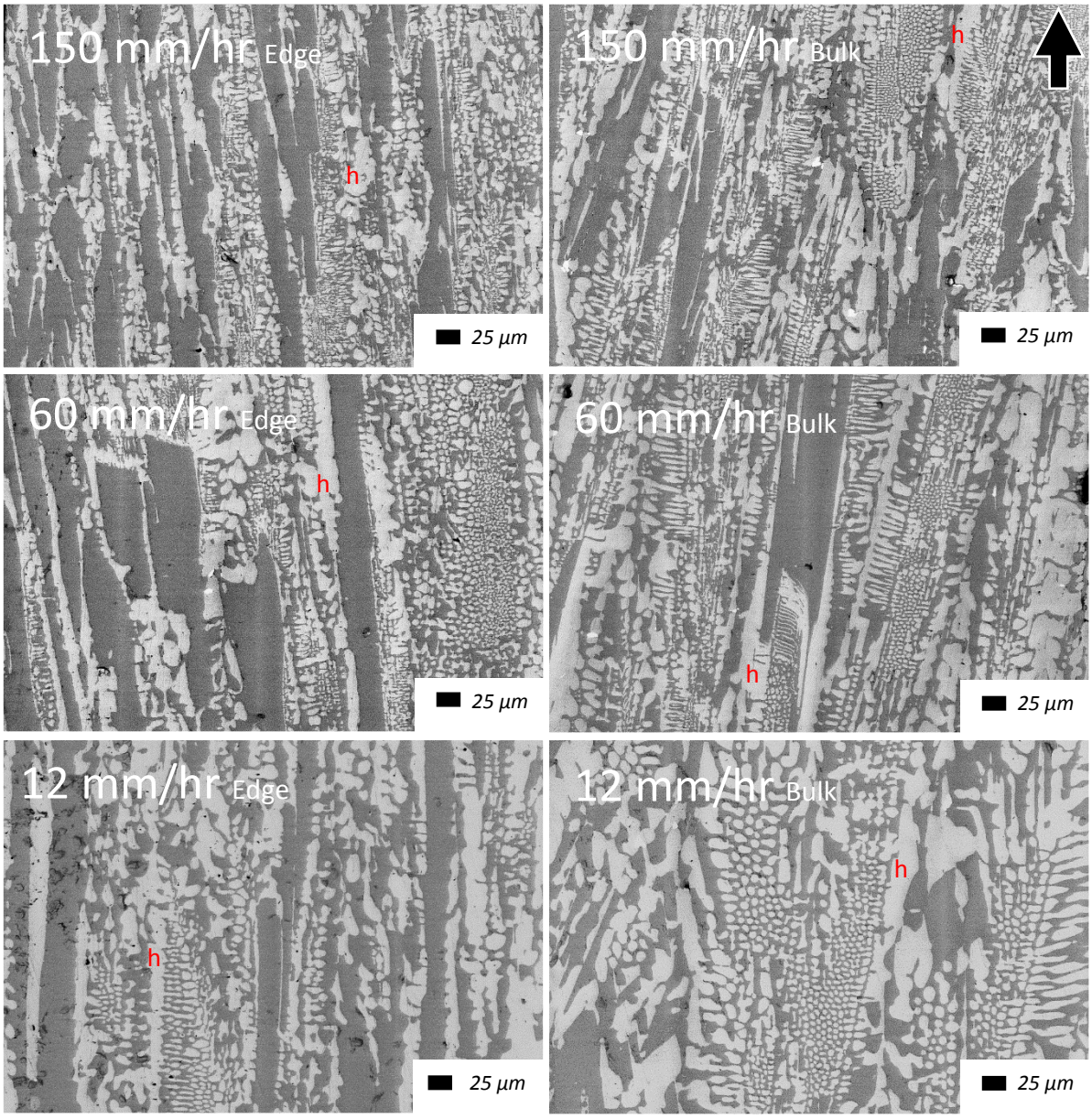

Figure 82: Backscattered electron images of the alloy CM1 processed using an optical float zone (OFZ) furnace at 3 different growth rates, 150 mm/hr, 60 mm/hr and 12 mm/hr from top to bottom respectively. Left hand images show the edge microstructure and right hand images the bulk microstructure. Arrow indicates the growth direction. Nb_{ss} haloes are indicated by h.

The EDS data also confirmed the existence of weak macrosegregation of Si, $C_{max}^{Si} - C_{min}^{Si} \geq 2\ at.\%Si$, for all growth rates. There was also macrosegregation of Ti at the lowest growth rate. Variations in the Si content within the large area and lamellar microstructure analysis were persistent

at all growth rates. This was especially evident at the two lower growth rates, for example at 12 mm/hr the Si results varied by 2 at.% or more in both the lamellar microstructure and large areas. For the 150 mm/hr growth rate the variation in Si content was limited to the edge of the sample. Large variation in the Ti concentration was observed in the lamellar microstructure in the 150 mm/hr grown sample and in the large area analysis of the 12 mm/hr grown sample. Considering the analyses of the phases there was significant variation in the concentrations of Ti and W in the solid solution. The data showed a distinct pattern of increased Ti levels with decreased W concentration (Figure 83). The concentrations of W within the solid solution showed a significant variation from the edge (highest) to the centre (lowest). This was mirrored in the Ti concentrations where the highest concentrations were seen in the bulk rather than in the edge. At the two slower growth rates, 60 and 12 mm/hr, the Si concentration in the silicide varied more than in the 150 mm/hr sample. However, the variations in Ti content were more pronounced in the silicide grains in the sample grown at the highest growth rate.

Table 23: Summary of EDS analysis (at.%) of the alloy CM1 processed using an optical float zone furnace at growth rates of 150, 60 and 12 mm/hr including SD, minimum and maximum values.

150 mm/hr								
Element	Large Area		Lamellar microstructure		Silicide		Solid Solution	
	Bulk	Edge	Bulk	Edge	Bulk	Edge	Bulk	Edge
Nb	60.2 ± 0.34 59.7 - 60.6	58.7 ± 0.47 58.1 - 59.3	60.6 ± 0.71 59.9 - 61.9	61.4 ± 0.53 60.9 - 62.2	52.6 ±0.92 50.9 - 53.5	53.3 ± 0.26 52.9 - 53.6	70.4 ± 0.90 69.1 - 71.8	69.8 ± 0.66 68.7 - 70.4
Ti	9.2 ± 0.39 8.8 - 9.7	8.6 ± 0.77 7.4 - 9.5	8.3 ± 1.05 7.0 - 9.7	7.2 ± 0.63 6.7 - 8.4	7.6 ± 1.19 6.7 - 9.7	7.0 ± 0.08 7.0 - 7.2	10.7 ± 1.91 8.5 - 13.5	6.6 ± 0.74 5.5 - 7.4
Si	20.6 ± 0.46 20.2 - 21.4	23.7 ± 1.31 22.1 - 25.2	20.3 ± 0.62 19.0 - 20.9	18.7 ± 0.96 17.3 - 19.9	37.4 ± 0.76 37.0 - 38.6	37.3 ± 0.66 36.5 - 38.1	1.8 ± 0.44 1.0 - 2.2	1.6 ± 0.45 1.2 - 2.4
Mo	6.3 ± 0.25 6.0 - 6.6	5.7 ± 0.38 5.2 - 6.2	6.8 ± 0.35 6.2 - 7.3	7.4 ± 0.42 6.7 - 7.9	1.7 ± 0.17 1.5 - 2.0	2.0 ± 0.32 1.6 - 2.6	12.0 ± 0.63 11.3 - 13.0	13.1 ± 0.41 12.8 - 13.8
Hf	1.2 ± 0.16 1.0 - 1.3	1.0 ± 0.13 0.8 - 1.2	1.0 ± 0.20 0.8 - 1.4	0.9 0.7 - 1.1	0.5 0.4 - 0.6	0.3 0.2 - 0.4	0.7 0.5 - 0.8	0.6 0.4 - 0.8
W	2.5 ± 0.16 2.3 - 2.7	2.4 ± 0.22 2.0 - 2.7	3.1 ± 0.65 2.2 - 4.0	4.3 ± 0.52 3.4 - 4.7	0.1 0.0 - 0.1	0.1 0.1 - 0.1	4.5 ± 1.19 3.2 - 6.5	8.3 ± 0.51 7.7 - 9.0

60 mm/hr								
Element	**Large Area**		**Lamellar microstructure**		**Silicide**		**Solid Solution**	
	Bulk	Edge	Bulk	Edge	Bulk	Edge	Bulk	Edge
Nb	61.2 ± 0.41	59.6 ± 0.21	61.1 ± 0.32	61.4 ± 0.68	53.3 ± 0.32	53.3 ± 0.39	71.0 ± 0.61	70.1 ± 0.53
	60.7 - 61.8	59.4 - 59.9	60.6 - 61.6	60.6 - 62.7	53.1 - 53.9	52.8 - 53.9	70.0 - 71.9	69.4 - 70.9
Ti	8.9 ± 0.68	7.7 ± 0.40	8.2 ± 0.61	7.3 ± 0.34	6.9 ± 0.13	6.9 ± 0.13	8.8 ± 0.46	7.3 ± 1.00
	8.1 - 9.6	7.2 - 8.3	7.1 - 9.0	6.9 - 7.9	6.8 - 7.1	6.7 - 7.1	7.9 - 9.2	5.8 - 8.8
Si	19.6 ± 0.88	22.5 ± 0.6	20.6 ± 0.88	19.5 ± 1.17	37.8 ± 0.55	37.5 ± 0.97	1.8 ± 0.64	1.7 ± 0.65
	18.5 - 21.0	21.6 - 23.3	19.4 - 21.4	17.4 - 20.8	36.9 - 38.5	36.0 - 39.0	0.9 - 2.8	1.0 - 2.7
Mo	6.4 ± 0.21	6.1 ± 0.23	6.4 ± 0.35	7.0 ± 0.40	1.6 ± 0.29	1.8 ± 0.34	12.1 ± 0.74	12.9 ± 0.62
	6.1 - 6.7	5.8 - 6.4	5.6 - 6.8	6.5 - 7.6	1.1 - 1.9	1.4 - 2.4	11.1 - 13.0	12.0 - 13.5
Hf	1.2 ± 0.2	1.0 ± 0.12	0.8	0.9	0.3	0.4	0.9	0.6
	0.9 - 1.4	0.9 - 1.2	0.8 - 0.9	0.7 - 1.2	0.2 - 0.4	0.3 - 0.5	0.6 - 1.0	0.4 - 0.8
W	2.8 ± 0.35	3.1 ± 0.21	2.9 ± 0.11	3.9 ± 0.56	0.1	0.1	5.4 ± 0.67	7.5 ± 137
	2.2 - 3.2	2.9 - 3.4	2.8 - 3.1	2.8 - 4.6	0.1 - 0.1	0.0 - 0.2	4.3 - 6.3	5.9 - 9.4
12 mm/hr								
Element	**Large Area**		**Lamellar microstructure**		**Silicide**		**Solid Solution**	
	Bulk	Edge	Bulk	Edge	Bulk	Edge	Bulk	Edge
Nb	59.7 ± 0.58	58.7 ± 0.26	60.3 ± 0.20	60.0 ± 0.82	52.8 ± 0.14	52.9 ± 0.22	70.1 ± 0.52	68.7 ± 0.96
	58.6 - 60.4	58.3 - 59.0	60.1 - 60.7	58.7 - 61.1	52.6 - 53.0	52.4 - 53.0	69.1 - 70.5	67.8 - 70.1
Ti	9.1 ± 1.27	7.3 ± 0.37	8.0 ± 1.41	7.6 ± 0.56	7.5 ± 0.31	7.3 ± 0.30	8.1 ± 0.87	6.7 ± 0.80
	7.6 - 11.2	6.8 - 7.8	6.7 - 10.5	6.9 - 8.4	7.2 - 8.1	6.8 - 7.7	7.2 - 9.3	5.8 - 7.6
Si	20.8 ± 1.69	21.0 ± 0.89	20.1 ± 0.63	19.6 ± 1.15	37.3 ± 0.56	37.1 ± 0.67	2.6 ± 0.49	1.7 ± 0.53
	18.7 - 23.2	20.1 - 22.4	19.0 - 20.8	18.8 - 21.9	36.6 - 38.0	36.2 - 38.2	1.7 - 3.3	0.7 - 2.1
Mo	6.2 ± 0.75	11.1 ± 0.50	6.8 ± 0.37	7.3 ± 0.39	1.9 ± 0.32	2.2 ± 0.26	11.7 ± 0.70	12.6 ± 0.69
	4.9 - 7.2	10.3 - 11.7	6.2 - 7.3	6.8 - 7.8	1.3 - 2.2	1.9 - 2.5	10.7 - 12.6	11.9 - 13.1
Hf	1.1 ± 0.12	0.2 ± 0.17	0.9 ± 0.10	0.9 ± 0.16	0.4	0.3	0.7	0.7
	1.0 - 1.3	0.0 - 0.4	0.8 - 1.1	0.7 - 1.1	0.3 - 0.5	0.2 - 0.5	0.5 - 0.8	0.5 - 1.0
W	3.1 ± 0.43	4.9 ± 0.12	3.8 ± 1.10	4.5 ± 0.39	0.1	0.1	6.7 ± 1.06	9.6 ± 1.59
	2.4 - 3.6	4.7 - 5.0	2.2 - 5.1	3.9 - 4.6	0.1 - 0.1	0.1 - 0.2	5.2 - 8.0	7.4 - 11.6

Figure 84 shows the internal microstructure in silicide grains of as-cast alloy CM1 solidified using OFZ at 150, 60 and 12 mm/hr. These images clearly show two distinct regions within the silicide; a lighter contrast area with light contrast precipitates and a darker contrast area located closer to the solid solution phase with no precipitates. The regions with precipitates were usually found in the larger

silicide grains but were sometimes found in the lamellar microstructure silicides, see Figure 84-150 mm/hr.

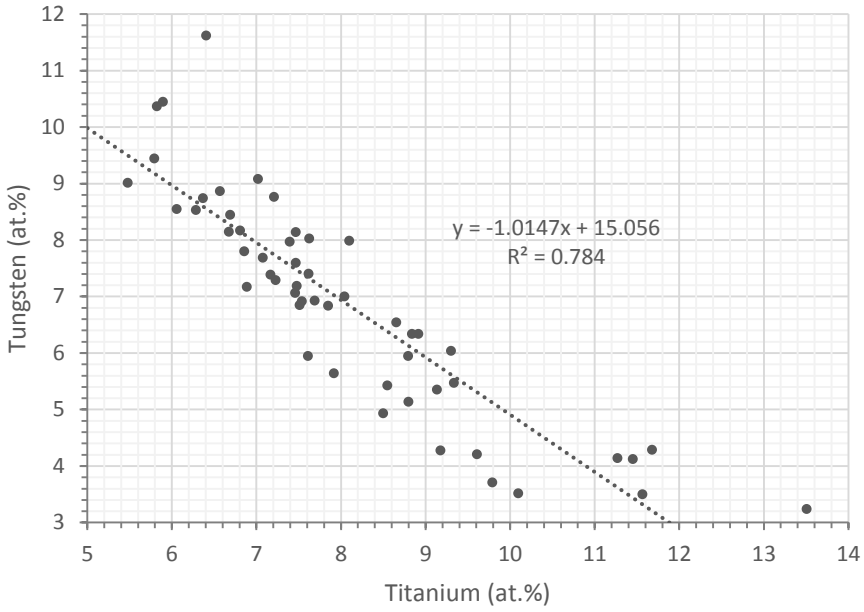

Figure 83: Relationship between the W and Ti concentration in the Nb_{ss} phase in the alloy CM1 cast using the OFZ process for all growth rates.

The precipitates seemed to form into two distinct morphologies at all growth rates; spherical and lamellar. Both morphologies were found in the same silicide grains suggesting that the precipitates grew perpendicular or parallel or at an angle to the section plane.

There was also evidence of thin, long and straight (Figure 85) or curved (Figure 84 60 mm/h and Figure 85E) lamellae precipitates in the 60 mm/h sample, and fine precipitates forming a “curve” seen in the 150 mm/h and 12 mm/h sample microstructures (Figure 85A, B, C, F, and G) which would suggest “break up” (spheroidisation) of the long thin lamellae. In Figure 85F and in (Figure 84 60 mm/h and Figure 85E) the curvature of the fine precipitates seemed to follow that of the Nb_{ss}/Nb_5Si_3 interface opposite.

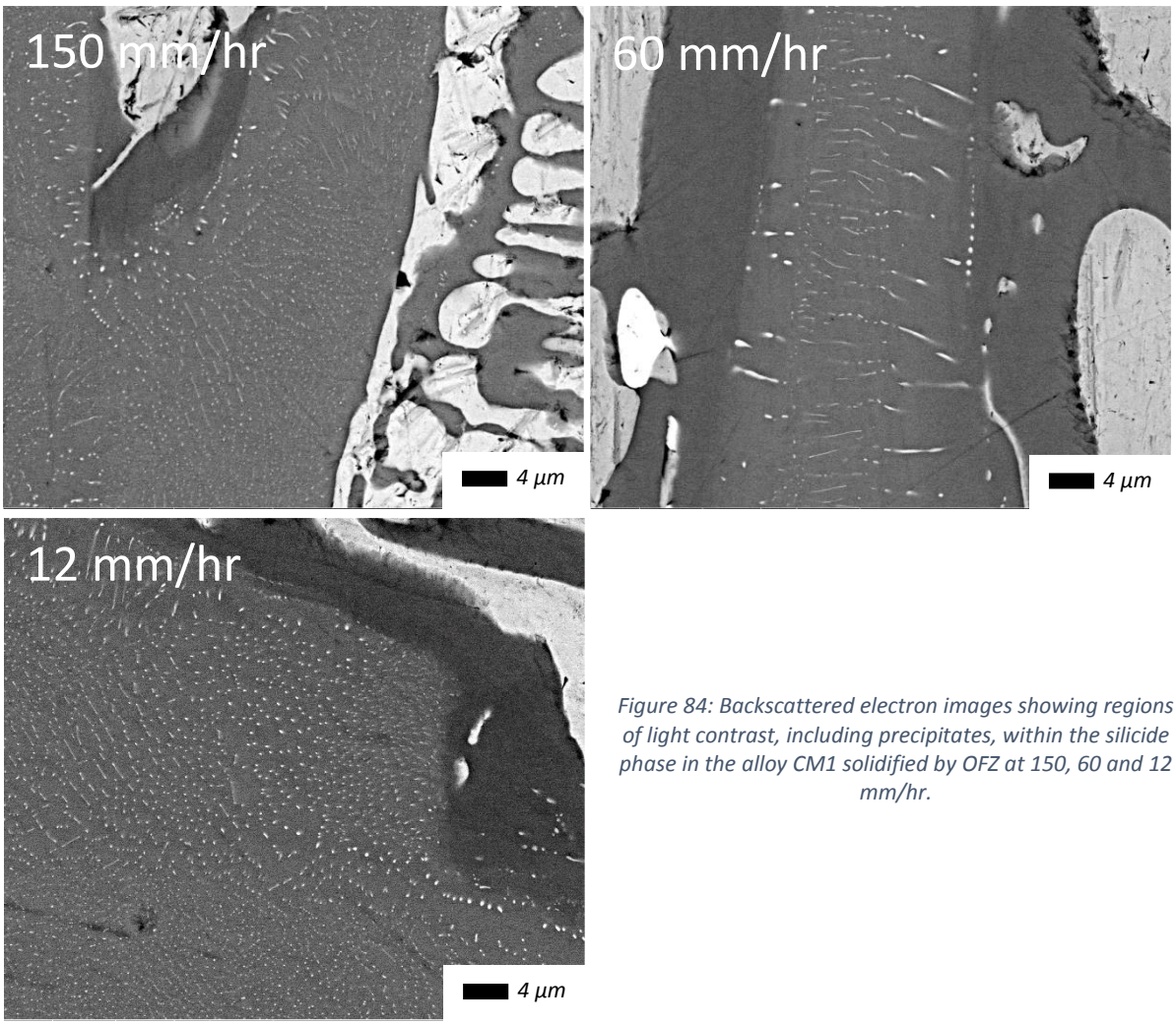

Figure 84: Backscattered electron images showing regions of light contrast, including precipitates, within the silicide phase in the alloy CM1 solidified by OFZ at 150, 60 and 12 mm/hr.

To determine whether elemental segregation was associated with the contrast change seen in the back scattered images, X-ray elemental maps were used, see Figure 86. Maps showed higher concentrations of Nb and Mo in the lighter contrast areas of the silicide and higher concentrations of Ti in the darker areas. Tungsten also seemed to show a slight affinity for the lighter contrast area of the silicide. However, due to the extremely low concentrations of W, 0.1 at.%, this segregation cannot be certain.

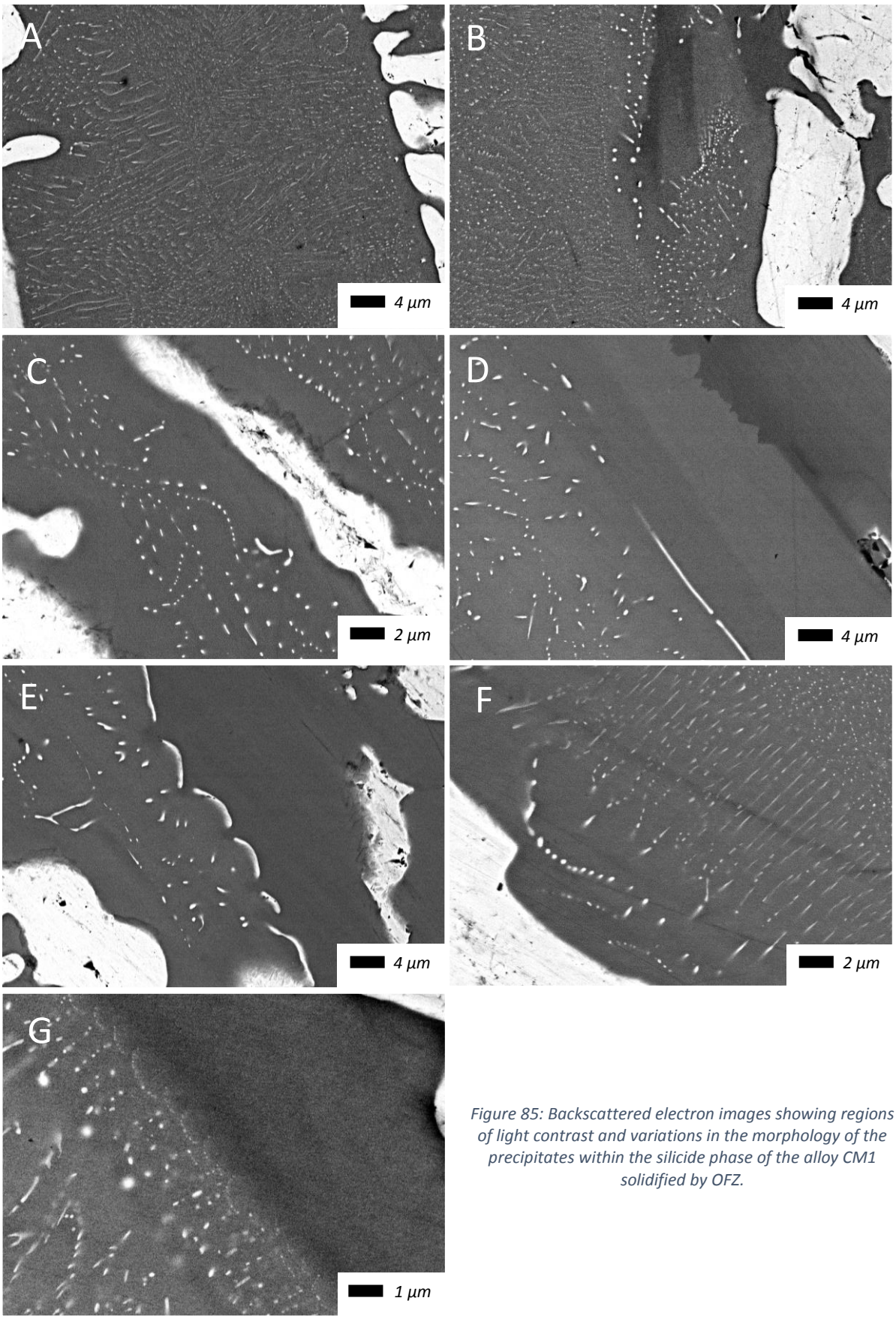

Figure 85: Backscattered electron images showing regions of light contrast and variations in the morphology of the precipitates within the silicide phase of the alloy CM1 solidified by OFZ.

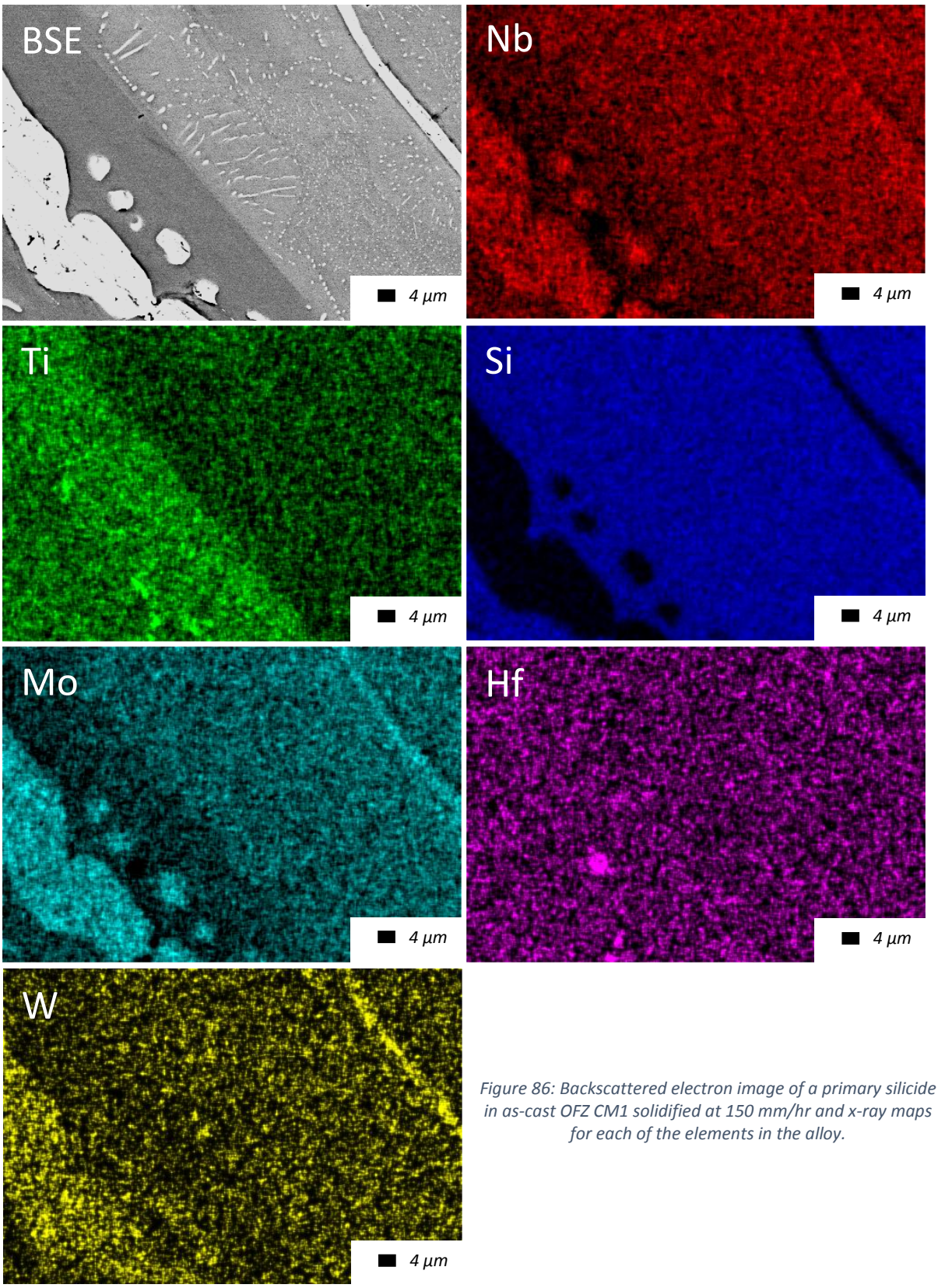

Figure 86: Backscattered electron image of a primary silicide in as-cast OFZ CM1 solidified at 150 mm/hr and x-ray maps for each of the elements in the alloy.

It should be remembered that evidence of fine precipitates in silicide grains was found in as-cast CM1 600 g and heat treated CM1 10 g, 600 g, 6 and 8 mm suction cast but not in the as-cast CM1 10g button and suction cast 6 mm or 8mm diameter bars of the alloy CM1.

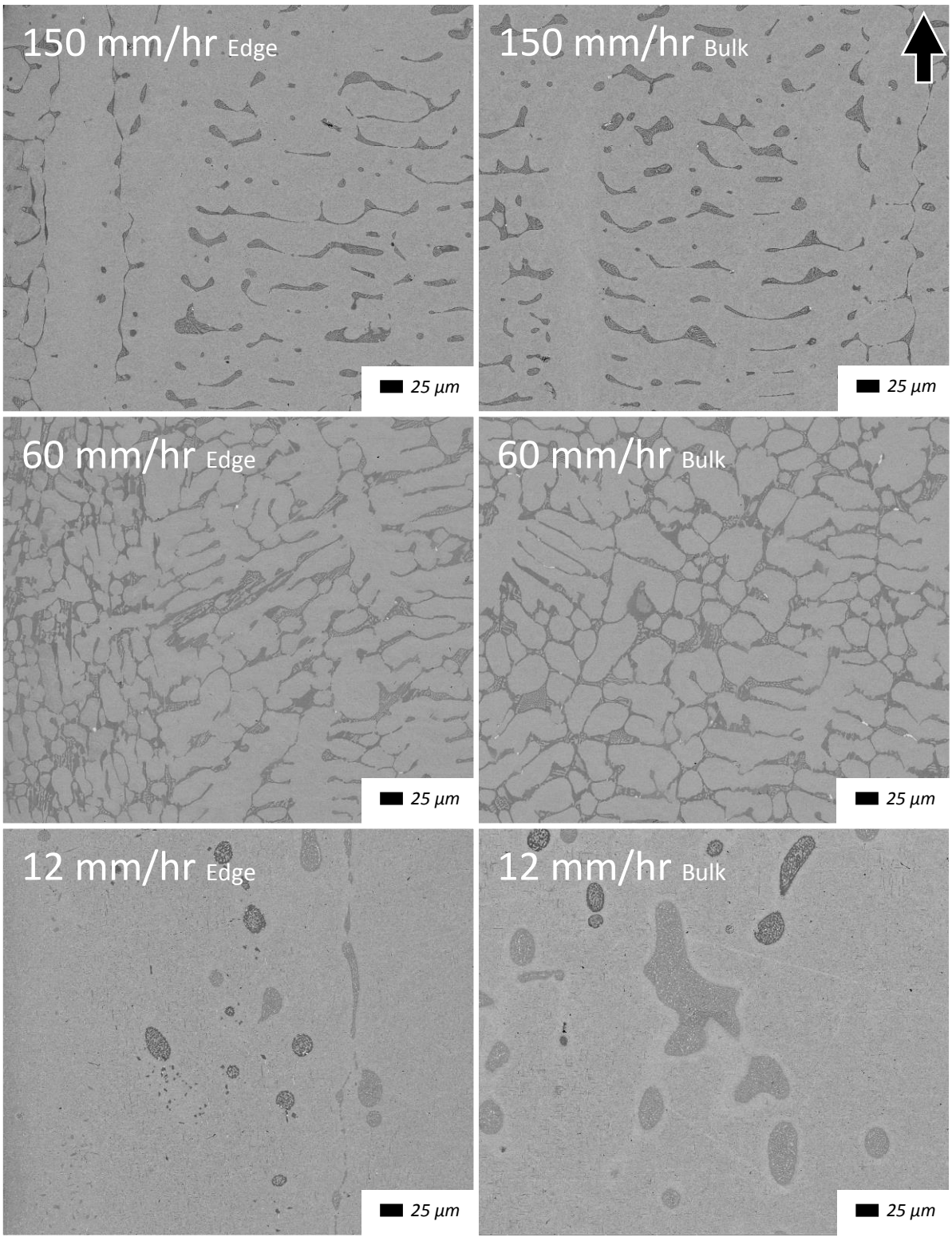

Figure 87: Backscattered electron images of the alloy CM2 processed using an optical float zone (OFZ) furnace at 3 different growth rates, 150 mm/hr, 60 mm/hr and 12 mm/hr from top to bottom respectively. Left hand images show the edge microstructure and right hand images the bulk microstructure. Arrow indicates the growth direction.

Figure 87 shows the microstructure of the alloy CM2 directionally solidified using an optical float zone furnace. These are typical microstructures grown at stable growth rates. Comparison of the microstructure of OFZ CM2 with those of the other methods used in this study, namely arc melting and suction casting shows significant differences. The OFZ microstructures consisted of a very high volume fraction of Nb_{ss} and α-Nb_5Si_3, confirmed by XRD and EDS, see Appendix B Fig 6 and Table 24, respectively. Such high vol% of Nb_{ss} would be possible for a low Si content hypoeutectic Nb-Si alloy.

At all growth rates for the stable OFZ growth of the alloy CM2 a small dark contrast plate shaped phase was present in the solid solution, see Figure 88. The existence of these secondary phase platelets in the Nb_{ss} might be the reason of the high Si content in the Nb_{ss} in all three growth rates, see Table 24. As the growth rate decreased these plates increased in size (≈ 1-2 μm in length at 150 mm/hr to ≈ 10 μm at 12 mm/hr). In the interdendritic area a lamellar microstructure was observed (Figure 87 and Figure 88). Decreasing the growth rate created an area around the eutectic cells with lamellar microstructure where the dark plates were not present. In the alloy solidified at 150 and 60 mm/hr growth rates the plates had two distinct orientations, perpendicular and parallel to the growth direction. In the 12 mm/hr sample there were also equiaxed dark contrast phases present in the Nb_{ss} (Figure 87) as well as the oriented dark contrast plates (Figure 88).

The OFZ sample solidified at 150 mm/hr, at both the edge and bulk, had larger dendrites (compared with the 60 mm/hr sample) grown in the same direction as the OFZ growth direction. Secondary dendrite arms had grown perpendicular to the growth direction. In the interdendritic regions a lamellar microstructure was observed. The latter consisted of a matrix of α-Nb_5Si_3 surrounding rods of Nb_{ss} of regular spacing (Figure 88).

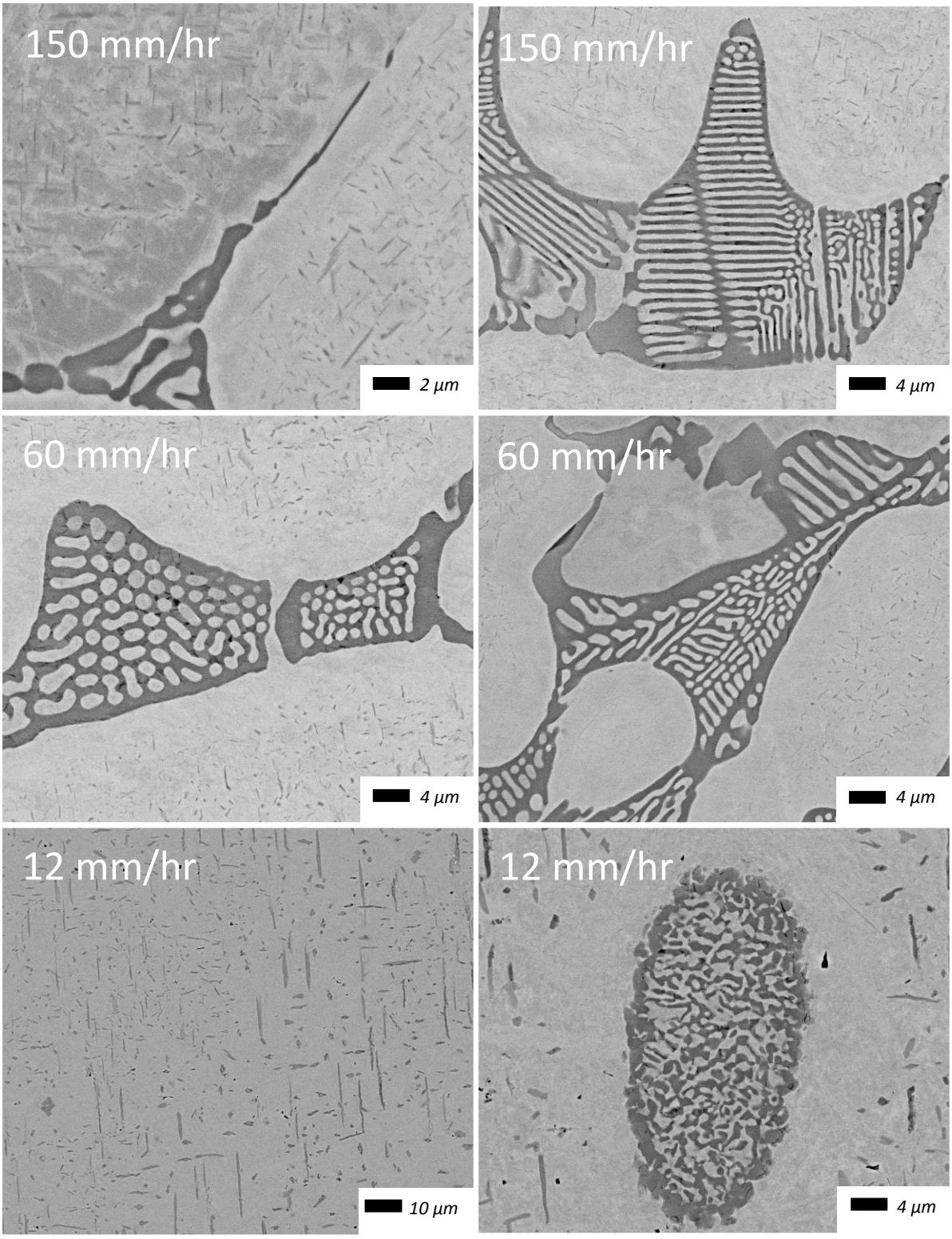

Figure 88: Backscattered electron images of fine precipitates in Nbss and lamellar microstructure cells in cast alloy CM2 processed by OFZ at 12, 60 and 150 mm/h

In the OFZ sample grown at 60 mm/hr, the volume fraction of the Nb_{ss} (61.8 %) was lower than in the 150 mm/hr sample (74.8 %) and significantly higher than in the alloy CM2 produced by arc-

melting (button and ingot) and suction casting (§ 3.4). The Nb_{ss} did not have the definite orientation relationship relative to the growth direction seen at 150 mm/hr. Interdendritic lamellar microstructure had the same morphology as seen at 150 mm/hr (Figure 88). There were however single phase silicide grains in this sample. This was not seen in the 150 mm/hr sample. The 60 mm/hr sample also had a larger volume fraction of α-Nb_5Si_3 towards the edge, as seen in the alloy CM1 OFZ, but not seen in the other two growth rates in the case of CM2 OFZ.

The 12 mm/hr growth rate sample had the largest lamellar microstructure cells of the three CM2 OFZ samples, see Figure 89. In the images from the Bulk and Edge for growth at 12 mm/hr in Figure 87, there is a distinct difference in contrast between neighbouring cells as well as different morphologies. The lighter contrast cells consisted of a silicide matrix with rods of Nb_{ss} (Figure 89) and, had a higher volume fraction of silicide than those in the other two growth rates. The darker contrast cells, although surrounded by a silicide shell, had predominantly a continuous mixture of both phases (Figure 88). Some cells contained both light and dark contrast silicide grains (Figure 89).

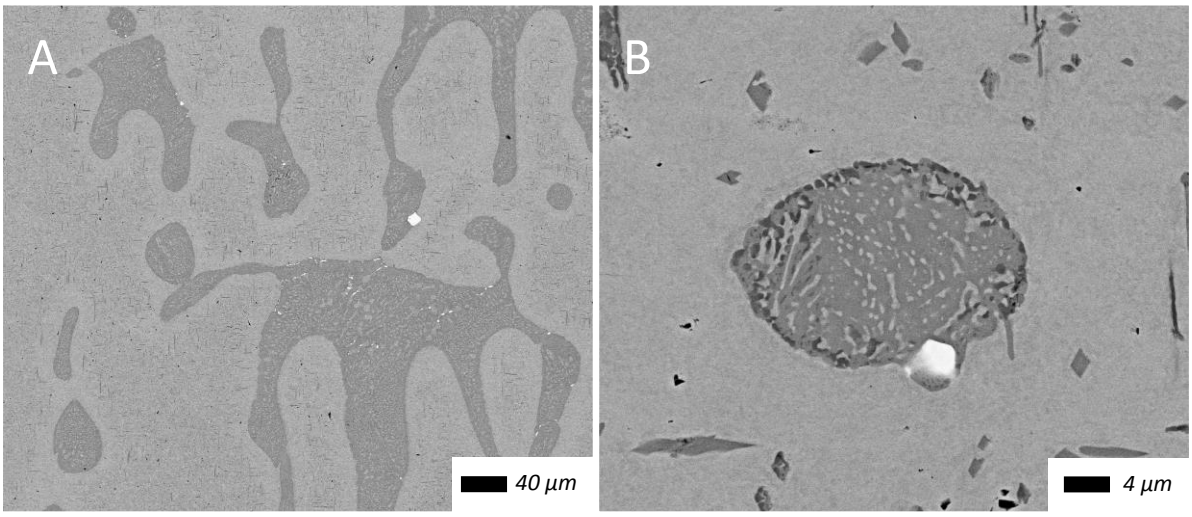

Figure 89: Backscattered electron images of Nb_{ss} with fine and coarse precipitates and lamellar microstructure (eutectic?) cells in cast alloy CM2 processed by OFZ at 12 mm/h

Beginning with the sample grown under steady state OFZ growth conditions (see below) at 150 mm/hr, the large area analysis in Table 24 shows that there were no differences in the concentration of the alloying elements between the edge and centre unlike the OFZ alloy CM1. There was however

variation of Nb content across the sample. The EDS analysis of the lamellar microstructure showed variation of Si in the bulk and no W in the lamellar microstructure. The silicide in both areas also did not contain any W. However, there was W solubility in the Nb_{ss}. The spot analysis showed that all elements, excluding W, had significant concentration variations between phases.

The sample grown under steady state OFZ conditions at 60 mm/hr showed insignificant variation of Si in both areas (Table 24). There was significant variation in the concentration of Si in the lamellar microstructure analysis in the edge area. The silicon concentration measured by large area analysis for this growth rate was much larger than that for the other two growth rates, and is consistent with the volume fraction differences of phases seen in the images in Figure 87. No W was analysed within the silicide and the lamellar microstructure was essentially W free. Significant variations of Si concentration were noted in the solid solution analysis in the edge area.

In the sample grown under steady state OFZ conditions at 12 mm/hr, the large area analysis of the edge and the bulk showed no significant difference in the concentration of the alloying elements. However, the analysis of the lamellar microstructure showed similarities with the sample grown at 150 mm/hr, for the Si concentration and no tungsten. In the silicide in the bulk of the sample the silicon concentration was only 25.4 at.%. This indicated that the contrast differences seen in Figure 87 was due to the silicides not being of the same form. The lighter contrast silicide was the Nb_3Si and the darker contrast silicide was the α-Nb_5Si_3. The presence of both silicides was confirmed by XRD, see Appendix B Fig 6. The large variation of Si concentration in the silicide grains at the edge would suggest that both silicide types, namely Nb_3Si and α-Nb_5Si_3 were presente in this area. This was confirmed by the individual analysis that showed two distinctly different levels of Si, corresponding to the Nb_3Si and Nb_5Si_3 phases. There was no evidence of Hf having a higher affinity for a specific form of silicide.

Table 24: Summary of EDS analysis (at.%) of the alloy CM2 processed using an optical float zone furnace at growth rates of 150, 60 and 12 mm/hr including SD, minimum and maximum values.

150 mm/hr								
Element	**Large Area**		**lamellar microstructure**		**Silicide**		**Solid Solution**	
	Bulk	Edge	Bulk	Edge	Bulk	Edge	Bulk	Edge
Nb	92.0 ± 0.87	92.0 ± 1.11	76.2 ± 0.87	76.0 ± 0.29	58.3 ± 1.65	59.2 ± 0.80	94.8 ± 0.38	94.5 ± 0.57
	91.0 - 93.1	90.4 - 93.1	74.9 - 77.3	75.4 - 76.2	55.4 - 61.3	58.0 - 59.9	94.2 - 95.5	93.9 - 95.4
Si	5.2 ± 0.41	5.3 ± 0.72	21.5 ± 0.88	21.4 ± 0.32	37.7 ± 1.10	37.5 ± 0.66	3.2 ± 0.35	3.3 ± 0.55
	4.6 - 5.7	4.6 - 6.4	20.2 - 22.5	21.1 - 21.9	35.8 - 39.2	36.9 - 38.4	2.6 - 3.7	2.3 - 4.0
W	1.4 ± 0.28	1.3 ± 0.32	0	0	0	0	1.0 ± 0.12	1.1 ± 0.11
	1.1 - 1.8	0.9 - 1.7					0.9 - 1.1	0.9 - 1.3
Hf	1.4 ± 0.24	1.3 ± 0.15	2.4 ± 0.29	2.6 ± 0.25	4.0 ± 0.81	3.3 ± 0.21	1.0 ± 0.22	1.6 ± 0.10
	1.1 - 1.6	1.1 - 1.5	1.8 - 2.7	2.1 - 2.8	2.9 - 5.4	3.0 - 3.5	0.8 - 1.5	1.0 - 1.3
60 mm/hr								
Element	**Large Area**		**lamellar microstructure**		**Silicide**		**Solid Solution**	
	Bulk	Edge	Bulk	Edge	Bulk	Edge	Bulk	Edge
Nb	84.7 ± 1.18	82.8 ± 1.15	74.8 ± 0.59	75.1 ± 1.04	57.1 ± 0.59	56.4 ± 0.28	94.2 ± 0.56	93.6 ± 1.06
	83.5 - 85.9	81.9 - 84.8	74.2 - 75.9	73.5 - 76.4	56.6 - 58.1	55.8 - 56.8	93.4 - 94.8	91.7 - 94.8
Si	9.6 ± 0.82	10.8 ± 0.95	22.1 ± 0.63	21.4 ± 1.03	38.7 ± 0.23	39.1 ± 0.10	2.2 ± 0.46	2.7 ± 1.11
	8.8 - 11.0	9.3 - 11.9	20.9 - 22.7	20.0 - 23.1	37.5 - 39.2	39.0 - 39.3	1.7 - 3.0	1.8 - 4.8
W	2.9 ± 0.66	3.3 ± 0.42	0.2	0.2	0	0	2.3 ± 0.11	2.0 ± 0.56
	2.2 - 3.9	2.8 - 3.9	0.2 - 0.3	0.0 - 0.73			2.2 - 2.5	1.5 - 3.0
Hf	2.7 ± 0.33	3.0 ± 0.37	2.9 ± 0.04	3.3 ± 0.23	4.2 ± 0.37	4.4 ± 0.31	1.2 ± 0.17	1.8 ± 0.10
	2.2 - 3.1	2.6 - 3.3	2.8 - 2.9	2.9 - 3.6	3.4 - 4.7	4.1 - 5.2	1.0 - 1.5	1.6 - 1.9
12 mm/hr								
Element	**Large Area**		**lamellar microstructure**		**Silicide**		**Solid Solution**	
	Bulk	Edge	Bulk	Edge	Bulk	Edge	Bulk	Edge
Nb	91.6 ± 0.71	92.0 ± 0.43	77.2 ± 0.67	76.4 ± 0.84	72.3 ± 0.22	67.6 ± 6.11	96.1 ± 1.01	97.2 ± 0.19
	90.8 - 92.6	91.5 - 92.6	76.2 - 78.3	75.0 - 78.5	71.9 - 72.6	60.0 - 73.1	94.1 - 97.2	96.7 - 97.3
Si	6.4 ± 0.67	6.2 ± 0.51	20.4 ± 0.51	21.3 ± 0.94	25.4 ± 0.41	30.6 ± 6.04	2.8 ± 0.86	3.4 ± 0.20
	6.2 - 7.7	5.5 - 6.6	19.2 - 21.2	20.3 - 22.6	24.8 - 25.8	25.2 - 38.0	1.9 - 4.5	2.1 - 2.7
W	0.6 ± 0.33	0.5	0	0	0	0	0	0
	0.3 - 1.2	0.4 - 0.6						
Hf	1.4 ± 0.2	1.3 ± 0.15	2.4 ± 0.18	2.3 ± 0.16	2.3 ± 0.60	1.8 ± 0.65	1.0 ± 0.16	0.4 ± 0.07
	1.1 - 1.6	1.1 - 1.5	2.1 - 2.6	1.9 - 2.6	1.6 - 3.0	1.2 - 3.0	0.8 - 1.3	0.3 - 0.4

3.3.1.1 Chemical and Microstructure inhomogeneity in the alloy CM2 processed using OFZ

Table 25 gives the average EDS analysis data of the alloys CM1 and CM2 processed using OFZ, across all growth rates and areas and their respective feed stock ingot, CM1 600 g and CM2 500 g. Focusing first on the alloy CM1, there are differences in the concentrations of Si, Mo and W. These differences are less than 2 at.% and thus were not considered significant. The alloy CM2 on the other hand showed significant differences of the concentrations of all elements between the large area EDS analysis of the feed stock, as-cast 500 g ingot, and the average data for the OFZ processed alloy. This data combined with the extremely high volume fraction of Nb_{ss} in the alloy CM2 processed using OFZ over all the studied growth rates points to either segregation (chemical inhomogeneities) or loss of alloying elements during OFZ solidification processing.

Table 25: Average large area EDS analysis data (at.%) for as-cast CM1 600 g, CM2 500 g and OFZ CM1 and CM2 across all growth rates and areas.

CM1			*CM2*		
Element	Large Area 600 g	Large Area OFZ	Element	Large Area 500 g	Large Area OFZ
Nb	60.8	59.7	*Nb*	71.3	89.2
Ti	8.5	8.5	*Si*	18.2	7.3
Si	22.7	20.8	*W*	4.9	1.7
Mo	5.2	7.0	*Hf*	5.6	1.9
Hf	0.7	1.0			
W	2.1	3.1			

The OFZ solidification processing of the alloy CM2 did not proceed as smoothly and continuously as that of the alloy CM1. During OFZ solidification processing the molten zone became unstable. To keep the hot zone molten the temperature and growth rate had to be altered. It should be pointed out that all results presented in § 3.3.1 (and for the heat treated OFZ alloy in § 3.3.2.) were from the regions that were grown at a stable growth rate (stable OFZ growth conditions). The changes in the growth rate because of instability created bulbous regions within the final bar. Figure 90 shows the OFZ bar of the alloy CM2 solidified at 12 mm/hr, the circled regions show where the instabilities formed.

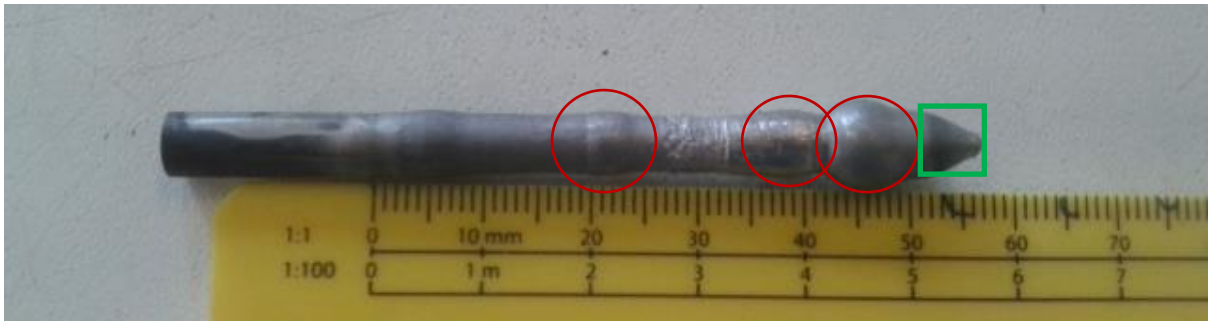

Figure 90: Cast CM2 alloy solidified using an OFZ furnace at 12 mm/hr, red circles highlight the regions where instabilities formed and the green square highlights the region within the hot zone at the end of solidification.

The bulk microstructure and chemistry of the samples did not alter from stable to unstable regions. However, in some specific regions there were some distinct differences. Figure 91A shows the region or boundary region between the stable (bottom of the image) and the unstable (top of the image) growths. The microstructure shows a distinct increase in the volume fraction of silicide, and therefore silicon, at and after the boundary region. The microstructure then gradually returned to the bulk microstructure seen in the stable area of as-cast OFZ alloy CM2 within a few millimetres of the boundary region. Figure 91B shows the edge region of the sample grown at 12 mm/hr as the solidification became unstable. The left hand side of the microstructure, closest to the edge, became silicide rich. This high Si concentration was only present within a millimetre of the edge and the microstructure returned to the bulk microstructure seen in the stable region. The Si-rich area at the edge remained present throughout the unstable growth region. This pattern of higher volume fraction silicide areas present at the boundary region and the edge was also seen in the sample grown at 60 mm/hr but the difference at the edge was not as profound due to the higher volume fraction of silicide present at the edge of the stable region grown at 60 mm/hr. The sample grown at 150 mm/hr, however, did not show any microstructural variation between the stable and unstable growths.

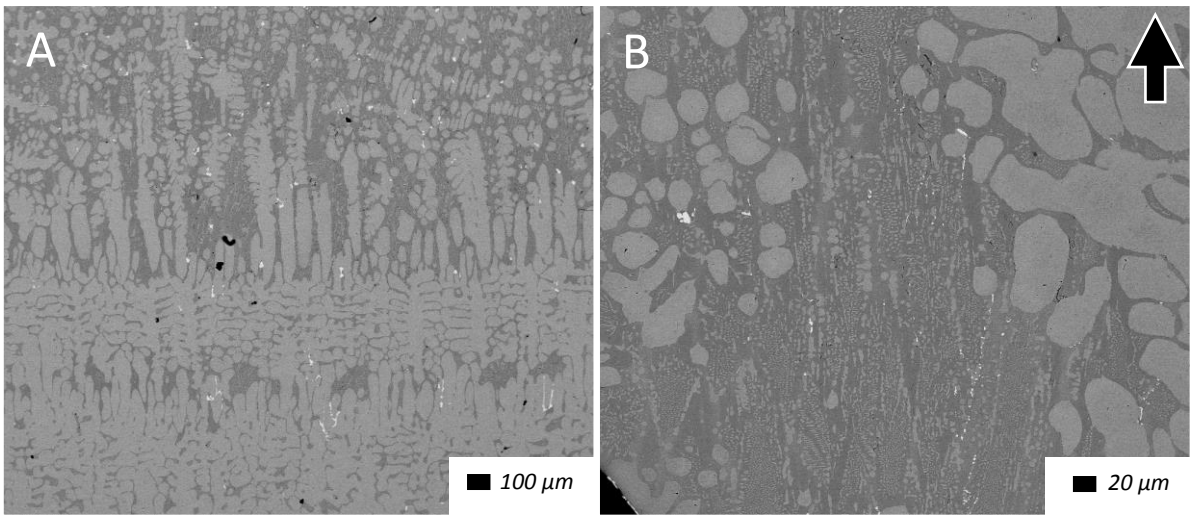

Figure 91: (A) The boundary region between the stable (bottom) and unstable (top) regions and (B) the microstructure at the edge of the unstable region in as-cast OFZ CM2 grown at 12 mm/hr.

The results of the microstructure studies of the boundary region between unstable and stable growth would suggest that there was segregation of elements at the solid/liquid interface. This segregation continued until there was a saturation of alloying elements causing the front to become unstable. To verify this the solid liquid boundary area must be looked at.

Figure 92 shows backscattered electron images of the microstructure of the portion of the bar grown at 12 mm/hr that was still in the hot zone when solidification stopped. This area is highlighted in Figure 90 with the green square. Image A shows the microstructure in the region just above the stable growth region in the hot zone. This region had a higher volume fraction of silicide than that which was present within the stable region of the bar. As the distance increased from the stable region towards the tip of the bar (images B to C in Figure 92) the volume fraction of the silicide increased and the size and number of Nb_{ss} dendrites decreased. At the tip of the bar the microstructure suddenly changed morphology to the structure seen in Figure 92D. The structure seen in image D was very similar to the structure seen in the as-cast CM2 500 g ingot, Figure 53C.

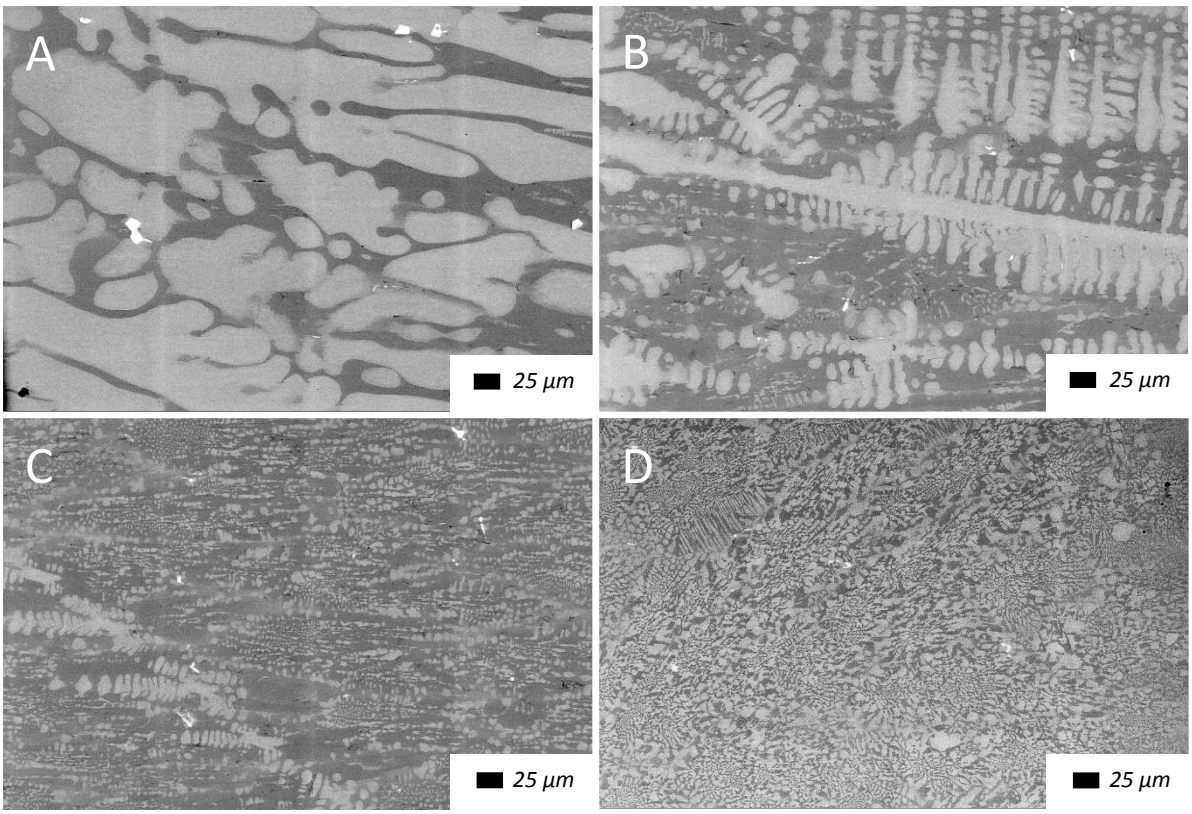

Figure 92: The evolution of the bulk microstructure in the sample grown at 12 mm/hr from just above the last area of stable directional growth (A) through 3 different areas that were still in the hot zone after solidification had been terminated (B to D), see also green square in Figure 90.

The microstructure at the edge of this section of the ingot showed much less change. In the region closest to the stable zone the microstructure was very similar to that seen in Figure 92B. The volume fraction of Nb_{ss} dendrites then decreased similarly to the bulk with the region just below the end of the bar containing no Nb_{ss} dendrites.

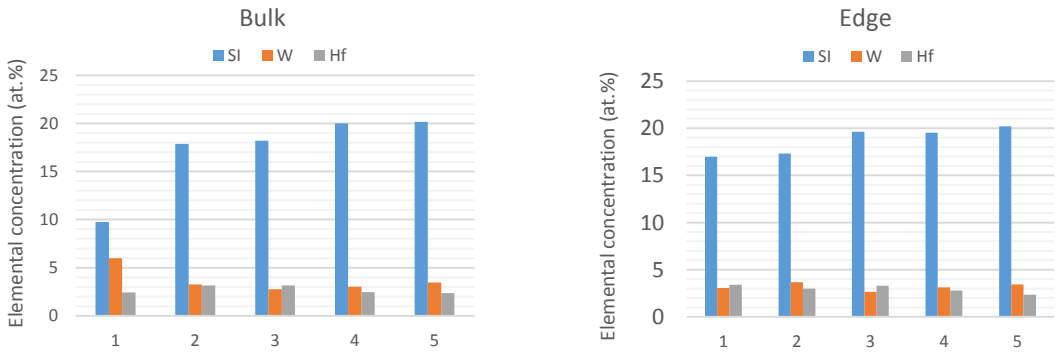

Figure 93: The average value of EDS large area analyses of Si, W and H from the area closest to the microstructure grown under stable conditions (1) to the last area to leave the hot zone after solidification (5)

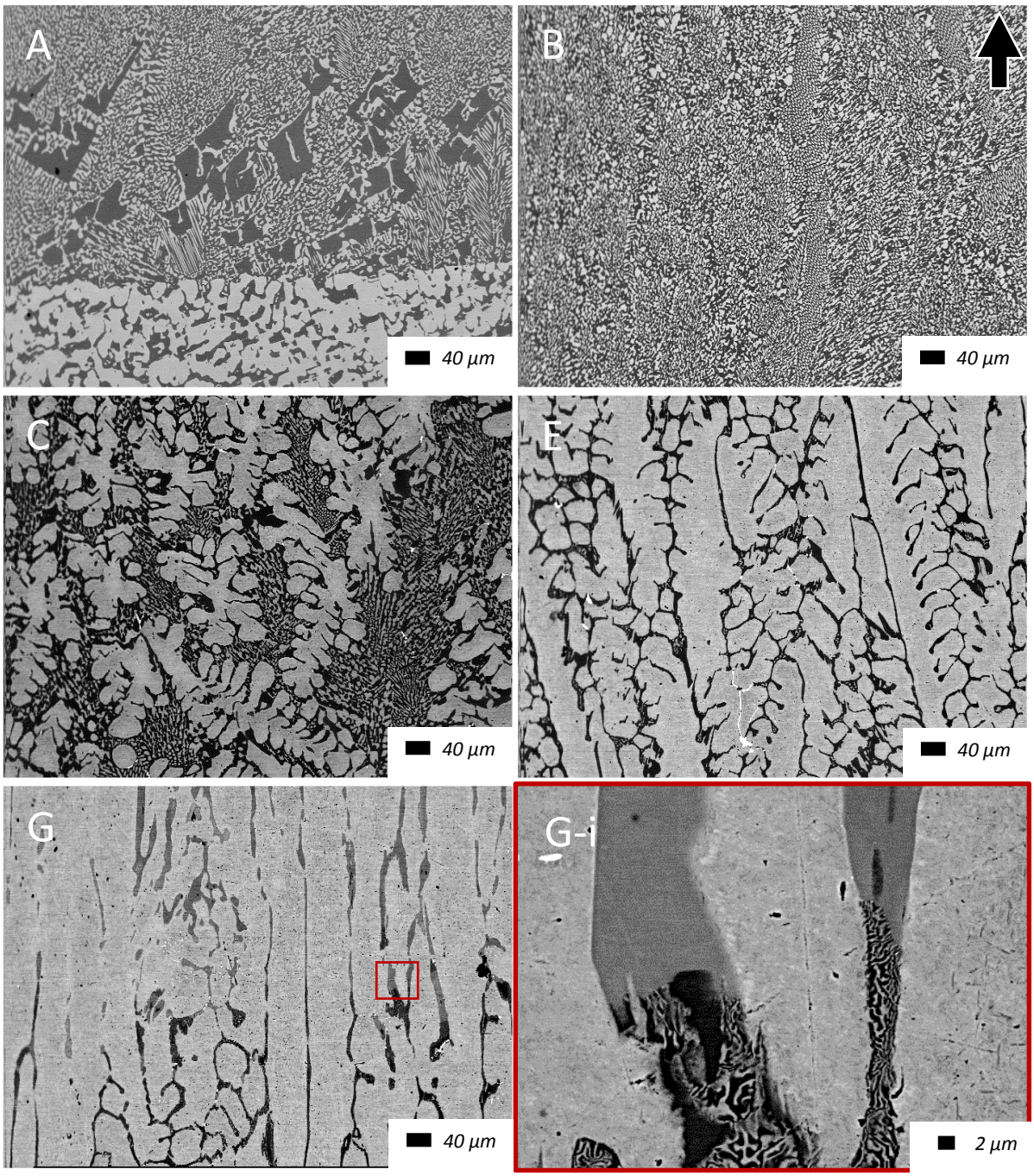

Figure 94: Backscattered electron images of the microstructural evolution of the as-cast alloy CM2 solidified in an OFZ furnace from the initial point of contact with the seed rod to the first unstable region.

The bar graph in Figure 93 shows how the concentration of Si, W and Hf varied from the area just above the region of stable growth (1) to the tip of the bar (5). The graphs clearly show a gradual increase of Si from 9.8 and 17.0 at.% at the edge and bulk respectively to 20.2 at.% at the tip of the bar. Tungsten was at a maximum, 6.0 at.%, in the bulk closest to the microstructure grown under stable conditions and remained at a relatively constant lower level after this, averaging 3.4 at.%,

higher than the average of the region of stable growth, 1.7at.%W. The Hf concentration showed a similar pattern with the individual area analysis never varying too much from the average of 2.9 at.%, again more than the 1.9 at.%Hf average seen in the OFZ bar cast under stable growth conditions.

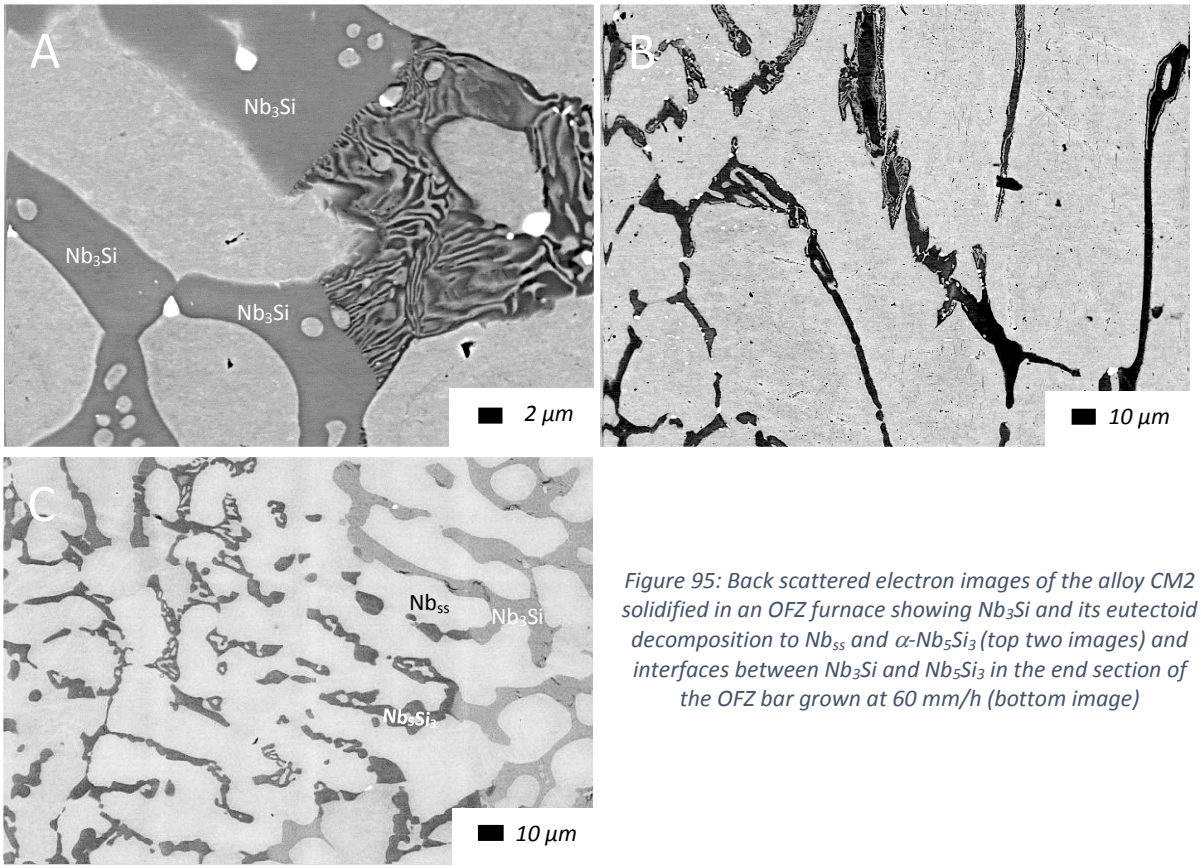

Figure 95: Back scattered electron images of the alloy CM2 solidified in an OFZ furnace showing Nb_3Si and its eutectoid decomposition to Nb_{ss} and α-Nb_5Si_3 (top two images) and interfaces between Nb_3Si and Nb_5Si_3 in the end section of the OFZ bar grown at 60 mm/h (bottom image)

To determine if there was any variation in the concentration of elements in the initial stages of solidification the sample grown at 12 mm/hr was also studied from the first area to melt where the DS bar came in contact with the seed rod. The images in Figure 94 show how the microstructure varied from the point of contact with the seed rod (A) to the first instability (just beyond image G). Initially (image A) the microstructure consisted of large silicide phases with an interdendritic eutectic structure. This structure then altered into a purely eutectic structure just above image A (about 250 µm from the boundary) as shown in image B. Within ~ 1 mm a distinct boundary formed where the eutectic spacing was reduced and Nb_{ss} dendrites formed. These dendrites initially formed in a seemingly random orientation in relation to the growth direction. As the distance from A increased the volume fraction of Nb_{ss} increased dramatically (images A-E) with the interdendritic eutectic

"squeezed" and only silicide formed in some regions. The Nb_{ss} dendrites also became more orientated towards the growth direction as the distance from A increased. Moving through the bar to the area, nearest to the unstable region, there was a contrast change in the silicide from dark, seen throughout the bar to this point, to a lighter contrast. Closer examination of the interface between the silicides, image G-I in Figure 94 and Figure 95, showed that the contrast change was due to the eutectoid decomposition $Nb_3Si \rightarrow (Nb_{ss} + \alpha\text{-}Nb_5Si_3)_{eutectoid}$.

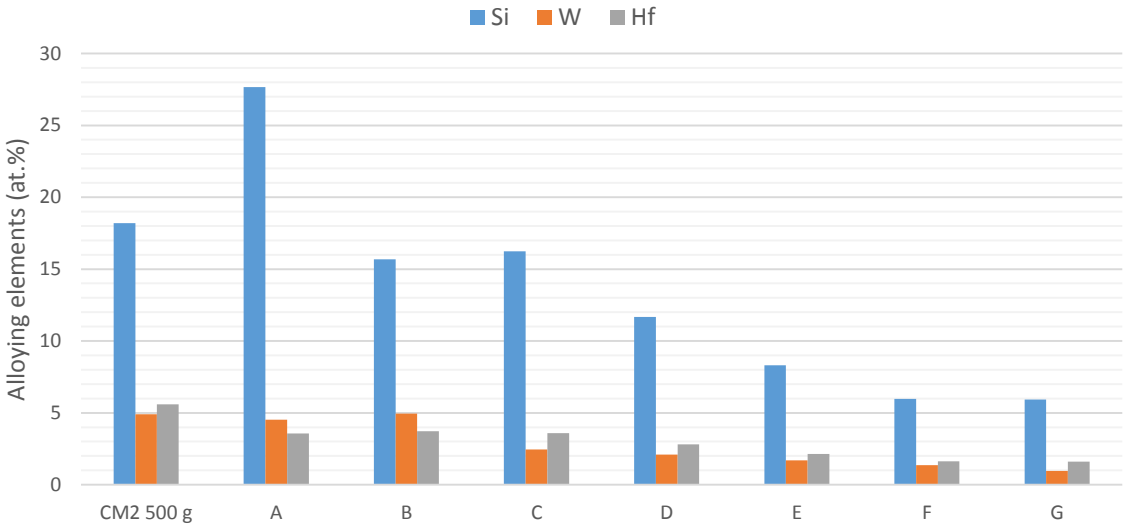

Figure 96: The average EDS analysis of the alloy CM2 bar attached to the seed rod at increasing distance from the rod. The average EDS analysis of as-cast CM2 600 g is also shown for reference.

The large area EDS analysis, Figure 96, confirmed the decreased amount of Si with increased distance from the seed rod. The silicon concentration showed a sudden drop from area A (27.7 at.%) to B/C (15.7/16.2 at.%) and then a more gradual decrease to area G (5.9 at.%). The W also showed a sudden decrease in concentration between areas B (4.9 at.%) and C (2.5 at.%) and then continued decreasing gradually throughout the bar. Areas A and B were the only two areas within 2 at.% of the average W concentration of the as-cast CM2 500 g ingot (4.9 at.%W). The Hf exhibited a gradual decrease throughout the length of the bar from area A (3.6 at.%) to G (1.6 at.%). All values for Hf however were below the average in the as-cast CM2 500 g ingot (5.6 at.%).

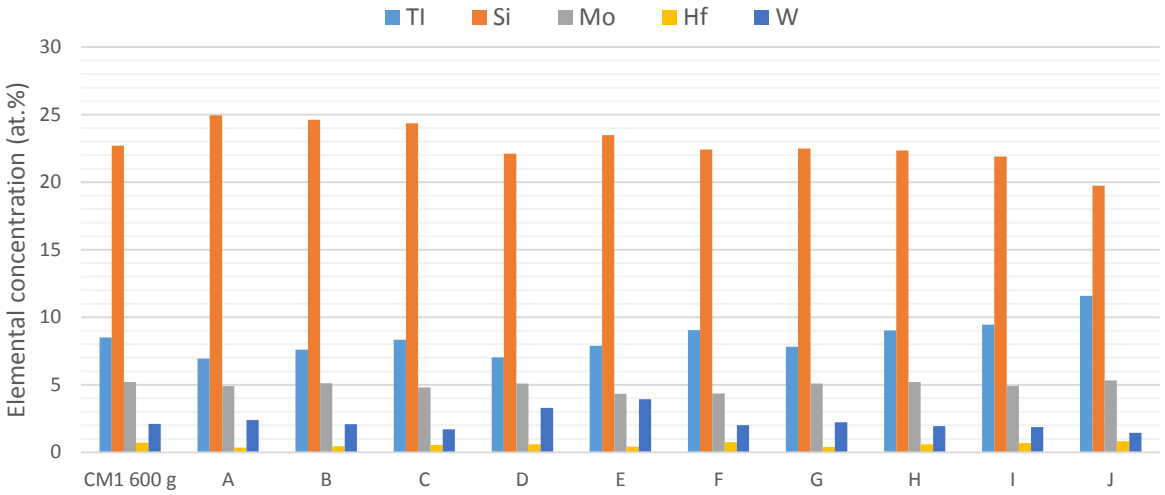

Figure 97: EDS analysis of the CM1 bar attached to the seed rod at increasing distance from the rod. The average EDS analysis of the as-cast CM1 600 g ingot is also shown for reference.

To eliminate any differences that may occur between using an OFZ furnace with 2 lamps (OFZ alloy CM1, Japan) and 4 lamps (OFZ alloy CM2, Cambridge) the alloy CM1 was also solidified using the OFZ furnace in Cambridge at 12 mm/hr growth rate. Figure 97 shows the change in elemental concentrations with increased distance from the seed rod (A to J) for as-cast alloy CM1 grown at OFZ 12 mm/hr (Cambridge). Average data for the as-cast CM1 600 g ingot is also added for reference.

Initially, (at areas A-C) the Si concentration was slightly higher than would be expected (25.0 – 24.4 at.% respectively) however this then decreased in area D and levelled out for the remainder of the bar. The Ti concentration remained relatively constant around the as-cast CM1 600 g ingot average value throughout the bar until it reached the final area where it jumped from 9.5 at.% in area I to 11.6 at.% in area J. The W concentration similarly increased from an expected level, ~.1 at.%, up to 3.3 and 3.9 at.% in areas D and E, respectively. This however was not as significant as the increase in Ti. The Mo and Hf levels remained relatively constant around the averages of the as-cast CM1 600 g ingot.

3.3.2 Heat Treated OFZ alloys

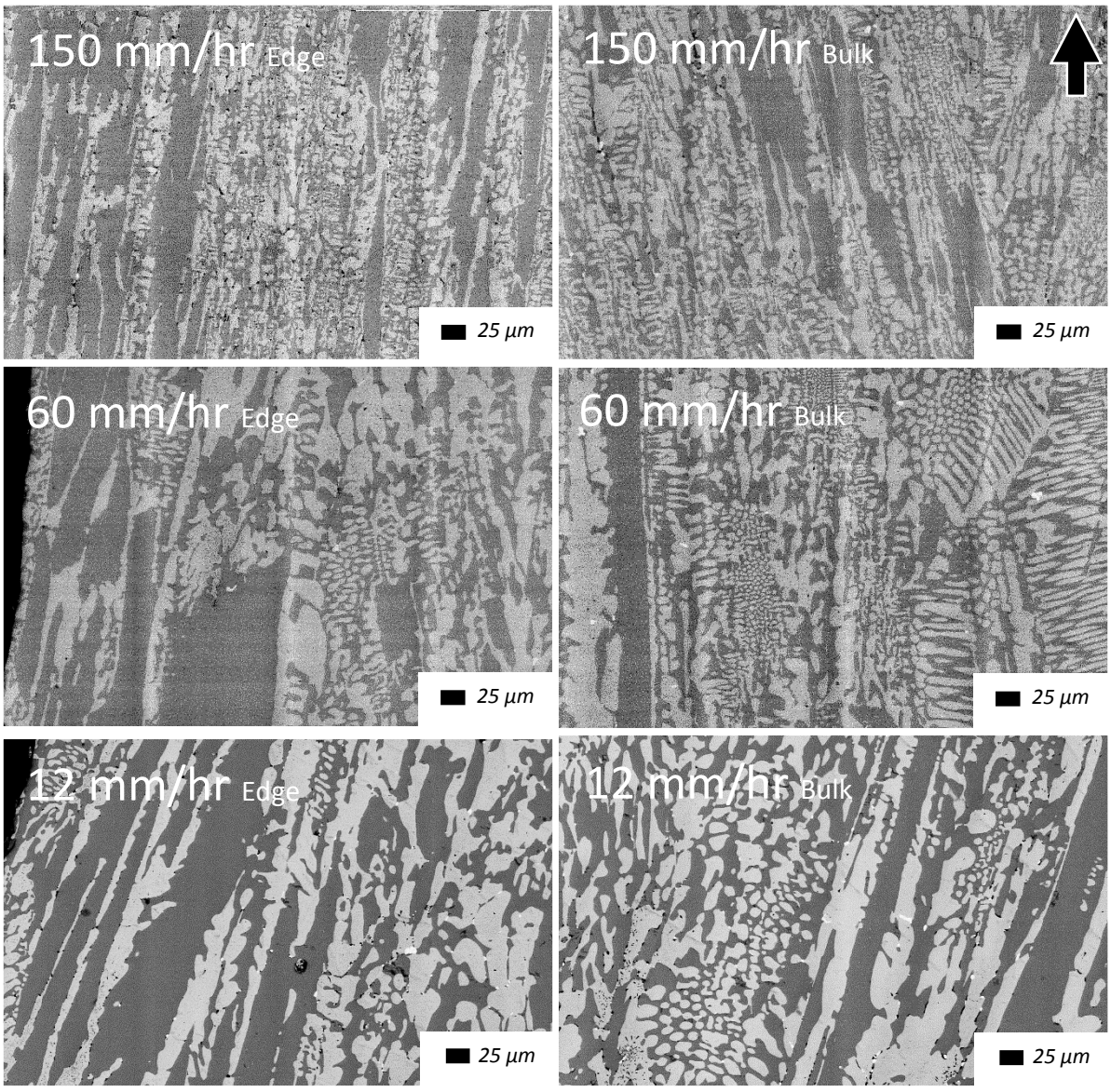

Figure 98: Backscattered electron images of the heat treated alloy CM1 processed using an optical float zone furnace at 3 different growth rates 150 mm/hr, 60 mm/hr and 12 mm/hr from top to bottom respectively. Left hand images show the edge microstructure and right hand images the bulk microstructure. Arrow indicates the growth direction

After the heat treatment at 1500 ^{O}C for 100 hrs the microstructure of the alloy CM1 solidified in the OFZ furnace was very similar to the as-cast OFZ microstructure, Figure 98. XRD, Appendix B Fig 7, showed that the same two phases, namely the α-Nb_5Si_3 and Nb_{ss}, were present pre- and post-heat treatment. The "periodic nature" of large, faceted silicide dendrites with the interdendritic prior-lamellar microstructure remained. The main difference between the two conditions was the spacing in the lamellar microstructure. This will be discussed in § 3.4.4.

In the sample grown at 150 mm/hr large area analysis showed inhomogeneity for Ti in the bulk and for Si in the bulk and in the edge and bulk of the lamellar microstructure. Compared with the OFZ cast alloy, the Si content in the bulk was lower. The average silicon content of the prior- lamellar microstructure area at the edge increased after the heat treatment. The concentrations of refractory alloying elements in the prior-lamellar microstructure were reduced after the heat treatment, Mo and W decreasing by 1.6 and 0.8 at.%, respectively. Ti-rich and -poor silicide still existed in the bulk after the heat treatment and the maximum Ti concentration had increased from 9.7 to 11.0 at.%. No Ti-rich silicide was detected at the edge. The concentrations of Ti and W in the solid solution were reduced after the heat treatment, particularly Mo. The variation in their concentrations was also reduced, particularly for W.

Table 26: Summary of EDS analysis data (at.%) of the heat treated alloy CM1 processed using an optical float zone furnace at growth rates of 150, 60 and 12 mm/hr, including the SD, minimum and maximum values.

150 mm/hr								
Element	**Large Area**		**Prior lamellar microstructure**		**Silicide**		**Solid Solution**	
	Bulk	Edge	Bulk	Edge	Bulk	Edge	Bulk	Edge
Nb	60.1 ± 0.41 59.7 - 60.8	59.0 ± 0.69 57.8 - 59.6	61.9 ± 0.85 60.2 - 62.6	62.2 ± 0.79 60.8 - 62.8	50.7 ± 1.81 49.1 - 53.3	53.7 ± 0.18 53.4 - 54.0	75.6 ± 0.51 75.0 - 76.3	75.7 ± 0.47 75.0 - 76.3
Ti	9.8 ± 0.86 8.5 - 10.9	8.7 ± 0.98 7.7 - 10.3	8.4 ± 0.26 8.0 - 8.3	7.5 ± 0.11 7.4 - 7.7	9.4 ± 1.66 6.8 - 11.0	6.5 ± 0.17 6.3 - 6.8	8.8 ± 0.34 8.4 - 9.4	4.4 ±0.37 4.1 - 5.0
Si	18.9 ± 1.04 17.4 - 20.0	22.9 ± 0.46 22.2 - 23.5	21.0 ± 1.20 19.9 - 23.3	20.8 ± 1.58 19.5 - 23.4	37.7 ± 0.42 36.9 - 38.1	37.1 ± 0.20 36.8 - 37.4	0.7 ± 0.32 0.3 - 1.3	0
Mo	7.3 ± 0.59 6.4 - 7.9	5.6 ± 0.45 4.9 - 6.1	5.6 ± 0.40 5.2 - 6.1	5.6 ± 0.44 4.9 - 6.1	1.1 ± 0.40 0.7 - 1.8	1.8 ± 0.22 1.5 - 2.1	10.5 ± 0.27 10.0 - 10.9	11.7 ± 0.35 11.2 - 12.1
Hf	1.2 ± 0.16 0.9 - 1.3	1.0 ± 0.10 0.8 - 1.1	0.6 0.3 - 0.8	0.6 0.2 - 0.8	1.1 ± 0.35 0.6 - 1.6	0.6 0.5 - 0.7	0.2 0.1 - 0.3	0
W	3.0 ± 0.4 2.9 - 3.6	2.7 ± 0.18 2.5 - 3.0	2.6 ± 0.48 2.0 - 3.4	3.4 ± 0.49 2.6 - 3.9	0.1 0.0 - 0.3	0.2 0.1 - 0.3	4.3 ± 0.46 3.9 - 5.2	8.2 ± 0.15 7.9 - 8.3

60 mm/hr								
Element	**Large Area**		**Prior lamellar microstructure**		**Silicide**		**Solid Solution**	
	Bulk	Edge	Bulk	Edge	Bulk	Edge	Bulk	Edge
Nb	61.0 ± 0.42 60.7 - 61.5	59.3 ± 0.58 58.7 - 60.2	61.7 ± 0.67 60.6 - 62.2	62.6 ± 1.15 60.6 - 63.8	51.8 ± 0.61 51.0 - 52.4	53.7 ± 0.12 53.5 - 53.9	75.1 ± 0.58 74.2 - 75.7	75.3 ± 0.89 74.2 - 76.6
Ti	9.4 ± 0.32 8.9 - 9.8	8.0 ± 0.31 7.6 - 8.3	7.4 ± 0.58 7.0 - 8.4	7.2 ± 0.18 6.9 - 7.5	8.2 ± 0.47 7.7 - 8.9	6.6 ± 0.11 6.4 - 6.7	9.0 ± 1.25 7.0 - 10.8	6.7 ± 0.50 6.2 - 7.4
Si	18.8 ± 0.67 18.1 - 19.8	22.8 ± 1.47 20.3 - 24.1	21.5 ± 1.26 20.5 - 23.7	20.4 ± 1.99 18.4 - 24.0	37.5 ± 0.21 37.2 - 37.7	37.2 ± 0.59 36.3 - 37.8	0.6 ± 0.41 0.0 - 1.3	0.1 0.0 - 0.3
Mo	7.1 ± 0.37 6.6 - 7.5	6.2 ± 0.62 5.6 - 7.2	5.4 ± 0.34 5.1 - 5.9	5.8 ± 0.47 5.2 - 6.4	1.7 ± 0.20 1.4 - 1.9	1.8 ± 0.47 1.2 - 2.5	10.6 ± 0.39 9.8 - 11.0	10.8 ± 0.35 10.3 - 11.2
Hf	1.1 ± 0.21 0.8 - 1.3	1.0 ± 0.08 0.9 - 1.1	0.6 0.4 - 0.6	0.6 0.4 - 0.7	0.8 0.7 - 1.1	0.5 0.4 - 0.8	0.3 0.1 - 0.4	0.1 0.0 - 0.3
W	2.6 ± 0.33 2.1 - 3.0	2.8 ± 0.57 2.1 - 3.6	3.4 ± 0.33 3.0 - 3.8	3.4 ± 0.49 2.5 - 4.0	0	0.2 0.0 - 0.4	4.4 ± 1.32 2.9 - 6.2	7.0 ± 1.18 5.3 - 8.6
12 mm/hr								
Element	**Large Area**		**Prior lamellar microstructure**		**Silicide**		**Solid Solution**	
	Bulk	Edge	Bulk	Edge	Bulk	Edge	Bulk	Edge
Nb	59.8 ± 0.68 58.7 - 60.9	58.9 ± 0.70 58.1 - 60.0	61.8 ± 0.58 60.9 - 62.4	62.1 ± 0.19 62.0 - 62.3	51.4 ± 1.77 48.0 - 53.0	53.5 ± 0.47 53.0 - 54.5	75.9 ± 0.58 75.1 - 76.7	75.3 ± 0.91 74.4 - 76.8
Ti	9.2 ± 0.69 8.2 - 10.3	8.1 ± 0.36 7.8 - 8.7	7.7 ± 0.71 6.9 - 9.0	7.3 ± 0.29 6.9 - 7.7	8.88 ± 1.60 8.2 - 12.0	6.6 ± 0.37 5.9 - 7.1	8.1 ± 0.30 7.6 - 8.4	6.9 ± 0.24 6.6 - 7.3
Si	19.3 ± 1.39 17.6 - 21.4	21.9 ± 1.15 20.2 - 23.4	21.6 ± 0.72 20.6 - 22.7	21.2 ± 0.72 20.8 - 21.6	37.1 ± 0.33 36.6 - 37.5	37.1 ± 0.41 36.6 - 37.8	0.5 0.1 - 1.4	0.7 0.2 - 1.5
Mo	6.8 ± 0.77 5.8 - 7.7	6.0 ± 0.58 5.5 - 7.0	5.4 ± 0.25 4.9 - 5.7	5.6 ± 0.21 5.4 - 5.9	1.7 ± 0.32 1.1 - 2.0	1.9 ± 0.21 1.6 - 2.2	10.3 ± 0.20 10.0 - 10.5	10.4 ± 0.27 10.1 - 10.8
Hf	1.2 ± 0.31 0.8 - 1.6	1.1 ± 0.20 0.8 - 1.4	0.6 0.6 - 0.7	0.6 0.5 - 0.6	0.9 0.6 - 1.4	0.6 0.4 - 0.7	0	0
W	3.8 ± 0.38 3.2 - 4.3	4.0 ± 0.26 3.7 - 4.4	2.8 ± 0.61 1.8 - 3.5	3.3 ± 0.61 3.2 - 3.6	0	0.2 0.0 - 0.4	5.1 ± 1.12 3.9 - 6.7	6.7 ± 0.87 5.0 - 7.3

Similar to the sample grown at 150 mm/hr the large area analysis showed chemical inhomogeneity of Si in the edge of the samples grown at 60 mm/hr. There was also chemical inhomogeneity of Si in the prior-lamellar microstructure where in both areas the Si content was slightly increased. Unlike the sample grown at 150 mm/hr, the large Ti and W chemical inhomogeneity in the solid solution was still present after the heat treatment. Ti and W-rich and -poor solid solution grains were still present in the system. Looking at the elemental differences between pre- and post-

heat treatment the lamellar microstructure analysis showed increased Si and Mo, 1 and 1.1 at.%, respectively, similar to those seen in the sample grown at 150 mm/hr. Also, similar to the latter was the increased Ti concentration in the silicide at the edge compared with the bulk. Reductions were also seen in the Si and Mo concentrations in the solid solution after the heat treatment, 1.4 and 1.7 at.%, respectively, similar to the sample grown at 150 mm/hr.

In the sample grown at 12 mm/hr large area analysis showed that the chemical inhomogeneity of Si was present in both areas after the heat treatment. In the prior-lamellar microstructure the Si concentration had increased in both areas and there was chemical inhomogeneity for Si in the bulk. The Ti macrosegregation seen in the larger area analysis of the cast OFZ alloy was still present in the bulk after the heat treatment but there was no evidence of chemical inhomogeneity of Ti in the prior lamellar microstructure. Increased Si, 1.6 at.%, and decreased Mo, 1.6 at.%, in the latter microstructure, similar to those seen in the sample grown at 150 and 60 mm/hr were seen after the heat treatment. Ti-rich and -poor phases, not seen in the cast OFZ alloy, formed in the bulk structure after the heat treatment. The solid solution had distinct W-rich and W-poor grains, as seen in the cast OFZ alloy but the variation in Ti was reduced. Average reductions of Si, Mo and W, 1.9, 1.7 and 2 at.% respectively, were seen in the solid solution post heat treatment.

Figure 99 shows backscattered electron images of silicide grains in the heat treated OFZ alloy CM1 solidified at the three growth rates. After the heat treatment silicide grains had internal structures (subgrains) with lighter contrast silicide areas bordered by darker ones. These structures formed a “crazy pavement” type pattern throughout the light contrast silicide which was more pronounced in the samples grown at the higher rate. The border regions made up of the dark silicide also contained the largest precipitates which seemed to preferentially form in these dark bands and especially in triple points.

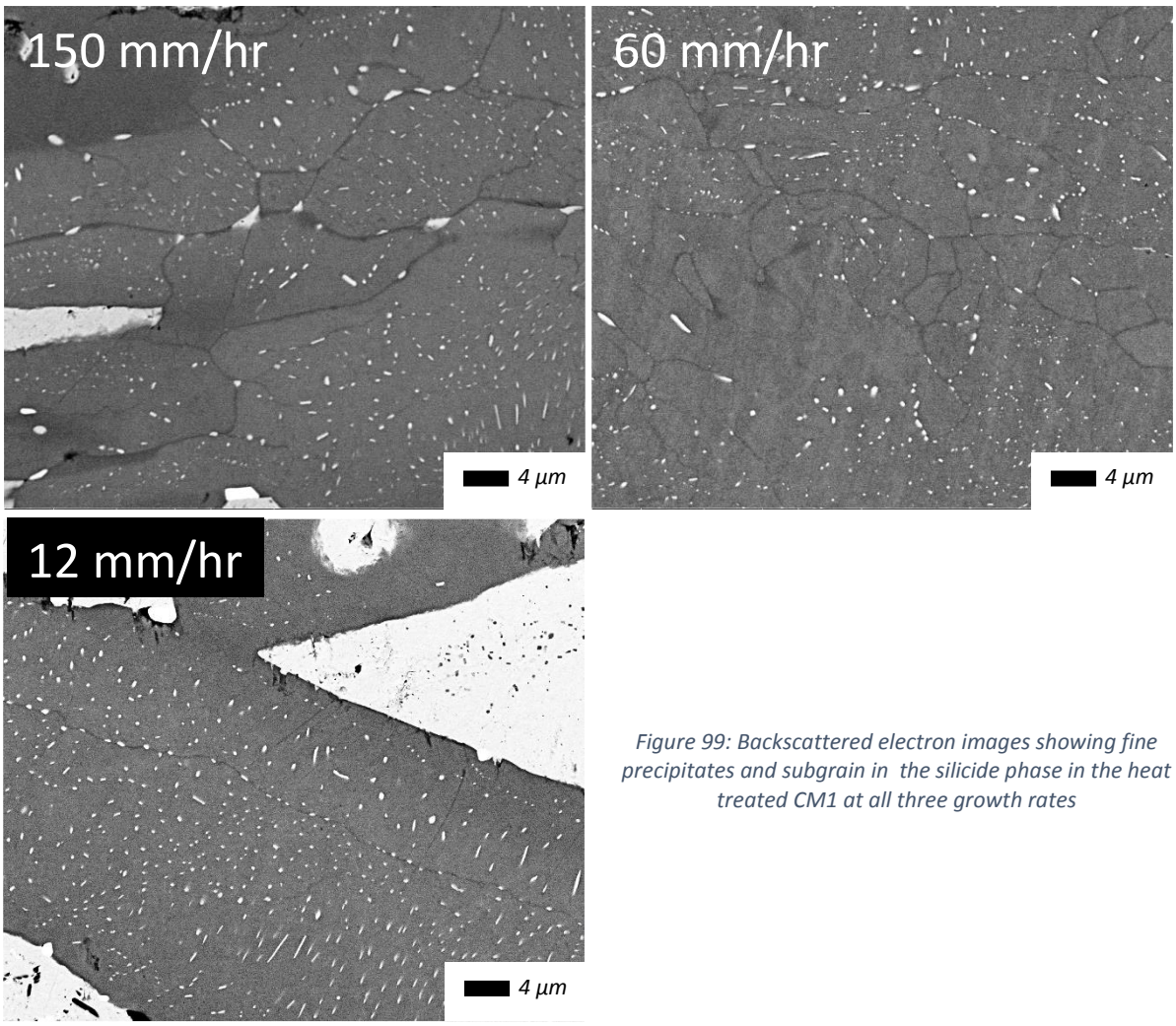

Figure 99: Backscattered electron images showing fine precipitates and subgrain in the silicide phase in the heat treated CM1 at all three growth rates

Similar to the OFZ alloy CM1 there were visually very little differences between the microstructures in the as-cast and heat treated conditions in the samples grown at 150 and 60 mm/hr, see Figure 100. The major difference was in the microstructure of the sample grown at 12 mm/hr and it was for the silicide phase. Whereas in the as-cast condition two distinct silicides were present only the darker contrast α-Nb_5Si_3 was present after the heat treatment as the Nb_3Si had fully transformed, see Figure 90. This was confirmed by the EDS analysis and XRD, Table 27 and Appendix B Fig 8 respectively. In the solid solution phase in the sample grown at 12 mm/hr there was, qualitatively, an increase in the size of the small dark phase present in this phase (Figure 88). There was also a dramatic increase in the volume fraction of hafnia after the heat treatment for all growth, rates Figure 90.

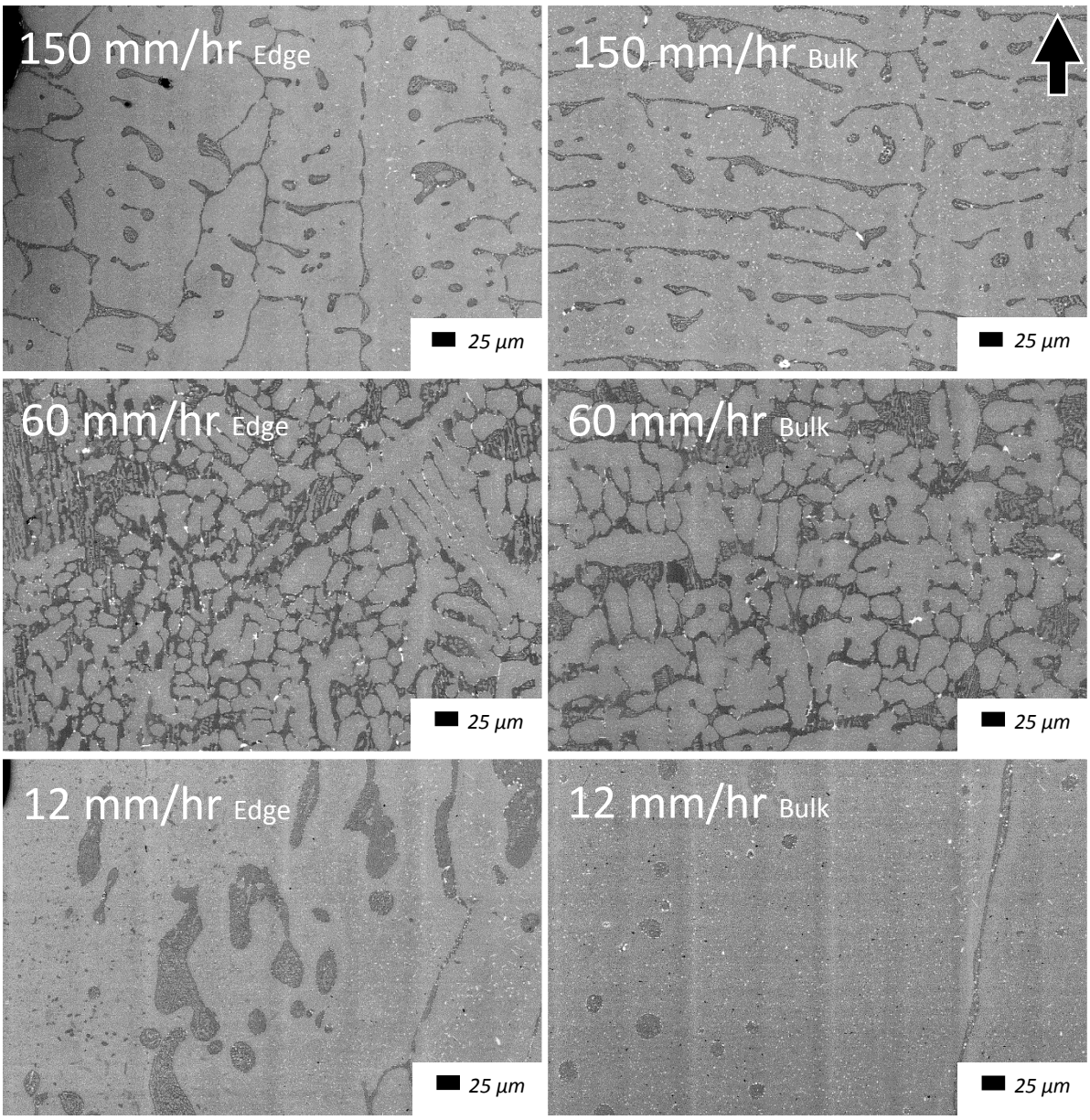

Figure 100: Backscattered electron images of the heat treated alloy CM2 processed using an optical float zone furnace at 3 different growth rates 150 mm/hr, 60 mm/hr and 12 mm/hr from top to bottom respectively. Left hand images show the edge microstructure and right hand images the bulk microstructure. Arrow indicates the growth direction.

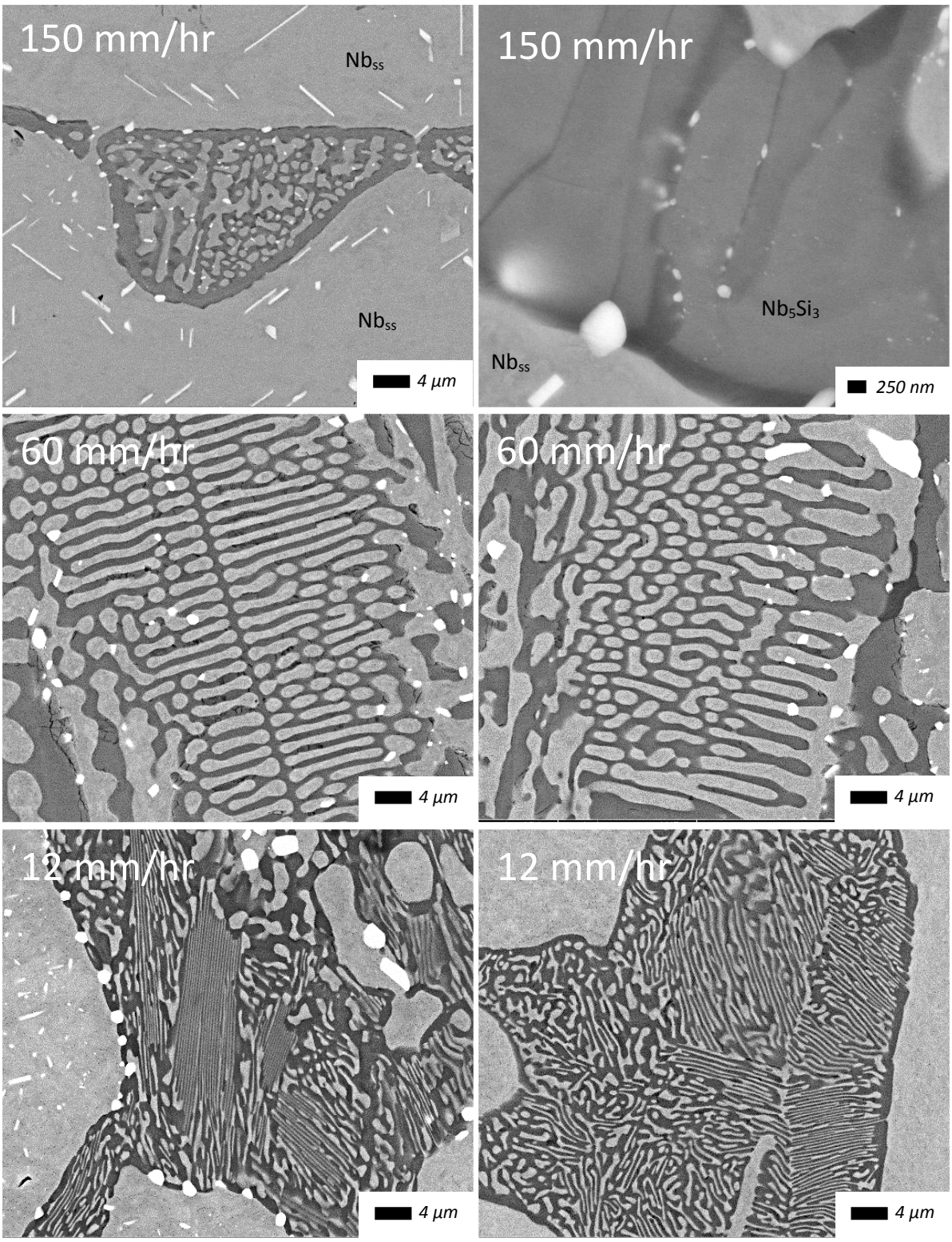

Figure 101: Backscattered electron images of lamellar microstructures and subgrains in Nb_5Si_3 taken from heat treated samples of alloy CM2 OFZ.

Table 27: EDS analysis (at.%) of the heat treated alloy CM2 processed using an optical float zone furnace at growth rates of 150, 60 and 12 mm/hr.

150 mm/hr								
Element	**Large Area**		**Prior lamellar microstructure**		**Silicide**		**Solid Solution**	
	Bulk	Edge	Bulk	Edge	Bulk	Edge	Bulk	Edge
Nb	92.0 ± 1.33 90.1 - 93.8	91.8 ± 2.06 88.8 - 93.8	75.5 ± 0.92 74.3 - 77.0	74.7 ± 0.32 74.2 - 75.1	58.6 ± 0.81 57.7 - 60.0	56.8 ± 0.74 55.7 - 58.2	96.2 ± 1.52 93.8 - 97.5	95.1 ± 1.99 91.7 - 97.1
Si	5.6 ± 1.08 4.0 - 7.0	5.8 ± 1.72 4.2 - 8.3	21.9 ± 0.83 20.4 - 23.0	22.4 ± 0.40 22.0 - 23.0	38.3 ± 0.62 37.1 - 39.1	38.8 ± 0.33 38.0 - 39.1	2.2 ± 1.61 0.82 - 4.9	2.3 ± 1.20 1.1 - 4.3
W	1.1 ± 0.16 0.9 - 1.3	1.1 ± 0.20 0.8 - 1.3	0	0	0	0	1.5 ± 0.08 1.4 - 1.6	1.5 ± 0.23 1.2 - 1.8
Hf	1.3 ± 0.27 0.9 - 1.7	1.3 ± 0.18 1.1 - 1.6	2.6 ± 0.22 2.2 - 2.9	2.9 ± 0.22 2.7 - 3.3	4.0 ± 0.33 3.7 - 4.7	4.4 ± 0.56 3.7 - 5.5	0.1 ± 0.1. 0.0 - 0.3	1.1 ± 1.17 0.0 - 2.7
60 mm/hr								
Element	**Large Area**		**Prior lamellar microstructure**		**Silicide**		**Solid Solution**	
	Bulk	Edge	Bulk	Edge	Bulk	Edge	Bulk	Edge
Nb	86.9 ± 1.74 84.6 - 89.2	84.3 ± 2.61 81.0 - 87.3	75.6 ± 1.41 73.8 - 77.9	75.3 ± 0.95 74.0 - 76.6	56.8 ± 1.21 55.5 - 59.1	58.7 ± 2.06 56.5 - 62.5	95.8 ± 0.50 94.8 - 96.4	96.0 ± 0.10 95.9 - 96.2
Si	9.0 ± 1.55 7.2 - 11.1	12.0 ± 2.55 8.9 - 13.7	20.5 ± 1.46 18.3 - 22.6	21.2 ± 0.80 20.0 - 22.2	38.5 ± 1.37 35.8 - 39.3	37.8 ± 0.93 36.4 - 38.8	0.8 ± 0.16 0.7 - 1.1	0.7 ± 0.12 0.5 - 0.8
W	2.1 ± 0.23 1.8 - 2.4	1.6 ± 0.17 1.4 - 1.9	0.7 0.5 - 1.0	0.6 0.5 - 0.8	0	0	3.1 ± 0.09 2.5 - 3.4	3.2 ± 0.17 3.1 - 3.6
Hf	2.0 ± 0.11 1.9 - 2.2	2.1 ± 0.15 1.9 - 2.2	3.0 ± 0.17 2.8 - 3.2	3.0 ± 0.24 2.6 - 3.3	4.7 ± 0.5 4.4 - 5.5	3.6 ± 1.58 0.5 - 4.9	0.2 ± 0.41 0.0 - 0.5	0.1 ± 0.06 0.0 - 0.2
12 mm/hr								
Element	**Large Area**		**Prior lamellar microstructure**		**Silicide**		**Solid Solution**	
	Bulk	Edge	Bulk	Edge	Bulk	Edge	Bulk	Edge
Nb	93.8 ± 0.59 93.2 - 94.7	92.5 ± 0.55 91.9 - 93.1	75.2 ± 1.59 71.7 - 76.4	73.2 ± 1.66 71.6 - 75.8	59.4 ± 0.52 58.9 - 60.2	61.0 ± 1.23 58.8 - 62.7	97.7 ± 0.73 96.1 - 98.2	97.4 ± 0.36 96.9 - 97.9
Si	5.1 ± 0.59 4.5 - 5.8	6.1 ± 0.13 6.0 - 6.3	22.2 ± 1.59 21.0 - 25.7	25.1 ± 1.50 22.7 - 26.6	37.6 ± 0.80 36.3 - 38.6	37.0 ± 0.87 35.9 - 38.5	2.1 ± 0.68 1.5 - 3.6	2.4 ± 0.31 1.9 - 2.9
W	0.2 0.1 - 0.4	0.2 0.0 - 0.5	0	0	0	0	0.2 ± 0.09 0.1 - 0.3	0.1 ± 0.06 0.0 - 0.2
Hf	0.9 0.7 - 1.1	1.1 ± 0.48 0.6 - 1.7	2.6 ± 0.27 2.3 - 3.2	1.7 ± 0.36 1.1 - 2.1	3.0 ± 0.41 2.5 - 3.5	2.0 ± 0.41 1.4 - 2.7	0.1 ± 0.12 0.0 - 0.3	0.2 ± 0.26 0.0 - 0.7

Considering the EDS analysis data in Table 27, significant chemical inhomogeneity of Si was noted for the two highest growth rates in the larger area analyses and for all three growth rates for

the lamellar microstructure analysis. Thus the chemical inhomogeneity of Si that was present in the latter lamellar microstructure of the cast OFZ samples was still present after heat treatment. Differences in Si content were also noted in the silicide and solid solution, in the former presumably due to the transformation of Nb_3Si and in the latter due to the second dark contrast phase. At 150 mm/hr both silicide and solid solution phases showed variations in their Si content. In the samples grown at 60 and 12 mm/hr variations in Si content were found only in the silicide at 60 mm/hr and in both phases for 12 mm/hr but to a lesser extent than that seen in the sample grown at 150 mm/hr.

Comparing the pre-and post-heat treatment samples grown at 60 mm/hr, the solid solution had reduced Si and Hf concentrations by almost 2 at.% and 1.5 at.%, respectively. At the same growth rate there was also an increase of over 1 at.% in tungsten. These changes in elemental concentrations within the phases were not seen at the other two growth rates. The only other significant change in elemental concentrations pre-and post-heat treatment in the sample grown at 12 mm/hr was in the Si concentration in the silicide due to the Nb_3Si phase not existing after the heat treatment.

3.3.4 Conclusions

Two near eutectic alloys with nominal compositions Nb-8.3Ti-21.1Si-5.4Mo-4W-0.7Hf (CM1) and Nb-20.5Si-5.8W-4Hf (CM2) were prepared using OFZ solidification processing at three growth rates, 12, 60 and 150 mm/h and were studied in the cast and heat treated (1500 ^{O}C/100 hrs) conditions.

The feed materials of the OFZ alloys were the CM1 600 g and CM2 500 g ingots. The alloys grown under stable OFZ conditions were studied. In the case of the alloy CM2, significant deviations of the microstructure compared with those observed in the feed ingot were observed. Thus, the cast alloy CM2 was also studied for conditions of non-stable growth at the beginning, during and the end of the OFZ process.

In the alloy CM1 OFZ the microstructures were similar for the three growth rates in both the cast and heat treated conditions. In the cast alloy, there was macrosegregation of Si in all three growth

rates and of Ti at 12 mm/h. The microstructures consisted of Nb_{ss} and α-Nb_5Si_3 and there was no evidence of subgrains in the latter. There were differences in chemical composition between the edge and centre of the OFZ bar, the edge was richer in Si and poorer in Ti. There were also differences in chemical composition of the lamellar microstructures between edge and centre, in the edge the latter was poorer in Si and in Ti. The Nb_{ss} in the edge was poorer in Ti, richer in Mo, W. Light and dark contrast areas were formed in Nb_5Si_3 grains in all three growth rates, in the former areas fine spherical or needle like precipitates of light contrast second phase particles of different morphology were observed in the same Nb_5Si_3 grain.

In the heat treated alloy CM1 OFZ there was chemical inhomogeneity over large areas and in phases, the latter were the Nb_{ss} and α-Nb_5Si_3. In the 150 mm/h sample there were chemical inhomogeneities in the bulk for Ti and Si and of Si in the bulk and edge of lamellar microstructures, and the Nb_{ss} was Si free. In the 60 mm/h there was chemical inhomogeneity of Si in the edge and of Si in the bulk and edge of lamellar microstructures, and of Ti and W in the Nb_{ss}. In the 12 mm/h sample there was chemical inhomogeneity of Si and Ti in the bulk and of Si in the bulk in the lamellar microstructures. Subgrains and fine precipitates were observed in Nb_5Si_3 grains in all three growth rates, the former were more pronounced in the samples grown at 60 and 150 mm/h.

In the case of the alloy CM2 OFZ, in the bars that solidified under stable OFZ conditions, the average chemical composition was significantly different than that of the parent (feed) ingot, particularly for Si, Hf and W. This was attributed to strong segregation (chemical inhomogeneities) developing at the start of OFZ, during OFZ and at the end of OFZ.

In the bars that were grown under stable OFZ conditions at 150 and 60 mm/h the phases were Nb_{ss} and α-Nb_5Si_3. In the bar grown under stable conditions at 12 mm/h the phases were the Nb_{ss}, Nb_3Si and α-Nb_5Si_3. In the 12mm/h bar there were precipitates in the Nb_{ss}. In all three growth rates cells of lamellar microstructure were formed between the Nb_{ss}. The cells in the 12 mm/h sample exhibited different contrast owing to the presence of the Nb_3Si and αNb_5Si_3 silicides.

Only the samples of the alloy CM2 that were grown under stable OFZ conditions were heat treated at 1500 C for 100 h. There was chemical inhomogeneity of Si in the samples grown at 150 and 60 mm/h. Similar microstructures with the cast CM2 OFZ were observed for 150 and 60 mm/h, with the microstructure consisting of Nbss and α-Nb_5Si_3. In the 12 mm/h sample the same phases were observed, in other words the Nb_3Si had fully transformed. The Nbss contained Si for all three growth rates. There were second phase particles in the Nb_{ss} and the Si content in the Nb_{ss} was high (compared with other heat treated Nb silicide alloys) for 150 and 12 mm/h.

3.4 Eutectic Spacing and Volume Fraction

3.4.1 10 g and 600/500 g Buttons

Figure 102 and Figure 103 respectively show plots of the eutectic spacing (λ) verses silicide volume fraction (V_f) in the eutectic in the alloy CM1 and CM2 buttons before and after heat treatment. In the alloy CM1 and CM2 10g buttons the λ and V_f were measured at 5 different evenly spaced locations through the sample, from the bottom next to the water cooled copper crucible (location A) to the top open to the argon atmosphere (location E). In the 600/500 g ingots the measurements were only taken from the bulk.

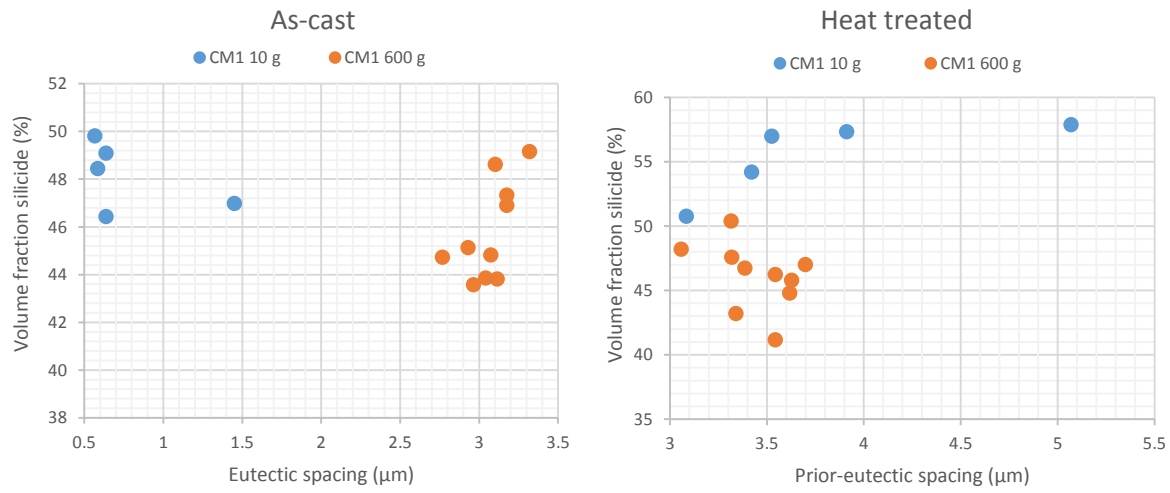

Figure 102: The volume fraction of silicide and the (prior) eutectic spacing in different areas of the 10 g and 600 g CM1 ingot in the as-cast and heat treated conditions.

In the bulk of the as-cast alloy CM1 10 g sample (B-D) the V_f silicide was between 48 and 50 % and the λ values did not vary significantly from 0.5 µm, Figure 102. The average λ for location A (anomalous eutectic) was significantly larger (1.44 µm) and the silicide V_f in the eutectic was slightly lower (47.0 %). Figure 104I shows the region of anomalous eutectic (coarse two phase Nb_{ss} and Nb_5Si_3) in location A. The λ values of location E were similar to that of the bulk but the V_f of the silicide was closer to that of location A. In the case of the alloy 600 g as-cast ingot there was less of a spread of the λ values, 2.8 - 3.3 µm, than in the 10 g button. There was however two distinct groups of the data;

highest silicide V_f (average 48.0 %) with highest λ (average 3.2 µm) and lowest silicide V_f (average 44.3 %) with lowest λ (average 3.0 µm). The average eutectic spacing and the average V_f of silicide for the bulk of the alloy CM1 10 g button and 600 g as-cast ingots were 0.6 µm and 49.1 % and 3.1 µm and 45.8 %, respectively.

The data for the heat treated alloy, Figure 102, for the 10 g ingot showed a large increase in spacing between the phases in the prior-eutectic and V_f, where the average increase in the bulk was 2.7 µm and 4.9 %, respectively. Therefore still a marked difference between the bulk and the edges. In location E the silicide V_f was reduced and the spacing increased slightly more than the bulk average. In the location A on the other hand, there were increases in both spacing and V_f by more than the bulk average. The spacing of phases in the prior-eutectic and V_f in the 600 g sample only increased by 0.4 µm and 0.3 % respectively.

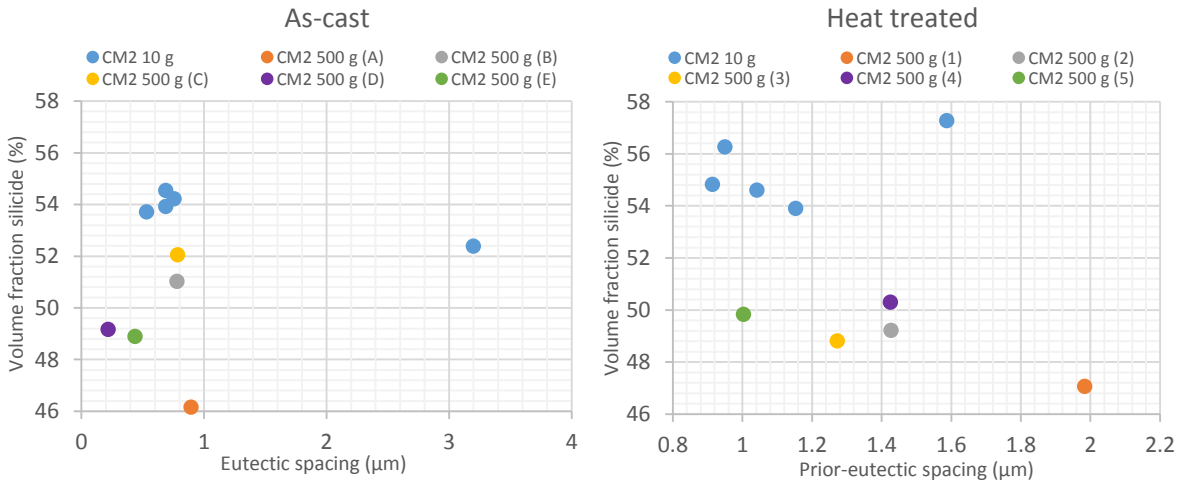

Figure 103: The volume fraction of silicide and the (prior) eutectic spacing in different areas of the 10 g and 500 g CM2 ingot in the as-cast and heat treated conditions

In the as-cast alloy CM2 10 g button the majority of results (locations B to E) were within the range 53.7 to 54.5 % and 0.5 to 0.8 µm for V_f and λ respectively, Figure 103. However, similar to the CM1 counterpart, the λ and V_f for the location of highest cooling (A) were significantly different, with average values 3.2 µm and 52.4 %, respectively. Figure 104II shows a zone of Nb_{ss} and Nb_5Si_3 (anomalous eutectic) in the bottom followed by the "regular" microstructure associated with alloy

CM2 10 g cast button. As shown in § 3.1.2 there were 5 distinctive microstructures of interest in the alloy CM2 500 g ingot. An average value for both λ and V_f was calculated for each area. Areas (locations) A, B and C all had very similar eutectic spacing; 0.9, 0.8 and 0.8 µm respectively. However the area A had significantly less silicide in the eutectic compared with the areas B and C where the V_f was 46.2, 51.0 and 52.2 %, respectively. The values of λ and V_f in the areas D and E were only 0.2 µm and 49.2 % and 0.4 µm and 48.9 %, respectively. The overall average values for the bulk of the alloy CM2 500 g was 0.6 µm and 49.9 % for λ and the silicide V_f, respectively. The average value for the bulk of the alloy CM2 10 g button were 0.7 µm and 54.1 %, respectively.

Similar to the λ and V_f values for the bulk of the alloy CM1 the average values for λ and V_f for the bulk of the alloy CM2 10 g button increased after the heat treatment. However, the increases of V_f and λ for the alloy CM2 10 g button were much smaller, 0.8 % and 0.3 µm, respectively. In the area of highest cooling the λ decreased by 1.6 µm and the V_f increased by 4.9 %. The overall average eutectic spacing of the alloy CM2 500 g ingot increased by 0.8 µm whereas the V_f of the silicide decreased by 0.4 %. However, owing to the dissimilarity between the as-cast and heat treated microstructures and EDS analysis a direct comparison of CM2 500 g pre and post heat treatment could not be made.

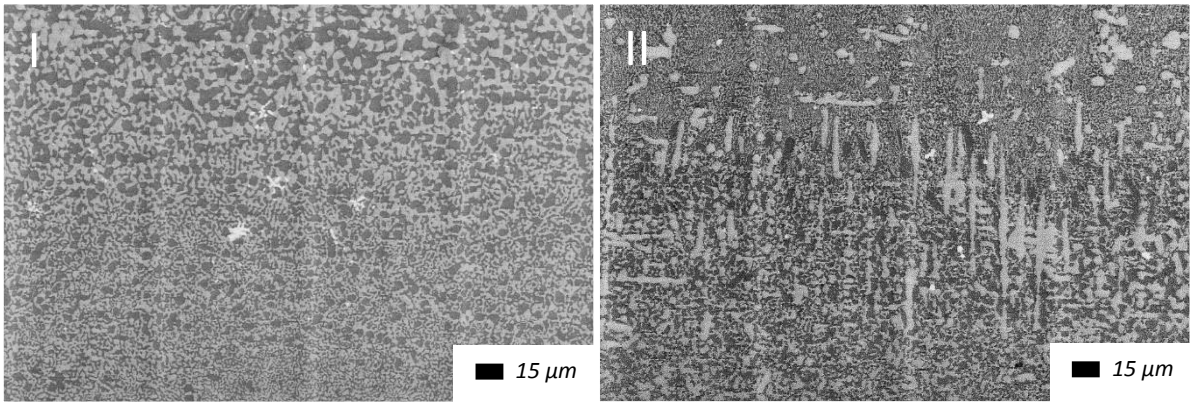

Figure 104: Backscattered electron images of location A for (I) alloy CM1 10 g cast button and (II) alloy CM2 10 g cast button

3.4.2 6 mm Suction Cast Ingots

In the suction cast bars the silicide volume fraction and the eutectic spacing were measured in different areas along the edge and centre of the bar, from the area of highest cooling, area A. The graphs in Figure 105 to Figure 108 represents an area (A to J) of the suction cast bar.

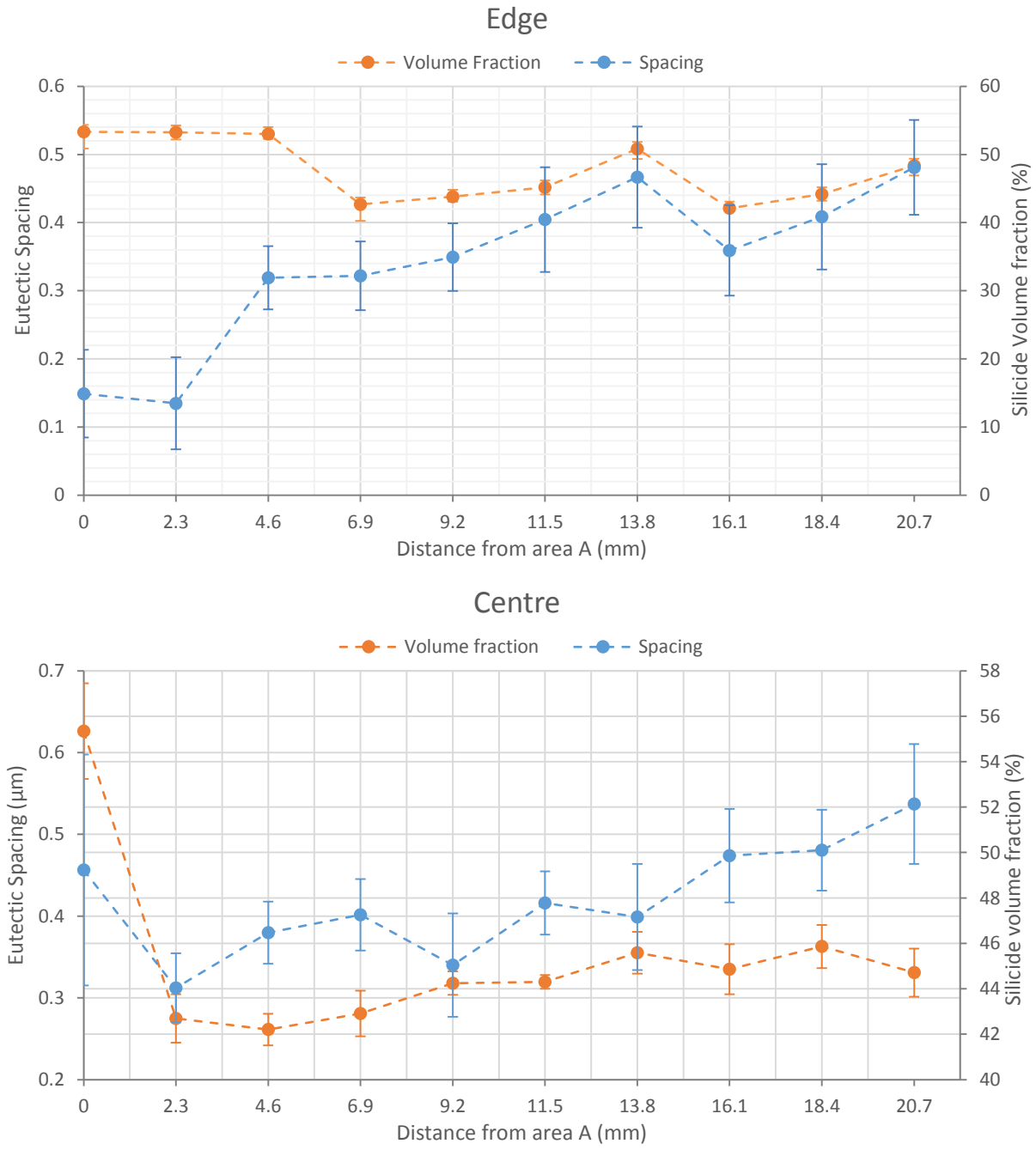

Figure 105: The change in λ and silicide V_f with distance from the area of highest cooling rate along the edge and centre of the as-cast alloy CM1 6 mm suction cast bar including SD.

Figure 105 shows how the silicide V_f and average λ along the edge and centre of the as-cast CM1 6 mm suction cast bar changed with distance from the area of highest cooling, i.e. area A. Along the edge from area A to area D, there was no trend between these two parameters. The V_f decreased significantly between areas C and D while λ remained relatively constant. From area D to area J the two parameters "traced" each other. A similar pattern was not seen along the centre of the bar. Following the initial drop in V_f and λ from area A to B, there was a general increase in both parameters from area B to area J, but the trend in the change of end parameters with the changing cooling rate was not the same, in fact, in most cases it was opposite to each other, i.e. as one increased the other decreased. The λ along the centre and edge increased with increasing distance from area A. The V_f increased in the centre with distance from area B. The relatively large standard deviation of the λ in area A at the centre should also be noted. This is attributed to the large variation in microstructure in this area due to the high cooling rates. A slightly higher SD can also be seen in the V_f in this area, but it is not as dramatic as that for λ. The average silicide V_f, was 46.4 and 45.3 % along the edge and centre, respectively and the average λ along the edge and centre of the bar was 0.34 and 0.42 µm, respectively.

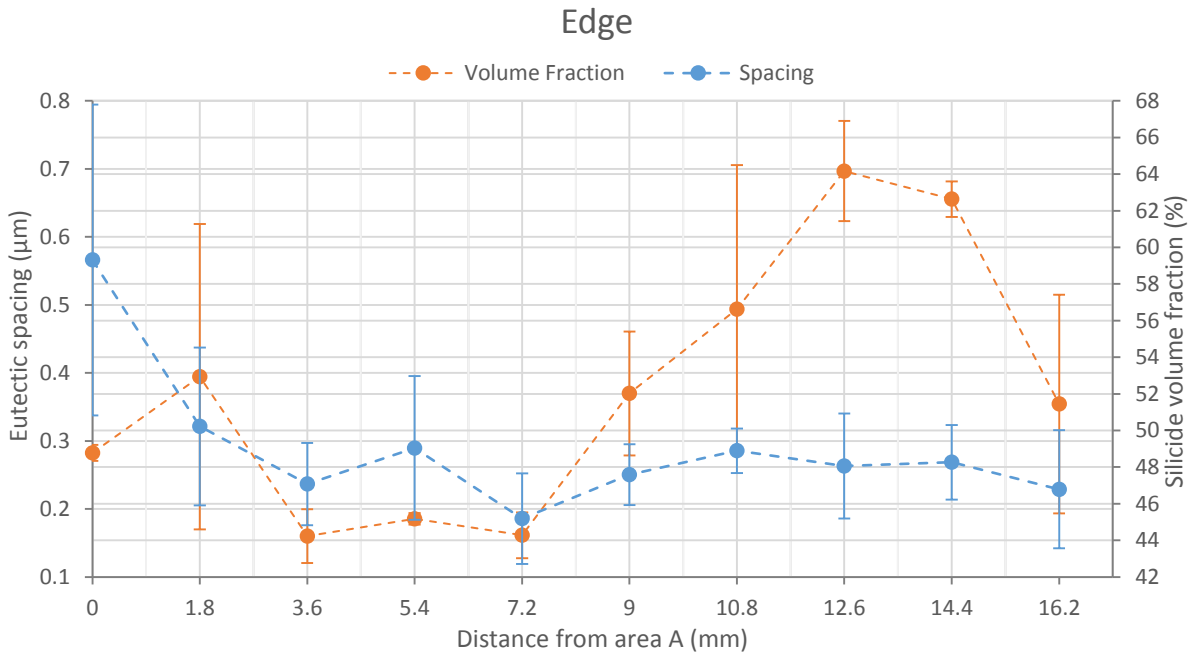

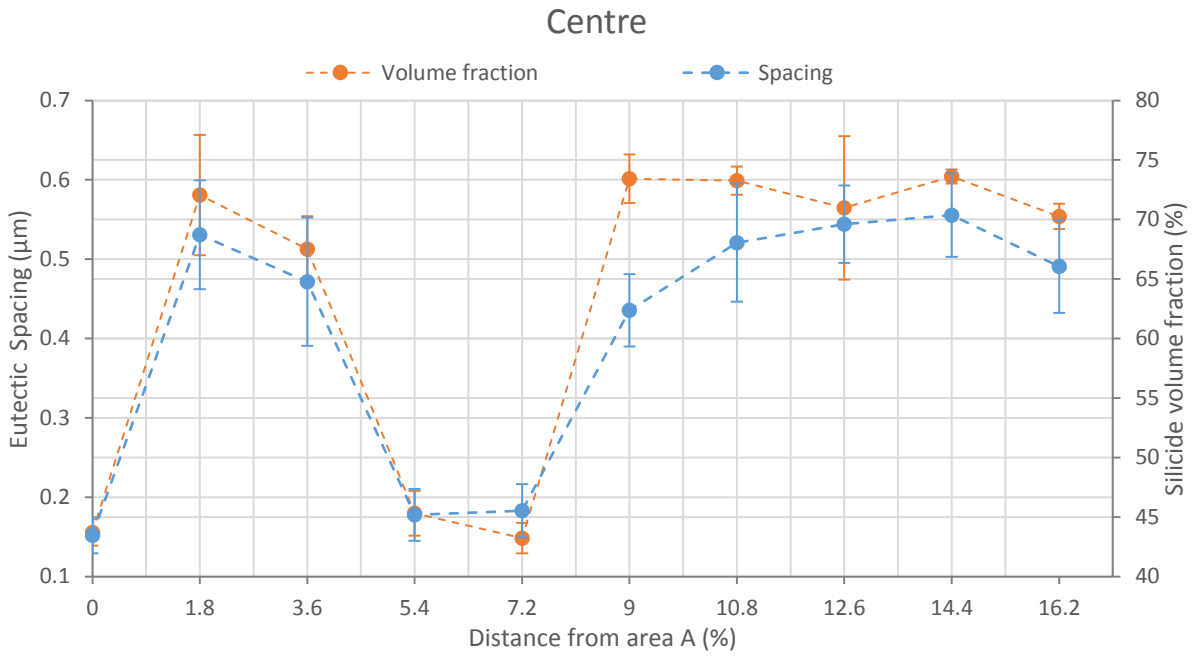

Figure 106: The change in λ and silicide V_f with distance from the area of highest cooling rate along the edge and centre of as-cast alloy CM2 6 mm suction cast bar including SD.

For the as-cast alloy CM2 6 mm bar, similar to the alloy CM1 6 mm bar, average values of λ and V_f along the edge and the centre of the bar were plotted against distance from the area of highest cooling rate (A), Figure 106. It should be remembered that in this alloy there was evidence of Nb_3Si and its eutectoid, formation to a fine mixture of Nb_{ss} and α-Nb_5Si_3. Along the edge the two parameters seemed to follow each other from areas B to area J. Between A and B the λ decreased and the V_f increased and from H to J the decrease of the V_f was more dramatic. Along the centre of the bar the trend in the changing of both parameters was almost identical. Comparing the data for λ and V_f along the edge and the centre of the CM2 6 mm bar showed very little similarities in either λ or V_f. High standard deviations can be seen for the λ in area A and in the V_f in areas B and G along the edge. The high deviation in the λ, similar to the alloy CM1 6 mm bar, can be explained by the solidification conditions causing large changes in the microstructure in these areas. The high deviations in volume faction occurred in areas where a contrast difference can be seen in the anomalous eutectic (see, § 3.2.1) which could indicate a change in volume fraction between the two contrast areas. The spacing in the centre was also more varied in the areas B, C and G; the areas where there was a dramatic

change in structure as stated in § 3.2.1. The average λ increased from the edge, 0.29 µm, to the centre, 0.41 µm. The average value of the silicide V_f along the edge and centre were 51.9 and 63.3 %, respectively.

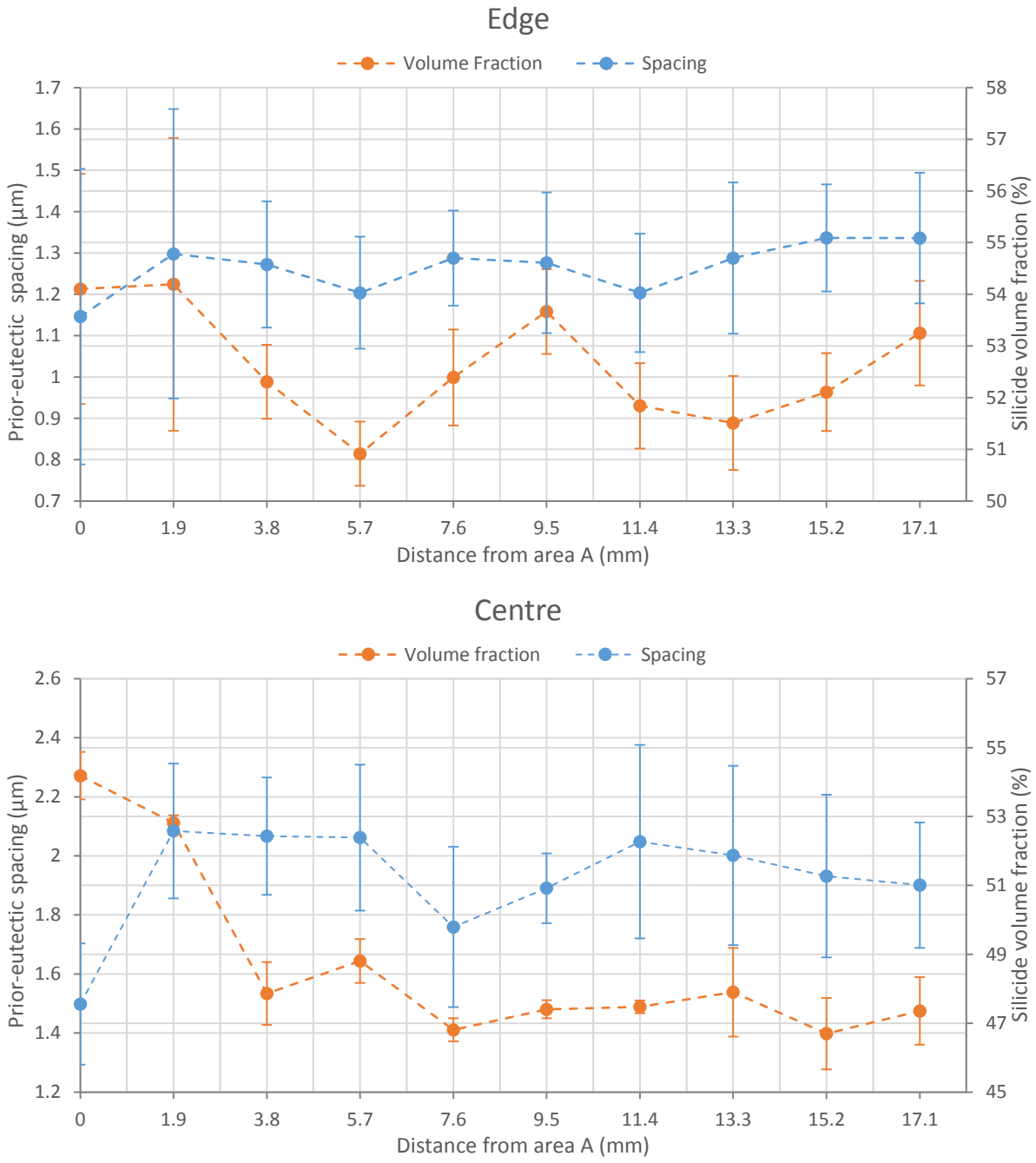

Figure 107: The change in λ and silicide V_f with distance from the area of highest cooling rate along the edge and centre of the heat treated alloy CM1 6 mm suction cast bar including SD.

Figure 107 shows how the prior-eutectic spacing (prior-λ) and silicide V_f changed along the edge and centre of the heat treated alloy CM1 6 mm bar with distance from area A. Along the edge the trend in λ and V_f was the same from area B to G. From A to B the increase in λ was more dramatic. Along the centre the trend in the changes of λ and V_f was the same from area D to G with a dramatic decrease in V_f from A to C and increases in the λ from A to B. The trend of λ increasing with distance from area A seen in the cast bar was not seen for the prior- λ.

The average spacing differences pre- and post-heat treatment along the edge of the alloy CM1 6 mm bar was 0.92 µm (i.e. $\lambda_{post}^{average} - \lambda_{pre}^{average} = 0.92\ \mu m$) with a maximum increase, in area B, of 1.6 µm. The silicide V_f had increased on average by 6.0 % (i.e. $V_{f\ post}^{average} - V_{f\ pre}^{average} = 6.0\ \%$). Unlike the spacing there was a decrease in silicide V_f in one area, C, but only by 0.7 %. The maximum increase in V_f was in area H (9.4 %). In the centre of the bar the average spacing had increased by 1.50 µm, with a maximum, in area B, of 1.77 µm. The average V_f increased by only 3.5 % with a maximum increase of 5.7 %, area C. Similar to the centre there was only one area that decreased in V_f silicide after heat treatment, area A.

The heat treated alloy CM2 6 mm bar showed two distinct and opposing patterns along the edge, see Figure 108. In the initial section of the bar, A to E, the change in prior-λ and the V_f exhibited a very similar trend with increasing distance from A. In the second half of the bar, E to J, the two parameters showed opposite trends, when the prior-λ increased the V_f decreased. Opposite trends in the changes of prior-λ and V_f were also seen along the centre of the bar.

Comparing the pre-and post-heat treatment data showed an increase in spacing by 1.20 µm and 0.51 µm along the edge and the centre, respectively. The maximum increase was seen in area D, 1.73 µm, along the edge and in area A, 1.52 µm, along the centre. However, unlike the alloy CM1 6 mm heat treated bar there was a decrease in the average silicide V_f of 3.5 % and 5.5% at the edge and the centre, respectively. Along the centre of the bar there were some significant increases (18.9 %

area E) and decreases (20.0 % area I) in V_f values compared with the as-cast condition. Only one area, D, along the edge and three areas, A C and E, along the centre showed increases.

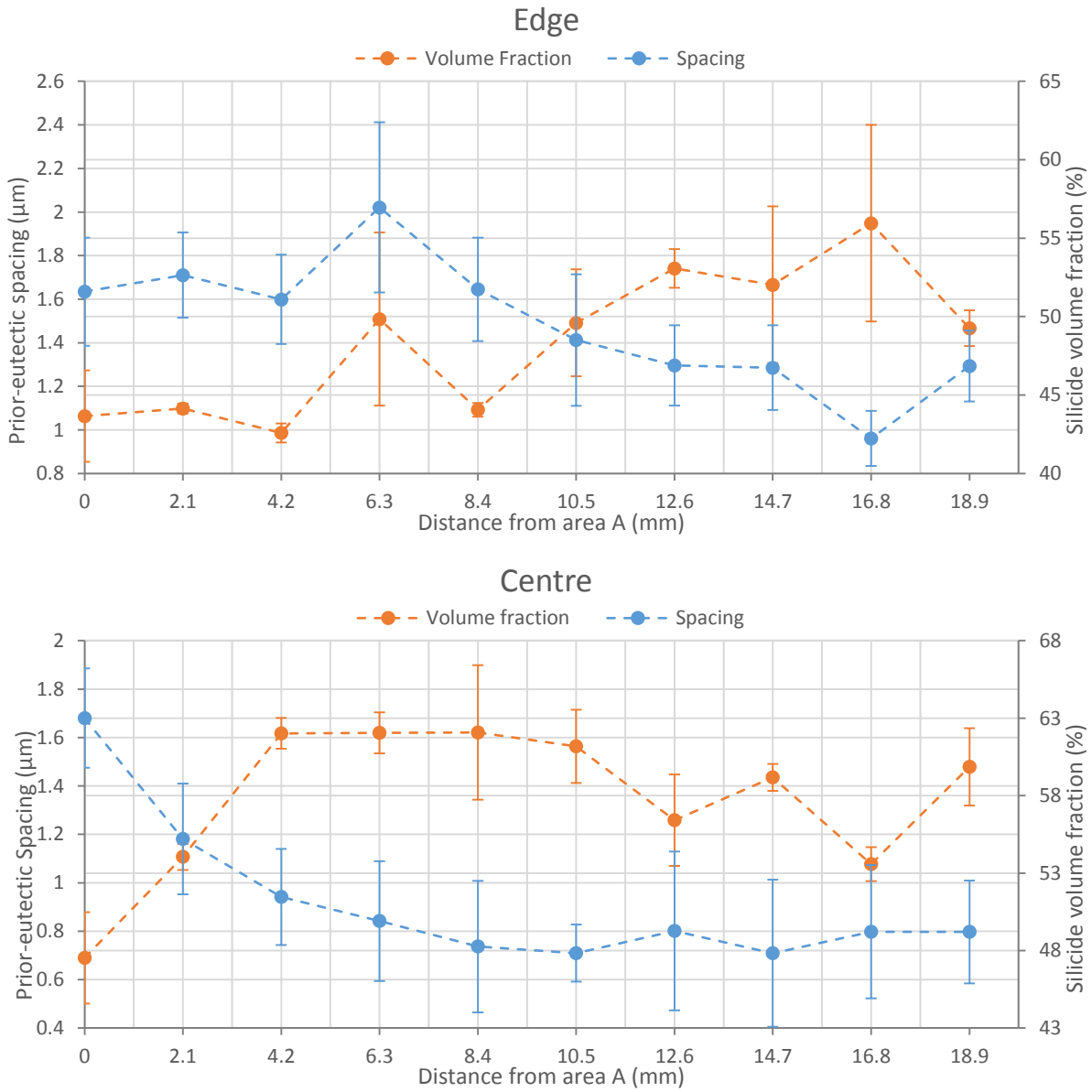

Figure 108: The change in λ and silicide V_f with distance from the area of highest cooling rate along the edge and centre of the heat treated alloy CM2 6 mm suction cast bar including SD.

3.4.3 8 mm Suction Cast Ingots

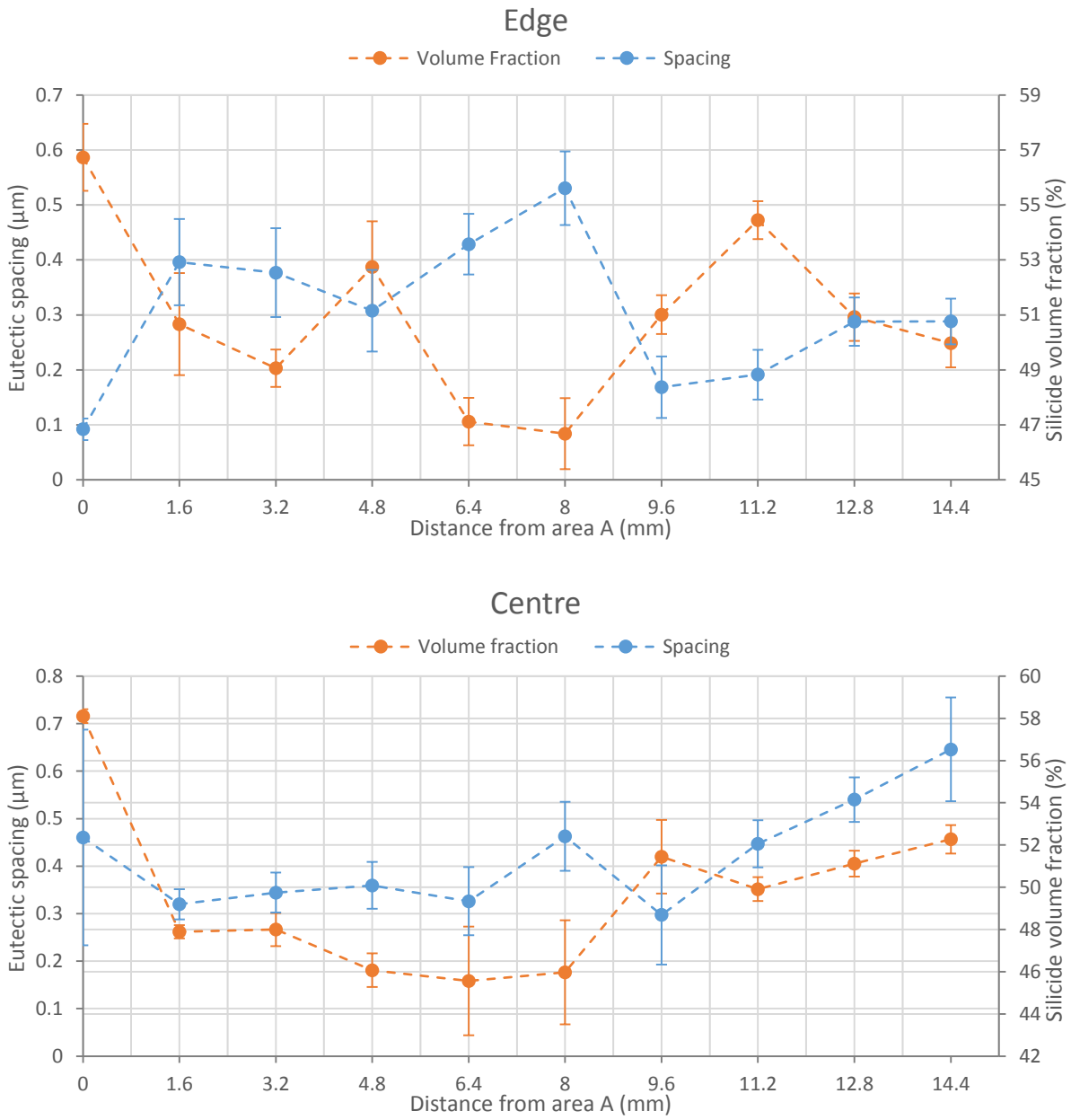

Figure 109: The change in λ and silicide V_f with distance from the area of highest cooling rate at the edge and centre of the as-cast alloy CM1 8 mm suction cast bar including SD.

Figure 109 shows how the λ and silicide V_f changed with increasing distance from area A along the centre and edge of the as-cast alloy CM1 8 mm suction cast bar. Along the edge the trends of the two parameters were opposing from area A to I. Along the centre similar trends were followed from area B to F. Along the edge from A to B the λ and V_f increased and decreased respectively and along the centre both parameters decreased, the latter was the case in alloy CM1 6 mm as-cast bar, see

Figure 105. There was, similar to the alloy CM1 6 mm bar, a large SD in the data for the λ in the centre at area A. There was however a relatively small deviation from the average at the areas along the edge even though there is a high variation in the microstructure. This indicates that the structure varied greatly from area to area but did not vary greatly within the selected area. Comparing the averages along the edge and the centre indicated that spacing at the centre was on average 0.11 μm larger than at the edge. On the other hand the V_f silicide along the edge was, on average, 1.0 % less than that along the centre (centre average = 51.6 %).

In the case of the as-cast alloy CM2 8 mm suction cast bar, the trend in the change of λ and silicide V_f were similar from B to J along the edge and from A to F along the centre, Figure 110. It should be remembered that in the cast microstructure of the alloy CM2 8 mm bar there was evidence of Nb_3Si and its eutectoid decomposition to Nb_{ss} and Nb_5Si_3 between A and B. Along the edge there was a large standard deviation in the λ in the areas B, H and J and in the V_f in area H. The variation in the λ was again most likely due to different eutectic morphology existing in the same area, fine lamellar cells within coarser anomalous eutectics. The large variation in V_f at the edge occurs, similar to the cast alloy CM2 6 mm bar, in an area where there were contrast differences in the anomalous eutectic. In the centre of the bar there was only one area where the standard deviation of the λ became relatively large; Area F, which could indicate the meeting point of the two different eutectic morphologies shown in Figure 75. Comparing the average spacing along the entire edge to the average along the centre showed that the average along the centre (0.41 μm) was 0.12 μm higher than that at the edge. The average silicide V_f was also slightly higher along the centre (49.7 %) compared to the average along the edge 49.1 %.

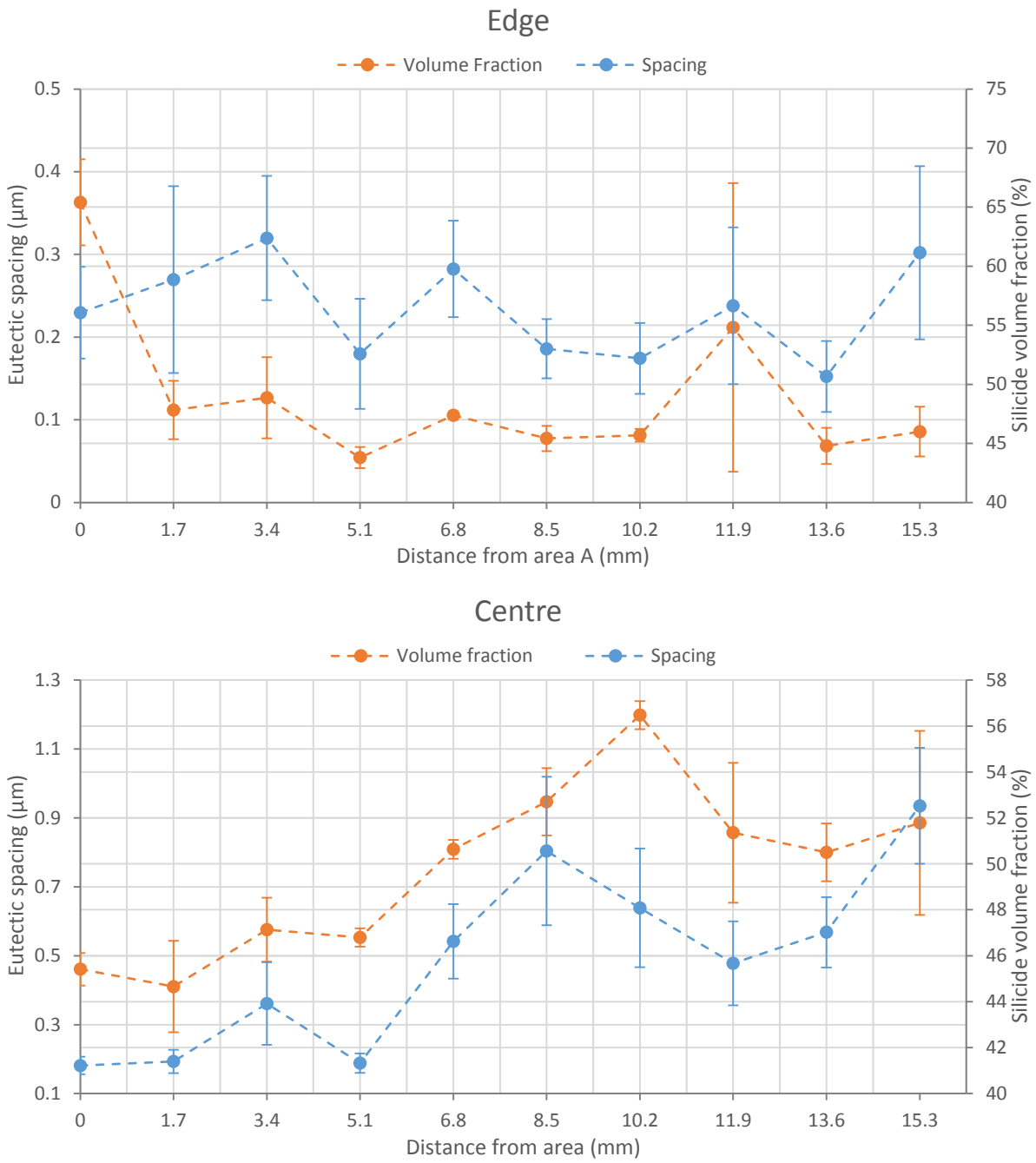

Figure 110: The change in λ and silicide V_f with distance from the area of highest cooling rate at the edge and centre of the as-cast alloy CM2 8 mm suction cast bar including SD.

Data for prior-λ and silicide V_f in the alloy CM1 8mm heat treated bar, Figure 111, show that along the edge the trends in the change of the parameters was very different. In certain areas, e.g. C to D, F to G and I to J the trend was the same. Along the centre, on the other hand, the trend was the same between A to F. The results revealed that the average eutectic spacing increased from along the

edge (prior-λ = 1.79 µm) to along the centre by 0.44 µm. The average silicide V_f on the other hand decreased from an average of 52.5 % along the edge to an average of 50.0 % along the centre.

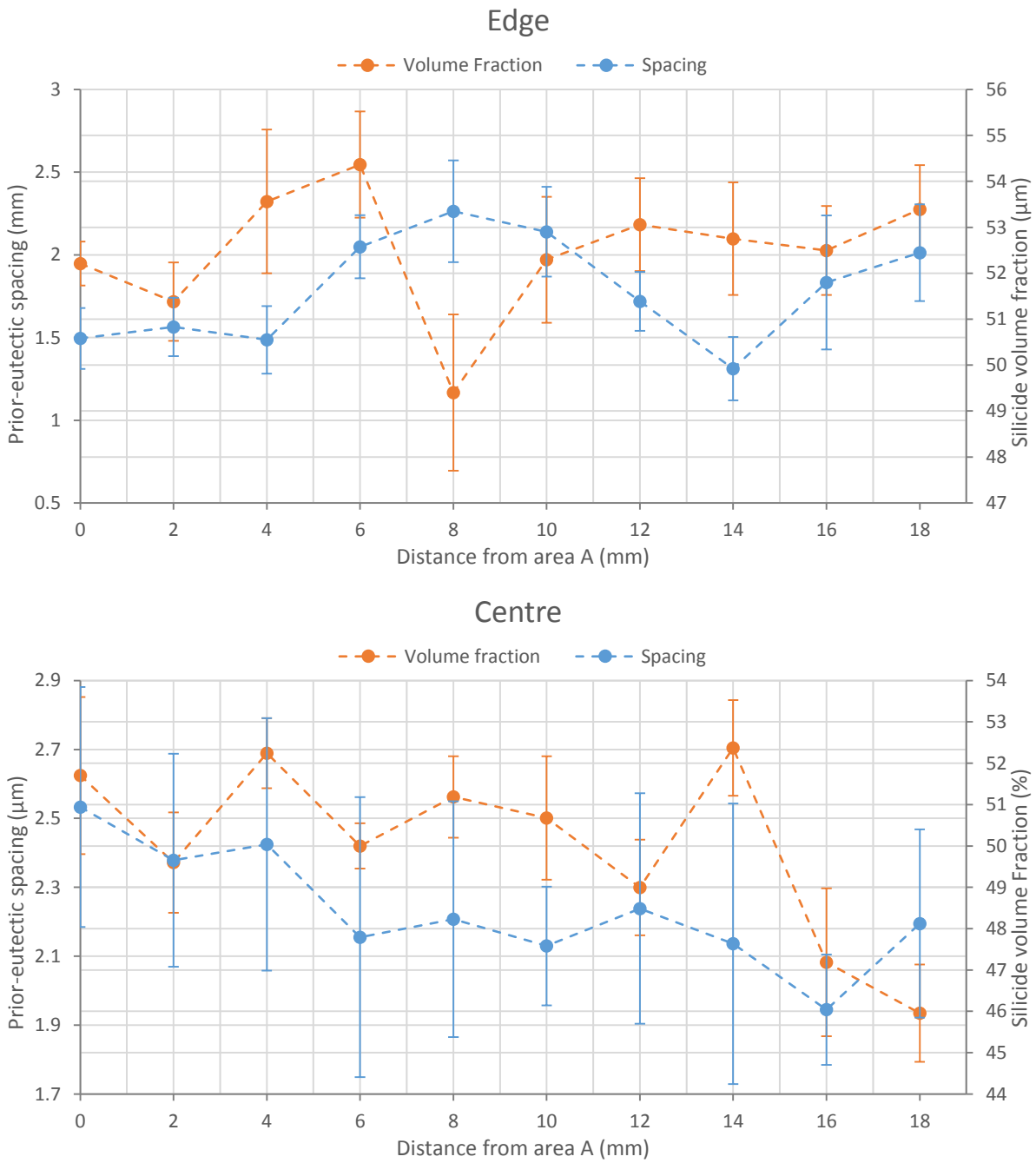

Figure 111: The change in λ and silicide V_f with distance from the area of highest cooling rate at the edge and centre of the heat treated alloy CM1 8 mm suction cast bar including SD.

Comparing the results of the cast with the heat treated alloy CM1 8 mm bar shows that the average spacing increased along the edge by 1.48 µm after heat treatment and along the centre the

increase was 1.81 µm after heat treatment. The volume fraction of the system also increased post heat treatment along the edge and along the centre by 1.9 and 0.4 %. However individual results showed that the V_f both increased and decreased post heat treatment compared to pre, whereas the λ only increased post heat treatment compared to pre. The largest increase in spacing was in areas D (1.74 µm) and C (2.08 µm) along the edge and centre, respectively.

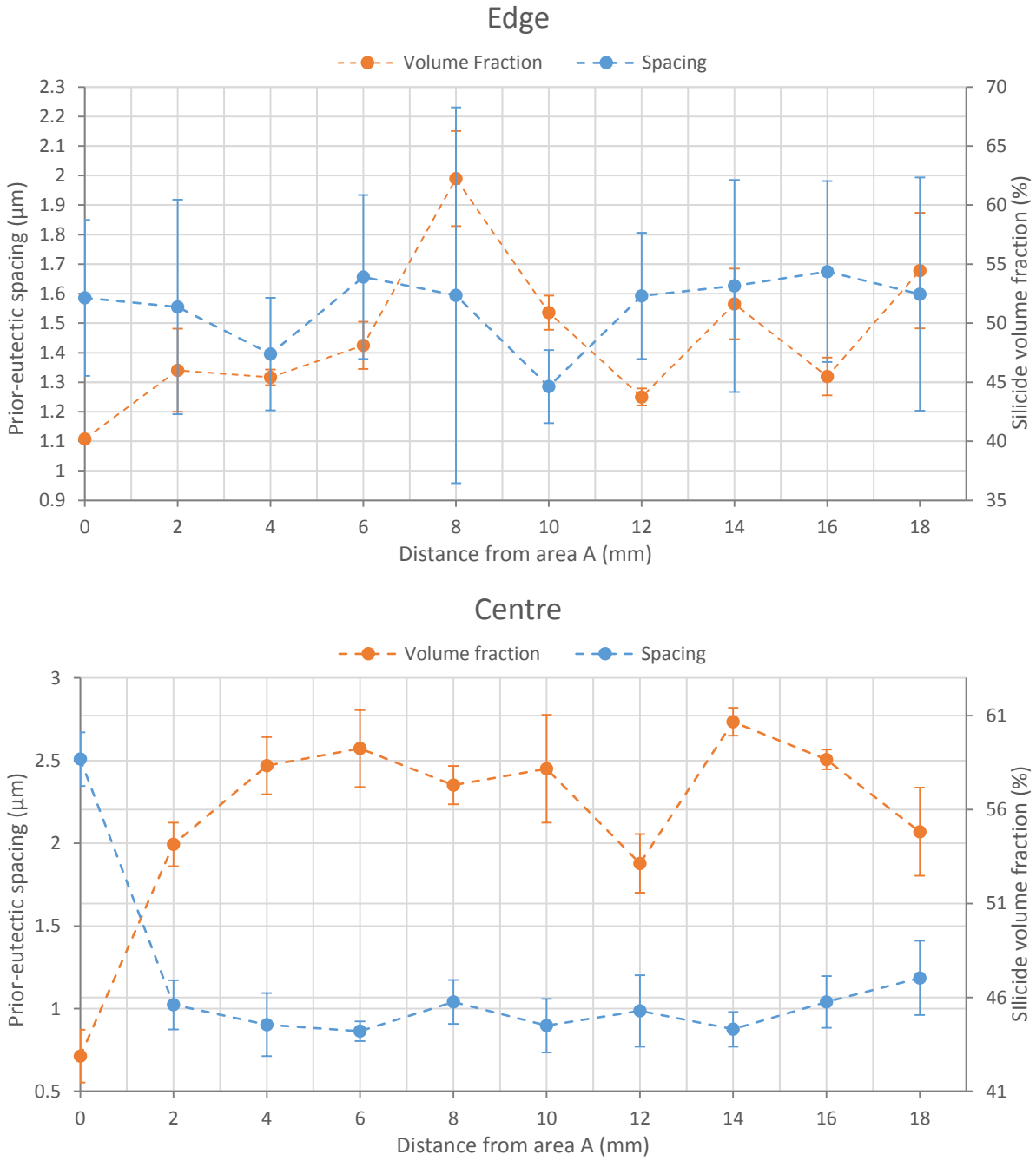

Figure 112: The change in λ and silicide V_f with distance from the area of highest cooling rate at the edge and centre of the heat treated alloy CM2 8 mm suction cast bar including SD.

The data for prior-λ and silicide V_f for the heat treated alloy CM2 8mm bar with increasing distance from the area of highest cooling rate along the edge and centre of the bar are shown in Figure 112. Along the edge of the bar the trend in prior-λ and V_f was the same from B to F. Along the centre of the bar the two parameters exhibited opposite trend from A to J, i.e. throughout the length of the bar. The results showed that the overall average central prior-λ results (1.98 μm) are 0.42 μm larger than the overall average along the edge (1.56 μm). Whereas there was a substantial increase in the average silicide V_f from the overall average along the edge (48.8 %) compared to the overall average along the centre (55.7 %). The data for the cast and heat treated alloy CM2 8 mm bar showed an overall increase in the average spacing post heat treatment compared to pre heat treatment along the edge and centre by 1.32 μm and 0.64 μm, respectively. Along the edge the silicide V_f decreased by 25.2 % in area A and increased in area E by 14.9 % post heat treatment compared to pre. However, comparing the overall average along the edge pre and post heat treatment there is very little change. Along the centre on the other hand there was an overall average increase of 6.0 % in the as cast to heat treated condition while only two areas, A and G, reported decreases in silicide V_f in the heat treated bar compared to the cast.

3.4.4 Directionally Solidified Ingots

The average lamellar spacing versus growth rate for the alloys CM1 and CM2 is shown in Figure 113. For the alloy CM1 the spacing increased with decreasing growth rate. In the samples grown at 150 and 60 mm/hr the spacing increased after the heat treatment. This difference depended on the growth rate and decreased with decreasing growth rate. For 150 mm/hr sample the difference between the as cast and heat treated conditions is 1.1 μm whereas for the 60 mm/hr it was 0.6 μm. In the case of the sample grown at 12 mm/hr after heat treatment the spacing slightly decreased by 0.4 μm. The aforementioned differences are indeed small, and could be attributed to measurement error. The latter is thought unlikely, as similar behaviour was observed for the alloy CM2 OFZ.

In the OFZ alloy CM2 the relationship between growth rate and the lamellar spacing was different. At the low growth rate, 12 mm/hr, where Nb_3Si was observed together with the fine microstructure of the Nb_{ss} + α-Nb_5Si_3 eutectoid the spacing was small (1.3 µm) and the maximum spacing in the as-cast condition (1.9 µm) was measured in the sample grown at 60 mm/hr while the spacing in the sample grown at 150 mm/hr was smaller (1.0 µm) than that at 12 mm/hr. Similarly to the OFZ alloy CM1 the lamellar spacing of the 60 and 150 mm/hr grown sample increased post heat treatment and decreased for the 12 mm/hr sample.

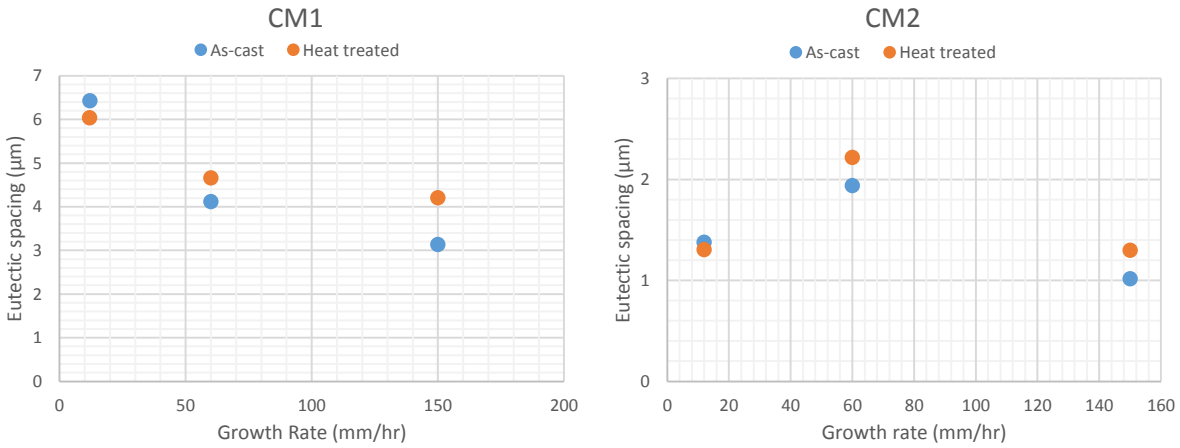

Figure 113: The average lamellar microstructure spacings against the growth rate of the as-cast and heat treated alloys CM1 and CM2 solidified using OFZ. Data for the OFZ alloys is for the bars grown under stable OFZ conditions.

Figure 114 shows the data for lamellar spacing and the volume fraction silicide for the alloy CM1 for the three growth rates. The lamellar spacing increased with decreasing growth rate, in agreement with Figure 113. For the sample grown at 150 mm/hr the V_f of silicide was below 55 %, with an average of 51.4 %. For the growth rate of 60 mm/hr the average V_f increased to 58.3 %. At 12 mm/hr the average V_f was reduced to 53.4 %.

Compared with the as-cast sample the range of V_f was reduced after the heat treatment. The as-cast alloy had V_f in the range 45.3 to 64.4 %silicide and λ in the range 2.2 to 8.1 µm. In the heat treated alloy the corresponding ranges were 41.4 to 56.1 % and 2.6 to 6.8 µm. The overall average V_f of the silicide was also reduced from 54.4 % to 49.6 %.

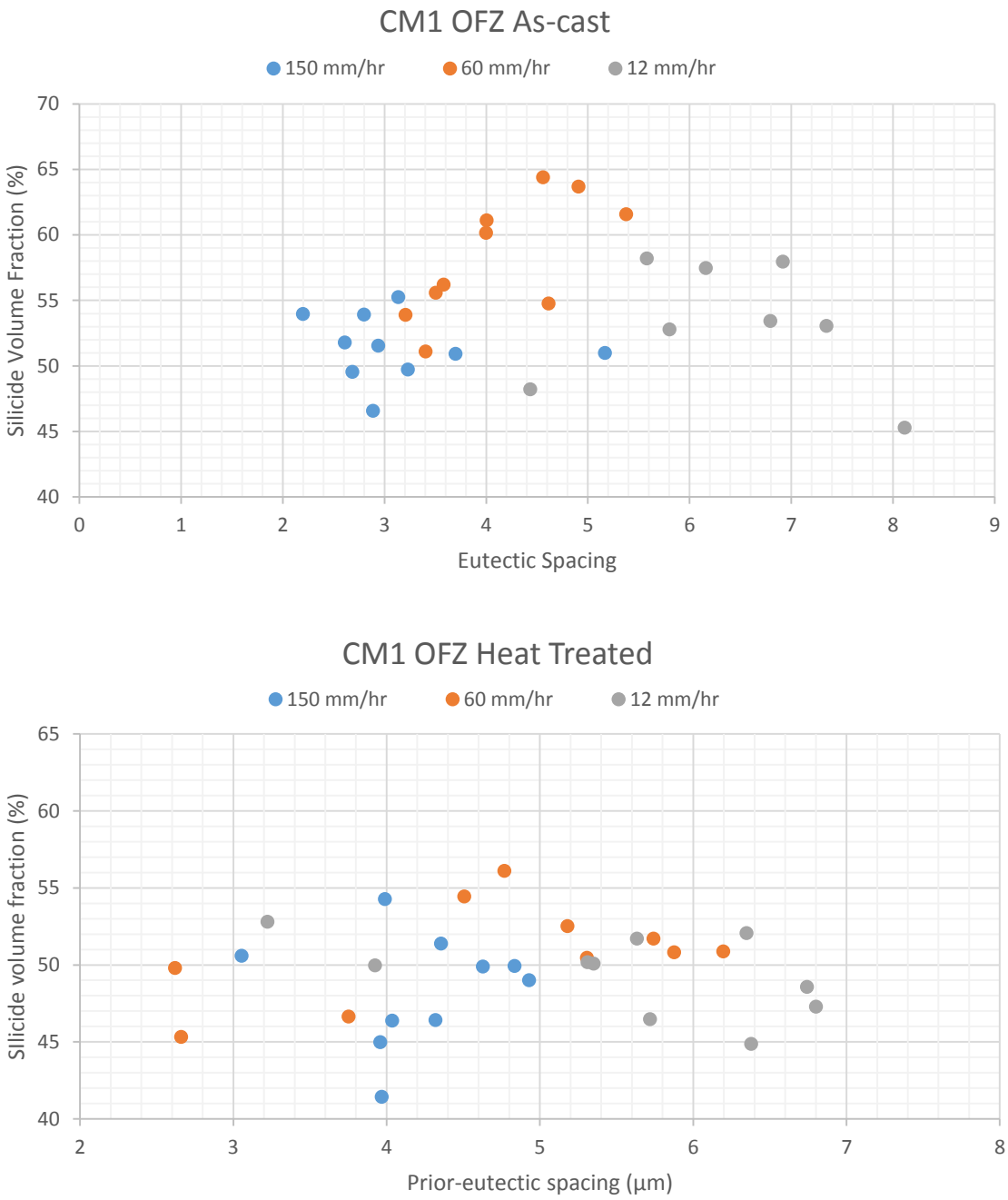

Figure 114: Lamellar microstructure spacing verses silicide volume fraction for the alloy CM1 solidified using an OFZ furnace in the as-cast and heat treated condition.

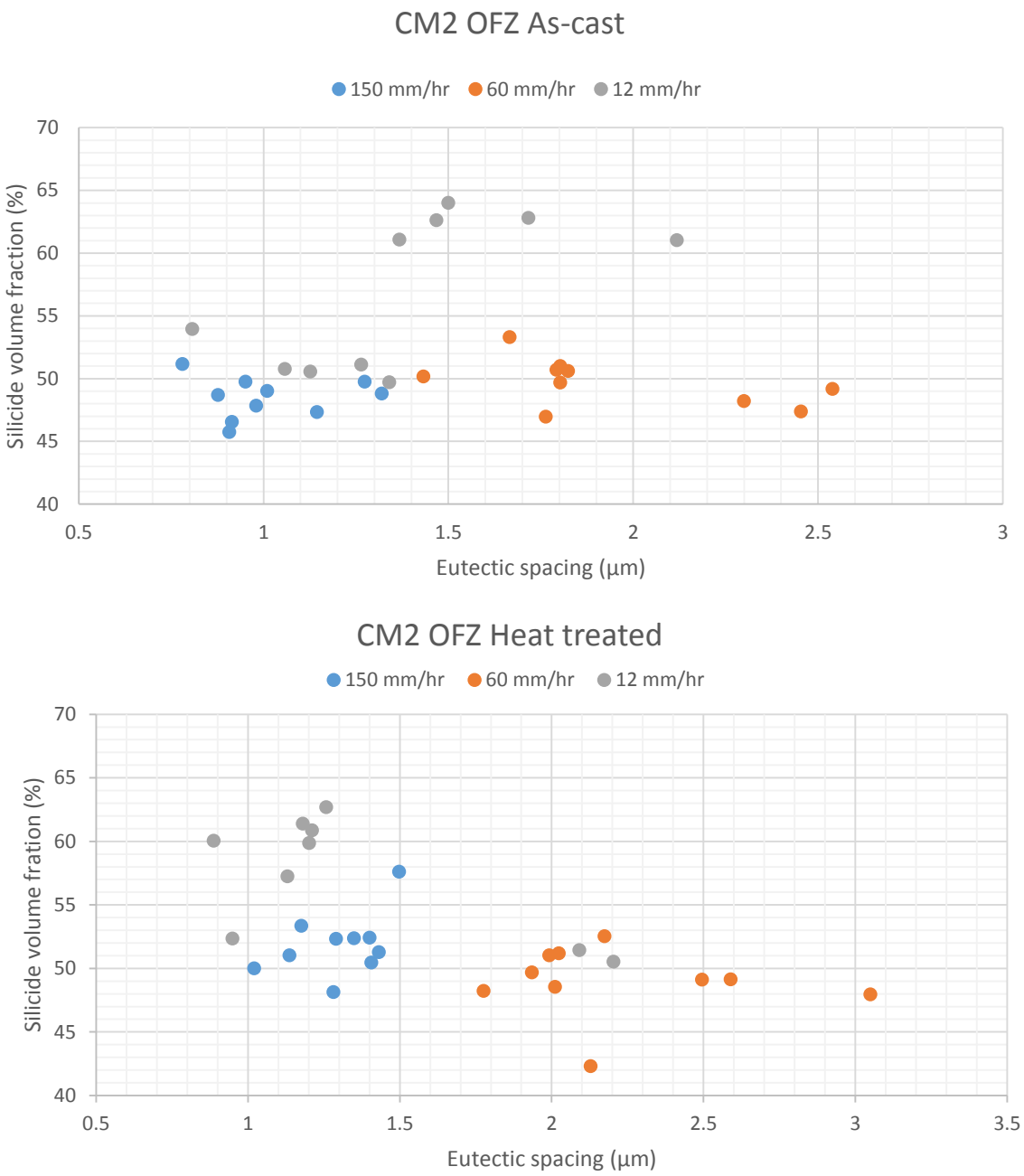

Figure 115: Lamellar microstructure spacing verses silicide volume fraction for the alloy CM2 solidified using an OFZ furnace in the as-cast and heat treated condition. Data for the OFZ alloys is for the bars grown under stable OFZ conditions.

The data for the λ and V_f for the alloy CM2 OFZ is shown in Figure 115. In the cast alloy the V_f of silicide was in the same range in the sample grown at 150 mm/hr and 60 mm/hr. In the 12 mm/hr grown sample, where there was Nb_3Si and the fine lamellar Nb_{ss} + Nb_5Si_3 eutectoid microstructure, the lamellar spacing was fine and the V_f silicide slightly higher. At low λ (average = 1.1 µm) and V_f (average = 49.4 %) there was a group of data made up mainly of 150 and 12 mm/hr grown samples.

The data for the 60 mm/hr grown sample seemed to form into two main groups one at low V_f and medium λ and the other at similar V_f but higher λ. A third group was made from the data from the 12 mm/hr grown sample with at a higher V_f (average = 62.3 %) and medium spacing (average = 1.6 μm).

Unlike the alloy CM1 after the heat treatment the range of the data increased. The data from the 150 mm/hr and 12 mm/hr samples formed one group and the data for the 60 mm/hr sample formed another.

3.4.5 Conclusions

Spacing, λ, of lamellae in eutectics and lamellar structures and volume fractions V_f of silicide in these structures was measured in two near eutectic alloys with nominal compositions Nb-8.3Ti-21.1Si-5.4Mo-4W-0.7Hf (CM1) and Nb-20.5Si-5.8W-4Hf (CM2) that had been prepared in the form of 10 g button ingots, 600 g and 500 g ingots and 6 and 8 mm suction cast bars. The alloys had also been processed using OFZ solidification processing at three growth rates, 12, 60 and 150 mm/h. The studies of λ and V_f in the OFZ alloy CM2 were made in microstructures grown under stable OFZ conditions, under which the chemical composition of the alloy CM2 was significantly different than that in the other forms of this alloy, as discussed in the § 3.3. The λ and V_f values were measured in the alloys in the cast and heat treated (1500 ^{O}C/100 hr) conditions.

In the suction cast bars similar trends in the variation of λ and V_f were observed along sections of the edge and centre of the bars were different depending on alloy and condition. Differences in trends were noticeable when Nb_3Si and its fine Nb_{ss} and α-Nb_5Si_3 products of its eutectoid transformation were in the microstructure.

4. DISCUSSION

4.1 INTRODUCTION

The two alloys studied in this thesis showed a variety of microstructures depending on solidification conditions. Before we attempt to discuss how the various microstructures of the two alloys formed, it is worth remembering some "facts" from the literature review that are "accepted" in the open literature.

Phase equilibria: In the Nb rich part of the binary Nb-Si phase diagram (§ 1.3.1, Figure 11) phase transformations that include the liquid phase are; the stable and metastable eutectics L → Nb_{ss} + Nb_3Si (at T ≈ 1920 ^{O}C) and L → Nb_{ss} + β-Nb_5Si_3 (at T < 1920 ^{O}C), respectively, and the peritectic L + β-Nb_5Si_3 → Nb_3Si (at T ≈ 1980 ^{O}C), but there is no data reported for a L → Nb_{ss} + α-Nb_5Si_3 eutectic. Reactions in the solid state are; the eutectoids Nb_3Si → Nb + α-Nb_5Si_3 (at T ≈ 1770 ^{O}C) and β-Nb_5Si_3 → α-Nb_5Si_3 + $NbSi_2$ (at T ≈ 1650 ^{O}C) and the peritectoid β-Nb_5Si_3 + Nb_3Si → α-Nb_5Si_3 (at T ≈ 1947 ^{O}C). There are metastable Nb_3Si and Nb_5Si_3 silicides. One metastable form of the former is A15 Nb_3Si. The metastable Nb_5Si_3 has the hexagonal Mn_5Si_3 as prototype, the same is the case for the Ti_5Si_3 and Hf_5Si_3 silicides.

The composition of the stable eutectic in the Nb-Si binary is reported to be in a wide composition range, 15.3 to 18.7 at.% Si (see § 1.2.1) and the temperature and composition of the metastable eutectic has been proposed to be 1850 ^{O}C and 19 at.% or 20 at.% (see § 1.3.1). Though the latter two values depend on the version of the Nb-Si binary used and the composition of the stable eutectic in the latter. Research in our group would suggest that the composition of the metastable eutectic in ternary and higher order Nb silicide based alloys is around 22 at.% Si.

Equilibrium solidification paths: The equilibrium solidification path of hypoeutectic Nb-Si binary alloys is L → L + $(Nb_{ss})_{primary}$ → $(Nb_{ss})_{primary}$ + $(Nb_{ss}$ + $Nb_3Si)_{eutectic}$ → $(Nb_{ss})_{primary}$ + (Nb_{ss} + α-$Nb_5Si_3)_{eutectoid}$. For hypereutectic alloys, depending on the Si concentration the primary phase can be

Nb_3Si or β-Nb_5Si_3. In the former case the equilibrium solidification path is L → L + $(Nb_3Si)_{primary}$ → $(Nb_3Si)_{primary}$ + $(Nb + Nb_3Si)_{eutectic}$ → $(Nb_3Si)_{primary}$ + Nb_{ss} + $(Nb_{ss} + \alpha\text{-}Nb_5Si_3)_{eutectoid}$ and in the latter L → L + β-$Nb_5Si_{3primary}$ → Nb_3Si → $(\beta\text{-}Nb_5Si_3)_{primary}$ + $(Nb_{ss} + \alpha\text{-}Nb_5Si_3)_{eutectoid}$.

Eutectic coupled zone: The coupled zone is used to study the solidification microstructures of eutectic and near eutectic alloys. This zone gives the range of compositions and growth temperatures (growth velocities or growth rates $V_{S/L}$) for which the coupled eutectic morphology leads the growth front. For shapes of coupled zones see Figure 5. The Nb-Si binary has eutectic coupled zones skewed towards the silicides Nb_3Si or β-Nb_5Si_3 (see § 1.3.1).

In Chapter 1, § 1.1.2.1, it was discussed that the coupled zone depends on the relative change of the interface (growth) temperature of different morphological forms (meaning eutectic, dendrites) as a function of composition and growth rate. Under a set of given growth conditions the growth form (meaning eutectic, dendrites) with the highest interface temperature (or in other words the lowest interfacial undercooling) will lead the growth front, see Figure 6. It was also discussed that the theories of coupled eutectic growth are based on steady state directional solidification ($G_L > 0$) where *both phases are present during growth* from the liquid. Thus, for a given alloy composition, eutectic microstructures can be controlled via temperature gradients (K/m) and growth rates (m/s) i.e., cooling rate [(K/m).(m/s) = K/s].

When a melt is undercooled significantly (bulk undercooling) the evolution of the solidification microstructures depends on the hierarchy of nucleation of phases and the potency of heterogeneous nucleants, see § 1.1.1. The literature on rapid solidification shows that different microstructures can be formed for a given alloy composition depending on the undercooling, namely metastable phases, mixed stable/metastable eutectics and coupled eutectics. Such microstructures can form when the melt spreads on a substrate of high thermal conductivity, like a copper plate in splat quenching.

The two alloys in this research exhibited a variety of microstructures, most of which comprised the Nb_{ss} and Nb_5Si_3, the latter being either the high temperature β-Nb_5Si_3 or the low temperature α-

Nb_5Si_3 polymorph. In some cases the Nb_3Si and the fine products of its eutectoid decomposition were also observed, usually in areas of ingots that had experienced high cooling rate during solidification. In both alloys microstructures exhibiting features of eutectics and/or eutectoids were observed, sometimes with microstructure transitions. In most cases "embedded" in the lamellar microstructures were dendrites of Nb_5Si_3 (e.g., Figure 46) or Nb_{ss} (e.g., Figure 48) and in most cases Nb_{ss} haloes were formed in-between Nb_5Si_3 grains and lamellar microstructure (e.g., Figure 51C, Figure 53A, B and C, Figure 60J, Figure 71F, Figure 75J and Figure 82).

Below, we shall discuss the microstructures of the two alloys, first using arguments based on our knowledge of the Nb-Si binary system and its invariant reactions. Then, the discussion will expand to consider available data about ternary phase equilibria.

4.2 CAST ALLOYS CM1 AND CM2

We start with the eutectic between Nb_{ss} and β-Nb_5Si_3 (metastable in the Nb-Si binary, see § 4.1). This was observed in the alloy CM1 10 g cast button and CM1 6 mm cast bar, where the presence of β-Nb_5Si_3 was confirmed by XRD that did not provide any evidence for α-Nb_5Si_3. In the alloy CM1 8 mm cast bar the XRD confirmed only the β-Nb_5Si_3 but there was EDS evidence for Nb_3Si in areas A and B of the bar (high cooling rates) and of its eutectoid transformation to Nb_{ss} and α-Nb_5Si_3. In the microstructures of the above three cases there were dendrites of β-Nb_5Si_3 surrounded by eutectic (the case for the alloy CM1 600 g will be discussed below separately). Furthermore, the alloy CM1 10 g cast button and 6 mm cast bar transitioned from a coarse two phase Nb_{ss} and β-Nb_5Si_3 microstructure (anomalous eutectic, see below) to the "standard eutectic" for these specimens (Figure 46B) in areas of highest cooling rate. The Si content of the alloy CM1 in the 10 g cast button, 6 mm and 8 mm cast bars was above the eutectic composition in the binary and the Si content of the eutectic was in the range of values for the metastable Nb_{ss} and β-Nb_5Si_3 eutectic in the binary. Nb_{ss} haloes were observed in all the microstructures.

In § 1.1.2.1 we discussed that the growth temperature of a phase "i" growing under positive temperature gradient in the liquid $G_L > 0$ is $T_i = T_L^i - B_i\sqrt{V_{S/L}} - {G_L D_L}/{V_{S/L}}$ where B_i is a function of physical constants of the alloy and T_L^i is the liquidus temperature of the alloy and that the growth temperature of coupled eutectic is $T_{Eu} = T_{eut} - B_{eu}(\sqrt{V_{S/L}})$ where B_{eu} is a function of physical constants of the alloy.

The above equations are applied to coupled eutectics on the assumption that both solid phases (of the eutectic) are already present. Directional solidification is the technique that is used to determine experimentally the coupled zone. The aforementioned assumption may not be true for the solidification of deeply undercooled melts. In the latter case one of the phases may nucleate first (and lead the growth) and thus the composition of the remaining liquid will change and even move outside the coupled zone.

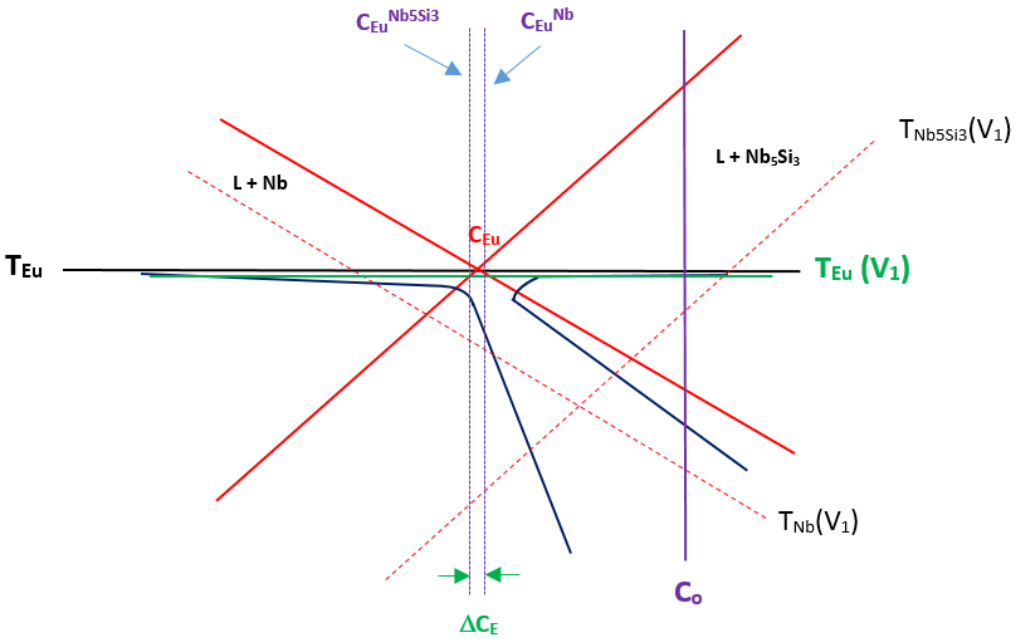

Figure 116: Schematic diagram of the skewed coupled zone of the Nb + β-Nb_5Si_3 metastable eutectic. Red continuous lines show the liquidus of Nb and β-Nb_5Si_3 and dashed red lines the growth temperatures T_i (i = Nb, β-Nb_5Si_3) of dendrites at growth rate V_1. The black horizontal line is the eutectic temperature T_{Eu}.

Figure 116 (drawing based on (Li et al. 2007)) shows a schematic of the skewed eutectic zone for the metastable eutectic in the Nb-Si binary. For the shape of the coupled eutectic zone see § 1.1.2.1. The composition of a hypereutectic alloy is shown by C_o.

Haloes form because of competitive growth of different phases in a eutectic. Theories about halo formation in eutectic solidification state that it occurs in those cases where the extension of the liquidus of halo forming (Nb_{ss} in our case) phase is outside the skewed zone. This is the case in Figure 116, which we shall consider below.

At the low growth rate $V_{S/L} = V_1$ in Figure 116 the growth temperature $T_{Eu}(V_1)$ of the coupled Nb + β-Nb_5Si_3 eutectic is higher than the growth temperatures of each phase, namely $T_{Nb}(V_1)$ and $T_{Nb5Si3}(V_1)$ and thus according to the criterion of maximum growth temperature (§ 1.1.2.1) the alloy of composition C_o will solidify as coupled Nb_{ss} + β-Nb_5Si_3 eutectic. From constitutional supercooling theory (§ 1.1.1) the maximum $V_{S/L}$ for coupled Nb_{ss} + β-Nb_5Si_3 eutectic will be $V_{S/L}^{CS} = G_L D_L[m_{\beta\text{-}Nb5Si3}(C_o - C_{Eu})]$ where $m_{\beta\text{-}Nb5Si3}$ is the slope of the liquidus of β-Nb_5Si_3.

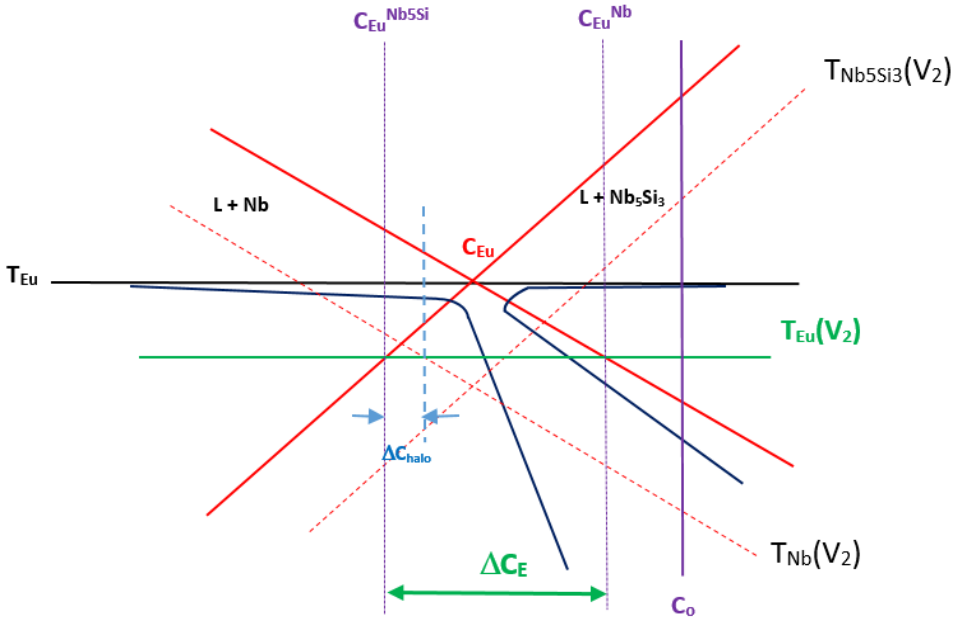

Figure 117: Schematic diagram of the skewed coupled zone of the Nb_{ss} + β-Nb_5Si_3 metastable eutectic. Red continuous lines show the liquidus of Nb and β-Nb_5Si_3 and dashed red lines the growth temperatures T_i (i = Nb_{ss}, β-Nb_5Si_3) of dendrites at growth rate V_2. The black horizontal line is the eutectic temperature T_{Eu}.

Next we consider the case when $V_{S/L}$ exceeds $V_{S/L}^{CS}$ ($V_2 > V_{S/L}^{CS} > V_1$), Figure 117. Notice that in this figure the extension of the Nb liquidus is also outside the skewed zone, as was the case in Figure 116. For the alloy of composition C_o the growth temperature of the β-Nb_5Si_3 is above that of $T_{Eu}(V_2)$. The liquid composition between the primary β-Nb_5Si_3 and the coupled eutectic S/L interface will be in the range $\Delta C_E = C_{Eu}^{Nb} - C_{Eu}^{Nb5Si3}$. However, in the composition range ΔC_{halo} the growth temperature of Nb will be above that of the eutectic, i.e., $T_{Nb}(V_2) > T_{Eu}(V_2)$ and thus the Nb_{ss} can form, in other words Nb haloes will form. The critical condition for halo formation is between the two cases shown in Figure 116 and Figure 117.

The critical condition for Nb_{ss} halo formation is shown in Figure 118. Notice that in this figure the extension of the Nb_{ss} liquidus is also outside the skewed zone, as was the case in the previous two figures.

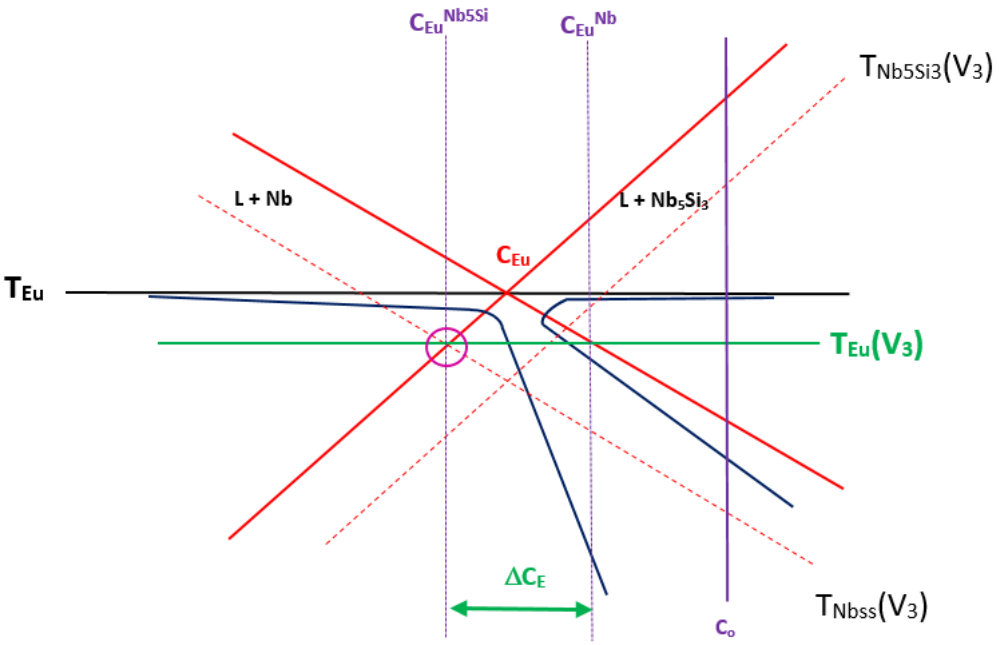

Figure 118: Schematic diagram of the skewed coupled zone of the Nb_{ss} + β-Nb_5Si_3 metastable eutectic. Red continuous lines show the liquidus of Nb_{ss} and β-Nb_5Si_3 and dashed red lines the growth temperatures T_i (i = Nb_{ss}, β-Nb_5Si_3) of dendrites at growth rate V_3. The black horizontal line is the eutectic temperature T_{Eu}.

Figure 118 shows that there is a critical $V_{S/L}$ (V_3 in the figure) above which Nb_{ss} haloes can form. This growth velocity is the velocity at which the growth temperature of the coupled eutectic and the Nb_{ss} are equal and simultaneously intersect the extension of the β-Nb_5Si_3 liquidus, circle in Figure 118.

We now consider the Nb_{ss} + β-Nb_5Si_3 metastable eutectic with the growth temperatures of the β-Nb_5Si_3 and the coupled eutectic, see Figure 119 (and Figure 6). The growth temperatures are described by the equations for T_i and T_{Eu} given above. Notice that in Figure 119 the extension of the Nb liquidus is also outside the skewed zone. At growth rate V_1 the composition of the coupled eutectic is C_{Eu1} and the composition of Nb in the liquid is $C_1 = C_o$ (where C_o is the alloy composition). At growth rate $V_2 > V_1$ the composition of the coupled eutectic is C_{Eu2} and the composition of Nb in the liquid is C_2. As the growth rate increases the Nb_{ss} will lead the coupled eutectic with undercooling ΔT. For small undercooling nucleation of Nb_{ss} on Nb_5Si_3 will lead to formation of Nb_{ss} halos. But if the undercooling were to exceed some critical value the Nb_{ss} could nucleate independently and form not only Nb_{ss} halo around the Nb_5Si_3 but also form Nb dendrites.

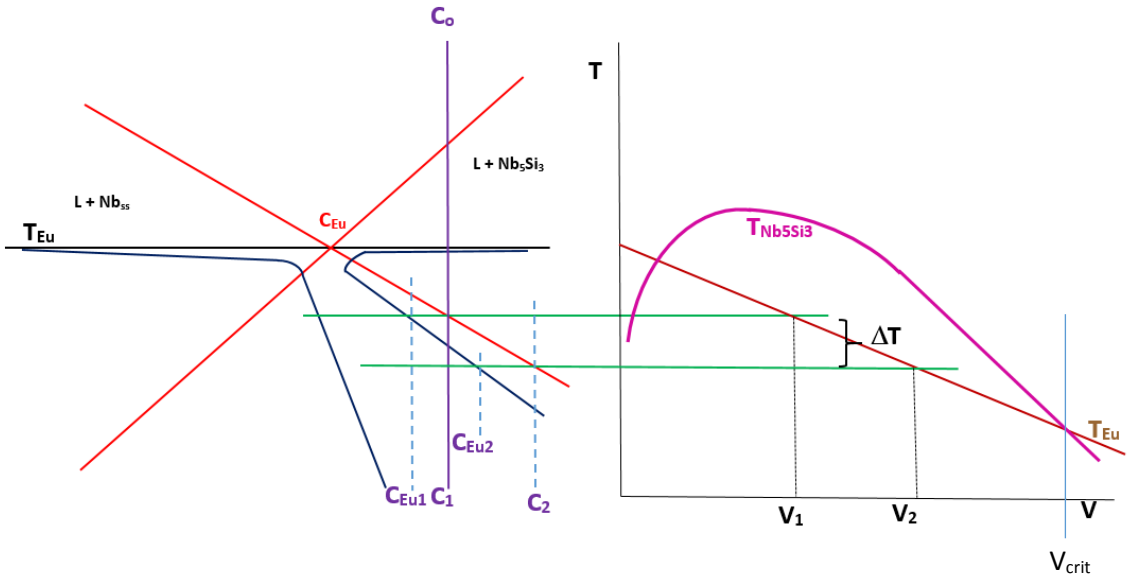

Figure 119: Schematic diagrams of the skewed coupled zone of the Nb_{ss} + β-Nb_5Si_3 metastable eutectic (left) and growth temperatures (right). Red continuous lines show the liquidus of Nb_{ss} and β-Nb_5Si_3. The black horizontal line is the eutectic temperature.

Figure 116 to 108 and the accompanying discussion could explain the microstructures seen in CM1 10 g cast button, CM1 6 mm and CM1 8 mm cast bar (away from areas of high cooling rate, i.e., after the transition from the anomalous to normal eutectic, see below) that formed at different growth rates (growth temperatures) under conditions with $G_L > 0$. As the solidification conditions changed coupled Nb_{ss} + β-Nb_5Si_3 eutectic with/out primary β-Nb_5Si_3 and Nb_{ss} haloes formed.

We turn our attention next to the formation of Nb_3Si in the high cooling rate areas of CM1 8 mm cast bar. There was no macrosegregation in this bar. Its Si content was lower than that of the CM1 6 mm cast bar but close to C_{Lp} (Figure 10A) for the L + β-Nb_5Si_3 → Nb_3Si peritectic in the binary, for which the values of 20.2 and 19.5 at% Si have been reported. Thus, it is possible that the alloy CM1 8 mm cast bar was either to the left or to the right of the C_{Lp} for the peritectic reaction in the Nb-Si binary phase diagram, Figure 11.

Let us see what is possible regarding Nb_3Si formation from the liquid. As discussed in § 4.1, with Nb_3Si as the primary phase (alloy composition to the left of C_{Lp}) a possible solidification path is L → L + $(Nb_3Si)_{primary}$ → $(Nb_3Si)_{primary}$ + $(Nb_{ss} + Nb_3Si)_{eutectic}$ → $(Nb_3Si)_{primary}$ + Nb_{ss} + $(Nb_{ss}$ + α-$Nb_5Si_3)_{eutectoid}$. In this case no β-Nb_5Si_3 is formed and the α-Nb_5Si_3 is the product of the eutectoid transformation of

Nb_3Si. If all the Nb_3Si transforms there will be the fine mixture of eutectoid Nb_{ss} and α-Nb_5Si_3, if not, then there will also be some remnant of Nb_3Si. The evidence in the bottom of CM1 8 mm cast bar (

Figure 73) is for the latter. However, it is not possible from the present results to eliminate the possibility that some of the fine lamellar microstructure in this alloy is the Nb_{ss} + β-Nb_5Si_3 eutectic instead of Nb_{ss} + α-Nb_5Si_3 eutectoid. Could a eutectic between Nb_3Si and β-Nb_5Si_3 form? This is considered below with the help of Figure 120.

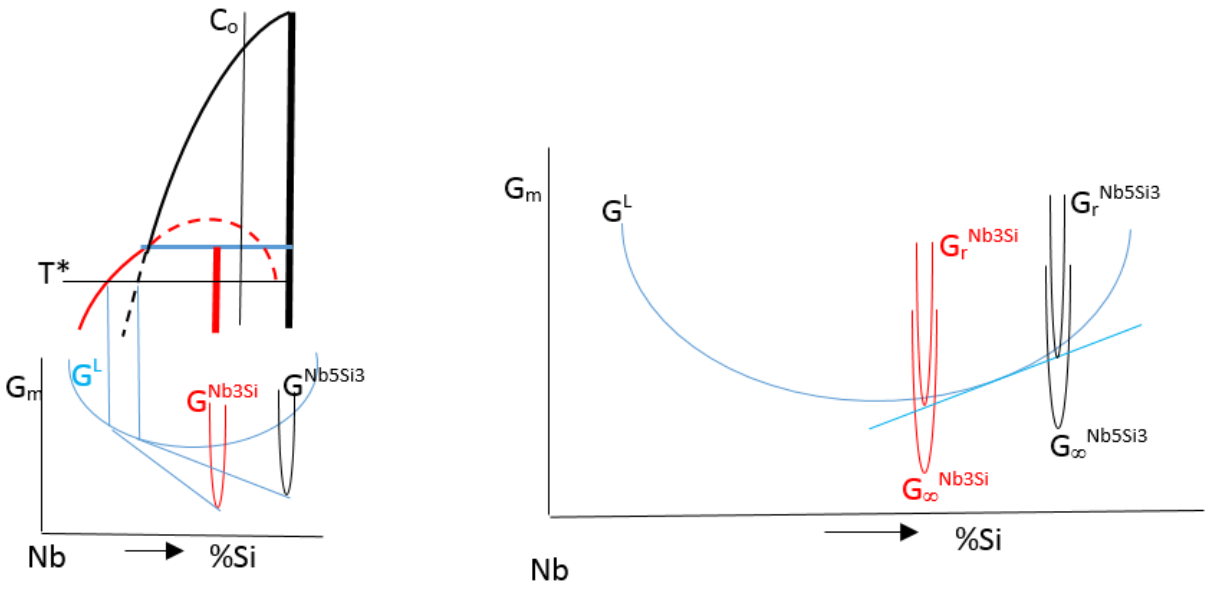

Figure 120: Schematic part of the Nb-Si binary phase diagram of the peritectic at about 1980 ^{O}C (left) and molar Gibbs free energy plots (bottom left and right). Metastable extensions of the liquidus lines of β-Nb_5Si_3 and Nb_3Si are shown with black and red dashed lines, respectively.

Figure 120 shows part of the Nb-Si binary with the peritectic reaction that occurs at about 1980 ^{O}C (Figure 11) and below it are the molar free energy curves of the phases at T = T*. For alloy of composition C_o, at T = T* Nb rich liquid and Si rich liquid can be in equilibrium with the Nb_3Si and β-Nb_5Si_3. Increased pressure arising from curvature of the two phases could shift their free energy curves to less negative free energy values leading to the situation shown on the right of the schematic phase diagram in Figure 120. This hypothetical situation would lead to the eutectic reaction L $\rightarrow$ β-Nb_5Si_3 + Nb_3Si (in which the former silicide would exhibit darker contrast than the latter) and shows another

(hypothetical) way that very fine Nb_3Si can form with very fine β-Nb_5Si_3. Such a eutectic was not observed.

Another possibility regarding formation of Nb_3Si with/without β-Nb_5Si_3 can be considered with the help of Figure 121, which shows an alloy of composition C_o undercooled to T = T*. At temperature T* the alloy will be supersaturated with respect to both phases because the intercept of the C_o and T* lines are below the liquidus curves of both phases. If β-Nb_5Si_3 were to form in the melt, the partitioning of atoms will move the composition of the melt towards the intercept of the liquidus extension of β-Nb_5Si_3 with T* and the undercooling (with respect to β-Nb_5Si_3) will decrease towards zero as will the undercooling with respect to Nb_3Si, however the undercooling will decrease slower with respect to the latter phase. When the former undercooling becomes zero, the growth of β-Nb_5Si_3 will stop and only Nb_3Si will form. In this scenario some β-Nb_5Si_3 forms (at low vol.%) followed by Nb_3Si and then the Nb_3Si transforms as discussed above. We can take this a little further by considering modes of growth in peritectics.

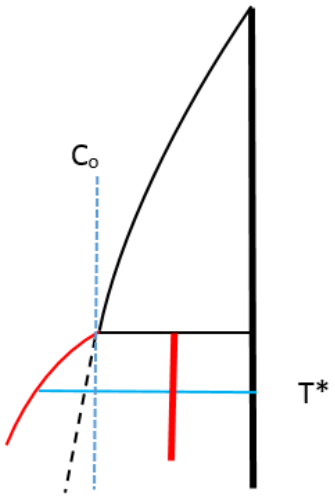

Figure 121: Schematic part of the Nb-Si binary phase diagram of the peritectic at about 1980 ^{O}C. Thick black and red vertical lines represent the β-Nb_5Si_3 and Nb_3Si, respectively.

In a typical peritectic different modes of growth under $G_L > 0$, meaning solidification of a phase with planar S/L front or cellular/dendritic solidification, are possible depending on solidification

conditions. We follow here the approach of Hillert (1977). Consider Figure 10A. For planar growth of each of the two phases, the constitutional supercooling theory (§ 1.1.1) gives for the phases α and β in Figure 10A, respectively $D_LG_L/V_{S/L} = |m_\alpha|C_o(1-k_\alpha)/k_\alpha$ and $D_LG_L/V_{S/L} = |m_\beta|C_o(1-k_\beta)/k_\beta$. In Figure 122 these two equations are represented by the lines A and B, respectively. The $D_LG_L/V_{S/L}$ value for planar growth of α is higher than for β. Above the line A both α and β can grow with planar S/L interfaces. The region between planar growth of β and cellular/dendritic growth of α can be obtained by equating the equations $T_\beta = T_{per} + |m_\beta|(C_{Lp} - C_o/k_\beta)$ with $T = T_{per} + |m_\alpha|(C_{Lp} - C_o) - D_LG_L/V_{S/L}$ where the former equation gives the temperature of the planar front of β and the latter equation has been derived by equating the composition of the liquid at temperature T, which is $C_L = C_{Lp} + (T_{per} - T)/|m_\alpha|$, with $D_LG_L/V_{S/L} = |m_\alpha|(C_L - C_o)$, which gives the tip temperature of α cells or dendrites. We get the equation $D_LG_L/V_{S/L} = (|m_\alpha| - |m_\beta|)(C_{Lp} - C_o) + |m_\beta|C_o(1 - k_\beta)k_\beta$. The line F in Figure 122 represents this equation. It intercepts the line B at $C_o = C_{Lp}$, line J in Figure 122 (this is found by equating the above equation with that for line B and the line A at $C_o = C_{Lp}k_\alpha k_\beta(|m_\alpha| - |m_\beta|)/(k_\beta|m_\alpha| - k_\alpha|m_\beta|)$). The latter equation is derived by equating the temperatures of the planar growth fronts for β (see above) and α, namely $T_\alpha = T_{per} + |m_\alpha|(C_{Lp} - C_o/k_\alpha)$. The line H (vertical blue line) in Figure 122 is the boundary between the regions of planar growth of α and β.

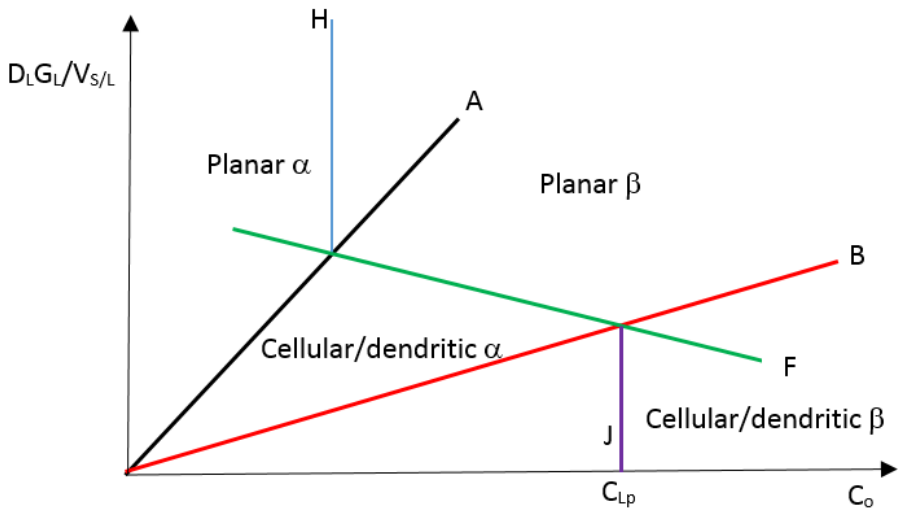

Figure 122: Schematic diagram of $D_LG_L/V_{S/L}$ versus alloy composition for a typical peritectic showing areas of different growth. Drawing based on Hillert (1977).

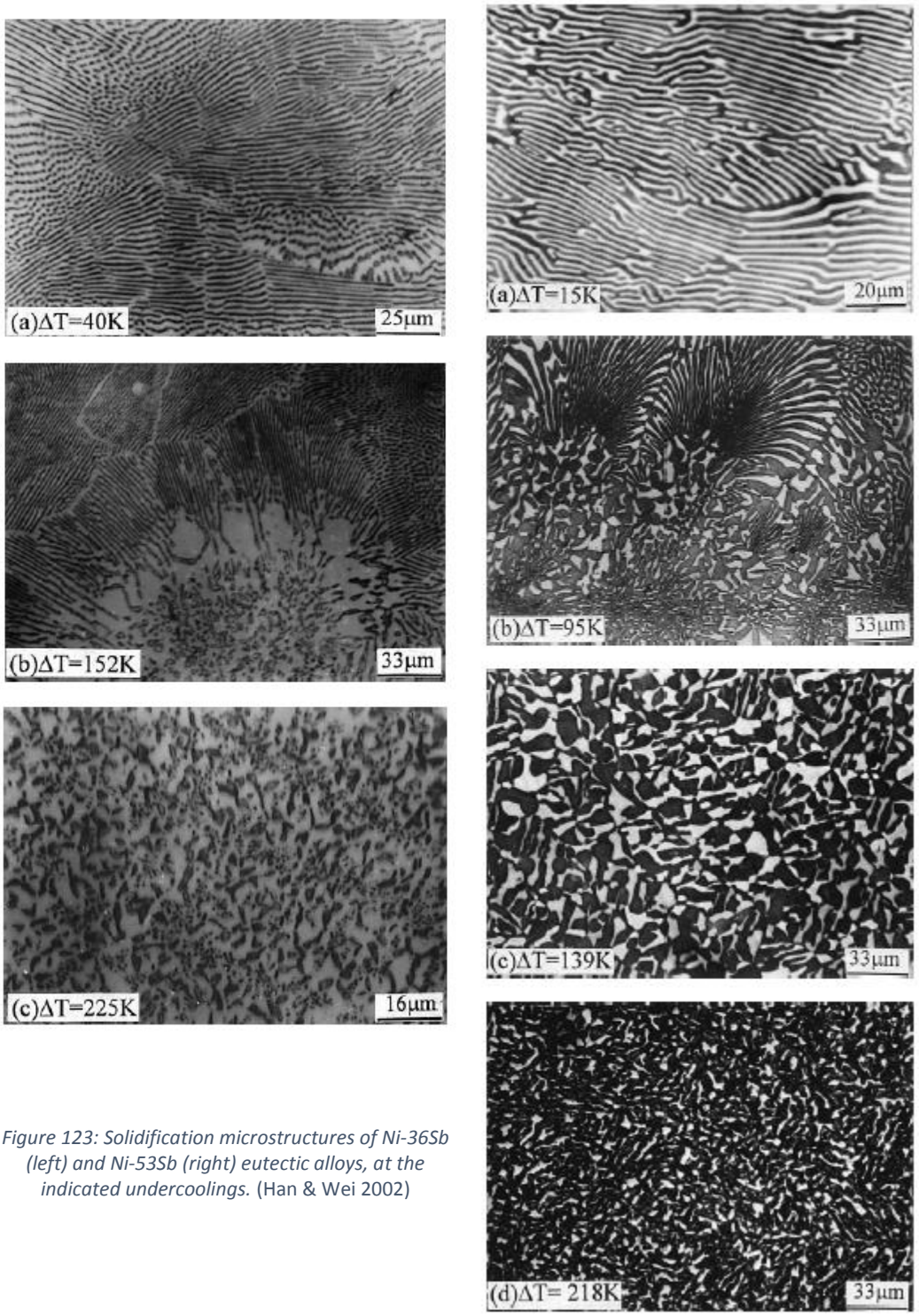

Figure 123: Solidification microstructures of Ni-36Sb (left) and Ni-53Sb (right) eutectic alloys, at the indicated undercoolings. (Han & Wei 2002)

Figure 122 shows four regions of growth. In the region to the left of lines A and H planar growth of α will occur and β could also form (metastable if $C_o < C_{\beta p}$ (see Figure 10A)) at a temperature significantly lower than T_{per}. Primary (cellular/dendritic) β will form in the area to the right of line J and below line B. In the area of primary (cellular/dendritic) α subsequent formation of β is possible if diffusion is slow in the α phase. The β would be planar if it falls above the line B.

The above shows that depending on growth (solidification) conditions it is possible to get β (which would be the Nb_3Si for the peritectic in the Nb-Si binary, the α phase being the β-Nb_5Si_3) growing with a planar interface or in the form of dendrites.

Transitions between microstructures, including eutectics, were observed in the cast alloy CM1 10 g button, 6 mm and 8 mm bars. Studies of the unconstrained solidification of binary NF/F eutectics (constrained solidification is growth controlled, and unconstrained solidification is nucleation controlled, see § 1.1.1), for example using electromagnetic levitation melting, have shown that melt undercooling plays a critical role on the type and scale of eutectic formed and in transitions between eutectic microstructures. These eutectics are referred to as anomalous eutectics in the literature (see § 1.1.2.1 and below). Figure 123 and Figure 124 show selected images of eutectic microstructures and transitions between eutectic microstructures taken from the literature. Figure 125 and Figure 126 show typical eutectics and eutectic microstructure transitions taken from this research.

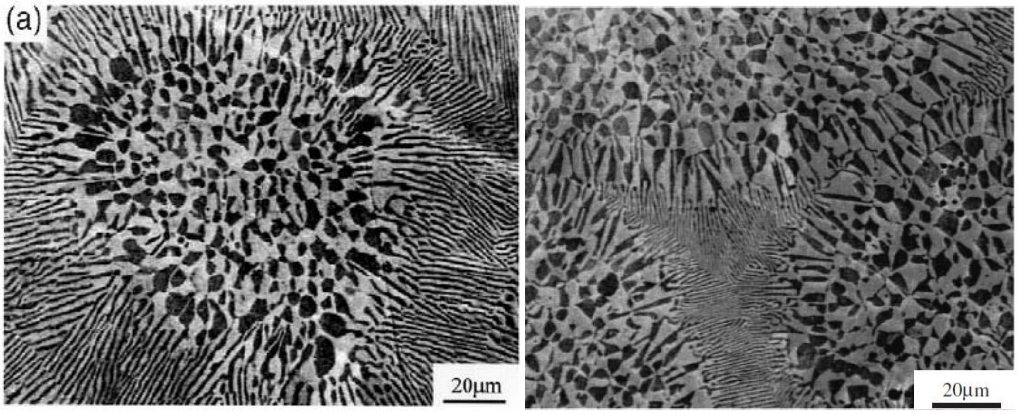

Figure 124: SEM images of eutectic colonies in Ni-18.7Sn eutectic alloy solidified at ΔT = 70 K from (Li et al. 2002) *left and* Li & Kuribayashi (2006) *right.*

It should be noted that the use of the term anomalous eutectic in this discussion is not the "usual" one. The term anomalous eutectic is often used to signify a lamellar eutectic in which the lamellar spacing deviates from the expected spacing owing to directional growth of one or both phases. Here, the term anomalous eutectic is used to indicate a eutectic where there is a transition between a regular two phase lamellar structure to a two phase one that is more globular in nature,

and depending on solidification conditions sometimes significantly coarser than the equivalent lamellar structure, with which it coexists or evolves to (Mullis et al. 2014).

In an anomalous eutectic the fine alternating lamellar structure is replaced with an essentially random globular structure of the two phases the scale of which depends on level of undercooling and gets finer the higher ΔT is (Figure 123, images for highest ΔT values), and the random globular structure is either interspersed with lamellar regions (Figure 124) or evolves (Figure 123, images for intermediate ΔT values) into lamellar eutectic (Figure 123, images for lowest ΔT values). In eutectics that exhibit the anomalous to lamellar transition with decreasing melt undercooling, usually one phase is a non-facetted solid solution and the other a facetted intermetallic.

Figure 123 shows a transition from anomalous to lamellar eutectic with decreasing undercooling ΔT for two Ni-Sb eutectic alloys (Han & Wei 2002). In the images on the left the grey phase is the Ni_{ss} and the white one is the intermetallic Ni_5Sb_2 and in the images on the right the black phase is Ni_5Sb_2 and the white is NiSb. Figure 123 shows that as ΔT decreases the microstructure changes to a mixture of anomalous + lamellar eutectic to lamellar eutectic. The lamellar eutectic grows epitaxially from the anomalous eutectic. Han & Wei (2002) reported significant refinement of the Ni-52.8Sb anomalous eutectic when the undercooling increased from 139 K to 218 K (images shown in Figure 123). Figure 114 (this work) shows a transition from fine to coarser anomalous eutectic (Figure 125A and C) to a mixture of anomalous and lamellar eutectic (Figure 125A and B) to lamellar eutectic (Figure 125B), and coarse anomalous eutectic to lamellar eutectic (Figure 125D).

In Figure 124 the image on the left shows regular lamellae growing epitaxially from an anomalous Ni-Sn eutectic “grain” and the image on the right shows several anomalous eutectic colonies surrounding regular eutectic colony(ies?). A similar microstructure is shown in Figure 126 (this work).

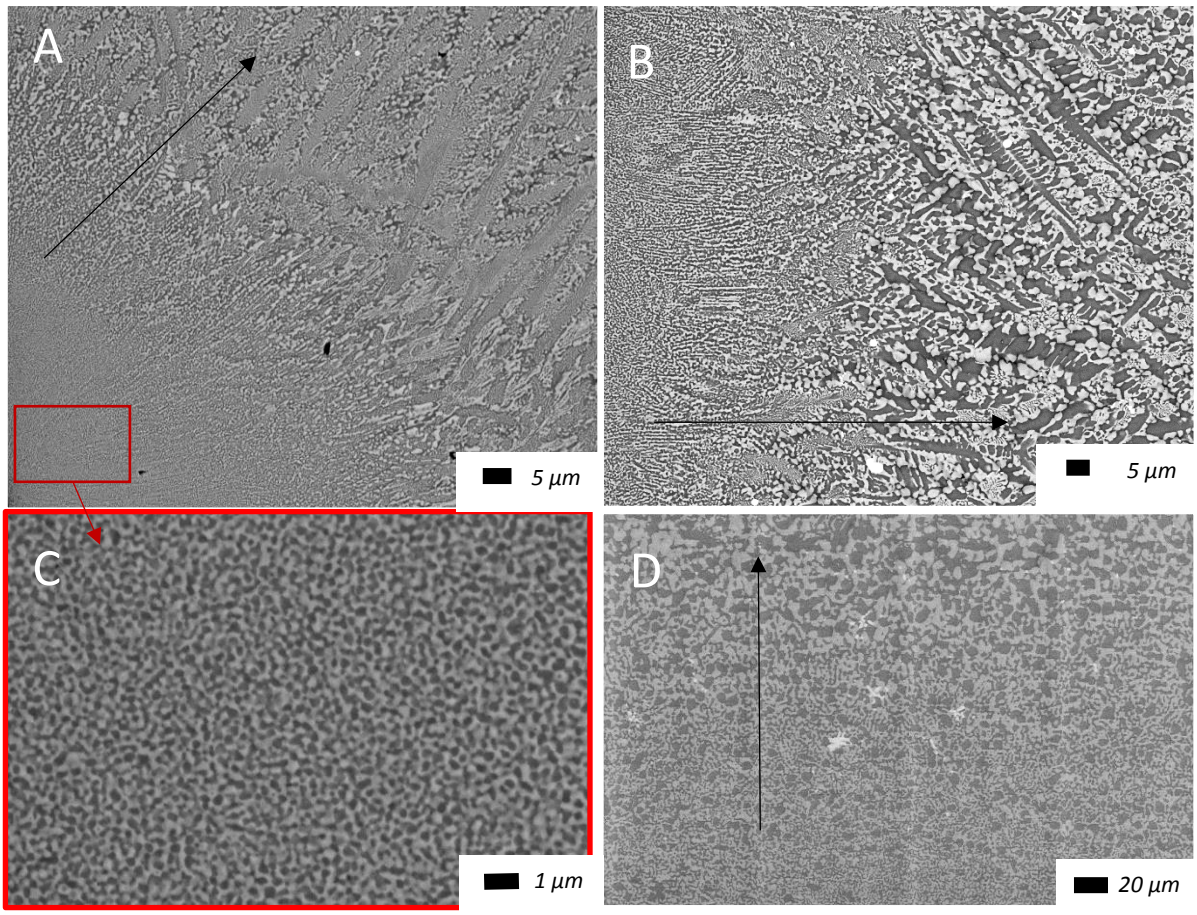

Figure 125: SEM backscattered images of anomalous eutectic in CM1 8 mm SC AC bar (a to c), (c) anomalous eutectic in area of highest cooling rate, (b) is high magnification of area in bottom right hand corner of (a). Image (d) is from the bottom of the CM1 10 g AC button ingot. Arrows point towards decreasing cooling rate.

In the literature anomalous eutectics have been discussed using different mechanisms, which include decomposition of a supersaturated solid solution, cooperative or uncoupled dendritic growth of two phases, re-melting of single-phase dendrites and re-melting of fine lamellar eutectic. The aforementioned mechanisms were assumed to operate alone in a given eutectic alloy. It was assumed that an anomalous eutectic formed via only one of these formation methods. However, a dual mechanism that includes re-melting of eutectic dendrites and single-phase dendrites has also been proposed for anomalous eutectic formation in undercooled Ni–Sn eutectic alloys. References to the relevant literature can be found in Yang et al. 2011 and Li et al. 2005.

Some researchers have proposed that the transitions from anomalous to anomalous + lamellar to lamellar eutectic occur at some critical undercooling value for *each* transition that tends to increase

with increasing cooling rate (in other words the tendency to observe these transitions decreases as the cooling rate is increased), while others (Li & Kuribayashi 2006) have suggested that a critical undercooling $\Delta T_{crit} \approx 0.25\ \Delta T_{max}$, where ΔT_{max} is the maximum achievable undercooling in the eutectic, is required only for anomalous eutectic formation. For $\Delta T > \Delta T_{crit}$ the vol.% of the anomalous eutectic increases and the microstructure of the latter is refined.

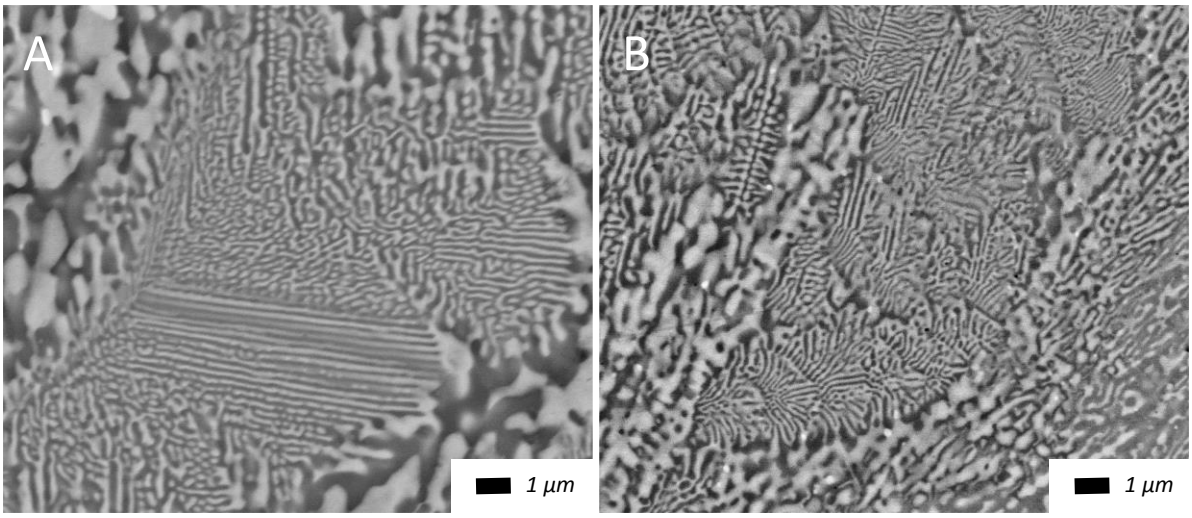

Figure 126: SEM backscattered electron images of eutectic colonies in (A) cast alloy CM1 8 mm and (B) cast alloy CM2 6 mm

The undercool-ability of Nb-Si melts has been demonstrated in rapid solidification studies of binary Nb-Si melts that formed amorphous (glassy) alloys and metastable phases, such as A15 Nb_3Si, e.g. (Masumoto et al. 1980). In hypereutectic binary Nb-Si alloys undercoolings of 670 K have been achieved (Robinson et al. 1989).

The solidification of an undercooled melt is unconstrained solidification (§ 1.1.1) and as shown in Figure 1 there exists a negative temperature gradient ahead of the S/L interface, which implies that the advancement of the latter is limited by the transport of heat in the melt ($\Delta T_{heat\ transfer}$ in Figure 1) and that the interfacial kinetics ($\Delta T_{attachement}$ in Figure 1) is important, meaning the transport of solute atoms and their attachment to the interface, see § 1.1.1, must be considered. The growth rate ($V_{S/L}$) in a deeply undercooled melt can be high, in which case the thermal and solutal conditions are far from equilibrium (see § 1.1.1).

In § 1.1.1 the distinction between melt undercooling (ΔT_L in Figure 1) and interface undercooling ($\Delta T_{attachment}$ in Figure 1) was made. The former provides the driving force for nucleation of solidification and the latter the driving force for the attachment of atoms at the S/L interface. As ΔT_L increases, the $\Delta T_{attachment}$ increases too.

In the solidification of an undercooled melt, which is non-isothermal, the $V_{S/L}$ decreases as the temperature increases owing to recalescence and beyond the recalescence temperature solidification proceeds under conditions that depend on the removal of heat. The effect of recalescence can be controlled when the deeply undercooled melt is in contact with a very good conductor of heat such as a water cooled copper surface.

It is expected (or it is reasonable to assume) that on the water cooled copper crucible wall in the button ingots and suction cast ingots the melt became undercooled as it experienced high cooling rate and nucleation occurred in the undercooled melt, most likely at different ΔT values.

In § 1.1.1 we discussed that kinetic undercoolings are different for non-facetted and facetted phases and that the structure of the S/L interface depends on the entropy of fusion. Let us consider further the contributions to interface undercooling. This discussion will be based on Li & Kuribayashi (2006).

In constrained eutectic solidification the undercooling has contributions from constitutional and curvature undercoolings. In unconstrained solidification in addition to these terms the kinetic and thermal undercoolings become important, particularly for large undercoolings. The kinetic undercooling can be written as $\Delta T_{attachment} = V_{S/L}/\mu$ where $V_{S/L}$ is growth rate and μ is linear interface kinetic coefficient, which for collision limited growth of a non-facetted disordered phase without strong lattice anisotropy is given by $\mu = V_S \Delta H_f/RT_i^2$ where V_S is the velocity of sound, ΔH_f is the heat of fusion and T_i is the temperature of the interface (T_{Eu} could be used for T_i). For diffusion limited growth, typical for an ordered intermetallic, the higher the complexity of a unit cell and the more complicated the chemical structure of a phase the lower the value of μ or the higher $\Delta T_{attachment}$. For

diffusion limited growth the V_S is replaced by V_D (diffusive speed). The former is three orders of magnitude greater than the latter, V_S is about 1 to 10 km/s compared with V_D of 1 to 10 m/s (Li & Kuribayashi 2006). The above argument points to difficulties of growth for a phase of high entropy of fusion (i.e., a facetted phase), like Nb_5Si_3 and Nb_3Si compared with the Nb_{ss}.

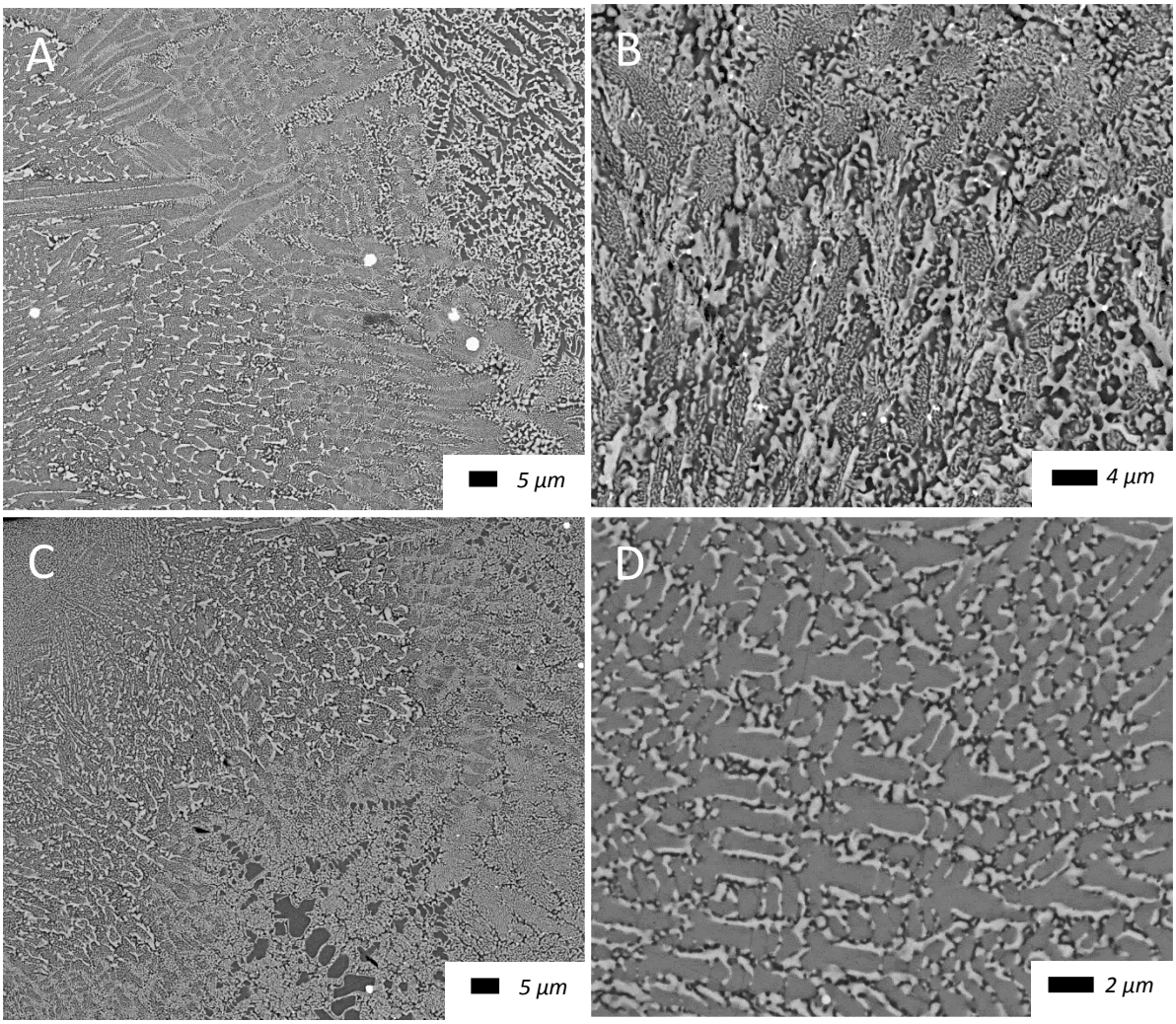

Figure 127: Backscattered images of the alloy CM1 8 mm bar from the areas of highest cooling. A, B and C show the transition regions between the anomalous and "regular" microstructures and D shows the area where Nb_3Si was found.

Considering the case of the alloy CM1, in highly undercooled melt near the water cooled copper crucible walls there was heterogeneous nucleation of Nb_{ss} and Nb_5Si_3. Owing to the different interface attachment kinetics of Nb_{ss} and Nb_5Si_3 (see above) the former phase grew faster than the latter, i.e., the growth of the two phases could become de-coupled. Indeed, the different attachment kinetics distorted the solute distribution ahead of the growing eutectic S/L interface. When the Nb_{ss} grew to a

length that was larger than the effective diffusion distance ($D_L/V_{S/L}^{\beta Nb5Si3}$) ahead of the Nb_5Si_3, the former could grow with no constraints, meaning the Nb could grow freely into the undercooled melt and thus the decoupled growth was established. The (leading) Nb_{ss} phase could not form "complete" dendrites owing to the chemical limitations (partitioning) of the eutectic alloy affecting the diffusion of Nb atoms. As both phases grew the release of heat of crystallization increased the temperature of the melt ahead of the growing interface (recalescence), and thus lowered the growth rate and the driving force to the growth temperature where coupled eutectic solidification occurred. The higher the melt undercooling the higher the nucleation rate and thus the finer the anomalous eutectic and the higher its volume fraction (Li & Kuribayashi 2003b).

The formation of the "regular" structure did not occur directly from the anomalous eutectic in all areas of the suction cast bars. In the areas of highest cooling, area A at the edge, the CM1 8 mm sample was a region between the anomalous and "regular" where Nb_3Si was observed. As can be seen in Figure 73 and Figure 127D the Nb_3Si grains were surrounded by the Nb_{ss} halos (with some regions of darker silicide assumed to be Nb_5Si_3). This microstructure can be seen throughout the highest cooling areas of the 8 mm suction cast alloy CM1 with a fine lamellar microstructure replacing the Nb_3Si grains, examples of this can be seen in Figure 71A and G and Figure 127, the latter were taken from area A and B at the edge of alloy CM1 8 mm suction cast bar. Using the previous two areas discussed in this work, the formation of Nb_3Si and the formation of anomalous eutectic, it is reasonable to conclude that Nb_3Si grew as a dendrite from the edge of the anomalous eutectic due to the change in solidification conditions brought on by the increased heat due to recalescence. In the initial stage of Nb_3Si dendrite growth there was a high V_f of Nb_3Si reducing the levels of Si in the liquid causing the liquid to solidify primarily as Nb_{ss} (Figure 127D). As can be seen in Figure 127A, B and C this then transformed into a region where darker contrast lamellar cells were surrounded by a lighter contrast lamellar structure, the latter of which is assumed to be Nb_{ss} + β-Nb_5Si_3 eutectic due to the morphological similarities to that of the "regular" interdendritic region. In this region the Nb_3Si formed in much lower concentrations pushing the liquid into the coupled zone of the eutectic in a similar way

to that of "regular" microstructure with Nb_3Si forming as the primary phase instead of β-Nb_5Si_3. The Nb_3Si that formed in these regions then decomposed vai a eutectoid leaving the darker lamellar cells surrounded by the lighter eutectic. Microstructures indicating the prior presence of Nb_3Si are also seen in the 6 mm sample however no evidence of Nb_3Si was found in this alloy (Figure 59)

In the cast alloy CM1 600 g the SEM studies confirmed microstructures similar to those observed in cast CM1 10 g (i.e., primary β-Nb_5Si_3 dendrites and Nb_{ss} + β-Nb_5Si_3 eutectic) but the XRD of the larger ingot confirmed the presence of Nb_{ss} and α-Nb_5Si_3. The other difference between the large and small ingots was the "subgrain" formation with fine precipitates of a second phase exhibiting same contrast as the Nb_{ss}, in the large ingot, Figure 51D. It should be noted that in the small ingot the β-Nb_5Si_3 had no subgrains and no fine second phase precipitates of a phase with contrast similar to that of the Nb_{ss}, and that both the latter (meaning subgrains and fine precipitates) formed in the small ingot after the heat treatment. It should also be noted that formation of subgrains and fine precipitates in α-Nb_5Si_3 were not observed in all silicide grains, which would suggest that orientation of the grain might have been important. Table 28 summarises the phases in the alloy CM1.

Considering only the Nb-Si binary (meaning, ignoring for the time being the role of the other solutes) the subgrain formation seems to be linked with the β-Nb_5Si_3 → α-Nb_5Si_3 transformation (cast alloy CM1 600 g) and could be attributed to "recovery" of the 5-3 silicide during solid state cooling driven by the strain energy arising from differences in thermal contraction between Nb_{ss} and Nb_5Si_3.

First-principles calculations performed in our group show that the moduli of elasticity of Nb, βNb_5Si_3 and αNb_5Si_3 respectively are 105, 269 and 291 (Papadimitriou et al. 2015a). The CTE (coefficient of thermal expansion) of Nb is 7.6 10^{-6} K^{-1}. The β-Nb_5Si_3 and α-Nb_5Si_3 exhibit anisotropy in CTE and the ratio of CTE values α_a/α_c along the a and c axes of their lattices (i.e., the CTE anisotropy ratio) is different for each phase, namely 0.783 and 0.658 for α-Nb_5Si_3 and β-Nb_5Si_3, respectively. The CTE values of β-Nb_5Si_3 and α-Nb_5Si_3 along their a axes are very close (8.961 10^{-6} K^{-1} and 8.777 10^{-6} K^{-1}) but those along their c axes are different, namely 11.095 10^{-6} K^{-1} and 13.331 10^{-6} K^{-1}, respectively,

according to our group's first-principles calculations (Papadimitriou et al. 2015b). All the aforementioned values are for the unalloyed phases and are expected to change as they become alloyed (see below).

Considering strain energy in β-Nb_5Si_3 to arise from the CTE anisotropy, meaning the lower the α_a/α_c ratio the higher the anisotropy, the subgrain formation as the β-Nb_5Si_3 transformed to α-Nb_5Si_3 would be accompanied by a reduction in strain energy (the "driving force") the latter driving "recovery" etc. and subgrain formation in the silicide.

In CM1 OFZ and for all growth rates the α-Nb_5Si_3 was present in the cast microstructures but no subgrains were observed. Given that thermal stresses in the "grown" solid can arise during solidification (see § 4.4) and that the sign and magnitude of these stresses depends on changes in cross section during OFZ and transport phenomena (heat and mass transfer) in the melt zone (§ 4.4), the absence of subgrains is attributed to reduced strain energy, the latter arising from the thermal stresses during OFZ counter-balancing stresses from the anisotropy of CTE of the 5-3 silicide, as discussed above.

Subgrain formation was not observed in the cast 10 g button ingot and the suction cast bars owing to the faster cooling during solid state cooling which did not give enough time for "recovery" processes. It should be noted that subgrain formation in Nb_5Si_3 in *binary* Nb-Si alloys has not been reported in the literature.

The data in Table 28 would suggest that the α-Nb_5Si_3 in cast CM1 600 g was the product of the β-$Nb_5Si_3 \rightarrow \alpha$-$Nb_5Si_3$ transformation that occurred under slow cooling conditions during solid state cooling of the solidified ingot and that the lamellar microstructures in the large cast ingot were indeed prior eutectics (formed as discussed above for the cast alloy CM1 10 g, CM1 6mm, and CM1 8mm) in which the silicide had transformed. Considering current knowledge of the Nb-Si binary, the above argument makes sense as there is no eutectic between Nb_{ss} and α-Nb_5Si_3. The fact that the Nb_3Si and its eutectoid transformation were observed in the area of highest cooling rate of cast CM1 8 mm bar

is attributed to the solidification path of the melt in that area (see above). The high cooling rate allowed us to "catch" the formation of Nb_3Si and its early stages of eutectoid decomposition.

Table 28: Phases in alloy CM1 arc melted and solidified button ingot, suction bars and large ingot

Alloy	*As Cast*	*Heat Treated*
CM1 10 g	Nb_{ss}, β-Nb_5Si_3 Si in eutectic = 19.9 at%	Nb_{ss}, α-Nb_5Si_3, in **α-Nb_5Si_3 subgrains + fine ppts*** Si in prior eutectic = 21.1 at%
CM1 6 mm SC	Nb_{ss}, β-Nb_5Si_3 Si in eutectic = 22.5 at%	Nb_{ss}, α-Nb_5Si_3, from location B to J in **α-Nb_5Si_3 subgrains + fine ppts*** Si in prior eutectic = 19.9 at%
CM1 8 mm SC	Nb_{ss}, β-Nb_5Si_3 in edge locations A and B Nb_3Si and $Nb_3Si \rightarrow Nb_3Si+\alpha$-$Nb_5Si_3$ Si in eutectic = 20.4 at%	Nb_{ss}, α-Nb_5Si_3, along centre of bar from location A to J in **α-Nb_5Si_3 subgrains + fine ppts*** Si in prior eutectic = 21.2 at%
CM1 600 g	Nb_{ss}, α-Nb_5Si_3, in **α-Nb_5Si_3 subgrains + fine ppts*** Si in lamellar microstructure = 19.4 at%	Nb_{ss}, α-Nb_5Si_3, in **α-Nb_5Si_3 subgrains + fine (coarser) ppts, *** Si in lamellar microstructure = 21.1 at%

* Similar volume fractions of silicide in lamellar microstructure, and similar spacing in lamellar microstructure

To summarize, using arguments based on the phase equilibria in the *binary* Nb-Si system and solidification theory the microstructure changes observed in the cast alloy CM1 10 g, 6 mm bar, 8 mm bar and 600 g can be explained with the help of Figure 116 to Figure 122. For melts with "fixed" C_o values higher than 19.5 at.%Si the observed microstructures can be accounted for by changes in $V_{S/L}$ that alter $T_{Eu}(V)$ (Figure 116 to Figure 118), the undercooling ΔT (Figure 119) and $D_L G_L/V_{S/L}$ (Figure 122). For cases with "fixed" $V_{S/L}$ and allowing for changes in melt composition C_o (> 19.5 at.%Si) the observed microstructures can be accounted for using the criterion of growth at maximum temperature (change of growth temperature of phases, Figure 116 to Figure 118), undercooling ΔT (Figure 119) and mode of growth (Figure 122). For melts with C_o close and/or below 19.5 at.%Si observed microstructures where the Nb_3Si is present can be accounted for with Figure 121 and Figure 122. Transitions between eutectic microstructures near the water cooled copper crucible walls can be attributed to decoupled growth between Nb_{ss} and Nb_5Si_3 being responsible for anomalous eutectic formation.

We shall now discuss the microstructures of the alloy CM2, first using arguments based on our knowledge of the Nb-Si binary system and its invariant reactions. Then, the discussion will expand to consider available data about ternary phase equilibria for both alloys.

The microstructures observed in the cast alloy CM2 10 g, CM2 6mm, CM2 8mm and CM2 500 g, were similar to those observed in the alloy CM1, including microstructure transitions, with the exception of large primary Nb_{ss} dendrites in CM2, e.g., see Figure 48A and Figure 53A.

The average Si concentration in the cast alloy CM2 was higher than the eutectic in the Nb-Si binary diagram, but lower than that in the alloy CM1 (e.g., 19.9 at.%Si in CM2 6mm vs 23.4 at.%Si in CM1 6mm, 19.8 at.%Si in CM2 500 g vs 22.7 at.%Si CM1 600 g) and in all forms of the alloy CM2 the Si content of the lamellar microstructure (eutectic?, see below) was in the range of the values for the metastable Nb_{ss} + β-Nb_5Si_3 eutectic.

The XRD confirmed the presence of α-Nb_5Si_3 in ***all*** forms of the cast alloy CM2 (the same was the case ***only*** in the alloy CM1 600 g) but in the cast alloy CM2 6mm also there was evidence of Nb_3Si and its eutectoid decomposition. The latter was also observed in the alloy CM1 8mm (see Table 28).

For the same reasons as discussed for the alloy CM1 600 g in the previous section, it is accepted that lamellar microstructures in the alloy CM2 were prior-eutectic Nb_{ss} + β-Nb_5Si_3, in which the β-Nb_5Si_3 transformed to α-Nb_5Si_3 upon solid state cooling and that in the case of the alloy CM2 6mm in addition to the aforementioned microstructure there were also areas of lamellar Nb_{ss} + α-Nb_5Si_3 resulting from the eutectoid transformation of Nb_3Si.

The formation of Nb_{ss} + β-Nb_5Si_3 eutectic microstructures in the alloy CM2 can be discussed using Figure 128 and Figure 129 in which the composition C_o of the alloy CM2 is to the left (lower Si) of that of the alloy CM1 (not shown in Figure 128 and Figure 129), for the alloy CM1 see C_o in Figure 116 to Figure 122.

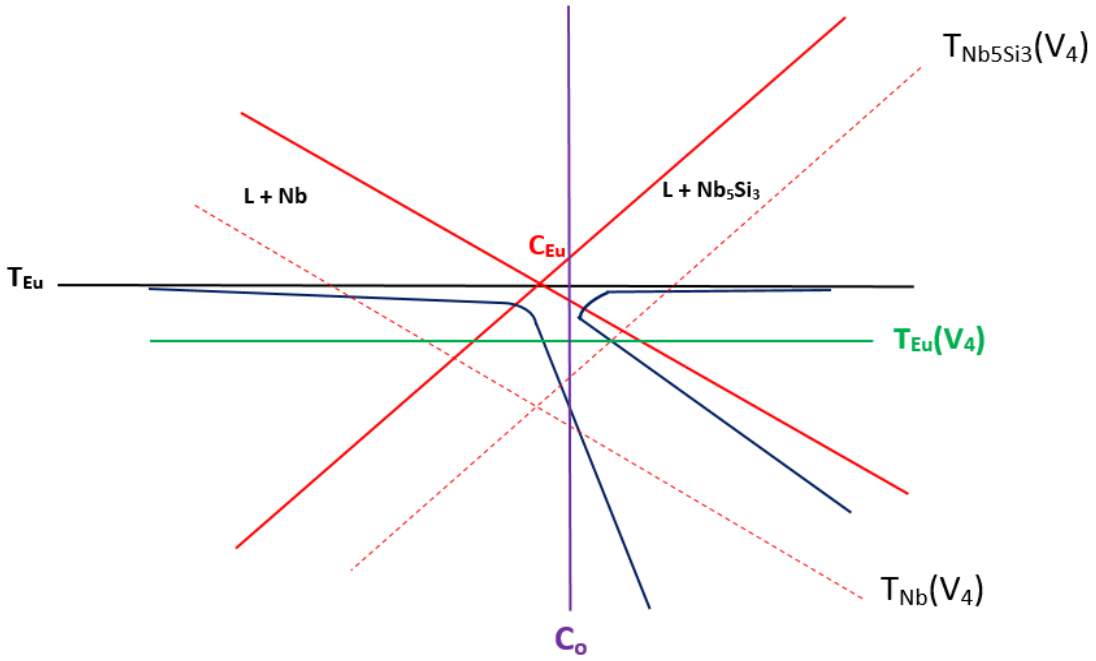

Figure 128: Schematic diagram of the skewed coupled zone of the Nb + β-Nb_5Si_3 metastable eutectic. Red continuous lines show the liquidus of Nb_{ss} and β-Nb_5Si_3 and dashed red lines the growth temperatures T_i (i = Nb_{ss}, β-Nb_5Si_3) dendrites at growth rate V_4. The black horizontal line is the eutectic temperature T_{Eu}.

At the growth rate V_4 in Figure 128 the growth temperature $T_{Eu}(V_4)$ of the coupled Nb + β-Nb_5Si_3 eutectic is higher than the growth temperatures of each phase, namely $T_{Nb}(V_4)$ and $T_{Nb5Si3}(V_4)$ and thus according to the criterion of maximum growth temperature (see § 1.1.1) the liquid of composition C_o will solidify as coupled Nb_{ss} + β-Nb_5Si_3 eutectic. At the growth rate V_5 in Figure 129 the liquid of composition C_o is outside the coupled zone and the solidification starts with primary Nb_{ss} dendrites with composition C_{Nb} as indicated in the figure.

Transitions in microstructure near the water cooled copper crucible are shown in Figure 130. These are similar to those observed in the alloy CM1 (see Figure 125 and Figure 126). The formation of anomalous eutectic in CM2 is attributed to the same reasons as for the alloy CM1, i.e., to decoupled growth of Nb_{ss} and β-Nb_5Si_3 in undercooled liquid.

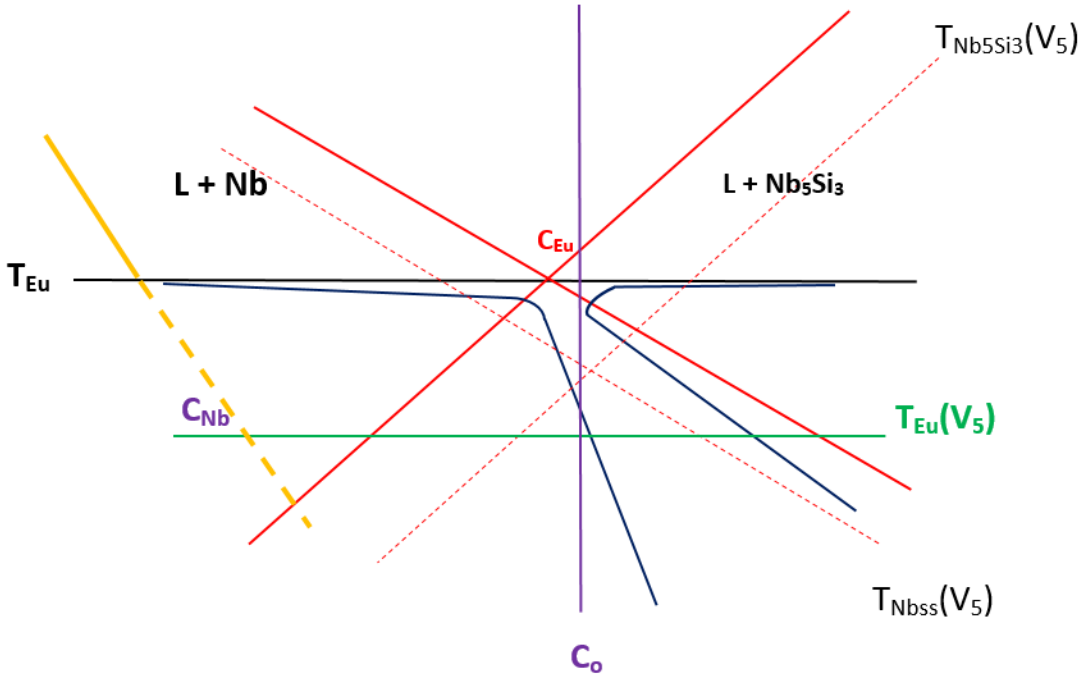

Figure 129: Schematic diagram of the skewed coupled zone of the Nb + β-Nb_5Si_3 metastable eutectic. Red continuous lines show the liquidus of Nb_{ss} and β-Nb_5Si_3 and dashed red lines the growth temperatures T_i (i = Nb_{ss}, β-Nb_5Si_3) dendrites at growth rate V_5. The solidus of Nb_{ss} and its extension are indicated by brown lines. The black horizontal line is the eutectic temperature T_{Eu}.

Closer inspection of the top right image in Figure 130 shows evidence of microsegregation (solute partitioning) in the Nb_{ss}. In the lower part of this image the core of the Nb_{ss} grains exhibits bright contrast compared with the Nb_{ss} grains in the upper part of this image which exhibit grey (darker) contrast. The former was also observed in Nb_{ss} dendrites in the bulk of cast alloy CM2 10 g, see Figure 48C, and would arise from high atomic number solutes like Hf and W in the core and low atomic number solutes like Si in the periphery. This means that the high atomic number solutes (Hf, W) might have played a role in the formation of the anomalous eutectic where the Nb_{ss}, that was formed was first, was Hf and W-rich and as the Nb_{ss} grew the Si was rejected to the periphery of the Nb_{ss} (which is supported by Figure 52 that shows that W (like Mo) does not like Si (and Ti)). The transition from anomalous to "normal" eutectic occurred when the liquid was poorer in Hf and W (the Nb_{ss} after the transition exhibited grey (darker) contrast). This would also explain why after HT the Nb_{ss} were rich in refractory metal (W) and with no Si, see § 4.3.

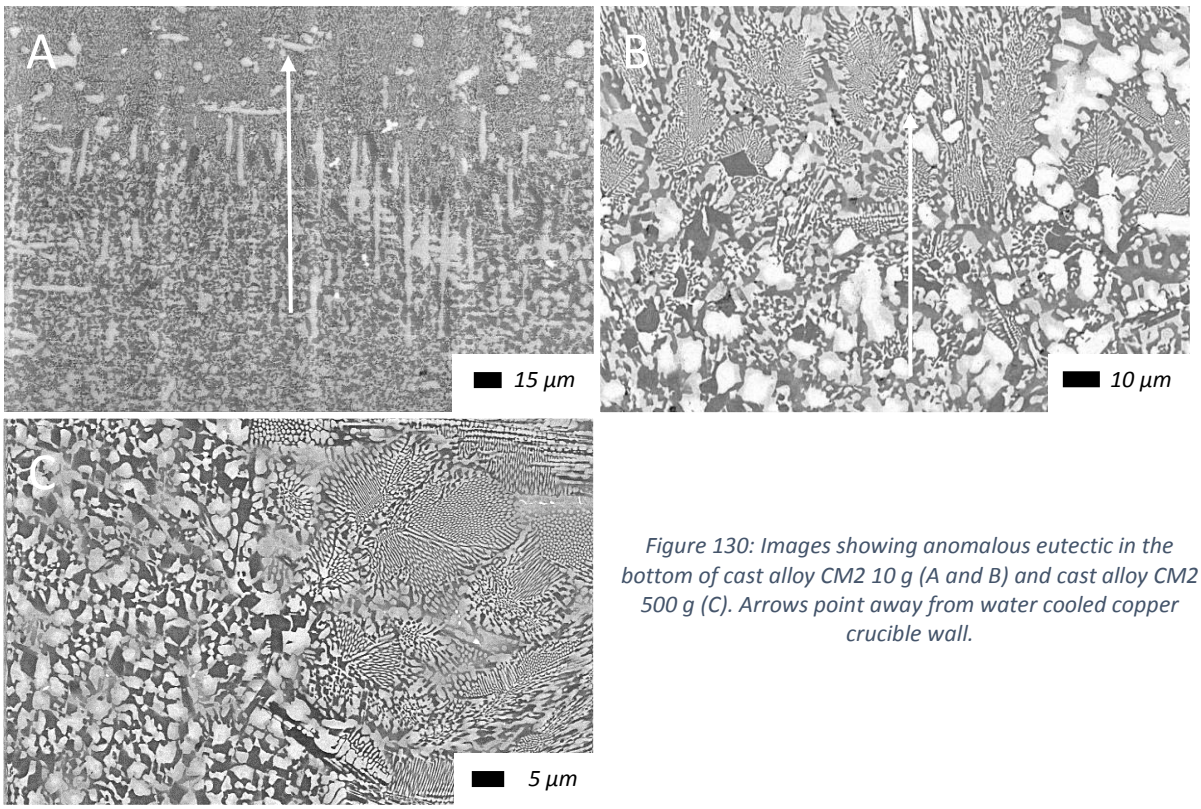

Figure 130: Images showing anomalous eutectic in the bottom of cast alloy CM2 10 g (A and B) and cast alloy CM2 500 g (C). Arrows point away from water cooled copper crucible wall.

An additional scenario for solidification is considered in Figure 131, and it is about nucleation in undercooled liquid near the crucible wall. Figure 131 schematically shows the case of the alloy CM2 of composition C_o undercooled to T_{nul}^{Nb5Si3} where β-Nb_5Si_3 nucleates first with composition C_{Nb5Si3} (intercept with solidus of Nb_5Si_3). The remaining liquid becomes leaner in Si *and if it were to undercool further* (while the β-Nb_5Si_3 nuclei continue to grow) a certain Si concentration and undercooling would be reached where Nb_{ss} of composition C_{Nb} nucleates. The Nb_{ss} dendrites would be leaner in Si compared with the liquid composition C_o. As recalescence occurs the growth of Nb_{ss} dendrites would enrich the melt in Si and the solidification enters the coupled zone (indicated by the purple arrow in Figure 131) and coupled Nb_{ss} + β-Nb_5Si_3 eutectic solidifies. The Nb_{ss} would grow rapidly under the higher undercooling ΔT_{Nb} of the Nb/L interface compared with the β-Nb_5Si_3/L interface and as it grows heat of fusion is released into the liquid causing recalescence. The latter is accompanied by a change in the composition of the liquid (see above). At the recalescence temperature and composition the liquid is in the coupled zone and thus the liquid solidifies as coupled eutectic of Nb_{ss} and Nb_5Si_3 (see

above). Following recalescence the solidification of the remaining liquid will be slow, meaning coarse spacing in the coupled eutectic.

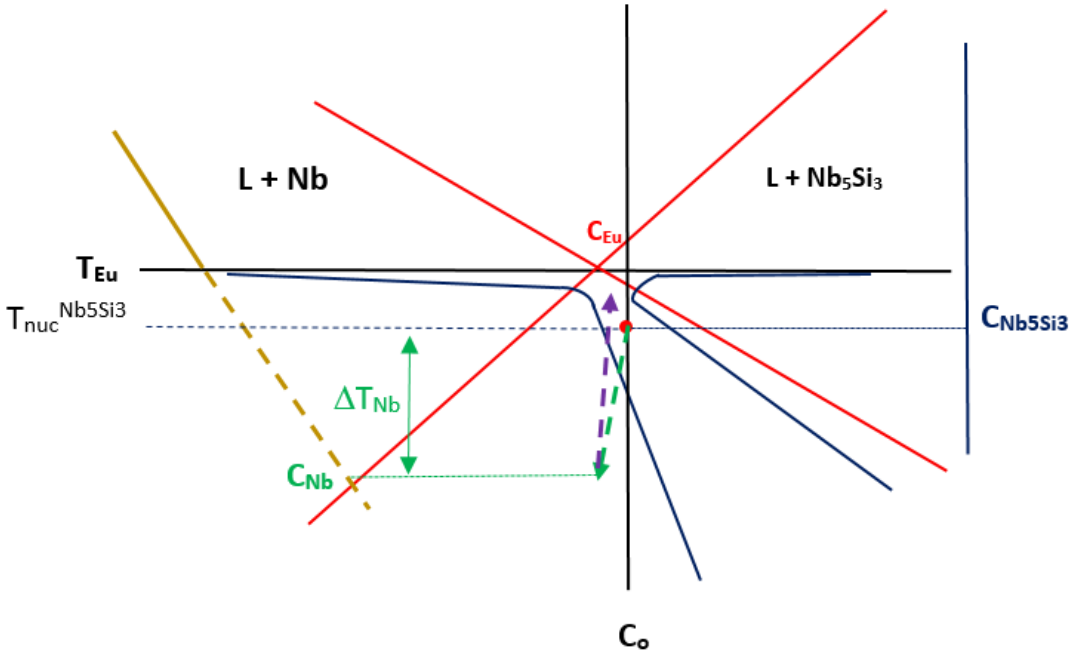

Figure 131: Schematic diagram of the skewed coupled zone of the Nb_{ss} + β-Nb_5Si_3 metastable eutectic. Red continuous lines show the liquidus of Nb_{ss} and β-Nb_5Si_3. The solidus of Nb_{ss} and its extension are indicated by brown lines. The alloy composition is C_o.

As discussed above, for the C_{Lp} (Figure 10A) of the L + β-Nb_5Si_3 → Nb_3Si peritectic in the Nb-Si binary (Figure 11) the values of 20.2 and 19.5 at.%Si have been reported. Thus, the C_o of the cast alloy CM2 6mm (19.9 at% Si) was very close to the C_{Lp} of the peritectic and it is possible that in liquid with composition to the left of C_{Lp} (i.e., lower than the above values) the Nb_3Si was formed (primary phase). There was evidence of very fine lamellar spacings in cast CM2 6mm and CM2 8mm, Figure 106 and Figure 110 respectively. In both cases these spacings were observed in the same areas (see Table 29) where evidence for the eutectoid transformation of Nb_3Si was observed, Figure 63 and Figure 78.

In the cast alloy CM2 no subgrain formation was observed in the α-Nb_5Si_3 in any of the specimens, which is different from the alloy CM1 (see above). This observation and the calculations of the stress σ using data for unalloyed Nb and β-Nb_5Si_3 (see above), would suggest that the Mo and

Ti solutes played a role in subgrain formation, meaning these solutes had an effect of the thermal contraction of Nb and Nb_5Si_3.

Table 29: Phases in alloy CM2 arc melted and solidified button ingot, suction bars and large ingot

Alloy	*As Cast*	*Heat Treated*
CM2 10 g	Nb_{ss}, α-Nb_5Si_3 Si in eutectic = 21.3 at.% Si in alloy = 20.7 at.% Anomalous eutectic. λ<1µm No subgrains, no precipitates (ppts).	Nb_{ss}, α-Nb_5Si_3 Si in eutectic = 23.7 at.% (21.7-26.1) Si in alloy = 22.3 at.% Coarsening, 1<λ<1.6µm No subgrains, no ppts.
CM2 6 mm	Nb_{ss}, α-Nb_5Si_3, Nb_3Si + eutectoid Si in eutectic = 20 Si in alloy = 19.9 at% Anomalous eutectic in areas D, E Edge very fine λ in C, D, E Centre very fine λ in A, D, E No subgrains, no ppts	Nb_{ss}, α-Nb_5Si_3, no Nb_3Si Si in eutectic = 22.4 Si in alloy = 16.9 at% (15.7 – 17.5) Coarsening Edge coarsening of λ Centre strong coarsening of λ in A, D, E not strong coarsening in other areas No subgrains, ***ppts in Nb_5Si_3 only in B2***
CM2 8 mm	Nb_{ss}, α-Nb_5Si_3, some eutectic very fine as in eutectoids. Si in eutectic = 21.7at.% Si in alloy = 21.8 at.% Anomalous eutectic along edge in areas A, D and along centre in A, J Edge $\lambda \approx$ constant Centre fine λ in A - D, then increases Edge transitions in microstructure, evidence of eutectoids, transition area lean in W, rich in Hf, Nb, evidence of Nb_3Si + eutectoid No subgrains, no precipitates	Nb_{ss}, α-Nb_5Si_3 Si in eutectic = 21.3at% (17.4-24.6) Si in alloy = 17.6 at% Edge λ varies widely, low in C, F and increased compared to AC Centre $\lambda \approx$ constant B- J and ≈1µm, coarsened particularly in A to E when compared with AC Edge, variations in microstructure No subgrains, ***weak precipitation in Nb_5Si_3***
CM2 500 g	Nb_{ss}, α-Nb_5Si_3 Si in eutectic = 20.6 at% (19-22.4) Si in alloy = 19.8 at% Anomalous eutectic λ<1µm Anomalous eutectic No subgrains, no precipitates	Nb_{ss}, α-Nb_5Si_3 Si in eutectic = 20.6 at% (17.3-23.6) Si in alloy = 17.1 at% (12.9-21.9) Ppts in centre of large Nb_{ss} grains No ppts in small Nbss grains Coarsening, 1<λ<2µm No subgrains, ***fine precipitates in Nb_5Si_3***

To summarize, using arguments based on the phase equilibria in the *binary* Nb-Si system and solidification theory the microstructure changes observed in the cast alloy CM2 10 g, CM2 6 mm bar,

CM2 8 mm bar and CM2 500 g can be explained with the help of Figure 116 to Figure 131. For melts with C_o close and/or below 19.5 at.% Si the presence of Nb_3Si in microstructures can be accounted for the same reasons as for the alloy CM1. Transitions between eutectic microstructures near the water cooled copper crucible walls can be attributed to decoupled growth between Nb_{ss} and Nb_5Si_3 being responsible for anomalous eutectic formation. The absence of subgrains and fine precipitates exhibiting similar contrast to Nb_{ss} in the α-Nb_5Si_3 in the cast alloy CM2 would suggest that the solutes Mo and Ti played a role in their formation.

We continue with the discussion of the results of this thesis by summarising the available data in the literature about Nb-Si-Mo, Nb-Si-W, Nb-Ti-Si and Mo-Si-W phase equilibria.

The first point to be appreciated is that the data about liquidus projections and solidification paths that is available in the literature is from studies in which arc melted alloys were solidified in water cooled copper crucibles, in other words under high cooling rates. Thus it is highly likely that the data might deviate from that that would have been acquired under equilibrium solidification. Below, alloy compositions are given in at%.

The Nb_3Si is destabilised by small Mo additions in Nb-Si-Mo alloys (Ma et al. 2004). Indeed, in Nb-16Si-xMo alloys with $x \leq 83$ the primary phase is the Nb_{ss} and when $x > 2$ the β-$(Nb,Mo)_5Si_3$ + Nb_{ss} eutectic replaces the $(Nb,Mo)_3Si$ + Nb_{ss} eutectic while in Nb-19Si-xMo alloys the primary phase is the $(Nb,Mo)_3Si$ when $x \leq 2$ and the β-$(Nb,Mo)_5Si_3$ when $x > 2$. In the latter alloys only the β-$(Nb,Mo)_5Si_3$ + Nb_{ss} eutectic is stable when $x \geq 4$ but both the β-$(Nb,Mo)_5Si_3$ + Nb_{ss} and $(Nb,Mo)_3Si$ + Nb_{ss} eutectics are formed when x = 3. Furthermore, in Nb-20Si-xMo alloys the primary phase is the β-$(Nb,Mo)_5Si_3$, and peritectic $(Nb,Mo)_3Si$ and $(Nb,Mo)_3Si$ + Nb_{ss} eutectic form when x = 1 and only β-$(Nb,Mo)_5Si_3$ + Nb_{ss} eutectic when $x \geq 3$ (Ma et al. 2000). Ma et al. (2000) reported that the composition of β-Nb_5Si_3 in the alloy Nb-19Si-3Mo was Nb-38.6Si-0.8Mo. On the contrary, Sekido et al. (2013) reported higher Mo solubilities in 5-3 silicides, namely 3.6 at% and 5.2 at% in α-Nb_5Si_3 and β-Nb_5Si_3, respectively. Solubilities of 2.5 at% Mo and 0.6 at% Mo in β-Nb_5Si_3 and α-Nb_5Si_3 were reported respectively for the

cast and heat treated conditions of the alloy Nb-18Si-5Al-5Cr-5Mo and slightly lower Mo concentration in the β-Nb_5Si_3 when Ti was added in the cast alloy Nb-24Ti-18Si-5Al-5Cr-5Mo (Geng et al. 2006b). In other words the data in the literature shows that the solubility of Mo is different in β-Nb_5Si_3 and α-Nb_5Si_3, depends on the presence or not of Ti in the silicide and also on the concentration of Mo in the alloy.

The recent study of Sekido et al. (2013) also confirmed that Mo stabilises the β-Nb_5Si_3 polymorph. The same authors reported that the transformation β-Nb_5Si_3 → α-Nb_5Si_3 (i) did not occur when the concentration of Mo in Nb_5Si_3 exceeded 6 at% and (ii) depended on the cooling rate. However, after heat treatment at 1400 ^{O}C for 100 hrs a mixture of both polymorphs was obtained (meaning both β-Nb_5Si_3 and α-Nb_5Si_3 were observed) when the Mo concentration in Nb_5Si_3 was 4 or 5 at%. It also confirmed that with Mo a two phase Nb_{ss} + α-Nb_5Si_3 or Nb_{ss} + β-Nb_5Si_3 phase equilibria can be attained in the Nb-Si-Mo ternary at 1700 ^{O}C, see Figure 22.

Tungsten has the same effect as Mo in the Nb-Si-W ternary phase equilibria, namely it destabilises the Nb_3Si and stabilises the Nb_{ss} and β-Nb_5Si_3 eutectic at W above 3 at% (Ma et al. 2004)

10W allowed formation of amorphous alloys (Masumoto et al. 1980), meaning that W enhances the undercool-ability of Nb-Si-W alloys at the level of Si and W concentrations considered in this thesis. Continuous solid solutions between β-Nb_5Si_3 and W_5Si_3 have been reported in cast ternary alloys (Cornish & Watson 2010) but the transformation of β-Nb_5Si_3 to α-Nb_5Si_3 does not allow the continuous solid solutions to persist to lower temperatures and the W solubility is about 1 at.% in α-Nb_5Si_3 (Ma et al. 2004). Mo and W form continuous solid solutions and Mo_5Si_3 and W_5Si_3 (and β-Nb_5Si_3) have the same crystal structures.

The early data that supported the construction of the Nb-Ti-Si liquidus projection(s) (Liang & Chang 1999) did not identify the structure of 5-3 compounds in the studied alloys (i.e., authors did not clarify which 5-3 allotrope was formed) and the projection gave a Nb_5Si_3 field, without specifying

whether this was the β-Nb_5Si_3 or the α-Nb_5Si_3 or the hexagonal Ti_5Si_3 based 5-3 silicide. Geng et al. (2009) "optimised" the Nb-Ti-Si ternary using published experimental data from GE researchers and proposed a liquidus projection with a large α-Nb_5Si_3 field, which did not agree with the literature. Li et al. (2013) recently revised the Nb-Ti-Si liquidus projection and performed a careful study of ternary alloys in the Nb_5Si_3-Ti_5Si_3 region. The proposed liquidus projection has only a very narrow field for the α-Nb_5Si_3 in the centre of the projection.

Like the Nb-Ti-Si ternary liquidus projection that does not indicate the Nb_5Si_3 polymorph forming from the liquid, the Nb-Hf-Si projection calculated by the same group based on data from GE researchers shows a field for $Nb(Hf)_5Si_3$ and the Scheil solidification path for Nb-19Si-5Hf is given as L → L + $Nb(Hf)_3Si$ → $(Nb,Hf)_3Si$ + $(Nb,Hf,Si)_{ss}$, meaning that Hf tends to stabilise the 3-1 silicide (Yang et al. 2003)

Sekido et al. (2013) reported that Nb_{ss} precipitates formed in both β-Nb_5Si_3 and α-Nb_5Si_3 after heat treatment even at 1300 ^{O}C for 20 hrs. Precipitation of Nb_{ss} in βNb_5Si_3 was not observed in the cast condition but after heat treatment at 1500 ^{O}C for 100 hrs plate shaped Nb_{ss} precipitates were formed in β-Nb_5Si_3 and the orientation relationship $\{-101\}_{Nb}$ // $\{2-10\}_{\beta Nb5Si3}$, $<111>_{Nb}$ // $<121>_{\beta Nb5Si3}$ was observed. In α-Nb_5Si_3 that formed from the β-Nb_5Si_3 → α-Nb_5Si_3 transformation during heat treatment at 1500 ^{O}C for 100 hrs there was Nb_{ss} precipitation in α-Nb_5Si_3 and for these precipitates two orientation relationships were observed, namely $(01-1)_{Nbss}$ // $(12-3)_{\alpha-Nb5Si3}$, $[133]_{Nbss}$ // $[111]_{\alpha-Nb5Si3}$ and $(-112)_{Nbss}$ // $(1-10)_{\alpha-Nb5Si3}$, $[110]_{Nbss}$ // $[110]_{\alpha-Nb5Si3}$ which were in agreement with the OR reported for eutectoid Nb_{ss}/α-Nb_5Si_3 lamellae by Sekido, Wei, et al. (2006) and Miura et al. (2005). Sekido et al. (2013) concluded that the β-Nb_5Si_3 → α-Nb_5Si_3 transformation occurs before the Nb_{ss} precipitates or simultaneously and attributed the precipitation of the Nb_{ss} to the β-Nb_5Si_3 exhibiting temperature dependent solubility owing to anti-site substitution of Nb and Mo atoms for Si sites (the β-Nb_5Si_3 and α-Nb_5Si_3 have solubility ranges (see Figure 11), for the former the off-stoichiometry towards the Si

rich side of the phase diagram is believed to be attained by substitutional, i.e., anti-site, defects and not by vacancies on Nb sites).

Regarding the alloy CM1 the formation of primary β-Nb_5Si_3 is consistent with the liquidus projections in the Nb-Si-Mo, Nb-Si-W and Nb-Ti-Si phase equilibria. It should be noted that using the Nb-Ti-Si liquidus projection (Li et al. 2013) the primary phase in the alloy CM1 is the β-Nb_5Si_3 when Nb, Mo, Hf and W are considered as equivalent, meaning the alloy CM1 is considered as a (Nb,Mo,Hf,W)-Ti-Si alloy. The Nb-Si-Hf liquidus projection according to (Yang et al. 2003) is of little use to this research owing to the lack of information about the type of 5-3 silicide formed from the liquid. The suppression of Nb_3Si and the formation of the Nb_{ss} + β-Nb_5Si_3 eutectic is also consistent with the liquidus projections in the Nb-Si-Mo and Nb-Si-W, see Figure 21 and Figure 24. The solidification of the Nb_{ss} + β-Nb_5Si_3 eutectic and the formation of Nb_{ss} haloes can be explained as discussed above with the help of Figure 116 to Figure 119. The formation of Nb_3Si in some of the forms of CM1 studied in this thesis (see Table 28) can be explained as discussed above and with the help of Figure 121 and Figure 122 but can also be linked with variations in Si and Mo content of the melt and the data from Ma et al. (2000) for Nb-19Si-xMo and Nb-20Si-xMo alloys. It should be remembered that both Hf and Ti at the concentrations in the alloy CM1 would tend to promote the Nb_3Si in the ternaries. The presence of α-Nb_5Si_3 in cast CM1 600 g can be attributed to the β-Nb_5Si_3 $\rightarrow$ α-Nb_5Si_3 transformation during solid state cooling that depends on the Mo concentration in the β-Nb_5Si_3 and on cooling rate and is also supported by phase equilibria data for 1700 ^{O}C for Nb-Si-Mo (Ma et al. 2004) and Nb-Si-W (Ma et al. 2000), see Figure 22 and Figure 25, that shows that the α-Nb_5Si_3 (with low solubilities for Mo or W) is in equilibrium with Nb_{ss} (in the Nb-Si binary the α-Nb_5Si_3 is stable below about 1940 ^{O}C, see Figure 11). The observation of α-Nb_5Si_3 only in cast CM1 600 g and not in cast CM1 10 g, CM1 6mm or CM1 8mm would suggest that the slower cooling of the larger ingot was essential for the sluggish β-Nb_5Si_3 $\rightarrow$ α-Nb_5Si_3 transformation taking place, consistent with the observations of (Sekido et al. 2013).

In the alloy CM2, the presence of W enhanced its undercool-ability (as was the case for the alloy CM1). For the alloy CM2 the formation of primary β-Nb_5Si_3 is consistent with the liquidus projections in the Nb-Si-W phase equilibria. The Nb-Si-Hf liquidus projection according to Yang et al. (2003) is of little use to this research owing to the lack of information about the type of 5-3 silicide formed from the liquid. The formation of Nb_3Si and eutectoid Nb_{ss} + α-Nb_5Si_3 can be accounted for as for the alloy CM1. The observation of α-Nb_5Si_3 in all cast forms of the alloy CM2 studied in this thesis is attributed to; (i) the β-Nb_5Si_3 → α-Nb_5Si_3 transformation during solid state cooling, which is also supported by phase equilibria data for 1700 ^{O}C for Nb-Si-W from Ma et al. (2004), see Figure 25, that shows that the α-Nb_5Si_3 (with low solubility for W) is in equilibrium with Nb_{ss} (in the Nb-Si binary the α-Nb_5Si_3 is stable below about 1940 ^{O}C, see Figure 11) and (ii) the absence of Ti in CM2. Indeed, according to first principles calculations performed in our group, Ti in Nb_5Si_3 decreases the temperature of the β-Nb_5Si_3 → α-Nb_5Si_3 transformation, meaning it tends to stabilise the β-Nb_5Si_3 (Papadimitriou et al. 2015b). Thus, with no Ti present in the alloy CM2, the aforementioned transformation was easier to occur and at a higher temperature during solid state cooling of all cast forms of the alloy CM2.

Subgrains were not observed in the α-Nb_5Si_3 in all the cast forms of the alloy CM2 (no β-Nb_5Si_3 was observed in the cast alloy CM2), but were observed in the α-Nb_5Si_3 in the cast alloy CM1 600 g ingot. First-principles calculations have also been performed in our group to show the effect of Ti substituting Nb in the β-Nb_5Si_3 and α-Nb_5Si_3 on the moduli of elasticity of β-Nb_5Si_3 and α-Nb_5Si_3 and their CTE values (Papadimitriou et al. 2015b). The Young's modulus of α-Nb_5Si_3 increases with Ti substituting Nb but that of β-Nb_5Si_3 decreases. For 12.5 at% Ti in the two silicides the E values are ≈ 314 and 244 GPa, respectively. The CTE (coefficient of thermal expansion) of the β-Nb_5Si_3 and α-Nb_5Si_3 also change and continue to exhibit anisotropy and the ratio of CTE values α_a/α_c along the a and c axes of their lattices (i.e., the CTE anisotropy ratio) is different for each phase, namely 0.797 and 0.611 for α-Nb_5Si_3 and β-Nb_5Si_3, respectively with 12.5 at% Ti substituting for Nb. The CTE values of β-Nb_5Si_3 and α-Nb_5Si_3 along their c axes are very close (10.682 10^{-6} K^{-1} and 10.980 10^{-6} K^{-1}) but those along their a-

axes are different, namely 8.510 10^{-6} K^{-1} and 6.709 10^{-6} K^{-1}. In other words, the substitution of Nb by Ti in the tetragonal 5-3 silicide makes the low temperature α-Nb_5Si_3 polymorph more isotropic (the ratio of CTE values α_a/α_c increases) and the high temperature polymorph more anisotropic.

In the alloy CM2 (no Ti present, and essentially no solubility of W in the 5-3 silicide, e.g., Table 8, Table 12 and Table 20) the difference between the ratios of CTE values α_a/α_c was 0.125 (the same as for the unalloyed silicide, see above. There is no data for Hf substituting Nb in the silicide but in CM2 no subgrains were observed in Hf rich and Hf poor 5-3 silicide, see end of § 3.2.1. This would suggest that the substitution of Nb by Hf did not have a strong effect on the CTE anisotropy according to our hypothesis for the formation of subgrains) but with the addition of Ti in the alloy CM1 (essentially no solubility of Hf and W in 5-3 silicide, e.g., see Table 7, Table 11, Table 15, Table 19 and Table 23) it increased to 0.186. Considering strain energy in β-Nb_5Si_3 to arise from the CTE anisotropy, meaning the lower the α_a/α_c ratio the higher the anisotropy, the subgrain formation as the Ti alloyed β-Nb_5Si_3 transformed to (Ti alloyed) α-Nb_5Si_3 would be accompanied by a reduction in strain energy (the "driving force"), but with the "driving force" increasing compared with the alloy CM2 (no Ti) owing to the substitution of Nb atoms by Ti atoms in the 5-3 silicide.

The above discussion ignores the role of Mo substituting Nb atoms in the 5-3 silicide because no data is available, but points to some special role played by Ti and Mo in the alloy CM1 (owing to the formation of subgrains + fine Nb_{ss} precipitates in α-Nb_5Si_3 in the cast CM1 600 g). We shall expand on this point in the next section.

4.3 HEAT TREATED ALLOYS CM1 AND CM2

In the alloys CM1 cast and OFZ and CM2 cast after the heat treatment the phases present in their microstructures were the Nb_{ss} and α-Nb_5Si_3 and HfO_2 and TiN were formed owing to interstitial contamination. The former two phases (and the absence of Nb_3Si) is in accordance with the ternary Nb-Si-Mo and Nb-Si-W phase equilibria at 1700 ^{O}C, see Figure 22 and Figure 25 and the 1500 ^{O}C isothermal Nb-Ti-Si isothermal section in (Bulanova & Fartushna 2010).

With the exception of the alloy CM1 600 g HT, in which there were Nb_{ss} grains with no Si and grains where the solubility of Si in the Nb_{ss} was low and at similar level to that reported for the Nb_{ss} in heat treated Nb silicide based alloys, in all other forms of the alloy CM1 the Nb_{ss} was free of Si, in agreement with other research in the group for arc melted Nb silicide alloys with refractory metal additions. The same was the case for the Nb_{ss} in the alloy CM2 500 g HT ingot and the other forms of CM2.

In some large ($\geq$ 30 μm) grains in the CM2 500 g HT second phase particles (precipitates) some of which were cuboidal in outline and exhibiting dark contrast were observed, see Figure 58B and C. The contrast of these precipitates was similar to that of Nb silicides, meaning they were Si rich. The presence of these precipitates was the reason for CM2 500 g HT having Nb_{ss} grains with Si. According to the literature, these precipitates were metastable Nb_3Si, as observed in binary Nb-Si and ternary Nb-Ti-Si alloys (Cockeram et al. 1991; Grylls et al. 2001; Bewlay, Grylls, et al. 1998) or δ-$Nb_{11}Si_4$ as observed in ternary alloys (Kashyap et al. 2013a; Cheng et al. 2010)], most likely (due to more advanced characterisation techniques) the latter intermetallic. Confirmation of the identity of the second phase precipitates observed in the large Nb_{ss} grains in the CM2 500 g HT alloy requires TEM studies, which were beyond the scope of the research presented in this thesis. There was strong partitioning of W in the Nb_{ss} compared with the α-Nb_5Si_3 (see § 3.1.2). We have seen (data for the alloy CM1, Figure 52) that Si and W “do not like” each other. Thus, it is suggested that the bulk of the large grains where this precipitation occurred was W and Si rich and the precipitation occurred as the

W "pushed" away the Si atoms creating the supersaturation required for the nucleation of the (Si rich) Nb_3Si or δ-$Nb_{11}Si_4$.

In both alloys the Nb_{ss} had high concentration of refractory metals, which in some cases increased slightly after the heat treatment, and most importantly the W + Mo content is the Nb_{ss} in the alloy CM1 tended to be similar to the W content in the Nb_{ss} in the alloy CM2. Such high levels of RM in the Nb_{ss} are expected to provide significant solid solution strengthening, which is essential for the mechanical properties (strength, creep) of the alloys at high temperatures, see Table 6.

There was coarsening of the microstructure, which was less severe in the alloy CM2 owing to more sluggish kinetics due the lower homologous heat treatment temperature for this alloy compared with the alloy CM1 (the Ti addition in the alloy CM1 is expected to reduce the liquidus compared with the Ti free CM2) and prior eutectic areas were retained in some cases.

Precipitation of second phase with contrast similar to that of Nb_{ss} has been reported by our group in α-Nb_5Si_3 in the *heat treated* Nb-24Ti-18Si-5Al (Zelenitsas & Tsakiropoulos 2006a) and Nb-18Si-5Al-5Cr-5Mo alloys (Geng et al. 2006b) in α-Nb_5Si_3 and/or β-Nb_5Si_3 in the *heat treated* Nb-24Ti-18Si-5Al-5Cr, Nb-24Ti-18Si-6Ta-5Al-5Cr, Nb-24Ti-18Si-8Cr-4Al, Nb-24Ti-18Si-6Ta-8Cr-4Al (Zelenitsas & Tsakiropoulos 2005; Zelenitsas & Tsakiropoulos 2006b), Nb-24Ti-18Si-5Al-5Cr-5Mo, Nb-24Ti-18Si-5Al-5Cr-2Mo (Geng et al. 2006b), Nb-24Ti-18Si-5Al-5Cr-5Hf-5Sn-2Mo (Geng et al. 2007) and Nb-18Si-5Al-5Ge and Nb-24Ti-18Si-5Al-5Ge (Li & Tsakiropoulos 2013) alloys, and in α-Nb_5Si_3 in Nb-20Ti-18Si-4Hf-5Cr-3Al-1.5Sn (Cheng et al. 2009). In the latter alloy the orientation relationship was $(222)_{Nbss}$ // $(002)_{\alpha\text{-}Nb5Si3}$ and $[1\text{-}10]_{Nbss}$ // $[1\text{-}10]_{\alpha\text{-}Nb5Si3}$ and the interface between Nb_{ss} and α-Nb_5Si_3 was found to be enriched in Hf.

Based on their results for the *heat treated* alloy Nb-24Ti-18Si-5Al Zelenitsas & Tsakiropoulos (2005) suggested that the Nb_{ss} precipitates were the product of the β-Nb_5Si_3 $\rightarrow$ α-Nb_5Si_3 + Nb_{ss} phase transformation. Furthermore, the data in (Zelenitsas & Tsakiropoulos 2005; Zelenitsas & Tsakiropoulos 2006b) showed that in *heat treated* Nb-24Ti-18Si-5Al, Nb-24Ti-18Si-6Ta-5Al-5Cr, Nb-24Ti-18Si-8Cr-4Al

and Nb-24Ti-18Si-6Ta-8Cr-4Al alloys the Nb_{ss} tended not to form in Ti rich areas in the α-Nb_5Si_3 and/or β-Nb_5Si_3. The data from our group and Cheng et al. (2009) would suggest that precipitation of Nb_{ss} in β-Nb_5Si_3 and/or α-Nb_5Si_3 is a more general phenomenon in Nb silicide based alloys and that many solutes contribute to this precipitation.

Precipitation of Nb_{ss} was observed in the (subgrained) α-Nb_5Si_3 in *cast* CM1 600 g, and in the non-subgrained α-Nb_5Si_3 in cast CM1 OFZ 150 mm/h, 60 mm/h and 12 mm/h, and in all the (subgrained) α-Nb_5Si_3 in the *heat treated* CM1 10 g, CM1 6mm, CM1 8mm, CM1 600 g, and CM1 OFZ 150 mm/h, 60 mm/h and 12 mm/h, and in non-subgrained α-Nb_5Si_3 in the *heat treated* CM2 10 g, CM2 6mm, CM2 8mm, CM2 500 g.

The formation of subgrains in the α-Nb_5Si_3 in the heat treated CM1 OFZ at all growth rates is attributed to the strain energy reduction via "recovery" phenomena, the strain energy (not counter-balanced by that due to other stresses as in the cast OFZ alloy) and attributed to the anisotropy of CTE due to the alloying with Ti and the changes in the chemistry of the silicide after the heat treatment (see data in Table 23 and Table 26).

Figure 132 shows the detailed microstructure of an α-Nb_5Si_3 grain with subgrain and fine precipitates. The subgrain boundary exhibits dark contrast but the bulk of the subgrains are lighter in contrast, meaning the latter must be richer in high atomic number elements (Hf, W). In this alloy the Nb_{ss} is also rich in W. Notice that near the boundary some precipitates are larger in size. Overall the precipitates are nanometre size and the spacing between them is also in the nanometre scale. Precipitates with high aspect ratio together with fine spherical precipitates can be seen in Figure 55C, where it should be noticed that there is a precipitate free area (zone) near the interface of Nb_{ss} and α-Nb_5Si_3. The latter can be seen also in Figure 58A for the alloy CM2.

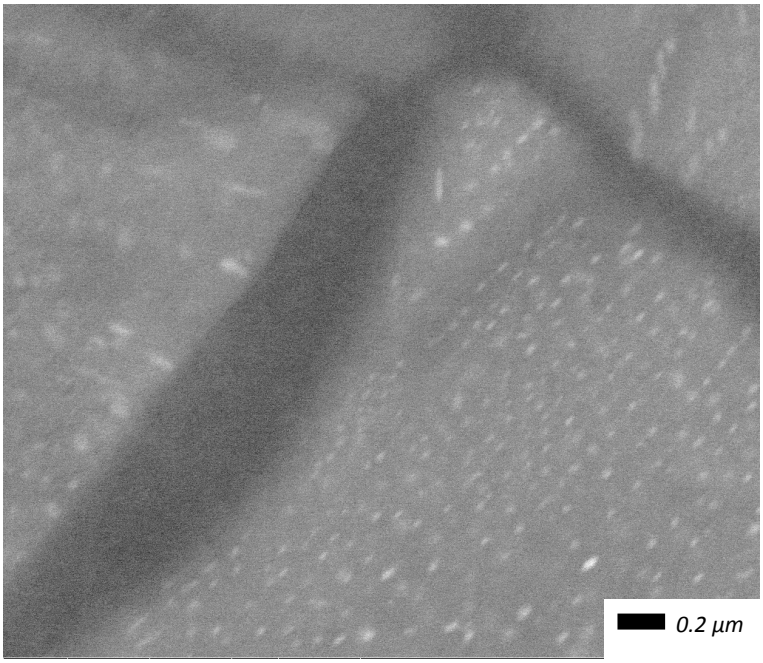

Figure 132: Backscattered electron image of heat treated alloy CM1 10 g showing subgrain boundary (dark contrast area) and fine brighter contrast precipitates.

In the alloy CM1, in the β-Nb_5Si_3 the high Ti (and Hf) content was associated with low Mo (and W) content (the Hf and W concentrations were extremely low, practically zero), for example see § 3.1.1, and Nb_{ss} precipitates formed in the large silicide grains in areas where X ray maps indicated low Ti high Mo content, see § 3.3.1 and Figure 86 and there was a "band" of Ti rich Mo poor silicide that was precipitate free and was formed next to the Nb_{ss} surrounding the 5-3 silicide, see Figure 85. In the Nb_{ss} the high Ti and Hf content was associated with low Mo and W content , for example see § 3.1.1 and Figure 47, there were Ti rich and Ti poor areas in the Nb_{ss} after the heat treatment, and the W in the Nb_{ss} also varied significantly, for example see § 3.2.2. Given that no precipitates were observed in the Ti rich (and Mo poor) areas (bands) formed at the interface between Nb_{ss} and Nb_5Si_3 (which according to the literature (Zelenitsas & Tsakiropoulos 2005; Zelenitsas & Tsakiropoulos 2006b) are the areas where Ti segregates during the solidification of Nb silicide based alloys), the precipitation of Nb_{ss} occurred in the Ti poor and Mo rich areas in the bulk of the silicide. Which is in agreement with previous research in our group (see above) and the role of Mo in the precipitation of Nb_{ss} according

to the work of Sekido et al. (2013). The evidence in this thesis would suggest that there was some orientation relationship of the Nb_{ss} precipitates in the silicide grain, see § 3.3.

In the alloy CM2 in the 5-3 silicide there were Hf rich and Hf poor areas and the W concentration was essentially zero and in the Nb_{ss} the refractory metal content (i.e. W) was similar to that (i.e. Mo + W) in the alloy CM1 and there was variation in the W concentration as was the case in the alloy CM1. Low Hf content in the Nb_{ss} was associated with high W concentration and vice versa. It should be remembered that in Ti and Hf containing Nb silicide based alloys, our group showed that during solidification Ti and Hf partition in the 5-3 silicide and in the Nb_{ss} forming Ti and Hf rich areas in both phases, which are found on either side of their interfaces. It is suggested that the precipitation of Nb_{ss} in the silicides in the alloy CM2 occurred with Hf and W acting as did Ti and Mo in the alloy CM1 (evidence for precipitate free Hf rich area (light contrast) as "equivalent" to precipitate free Ti rich area (see above) can be seen in Figure 133).

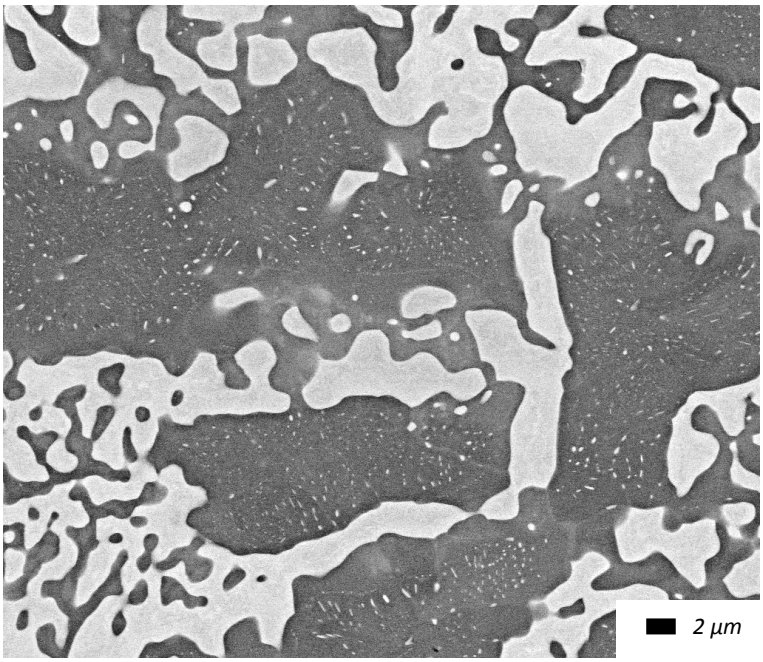

Figure 133: Backscattered electron image of alloy CM2 500 g HT showing precipitate free areas (zones) exhibiting lighter contrast and fine precipitates in areas exhibiting darker contrast.

To summarise, in the alloy CM1 the addition of Ti was responsible for subgrain formation in β-Nb_5Si_3 during the β-Nb_5Si_3 → α-Nb_5Si_3 transformation and Ti and Mo for the precipitation of Nb_{ss} in

the α-Nb_5Si_3 during solid state cooling in *cast* CM1 600 g and during heat treatment in all forms of CM1, with growth of the precipitates formed on subgrain boundaries owing to enhanced diffusivity. In the alloy CM2 the absence of Ti was responsible for the non-formation of subgrains during the β-$Nb_5Si_3 \rightarrow \alpha$-$Nb_5Si_3$ transformation and Hf and W for the precipitation of Nb_{ss} in the α-Nb_5Si_3 during heat treatment, with the precipitation of the Nb_{ss} being sluggish (compared with CM1) owing to the absence of short diffusivity paths (no subgrains and subgrain boundaries) and the slower diffusivity of W (compared with Mo) in the silicide grain.

4.4 OPTICAL FLOATING ZONE PROCESSING

The two alloys studied in this thesis were processed using OFZ with xenon lamps, counter-rotation of the support and feeder rods at 30 rpm and pulling of the system downwards at the said velocities in an Ar atmosphere (i.e., the S/L interface moved upwards, see Figure 35 and Figure 36i during OFZ). After the supporting and feeder rods were in place (t = 0) melting was initiated on the bottom of the feeder rod melted first ($t = t_1$). The feeder rod was then lowered to come into contact with the support rod at which point solidification began and entire system moved downward at the assigned rate to establish "steady state" growth conditions. The shape of the melt zone, of the S/L interface and of solidification conditions were determined by a large number of inter-related parameters and phenomena. These was discussed for OFZ processing using data in the literature. The data is from modelling studies of Si and/or $NaNO_3$ under normal gravity or zero gravity, with the interest in OFZ Si arising from its use in functional applications and the possibility of growing Si single crystals in microgravity or zero gravity conditions (to our knowledge there is one modelling study of the floating zone growth of the refractory metal Mo by Chen & Chu (1995), and the OFZ of Ge has also been modelled (Young & Chait 1990). The actual solidification microstructures of each alloy will then be discussed in § 4.5 and 4.6.

4.4.1 Highlights from the literature on OFZ processing

The highlights of the literature described in § 1.6.3.1 can be "summarised" as shown below in A to L and show that the microstructures developed in OFZ processing depend on twelve inter-related parameters – phenomena – processes.

A - Surface tension:

A1: The surface tensions γ_{SV}, γ_{SL} and γ_{LV} will vary with temperature and composition and the former two will also vary with the orientation of the solid surface.

A2: The γ_{LV} will change along the liquid surface owing to changes in temperature along the surface. There will be movement of liquid from areas of low surface tension to areas of high surface tension.

A3: The surface tension parameter M depends on liquid density and viscosity and $|\partial\gamma_{LV}/\partial T|$.

A4: There is no data for γ_{ij} (i, j= L, S, V), viscosity and $|\partial\gamma_{LV}/\partial T|$ for Nb silicide based alloys.

B - Convection and transport phenomena in melt zone:

B1: Convection in the melt zone can be (i) from surface tension driven flow, (ii) from buoyancy driven natural convection, (iii) from rotation of the feeder and (grown) solid and (iv) from flow generated by melting at the liquid interface and solidification at the solid interface.

B2: The liquid will move from areas of low surface tension to areas of high surface tension.

B3: The magnitude of convection will depend on the processing conditions (e.g., counter-rotation or not of rods, number, type and shape of lamps, de-focussing or not of lamps, diameter of rods, growth velocity, surrounding atmosphere, non-steady state and steady state growth) and material.

B4: The flow can change from laminar to oscillatory to turbulent. Moderate convection will result in laminar flow. Increase in rotation speed can lead to turbulent flow.

B5: Models have considered liquid flow within the liquid boundary layer parallel to the S/L interface in DS solidification of eutectic alloys.

B6: There will be Marangoni convection in temperature gradient (MCT) and Marangoni convection in concentration gradient (MCC).

B7: The surface tension parameter M can be used to characterise thermocapillary flow in OFZ.

B8: For Nb and Mo (materials with very low Prandtl number Pr << 1, like Si, where Pr is 0.026 and 0.025, respectively for Nb and Mo)) laminar flow will have a small influence on the heat transfer.

B9: The Pr values for Mo, Nb and Si indicate that if these elements were to be grown using floating zone melting, it is most likely that they will exhibit thermocapillary flow.

B10: Convection arising from rotation of the feeder and grown solid can be described using the dimensionless numbers $S = \omega_f/\omega_s$ and $A = l/\alpha$, where ω_f and ω_s are the rotation speeds of the feeder and solidified specimen, respectively, and l and α are the half zone length and the rod radius. For no free convection when S = -1 the flow in the zone is divided into two equal cells by the mid-plane of the zone.

B11: Models for OFZ Si have indicated (a) that the streamlines are concentrated at the L-V surface, with the centre of the vortex being near the liquid surface, (b) that the direction of the streamlines is from hot to cold, (c) that the flow of hot liquid is along the surface and directed to the interface, (d) that flow and mixing in the floating zone are significant and (e) that secondary cells form and move towards the S/L interface as M increases.

B12: Experiments would suggest (i) that the contribution of MCT to diffusion becomes significant when the melt zone length increases, (ii) that the Marangoni vortices move from near the surface towards the zone interior as the melt zone length increases, (iii) that flow instability occurs when the Marangoni number exceeds some critical value, which depends strongly on the aspect ratio of the melt zone and the properties of the liquid and (iv) that *in the presence of solute* the flow velocity induced by MCC is significantly lower than that of MCT.

B13: Models for OFZ with upward growth for three different counter-rotation speeds (higher than those used in this research) showed that four flow cells were formed in the melt zone, two near the L-V surface and two further in. The former were attributed to MCT and the latter to the centrifugal force arising from the counter-rotation, i.e., were attributed to forced convection.

C - Shape and stability of melt zone:

C1: The shape of the melt zone depends on the angle φ of the meniscus formed at the S-L-V junction.

C2: Every material has a characteristic φ^* that depends on the crystal orientation and the type of solutes and their concentrations in the liquid and the gaseous environment in the OFZ process.

C3: If φ deviates significantly from φ^* then the shape will become unstable.

C4: No φ^*data is available for Nb silicide based alloys.

C5: The length beyond which the melt zone becomes unstable and collapses is proportional to $(\gamma_{LV}/\rho g)^{1/2}$.

C6: Shape, length and stability of melt zone are affected by convection and transport phenomena in the liquid zone.

D - Change in cross section:

D1: When growth occurs with $\varphi \neq \varphi^*$ change in cross section should be expected.

D2: Radiation heat losses to the surroundings will increase with increasing cross section of the grown crystal.

D3: Changes in cross section area will have an effect on the magnitude and sign of thermal stresses in the solid at the S/L interface.

E - Shape of S/L and L/V interfaces:

E1: The shape of the S/L interface will change with increasing power input from convex towards the liquid to flat to concave.

E2: Large deformation of the L/V interface can modify the flow and temperature fields.

E3: The shape of the S/L interface depends on transport phenomena (mass and heat transfer) in the melt zone.

E4: For $|\partial\gamma_{LV}/\partial T| = 0$ the shape of the growth front will change when the peak temperature T_{peak} changes. Convex interfaces will form for low T_{peak} and concave for higher T_{peak}.

F - Oscillations:

F1: Oscillations about the steady state can occur when growth occurs with $\varphi \neq \varphi^*$.

F2: Transitions to oscillatory state could occur at a critical Marangoni number.

F3: Solute inhomogeneities could lead to periodic and irregular oscillations.

F4: At intermediate M values oscillations and formation of striations parallel to the S/L interface are likely.

G - Temperature gradients $(dT/dx)_S$ and $G_L = (dT/dx)_L$:

G1: Highest value of $(dT/dx)_S$ will occur when there is no change in cross section in melt zone.

G2: The value of $(dT/dx)_S$ will decrease as the change in cross section becomes severe.

G3: For constant growth rate a decrease in $(dT/dx)_S$ means a decrease in $(dT/dx)_L$.

G4: As $(dT/dx)_S$ decreases with increasing change in cross section of the crystal there will be a reduction of $G_L = (dT/dx)_L$.

G5: Long cylindrical lamps will produce sharper axial energy distribution and thus higher $G_L > 0$ at the S/L interface.

G6: The $(dT/dx)_S$ can be as high as 973 and 1365 K/cm for DS Nb and W, respectively.

H - Stress in solid:

H1: Thermal stresses in the solid will develop from the initial stages of crystal growth.

H2: The magnitude and sign of the thermal stresses will depend on the change in cross section area with distance from the growth (i.e., S/L) interface.

H3: Tensile thermal stresses will set in when there is no change in cross section or the change of angle ξ (Figure 37) is very small.

H4: Compressive thermal stresses will set in when the angle ξ increases.

I - Temperature fields:

I1: In OFZ with mirror based heating it is difficult to measure and control the temperature distribution.

I2: Long cylindrical lamps will produce sharper axial energy distribution.

I3: For small Pr number materials (like Nb, Mo, W, Ti, Si, Hf) when $PrRe_S = 1$ the temperature field is determined by conduction.

I4: When $PrRe_S = 100$ the temperature field depends strongly on fluid flow. When $S = \omega_f/\omega_S = -1$ the isotherms near the axis are pushed to each rod and those near the periphery move away from each rod along the flow direction.

I5: For large Schmidt number materials ($Sc^{Si} = 5$, $Sc^{Nb} = 145$) the feeder and crystal fronts will be non-isothermal owing to variation in solute concentration.

J - Solute distribution:

J1: Mixing affects the mass flow more strongly compared with the thermal flow.

J2: The convective motion in the liquid distributes solute laterally.

J3: Increased rotation speed that leads to turbulent flow will result to the development of transverse macrosegregation.

J4: At low M values if the growth rate is not low there will be radial variations in solute concentration.

J5: The distribution of solute and the development or not of chemical in-homogeneities in the solid depend on the mass and heat transfer in the melt zone.

J6: Experiments would suggest that in the presence of solute the flow of the hot liquid is to the interior of the melt zone.

J7: Models indicated that in the presence of laminar flow the convection has a small influence on heat transfer for small Prandtl number Pr (<< 1) materials and that the laminar flow cells would lead to significant inhomogeneities in the melt and the solidified material.

J8: In the presence of convection the iso-concentration lines and the point where the eutectic composition is reached shift in the direction of the flow.

J9: For large Schmidt number materials the axial concentrations gradients near the feeder and crystal fronts are steep.

J10: For $|\partial\gamma_{LV}/\partial T|$ = 0 and k<1, for a strongly convex interface the solute diffuses to the L-V surface (radial segregation) and for concave interface the solute segregates towards the centre of the crystal.

J11: For increasing $|\partial\gamma_{LV}/\partial T|$ and k<1 the solute moves inward towards the centre and segregates there. Upon further increase of $|d\gamma/dT|$ the flow mixes the solute and the radial segregation in the centre decreases. The solute concentration varies along the axis but not near the L-V interface.

J12: For increasing $|\partial\gamma_{LV}/\partial T|$ and k>1 at high $|\partial\gamma_{LV}/\partial T|$ values the melt zone is shorter and the concentration field is reversed, meaning the maximum solute concentration is at the feeder front and the minimum at the crystal front, and the solute segregates toward the surface. With increasing $|\partial\gamma_{LV}/\partial T|$ the solute segregation increases and then decreases due to mixing. There is longitudinal variation in solute concentration but not near the L-V interface.

K - Undercooling, stability of S/L interface:

K1: MCT and MCC will affect the morphological stability of the S/L interface.

K2: The convective motion in the liquid will distribute solute laterally and thus should be expected to morphologically stabilise the S/L interface.

K3: The formation of constitutionally undercooled liquid and therefore the "breakdown" of the interface is most likely to occur at the centre rather than at the periphery of the solidifying solid.

K4: Long cylindrical lamps will produce sharper axial energy distribution and thus higher $G_L > 0$ at the S/L interface that prevents formation of constitutionally undercooled liquid.

K5: For constant growth rate a change in $(dT/dx)_S$ means a change in $(dT/dx)_L$ and thus an effect on the formation of constitutionally undercooled liquid ahead of the S/L interface and the morphological stability of the latter. As $(dT/dx)_S$ decreases with increasing ξ (Figure 37b) a change in cross section of the crystal that reduces $(dT/dx)_L$ will encourage the onset of constitutional undercooling.

K6: For rigid boundary layer, convection makes the S/L interface less morphologically stable for solute with $k > 1$ but could either increase or decrease morphological stability for $k < 1$.

K7: For deformable boundary layer, convection stabilises morphologically the S/L interface for solute with $k < 1$, and for $k > 1$ convection destabilises the S/L interface and capillary stabilises the interface quickly when convection is strong.

K8: Models predict that the undercooling ΔT at the S/L interface will decrease linearly with the intensity of convection, especially at low $V_{S/L}$.

L - Eutectic spacing:

L1: The spacing λ will depend on how the S/L interface "breaks down" (i.e., becomes destabilised).

L2: Liquid flow within the liquid boundary layer parallel to the S/L interface in DS solidification of eutectic alloys affects the size of eutectic phases and the lamellar $\leftrightarrow$ fibre eutectic microstructure transitions.

L3: Models would suggest that the eutectic spacing λ increases as forced convection increases and that the lamellar $\rightarrow$ fibre eutectic microstructure transition becomes easier in the presence of convection, particularly at low growth rates (or large eutectic spacing λ).

L4: The dependence of eutectic spacing on convection intensity, particularly at low $V_{S/L}$ is also dependent on eutectic volume fraction.

L5: Convection has less influence on λ at high $V_{S/L}$, and the change in λ depends on the orientation of the lamellae relative to the flow.

L6: In the presence of convection the lamellae could grow at an angle to the S/L interface.

4.5 OFZ ALLOY CM1

The cast microstructures of the alloy CM1 OFZ were similar in all three growth velocities regarding "architecture" and phases present (Figure 82), and the scale of the microstructure became finer as the growth rate increased (Figure 113 and Figure 114). Compared with the suction cast alloy, the size of the eutectic cells was significantly larger, see Figure 59 and Figure 82.

In the OFZ processing of the alloy CM1 it is expected that γ_{SV}, γ_{SL} and γ_{LV} would have varied with temperature and composition of the melt and solid (partitioning of solutes between solid phases and liquid), and that γ_{SV}, γ_{SL} could have also varied with the orientation of the solid surface (facetted 5-3 silicide), that the parameter M would have changed as the liquid density, viscosity and $|\partial\gamma_{LV}/\partial T|$ changed, that there were slight changes in cross section as "*conditions were adjusted to achieve steady growth and/or uniform melt zone*" and that oscillations occurred as φ would have deviated significantly (?) from φ^*_{Nb} and solute in-homogeneities developed. There is no data available for Nb silicide alloy melts to allow us to calculate such changes. Available data for elemental Nb and Si has been given in the § 4.4.

The solidification microstructures were formed as discussed in § 4.2 with the help of Figure 116 to Figure 119 for the other forms of the alloy CM1, meaning the primary phase was the β-Nb_5Si_3, haloes of Nb_{ss} and coupled Nb_{ss} + β-Nb_5Si_3 formed and during solid state cooling during OFZ processing the transformation β-$Nb_5Si_3 \rightarrow \alpha$-$Nb_5Si_3$ occurred. The reasons for the absence of subgrains in α-Nb_5Si_3 and the precipitation of second phase in α-Nb_5Si_3 were discussed in § 4.2.

The undercooling at the S/L interface (and the temperatures $T_{Eu}(V)$ in Figure 116 to Figure 118) that drove the formation of the solidification microstructure is attributed to (see § 4.4.1) K3 (inter-related with J2, J4 (for the high growth rate), J6, J9 (inter-related with I5), J11, J12 and B11) and K5 (inter-related with G2 to G4), then K1 and K2 (inter-related with A1, A2, B1 (inter-related with A1, A3), B2, B3, B9, B10 and B13) and then K8, K7 (partition coefficients of Mo and W in Nb_{ss}, respectively $k_W > 1$, $k_{Mo}>1$) and K6 (partition coefficient of Si in Nb_{ss} $k_{Si} < 1$).

The scale of the microstructure and eutectic spacing is attributed to (see § 4.4.1) L1 (inter-related with K1 and K5 to K7), L2 (inter-related with E1 to E3, A2, B1, B2, B4, B5, B8, B9, B11, B12 (inter-related with C5 and C6)), L3 (inter-related with B1, B2, B4, B5, B8, B9, B11, B12), L4 (inter-related with J1 to J12) and L5.

The higher Si content in the edge compared with the centre of the "grown" bars is attributed to (see § 4.4.1) J9 (inter-related with I5), J10, J12 and J11 for large $\left|\partial\gamma_{LV}/\partial T\right|$. Difference in composition (Ni content) between the edge and centre in DS Fe-xNi (x=4, 4.2, 4.5) alloys has been reported by Vandyoussefi et al. (2000) and was attributed to a changing solute distribution across the interface caused by the macroscopically non-planar S/L interface and to lateral macrosegregation from thermosolutal convection during solidification.

Differences in the Si content of the eutectic between the edge and centre are attributed to the different Si contents of the melt in these two areas (see above), the $(dT/dx)_L$ in these areas (affected by parameters discussed above for the undercooling at the interface) and the fact that in the alloy CM1 the eutectic is not an invariant reaction.

How does the data for the alloy CM1 OFZ compare with the literature on OFZ and DS Nb silicide based alloys? The data in the literature is limited and falls in three groups. In the first group we have OFZ "advanced" alloys such as Nb-24Ti-16Si-7Cr-3Al-2Hf (Huang et al. 2011) and Nb-22Ti-16Si-7Cr-3Al-3Ta-2Hf-0.2Ho (Cheng & He 2011) grown at growth rates $\leq$ 16 mm/h in an Ar atmosphere with no data provided regarding rotation or not of feeder and grown rods, direction of pulling and type and size of lamps used. These studies reported microstructures that were similar to those of the alloy CM1 OFZ and that in the former alloy the directionality and large aspect ratio of the 5-3 silicide were "destroyed" above some critical growth rate (5 mm/h). However, no attempt was made to discuss the "directional" solidification of the alloys using the parameters and phenomena that are important in OFZ processing.

The second group is for "advanced" alloys processed using electron beam floating zone melting-EBFZM (Nb-24.6Ti-14.5Si-5.3Cr-4.2Hf-2.8Al-1B-0.05Y (Guo, Gao, Guan, et al. 2007)) and Bridgman (Nb-24Ti-16Si-10Cr-2Al-2Hf (Wang et al. 2013), Nb-22Ti-12Si-14Cr-2Al-2Hf (Su et al. 2013)). For the EBFZM processed alloy a critical growth rate was required for obtaining a directional microstructure and no attempt was made to discuss the "directional" solidification of the alloy using the parameters and phenomena that are important in OFZ processing. However, for the Bridgman processed alloys, microstructures similar to those of the alloy CM1 (meaning directional large aspect ratio 5-3 silicide and eutectic) were obtained for growth rates of 14, 72, 360, 1080, 2160 and 3000 mm/h, and no critical growth rate was reported above which the directionality of the microstructure was "destroyed".

The third group is for "simple" binary and ternary alloys, namely (a) Nb-17.5Si and Nb-17.5Si-10Ti (Sekido, Kimura, et al. 2006) OFZ "grown" in Ar atmosphere at withdrawal speeds of 10 and 100 mm/h (no further processing data given), (b) Nb-17.5Si and Nb-17.5Si-xTi (x=2, 5, 10) (Sekido et al. 2007) where the binary was OFZ "grown" in Ar atmosphere at withdrawal speeds of 10, 30, 100 and 200 mm/h and the ternary at 10, 30 and 100 mm/h (no further processing data given but the authors claimed that *"during unidirectional solidification the amount of floating liquid was kept constant"*), (c) Nb-18.1Si (Miura, Murasato, et al. 2007) that was OFZ grown in Ar atmosphere using four xenon lamps, with counter-rotation of rods at 30 rpm, and growth rates in the range 5 to 4200 mm/h, where the highest rate was used in order to compare the OFZ "grown" structure with the arc melted one, (d) near eutectic Nb-17Si-10Mo-3Al (Li, Miura, et al. 2011) that was OFZ "grown" using four xenon lamps in Ar atmosphere with different rotation speeds of feeder and grown rod and growth rates of 3, 5 and 10 mm/h, (e) Nb-17Si-10Mo-xGa (x=0.1, 1) and Nb-17Si-10Mo-3Al (Li, Ma, et al. 2011) that were OFZ "grown" using rotation of the feeder at 10 rpm with the support rod (they call this the seed rod) stagnant and withdrawal rate of 5 mm/h and (f) Nb-18Si (Gang & Heilmaier 2014) grown using floating zone melting with high frequency heating with counter-rotation of the feeder and seed rods (rotation speed(s?) not given) at 36 mm/h.

The data for the third group of alloys shows that some OFZ alloys that have been processed using lamps for heating have been studied “more carefully” compared with the other two groups but not systematically. The more “comprehensive” study was for (d). In this alloy, though not reported by the authors, the Mo will partition strongly to the Nb_{ss} ($k_{Mo}>1$) and Al to both the Nb_{ss} and the Nb_5Si_3. Thus, during solidification the composition of the melt will be different near the solid solution and the silicide, meaning MCT and MCC and changing M. Furthermore, the temperature distribution in the melt zone would have changed between experiments if there were to be de-focusing, see § 4.4, and the conditions at the S/L interface would have changed if there were to be changes in cross section during growth (as suggested by Figure 6 in their paper). For counter-rotation of both rods of 5-5 rpm at 5 mm/h the morphology of the near eutectic alloy changed in the radial direction. No chemical analysis data was given regarding the chemical composition of the inner and outer areas. Spherical primary Nb_{ss} and Nb_{ss} + Nb_5Si_3 eutectic regions were observed in the centre but in the outer parts there was irregular blocky structure and the growth direction was not obvious in the longitudinal cross section of the grown specimen. This was attributed to the rotation of the seed rod. When OFZ growth was done with 10-0 rpm rotation (i.e., feeder rod rotates at 10 rpm and seed rod not rotating) and 5 mm/h fully lamellar microstructures were obtained and the S/L interface was convex. When the rotation speed of the feeder rod was increased to 40 rpm (seed rod not rotating) regular lamellar microstructures were observed only in the outer part of the grown rod. No chemical analysis data was given for the inner and outer regions as the rotation speed of the feeder rod increased. The authors selected the 10-0 rpm condition as “the critical one” for producing fully-lamellar microstructure of this near eutectic alloy. This was achieved only at growth rates of 3 and 5 mm/h but at 10 mm/h lamellar microstructure and eutectic cells were formed. For the latter case the authors did not check for any chemical in-homogeneities in the cross section. The mode of rotation affects the flow patterns as does the parameter M (Figure 40) and both affect temperature fields, solute profiles along the axis and near the L-V interface, as discussed in § 4.4. The data for the eutectic spacing for 10-0 rpm and growth

rates of 3, 5 and 10 mm/h obeyed the Jackson Hunt relationship with the constant being $\lambda^2 V_{S/L}$ = 170 $\mu m^2 mmh^{-1}$.

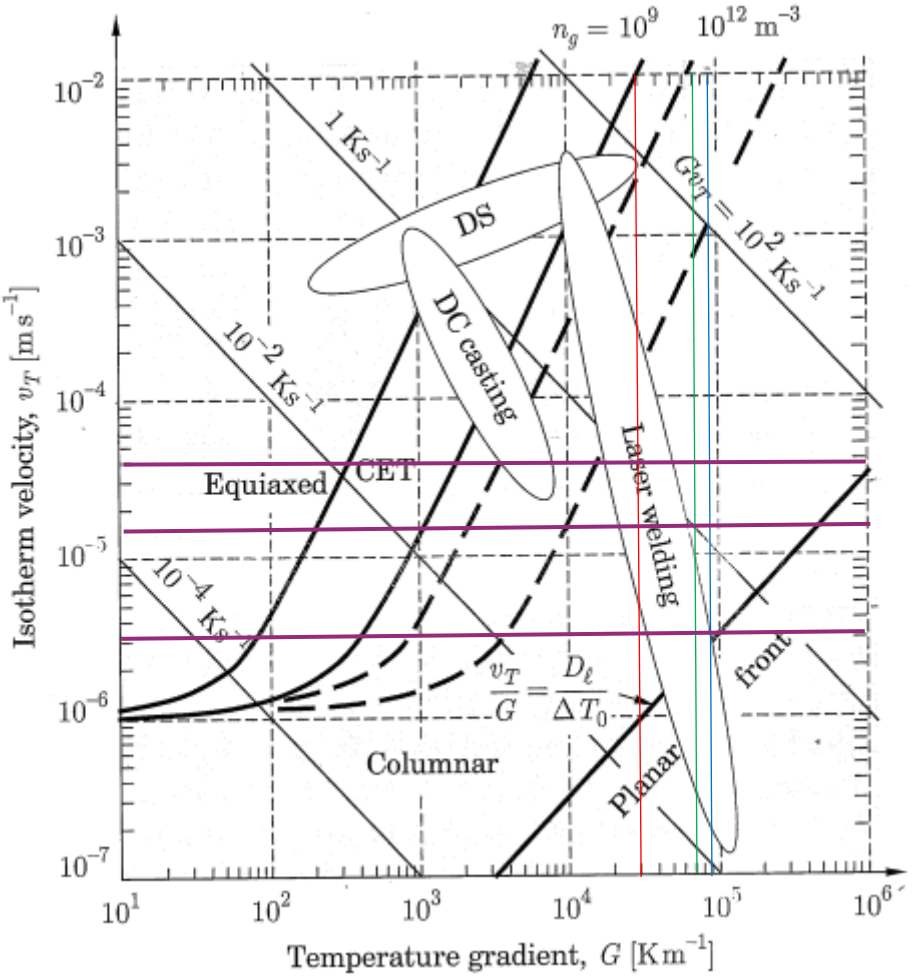

Figure 134: Plot of isothermal velocity (growth rate) versus temperature gradient showing the transitions between equiaxed, columnar and planar morphologies (Dantzig & Rappaz 2009)*. The vertical red green and blue vertical lines present the three temperature gradients and the three horizontal lines the growth rates.*

In the alloy (c) the size of the eutectic cells did not change as the OFZ growth rate increased to 4200 mm/h and was almost five times larger than the size of the eutectic cells in the arc melted sample. This observation about the size of eutectic cells is in agreement with the results of this thesis (see above.) As the growth rate in OFZ increased from 20 to 4200 mm/h the size of the Nb_{ss} decreased significantly. Assuming a temperature gradient of 30 K/mm (see below), the cooling rates associated with these velocities will be 0.17 K/s and 35 K/s, significantly lower than the cooling rates in the suction

casting used in this research (≤ 1000 K/s at the bottom of the suctions cast bar). Comparison of Figure 59 and Figure 82 shows a significant refinement in the size of the Nb_{ss} at the higher cooling rate.

In the alloys in (b) the microstructure of the binary eutectic alloy became finer as the growth rate increased. Cellular Nb_{ss} + Nb_3Si eutectic microstructures surrounded by coarser Nb_{ss} + Nb_3Si eutectic were formed at growth rates above 30 mm/h. In the ternary alloy, owing to the addition of Ti, cellular eutectic microstructures developed at *all* growth rates, with better alignment of the Nb_{ss} at the low growth rates. In the ternary alloys, for a given Ti concentration, as the growth rate increased the directionality of the microstructure became stronger, the size of Nb_3Si became finer and the microstructure inside the eutectic cells became finer. For fixed growth rate, as the Ti concentration in the alloy increased the size (length and aspect ratio) of the Nb_3Si increased too. No data was provided in the paper regarding the chemical composition of the grown rods at the edge and centre.

A major issue with "directional" solidification using OFZ compared with traditional DS experiments is the fact that the temperature gradient in the liquid ahead of the S/L interface cannot be fixed. A number of reasons why this is the case were discussed in the § 4.4. In the open literature on OFZ grown crystal this temperature gradient is not given (because it is not known). In the alloy (f) the authors reported G_L in the range 30 to 40 K/mm which for their $V_{S/L}$ = 36 mm/h corresponds to very low cooling rates (0.3 to 0.4 K/s). Bei & George (2007) for the OFZ processing of a NiAl-Mo eutectic reported G_L = 30 K/mm and that their data obeyed the Jackson-Hunt relationship with $\lambda^2 V_{S/L}$ = 95.25 $\mu m^2 mmh^{-1}$ while (Koohpayeh 2007) attempted to measure the temperature gradient in his experiments for the OFZ growth of functional oxides and reported the estimated value of 70 K/mm. The highest reported value for the temperature gradient for OFZ processing of intermetallic alloys was given at a TMS conference as 90 K/mm (paper not published, (Tsakiropoulos 2008)). Using the above data for temperature gradient and the growth rates used in this research, the cooling rates for CM1 OFZ were 0.1, 0.5 and 1.25 K/s (for G_L = 30 K/mm), 0.23, 1.17 and 2.9 K/s (for G_L = 70 K/mm) and 0.3, 1.5 and 3.75 K/s (for G_L = 90 K/mm). Figure 134 shows that in all cases the intercepts for the alloy

CM1 OFZ are in the "columnar growth" region and (for the 30 K/mm temperature gradient) in the area occupied in the diagram by laser welding.

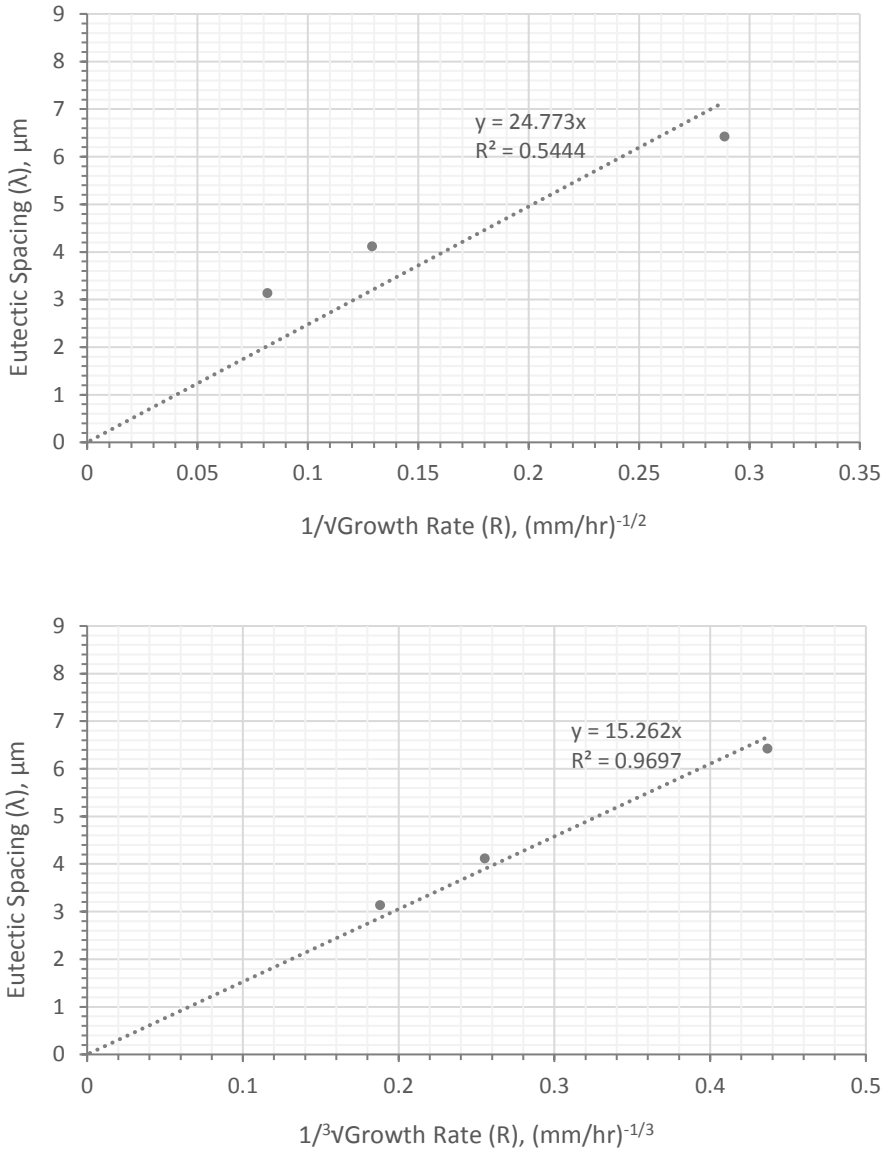

Figure 135: Plot of eutectic spacing for CM1 OFZ versus $1/\sqrt{R}$ (top) and $1/\sqrt[3]{R}$ (bottom) where R is growth rate.

The data for eutectic spacing in CM1 OFZ in Figure 113 is plotted as function of growth rate R (mm/h) in Figure 135. When the data is fitted to the Jackson-Hunt theory ($\lambda^2 V_{S/L}$ = constant) the fit is poor (($\lambda^2 V_{S/L}$ = 613.7 $\mu m^2 mmh^{-1}$, fit parameter R^2 = 0.5444, Figure 135 top). However, when the data is fitted to $\lambda^3 V_{S/L}$ = constant, i.e., to $1/\sqrt[3]{R}$ the fit is significantly better, see Figure 135 bottom where

the fit parameter is 0.9679. The deviation from the Jackson-Hunt theory is attributed to the parameters and phenomena that were discussed above to have an effect on the scale of the microstructure and eutectic spacing of CM1 OFZ. This non-Jackson-Hunt relationship has also been seen in other work (Racek et al. 1974) where the solidification of eutectic Cd-Sn at low growth rates conformed to $\lambda^3 V_{S/L}$ = constant rather than the $\lambda^2 V_{S/L}$ = constant seen at higher growth rates. It is determined in this work that the power that λ is raised to depends on the shape parameter which in turn is dependent on the growth rate.

4.6 OFZ ALLOY CM2

4.6.1 Steady state OFZ

Compared with the alloy CM1 OFZ, in the steady state "grown" CM2 using the same processing parameters as for the alloy CM1, there were no differences in the composition of the near edge and centre areas of the grown rod. This can be explained using (see § 4.4.1) J5 (inter-related with B8, J7 and J3) and J11 with $k_W < 1$, $k_{Hf} < 1$, $k_{Si} < 1$ (see data for Nb_{ss} in Table 24) and $|\partial\gamma_{LV}/\partial T|_{Nb} = 0.43$ (see § 4.4), which is significantly higher than $|\partial\gamma_{LV}/\partial T| = 0.056$ in Figure 44g. In other words, as discussed in § 4.4, at this high $|\partial\gamma_{LV}/\partial T|$ value the flow in the melt zone mixed the solute in the centre (see square in Figure 44f) and reduced the difference between the solute concentration in the centre and edge, as indicated by the change in the solute concentration line with increasing $|\partial\gamma_{LV}/\partial T|$ in the Figure 44g. Assuming the same temperature gradients in the liquid as for the OFZ of CM1, for the three growth rates the alloy CM2 falls in the "columnar growth" region.

Long thin precipitates grown in orthogonal directions (i.e., with some orientation relationship) and exhibiting dark contrast were observed in the Nb_{ss} in all three growth rates. Their aspect ratio increased as the growth rate decreased. Spherical junkier precipitates were also observed for the 12 mm/h growth rate. The latter was also observed in some large Nb_{ss} grains in the alloy CM2 500 g HT. It is suggested that these precipitates were metastable Nb_3Si or (most likely) δ-$Nb_{11}Si_4$, as discussed in § 4.3.

Microstructures similar to those of the steady state "grown" CM2, including the second phase long thin precipitates in Nb_{ss} grains exhibiting some orientation relationship, have been reported for the hypoeutectic Nb-xSi-22Ti-3Cr-3Al-2Hf (x = 3, 9) alloy OFZ grown at 9 mm/h with/out rotation of the feeder rod (10 rpm) (Wu et al. 2012).

4.6.2 Non-steady state OFZ

The OFZ solidification processing of the alloy CM2 did not proceed as smoothly and continuously as that of the alloy CM1. During OFZ processing the molten zone became unstable. This required the temperature and growth rate to be altered. These changes created bulbous regions within the final bar. Figure 90 shows the OFZ bar of the alloy CM2 solidified at 12 mm/hr, the circled regions show the areas where the instabilities formed.

The beginning and end of OFZ was studied in more detail for the low growth rate. For the beginning of OFZ the microstructure changes are shown in Figure 94 and chemical analysis data in Figure 96, for the end of OFZ in Figure 92 and Figure 93, and Figure 91 shows the change in microstructure as "OFZ growth conditions were adjusted" and lead to formation of bulbous regions. The microstructure changes were associated with changes in Si content, see Figure 93 and Figure 96.

The data for the non-steady OFZ grown alloy CM2 would suggest that the concentration of Si in the melt ahead of the solidifying front played a crucial role (i) in how the non-steady state grown microstructure evolved to the steady state grown one, (ii) the transitions (via adjustments of temperature and (minor adjustment of) growth rate) to ensure steady state growth (leading to formation of bulbous areas) and (iii) the final "transient" (green square in the Figure 90).

Table 30: Data for Si content (at%) of the alloy CM2 and its eutectic/lamellar microstructures

	Eutectic/lamellar microstructure	*Alloy*
Si_{max}	26.1	23.1
$Si_{max}^{average}$	23.1	20.9
Si_{min}	17.4	12.9
$Si_{min}^{average}$	19.6	18.1
$Si^{average}$	21.5	19.5

Table 30 shows data for the Si concentration in all forms of the alloy CM2 *excluding* the OFZ alloy. The data for the latter is given in Table 25. In Table 30 Si_{max} and Si_{min} respectively are the highest and lowest measured values and $Si_{max}^{average}$ and $Si_{min}^{average}$ respectively are the averages of the highest

and lowest measured values (data in the Table 8, Table 10, Table 12, Table 14, Table 16, Table 18, Table 20 and Table 22). $Si_{average}$ is the average of all data.

We shall consider first the early stages of growth at 12 mm/h (Figure 94 and Figure 96). Table 30 shows that the Si content of the eutectic/lamellar microstructure in the alloy CM2 was always higher than that of the alloy. This data can help us account for (i.e., justify) the high difference in Si content between the starting alloy (lower part of image A in Figure 94) and OFZ stage A (eutectic in top part of image A in Figure 94). The data in Figure 96 and Table 25 and Table 30 gives 27.5 – 18.2 = 9.3 at% (Figure 96 and Table 25) as the difference between the starting alloy and the eutectic at the top of image A in Figure 94, and the data in the Table 30 gives the maximum and minimum differences as 26.1 – 12.9 = 13.2 at% and 26.1 – 18.1 = 8 at%, in other words the former (9.3 %) in the range of values that could be expected for the alloy CM2. The difference between the compositions of the eutectic/lamellar microstructures in the top of image A and in image B in Figure 94 is 27.5 – 15.5 = 12 at% (Figure 96) and the maximum difference between the eutectic/lamellar microstructures in the alloy CM2 is 26.1 – 17.4 = 8.7 at% (Table 30).

In area A (Figure 94) as the Si rich eutectic formed the melt ahead of it was poorer in Si, which explains the lower Si in area B (Figure 94). The eutectic in B had essentially the same composition as the alloy but as W partitioned to the Nb_{ss} (see data for the Nb_{ss} in the Table 8, Table 10, Table 12, Table 14, Table 16, Table 18, Table 20 and Table 22), the W content of the liquid dropped, thus in area C (Figure 94) the Si content was lower than the metastable Nb_{ss} + β-Nb_5Si_3 eutectic, therefore the microstructure consisted of Nb_{ss} and Nb_{ss} + β-Nb_5Si_3 eutectic (no Nb_3Si because 2 < W < 5 at.%) and solidification occurred as shown in Figure 129. In area C the Si content was ≈ 16 at.%, W ≈ 2 at.% and Hf ≈ 3 at.%, the eutectic composition was richer that the alloy one, thus the melt ahead of the solidifying front was poorer in Si, and with W partitioning to the Nb_{ss} the melt was also poorer in W. This would explain the increased volume fraction of Nb_{ss} (and decrease in the volume fraction of the 5-3 silicide) in areas D, E, F and G. The Nb_3Si formed in area G where the transition from non-steady

state to steady state growth occurred (Figure 94, image Gi) and in the part of CM2 steady state grown at 12 mm/h (Figure 95) when the W content in the melt was too low to suppress the 3-1 silicide. Its eutectoid decomposition (Figure 94, image G-I, Figure 95) was possible owing to the slow cooling conditions.

Most of the Si in the bar of the alloy CM2 that was processed by OFZ (non-steady and steady state growth stages) was "consumed" in the early stages (area A) and end of the bar (Figure 93). How did (top of) area A and area B solidify giving fully eutectic microstructures? Consider Figure 136. The melt of composition C_o^A corresponding to that of the top of image A in Figure 94 solidified at growth temperature $T_{Eu}(V_1)$ owing to its proximity with the efficient heat sink provided by the support rod. The melt of composition C_o^B corresponding to that of the image B in Figure 94 solidified at growth temperature $T_{Eu}(V_2)$ owing to recalescence reducing the growth temperature.

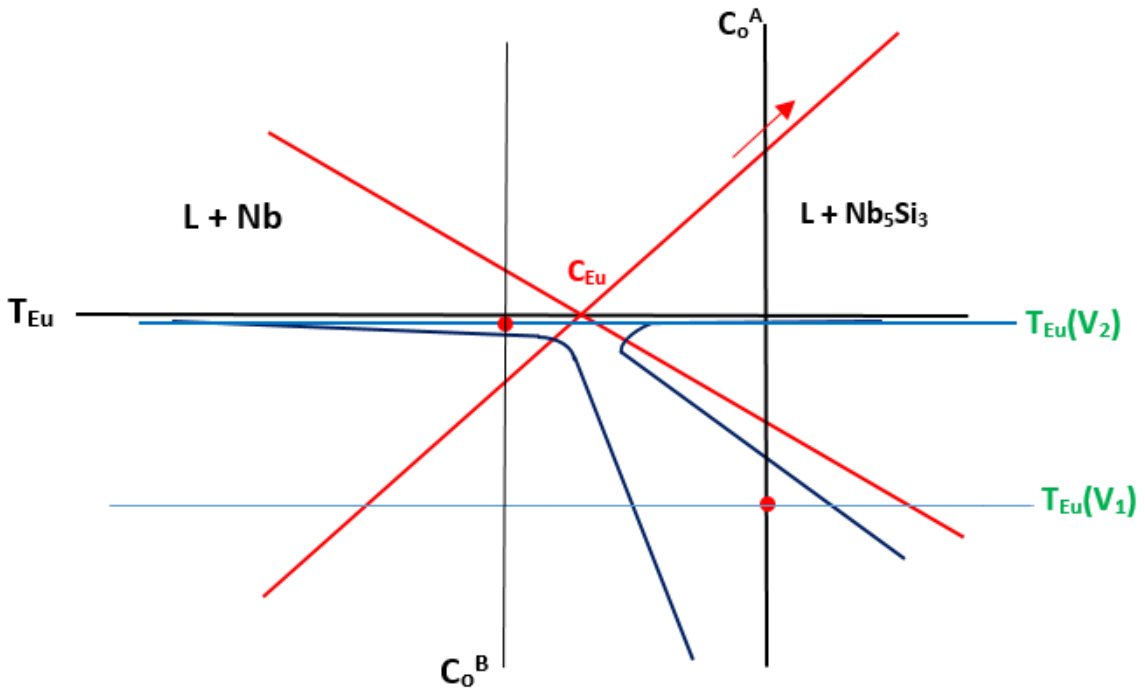

Figure 136: Schematic diagram of the skewed coupled zone of the Nb_{ss} + β-Nb_5Si_3 metastable eutectic. Red continuous lines show the liquidus of Nb_{ss} and β-Nb_5Si_3 and their extensions.

As OFZ processing started the liquidus temperature of CM2 was that of the alloy CM2 500 g ingot that was used to machine the bar. In area A as the Si content of the melt increased the liquidus temperature increased (the liquidus moves upwards on the Nb_5Si_3 liquidus, see red arrow above liquidus of Nb_5Si_3 in Figure 136). This required more power to be supplied to melt the alloy. When the Si content dropped the liquidus temperature was reduced (moved in the opposite direction to that shown by the arrow above the Nb_5Si_3 liquidus in Figure 136) and this required the power to be adjusted again. These operations mean that (see § 4.4.1) A1 to A3, B1, B2, B9, C2, C3, D1, E1, E2, F1, F3, H1, G1, I5, J1, J2 (inter-related with J4, J5, J7, J8, J11), K1 (inter-related with K2, K5 to K7), K8 (for change from C_o^A to C_o^B see Figure 136) kicked-in ("operated").

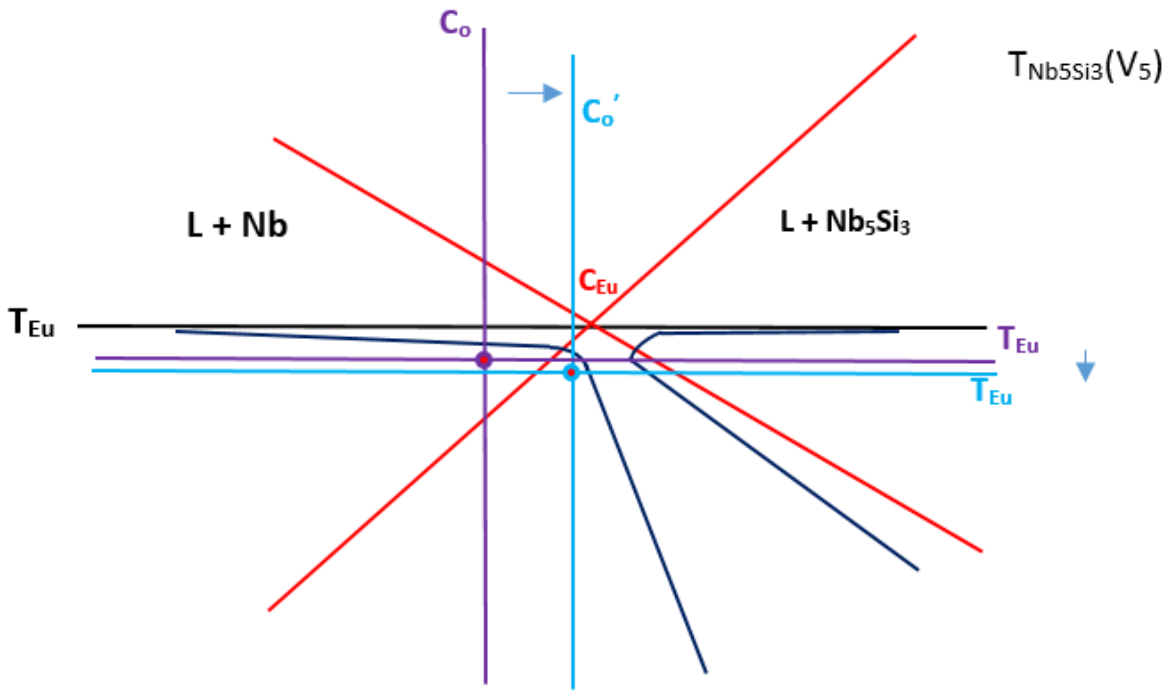

Figure 137: Schematic diagram of the skewed coupled zone of the Nb_{ss} + β-Nb_5Si_3 metastable eutectic. Red continuous lines show the liquidus of Nb_{ss} and β-Nb_5Si_3 and their extensions. Two melts of compositions $C_o' > C_o$ are shown with growth temperatures $T_{Eu} > T_{Eu}'$.

During steady state growth instabilities leading to formation of bulbous regions occurred (Figure 90). Instability(ies) set in as the Si content of the melt ahead of the solidification front changed. Because in steady state growth the Si content was well below the eutectic composition (see Table 24),

an increase in Si content meant a decrease in liquidus temperature, meaning a decrease in the undercooling driving the solidification. While the power was not adjusted phenomena A1, A2 (inter-related with C2), A3, B1 to B4, C3 (inter-related with F1, F3) C6, D1, E1 to E3, G2, G3, I5, J2, J4, J5, J11, K1 (inter-related with K2, K6 to K8), L3, L4 (and L5 for the 150 mm/h growth rate) became important. While the power was adjusted the melt superheat increased or T_{max} (or T_{peak}) increased, meaning an increase in the undercooling driving the solidification. Thus, a shift of the melt composition C_o to C_o' (see vertical lines in Figure 137) and a decrease of T_{Eu} brought the alloy closer and into the skewed zone giving the Nb_{ss} and (Nb_{ss} + β-Nb_5Si_3) eutectic.

Figure 91 shows the change in microstructure as "OFZ growth conditions were adjusted" (i.e., changes were made to temperature and growth rate) and lead to formation of bulbous regions (i.e., change in cross section). The area above the "transition interface" and the edges (i.e., the parts of the melt zone close to the liquid surface) were Si rich. The zone instability meant that C1 [inter-related with C3 (inter-related with F1), D1 (inter-related with D2), D3 (inter-related with G2 (inter-related with H2 (inter-related with G3 (inter-related with K5 to K6, J11, J12)], C2 [as the Si, W and Hf contents changed (inter-related with F3 (inter-related with K5, J11, J12))], C5 (inter-related with C2), E2 [inter-related with D2 (inter-related with G1 to G4, K5 to K7, J11, J12] kicked-in. As the temperature and growth rate were adjusted the B1 (inter-related with B2 to B4, B6, B11, B12), F2, E2 [inter-related with D2 (inter-related with G1 to G4, K5 to K7, J11, J12], E3 (inter-related with D3, G3, J5, J11, J12, K5 to K7) "operated".

The Si rich centre of the "transition interface" is attributed to k<1 with $\partial\gamma/\partial T < 0$, see Figure 44g and J11. The Si rich area at the edge is attributed to k < 1 but with lower $\partial\gamma/\partial T$ than for the centre. Changes in γ were caused by changes in solute concentrations and B1 to B3, B11, B12 and changes in the shapes of the S/V and L/V interfaces (E in § 4.4.1).

Changes in Si content at the end of OFZ at 12 mm/h (square in Figure 90), see Figure 93 can be understood with the help of Figure 44h, see end of § 4.4.

4.7 Summary of Cast OFZ Microstructure

Sections 4.6 and 4.5 reviews the causes for the development of the cast OFZ microstructure which have been assessed using previous work, focusing mainly on the work done on the solidification of Si and Ge. Work in this thesis in conjunction with the literature highlights how difficult it is to control the microstructural evolution of these alloys during OFZ solidification, even when the solidification is considered stable. It has been shown how 12 different processes (A – L § 4.4.1) can be in operation to create the stable growth, seen in CM1 and CM2, or create unstable growth, seen in CM2. Each of the processes can create a flow within the melt zone moving elements and heat within the system, which in turn, can cause further disturbances within the melt zone. I.e. inhomogeneity in the liquid can cause buoyancy convection currents to occur which can create more concentration variations due to the creation of a number of flows in the melt. If these concentration variations form Si-rich regions at the surface a high V_f of faceted phase can solidify whose growth can cause changes in the meniscus angle creating oscillations around the stable angle forcing changes in the entire melt shape. This can in turn cause variations in heating through the cross section due to changes in the size of the melt zone. The significant issue in determining the initial problem is that any one of these steps can start a cascade resulting in instabilities and determining which is the culprit demands systematic studying beyond the scope of this thesis.

Looking at the cast OFZ microstructure for CM1 there is segregation between the edge and the bulk of the bar created by variations in the surface tensions between the liquid and the atmosphere segregating elements. The grains within the microstructure, both primary Nb_5Si_3 and the eutectic grains form a columnar morphology in the direction of growth which is consistent with the work of Dantzig & Rappaz (2009) at the three temperature gradients determined in the literature. The morphology of the eutectic however does not conform to the Jackson-Hunt relationship ($\lambda^2 V_{S/L}$ = constant) but when the results are plotted on a graph of λ vs. $1/\sqrt[3]{R}$ (i.e. $\lambda^3 V_{S/L}$ = constant) the results show a fit parameter, $R^2 = 0.97$.

In the cast OFZ microstructure of alloy CM2 there are two distinct regions; stable and unstable. The stable region, unlike the CM1 OFZ microstructure, does not have any macrosegregation in the radial direction. This is due to the mass and heat transfer in the melt zone likely caused by the changing surface tension at the L/V surface mixing the elements in the radial direction. In this stable region, assuming the same temperature gradients as in the alloy CM1, the growth should, according to the literature, be columnar. However, columnar morphology is not as readily seen in CM2 OZF alloys as it was in CM1. Unlike the alloy CM1 OFZ ingot CM2 does not show any relationship between the growth rate and the lamellar spacing observed. This is most likely due to the 12 mm/hr ingot containing both eutectic and eutectoid structures. The oscillation between stable and unstable growth could also have affected the morphology of the eutectics in the alloy CM2 OFZ.

The creation of an unstable melt, which in turn created the bulbous regions in the solidified ingot, were shown to be associated with the segregation of elements, especially silicon. The variation of the microstructure seen in the stable region has been explained with the help of Figure 136 and Figure 137 and the associated EDS analysis in the results section. This shows the formation of Si-rich eutectics and reducing W concentration throughout the length of the ingot created the high Nb_{ss} V_f and the formation of the Nb_3Si. As the growth continued it is thought that concentration changes in the melt created variations in the surface tension, density and the liquidus temperature of the melt. However, the solidification continued until a critical point where the solidification conditions, temperature and growth rate, had to be altered to continue solidification. This change in solidification conditions then created conditions where the convection flow was altered, for reasons explained above, causing a Si-rich region (in comparison to the regions around it) to solidify.

4.8 HEAT TREATED OFZ ALLOYS CM1 AND CM2

The discussion for the other forms of the alloy CM1 HT, see § 4.3, applies here regarding phase equilibria and precipitation of Nb_{ss} in α-Nb_5Si_3 grains. The "architecture" of the micro-structure of alloy CM1 OFZ HT was essentially the same as that of the cast alloy with slight coarsening of the lamellar structure (Figure 113) particularly for the 60 mm/h and 150 mm/h growth rates. The slight reduction of the lamellar spacing for the 12 mm/h growth rate could be attributed to the fine spacing of the products of the eutectoid transformation of Nb_3Si if the latter were indeed present in the cast alloy. However, no evidence for this was found. There was no Nb_3Si in the heat treated microstructures which means that even if there was some Nb_3Si in the 12 mm/h grown specimen, the transformation of the Nb_3Si had been completed. The slightly smaller lamellar spacing for the 12 mm/h growth rate is attributed to errors in the measurement of lamellar spacing. Subgrains were formed owing to the effect of Ti on the anisotropy of CTE of the 5-3 silicide (see discussion in § 4.2 and 4.3 about subgrain formation in Nb_5Si_3) and the changes in Ti content in the α-Nb_5Si_3 in the centre of the OFZ alloy after the heat treatment (Table 23 and Table 26).

The "architecture" of the microstructure of the steady state grown alloy CM2 OFZ HT was essentially the same as that of the cast alloy and had coarsened slightly (see Figure 113). The phases present, namely Nb_{ss} and α-Nb_5Si_3 are in agreement with the 1700 ^{O}C isothermal section for the Mo-Si-W system. There was no Nb_3Si present in the HT microstructure which means that the latter silicide had fully transformed eutectoidally to Nb_{ss} and α-Nb_5Si_3. Evidence for the fine product of the latter transformation was observed, see Figure 101, microstructures for 12 mm/h. This could account for the lamellar spacings in the cast and HT alloy grown at 12 mm/h being essentially the same (see Figure 113), owing to the fact that the data in this figure cannot differentiate between the coarsened Nb_{ss} + α-Nb_5Si_3 lamellar microstructure and the fine lamellar structure of the eutectoid Nb_{ss} and α-Nb_5Si_3. The aspect ratio of orthogonally grown long thin precipitates in the Nb_{ss} had increased.

5. CONCLUSIONS AND SUGGESTIONS FOR FUTURE WORK

5.1 CONCLUSIONS

Two near eutectic alloys with nominal compositions Nb-8.3Ti-21.1Si-5.4Mo-4W-0.7Hf at. % (CM1) and Nb-20.5Si-5.8W-4Hf at. % (CM2) were studied in the cast and heat treated (1500 ^{O}C/100 hrs) conditions in the form of 10 g button ingots, 6 mm and 8 mm suction cast bars and as OFZ grown bars at three growth rates, namely 12, 60 and 150 mm/h and as 600 g (CM1) g and 500 g (CM2) ingots.

The feed materials of the OFZ alloys were the CM1 600 g and CM2 500 g ingots. The alloys grown under stable OFZ conditions were studied. In the case of the alloy CM2, significant deviations of the microstructure compared with those observed in the feed ingot were observed. Thus, the OFZ alloy CM2 was also studied for conditions of non-stable growth at the beginning, during and the end of the OFZ process.

The conclusions of the research presented in this thesis were as follows.

5.1.1 Microstructures

This study revealed dependence of cast microstructures on cooling rate or (specific) solute concentration as well as the formation of Nb_3Si and its eutectoid decomposition in suction cast bars and OFZ grown bars (stable OFZ growth for CM2), in other words the range of solidification conditions employed in this research allowed us to capture the formation of Nb_3Si and its eutectoid decomposition in both alloys as well as the β-$Nb_5Si_3 \rightarrow \alpha$-$Nb_5Si_3$ transformation.

The microstructures developed during OFZ processing of both alloys depended on twelve inter-related parameters (phenomena) processes, according to the literature on floating zone melting/processing.

In the cast alloys CM1 and CM2 the Nb_{ss} and Nb_5Si_3 and eutectic of these two phases with/out Nb_{ss} haloes were formed in the all studied forms.

In the cast alloy CM1 in the 8 mm suction cast bar the Nb_3Si and the products of its eutectoid decomposition were observed. In the CM1 600 g ingot and the CM1 OFZ grown bars at all three growth rates the β-$Nb_5Si_3 \rightarrow \alpha$-$Nb_5Si_3$ transformation had occurred during solid state cooling.

In the cast CM1 OFZ there were differences in chemical composition between the edge and centre of the bar, the edge was richer in Si and poorer in Ti. There were also differences in chemical composition of the lamellar microstructures between edge and centre, in the edge the latter was poorer in Si and in Ti.

In the cast alloy CM2 the β-$Nb_5Si_3 \rightarrow \alpha$-$Nb_5Si_3$ transformation had occurred during solid state cooling in all forms of the studied alloy (steady state OFZ grown bars) and in the 6 mm and 8 mm suction cast bars also the Nb_3Si and the products of its eutectoid decomposition were observed.

In the cast alloy CM2 OFZ, in the bars that solidified under stable OFZ conditions, the average chemical composition was significantly different than that of the parent (feed) ingot, particularly for Si, Hf and W. This was attributed to strong Si segregation (Si chemical inhomogeneities) developing at the start of OFZ, during OFZ and at the end of OFZ.

In the cast alloy CM2 OFZ grown under non stable conditions the Nb_{ss} and $Nb_{ss} + Nb_5Si_3$ eutectic were formed and in areas of low Si content the Nb_3Si and the products of its eutectoid decomposition were observed.

Relationships between solutes in the prior-eutectic areas in the heat treated alloys were found for both alloys.

Anomalous eutectics were observed near the water cooled copper crucible walls and were attributed to de-coupled growth of the eutectic phases.

In both the heat treated alloys in all studied forms (steady state OFZ grown bars of CM2) the microstructure had coarsened, and only the Nb_{ss} and αNb_5Si_3 were observed, in agreement with available phase equilibria data.

5.1.2 Nb solid solution

The refractory metals partitioned to the solid solution in both alloys in all their cast and heat treated forms (steady state OFZ grown bars of CM2).

Nb_{ss} free of Si was formed after heat treatment in both alloys, in agreement with other data in the literature.

Relationships between solutes in the Nb_{ss} have been found for both alloys. Ti and Mo and W *did not like each other* in the Nb_{ss}.

Bulky and/or long thin precipitates, most likely metastable Nb_3Si or δ-$Nb_{11}Si_4$ (according to the literature) and probably forming with some orientation relationship were observed in the heat treated Nb_{ss} in CM2 500 g ingot (bulky) and in the cast and heat treated stable OFZ grown alloy CM2 (long and thin) at all three growth rates.

5.1.3 Nb_5Si_3

The β-$Nb_5Si_3 \rightarrow \alpha$-$Nb_5Si_3$ transformation occurred during solid state cooling depending on alloy and condition, see above.

In the Ti containing CM1 subgrains were observed in the α-Nb_5Si_3. Their formation has been attributed to the effect of Ti on the anisotropy of CTE of the 5-3 silicide.

Light and dark contrast areas were formed in α-Nb_5Si_3 grains in all three growth rates in the cast CM1 OFZ, in the former areas fine spherical or needle like precipitates of light contrast (like the Nb_{ss}) second phase particles of different morphology were observed in the same Nb_5Si_3 grain.

No subgrains were observed in the α-Nb_5Si_3 in all forms of the cast and heat treated alloy CM2.

Precipitates in the α-Nb_5Si_3 exhibiting contrast similar to that of the Nb_{ss} were observed when the α-Nb_5Si_3 was present in the microstructures of all forms of the alloy CM1 and were attributed to the β-$Nb_5Si_3 \rightarrow Nb_{ss} + \alpha$-$Nb_5Si_3$ transformation.

Precipitates exhibiting contrast similar to that of the Nb_{ss} were rarely observed in the α-Nb_5Si_3 and only in some of the heat treated microstructures of the alloy CM2, namely the 6 mm suction cast bar and the 500 g ingot.

5.1.4 Eutectic spacing

The data for eutectic spacing in CM1 OFZ did not follow the Jackson-Hunt relationship $\lambda^2 V_{S/L}$ = constant. Instead, it obeyed the relationship $\lambda^3 V_{S/L}$ = constant, with fit parameter 0.9679.

In the suction cast bars similar trends in the variation of λ and V_f were observed along sections of the edge and centre of the bars that were different depending on alloy and condition. Differences in trends were noticeable when Nb_3Si and the fine Nb_{ss} and α-Nb_5Si_3 products of its eutectoid transformation were present in the microstructure.

5.2 SUGGESTIONS FOR FUTURE WORK

OFZ processing, though not the ideal method for making directionally solidified Nb silicide based alloys commercially, has been the research tool of choice for preparing "*DS*" intermetallic alloys to evaluate their mechanical properties. Systematic studies of the OFZ processing of intermetallic alloys are missing in the open literature, with the exception of single crystal Ni and Ti aluminides to study the dependence of specific properties on single crystal orientation.

Bridgman and/or Czochralski processing of Nb silicide based alloys has been tried, but the limited studies published in the open literature have not been systematic. Until these two processes are better understood for Nb silicide based alloys and become widely available, the OFZ processing of Nb silicide alloys is the only alternative option for forming "*directionally solidified*" microstructures. The latter however depends on (at least) twelve inter-related phenomena and processes, and data about thermo-physical properties of Nb silicide based alloys to help us understand all types of DS is missing.

The OFZ processing of the alloys CM1 and CM2, which are more complicated than the alloys studied by Miura and co-workers, but still simple compared with the latest generation of developmental alloys, has demonstrated that the behaviour of Si (and of refractory metals) is very important regarding the final microstructure. A systematic study of OFZ processing of selected latest generation alloy that meets (or is close to meeting) the property goals is essential. Without similar evidence of macrosegregation and destabilisation of the steady state growth in the literature the results of this thesis will become a starting point for research. Understanding of the solidification conditions for multi-phase and multi-element alloys and how different alloying elements interact with each other and change these conditions requires a systematic study. Evidence within the research group at Sheffield, obtained since writing this thesis, points to opposing consequences for the solidified microstructure with different alloying elements. Namely a high concentration of Si in the bulk compared to the edge when different alloys are solidified using the OFZ method.

Thus, Nb-18Si based alloy(s) with solute additions of Ti, refractory metals and simple metal(s) (and metalloid(s)) and other transition metals that are important for achieving a balance of high temperature strength and oxidation resistance should be studied systematically under "controlled" conditions of (i) type, shape and/or de-focusing of heating lamp(s), (ii) bar diameter, (iii) counter-rotation, or single rotation or no-rotation of feeder and seed bars, (iv) alloy density and viscosity.

The dependence of the formation of sub-grains in α-Nb_5Si_3 on alloy chemistry and DS processing conditions must also be understood as the latter (and the associated precipitation of Nb_{ss} in the silicide) will have an effect on its properties and behaviour at different temperatures, including oxidation. The work within this thesis will form the basis of future work within the group at Sheffield on sub-grain formation; as sub-grains in niobium silicide phases have yet to be described in open literature. Further study is not only required to determine the affect sub-grains will have on the mechanical and oxidation properties but also to test the hypothesis of their formation and the effect that alloying additions (such as Mo and Ti) have on the formation of sub-grains, outlined in this thesis.

The dependence of the formation of second phase precipitates in Nb_{ss} on alloy chemistry and DS processing conditions must also be understood given the importance of the solid solution for room temperature fracture toughness, high temperature strength and oxidation resistance.

REFERENCES

Abbaschian & Lipschutz, 1997. Eutectic solidification processing via bulk melt undercooling. *Materials Science and Engineering: A*, A226-A228, pp.13–21.

Amancherla et al., 2007. Thermodynamic and Microstructural Modeling of Nb-Si Based Alloys. *Journal of Phase Equilibria and Diffusion*, 28(1), pp.2–8.

Andreeta, Andreeta & Hernandes, 2002. Laser heated pedestal growth of Al2O3/GdAlO3 eutectic fibers. *Journal of Crystal Growth*, 234, pp.782–785.

Antonova, Firstov & Miracle, 2003. Investigation of phase equilibria in the Ti-Al-Si-Nb system at low Nb contents. *Acta Materialia*, 51(11), pp.3095–3107.

Baragar, Sahoo & Smith, 1977. The structural modification of the complex-regular eutectics of bismuth-lead, bismuth-tin and bismuth-thallium. *Journal of Crystal Growth*, 41.

Baskaran & Wilcox, 1984. Influence of convection on lamellar spacing of eutectics. *Journal of Crystal Growth*, 67, pp.343–352.

Becker, 1949. Kinetics of the formation of nuclei and statistical theory of condensation. *Discussions of the Faraday Society*, 5, pp.55–61.

Bei & George, 2007. Microstructures and Mechanical Properties of Directionally Solidified Intermetallic Composites. *Materials Science Forum*, 539-543, pp.1495–1500.

Bendersky et al., 1987. Microstructural characterization of rapidly solidified Nb-Si alloys. *Materials Science and Engineering*, 89, pp.151–159.

Bewlay et al., 2003. A review of very-high-temperature Nb-silicide-based composites. *Metallurgical and Materials Transactions A*, 34(10), pp.2043–2052.

Bewlay et al., 2004. Analyses of eutectoid phase transformations in Nb-silicide in situ composites. *Microscopy and microanalysis : the official journal of Microscopy Society of America, Microbeam Analysis Society, Microscopical Society of Canada*, 10(4), pp.470–80.

Bewlay et al., 1995. Solidification processing of high temperature intermetallic eutectic-based alloys. *Materials Science and Engineering A*, 192-193, pp.534–543.

Bewlay, Grylls & Fraser, 1998. On the Formation of Silicide Precipitates in Niobium-Silicide Based Composites. *Mat. Res. Soc. Symp. Proc.*, 552, pp.1–5.

Bewlay, Jackson & Bishop, 1998. The Nb-Ti-Si ternary phase diagram: Determination of solid-state phase equilibria in Nb-and Ti-rich alloys. *Journal of phase equilibria*, 19(6), pp.577–586.

Bewlay, Jackson & Gigliotti, 2002. *Intermetallic Compounds: Vol. 3, Principles and Practice*, John Wiley and sons, Ltd.

Bewlay, Jackson & Lipsitt, 1996. The Balance of Mechanical and Environmental Properties of a Multielement Niobium-Niobium Silicide-Based In Situ Composite. *Metallurgical and Materials Transactions A*, 27(December), pp.3801 – 3808.

Bewlay, Jackson & Lipsitt, 1997. The Nb-Ti-Si ternary phase diagram: Evaluation of liquid- solid phase equilibria in Nb-and Ti-rich alloys. *Journal of phase equilibria*, 18(3), pp.264–278.

Bewlay, Jackson & Subramanian, 1999. Processing high-temperature refractory-metal silicide in-situ composites. *JOM*, (April).

Bewlay, Sutliff & Bishop, 1999. Evidence for the existence of Hf 5 Si 3. *Journal of phase equilibria*, 20(2), pp.109–112.

Birmingham, U. of, 2016. Casting and Research Facility. *Birmingham, University of*. Available at: http://www.birmingham.ac.uk/research/activity/irc-materials-processing/themes/castings/facilities.aspx.

Bowman, 2000. Superalloys: A primer and History. *Minerals, Metals and Materials Society*. Available at: http://www.tms.org/meetings/specialty/superalloys2000/superalloyshistory.html.

Brice, 2000. Characterization of laser deposited niobium and molybdenum silicides. *Materials Research Scoiety Sym. Proc.*, 625, pp.31–36.

Bulanova & Fartushna, 2010. *Landolt-Bornstein Database*, Berlin: Springer.

Burton, Cabrera & Frank, 1951. The Growth of Crystals and the Equilibrium Structure of their Surfaces. *Philosophical Transactions of the Royal Society A: Mathematical, Physical and Engineering Sciences*, 243(866), pp.299–358.

Cahn, 1960. Theory of crystal growth and interface motion in crystalline materials. *Acta Metallurgica*, 8(8), pp.554–562.

Chan, 2002. Alloying effects on fracture mechanisms in Nb-based intermetallic in-situ composites. *Materials Science and Engineering: A*, 329-331, pp.513–522.

Chan, 2005. Alloying effects on the fracture toughness of Nb-based silicides and Laves phases. *Materials Science and Engineering: A*, 409(1-2), pp.257–269.

Chan & Davidson, 2003. Improving the fracture toughness of constituent phases and Nb-based in-situ composites by a computational alloy design approach. *Metallurgical and Materials Transactions A*, 34(September).

Chandrasekhar, Eisa & Wilcox, 1986. Influence of convection on lamellar spacing of eutectics. *Journal of Crystal Growth*, 76, pp.485–488.

Chang, C.E. & Wilcox, W.R., 1976. Analysis of Surface Tension Driven Flow in Floating Zone Melting. *Int. J. Heat Mass Transfer.*, 19, pp.355–366.

Chang, C.E. & Wilcox, W.R., 1975. Inhomogeneities due to thermocapillary flow in floating zone melting. *Journal of Crystal Growth*, 28(1), pp.8–12.

Chattopadhyay et al., 2007. Effect of Mo and Si on morphology and volume fraction of eutectic in Nb–Si–Mo alloys. *Materials Science and Engineering: A*, 456(1-2), pp.358–363.

Chattopadhyay et al., 2006. Effect of Mo on microstructure and mechanical behaviour of as-cast Nbss–Nb5Si3 in situ composites. *Intermetallics*, 14(12), pp.1452–1460.

Chen, J. & Chu, C., 1995. Numerical computation of fluid flow of floating- zone crystal growth of molybdenum Abstract--The. , 38(10), pp.1841–1853.

Chen, J.C., Chu, C.F. & Ueng, W.F., 1994. Thermocapillary convection and melt-solid interface in the floating zone. *International Journal of Heat and Mass Transfer*, 37(12), pp.1733–1748.

Chen, Shang & Zhang, 2007. Bonding characteristics and site occupancies of alloying elements in different Nb5Si3 phases from first principles. *Physical Review B*, 76(18), p.184204.

Cheng, G. et al., 2010. Characterization of a new Nb-solicide (d-Nb11Si4) in Nb–Si binary systems. *Philosophical Magazine*, 90(19), pp.2557–2568.

Cheng & He, 2011. Microstructure evolution and room temperature deformation of a unidirectionally solidified Nb-22Ti-16Si-3Ta-2Hf-7Cr-3Al-0.2Ho (at.%) alloy. *Intermetallics*, 19(2), pp.196–201.

Cheng, Tian & He, 2009. Orientation relationship and interfacial structure between Nb solid solution precipitates and a-Nb5Si3 intermetallics. *J. Mater. Res*, 24(1), pp.3701–3710.

Cockeram et al., 1991. Characterization of Silicide Precipitates in Primary Nb Phase in Nb - 10% Si In-situ Composites B. *Scripta Metallurgica;(United States)*, 25, pp.393–398.

Coriell, S.R. & Sekerka, R.F., 1976. The effect of the anisotropy of surface tension and interface kinetics on morphological stability. *Journal of Crystal Growth*, 34(2), pp.157–163.

Cornish & Watson, 2010. *Landolt-Bornstein Database*, Berlin: Springer.

Croker, McParlan, et al., 1975. Anomalous eutectic growth. *Journal of Crystal Growth*, 29(1), pp.85–97.

Croker, Baragar & Smith, 1975. Anomalous eutectic growth: II. The relationship between faceted/non-faceted eutectic structures. *Journal of Crystal Growth*, 30.

Dantzig & Rappaz, 2009. *Solidification* 1 st. M. Rappaz, ed., United States of America: CRC Press.

David et al., 2006. Thermodynamic description of the Cr-Nb-Si isothermal section at 1473 K. *Intermetallics*, 14(4), pp.464–473.

Dicks, Wang & Wu, 2009. The manufacture of a niobium/niobium-silicide-based alloy using direct laser fabrication. *Journal of Materials Processing Technology*, 209(4), pp.1752–1757.

Favier, J.J. & Rouzaud, A., 1983. Morphological stability of the solidification interface under convective conditions. *Journal of Crystal Growth*, 64(2), pp.367–379.

Fei et al., 2013. Microstructure evolution of a hypereutectic Nb-Ti-Si-Cr-Al-Hf alloy processed by directional solidification. *Chinese Journal of Aeronautics*.

Fidler, Croker & Smith, 1972. The thermodynamics and morphologies of eutectics containing compound phases. *Journal of Crystal Growth*, 13114, pp.739–746.

Fisher & Kurz, 1977. Solidification and Casting of Metals. In *Proc. Intern. Conf. Univ. of Sheffield*. p. 57.

Fleischer, 1989. Intermetallic compounds for strong high-temperature materials: status and potential. *Annual Review Materials Science*, 19, pp.231 – 263.

Flood, 1985. *DPhil Thesis*. University of Oxford.

Frenkel, 1932. Note on a relation between the speed of crystallization and viscosity. *Phys. Z. Sowjetunion*, 1, p.498.

Fu et al., 2008. *Directional Solidification and Processing of Advanced Materials* 1st ed., Beijing: Science Press.

Gandin, 2000. From constrained to unconstrained growth during directional solidification. *Acta Materialia*, 48(10), pp.2483–2501.

Gang, F. & Heilmaier, M., 2014. Influence of Directional Solidification on the Creep Properties of a Binary NbSi Eutectic Alloy. *Jom*, 66(9), pp.1908–1913.

Geng, T. et al., 2009. Thermodynamic assessment of the Nb-Si-Ti system. *Intermetallics*, 17(5), pp.343–357.

Geng & Tsakiropoulos, 2007. A study of the microstructures and oxidation of Nb–Si–Cr–Al–Mo in situ composites alloyed with Ti, Hf and Sn. *Intermetallics*, 15(3), pp.382–395.

Geng, Tsakiropoulos & Shao, 2007. A study of the effects of Hf and Sn additions on the microstructure of Nbss/Nb5Si3 based in situ composites. *Intermetallics*, 15(1), pp.69–76.

Geng, Tsakiropoulos & Shao, 2006a. Oxidation of Nb–Si–Cr–Al in situ composites with Mo, Ti and Hf additions. *Materials Science and Engineering: A*, 441(1-2), pp.26–38.

Geng, Tsakiropoulos & Shao, 2006b. The effects of Ti and Mo additions on the microstructure of Nb-silicide based in situ composites. *Intermetallics*, 14(3), pp.227–235.

Goetzinger, Barth & Herlach, 1998. Mechanism of formation of the anomalous eutectic structure in rapidly solidified Ni–Si, Co–Sb and Ni–Al–Ti alloys. *Acta Materialia*, 46(5), pp.1647–1655.

Gokhale & Abbaschian, 1990. Mo-Si (Molybdenum-Silicon). *Binary Alloy Phase Diagrams, Second Edition/ed. TB …*.

Gonzales & Rappaz, 2006. Dendrite growth directions in aluminum-zinc alloys. *Metallurgical and Materials Transactions A*, 37(9), pp.2797–2806.

Grammenos & Tsakiropoulos, 2011. Study of the role of Hf, Mo and W additions in the microstructure of Nb–20Si silicide based alloys. *Intermetallics*, 19(10), pp.1612–1621.

Grylls et al., 2001. Characterization of silicide precipitates in Nb–Si and Nb–Ti–Si alloys. *Philosophical Magazine A*, 81(April 2015), pp.1967–1978.

Guillermet, 1996. Gibbs energy coupling of phase stability and thermochemistry in the Hf Nb system. *Journal of alloys and compounds*, pp.1–2.

Guo, Gao, Guan, et al., 2007. Microstructure and Mechanical Properties of an Advanced Niobium Based Ultrahigh Temperature Alloy. *Materials Science Forum*, 539-543, pp.3690–3695.

Guo, Gao & Guan, 2007. Microstructure and mechanical properties of an advanced niobium based ultrahigh temperature alloy. *Materials Science and Engineering A*, pp.2–7.

Guo & Guo, 2011a. Effect of high temperature treatments on microstructure of Nb-Ti-Cr-Si based ultrahigh temperature alloy. *Transactions of Nonferrous Metals Society of China*, 21(8), pp.1710–1716.

Guo & Guo, 2011b. Microstructure evolution and room temperature fracture toughness of an integrally directionally solidified Nb–Ti–Si based ultrahigh temperature alloy. *Scripta Materialia*, 64(7), pp.637–640.

Han & Wei, 2002. Microstructural characteristics of Ni-Sb eutectic alloys under substantial undercooling and containerless solidification conditions. *Metallurgical and Materials Transactions A*, 33(4), pp.1221–1228.

Hellawell & Herbert, 1962. The development of preferred orientations during the freezing of metals and alloys. In *Proc. R. Soc. Lond. A*. pp. 560 – 573.

Hillert, 1977. Solidification and Casting of Metals. *Proc. Intern. Conf. Univ. of Sheffield*, Institute , p.157.

Hillig & Turnbull, 1956. Theory of Crystal Growth in Undercooled Pure Liquids. *The Journal of Chemical Physics*, 24(4), p.914.

Huang et al., 2011. Microstructures and mechanical properties of directionally solidified multi-element Nb-Si alloy. *Progress in Natural Science: Materials International*, 21(2), pp.146–152.

Hunt, 1977. Solidification and Casting of Metals. In *Proc. Intern. Conf. Univ. of Sheffield*. p. 1.

Hunt & Jackson, 1966. Binary eutectic solidification. *Transactions Of The Metallurgical Society Of Aime*, 236(6), pp.843–852.

Hurle, D.T.J., 1969. Interface stability during the solidification of a stirred binary-alloy melt. *Journal of Crystal Growth*, 5(3), pp.162–166.

Jackson, 1958. *Growth and Perfection of Crystals* 1st ed. Doremus, ed., New York: Wiley.

Jing et al., 2008. Liquid-Solid Phase Equilibria of Nb-Si-Ti Ternary Alloys. *Chinese Journal of Aeronautics*, 21(3), pp.275–280.

Jurisch & Loser, 1990. Analysis of periodic non-rotational W striations in Mo single crystals due to nonsteady thermocapillary convection. *Journal of Crystal Growth*, 102(1-2), pp.214–222.

Jurisch, M., 1990. Surface temperature oscillations of a floating zone resulting from oscillatory thermocapillary convection. *Journal of Crystal Growth*, 102(1-2), pp.223–232.

Kashyap, Tiwary & Chattopadhyay, 2013a. Microstructural and mechanical behavior study of suction cast Nb–Si binary alloys. *Materials Science and Engineering: A*, 583, pp.188–198.

Kashyap, Tiwary & Chattopadhyay, 2013b. Microstructure and mechanical properties of oxidation resistant suction cast Nb–Si–Al alloy. *Materials Science and Engineering: A*, 559, pp.74–85.

Kerr, Cisse & Bolling, 1974. On equilibrium and non-equilibrium peritectic transformations. *Acta Metallurgica*, 22(6), pp.677–686.

Kerr & Winegard, 1967. Eutectic Solidification. *Crystal Growth*, Oxford(ed. Peiser), p.179.

Kim et al., 2001. Microstructure and room temperature fracture toughness of Nbss/Nb5Si3 in situ composites. *Intermetallics*, 9, pp.827–834.

Kim, Tanaka & Hanada, 2002a. Effect of W alloying and NbC dispersion on high temperature strength at 1773 K and room temperature fracture toughness in Nb5Si3/Nb in-situ composites. *Materials Transactions*, 43(6), pp.1415 – 1418.

Kim, Tanaka & Hanada, 2002b. Microstructure and high temperature strength at 1773 K of Nb ss/Nb 5 Si 3 composites alloyed with molybdenum. *Intermetallics*, 10, pp.625–634.

Kobayashi, N. & Wilcox, W.R., 1982. Computational Studies of Convection Due To Rotation in a. *Journal of Crystal Growth*, 59, pp.616–624.

Koohpayeh, 2007. *Crystal growth of functional oxides using an image furnace*. University of Birmingham.

Kotler & Tiller, 1966. The Instability of a Cylindrical Crystal During Growth from an Alloy Melt. *Proc. Intern. Conf. Crystal Growth*, Boston(H S Peiser ed.), p.721.

Kuo & Wilcox, 1972. Influence of crystal dimensions on the interfacial temperature gradient. *Journal of Crystal Growth*, 12(3), pp.191–194.

Kurz & Fisher, 1979. Dendrite growth in eutectic alloys: the coupled zone. *International Materials Reviews*, 24(1), pp.177–204.

Kurz & Fisher, 1968. *Fundamentals of Solidification* 4th ed., CRC PRess.

Lan, C.W. & Kou, S., 1992. Shortened floating zone crystal growth under normal gravity. , 119.

Lan, C.W. & Tsai, C.H., 1997. Modeling of ellipsoid mirror furnace for floating-zone crystal growth. *Journal of Crystal Growth*, 173(3-4), pp.561–573.

Lan & Kou, 1991a. Effects of rotation on heat transfer, fluid flow and interfaces in normal gravity floating-zone crystal growth. *Journal of Crystal Growth*, 114(4), pp.517–535.

Lan & Kou, 1991b. Heat transfer, fluid flow and interface shapes in floating-zone crystal growth. *Journal of Crystal Growth*, 108(1-2), pp.351–366.

Lan & Kou, 1993. Radial dopant segregation in zero-gravity floating-zone crystal growth. *Journal of Crystal Growth*, 132(3-4), pp.578–591.

Li et al., 2013. As-cast microstructures and solidification paths of the Nb-Si-Ti ternary alloys in Nb5Si3-Ti5Si3 region. *Rare Metals*, 32(5), pp.502–511.

Li et al., 2006. Effect of Mo addition on the phase stability of β-Nb5Si3 phase. *Intermetallics*, 14(4), pp.392–395.

Li et al., 2007. Halo formation in directional solidification of Ni-Ni3Nb hypereutectic alloy. *Journal of Crystal Growth*, 299(1), pp.178–183.

Li, Ma, et al., 2011. Mechanical properties of directionally solidified Nb–Mo–Si-based alloys with aligned Nbss/Nb5Si3 lamellar structure. *Materials Science and Engineering: A*, 528(18), pp.5772–5777.

Li et al., 2010. The effects of melting technologies on the microstructures and properties of Nb–16Si–22Ti–2Al–2Hf–17Cr alloy. *Materials Science and Engineering: A*, 527(23), pp.6140–6152.

Li, Miura, et al., 2011. Ultrahigh-temperature Nbss/Nb5Si3 fully-lamellar microstructure developed by directional solidification in OFZ furnace. *Intermetallics*, 19(4), pp.460–469.

Li & Kuribayashi, 2006. Free Solidification of Undercooled Eutectics. *Materials Transactions*, 47(12), pp.2889–2897.

Li & Kuribayashi, 2003a. Further discussion on the free growth behavior in the solidification of undercooled eutectic melts. *Metallurgical and Materials Transactions A*, 34(June), pp.1393–1396.

Li & Kuribayashi, 2003b. Nucleation-controlled microstructures and anomalous eutectic formation in undercooled Co-Sn and Ni-Si eutectic melts. *Metallurgical and Materials Transactions A*, 34(December), pp.2999–3008.

Li, M. et al., 2005. Microtexture and macrotexture formation in the containerless solidification of undercooled Ni-18.7 at.% Sn eutectic melts. *Acta Materialia*, 53(3), pp.731–741.

Li, Nagashio & Kuribayashi, 2002. Reexamination of the solidification behavior of undercooled Ni–Sn eutectic melts. *Acta materialia*, 50, pp.3239–3250.

Li & Peng, 2007. Microstructural and mechanical characterization of Nb-based in situ composites from Nb–Si–Ti ternary system. *Acta Materialia*, 55(19), pp.6573–6585.

Li & Tsakiropoulos, 2013. The microstructures of Nb–18Si–5Ge–5Al and Nb–24Ti–18Si–5Ge–5Al in situ composites. *Journal of Alloys and Compounds*, 550, pp.553–560.

Liang & Chang, 1999. Thermodynamic modeling of the Nb–Si–Ti ternary system. *Intermetallics*, 7(June 1998).

Louchev et al., 2004. Thermally induced effects during initial stage of crystal growth from melts. *Journal of Crystal Growth*, 273(1-2), pp.320–328.

Ma et al., 2012. Interactions between Nb-silicide based alloy and yttria mould during directional solidification. *International Journal of Refractory Metals and Hard Materials*, 30(1), pp.96–101.

Ma et al., 2004. Microstructure and mechanical properties of Nb/Nb5Si3 in situ composites in Nb–Mo–Si and Nb–W–Si systems. *Materials Science and Engineering: A*, 386(1-2), pp.375–383.

Ma et al., 2000. Phase equilibria in Nb-Mo-rich zone of the Nb-Si-Mo ternary system. *Materials Transactions, JIM*, 41(10), pp.1329 – 1336.

Ma et al., 2002. Phase Equilibria in Nb-W-rich Zone of the Nb-W-Si Ternary System. *Materials Transactions*, 43(4), pp.688–693.

Masumoto et al., 1980. Superconductivity of Ductile Nb-Based Amorphous Alloys. *Trans. Jpn. Inst*

Met., 21, pp.115–122.

Mendiratta & Dimiduk, 1991. Phase relations and transformation kinetics in the high Nb region of the Nb-Si system. *Scripta Metallurgica;(United States)*, 25.

Meng et al., 2010. Thermodynamic modeling of the Mg-Sn-Zn ternary system. *Journal of Alloys and Compounds*, 508(2), pp.570–581.

Miura et al., 2009. Effect of microstructure on the high-temperature deformation behavior of Nb–Si alloys. *Materials Science and Engineering: A*, 510-511, pp.317–321.

Miura, Murasato, et al., 2007. Microstructure Control of Nb-Si Alloy Doped with Zr and Mg through Eutectic and Eutectoid Reactions and its Deformation Behavior. *Mat. Res. Soc. Symp. Proc.*, 980, pp.33–38.

Miura, Ohkubo & Mohri, 2007. Microstructural control of Nb–Si alloy for large Nb grain formation through eutectic and eutectoid reactions. *Intermetallics*, 15(5-6), pp.783–790.

Miura, S. et al., 2005. Effects of Zr on the eutectoid decomposition behavior of Nb3Si into (Nb)/Nb5Si3. *Metallurgical and Materials Transactions A*, 36(March), pp.489–496.

Mullins & Sekerka, 1963. Morphological Stability of a Particle Growing by Diffusion or Heat Flow. *Journal of Applied Physics*, 34(2), pp.323–329.

Mullis, Clopet & Cochrane, 2014. Determination of the Origin of Anomalous Eutectic Structures from In-situ Observation of Recalescence Behaviour. *Material Science Forum*, pp.349–354.

Naidu, 1990. Nb-W (Niobium-Tungsten). *Binary Alloy Phase Diagrams, Second Edition/ed. TB …*, pp.2–3.

Okamoto, 2005. Nb-Si (niobium-silicon). *Journal of Phase Equilibria and Diffusion*, 26, pp.9–11.

Okamoto, 2002. Nb-Ti (niobium-titanium). *Journal of phase equilibria*, pp.1–2.

Papadimitriou, Utton & Tsakiropoulos, 2015a. Ab initio investigation of the intermetallics in the Nb-Sn binary system. *Acta Materialia*, 86, pp.23–33.

Papadimitriou, Utton & Tsakiropoulos, 2015b. Unpublished Research. *University of Sheffield*.

Quenisset & Naslain, 1981. Effect of forced convection on eutectic growth. *Journal of Crystal Growth*, 54(3), pp.465–474.

Quenisset, Sokolowski & Glicksman, 1983. Effects of forced convection flow on directional solidification of Pb-Sn and Cd-Zn eutectic alloys. *Journal of Crystal Growth*, 63(2), pp.389–399.

Racek, Lesoult & Turpin, 1974. The Cd-Sn eutectic structures at low growth rates. *Journal of Crystal Growth*, 22(3), pp.210–218.

Robinson et al., 1989. UNDERCOOLING STUDIES ON Nb — Pt and Nb-Si ALLOYS USING THE 105 METER DROP TUBE. , 8(12), pp.321–330.

Sainan et al., 2013. The microstructure evolution of directionally solidified Nb-22Ti-14Si-4Cr-2Al-2Hf alloy during heat treatment. *Intermetallics*, 38, pp.102–106.

Sakata et al., 2015. FT-IR emissivity measurements of Nb melt using an electrostatic levitation furnace. *Journal of Chemical Thermodynamics*, 91, pp.116–120.

Schaefer & Coriell, 1984. Convection-induced distortion of a solid-liquid interface. *Metallurgical and Materials Transactions A*, 15(12), pp.2109–2115.

Schlesinger et al., 1993. The Nb-Si (Niobium-Silicon) system. *Journal of Phase Equilibria*, 14(4), pp.502–509.

Schwabe et al., 1978. Experiments on Surface-Tension Driven Flow in Floating Zone-Melting. *Journal of Crystal Growth*, 43(3), pp.305–312.

Sekido, Kimura, et al., 2006. Fracture toughness and high temperature strength of unidirectionally solidified Nb–Si binary and Nb–Ti–Si ternary alloys. *Journal of Alloys and Compounds*, 425(1-2), pp.223–229.

Sekido et al., 2007. Microstructure development of unidirectionally solidified (Nb)/Nb3Si eutectic alloys. *Materials Science and Engineering: A*, 444(1-2), pp.51–57.

Sekido, Wei, et al., 2006. Orientation relationship between Nb and Nb 5 Si 3 (D8 l) phases in the eutectoid lamellar microstructure. *Philosophical Magazine Letters*, 86(2), pp.89–98.

Sekido et al., 2004. Solidification Process and Mechanical Behavior of the Nb/Nb5Si3 Two Phase Alloys in the Nb-Ti-Si System. *Materials Transactions*, 45(12), pp.3264–3271.

Sekido et al., 2013. Stability of the Nb5Si3 phase in the Nb–Mo–Si system. *Intermetallics*, 41, pp.104–112.

Sha, Hirai, Tabaru, et al., 2003. Effect of carbon on microstructure and high-temperature strength of Nbî—¸ Moî—¸ Tiî—¸ Si in situ composites prepared by arc-melting and directional solidification. *Materials Science and Engineering A*, 343, pp.282–289.

Sha et al., 2000. Effect of W Addition on Compressive Strength of Nb-10Mo-10Ti-18Si-Base In-Situ Composites. *Materials Transactions, JIM*.

Sha, Hirai, Ueno, et al., 2003a. Mechanical properties of as-cast and directionally solidified Nb-Mo-W-Ti-Si in-situ composites at high temperatures. *Metallurgical and Materials Transactions A*, 34(1), pp.85–94.

Sha, Hirai, Ueno, et al., 2003b. Toughness and strength characteristics of Nb-W-Si ternary alloys prepared by arc melting. *Metallurgical and Materials Transactions A*, 34(December).

Shah et al., 1992. Appraisal of other silicides as structural materials. *Materials Science and Engineering: A*, 155, pp.45–57.

Sheffield, T.U. of, 2016. List of Equipment and Facilities in the Sorby Centre. *Sheffield, The University of*. Available at: https://www.sheffield.ac.uk/materials/centresandfacilities/sorby/equipment.

Steen & Hellawell, 1975. The growth of eutectic silicon-contributions to undercooling. *Acta Metallurgica*, 23(4), pp.529–535.

Su et al., 2013. Microstructure and room-temperature fracture toughness of directionally solidified Nb–Si–Ti–Cr–Al–Hf alloy. *Materials Science and Engineering: A*, 560, pp.672–677.

Subramanian et al., 1997. Advanced intermetallic alloys—beyond gamma titanium aluminides. *Materials Science and Engineering: A*, 239-240, pp.1–13.

Subramanian, Mendiratta & Dimiduk, 1996. The development of Nb-based advanced intermetallic alloys for structural applications. *Jom*, 48(1), pp.33–38.

Surek, 1976. Theory of shape stability in crystal growth from the melt. *Journal of Applied Physics*, 47(10), p.4384.

Surek & Coriell, 1977. Shape stability in float zoning of silicon crystals. *Journal of Crystal Growth*, 37(3), pp.253–271.

Tarshis & Tiller, 1966. The Importance of Attachment Kinetics on the Stability of a Planar Solid-Liquid Interface. *Proc. Intern. Conf. Crystal Growth*, Boston(H. S. Peiser, ed.), p.709.

Taylor, Fidler & Smith, 1968. Broken lamellar eutectic growth; Structure of the silver-bismuth eutectic.

Journal of Crystal Growth, 3, pp.666–673.

Temkin, 1964. Crystallisation Processes. *English translation published by Consultants Bureau*, New York,(ed. Sirota & Gorskii).

Tewari & Chopra, 1992. Break-down of a planar liquid-solid interface during directional solidification; influence of convection. *Journal of Crystal Growth*, 118(1-2), pp.183–192.

Tian et al., 2009. Effect of growth rate on microstructure and mechanical properties in a directionally solidified Nb-silicide base alloy. *Materials & Design*, 30(6), pp.2274–2277.

Tian et al., 2008. Microstructure and room temperature fracture toughness of cast Nbss/silicides composites alloyed with Hf. *Materials Letters*, 62(17-18), pp.2657–2660.

Tiwary, Kashyap & Chattopadhyay, 2013. Effect of Mg addition on microstructural, mechanical and environmental properties of Nb–Si eutectic composite. *Materials Science and Engineering: A*, 560, pp.200–207.

Trivedi & Kurz, 1994. Solidification microstructures: A conceptual approach. *Acta Metallurgica et Materialia*, 42(1), pp.15–23.

Tsakiropoulos, 2009. Advanced Metallic Systems Lecture Notes. *University of Sheffield*.

Tsakiropoulos, 2008. Private Communications.

Utton & Tsakiropoulos, 2015. Unpublished Research. *University of Sheffield*.

Vandyoussefi, Kerr & Kurz, 2000. Two-phase growth in peritectic Fe–Ni alloys. *Acta Materialia*, 48(9), pp.2297–2306.

Wagner & Brown, 1962. Growth of Bismuth Crystals from the Melt by A Twin Plane Mechanism. *Trans. Met. Soc. of AIME*, 224, pp.1185–1188.

Wang et al., 2013. Microstructure optimization of directionally solidified hypereutectic Nb–Si alloy. *Transactions of Nonferrous Metals Society of China*, 23(10), pp.2874–2881.

Wang et al., 2006. Undercooling and rapid solidification of Nb-Si eutectic alloys studied by long drop tube. *Transactions of the Nonferrous Metals Society of China*, 16, pp.89 – 92.

Wang & Sundman, 2000. Thermodynamic Assessment of the. *Calphad*, 21(December), pp.6–18.

Wilson, 1900. On the velocity of solidification and viscosity of supercooled liquids. *Phil. Mag*, 50(303), pp.238–250.

Wu, M., Li, S. & Han, Y., 2012. Effect of rotation mode on microstructure and mechanical properties of directionally solidified Nb-Silicon based alloys. *Procedia Engineering*, 27(2011), pp.1179–1186.

Xiong et al., 2009. Effects of Si, W and W–Mo on isothermal oxidation behaviors of Nb/Nb5Si3 in situ composites at high temperature. *Journal of Alloys and Compounds*, 486(1-2), pp.330–334.

Xiong, Cai & Wang, 2014. Microstructures of Nb/Nb5Si3 composites and it alloyed with W, Mo and W–Mo fabricated by spark plasma sintering. *Journal of Alloys and Compounds*, 583, pp.574–577.

Xu et al., 2014. Temperature-dependent mechanical properties of alpha-/beta-Nb5Si3 phases from first-principles calculations. *Intermetallics*, 46, pp.72–79.

Yang et al., 2011. New evidence for the dual origin of anomalous eutectic structures in undercooled Ni-Sn alloys: In situ observations and EBSD characterization. *Acta Materialia*, 59(10), pp.3915–3926.

Yang et al., 2003. Thermodynamic modeling of the Nb–Hf–Si ternary system. *Intermetallics*, 11(5), pp.407–415.

Yang, Bewlay & Chang, 2007. Liquid-Solid Phase Equilibria in Metal-Rich Nb-Ti-Hf-Si Alloys. *Journal of Phase Equilibria and Diffusion*, 28(1), pp.107–114.

Young & Chait, 1990. Surface tension driven heat, mass, and momentum transport in a two-dimensional float-zone. *Journal of Crystal Growth*, 106(2-3), pp.445–466.

Yuan et al., 2012. The microstructure optimizing of the Nb–14Si–22Ti–4Cr–2Al–2Hf alloy processed by directional solidification. *Materials Letters*, 84, pp.124–127.

Zelenitsas & Tsakiropoulos, 2006a. Effect of Al, Cr and Ta additions on the oxidation behaviour of Nb–Ti–Si in situ composites at 800°C. *Materials Science and Engineering: A*, 416(1-2), pp.269–280.

Zelenitsas & Tsakiropoulos, 2005. Study of the role of Al and Cr additions in the microstructure of Nb–Ti–Si in situ composites. *Intermetallics*, 13(10), pp.1079–1095.

Zelenitsas & Tsakiropoulos, 2006b. Study of the role of Ta and Cr additions in the microstructure of Nb-Ti-Si-Al in situ composites. *Intermetallics*, 14(6), pp.639–659.

Zhao et al., 2000. Hf-Si binary phase diagram determination and thermodynamic modeling. *Journal of Phase Equilibria*, 21(1), pp.40–45.

Zhao, Bewlay & Jackson, 2001. Determination of Nb–Hf–Si phase equilibria. *Intermetallics*, 9(8), pp.681–689.

Zhao, Jackson & Peluso, 2004. Mapping of the Nb–Ti–Si phase diagram using diffusion multiples. *Materials Science and Engineering: A*, 372(1-2), pp.21–27.

Zheng et al., 2008. Effect of Hf on high-temperature strength and room-temperature ductility of Nb–15W–0.5Si–2B alloy. *Materials Science and Engineering: A*, 483-484, pp.656–659.

APPENDIX

A. EXAMPLES OF OBSERVED MICROSTRUCTURES

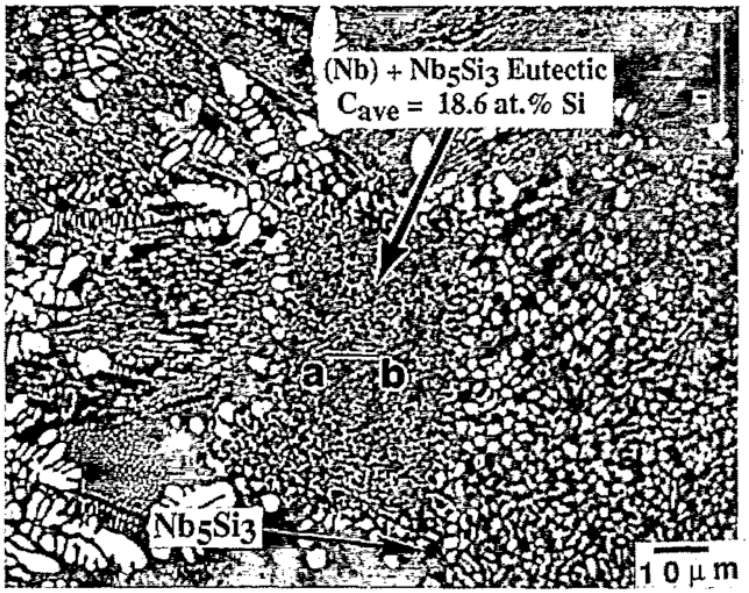

Figure 1: Showing an anomoluos eutectic between Nb and Si in a highly undercooled melt (Abbaschian & Lipschutz 1997)*, permission conveyed through Copyright Clearance Center, Inc.*

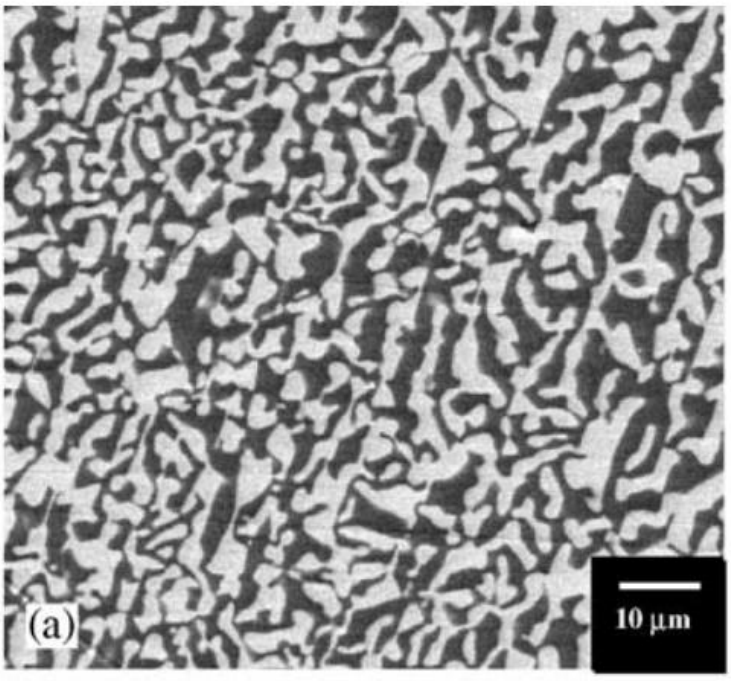

Figure 2: Showing the "Chinese script" or maze eutectic between Al_2O_3/$GdAlO_3$ (Andreeta et al. 2002)*. The major difference between this eutectic and the anomalous eutectic in Figure 1 is the continuous nature of both phases compared to the anomolous which has both a discontinuous and continuous phase, permission conveyed through Copyright Clearance Center, Inc.*

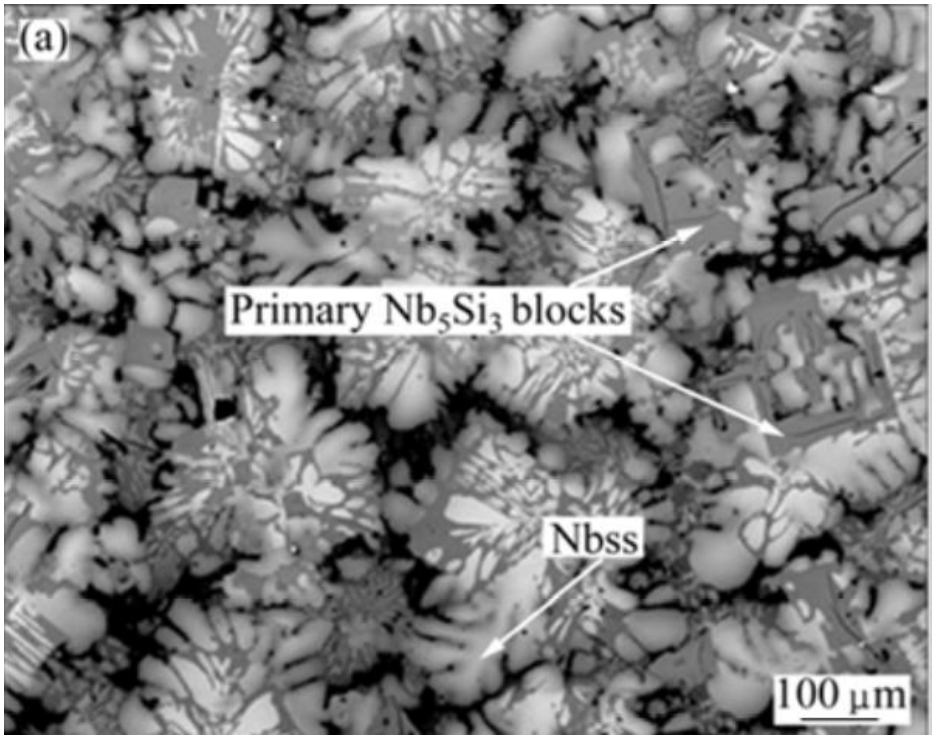

Figure 6: Showing back scattered electron images of petaloid eutectic microstructure on transversal-sections of steady-state zones of directionally solidified Nb−16Si−24Ti−10Cr−2Al−2Hf alloy with a withdrawal rate of 1.2 mm/min (Wang et al. 2013), permission conveyed through Copyright Clearance Center, Inc

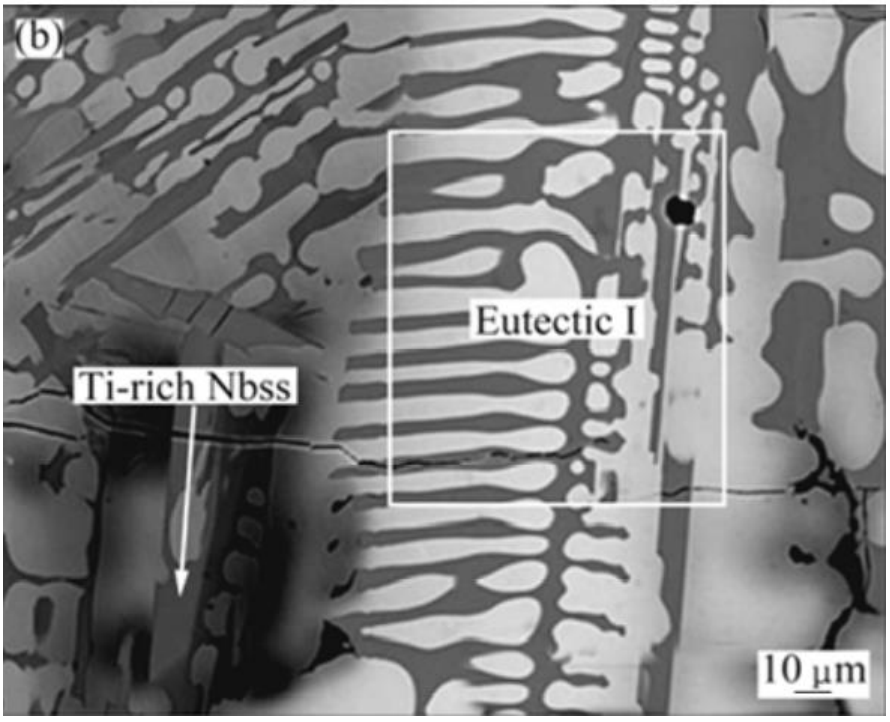

Figure 4: Showing back scattered electron images of a irregular lamellar eutectic microstructure on longitudinal-section of steady-state zones of directionally solidified Nb−16Si−24Ti−10Cr−2Al−2Hf alloy with a withdrawal rate of 1.2 mm/min (Wang et al. 2013)*, permission conveyed through Copyright Clearance Center, Inc.*

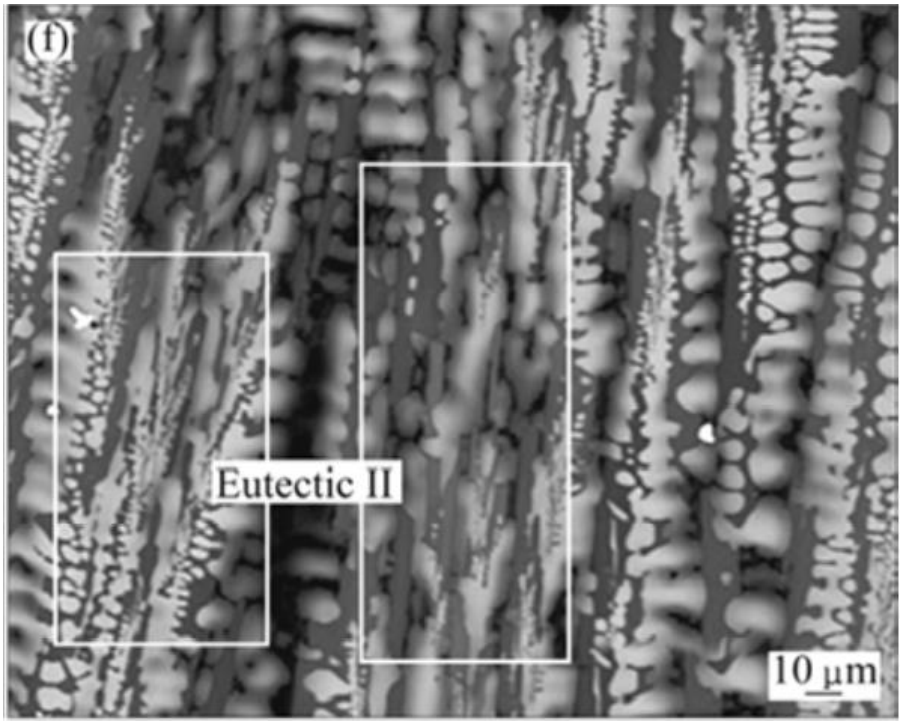

Figure 5: Showing back scattered electron images of a complex regular eutectic microstructure on longitudinal-section of steady-state zones of directionally solidified Nb–16Si–24Ti–10Cr–2Al–2Hf alloy with a withdrawal rate of 18 mm/min (Wang et al. 2013)*, permission conveyed through Copyright Clearance Center, Inc.*

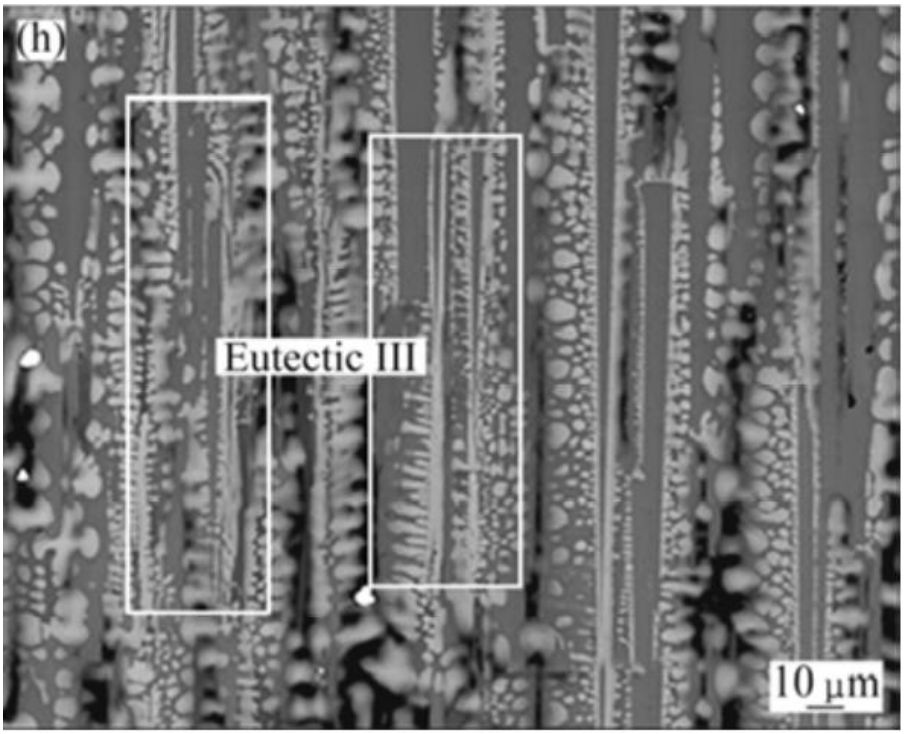

Figure 6: Showing back scattered electron images of a quasi-regular eutectic microstructure on longitudinal-section of steady-state zones of directionally solidified Nb–16Si–24Ti–10Cr–2Al–2Hf alloy with a withdrawal rate of 36 mm/min (Wang et al. 2013)*, permission conveyed through Copyright Clearance Center, Inc.*

B. X-RAY DIFFRACTOGRAMS

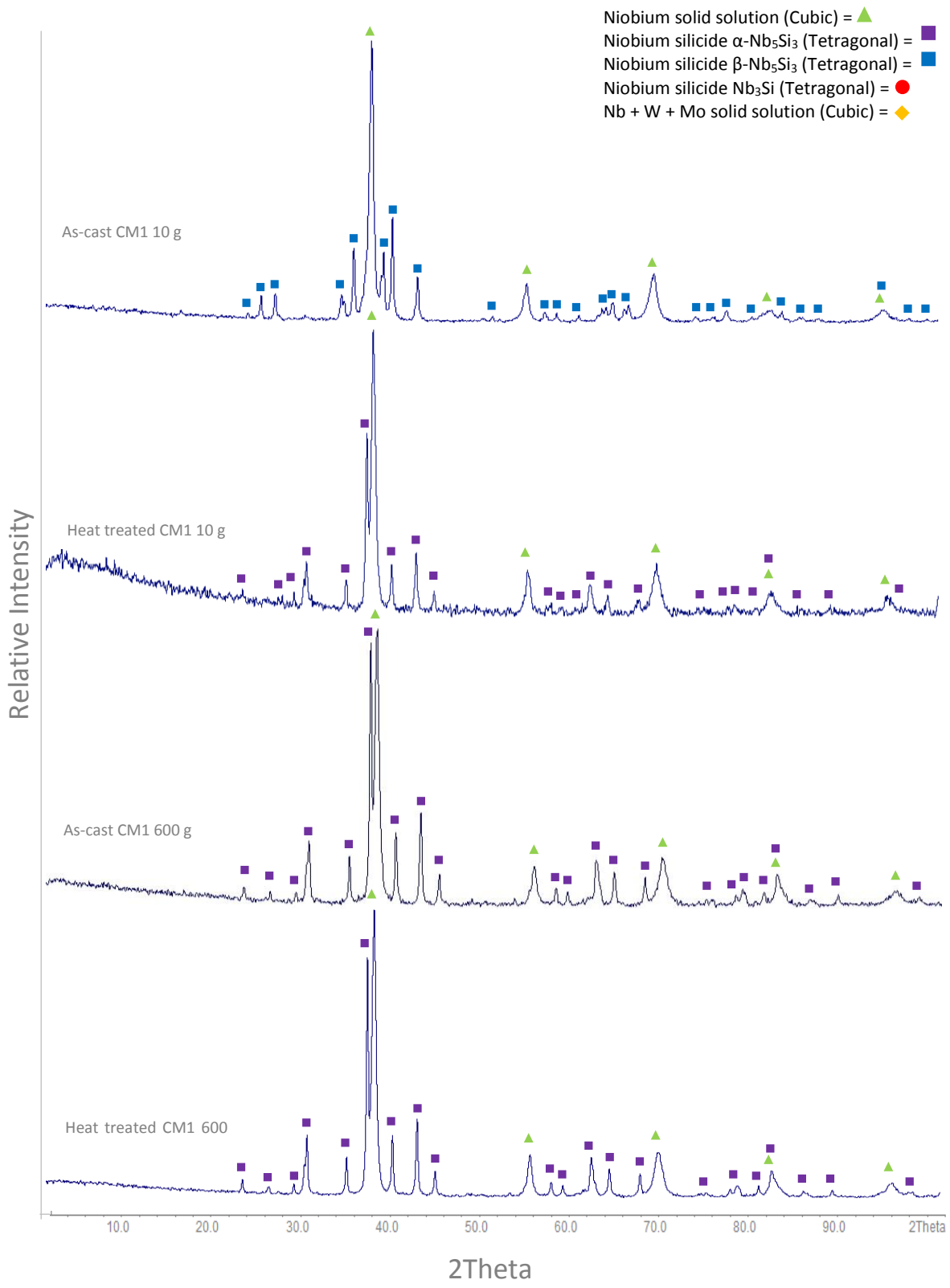

Figure 1: Showing x-ray diffractograms of as-cast and heat treated CM1 10 g and 600 g.

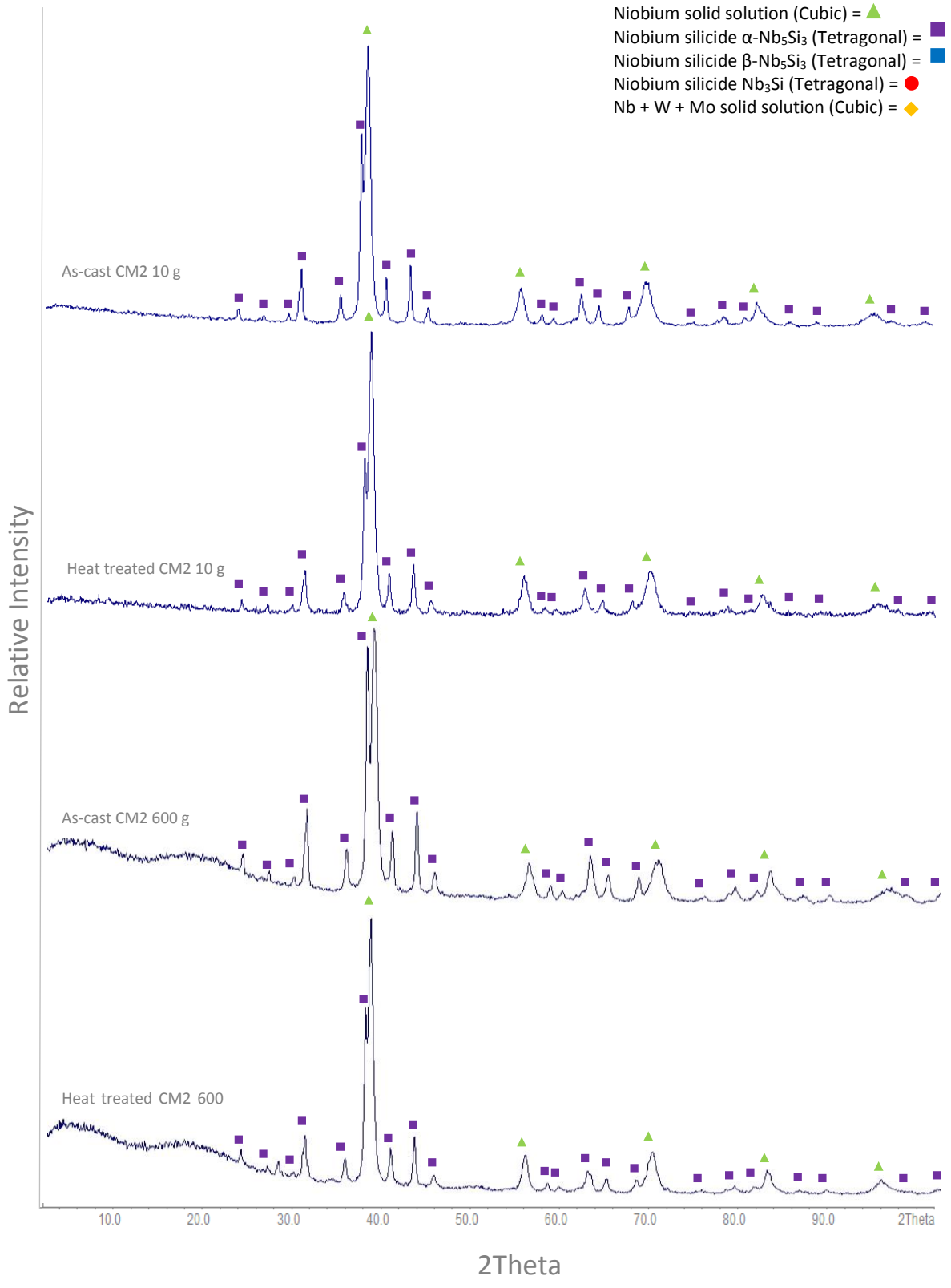

Figure 2: Showing x-ray diffractograms of as-cast and heat treated CM2 10 g and 500 g.

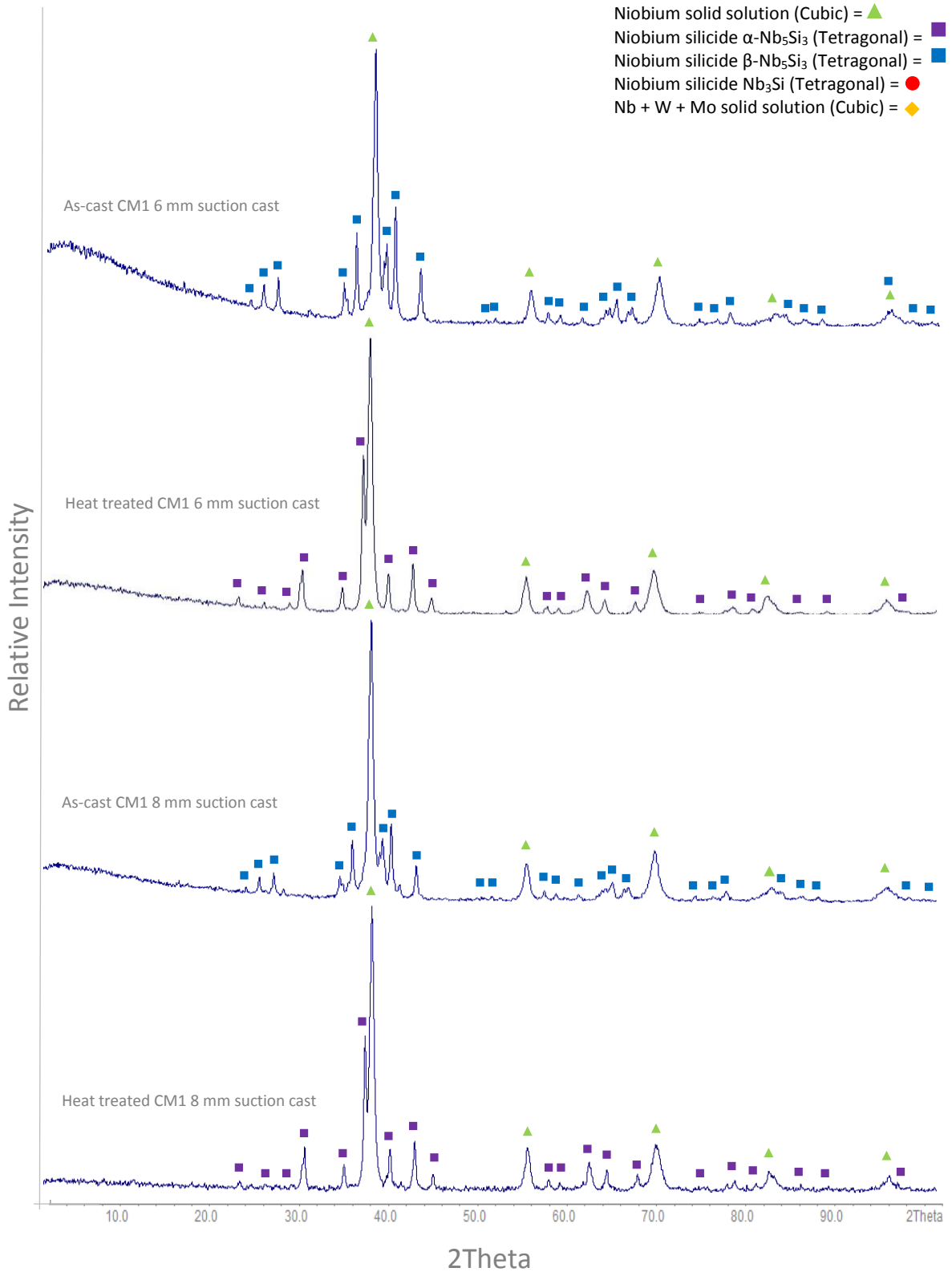

Figure 3: Showing x-ray diffractograms of as-cast and heat treated CM1 suction cast 6 mm and 8 mm.

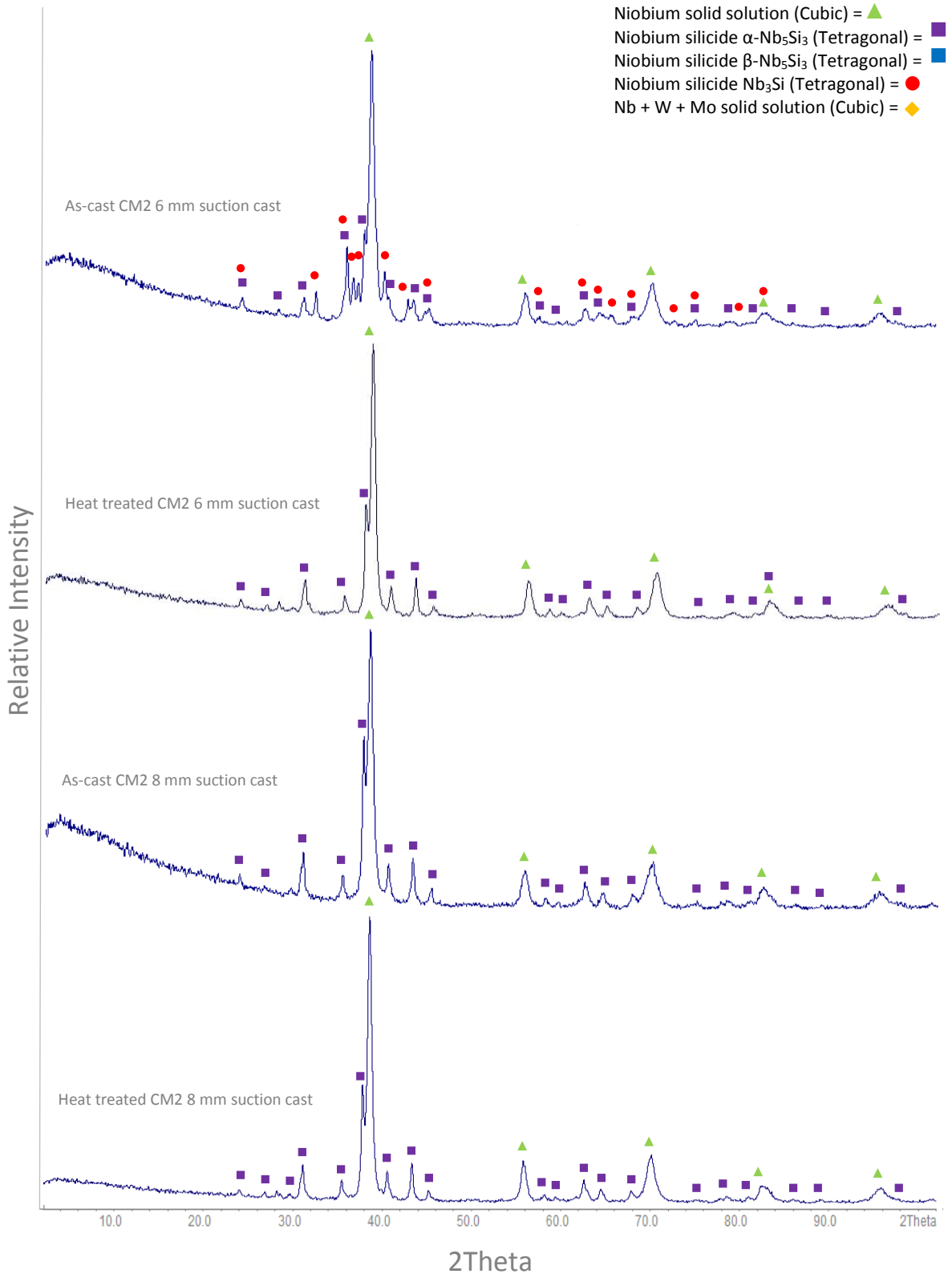

Figure 4: Showing x-ray diffractograms of as-cast and heat treated CM2 suction cast 6 mm and 8 mm.

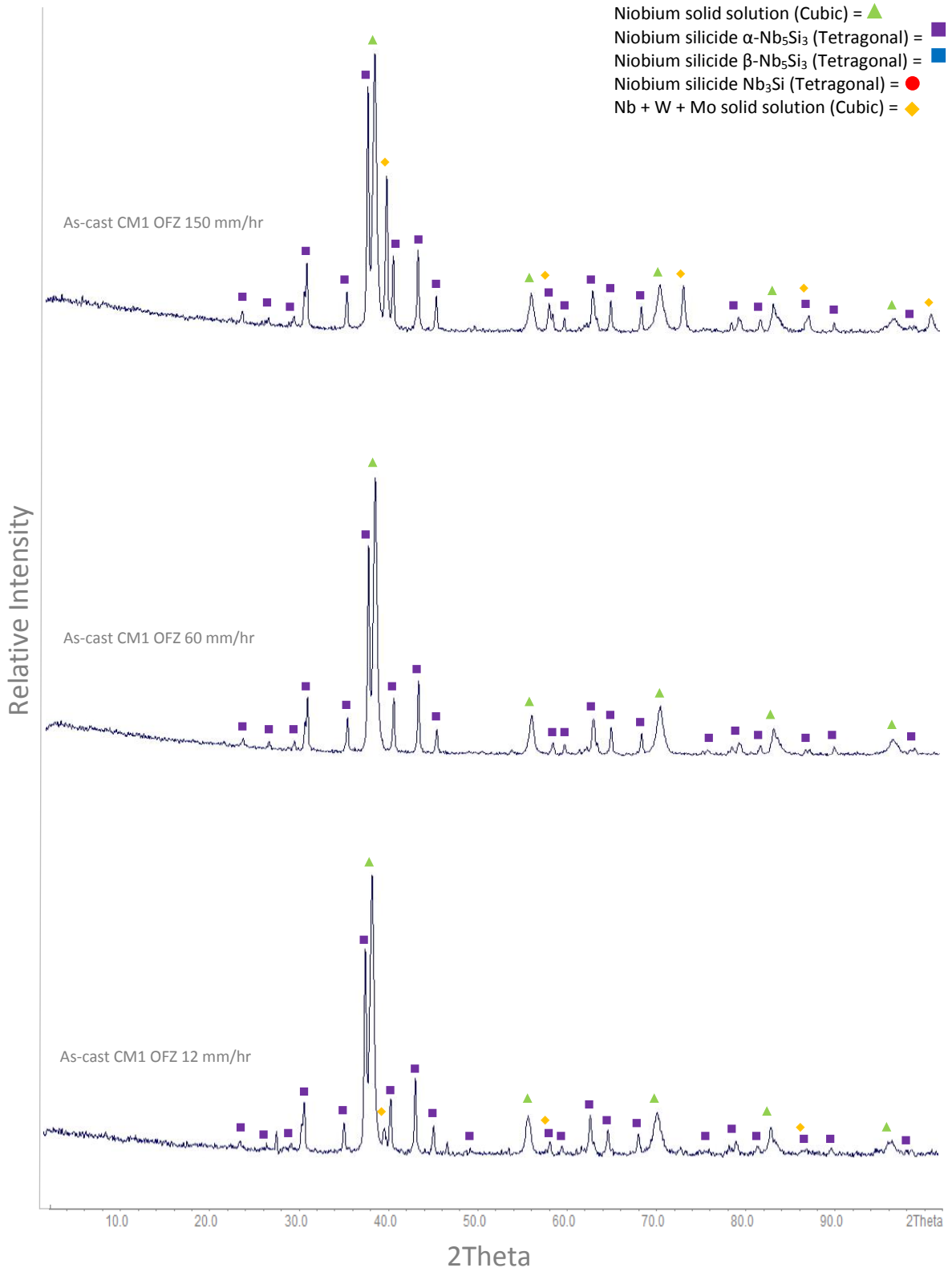

Figure 5: Showing x-ray diffractograms of as-cast CM1 solidified in an optical float zone furnace at 150, 60 and 12 mm/hr.

Figure 6: Showing x-ray diffractograms of as-cast CM2 solidified in an optical float zone furnace at 150, 60 and 12 mm/hr.

Figure 7: Showing x-ray diffractograms of heat treated CM1 solidified in an optical float zone furnace at 150, 60 and 12 mm/hr.

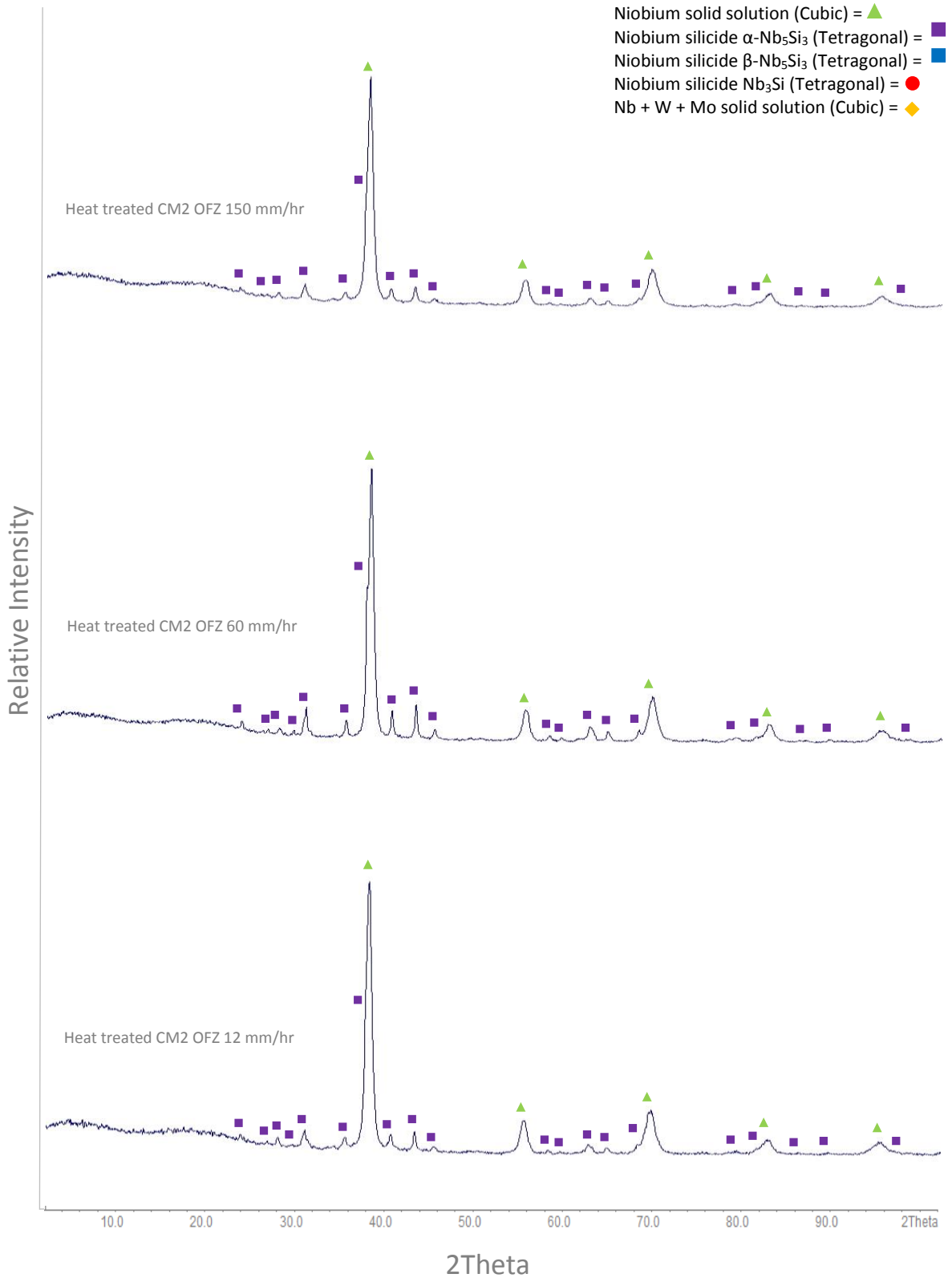

Figure 8: Showing x-ray diffractograms of heat treated CM2 solidified in an optical float zone furnace at 150, 60 and 12 mm/hr.